Towards Responsive Squaramides:

Anion Recognition, Sensing, and Transport

Maynooth University
National University of Ireland Maynooth

A thesis submitted to Maynooth University in fulfilment of the requirements for the degree of

Doctor of Philosophy

By

Luke Marchetti, B.Sc.

Department of Chemistry,

Maynooth University,

Maynooth,

Co. Kildare, Ireland.

February 2022

Research Supervisor: Dr. Robert Elmes

Head of Department: Prof. Denise Rooney

Table of Contents

Acknowledgements ……i

Abstract ……iv

Abbreviations ……..vi

1 Introduction ……2

1.1 Anions in a Biological Context ……3

1.1.1 Physiological Role of Anions ……3

1.1.2 Anion Binding in Cells ……8

1.1.3 Transmembrane Transport of Anions ……11

1.2 Anion Binding and Recognition ……19

1.2.1 Anion Binding Motifs ……19

1.2.2 Considerations and Challenges in Anion Receptor Design ……25

1.2.3 Anion Binding Units ……28

1.3 Anion Transport ……40

1.3.1 What Makes a Good Anionophore? ……40

1.3.2 Squaramides as Anion Transport Units ……42

1.3.3 Applications of Anion Transport ……43

1.4 Aims ……46

2 Amido-squaramides: A New Moiety in Anion Recognition and Transport ……48

2.1 Introduction ……48

2.2 Chapter Objective ……52

2.3 Synthesis and Characterisation of Amido-Squaramides ……53

2.4 pK_a Determination ……57

2.5 Geometry Optimisation ……60

2.6 Anion Binding Studies ……62

2.7 Anion Transport Assays ……68

2.8 Conclusion ……72

3 Towards Stimuli-Responsive Anion Transport ……75

3.1 Introduction…….. 75

3.2 Chapter Objectives ……81

3.3 Synthesis and Characterisation of Tertiary Squaramides ……83

3.4 Preliminary Analysis.……86

3.5 Synthesis Optimisation of Tertiary Squaramides.……..88

3.6 Synthesis and Characterisation of Tertiary Ureas.……..*94*

3.7 Conclusion……97

4 Squaramidoquinoxalines as Anion Sensors 102

4.1 Introduction 102

4.2 Chapter Objectives 107

4.3 Synthesis and Characterisation of Squaramidoquinoxalines 108

4.4 UV-Vis Absorption Properties……..109

4.5 UV-Vis Anion Titrations……112

4.6 ^{1}H NMR Titrations……..115

4.7 Applications of Squaramidoquinoxalines……116

4.8 Conclusions……117

5 Thesis Summary 121

5.1 Thesis Summary 122

5.2 Publications…… 125

6 Experimental Procedures 129

6.1 General Procedures and Instrumentation 129

6.2 Synthetic Procedures for Chapter 2 130

6.3 Synthetic Procedures for Chapter 3……138

6.4 Synthetic Procedures for Chapter 4……..144

6.5 Anion Binding Studies……146

6.6 UV-Vis pH spectrophotometric titrations……...146

6.7 Cl^-/NO_3^- exchange assays……..146

6.8 Computational Methods……..147

Bibliography……..150

Appendix……164

Acknowledgments

There is a long list of people that I would be remiss to not acknowledge for their support throughout the past four years. These people were there for me every step of the way, and I would have had a lesser experience if it were not for them.

First and foremost, I would like to thank my supervisor, Dr. Robert Elmes. I could not have made it this far without your patience, guidance, and mentorship. Thank you for your unwavering faith in me and my abilities, and for giving me every opportunity possible throughout the past four years. It was fantastic to work with you, and hopefully it will not be the last.

I'd like to thank the technical staff of the chemistry department for their continued, unwavering support of my research - Ria, Barbara, Karen, Ollie, Ann, Orla, Carmel, Noel, and Walter. Whether it was support in demonstrating, sorting out ordering chemicals, supplying chemicals for me to 'borrow', or even advice, I am very grateful. Thank you to all the academic staff of the chemistry department, who always provided advice or lend a hand when asked, I have and will always appreciate it. I'd like to thank Dr Trinidad Velasco Torrijos for taking a chance on me as a second-year undergrad and allowing me to conduct research as part of your group for a summer. In doing so, through your patience and guidance, you sparked a love of research and all things organic chemistry and is one of the reasons I chose to pursue a PhD.

To the admin staff, Donna and Carol, thank you for chasing me down to make sure I submitted timesheets on time, and sorting out any problems that arose over the past four years without hesitation. More importantly, thank you for the laughter that made my sides hurt on several occasions and for listening to me give out when needed. Without you, the chemistry department would be a much quieter, less vibrant place.

To the Old Guard who showed me the ropes and made me feel extremely welcome when I joined the department as a postgraduate – Ross, Jack, Justine, Caroline, Muhib, Mark Grace, Michelle Kickham, Matt, and Aoife, thank you for your friendship and for making the tea room a nice escape from the lab. In particular, I want to thank Drs Jessica Ramos and Andrew Reddy, and also Michelle Kickham, for acting as mentors early in my research career. Your teachings provided the foundation for the researcher I am today.

Thank you, also, to those who I started alongside but have since moved on - Grace, My, Alessandro, and Paddy. Thank you to Jason for your friendship (and abuse) early in the mornings (and sometimes last mornings) and thank you to Michelle Doran for always sticking up for me in the face of your bullying. Best of luck to the new postgrads, even if some of you aren't 'new' anymore – Caytlin, Eoin, Kyle, Darren, Sinead, Clara, Keela, and Adam. Thank you for all the laughs and friendship.

To the Elmes Group – Conor W, thank you for the supply of diet coke and chocolate and all the nights gaming, Conor G, thank you for keeping me young and up to date with all the new lingo. Thank you also to Hua, Luke B, and new additions Stephen Healy, Farhad and Xuanyang. Thanks to all the Elmes group for all for the laughs and for putting up with me in grumpy moods. Best of luck with the rest of your research, you will smash it.

There are two incredible women who I am honoured to call friends. Drs Harlei Martin and Amanda Doyle. Harlei, thank you for the never-ending supply of gossip, chocolate, and for listening to me rant and rave. Thank you for all the advice and mentorship over the past few years. Amanda, one of my first friends I made as a postgrad, thank you for minding me, looking out for me, and most importantly, thank you for letting me stay on your couch, even after I got sick in your bathroom. The two of you have been my agony aunts, and go-to people for nearly everything throughout my PhD. I will always cherish our friendship.

Outside of Maynooth, I had an incredible support structure by way of my friends. To the Core Four – Emma Costigan, my saltmate, I cannot thank you enough for your friendship from all the way in undergrad to where we are now. Thank you for making me feel a part of your family and making your home a safe haven (and for feeding me). Thank you for the additions of your loving husband, Mark, your gorgeous daughter, Ella, and equally gorgeous dog, Toby, to the Core Four. Niamh Doody – the other half of my power couple, thank you for your friendship from practically day one of undergrad. We've come a long, long way since sitting on Slevin's coach. Best of luck with your own PhD, I have no doubt you'll excel, as you do in everything you put your mind to. Ruth Doherty – your love, warmth, and kindness has made me cherish our friendship from day one. Thank you for being a wonderful person, and congratulations on achieving your dreams, you're going to be an excellent speech and language therapist.

My beloved Hens, my chosen family, Katie, Ash, Jen, Niamh Hayes, Mellon, and Beth. Thank you for your love, friendship, and understanding throughout the years. The Hens are a source of light and joy in my life, and I would be lost without you all. Rachel Kearns, my Jolene, We Are One, thank you for being a constant source of love and laughter, I cannot wait to see what the future holds for us both. Thank you to Grace Dignam for your friendship, love and for always wanting to get a Chinese. Nearly eleven years of friendship and we still haven't murdered each other, which is an achievement in itself. Charles, my ghost of Christmas future, I cannot thank you enough. Without your unreasonable patience and kindness, these past few months would have been bleak.

Most importantly, I would like to thank my family – my Mam, my Dad, my brother, Jamie, his partner Tonia, and my beautiful niece, Madison. Your love, constant support (both emotional and financial), and encouragement has helped me throughout my entire life and helped get me to where I am today. Lastly, to my late grandmother Elizabeth, thank you for all of your love, and always supporting and encouraging further education.

Abstract

Anions play a crucial role in both biological and environmental contexts to such an extent where the absence or the overabundance of anions can lead to severe health implications and environmental concerns. The recognition of the universal significance of anions has led to an explosion of research in the field of supramolecular chemistry, resulting in a solid foundation of the principles of synthetic anion receptors and transporters. Indeed, synthetic anion transporters show particular promise in medicinal chemistry where they are being developed as new approaches for anti-cancer agents, anti-microbials and as novel Cystic Fibrosis treatments. This thesis focuses on the use of squaramides as an anion binding motif, where novel recognition motifs, stimuli responsive transport, and selective anion sensing is explored.

The thesis commences with a literature review and introductory chapter that outlines the aims and objectives of the research. Chapter 2 details the design and synthesis of squaramides featuring an *N*-acyl linkage, termed 'amido-squaramides'. These novel compounds were investigated as potential anion binding units *via* a combination of experimental and computational techniques where it was shown that the amido-squaramides exist in the *anti*/*syn* conformation due to the presence of an intramolecular H-bond. The receptors' anion binding abilities were assessed and were shown to selectively bind to Cl^- *via* H-bond formation in a 1:1 binding mode. Finally, the receptors were found not to display anionophoric activity at pH 7.20, but at pH 4.20, anion transport was observed to 'switch on'. This established amido-squaramides as pH-switchable anion transport units.

The 3rd Chapter details attempts to synthesise tertiary squaramides, featuring enzyme- and fluoride- responsive triggers. This chapter reports four novel secondary amines, featuring a nitrobenzyl moiety, and triisopropylsilyl ether moiety and also outlines several synthesis optimisation studies to obtain the tertiary squaramides. Synthetic problems were encountered during the experimental work that prevented successful synthesis of the target molecules, however, it is envisaged that future work may focus on the use of metal-based catalysis to generate the desired stimuli-responsive anion transporters.

The 4th Chapter outlines the development and application of a squaramide based chemosensor. A small family of squaramidoquinoxalines were synthesised *via* a one-step synthesis. X-ray crystallographic analysis demonstrated the tendency of the squaramidoquinoxalines to participate in a number of intermolecular interactions and displayed selective sensing of F^- over other halide anions, resulting in visible to the naked-eye colour change from pink-red to green to yellow. Experimental and theoretical results suggest that the colourimetric change is brought about by two distinct deprotonation events. The squaramidoquinoxalines were also incorporated into test strips that allowed for the rapid and naked-eye detection of F^- in aqueous media.

Abbreviations

Å	Angstrom
ATR	Attenuated Total Reflection
$CDCl_3$	Deuterated chloroform
COSY	Correlation Spectroscopy
DCM	Dichloromethane
DEPT	Distortionless enhancement by polarization transfer
DIPEA	Diisopropylethylamine
DMF	Dimethylformamide
DMSO	Dimethylsulfoxide
EDCI	1-Ethyl-3-(3-dimethylaminopropyl)carbodiimide
e.g.	Exempli gratia (Latin for ‘for example’)
Equiv	Equivalents
ESI	Electrospray ionisation
Et2O	Diethyl ether
EtOAc	Ethyl acetate
EtOH	Ethanol
h	Hours
HCl	Hydrochloric acid
HMBC	Heteronuclear Multiple Bond Correlation
HRMS	High Resolution Mass Spectrometry H
HSQC	Heteronuclear Single Quantum Coherence
i.e.	Id est (Latin for ‘that is’)
IR	Infrared spectroscopy
K	Kelvin

LMCS	Liquid chromatography-Mass Spectrometry
MeCN	Acetonitrile
MeOH	Methanol
mg	Milligram
min	Minutes
mL	Millilitre
mm	Millimetre
µm	Micrometre
NO_2	Nitro group
NEt_3	Triethylamine
nm	Nanometre
NMR	Nuclear Magnetic Resonance
OH	Hydroxyl group
Pet Ether	Petroleum ether
rt	Room temperature
TFA	Trifluoroacetic acid
TLC	Thin Layer Chromatography
µL	microlitre
UV	Ultraviolet
Vis	Visible

Chapter 1

Introduction

1 Introduction

The International Union of Pure and Applied Chemistry (IUPAC) defines an anion as ‘a monoatomic or polyatomic species having one or more elementary charges of the electron’. Anions are ubiquitous in everyday life, from fluoride in tap water, nitrates and phosphates in soil fertilisers, sulfates in cosmetic products, and chloride and bicarbonate both play important roles in our very own physiology. Anions play roles in maintaining cellular pH,[1] cellular volume[2] and in the formation of membrane potentials, which aid electrical signals to propagate through our nervous system.

However, an imbalance of anions can result in serious health implications. Cystic fibrosis,[3] cardiac ischemic preconditioning, and cardiac arrhythmogenesis[4] are diseases brought about by the malfunctioning of anion transport channels in epithelial or cardiac cells, respectively. Furthermore, metabolic acidosis can be induced from a lack of bicarbonate in blood serum, which can cause loss of bone density, muscle wasting, and in severe cases death.[5]

An imbalance of anions also has negative impacts outside of human biology. Excess nitrates and phosphates from crop fertilisers leech into rivers and lakes which then leads to their eutrophication, causing a deficiency of oxygen in the bottom waters, further resulting in the death of aquatic animals and loss of biodiversity.[6] Sulfates are known to interfere with the vitrification process and safe storage of nuclear waste.[7,8]

Due to the recognition of the biological relevance of anions, the selective recognition, sensing, and transport of anions has become a rapidly developing area of research. Indeed, these topics have become firmly entrenched in the area of supramolecular chemistry, as evidenced by the large number of review papers detailing the significant advances in the field.[9]

In this chapter, the significance of anions in a biological context will be further discussed, from their physiological role to their implication in various diseases. The significant advances made in the fields of anion recognition, sensing and transport will be examined in detail and the aims of this research project will also be outlined.

1.1 Anions in a Biological Context

This section will detail the physiological role of anions, how they are recognised, bound, and transported in a biological setting, and the diseases that occur when anion homeostasis is perturbed. This will give important context as to why the field of anion recognition and transport is a burgeoning field in supramolecular chemistry. It will also lay the foundation of the common themes and chemical moieties seen in later in the chapter, describing where and how scientists drew inspiration from nature in their quest to synthesise anionophores to act as potential treatments for illness caused by malfunctioning anion channels.

1.1.1 Physiological Role of Anions

The physiology of anions is extremely important in the regulation of cellular function. A large majority of biotransformations either act on anionic substrates or involve anionic co-factors. The following section, while non-exhaustive provides several examples - from the oxygenation of red blood cells to the production of energy within cells

A process known as the chloride shift, or Hamburger phenomenon, occurs when bicarbonate (HCO_3^-) and chloride (Cl^-) exchange across the membrane of red blood cells. As CO_2 is produced as a by-product of metabolism it gets converted to carbonic acid (H_2CO_3) by carbonic anhydrase (Equation 1.1). Carbonic acid then dissociates to form bicarbonate and hydrogen ions (H^+). This decrease in CO_2 concentration causes more CO_2 to diffuse into the red blood cell, allowing for more CO_2 to be carried by cell. The membrane of red blood cells is permeable to HCO_3^- but not to H^+. Due to the rise of HCO_3^- concentration, bicarbonate diffuses down a concentration gradient out of the cell as Cl^- influxes into the red blood cell to prevent a build-up of electric potential on the inside of the cell.[10]

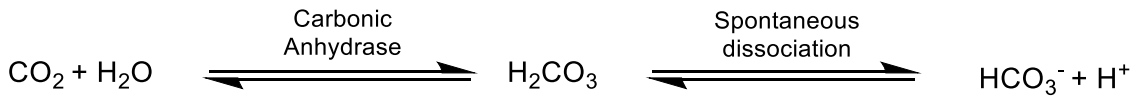

Equation 1.1. The conversion of carbon dioxide and water to bicarbonate and hydrogen ion.

This process can occur in the opposite direction during the oxygenation of red blood cells in the capillaries of the lungs. When CO_2 is released from haemoglobin (Hb), H^+ ions are also released into the cytoplasm which allows for carbonic anhydrase to convert HCO_3^- and H^+ back into CO_2 and H_2O. The drop in bicarbonate concentration causes chloride to efflux out of the red blood cell and for bicarbonate to influx in. This is represented schematically in Figure 1.1.

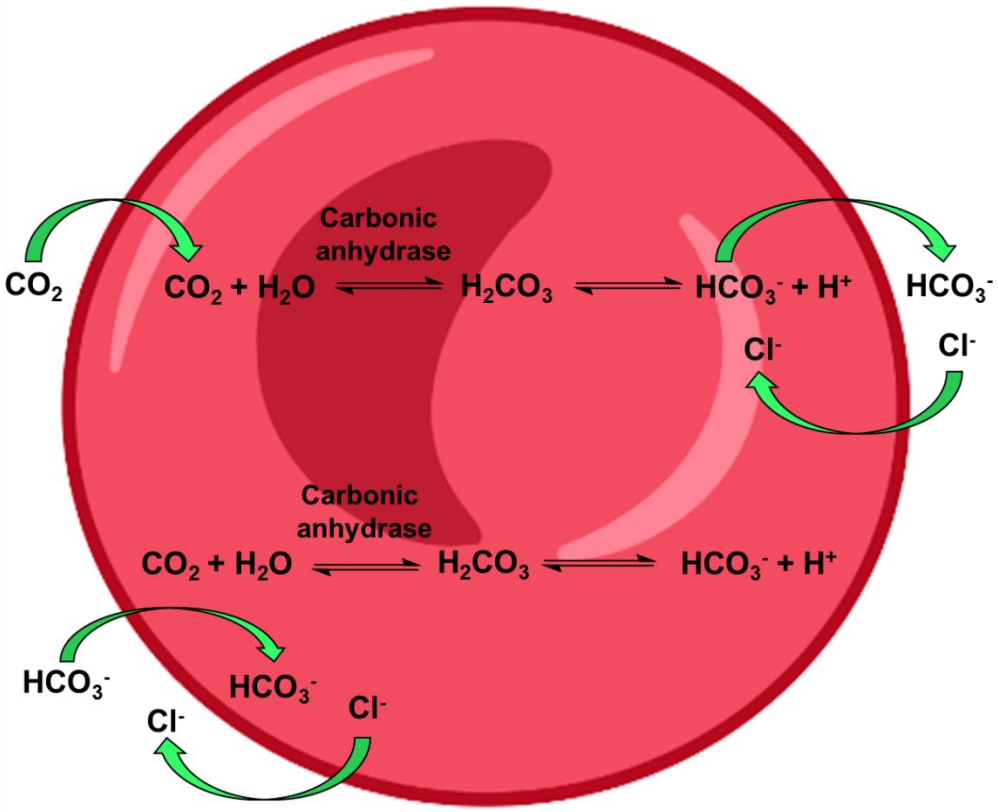

Figure 1.1. Diagram illustrating the chloride shift in red blood cells.

Chloride is a strong allosteric effector for Hb, altering the Hb from relaxed form (R) to taut (T) form, lowering its affinity for O_2. A study concluded that chloride binds to no specific site within Hb but rather resonates between cationic residues and reduces electrostatic repulsions – stabilising the T form of Hb.[11] The T form has a lower affinity for O_2 as there is an increase in binding sites which allows species such as 2,3-bisphosphoglyceric acid to compete for binding sites. This allows for the unloading of O_2 into surrounding tissues.

Cl^- is also heavily implicated in Cystic fibrosis (CF) - an inherited and fatal disease brought about by a mutation of the cystic fibrosis transmembrane conductance regulator (CFTR) protein. Under normal circumstances, CFTR allows for passage of Cl^-, along with other halide anions, across the cell

membrane into the cytoplasm. This creates a higher concentration of electrolytes in the mucus, resulting in water leaving the cell *via* osmosis.[3] There have been several mutations observed that either prevents CFTR from being produced or causes the protein to degrade rapidly. This loss in Cl^- transport across membranes causes a thickening of the mucus in lungs leading to chronic infection and decreased lung function, vastly reducing the expected life-span of the patient.[12]

Sulfate, a tetrahedral oxyanion, is the fourth most abundant anion in human plasma and is one of the most important cell nutrients, being the major source of sulfur in many organisms.[13] In human biology, sulfates are crucial in the formation of mucins - sulfated glycoproteins that are found in mucous membranes and secretions. It has been proposed that sulfated mucins aid in protecting mucous membranes from bacterial attack, and the sulfate residues of these glycoproteins have been implicated in binding to pathogenic bacteria.[14] Mucins with a higher level of sulfation have been found in those that suffer with CF, compared to those who do not. This higher level of sulfation has been proposed to be a factor in the higher impact of *Pseudomonas aeruginosa* on CF patients.[15]

Phosphate is another biologically relevant ion and plays a crucial role in skeletal development, cell metabolism, energy-transfer, as well as being components of the cell membrane, DNA and RNA.[16] Inorganic phosphate (Pi) is involved with the mineralisation of bone by forming hydroxyapatite crystals by complexing with calcium inside matrix vesicles (MVs), small structures produced from the plasma membrane of osteoblasts and chondrocytes. The MVs then propagate into collagen fibrils to mineralise the extracellular matrix. Chondrocytes are the cells that produce and maintain cartilage. High levels of Pi in chondrocytes induces apoptosis which is vital in endochronal ossification – the formation of bone.[17] Phosphate has also been identified in regulating gene expression of *cyclin* D_1 and Dmp_1, two genes involved in regulating the cell cycle in osteoblasts.[18-19] A lack of Pi can lead to the formation of diseases such as rickets and osteomalacia, diseases that affect bone development, cause bones to lose mineralisation causing them to soften and break more easily and can cause bone deformities.[20]

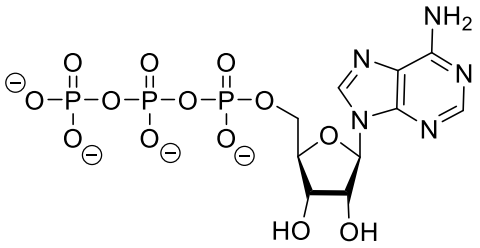

Figure 1.2. Structure of adenosine triphosphate at pH 7.

Adenosine triphosphate (ATP) (Figure 1.2) is the source of energy within a cell. It consists of three phosphate units, linked via phosphodiester bonds, bound to a ribose sugar which in turn is bound to adenine. When ATP undergoes hydrolysis, it forms adenosine diphosphate (ADP) and releases Pi, sometimes undergoing a second hydrolysis to form adenosine monophosphate (AMP) and a second Pi unit. This process is energetically favourable, yielding Gibbs-free energy of -7.3 cal/mol.[21] This provides the energy required for nearly every energy-demanding process in the cell. In turn, ADP and AMP can activate PFK1 and pyruvate kinase, stimulating further ATP production.

Deoxyribonucleic acid (DNA) and ribonucleic acid (RNA) are nucleic acids that carry the genetic information needed for all living organisms to build the proteins needed for the organism's development, growth, and reproduction. Both DNA and RNA consist of nucleotides – repeating units containing a nitrogenous base covalently bonded to a ribose sugar which in turn is bonded to a phosphate group. The ribose sugar and phosphate make up the backbone of DNA and RNA. Each phosphate acts as a bridging unit between ribose sugars and their conjugated nitrogenous base *via* a phosphodiester bond (Figure 1.3).

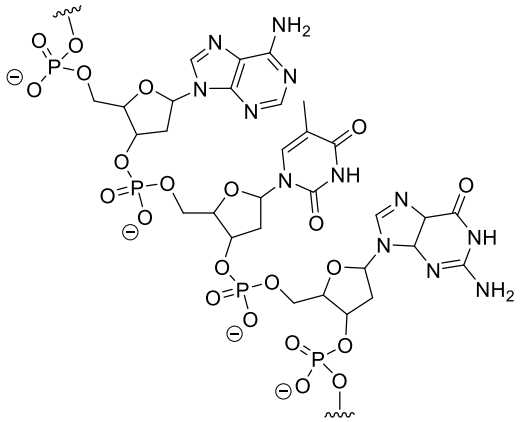

Figure 1.3. Example of a portion of DNA containing adenine, thymine and guanine linked together via the phosphate backbone.

Even the cell membrane's main component contains anions - phospholipids are amphiphilic molecules containing a negatively charged phosphate, a positively charged quaternary ammonium at the head and a long hydrocarbon tail (Figure 1.4). The four major phospholipids that constitute the cell membrane in animals are phosphatidylcholine, phosphatidylethanolamine, phosphatidylserine and sphingomyelin. The phospholipids contain three parts – a glycerol backbone, two long chain fatty acid and a phosphate head group. The phospholipids arrange themselves into a bilayer with the hydrophobic tails pointing inward and the hydrophilic head point outwards.[22]

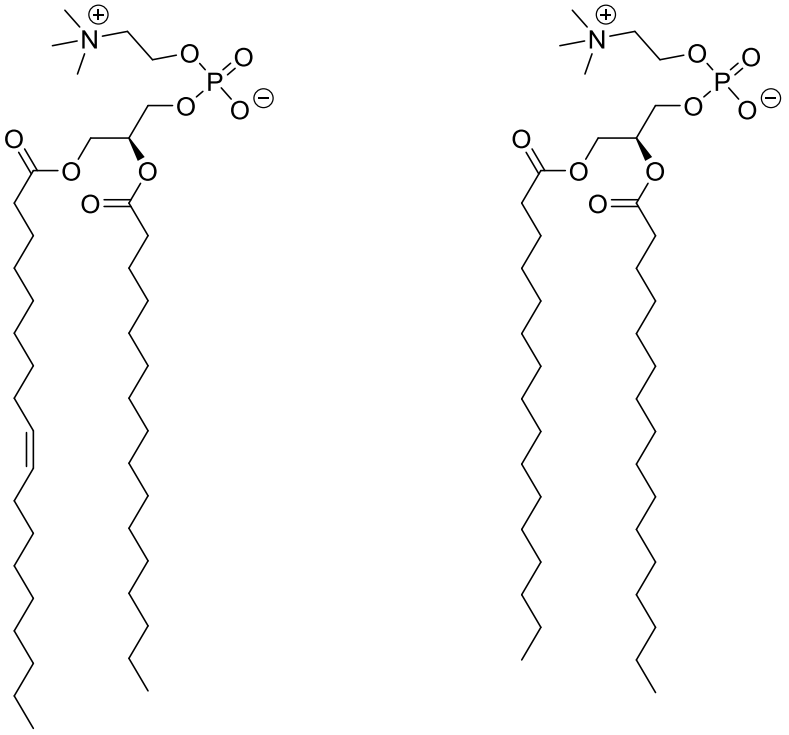

Figure 1.4. Structure of phospholipids 1-palmitoyl-2-oleoyl-sn-glycero-3-phosphocholine (POPC) and dipalmitoylphosphatidylcholine (DPPC), important components of mammalian cell membranes.

The above examples illustrate the breath and diversity of anionic species that perform crucial roles in biology. From the production of energy to the construction of membranes, life cannot function without anions. The following section will outline some of the methods nature uses to bind and recognise anions and will serve as inspiration to the design of anion receptors synthesised as part of this thesis.

1.1.2 Anion Binding in Cells

In the cellular environment, there exist proteins that are capable of recognising and selectively binding various anions. These anion-binding sites within proteins utilise various non-covalent interactions to bind to their target anions. A common feature is using charge interactions between the substrate anion and cationic residues of the protein. For example, arginine residues are employed to bind to phosphate and guanine of TAR RNA with what is known as the “arginine fork”.[23-24] The guanidinium NHs act as a two-pronged hydrogen bond donor, interacting with both the phosphate and the guanine (Figure 1.5).

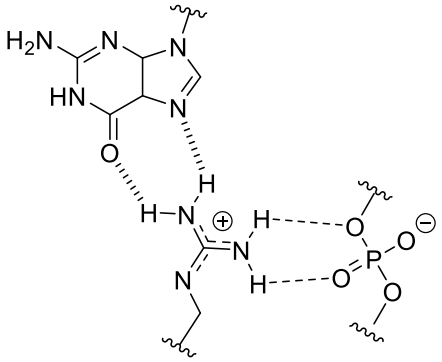

Figure 1.5. Arginine binding to phosphate and guanine of TAR RNA.[24]

Arginine, lysine, histidine and serine are the most common amino acids that utilise their side chain in the binding regions.[23] The side chains all contain hydrogen bond motifs such as hydroxyl, amino and imidazole functional groups that can bind to anionic species (Figure 1.6).

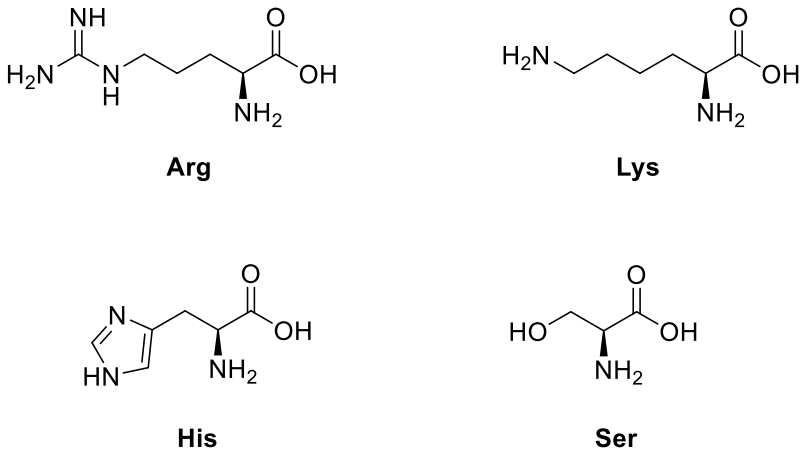

Figure 1.6. Arginine, lysine, histidine and serine – the most common amino acids that use their side chain for anionic binding.

In the majority of cases, however, the peptide backbone of the protein forms the binding site with the amide NHs forming hydrogen bonds with the substrate. For example, apotransferrin is a type of transferrin - an iron transport protein that binds to Fe(III), transports it around the body and allows for its cellular uptake.[25]

Apotransferrin has an anion binding site, which evidence suggests, has a high affinity for carbonate (CO_3^{2-}).[26] The carbonate-binding site consists of a positively charged arginine residue and amide NH groups originating from the peptide backbone of the protein (Figure 1.7). Spectroscopic and kinetic data indicates that carbonate-binding occurs before the binding of Fe(III), implying that anion-binding has a cooperative role. It is proposed that the carbonate neutralises any positive charges that may repel the cationic iron and provides two carbonate oxygens which may act as ligands, aiding in the metal-binding. It is also postulated that protonation of the carbonate could be the first step in the release of the iron from the metal-binding site.[27]

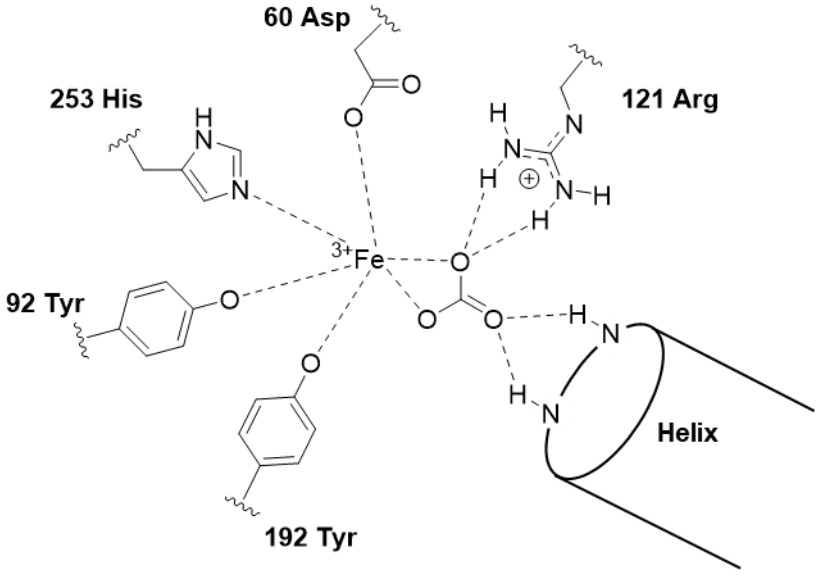

Figure 1.7. Binding pocket of human iron-lactoferrin.[28]

Sulfate-Binding Protein (SBP) is a protein found in *Salmonella typhimurium* (*S. typhimurium*) that acts as an anion transporter for sulfate.[29] SBP binds to sulfate by way of seven hydrogen bonds – five originating from the peptide backbone, one from the hydroxyl group of serine and the final hydrogen bond from the indole NH of a tryptophan side-chain (Figure 1.8). As the majority of the hydrogen bonds come from the peptide backbone, the binding site is considered rigid which implies that the geometry of the binding site is dependent

on the proper folding of the backbone. The binding site is classed as unusual due to the lack of positively charged residues and that the bound sulfate is inaccessible to the bulk solvent.[30]

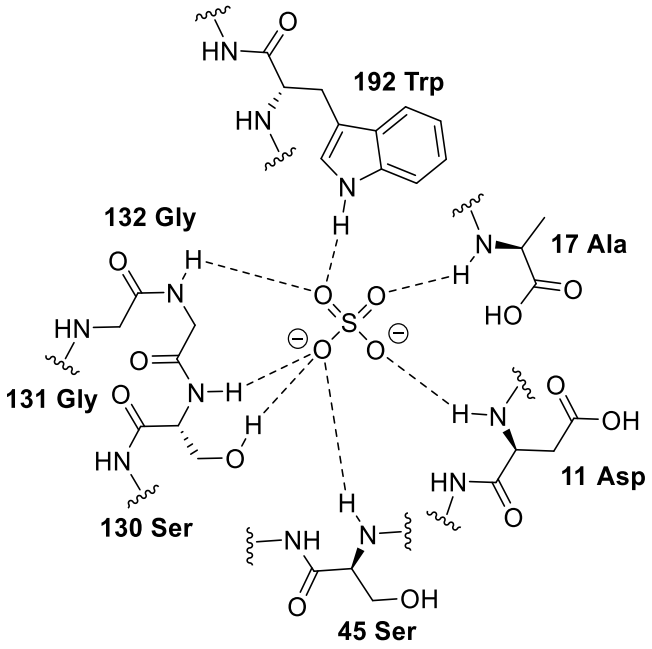

Figure 1.8. Binding pocket of Sulfate-binding Protein found in *Salmonella typhimurium.*[30]

Chloride channel proteins found in *Escherichia coli* (*E. coli*) and *S. typhimurium* show coordination of chloride to two NH protons of the amide backbone and two hydroxyl groups from amino acid side chains, tyrosine and serine (Figure 1.9). This binding site forms a narrow pore which allows for the selective movement of Cl^- through the protein.[31]

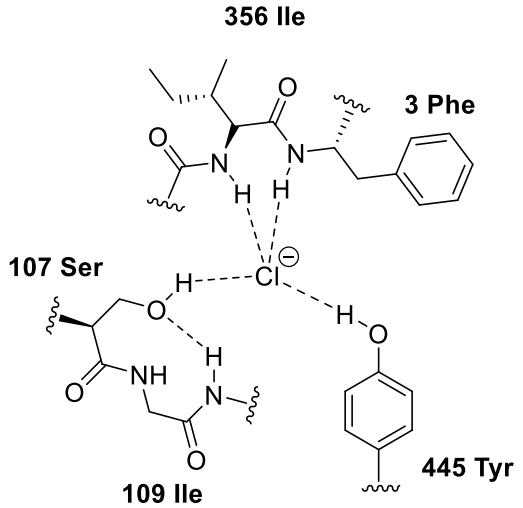

Figure 1.9. Binding pocket of the ClC chloride channel found in *E. coli* and *S. typhimurium*.[31]

As seen in the examples above, nature employs H-bonds to bind anionic species. The importance of judicious arrangement of the binding motif for strong and selective binding is also evident. These two factors are important considerations on the design of synthetic anion receptors. The following section examines the mechanisms nature uses to facilitate anion transport across lipid membranes.

1.1.3 Transmembrane Transport of Anions

The transport of anions is critical in maintaining anion homeostasis. The plasma membrane acts a barrier to maintain the internal composition of the cell due to its selective permeability. Small polar but neutral molecules, (e.g. H_2O) small non-polar molecules, (e.g. benzene), and gases (e.g. O_2) are able to diffuse across the membrane, in what is known as passive diffusion. During passive diffusion, a molecule can diffuse across the phospholipid bilayer following a concentration gradient from high to low concentration. Larger polar molecules, such as glucose or amino acids, and charged species, such as ions, are unable to passively diffuse across the plasma membrane due to the hydrophobic, non-polar nature of the interior of the phospholipid bilayer. For such molecules to enter or exit a cell, they must rely on facilitated diffusion by way of carrier and channel proteins to do so.[21] The various means by which natures facilitates anion transport are schematically represented in Figure 1.10.

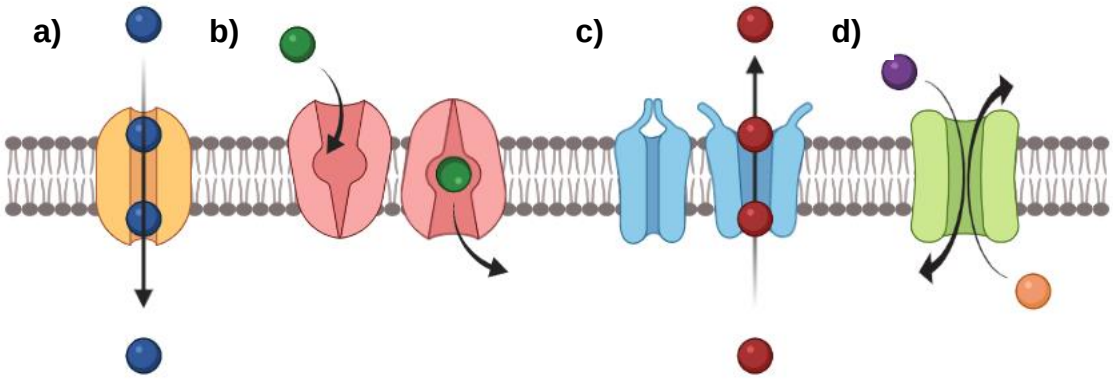

Figure 1.10. Schematic of four types of ion transport proteins embedded in the plasma membrane **a)** ion channel, **b)** ion transport protein, **c)** gated ion transporter **d)** anti-port ion exchanger.

Carrier and channel proteins are proteins embedded into the plasma membrane of the cell and facilitate transport of molecules across the membrane.

Ion transport carrier proteins generally use either ATP or an electrochemical gradient to transfer its substrates in a particular direction. Ion channel proteins allow for ions to passively diffuse through a pore down an electrochemical gradient. Most ion channels typically do not allow for ions to freely pass through the membrane at all times but are 'gated', allowing for the regulation of ionophoric activity. These gates are controlled by various stimuli such as voltage, ligand binding and cell volume, which open and close the channel by altering the conformation of the channel. Below, several specific examples of protein anion transport will be discussed.

1.1.3.1 ClC Proteins

The ClC family of chloride transport proteins was first discovered by Zdebik *et al*. in 1990.[32] ClC proteins are voltage-gated channels that rely on chloride concentration and pH to modulate its gating. ClC channels show selectivity for halide ions in the order of $Cl^- > Br^- > I^-$.[33] Even though ClC proteins share the same basic structure (Figure 1.11), some act as chloride-only channels, while the others act as chloride/proton exchangers.[34-35] ClC-1, ClC-2, ClC-Ka, and ClC-Kb function as chloride-only channels and are embedded in the plasma membrane. ClC-3 to ClC-7 are chloride/proton exchangers and are found localised to intracellular membranes.[36]

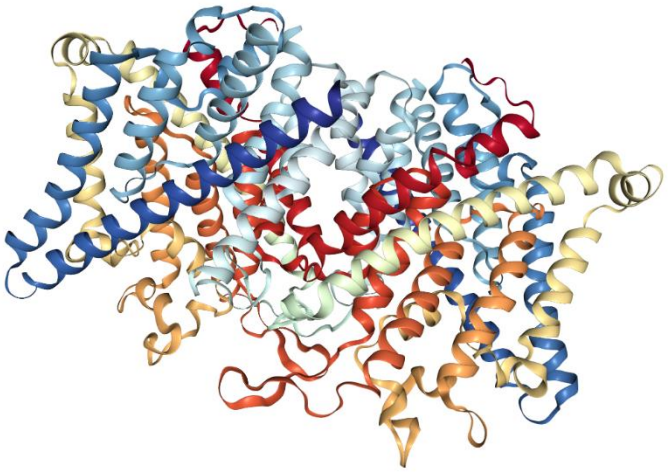

Figure 1.11. Crystal structure of chloride ion channel, Human ClC-1.[37]

ClC transporter structures reveal a narrow channel through the protein with three Cl^- binding sites, S_{ext} which is an external site, S_{cen} is found within the

phospholipid bilayer, and S_{int} being in contact with the cellular interior.[1,38]. ClC transporters commonly contain a glutamate residue in close proximity to S_{cen} and S_{ext} which allows for the carboxylate group to competitively bind to the binding sites with Cl^-.[39-40] This glutamate residue is postulated to act as a 'self-gating' mechanism while also facilitating proton transfer alongside chloride transfer. When the gating glutamate is mutated to Ala, Gln or Val, the channel has been observed to remain it its open state, indicating that the glutamate acts as a self-gating mechanism for ClC transporters.[41] In its anionic form, glutamate blocks the pore by coordinating to S_{ext}, while S_{cen} and S_{int} are each occupied by Cl^-. Upon protonation of the glutamate, the conformation changes, opening up the pore (Figure 1.12). This would give rise to the 2:1 Cl^-:H^+ stoichiometry classically seen in ClC transporters.[42] The importance of the gating glutamate is also seen in ClC-4, which upon mutation turns the transport protein from Cl^-/H^+ exchanger to a passive Cl^- conductor.[43-44]

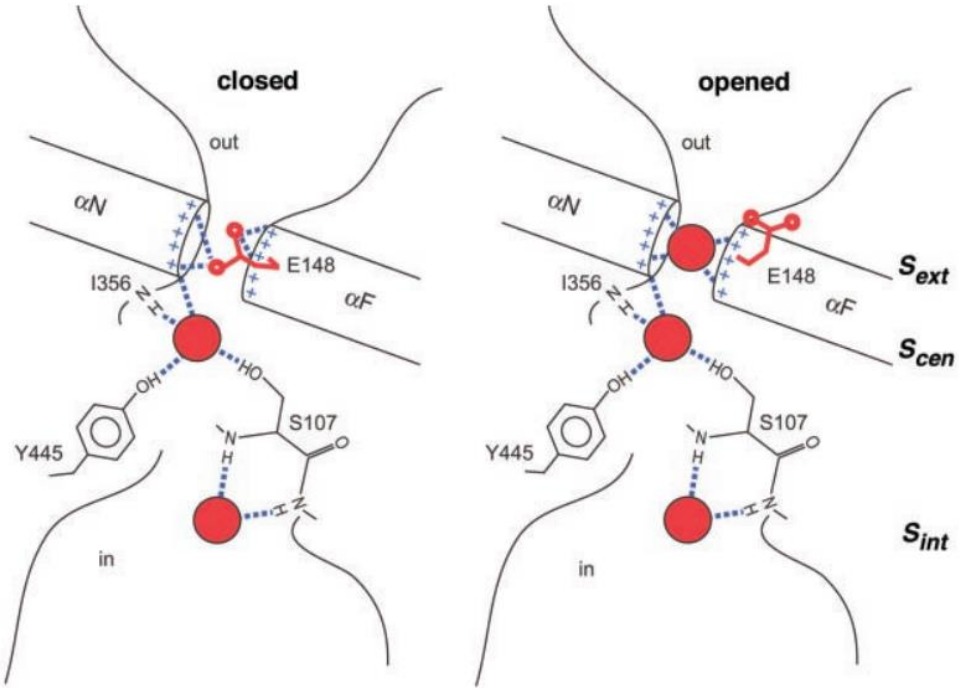

Figure 1.12. Schematic drawing of the open and closed conformations of a ClC chloride channel. In the closed state, glutamate occupies S_{ext} blocking the channel. In the open conformation, the glutamate moves away from S_{ext} to allow Cl^- binding to the binding site.[41]

MacKinnon *et al.* elucidated the structure of ClC-1 using cryo-EM to establish the transmembrane domain.[37] They found, as in other ClC structures, that ClC-1 contains a selectivity filter due to the pore being narrowly constricted through the membrane. ClC proteins can be found in a wide range of tissues

throughout the body though only some of the ClC family have their functions fully elucidated.

ClC-1 is found nearly exclusively in skeletal muscle and is postulated to re-polarise muscle fibres following activation of action potentials.[45] ClC-2 can be found expressed in the brain, lungs, kidney and skeletal muscles where it control Cl^- release into extracellular medium.[46] ClC-Ka and ClC-Kb are ClC channel proteins found in the nephrons of the kidney and in the inner ear.[47,48] These channel proteins lack the gating glutamate seen in other ClC proteins and display different halide selectivity, $Br^- > Cl^- > I^-$.[49] ClC-3 is expressed in most tissues and is localised in endosomal membranes.[50-51] While the exact function of ClC-3 has yet to be determined, the reduction of ClC-3 expression has been linked to inflammatory bowel disease[52] and atherosclerosis.[53] ClC-5 localisation is restricted to renal and intestinal epithelia and plays a role in endosomal acidification.[54] ClC-7 is mostly displayed in lysosomes and also found on the ruffled borders of osteoclasts.[55] Despite being the only ClC exchange protein needing a β-subunit to function, ClC-7 displays characteristic similar to the rest of the ClC exchange family such as $2Cl^-/H^+$ stoichiometry, inhibition of transport activity at low pH and the presence of gating glutamate residues. The exact physiological function of ClC-7 is yet to be determined but its dysfunction is implicated in osteopetrosis.

It is evident that ClC proteins are critical in a wide range of physiological processes. As ClC proteins are found expressed in plasma membranes and intracellular membranes their roles are diverse, ranging from acidification in intracellular vesicles and to restore proper polarisation of cells in muscle cells following action potentials.[56] Thusly, dysfunction of ClC proteins lead to several severe diseases.

Mutations in the ClC-1 gene results in a disease known as myotonia congenita. As ClC-1 is mainly responsible for Cl^- conductance in skeletal muscle, disruption of ClC-1 activity results in failure to repolarise the muscle fibres. The lack of repolarisation causes a delay in muscle relaxation after contraction causing ‘muscle stiffness’.[56] As myotonia congenita is a congenital disorder can occur in two forms, Thomsen disease (dominant trait) or Becker disease (recessive trait). Both diseases result in muscle weakness, skeletal deformities as well as hypercalcemia and hypermagnesemia.[57]

Disruption in ClC-2 function has been found to cause azoospermia (degeneration of sperm cells) due to a defect in the transepithelial transport in Sertoli cells in the testes. Patients with ClC-2 mutations have also been recorded to display symptoms similar to leukodystrophies, a set of diseases characterised by the degeneration of white matter in the brain resulting in mental retardation, muscle rigidity, ataxia and epilepsy.[58]

ClC-K plays a role in the absorption of salt and water in the kidneys and also the cycling of Cl^- from the epithelium of the inner ear and the interstitial fluid.[47,59] Bartter syndrome type III is caused by mutations in ClC-Kb, reducing salt absorption by the body. This results in hypokalemia and metabolic alkalosis. Mutations in the gene for barttin cause Bartter syndrome type IV resulting in congenital deafness combined with the loss of salt reabsorption in the kidneys.[60]

Mutations in ClC-5 causes Dent's disease, which is characterised by hypercalciuria, hyperphosphaturia, kidney stones, low molecular weight proteinuria, and nephrocalcinosis.[61] Mutations in ClC-5 reduce the acidification of endosomes while also causing ClC-5 to lose the ability to transport protons.[62] ClC-5 disruption also had a knock-on effect in mice models, where NHE_3 (Na^+/H^+ exchanger) and NaPi-2a (Na^+/Pi co-transport) also had reduced expression adding to further reduction of endocytosis in the proximal tubule of the kidney.[63]

1.1.3.2 Cystic Fibrosis Transmembrane Conductance Regulator (CFTR)

CFTR is another example of an anion transporter protein. It is an ATP-binding cassette (ABC) transporter that acts as an ion channel, located mainly in the plasma membrane of epithelial cells in the lungs and intestines.[64] The protein displays a number of positively charged arginine and lysine residues on the extra-cellular surface and in the transmembrane domain of the ion channel.[65] This positive extra-cellular surface and lining of the pore provides electrostatic interactions that attract anions into the pore and traffic the anions through the protein. These positively charged amino acids give CFTR selectivity towards anions over cations, while the pore size grants selectivity for monovalent over larger divalent anions but not does display selectivity for monovalent anions. The order of selectivity with the halide ions is in the order of $Br^- \geq Cl^- > I^-$.[66] Many other

monovalent anions have been found to permeate through CFTR, including nitrate, bicarbonate, formate and thiocyanate.[67]

As CFTR is localised to epithelial cell surfaces in the lungs and intestines, its main function is fluid secretion and electrolyte absorption in those tissues. CFTR is responsible for transporting chloride and bicarbonate as well as regulating other ion channels such as sodium, potassium, and other chloride channels.[68-69] As CFTR effluxes Cl^-, the salt concentration of interstitial fluid increases causing water to be secreted *via* osmosis or *via* aquaporins.[70] This secretion of water as an effect of ion transport is essential in maintaining the pH, thickness, and composition of the airway surface liquid (ASL) of the airways, which helps to protect the lining epithelia of the airways (schematically represented in Figure 1.13).[71] This process of regulating salt absorption and the secretion of water by CFTR is seen also in the pancreas and sweat glands.[72] As well as thiocyanate, CFTR has been identified in glutathione transport, both of which have a critical role in the regulation of immune response in the lungs.[73]

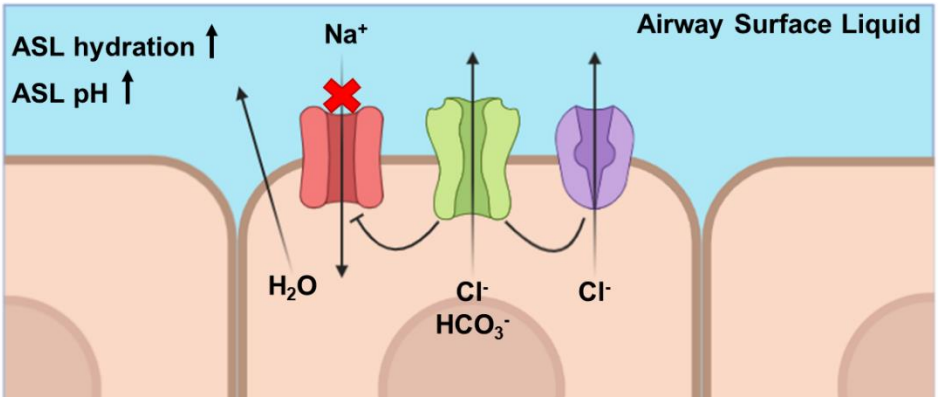

Figure 1.13. Schematic of ion transport in lung epithelia. CFTR (green) effluxes Cl^- and HCO_3^- into the airway surface liquid while inhibiting ENaC, reducing Na^+ absorption. HCO_3^- increases the pH of the ASL and the increased salt concentration drives the secretion of water into the ASL, increasing its hydration.

Cystic fibrosis is the most common fatal genetic disorder in populations of Northern European ancestry, with 34 new cases diagnosed in Ireland each year.[74] CF is caused by mutations in the CFTR gene which lead to the absence or malfunction of the protein. While there are many mutations that may cause CF, the phenotypes and clinical outcomes remain the same.[75] Cystic fibrosis primarily affects the lungs and their function although, other organs such as the pancreas, intestines, liver, and kidneys are also effected. Patients that suffer with CF display

inflammation, chronic lung infections, poor growth, infertility in males, and premature death.[76]

The main cause of premature death in CF patients is due to the lung pathology. Discussed previously, CFTR is involved with maintaining the ASL in the airways, which aids in mucociliary clearance – the process where cilia clear inhaled debris and helps eradicate bacterial infections. The lack of water secretions caused by non-functioning CFTR leads to severe mucus build-up in the lungs and, coupled with the depletion of the ASL, decreases patients' lung function due to damage to epithelia.[77]

1.1.3.3 Cl^-/HCO_3^- Exchange Proteins

Cl^-/HCO_3^- exchange proteins are critical in pH homeostasis and as seen previously, are involved with the chloride shift in RBCs. Cl^-/HCO_3^- exchange is performed by two families of membrane proteins called solute carrier transport proteins (SLC), SLC4 and SLC6.[78]

SLC4 proteins contain both Na^+ dependent and independent transporters. Cl^-/HCO_3^- exchangers are known as Anion Exchange proteins (AE). AE1-AE3 are Na^+ independent Cl^-/HCO_3^- exchangers.

AE1, previously known as band 3, is mainly found localised in the membranes of RBCs, where it facilitates the electroneutral exchange of Cl^- and HCO_3^- across the plasma membrane, but also can be found in the kidneys.[79] When CO_2 is converted to HCO_3^- by carbonic anhydrase II in erythrocytes, AE1 exchanges the bicarbonate for chloride existing in the plasma. In the lungs, this process is reversed, HCO_3^- is exchanged for Cl^-, allowing for the bicarbonate to be converted back into CO_2 that is exhaled. This process is critical to maintaining pH homeostasis since a build-up of CO_2 would results in acidosis.[80] In the kidney, AE1 reabsorbs HCO_3^- in the renal tubule, acidifying urine. The HCO_3^- reabsorbed here accounts for 5 of the total filtered HCO_3^-.[80]

AE2 and AE3's main role is in pH homeostasis by either absorbing or releasing HCO_3^- into the surrounding tissues. AE2 is the most widely expressed SLC4 Cl-/HCO3- exchanger with the highest expression found in the colon, kidney, and in acid-secreting cells in the stomach.[81] AE2 predominantly partakes

in pH homeostasis by regulating $HCO3^-$ concentration in tissues. In gastric epithelium, AE2 aids in the secretion of HCl. H^+/K^+-ATPase secrets H^+ into the stomach while AE2 effluxes Cl^- and absorbs HCO_3^- into the blood stream, preventing alkalinisation.[82] Similarly, AE2 found in osteoclasts removed HCO_3^- and introduces Cl^- into the matrix to allow for old bone tissue to be degraded.[83] AE3 is mainly located in the heart, brain, retina, and smooth muscle. In myocardial tissue, AE3 releases HCO3-, regulating the internal pH.[84]

Similar to the SLC4 family, SLC6 exchangers contribute to pH homeostasis in a wide variety of tissues, such as the GI tract, pancreas, sweat glands, kidneys, stomach, lungs and thyroid glands.[78]

SLC26A3 secretes high concentrations of HCO_3^- into the pancreatic lumen while absorbing Cl^- in the intestinal lumen, a major site for chloride reabsorption.[85-86] SLC26A6 is a major Cl^-/HCO_3^- exchanger in the heart ventricles and is postulated to aid in transport of the high loads of HCO_3^- present, due to the high metabolic rate in the ventricles.[87] SLC26A7 is expressed in the gastric parietal cells which indicate a role in acid secretion.[88] Little investigation has been performed in the physiological role of SLC26A9 but its presence in the lungs indicate that it may play a role in the maintenance of the airway surface liquid.[89]

Given how vital anion transport across plasma membranes is to correct physiological function, and the wealth of diseases that result when ion transport malfunctions, it is unsurprising chemists have sought to mimic the action of transport proteins through synthetic chemistry. This is an area of chemistry, specifically supramolecular chemistry, that has stimulated significant research interest in recent years. The following sections will examine the optimal design features of a successful anion receptor and give several examples from the recent literature.

1.2 Anion Binding and Recognition

Whether it be a naturally occurring molecule or a synthetic one, anion receptors utilise non-covalent interactions to bind to their substrates. In 1968, Simmons and Park produced ammonium-based macrobicyclic receptors capable of binding Cl^- (Figure1.14).[90]

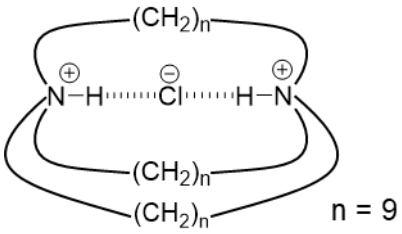

1.1

Figure 1.14. Structure of ammonium-based macrobicyclic receptor synthesised by Simmons and Park.

The protonated amines of these receptors pointing into the cavity in addition to the cationic ammoniums forms a binding pocket, in which chloride binds with K_a = 4 M^{-1}. This seminal work is regarded as the first example of a synthetic anion receptor and the birth of anion receptor chemistry. Since this landmark contribution, the scope of non-covalent interactions used in anion receptor chemistry has broadened considerably from electrostatic interactions including hydrogen bond formation, anion-π interactions, and halogen bonding to name but a few. The following sections will discuss several of the anion binding motifs that have been utilised in synthetic anion receptor design to date.

1.2.1 Anion Binding Motifs

As anions are, by definition, negatively charged it is unsurprising that the first example of a synthetic anion receptor was cationic. There are several examples of this approach to anion binding found in literature, however in more recent years, neutral receptors that employ hydrogen-bond donors became the spotlight focus in anion receptor chemistry.

1.2.1.1 Electrostatic interactions

Graf *et al.* added to the ammonium-based cohort of anion receptors by reporting the synthesis of **1.2** (Figure 1.15), utilising a cryptand consisting of four fused triaza[18]crown-6-rings.[91] In its tetraprotonated state, the molecule is able to form four hydrogen-bonds to Cl^-, supported by the electrostatic interactions of the ammonium cations. This receptor showed selectivity for Cl^- over Br^- due to the size of the respective anions resulting in a poor match for the cavity of the macrotricycle.

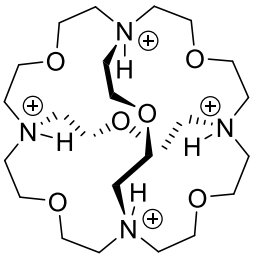

1.2

Figure 1.15. Structure of cryptand synthesised by Graf *et al.*

While **1.2** is perfectly spherical in shape which gives good complementarity for binding spherical anions, **1.3** synthesised and studied by Kintzinger displays an elliptical geometry which conveys complementarity for linear anion binding (Figure 1.16).[91] Spherical Cl^- displayed a much lower binding affinity to **1.3** compared to linear N_3^- (log K_a < 1.0 and log K_a = 4.6 respectively).

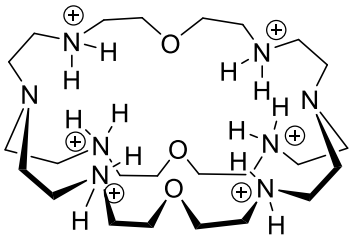

1.3

Figure 1.16. Cryptand produced by Kintzinger.

Schmidtchen synthesised a family of receptors, **1.4** (Figure 1.17), that did not employ hydrogen bond interactions but rather used quaternary ammonium groups to form a cationic cage for anion binding.[92] By varying the length of the alkyl chain between the quaternary ammonium groups, the size of the cage could be tuned to accommodate halide anions of different sizes. By altering the R group

on the ammonium vertice, zwitterionic structures could be generated that reduced the effect of competing counterions.

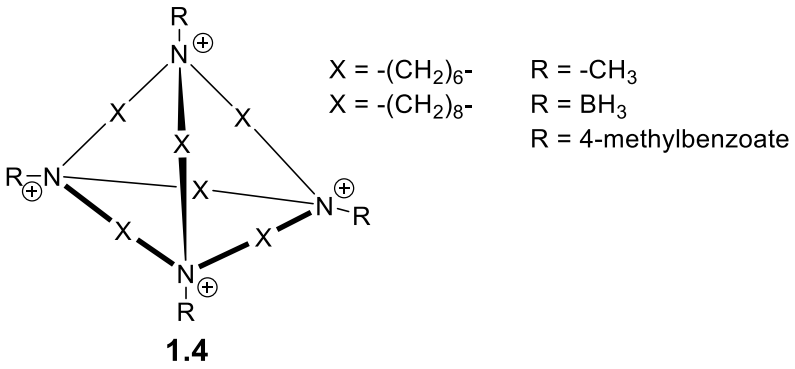

1.4

Figure 1.17. Tetrahedral quaternary ammonium cage with tunable cavity size.

Employing electrostatic interactions to bind anions provides its own challenges, however. As anions may be pH sensitive, becoming protonated at low pH, protonated receptors as seen above will have their own pH sensitivities. Therefore, the pH window of the anions of interest and their receptors must overlap for anion binding to occur. This challenge can be bypassed by using neutral receptors and hydrogen bonding motifs.

1.2.1.2 Hydrogen Bonding

A hydrogen bond can be viewed as a dipole-dipole interaction where a hydrogen atom bonded to an electronegative atom (known as the donor) is attracted to a dipole of a neighbouring electronegative atom (known as the acceptor) which often bears a lone pair of electrons or negative charge (Figure 1.18). The strength of a hydrogen bond can vary greatly, being affected by the electron-withdrawing strength of the atom attached, the acidity of the hydrogen bond donor, and the angle the hydrogen bond adopts. In general, the stronger the electronegativity of the atoms on either side of the hydrogen, the stronger the hydrogen bond.[93]

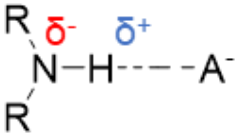

Figure 1.18. Example of hydrogen bond formation with a secondary amine acting as a hydrogen bond donor and generic anion A^- acting as an acceptor.

Typically, in anion receptor chemistry, the most common hydrogen bond donor is the N-H moiety, being found in anion binding units such as amides, sulfonamides, ureas, thioureas, squaramides, pyrroles, and indoles. Moieties such as ureas, thioureas, and squaramides are broadly employed as anion receptors as their dual hydrogen bond donors being seen as favourable for strong anion complexation (Figure 1.19).

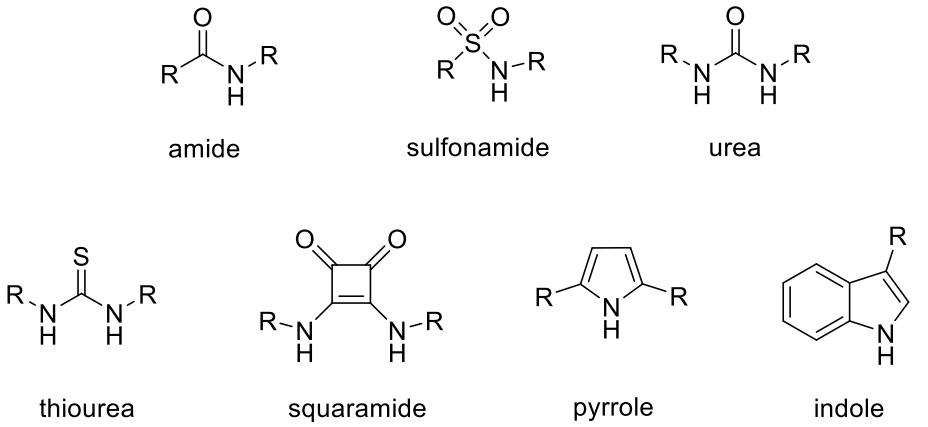

Figure 1.19. Some of the common scaffolds used in anion receptor chemistry.

Hydrogen bonding to anions can be seen extensively in nature, as seen in *Sections 1.1.2* and *1.1.3*, where the amide backbone of proteins and the side chains of their amino acid residues form hydrogen bonds to their anionic substrates. This approach is a popular one used be organic chemists to create synthetic anion receptors.

For example, Caltagirone and Quesada *et al*. reported a family of receptors exploiting the isophthalamide and picolineamide binding motifs (Figure 1.20) and investigated their anion binding and transport capabilities. Receptors lacking electron-withdrawing groups (**1.5** and **1.6**) displayed the lowest binding constants for Cl^- in DMSO-d_6. Receptor **1.12** displayed the highest binding constant which the authors attribute to the preorganisation of the binding motif due to the aromatic nitrogen. Anion transport studies using a chloride-selective electrode established that **1.5** and **1.6** showed no anionophoric activity while **1.8** was the most active Cl^-/NO_3^- exchanger.

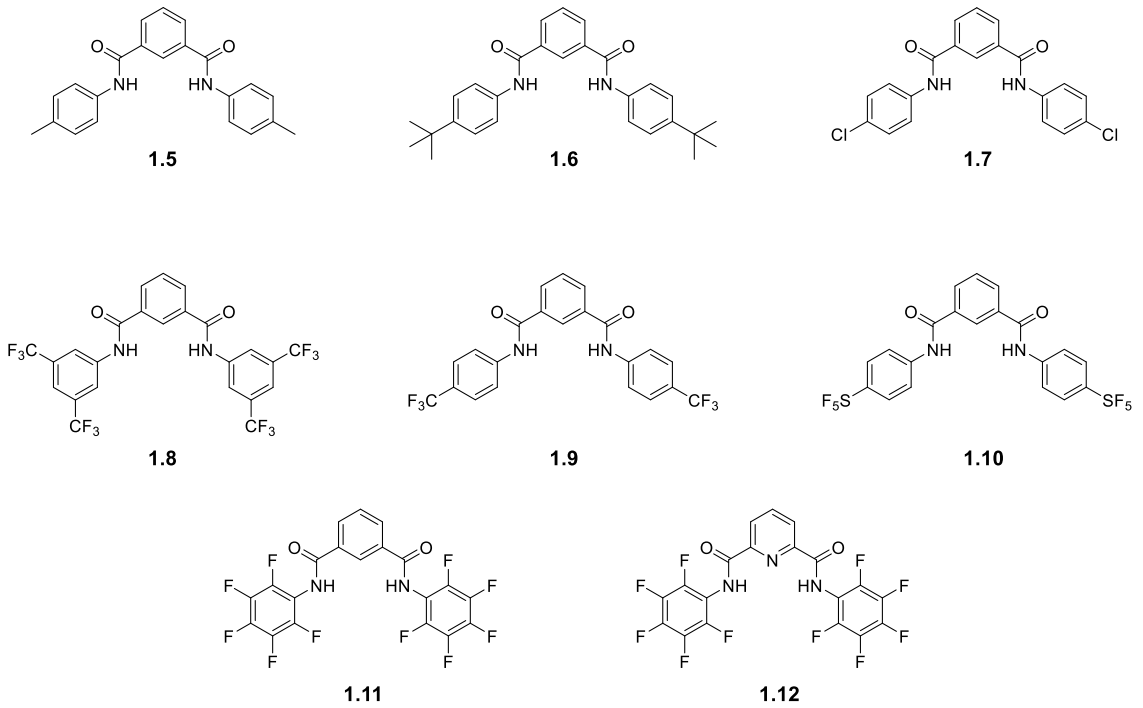

Figure 1.20 Structure of isophtalamides and picolineamides

More examples of hydrogen bonding-based anion receptors will be examined later on in the chapter, specifically squaramides and ureas, as they fall under the scope of this project.

1.2.1.3 Anion-π Interactions

While cation-π interactions have been well studied over the years, anion-π interactions have only been recently examined.[94] Anion-π interactions stem from electron-deficient aromatic rings and electron rich anions, where there is a charge-transfer between the two species.[95] Kochi *et al.* discovered with x-ray crystallography that halide anions lie offset to the centre of the ring with binding constants from 1-10 M^{-1} (Figure 1.21).

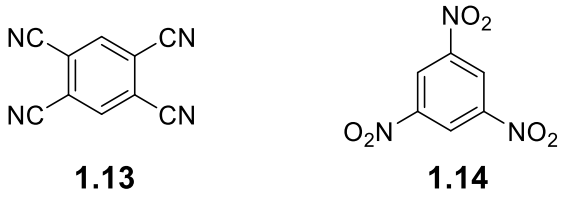

Figure 1.21. Two examples of electron deficient aromatic rings by Rosokha et al. employed as anion receptors.

1.2.1.4 Halogen Bonding

Halogen bonding as an anion binding motif is another area undergoing recent investigation. IUPAC defines a halogen bond as “occurring when there is evidence of a net attractive interaction between an electrophilic region associated with a halogen atom in a molecular entity and a nucleophilic region in another, or the same, molecular entity”. Due to the anisotropic distribution of electron density along an R-X bond, a region of low electron density exists known as a σ-hole. As the σ-hole is highly localised, the halogen bond interaction is strictly linear, bearing similarity to hydrogen bonds. The choice of halogen atom has a large influence of the properties of the halogen bond, as halogen bond strength increases with increasing polarizability and decreasing electronegativity, giving rise to the order of I > Br > Cl >> F.[96]

Work by Langton *et al.* illustrated that employing halogen bond donors gave rise to receptors, **1.15** (Figure 1.22), that show higher anion binding affinity and anion transport abilities than analogous hydrogen bonding systems.[97]

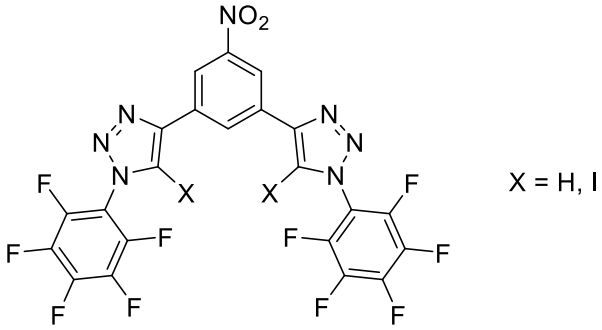

1.15

Figure 1.22. Bidentate halogen/hydrogen bonding receptors for anion binding and transport synthesised by Langton.

While anion-π interactions and halogen bonding are currently of interest in the field of anion recognition, they are beyond the scope of the work discussed in this thesis and will not be discussed in detail here. Instead, the general considerations of anion receptor design and the challenges that chemists face in this pursuit will be discussed in the next section.

1.2.2 Considerations and Challenges in Anion Receptor Design

There are a number of considerations to be made when designing anion receptors due to the varied nature of anion geometry, charge and propensity for solvation. As mentioned previously, the efficacy of charged or protonated receptors is dependent on the pK_a window of the receptor and the anion. If the anion becomes protonated at low pH, then it will lose its positive charge and binding will not occur. Conversely, at higher pH, the receptor may become deprotonated and will become defunct. These issues, however, can be overcome using neutral receptors.

In contradiction to this, hydrogen bond donors face their own set of hurdles. The acidity of NH protons has a direct effect on the strength of the hydrogen bond formed, with stronger hydrogen bonds being formed as pK_a descreases.[98] However, if the pK_a is too low deprotonation of the hydrogen bond donor will occur in the presence of basic anion such as F^- or AcO^-. Deprotonation of the receptor is unfavourable as it loses hydrogen bond donation ability, and the resulting negative charge will result in a charge repulsion between the anion and receptor in the event there are multiple binding sites.

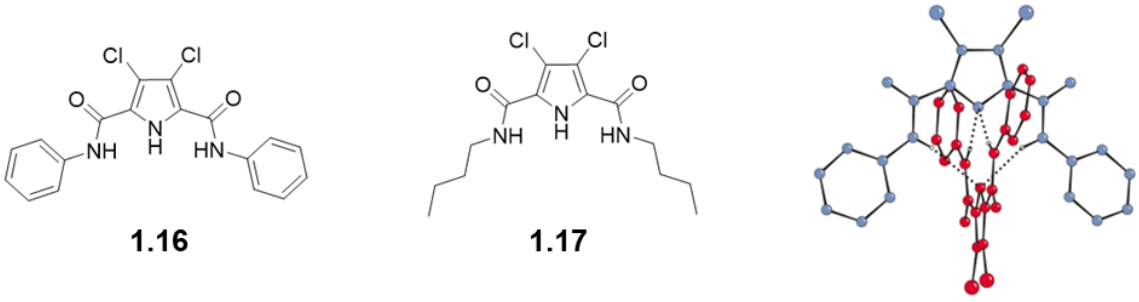

Figure 1.23. Structure of pyrrole-based receptors (left and middle) and crystal structure of narcissistic dimer formed upon deprotonation (right).

For example, treatment of **1.16** (Figure 1.23) with F^-, BzO^-, and $H_2PO_4^-$ in dichloromethane-d_2 resulted in deprotonation of the pyrrole NH.[99] The deprotonated receptor was found to form a what was termed a 'narcissistic dimer', formed from the amide protons of each molecule coordinated to the negative charge of the nitrogen. Using ^1H NMR spectroscopy, **1.17** (Figure 1.23) was observed to coordinate, *via* hydrogen bond formation, to the less basic Cl^- in acetonitrile-d_3, giving an association constant of $K_a = 2015\ M^{-1}$.

In the case of **1.18** (Figure 1.24), synthesised and studied by Caltagirone et al., basic anions F- and BzO- deprotonated the sulfonamide NH protons which led to intramolecular H-bonding from the urea NHs, thus introducing competition with anion complexation by way of intramolecular interactions.[100]

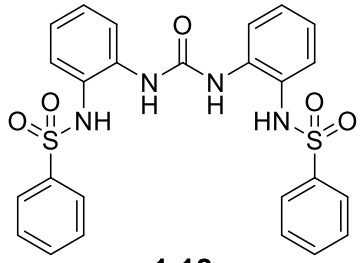

1.18

Figure 1.24. Structure on urea-based receptor with highly acidic sulfonamide NH moieties that deprotonate in the presence of basic anions.

Anions come in a wide range of sizes and geometries, e.g. spherical (halides), trigonal planar (NO_3^-), tetrahedral (SO_4^{2-}), and linear (N_3^-). When trying to create a receptor that displays selectivity for one anion over others, a high degree of design and complementarity is required. An example of this has already been discussed with Schmidtchen's quaternary ammonium cage, **1.18** (Figure 1.17).

Jolliffe and co-workers synthesised two macrocyclic tri/tetrathiourea carbazole-based receptors, **1.19** and **1.20**, and investigated their binding to dicarboxylate species (Figure 1.25).[101] Little difference was found in the binding affinity of these receptors and unsaturated, flexible guests, however, large differences in association constants were found with saturated, rigid guests which was ascribed to size complementarity of the macrocycles' pore size. Dicarboxylates with a short alkyl chain between the two moieties were too short to span the macrocycle pore, resulting in lower interaction. As the macrocycles have some degree of flexibility, larger guests that did not fit properly into the pore were able to bind, however this was not found to be energetically favourable.

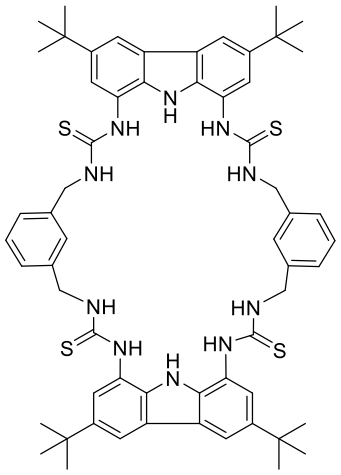

1.19

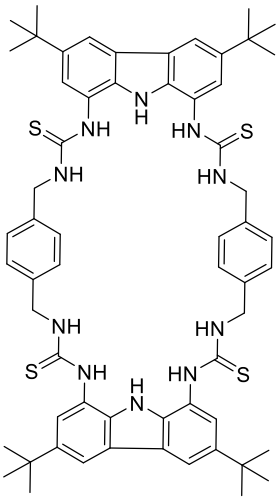

1.20

Figure 1.25. Tetrathiourea carbazole macrocycle used as ditopic receptors for dicarboxylate species.

The nature of the solvent anion-binding takes place in is also a critical component in determining selectivity and anion-binding strength. Polar protic solvents, such as water, can form solvation shells around anions through strong hydrogen bonds. A neutral receptor that relies on hydrogen bonding to bind to a target anion will face competition with water (or other hydroxylic solvents) and the resulting solvation 'net' around the anion. In non-polar solvents, this issue does not arise, yet ion-pairing becomes the new challenge.[102] While in polar solvents the ions are well solvated, reducing the effect of ion pairs, in non-polar solvents the ions are weakly solvated and the receptor must overcome this interaction to successfully bind to its substrate.

The hydrophobicity of anions also plays a role in a receptor's anion binding selectivity. The hydrophobicity of an anion is ordered in the Hofmeister series (Figure 1.26), established in 1888 by examining the effects of different anions and their ability to precipitate proteins out of water.[103] This is particularly of interest in the extraction of anions from aqueous solution and transport of anions across lipid membranes.

organic anions > ClO_4^- > SCN^- > I^- > NO_3^- > Br^- > Cl^- > HCO_3^- > F^-, SO_4^{2-} > HPO_4^{2-}

Figure 1.26. The Hofmeister series of anion hydrophobicity in descending order.

These are just some of the factors that must be considered when designing a synthetic anion receptor. These considerations have led to the identification of several optimal anion binding moieties that show particularly

strong chemical characteristics for anion binding. The following section will outline examples of anion binding structures with a focus on those that exploit hydrogen bonding to interact with their target anion.

1.2.3 Anion Binding Units

While an exhaustive review of the contributions that ureas and squaramides have made to the field of anion recognition is outside the scope of this thesis, contributions of relevance and note will be discussed herein. Both ureas and squaramides are anion binding units that have been the subject of intense investigation over a number of years due to their relative ease of synthesis and tuneable properties such as hydrogen bond donor strength, lipophilicity and solubility.

1.2.3.1 Ureas

Ureas as anion binding units have been the topic of several reviews, illustrating how central this motif has been in anion recognition.[104,9a,105]. In 1992, the use of neutral hydrogen bond donors for anion binding was stimulated by Wilcox, as he demonstrated that urea **1.21** (Figure 1.27) formed a 1 : 1 complex with phosphonates in dichloromethane via hydrogen bond formation.[106]

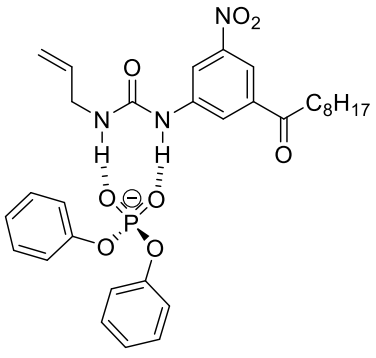

1.21

Figure 1.27. Urea synthesised by Wilcox bound to phosphonate in 1:1 stoichiometry.[106]

Ureas are seen to have many advantageous properties as an anion binding unit. Ureas contain two parallel hydrogen bond donors through the NH

moieties which grants geometric complementarity to a range of oxoanions that contain two oxygen atoms, as seen above (Figure 1.27). Upon complexation to spherical anions, such as halides, ureas form a pseudo six-membered ring. The anion binding strength of ureas can be tuned by varying the R groups attached to either NH moiety, and asymmetrical ureas are also relatively easily produced.

Synthetic routes to ureas often utilise phosgene, phosgene derivatives or similar carbonyl compounds, with the amine of choice. Two equivalents of amine to one equivalent of carbonyl derivative (**a**) will form a symmetrical urea (**c**), while one equivalent of amine reacted with the electrophile of choice will yield a carbamoyl product (**b**). This carbamoyl product can then undergo a second nucleophilic substitution by a different amine to yield an unsymmetrical product (**d**) (Scheme 1.1).

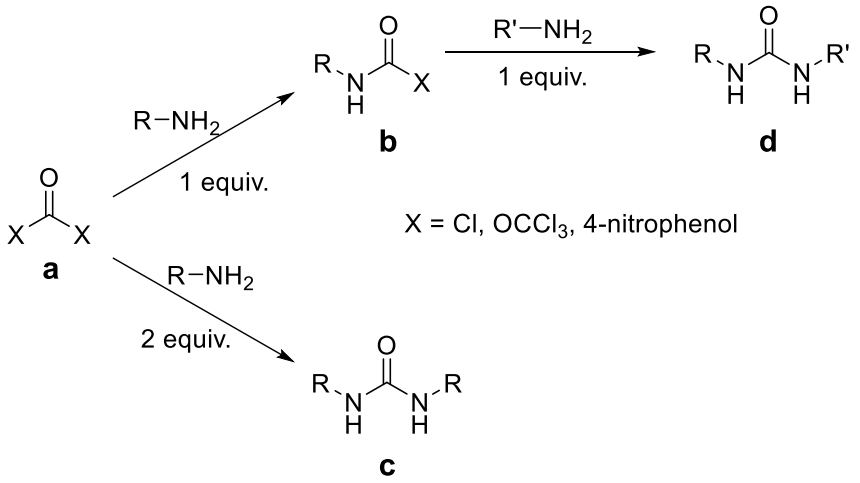

Scheme 1.1. Synthetic pathways to obtain symmetric or asymmetric ureas.

A wide commercial availability of isocyanates has allowed for easier access to unsymmetrical ureas. This synthetic pathway involves the nucleophilic substitution of an amine to the carbon of the isocyanate, which usually yields the product in high yield and purity.[9a]

The use of triphosgene, also known as bis(trichloromethyl) carbonate (BTC), has been extensively used in literature for urea synthesis.[107,108] Triphosgene is considered to be safer to handle than gaseous phosgene due to its crystalline nature. Triphosgene has been utilised to prepare symmetrical and unsymmetrical ureas, even in the presence of sterically 'bulky' groups on the amine of interest and under mild conditions in an aprotic solvent. Scheme 1.2 illustrates the reaction of one mole triphosgene with 3 moles of amine and a non-

nucleophilic base which forms 3 moles of isocyanate. The isocyanate can undergo a second nucleophilic substitution to yield an unsymmetrical urea or a symmetric urea, depending on the desired outcome.

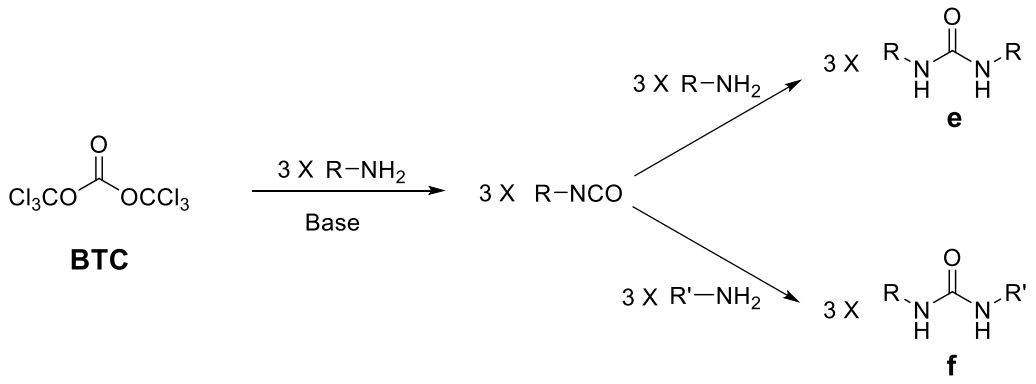

Scheme 1.2. Reaction of triphosgene (BTC) with primary amines to yield symmetric (**e**) and unsymmetric (**f**) ureas.

Ureas have the potential to act as strong anion binding units, especially when working cooperatively. Ureas are commonly conjugated to a scaffold to generate bis-ureas which display high affinity for anion binding.

Davis synthesised and studied a library of cholapod-based receptors which contain varying numbers of hydrogen bond donor systems, including ureas, which cooperatively bound to a range of anions (Figure 1.28).[109] The cholapod scaffold allowed for the preorganisation of the hydrogen bonds donors to align in the same direction. The binding constants were determined by measuring the extraction of a range of tetraethylammonium salts from water into chloroform and verified using ^{1}H NMR spectroscopy.

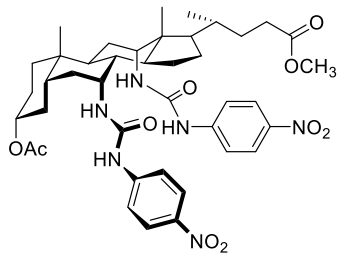

1.22

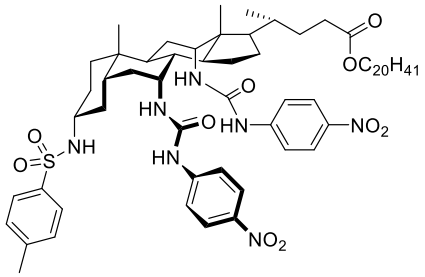

1.23

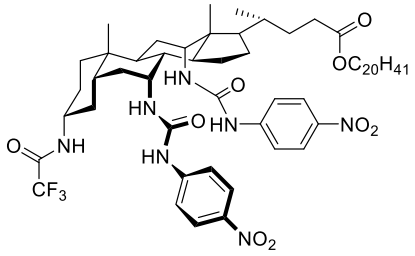

1.24

Figure 1.28. A selection of cholapod anion receptors from the library synthesised by Davis.

The family of cholapod receptors displayed startling results with many of the receptors displaying affinities exceeding $K_a = 10^{10}$ M^{-1} with several even displaying $K_a > 10^{11}$ M^{-1}. Unsurprisingly, the binding affinity increased with increasing numbers of hydrogen bond donors present. Anion selectivity was determined to arise from the geometry of the receptor as opposed to the acidity of the receptor or the basicity of the anion.

Another scaffold commonly employed is the calix[4]arene scaffold, with ureas decorating the lower rim. Puri and Mahajan investigated the properties of urea moieties conjugated to cone and 1,3-*alternate* conformations of calix[4]arenes, **1.25** and **1.26** respectively (Figure 1.29).[110] Interactions with anions were monitored using UV-Vis spectrophotometry and ^{1}H NMR spectroscopy. Receptors **1.25** and **1.26** demonstrated the ability to form hydrogen bonds with the halide anions, nitrate, and acetate. Examination of the binding constants revealed the receptors displayed no anion selectivity. Job plot analysis revealed that **1.25** formed a 1:1 (receptor:anion) complex with all anions tested, while **1.26** formed a 2:1 complex with chloride and a 1:1 complex with the other anions.

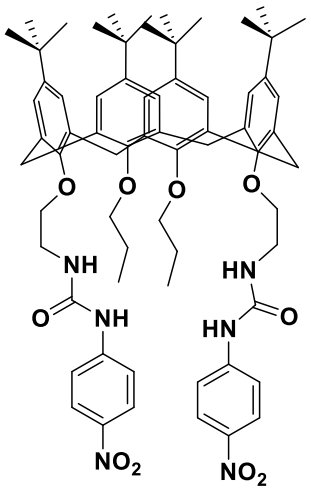

1.25

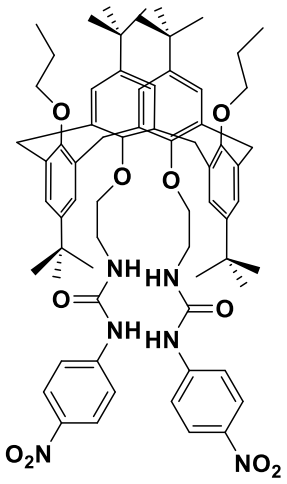

1.26

Figure 1.29. Calix[4]arene-urea conjugates for anion binding.

The anion binding properties of a tripodal urea (Figure 1.30), synthesised by Hossain *et al.,* were investigated using ^{1}H NMR spectroscopy.[111] The receptor formed a 1:1 complex by way of NH···anion interactions with all anions tested, and demonstrated a binding selectivity of $F^- > H_2PO_4^- > HCO_3^- > HSO_4^- > CH_3COO^- > SO_4^{2-} > Cl^- > Br^- > I^-$ in DMSO-d_6. The selectivity for HSO_4^- over SO_4^{2-} was ascribed to acid-base proton transfer to the nitrogen of the tris(3-aminopropyl)amine scaffold which was supported by DFT calculations.

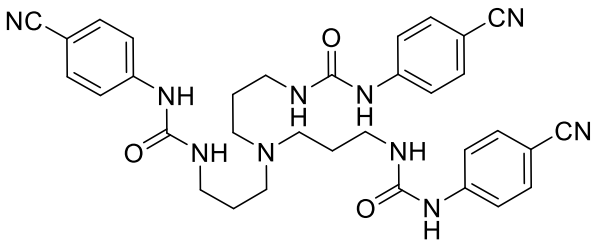

1.27

Figure 1.30. Tripodal urea

1.2.3.2 Squaramides

Squaramides are a more recent addition to the field of supramolecular chemistry and have garnered much attention due to their diverse application in biological and chemical sciences.[112,113]

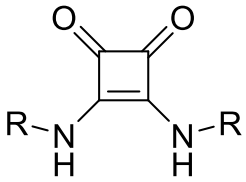

1.28

Figure 1.31. Generic structure of a squaramide.

Squaramides are composed of a cyclobutene ring containing two carbonyl groups neighbouring two NH groups (Figure 1.31). This arrangement of hydrogen bond acceptors and hydrogen bond donors in close proximity gives squaramides various applications in a diverse array of fields such as catalysis, self-assembly, bioconjugation, molecular recognition and transport.[114]

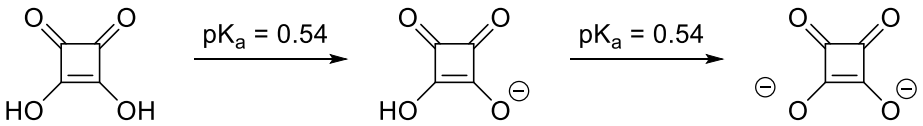

Scheme 1.3. Acidity of squaric acid.

Squaramides are derived from diketocyclobutenediol (otherwise known as squaric acid), which was first synthesised by Cohen *et al*. in 1959. It was noted that the hydroxyl groups displayed high double acidity, easily accommodating a double charge (pK_{a1} = 0.54, pK_{a2} = 3.58) (Scheme 1.3).[115] One year later, West et al. explained this by establishing the aromaticity of $C_nO_n^{2-}$ systems.[116] Squaramides also display this characteristic aromaticity, originating from the delocalisation of the lone pair of electrons of the nitrogen into the cyclobutenedione ring satisfying Hückel's rule (4n + 2 π electrons, n = 0).

Frontera et al. calculated the aromaticity of squaramide **1.29** (Figure 1.32) and its complexes with ammonium cations and carboxylate anions, inspecting bond length, magnetic and energetic properties.[117] Findings indicated that **1.29** had increased aromatic character when acting as a hydrogen bond donor or

acceptor. This offers insight in that squaramides benefit greatly in molecular recognition or self-assembly processes as it gains thermodynamic stability from increased aromatic character.

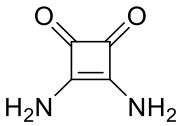

1.29

Figure 1.32. Squaramide used by Frontera *et al*. to investigate aromatic character.

Squaramides exhibit a rigid, planar structure due to the cyclobutenedione ring. While rotation is possible around the C-N bonds, albeit restricted rotation, squaramides exhibit a conformational bias towards the *anti*/*anti* conformation where the NH groups point in parallel directions (Figure 1.33).[118] This conformation is conducive towards anion binding as it allows cooperative binding of the two NH hydrogen bond donors. The *anti*/*syn* conformer is less often observed but it has been recorded in *N*-acyl squaramides where the carbonyl participates in an intramolecular H-bond with the adjacent NH (Figure 1.33).[119] The *syn*/*syn* state has never been observed, likely due to the steric clash that would occur from the amine substituents (Figure 1.33).

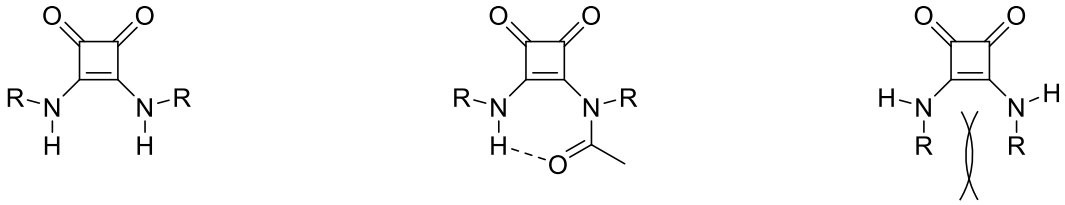

anti/*anti* *anti*/*syn* *syn*/*syn*

Figure 1.33. Possible squaramide conformations.

The utilisation of squaramides in supramolecular chemistry is made all the more attractive due to the relatively facile synthesis of alkyl squarates which can undergo nucleophilic substitution reactions to produce squaramides. The most common synthetic pathway (Scheme 1.4) relies on reactions of dialkoxysquarate derivatives (**g**) with primary or secondary amines that can be performed under mild conditions – room temperature (rt) with a mild base. Symmetrical squaramides (**h**) are generated through an excess of the appropriate amine and when unsymmetrical squaramides (**j**) are the target, a single equivalent of amine is used initially. Upon the first substitution, the now mono-substituted squaramide

(**i**) becomes less reactive due to the donation of electrons from the lone pair of the nitrogen, leading to aromatic gain. Zinc trifluoromethanesulfonate can be used as a lewis-acid catalyst in these reaction types to i) increase the electrophilicity of the squaramide to allow nucleophilic substitution with deactivated amines and ii) prevent the formation of squaraine (**k**) by-products.[120]

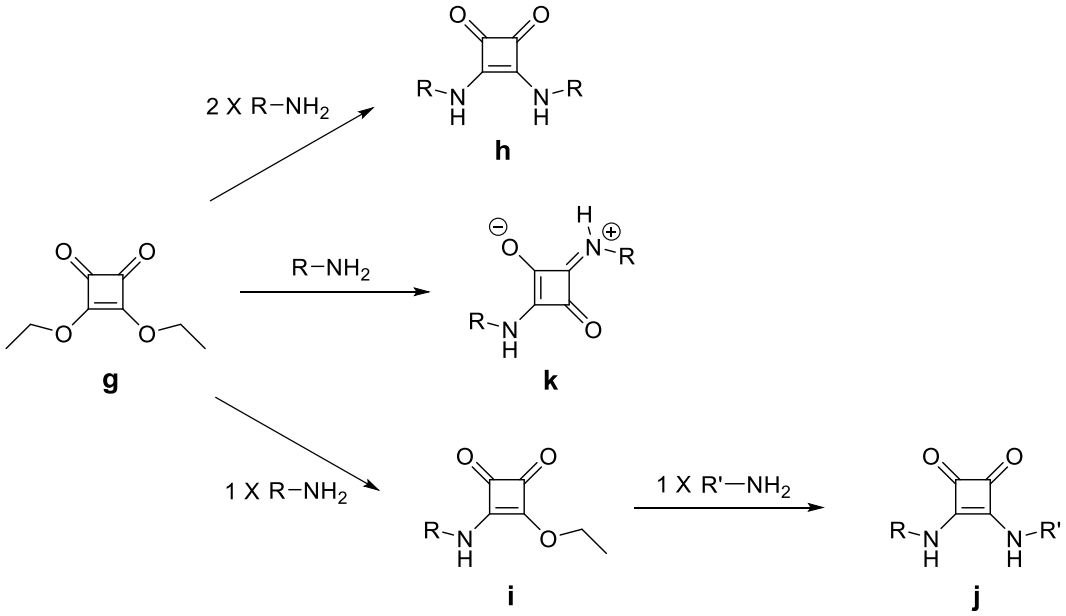

Scheme 1.4. Synthetic pathways to symmetrical and unsymmetrical squaramides, **h** and **j** respectively, and squaraine, **k**.

The early work of Costa and co-workers established squaramides as anion receptors.[121,122] These simple dialkyl-substituted squaramides (Figure 1.34) were capable of forming 1:1 complexes with acetate in highly competitive media. Association constants with anions were determined by ^{1}H NMR titrations which revealed a downfield shift of methylenic protons in addition to the downfield shift of the NH protons upon increasing anion concentrations, indicating weak C-H···anion interactions. The presence of the cationic ammonium moiety in **1.31** increased the association constant by up to ten-fold compared to **1.30**.

Figure 1.34. Chemical structures of the pioneering work of Costa et al. establishing squaramides as anion binding motifs.

Similar to ureas, squaramides are often appended to scaffolds for preorganisation of hydrogen bond donors and incorporating additional hydrogen bond donor motifs. Jolliffe *et al.* synthesised a family of peptide-based anion receptors, **1.32**-**1.38** (Figure 1.35), for SO_4^{2-} recognition.[123] The effect of varying chain length, backbone length, acidity of squaramide NH protons and inclusion of water-solubilising groups were investigated. A strong selectivity for SO_4^{2-} was observed for all receptors in DMSO-d_6 and the addition of hydrophilic TriTEG had no remarkable impact on the aqueous solubility of the receptors.

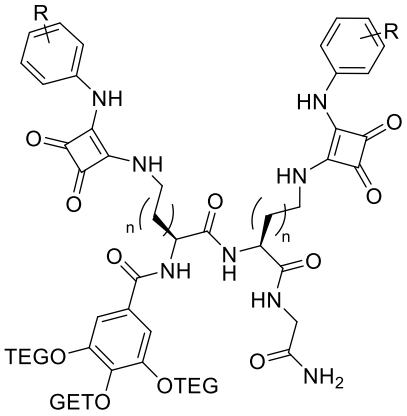

1.32; n = 3, R = *p*-CF_3
1.34; n = 3, R = bis-*m*-CF_3
1.35; n = 1, R = *p*-CF_3
1.36; n = 1, R = bis-*m*-CF_3

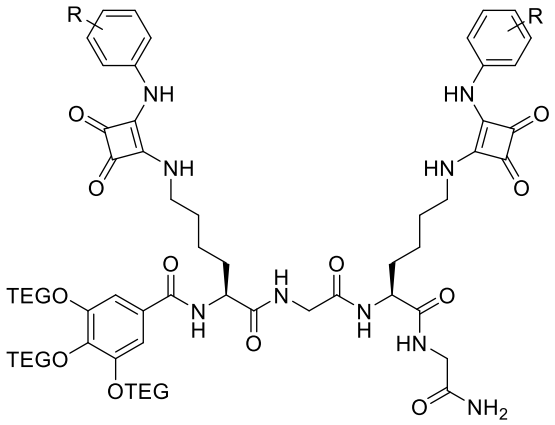

1.37; n = 3, R = *p*-CF_3
1.38; n = 3, R = bis-*m*-CF_3

Figure 1.35. Chemical structures of squaramide-based SO_4^{2-} receptors, **1.23**-**1.28**.

Continuing their work on cholapod-based anion receptors, Davis and co-workers synthesised squaramide analogues, **1.39** – **1.44** (Figure 1.36), to their urea examples discussed previously (Figure 1.28).[124] Similar to the urea analogues, squaramides placed in the axial position benefitted from preorganisation of the hydrogen bond donor motifs. These receptors displayed high selectivity for acetate over other anions (Cl^-, Br^-, I^-, and NO_3^-) while also displaying higher affinities than the previously studied ureas and thioureas with binding constants exceeding Ka = 10^{14} M^{-1}.[125]

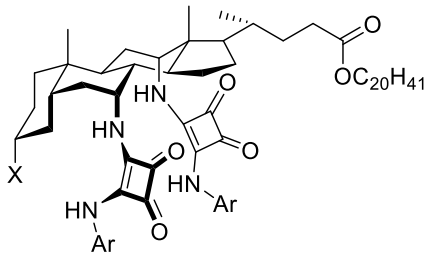

1.39; Z = OAc, Ar = 4-$MeOC_6H_4$
1.40; Z = OAc, Ar = Ph
1.41; Z = OAc, Ar = $CF_3C_6H_4$
1.42; Z = OAc, Ar = 3,5-$(CF_3)_2C_6H_3$
1.43; Z = $NHCOCF_3$, Ar = 4-$CF_3C_6H_4$
1.44; Z = $NHCOCF_3$, Ar = 3,5-$(CF_3)_2C_6H_3$

Figure 1.36. Family of squaramide-based cholapod receptors displaying higher binding constants than urea analogues.

1.2.3.3 Squaramides vs. Ureas

The above work by Davis and co-workers is not the only example of squaramides acting as higher affinity anion receptors than analogous hydrogen bonding motifs, indeed, the seminal report from the lab of Fabrizzi demonstrated that squaramides are able to challenge ureas as anion binding motifs (Figure 1.37).[126]

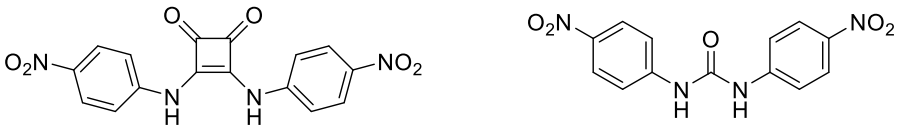

1.45 **1.46**

Figure 1.37 Chemical structure of analogous squaramide and urea receptors reported by Amendola *et al*. which established squaramides can challenge ureas as hydrogen bonding units.

^{1}H NMR studies showed that **1.45** formed 1:1 complexes with halide ions there were one to two orders of magnitude more stable than the corresponding urea-based receptor, **1.45**. X-ray diffraction studies on chloride and bromide complexes of **1.45** revealed four hydrogen bonds to the anion – two originating from the squaramide NH moieties and two originating from the *ortho*-H of the phenyl substituents. The squaramide receptor was found to form complexes with oxoanions (NO_2^-, NO_3^-, $H_2PO_4^-$, HSO_4^-) of comparable stability to that of the urea analogue. **1.45** shows 1:1 hydrogen-bond complexes with basic anions F^- and CH_3COO^-, while **1.46** shows deprotonation with F^- but not with CH_3COO^-.

Squaramides have also been reported to outperform thioureas, as reported by Jolliffe *et al*. when they examine peptide-based thiourea and squaramide receptors (Figure 1.38).[127] While the stereochemistry of the peptide scaffold proved to have no effect on the binding affinity of anions, the squaramide receptors (**1.48**, **1.50**, and **1.52**) displayed anion binding constants far higher than that of their thiourea counterparts. All of the reported receptors displayed an unusually high affinity for SO_4^{2-} in DMSO-d_6 (0.5% H_2O) with a $K_a > 10^4$ for receptors **1.47** and **1.48,** showing a high selectivity for SO_4^{2-} over halide anions and oxoanions such as AcO^-, BzO^-, $H_2PO_4^-$, HSO_4^- NO_3^-, and TsO^-.

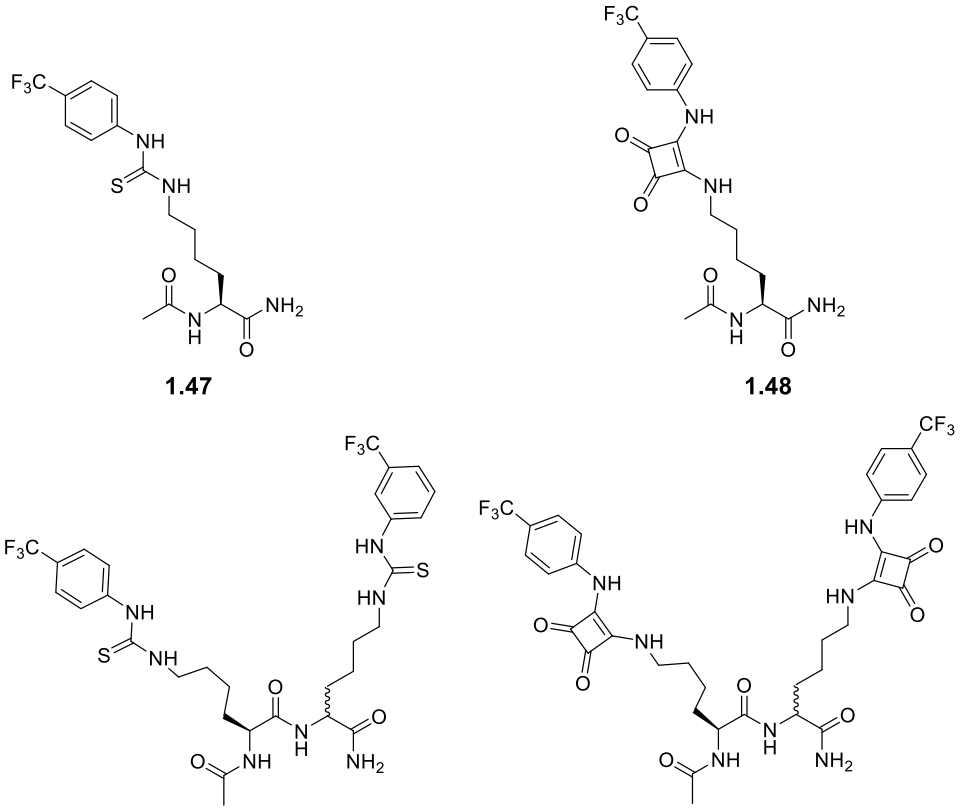

Figure 1.38 Structure of peptide-based thioureas and squaramide receptors investigated by Elmes *et al*.

Gale *et al*. demonstrated that squaramides not only display higher anion binding association constants compared to their urea analogues but also exhibit better anion transport abilities (Figure 1.39).[128]

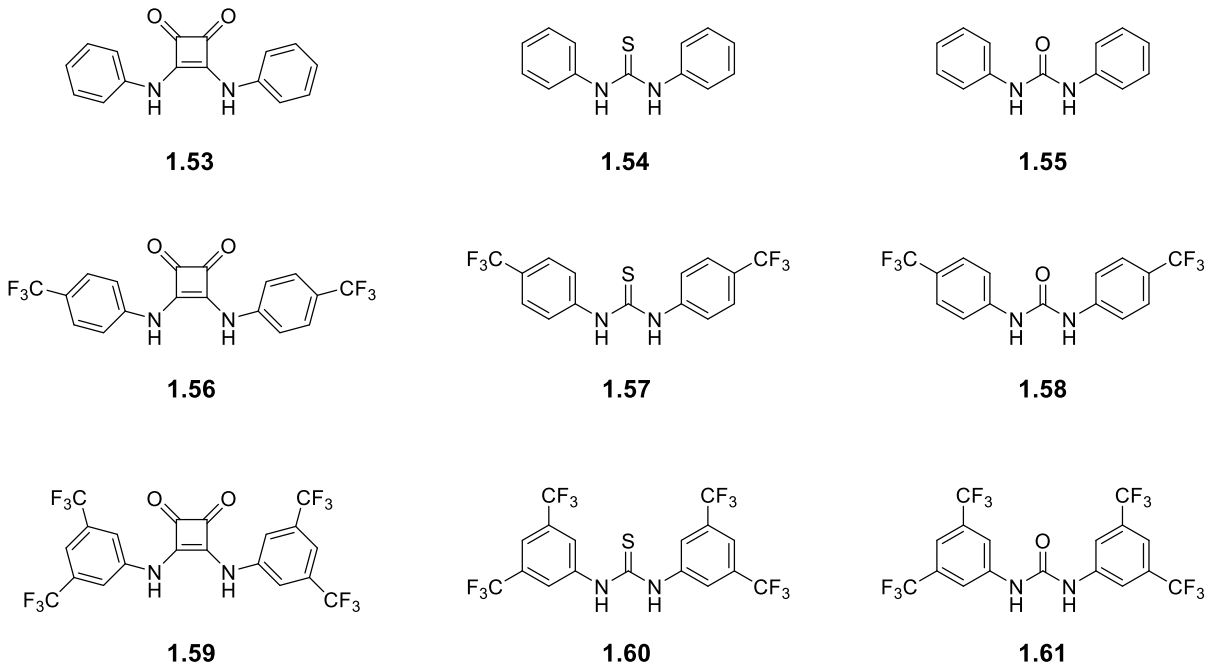

Figure 1.39. Structures of squaramide, thiourea and urea analogues Busschaert et al. used to compare anion binding and anionophoric activity.

Binding constants were determined using ^{1}H NMR spectroscopy and anion transport ability were assessed using POPC liposomes and a chloride selective electrode. The squaramide analogues displayed anion binding affinities one order of magnitude greater than those of their urea and thioureas analgoues while also displaying considerably lower EC_{50} values in Cl^-/NO_3^- exchange assays (see Table 1.1)

Table 1.1 Summary of chloride binding (K_a) and anion transport (EC_{50}) abilities of compounds **1.35** – **1.43**. [(a)]Association constant with receptors and Bu_4NCl in DMSO-d_6/0.5% H_2O at 298 K. [(b)] Concentration of transport (mol% carrier with respect to lipid) required to obtains 50% chloride efflux in 270s during Cl^-/NO_3^- assays. [(c)] Compound was not active enough to perform Hill analysis.

Compound	K_a [M^{-1}] [a]	EC_{50} [mol%] [b]
1.53	260	1.38
1.54	15	-[c]
1.55	31	-[c]
1.56	458	0.06
1.57	43	0.22
1.58	75	0.42
1.59	643	0.01
1.60	41	0.16
1.61	88	0.30

The authors postulated that the superior binding ability of squaramides arises from the increase in thermodynamic stability that occurs when squaramides bind to the anion, as discussed previously in this section.

It was first considered that the superior anion transport abilities demonstrated by the squaramides was due to increased lipophilicity. However, TPSA (total polar surface area) and Ghose–Crippin log*P* calculations determined that squaramides were in fact less lipophilic than urea and thiourea counterparts, which had also been proposed by other researchers.[113] The greater anionophoric ability was attributed to the greater anion binding properties of squaramides.

1.3 Anion Transport

Knowing the importance on anion transport in human biology and the diseases that stem from malfunctioning anion channels (as discussed in Section 1.1.3), it is no of surprise that anion transport became a burgeoning field in supramolecular chemistry. Synthetic receptors were designed and created in the hopes of creating small drug-like molecules that can transport anions across the plasma membranes of cells. The approach may find application to either replace malfunctioning transport proteins in patients suffering from channelopathies or, alternatively to disrupt cellular anion homeostasis and bring about cytotoxicity for cancer drug development.

1.3.1 What Makes a Good Anionophore?

Research investigating the features needed for effectual anionophores have revealed multiple factors that a play a role in determining anion transport activity. Quesada and Gale *et al*. performed a quantitative structure activity relationship (QSAR) study by varying the substituents on a series of 1-hexyl-3-phenylthioureas, **1.62** (Figure 1.40), to elucidate the factors that impact their anionophoric activity.[129] The study varied substituents in the *para*- position of the phenyl ring and anion binding and transport experiments were performed to examine the effects of the substituent variations. ^{1}H NMR experiments were used to determine the binding constants of the receptors and anion transport activity

was determined using POPC vesicles and a chloride-selective electrode to monitor Cl^- efflux from the vesicles.

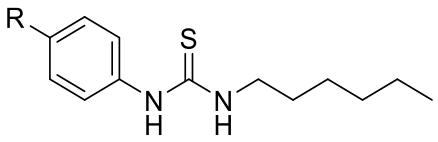

1.62

Figure 1.40. Generic structure of 1-hexyl-3-phenylthiourea in the QSAR study of Gale.

Their findings showed that in increase in lipophilicity led to an increase of anion transport activity. As transport of anions relies of the partitioning of the receptor through the lipid membrane, an effective anion transporter needs to be able to partition into the membrane when passing from one aqueous phase to another, carrying the inherently lipophobic anion with it. Therefore, an increase in lipophilicity increased the partitioning of the transporters into the lipid membrane, consequently increasing the anion transport activity. This effect has been reported previously, where Quesada demonstrated that an increase of alkyl chain length led to an increase of anionophoric activity in tambjamine-based anion receptors.[130] Indeed, further findings from the collaboration of Quesada and Gale showed there to be an optimal range of lipophilicity when considering tambjamine-based transporters.[130,131] Davis confirmed the importance of lipophilicity when he reported the findings of his own SAR study, where a positively charged receptor displayed limited anion transport activity compared to analogous neutral systems.[132]

The QSAR study from Quesada and Gale *et al*. also highlighted that an increase of anion binding ability correlated to an increase of anion transport ability, also. Receptors decorated with strongly electron-withdrawing groups, such as NO_2 or SO_2Me, displayed the highest anion transport ability with low EC_{50} values and inversely receptors decorated with electron-donating groups, such as OMe, displayed lower anionophoric activity with higher EC_{50} values.

When choosing which substituents to exploit in the design of an anion transporter, one can look to Hammett constants which act as a good quantifier of electron-withdrawing effects of substituents.[133] It has been documented previously that the presence of strong electron-withdrawing groups leads to stronger hydrogen bond formation to anions.[134,135] However, the inclusion of

strongly electron-withdrawing groups can also hinder receptor-anion complex formation as, mentioned previously, hydrogen bond donors with a low pK_a can undergo deprotonation when interacting with an anion, limiting their anion binding and transport capabilities.

While only contributing to a smaller extent, molecular size also impacts anion transport. Larger molecules display slower diffusion across lipid membranes thereby reducing anion transport. Smaller molecules diffuse quicker across membranes consequentially increasing the rate of anion transport.

1.3.2 Squaramides as Anion Transport Units

Gale et al. were the first to report squaramides as active anion transport units, **1.53**, **1.56**, **1.59**.[128] Investigation into the anion transport process of these simple *N*-diphenyl squaramides revealed that they acted via a Cl^-/NO_3^- antiport (anion exchange) process. Using NaCl loaded POPC vesicles suspended in an isotonic $NaNO_3$ solution, chloride efflux was observed using a chloride-selective electrode. When the external anion was substituted to SO_4^{2-}, no Cl^- efflux was observed. This is due to the highly hydrophilic nature of the SO_4^{2-} anion which precludes it from transport across a lipid membrane. However, when a pulse of HCO_3^- was added to the SO_4^{2-} external solution, release of Cl^- from the vesicles is observed. The dependence on the nature of the external anion indicated an antiport process. Squaramides were determined to act as mobile carriers, as opposed to forming ion channels, after U-tube experiments were able to verify that the squaramides facilitated anion transport through the organic phase.

Moving beyond simple monoatomic anionic species, Gale *et al*. exploited the squaramide motif to transport glycine across lipid membranes.[136] Creating a system of squaramide **1.59** and 3,5-bistrifluoromethylbenzaldehyde (BTFMB), the authors postulated that the squaramide NHs complex to the glycine carboxylate group while the amine of glycine forms an imine or hemiaminal with BTFMB, thus facilitating reversible binding and release of the amino acid. This two-part system increases the lipophilicity of glycine, allowing for transport across the non-polar lipid membrane. Influx of glycine was monitored using a novel fluorescence assay involving a Cu^{2+}-calcein complex, where copper quenches

the fluorescence of calcein but sequestration of the copper by glycine restores calcein fluorescence (Figure 1.41).

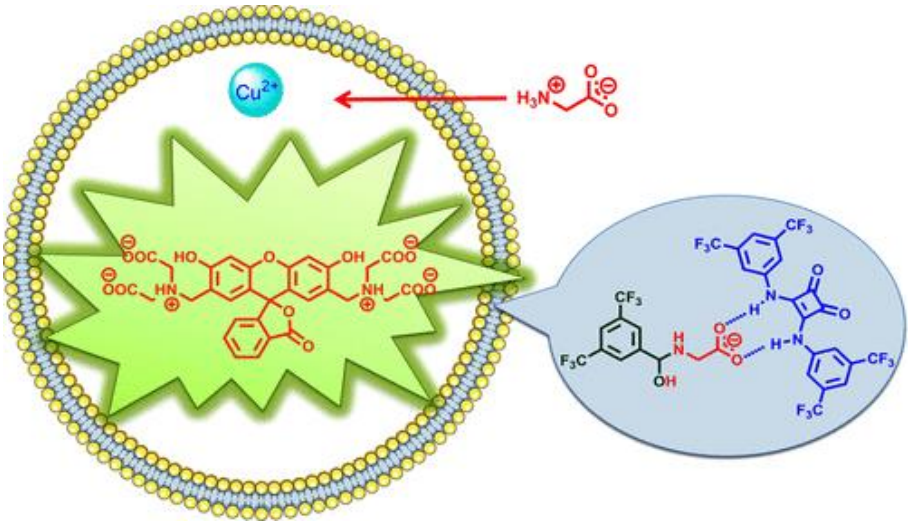

Figure 1.41. Schematic representation of two-part system with the capability of amino acid transport mediated by compound **1.41** and BTFMB.

The development of synthetic anionophores have inevitably led to their application in diverse areas of supramolecular chemistry from anion extraction[7,137] to fluorescent chemosensors,[138] but predominantly they have been investigated for biologically relevant uses such as drug development.[139,9d]

1.3.3 Applications of Anion Transport

In 2014, Sessler and Shin demonstrated the ability on ionophores, **1.63** and **1.64**, to induce apoptosis by facilitating Cl^- transport within a range of cell lines (Figure 1.42).[140] **1.63** and **1.64** were observed to influx Cl^- coupled with Na^+ into the cellular environment. The increase of intracellular chloride and sodium concentrations, resulting in an enhancement of intracellular ROS levels causing the release of cytochrome c from the mitochondria, in turn leading to apoptosis via caspase-dependent apoptosis. This finding further opened the door to the field of anion transport, giving ionophores clinical potential.

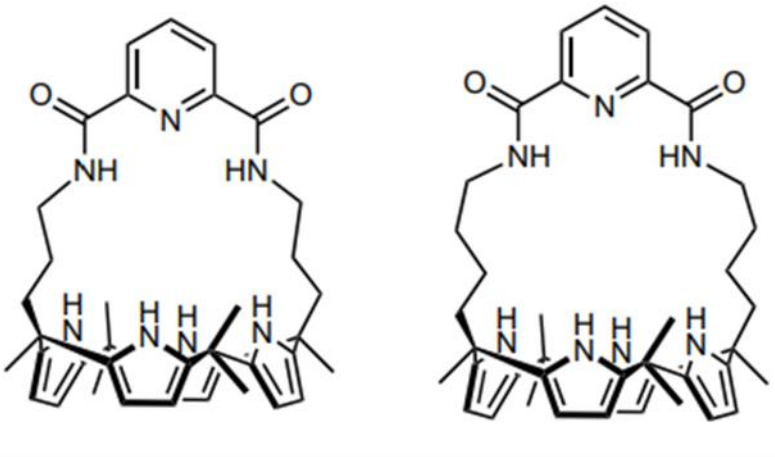

Figure 1.42. Structures of two pyridine diamide-strapped calix[4]pyrroles capable of inducing apoptosis in cells.

Research investigating the clinical potential of anionophores continued when Gale et al. examined the effect of squaramide-based anion transporters, **1.56** and **1.65** – **1.69**, on several mammalian cell types.[140] The anionophoric activity was first investigated using POPC vesicles and a chloride-selective electrode to monitor Cl^- efflux. Squaramide **1.56** was demonstrated to be the most efficient transporter, followed by **1.65** and **1.66**. Tripodal receptors **1.67** and **1.68** did not display any anionophoric activity which was attributed to their binding affinity for Cl^- to be too high, inhibiting the release of Cl^-.

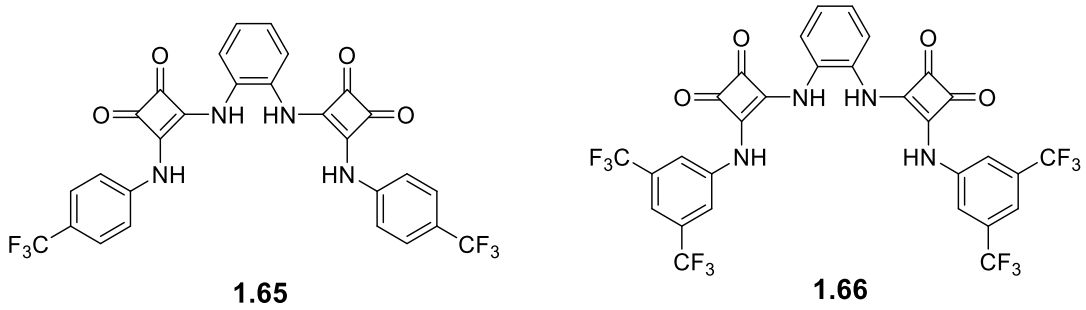

Figure 42. *o*-phenylenediamine-based squaramide receptors, **1.46** and **1.47**.

1.56, **1.65** and **1.66** were ascertained to act as Cl^- transporters with concomitant channel-mediated Na^+ transport in Fishcher rat thyroid epithelial (FRT) cells. In HeLa and A549 cells, the anionophores demonstrated the ability to induce caspase-dependent apoptosis by perturbing Cl^- concentrations intracellularly. Transporter **1.56** alone displayed the ability to efflux Cl^- out of lysosomes, decreasing lysosomal Cl^- concentrations this increasing the pH. This

effect led to the reducing of lysosomal enzyme activity, disrupting autophagy ultimately leading to apoptosis.

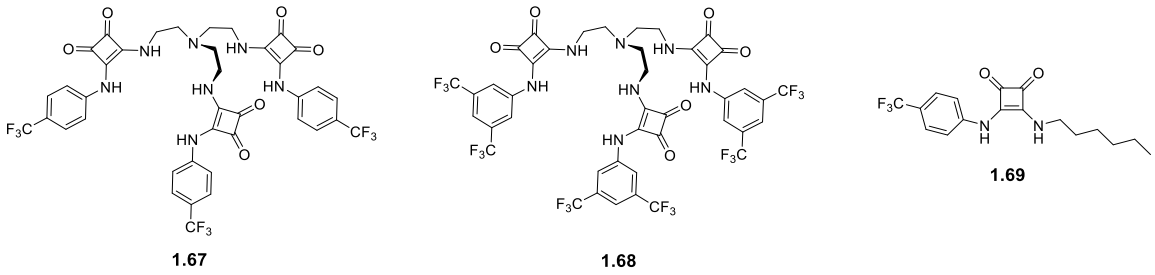

Figure 43. The least active anionophores described in the work of Busschaert et al.

The above sections have sought to give a background to the field of anion recognition and transport with a focus on neutral receptors that take advantage of hydrogen bonding. From the lessons learned from the vast amount of work already conducted in this area, it is clear that there are still several problems that still need to be solved and further work is required in the design of simple, efficient and selective anion receptors and transporters. This thesis will aim to expand the repertoire of anion binding receptors and seeks to create more diversity in receptor design. The following section will lay out the overall aims for the thesis and summarise the work discussed in each chapter.

1.4 Aims

Anion recognition and transport continues to be a rapidly developing field in supramolecular chemistry given the ubiquitous nature of anions, their crucial role in human biology and the impact of channelopathies on patient outcomes. While many advancements have been made in the past number of years which has highlighted the clinical applications of potent anionophores, there are many avenues left unexplored. The aim on this research is exploit the squaramide motif in developing new motifs in anion recognition and transport, explore their sensing abilities and to exert spatiotemporal control over anionophoric activity.

The first objective was to create a new anion recognition motif based on the squaramide moiety by including an *N*-acyl linkage between the squaramide and its substituent (Chapter 2). We postulated that this linkage would vary the pK_a of the squaramide NH which has been established to correlate to the hydrogen bond strength. With a family of these receptors in hand, pK_a determination, anion binding and transport studies would be carried out to investigate their physical properties and determine their efficacy.

The second objective featured the investigation in creating stimuli-responsive anionophores, few examples of which exist in the literature (Chapter 3). We envisaged tertiary squaramides with an enzyme-responsive trigger would allow us to exert spatiotemporal control over anionophoric activity.

The final aim of this research was to develop a family of squaramide-based chemosensors and examine the effect of electron-withdrawing and electron-donating groups have on anion selectivity, as well as further probing the applications of squaramides as building blocks in anion recognition and sensing (Chapter 4).

Chapter 2

Amido-squaramides: A New Moiety in Anion Recognition and Transport

2 Amido-squaramides: A New Moiety in Anion Recognition and Transport

2.1 Introduction

Squaramides have been proven to be highly efficient and effective anion receptors and transporters, as discussed in Chapter 1. The existence of their potent hydrogen bond donor NH groups, coupled with an increase in thermodynamic stability upon anion complexation, ranks squaramides above other anion binding and transport motifs.[128]

While squaramides have been appended to many different scaffolds with the aim of increasing their anion binding affinity,[141] optimising the geometry of their hydrogen bond donors,[124] or to grant selectivity to the receptor,[123,142,127] there are many examples of simple, disubstituted squaramides that achieve high binding constants and display high rates of anionophoric activity.

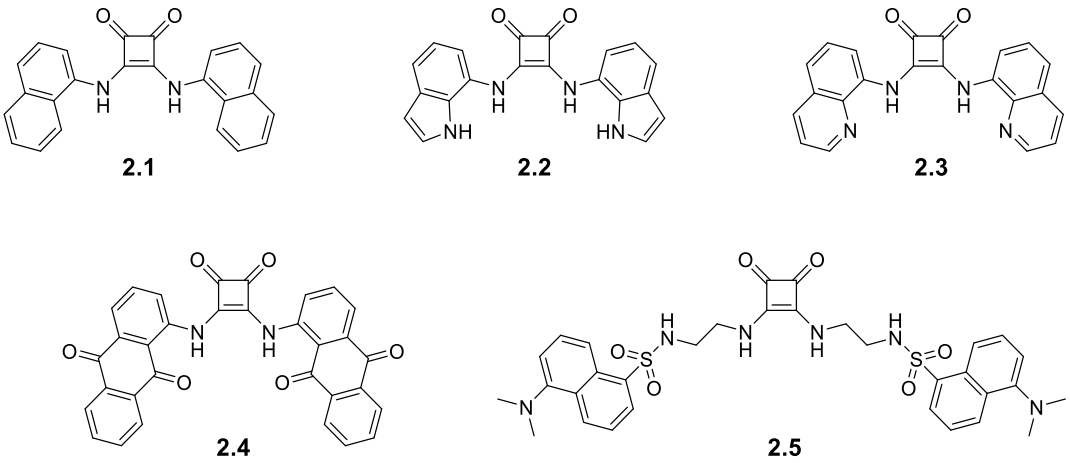

Figure 2.1. Series of acyclic squaramides synthesised by Picci *et al*.

Caltagirone *et al*. synthesised a family of acyclic, symmetric squaramides receptors with additional H-bond donor groups and assessed their affinity and transmembrane transport of anions (Figure 2.1).[143] All receptors underwent deprotonation with basic anions F^- and CN^-, with only receptors **2.1**, **2.2** and **2.5** forming anion : receptor complexes. Of these receptors, **2.2** displayed the highest affinity for the anions tested (AcO^-, BzO^-, $H_2PO_4^-$, and Cl^-) with binding constants reaching as high as $K_a > 10^4\ M^{-1}$ for Cl^-. Remarkably, **2.2** was also able to complex Cl^- in highly competitive solvent mixtures, DMSO-d_6 with 10% and 25% H_2O, surpassing the binding affinity of urea analogues.[144] The domination of **2.2**

continued in the anion transport assays, where the receptor displayed EC_{50} values as low as 0.55 μM, illustrating the benefit of additional hydrogen bond donor groups.

A squaramide-linked bis(choloyl)-conjugate (Figure 2.2) was synthesised by Chen *et al*. and its anionophoric activity was determined using EYPC-based vesicles in conjunction with a fluorescent pyranine assay and chloride-selective electrode measurements.[145] Potent anionophoric activity was observed, with an EC_{50} value of 3.82 ± 1.18 mol %, and it was found that Cl^- efflux was dependent on the external anion, suggesting that **2.6** acts as an anion-cation co-transporter as opposed to an anion-anion antiport process as demonstrated by other squaramide examples.[128]

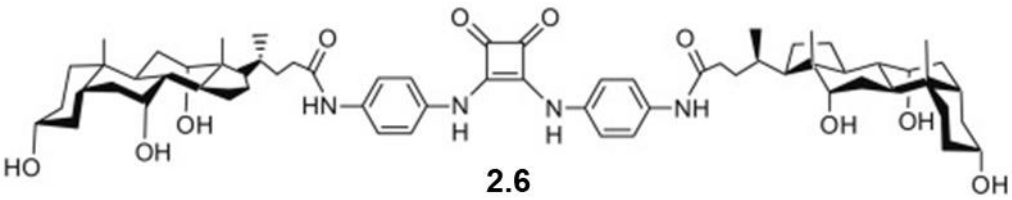

2.6

Figure 2.2. Bis(choloyl)-conjugated squaramide synthesised by Deng *et al*.

Gale *et al*. reported a family of 1,8-naphthalimide conjugated squaramides that acted as anion receptors and transporters, as well as the ability to act as cellular imaging agents, Figure 2.3.[146] The receptors were found to form 1 : 1 complexes with Cl^- and unsurprisingly, displayed anion binding constants in the order of the strength of their electron-withdrawing substituents; **2.7** > **2.9** > **2.8** > **2.10**. While little interaction was with NO_3^-, the receptors showed a high affinity for $H_2PO_4^-$ with the more basic receptors, **2.7** – **2.9**, reaching binding constants of $K_a > 10^4\ M^{-1}$. The same order was observed in the anion transport assays as in the anion binding affinity with the squaramide bearing the bis-CF_3 moiety reaching an EC_{50} value of 0.15 mol %, far lower than the urea analogue reported previously.[147] All receptors demonstrated the ability to perform antiport processes with Cl^-/NO_3^- but also symport processes with H^+/Cl^- by dissipating a pH gradient across a cell membrane.

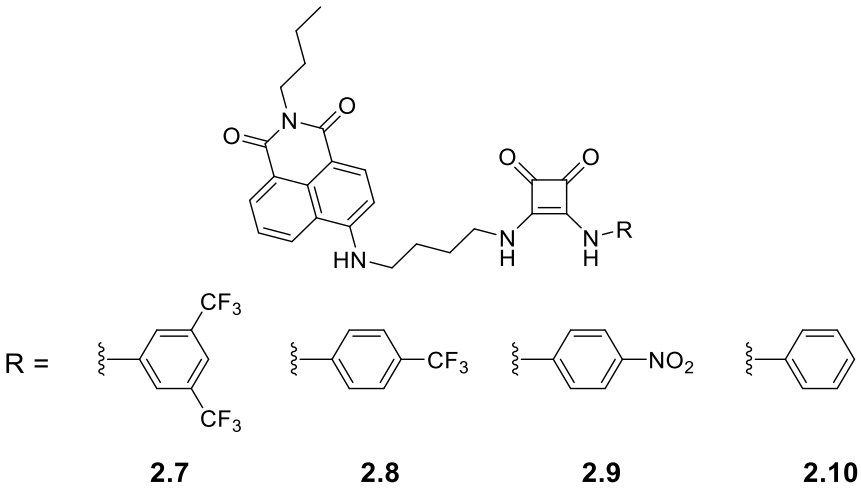

Figure 2.3. Family of fluorescent 1,8-naphthalimide conjugated squaramides.

The vast majority of squaramide-based molecules reported in the literature to date display either *N*-alkyl or *N*-aryl substituents, as seen in all of the examples discussed thus far. Examples of squaramides containing other linkages are scarce.

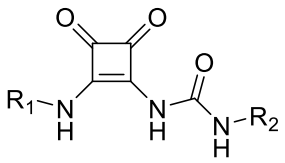

2.11: R_1 = Bu, R_2 = cyclohexyl
2.12: R_1 = R_2 = Bu

Figure 2.4. *N*-Carbamoyl squaramides capable of self-assembly.

For example, Early work by Ashton *et al*. produced *N*-carbamoyl squaramides capable of forming hydrogen-bonded dimers, Figure 2.4.[119] These squaramides underwent self-assembly through intermolecular hydrogen bonds and while also displaying intramolecular hydrogen bonds between the squaramide NH and the ureido carbonyl (Figure 2.5). These compounds were not screened for their anion binding affinity.

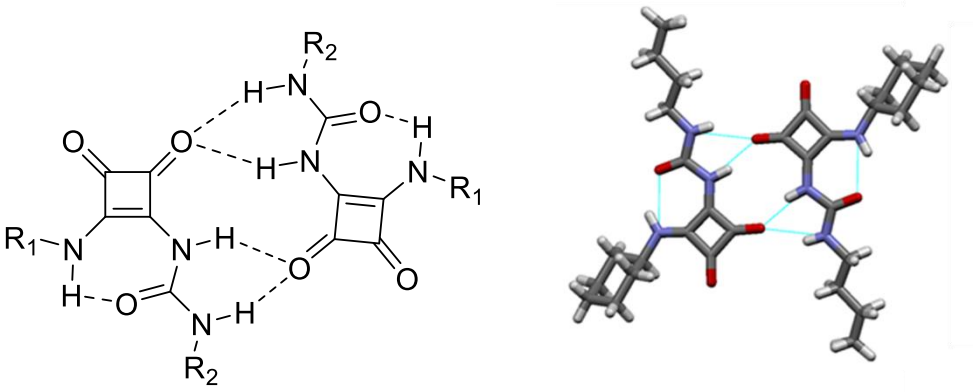

Figure 2.5. Dimer formation of *N*-carbamoyl squaramides (left). Crystal structure of **2.11** dimer (right).

Cheng *et al*. synthesised a series of *N*-*tert*-butyl sulfinyl squaramide receptors and examined their anion binding constants using ^{1}H NMR spectroscopy (Figure 2.6).[148] These receptors contained a direct linkage from the squaramide NH to a sulfoxide moiety. Due to the acidity of the sulfinyl group, the receptors displayed anion binding constants higher than previously reported simple squaramides in DMSO-*d*$_6$,[128] with binding constants for Cl^- reaching K_a = 820 ± 67 M^{-1} for receptor **2.15**. The increased anion binding constants were not due to the increased acidity alone; a downfield shift of the protons of the *tert*-butyl group in the ^{1}H NMR experiments, single-crystal analysis, and DFT calculations revealed weak C-H hydrogen bond formation with Cl^-. These results highlighted how the importance of the squaramide NH acidity, and the overall structure of the receptor can have a major influence of anion binding ability.

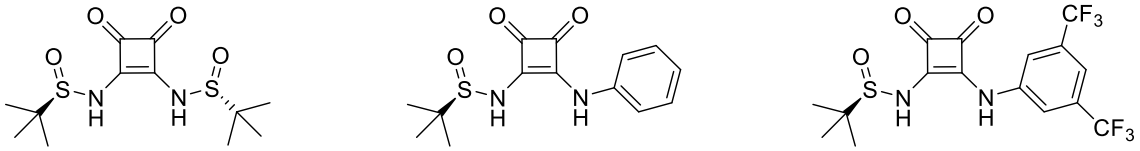

2.13 **2.14** **2.15**

Figure 2.6. Structures of N-tert-butyl sulfinyl squaramide receptors.

As seen in the examples above, simple, disubstituted squaramides have been shown to be highly efficient anion receptors and transporters. As seen in the example of Cheng *et al*. by linking a strongly electron-withdrawing group directly to a squaramide, a highly effective anion receptor is produced. However, the predominant substituents of squaramides reported in literature contain either an *N*-alkyl or *N*-aryl linkage. The lack of diversity when it comes to *N*-linkages in

squaramides is an opportunity for the exploration of novel moieties and the effect they might have on anion recognition and transport activity.

2.2 Chapter Objective

The objective of this chapter is to synthesise a family of disubstituted squaramides, where one substituent displays an *N*-aryl linkage as seen in previous literature examples and the second substituent displays a *N*-amide linkage to an aryl group, which we termed 'amido-squaramides' (Figure 2.7). By varying the substituents of these phenyl moieties, we expected to investigate the effect on the amido-squaramides' anion binding ability and anionophoric activity. These substituents would include moieties which have been reported to increase anion binding and anion transport abilities of receptors (*e.g.* $-CF_3$ and $-NO_2$) and halide substituents to widen the scope.

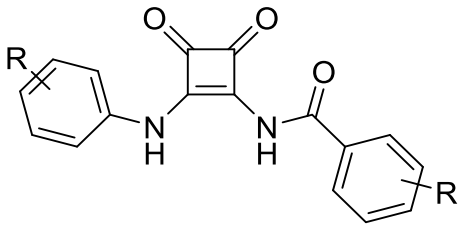

Figure 2.7 Generic structure of amido-squaramides.

We envisaged that this *N*-amide linkage would increase the acidity of the squaramide NH, consequently decreasing its pK_a, due to the electron-withdrawing effect of the carbonyl. According to literature precedent, this decrease in pK_a should result in higher anion binding constants and anionophoric activity compared to the aryl derivatives previously reported. To confirm this, we wished to determine the pK_a of the squaramide NH groups and subsequently evaluate their ability to bind and transport anions using a range of spectroscopic techniques. What follows are the results of both the synthetic study of these compounds in addition to a spectroscopic and computational analysis of their anion recognition ability and preliminary analysis of their anionophoric activity.

2.3 Synthesis and Characterisation of Amido-Squaramides

The synthetic route to amido-squaramides is a multi-step pathway involving several squarate intermediates before obtaining an amido-squaramide (Scheme 2.1).

The initial step is the synthesis of 3,4-diethoxy-3-cyclobutene-1,2-dione, otherwise referred to as diethyl squarate, **2.17**. Diethyl squarate is one of the most common alkoxy derivatives of squaric acid used in squaramide synthesis and is used almost exclusively as the starting point for the synthesis of squaramide derivatives. **2.17** was synthesised using methods adapted from those reported by Liu *et al*.[149] 3,4-diethoxy-3-cyclobutene-1,2-dione, **2.16**, also known as squaric acid, was reacted with triethyl orthoformate to form **2.17** with a yield of 91%. **2.17** was then converted to amino-squarate, **2.18**, using a method adapted from Ashton *et al*.,[119] where diethyl squarate was treated with a 20% ammonium in ethanol solution to yield **2.18** in 71% yield.

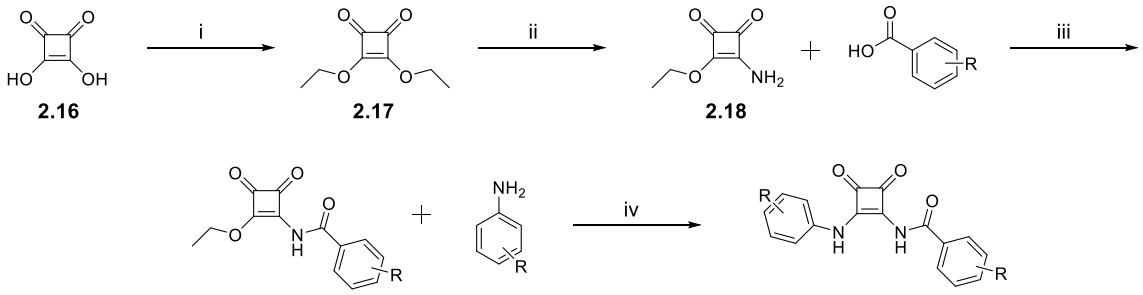

2.19: R = H
2.20: R = 4-CF_3
2.21: R = bis-3,5-CF_3
2.22: R = 4-NO_2
2.23: R = 2-iodo
2.24: R = 4-iodo
2.25: R = 3,4-dichloro
2.26: R = 4-chloro

2.27: R = H
2.28: R = 4-CF_3
2.29: R = bis-3,5-CF_3
2.30: R = 4-NO_2
2.31: R = 2-iodo
2.32: R = 4-iodo
2.33: R = 3,4-dichloro
2.34: R = 4-chloro

Scheme 2.1 Synthetic pathway to amido-squaramides. *Reagents and conditions:* i) triethyl orthoformate, EtOH, 80°C, 72 h, 91%; ii) 20% ammonium in ethanol, EtOH, rt, 18 h, 70%; iii) EDCI.HCl, DMAP, MeCN/DMF (anhydrous), N_2, rt - 80°C, 18 h, 10 - 83%; iv) $Zn(OTf)_2$, MeCN/DMF, 80° C, 3 - 18 h. 10 - 71%.

The conditions for the synthesis of amido-squarates **2.19** - **2.26** were optimised by using the synthesis of **2.19** as a model reaction. In the first instance, PyBOP was used as the coupling reagent to form an amide linkage between **2.18** and benzoic acid. LCMS analysis suggested some conversion to the desired product however, purification proved difficult due to incomplete separation of the product and the by-products of the coupling reaction during flash

chromatography. Pure product was obtained with a yield of 42%. TBTU was then trialled as a coupling reagent, however, the same difficulties persisted during purification, however, a slight increase of yield was observed at 51%.

Moving away from benzotriazol-1-yl based coupling reagents, EDCI.HCl was employed to mediate the coupling of **2.18** and benzoic acid (Scheme 2.2). DMAP deprotonates benzoic acid, increasing its nucleophilicity, which allows the carboxylate to attack the electrophilic carbon of the diimide, forming an activated ester. Nucleophilic substitution of amino-squarate, **2.18**, and the activated ester forms a tetrahedral intermediate which then collapses to form the desired amido-squarate, **2.19**, and a urea by-product.

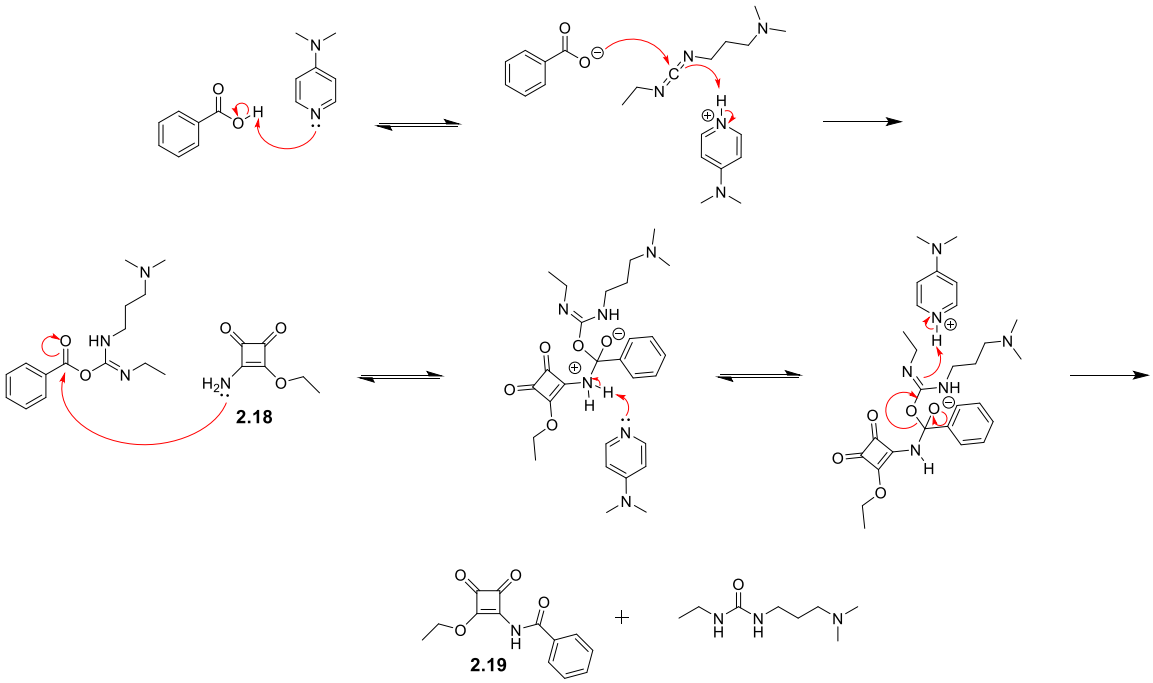

Scheme 2.2. Mechanism of EDCI mediated coupling of amino squarate, **2.18**, and benzoic acid to form amido-squarate, **2.19**.

These conditions proved fruitful as not only an increase of yield was observed (83%) but purification *via* flash chromatography became facile due to complete separation of the urea by-product of EDCI and the desired product. The yield of the amido-squarate intermediates varied greatly and seemed to be dependent on the electron-withdrawing strength of the substituents of the benzoic acid derivative, as with increasing electron-withdrawing strength of the aryl substituent, the yield of the amido-squarate intermediate decreased. The 4-nitro derivative displayed the lowest yield of 25% while the unsubstituted amido-squarate displayed a yield of 83%. We postulate that the nucleophilicity of the

benzoic acid decreases with stronger electron-withdrawing groups, reducing the ability of the benzoic acid to form the activated ester with EDCI.

The formation of the *N*-amido linkage of the amido-squarate intermediate was evident from the ^{1}H NMR spectra (Figure 2.8) with the characteristic NH of the amide linkage appearing as sharp singlet at 9.88 ppm with an integration of 1 H. The aromatic protons appear between 7.5 ppm – 8 ppm as poorly resolved multiplets. The *ortho*-H protons appear at 8.03 ppm while *meta*-H protons appear at 7.51 ppm, both with an integration of 2 H, and the *para*-H protons appear at 7.62 ppm with an integration of 1 H. The methylene protons of the ethyl ester appear at 4.95 ppm as a quartet, integrating for 2H. The methyl protons appear at 1.54 ppm as a triplet, integrating for 3 H. All amido-squarate intermediates share the same characteristic features, *i.e.* the amide NH and the ethyl peaks, with the aryl protons varying depending on substitution pattern (See Appendix).

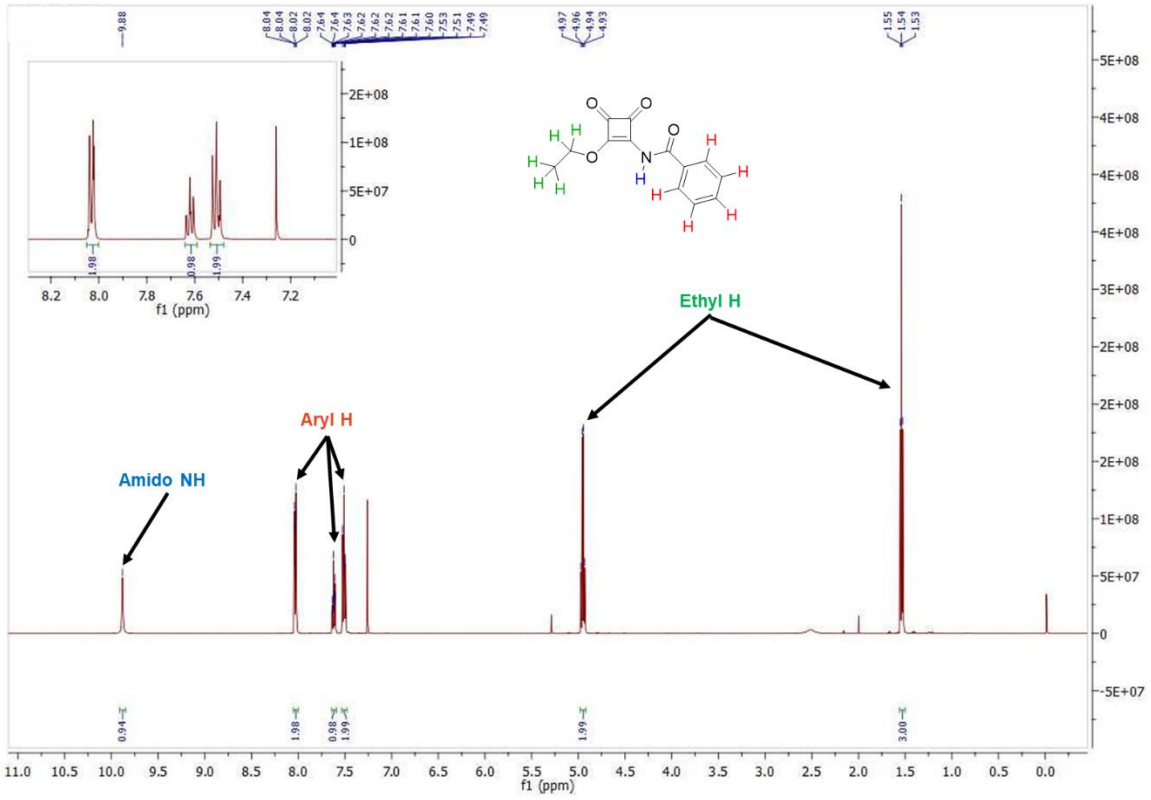

Figure 2.8 ^{1}H NMR spectra of amido-squarate intermediate **2.19**.

The final step of the synthetic pathway was to react the appropriate aniline with the amido-squarate intermediates to form the amido-squaramide (Scheme 2.3). Zinc trifluoromethanesulfonate was used as a lewis-acid catalyst to increase the electrophilicity of the squaramide and prevent squaraine formation (1,3

substitution). Nucleophilic substitution between aniline and amido-squarate intermediate, **2.19**, forms a tetrahedral intermediate. Intramolecular proton transfer occurs between the protonated amine and the ethoxy ester, allowing the ester to act as a leaving group. The tetrahedral intermediate collapses, forming the target compound, amido-squaramide, **2.27**, and releases ethanol.

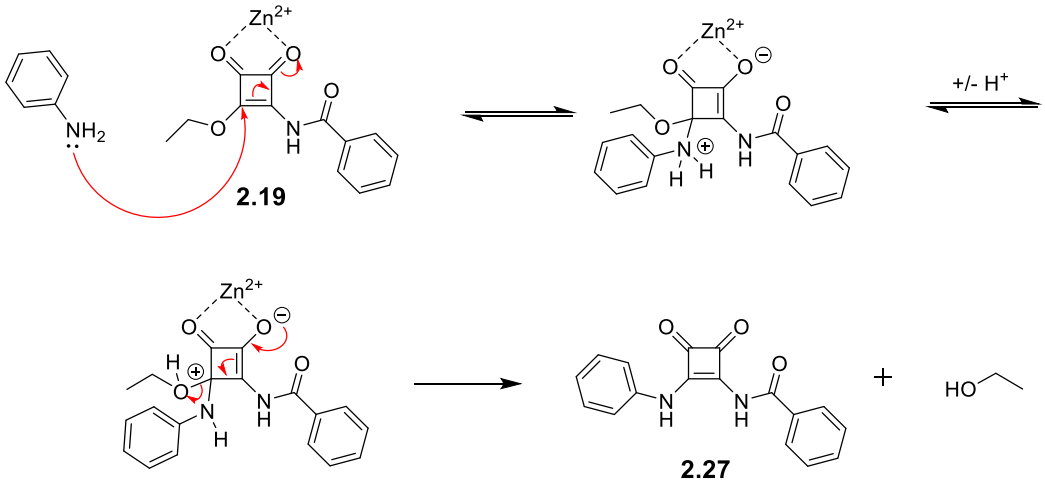

Scheme 2.3 Mechanism of nucleophilic substitution with aniline and amido-squarate, **2.19**.

Once again, the yields varied depending on the electron-withdrawing substituents of the aniline. As 4-nitroaniline is an electron-poor and weak nucleophile, the yields were the lowest at 10%, while the unsubstituted aniline gave a yield of 71%.

The successful synthesis of the amido-squaramides can be seen by the characteristic NH peaks of the amido-squaramide. Using **2.28** as an example, the amido-NH shifts downfield to 10.24 ppm while the phenyl NH appears at 12.26 ppm, both integrating for 1 H. Successful nucleophilic substitution is also indicated by the disappearance of the ethyl ester peaks in the aliphatic region. ^{13}C NMR, HRMS and IR confirmed successful formation of the amido-squaramides. Full characterisation data can be found in the experimental section and supporting spectra can be found in the Appendix.

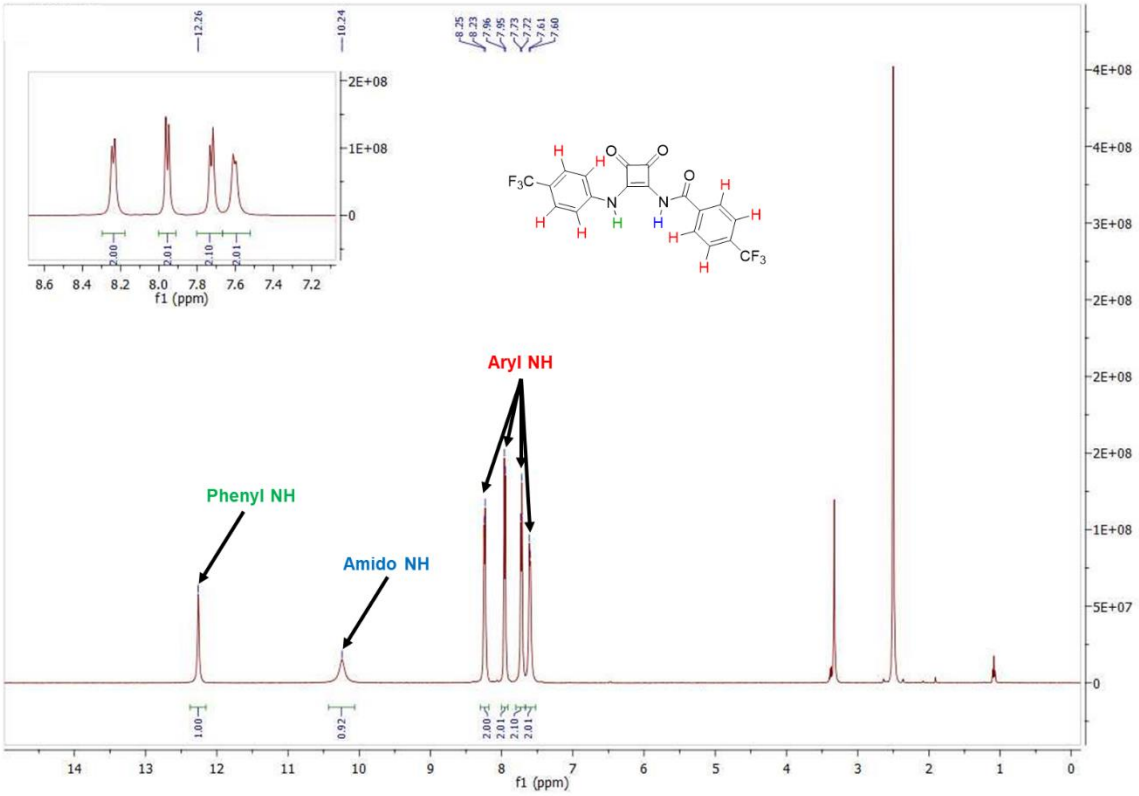

Figure 2.9 ^{1}H spectrum of amido-squaramide, **2.28**.

2.4 pK_a Determination

To examine the effect the carbonyl has on the pK_a of the amide NH, pH-spectrophotometric titrations were performed to obtain experimental pK_a values, using a method described by Schmidtchen *et al*.[150] These titrations were performed in a mixture of DMSO-water (9/1 v/v; in the presence of 0.1 M $TBAPF_6$ at a receptor concentration of 10 µM).

During the spectrophotometric titrations, deprotonation events were observed by hypo- and hyperchromism of absorbance bands at various wavelengths. This can be clearly seen in the example of **2.32** (Figure 2.10), where there is hypochromism at 284 and 320 nm and hyperchromism at 347 and 407 nm. The inset of Figure 2.10 details the changes of absorbance as a function of pH. A four parameter sigmoid curve was fitted through these data points using Sigma Plot (Systat Software Inc., Chicago, IL, USA) with the point of inflexion corresponding to the pKa (See Appendix), the results of which are summarised in Table 2.2.

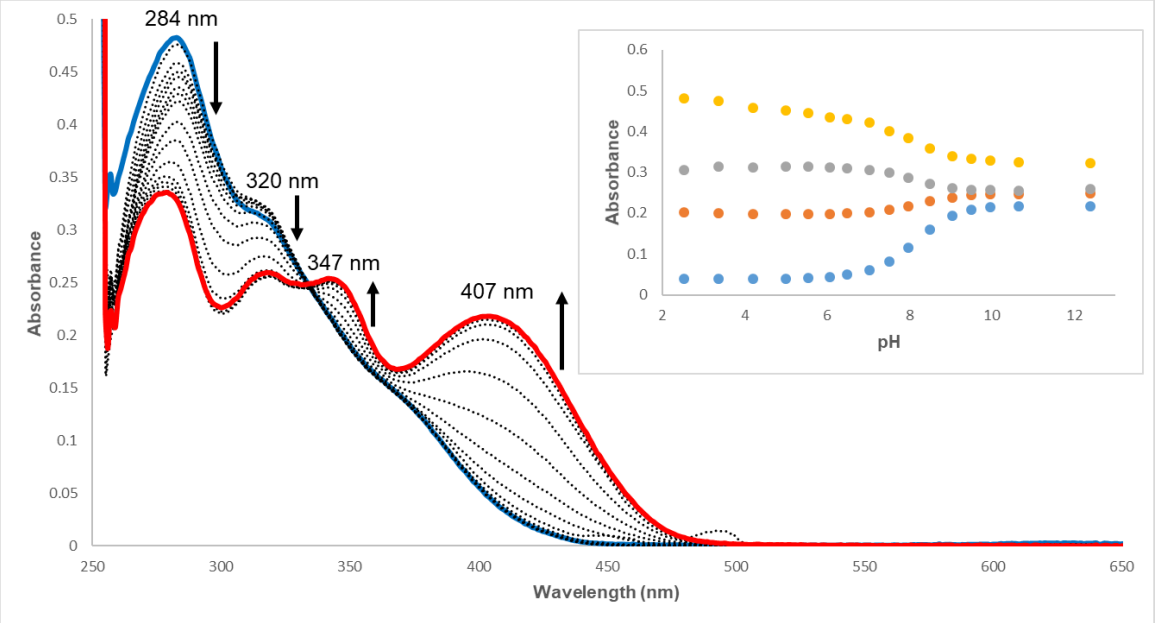

Figure 2.10 Absorption spectra taken over the course of a pH-spectrophotometric titration of **2.32** (10 µM) in an DMSO–water mixture (9/1 v/v; in presence of 0.1 M $TBAPF_6$) pH 2.52 (blue), pH 12.40 (red). *Inset*: Comparison plots of absorbance at 284 nm (yellow), 320 nm (grey), 347 nm (orange), and 407 nm (blue) vs. pH.

We expected to observe two deprotonation events, one for the *N*-amide NH and the second being the NH of the *N*-phenyl, however, only one deprotonation event could be observed for all receptors. This signified that the pK_a of only one NH was determined during the pH-spectrophotometric titrations.

We postulated that the pK_a of the *N*-amide NH would be lower than that of the *N*-phenyl pK_a due to the electron-withdrawing effect of the carbonyl. Thus, examining the results of the pH-spectrophotometric titrations, we expected that we had determined the pK_a values of the *N*-amide NH based on the range of values obtained, as they displayed lower pK_a values than those of analogous disubstituted *N*-phenyl squaramides previously reported in the literature (Table 2.1).[151] This was the first piece of evidence to suggest that we were correct in our assumption that the inclusion of the carbonyl would reduce the pK_a of the NH, increasing its acidity.

Table 2.1 Comparison of experimentally obtained pK_a of amido-squaramides vs. experimentally obtained pK_a of disubstituted *N*-phenyl squaramides.[151]

Receptor	pK_a	Receptor	pK_a
2.27	8.8	**1.53**	11.7
2.28	7.3	**1.56**	9.8
2.29	6.3	**1.59**	8.5

To further investigate the experimentally derived pK_a values, a collaboration with Dr. Tobias Krämer of the Chemistry Department, Maynooth University allowed us to obtain the pK_a for both the *N*-phenyl and *N*-amide NH. Dr. Krämer calculated the pK_a values of all receptors using a direct method *via* the thermodynamic cycle depicted in Scheme 2.4, utilising a proton solvation free energy of –273.30 kcal mol^{-1} in DMSO.

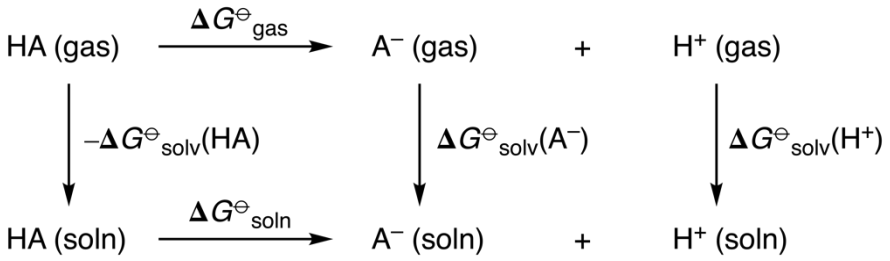

Scheme 2.4 Thermodynamic cycle used to determine the pK_a values of amido-squaramide receptors.

The results obtained by Dr. Krämer confirmed our belief that we had determined the pK_a of the *N*-amide NH, illustrated by the good agreement between the two values (Table 2.2). The calculated values of the *N*-phenyl NH also shows alignment with previous reports in the literature from Ni *et al*.[152] The pK_a values correlate with the Hammett constants of the substituents as the pK_a decreases as the Hammett constant increases,[133] *i.e.* **2.29** bearing two (trifluoro)methyl moieties displayed the lowest pK_a while the unsubstituted **2.27** displayed the highest pK_a. The calculations also confirmed that the *N*-amide linkage decreased the pK_a of the amido-squaramide receptors.

Table 2.2. Summary of experimentally obtained pK_a values for *N*-phenyl NH and calculated values for both *N*-phenyl and *N*-amide NH. [a] no Hammett constant reported for *o*-iodo substituent.

	pK_a					
Receptor	***N*-amide (Exp.)**	***N*-amide (Calc.)**	***N*-phenyl (Exp.)**	***N*-phenyl (Calc.)**	**Substituent**	**Hammett Constant**
2.27	8.8	8.9	-	12.7	H	0.0 σ_p
2.28	7.3	7.9	-	11.6	4-CF_3	0.54 σ_p
2.29	6.3	6.6	-	10.3	Bis-3,5-CF_3	0.43 σ_p
2.30	7.5	7.5	-	10.4	NO_2	0.78 σ_p
2.31	8.8	8.9	-	12.4	2-Iodo	-[a]
2.32	8.1	9.8	-	11.4	4-Iodo	0.18 σ_p
2.33	7.1	7.1	-	9.3	3,4-dichloro	0.23 σ_p 0.37 σ_m
2.34	8.2	7.8	-	11.0	4-Chloro	0.23 σ_p

2.5 Geometry Optimisation

Further work performed by Dr. Krämer produced optimised geometries of amido-squaramides in the solution phase. The geometries of the amido-squaramides were optimised with M06-2x/6-31+G(d) and then single point calculations with DLPNO-CCSD(T)/CBS (3/4 extrapolation to complete basis set limit with def2-*n*ZVP basis set with *n* = 3 and 4).

From these calculations, the energy-minimised structure of amido-squaramide **2.27** showed that the carbonyl of the amide-linkage participates in an intramolecular hydrogen bond to the NH of the *N*-phenyl NH (Figure 2.11). This is unsurprising as similar behaviour was observed by Ashton *et al.* (Figure 2.5).

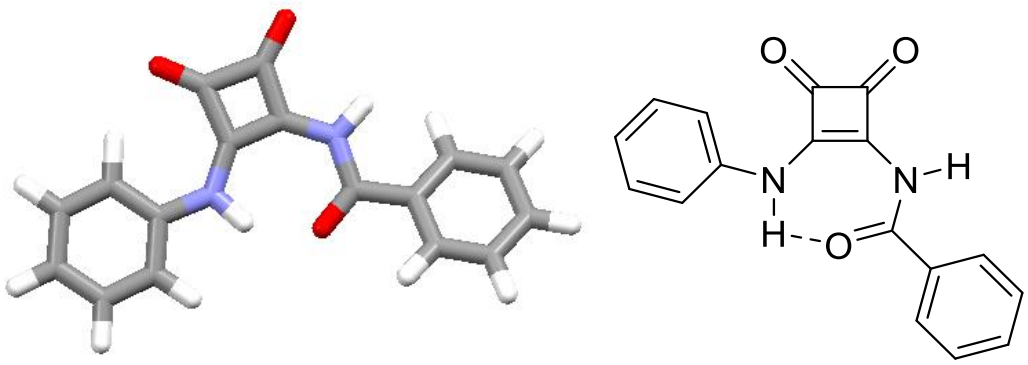

Figure 2.11 Energy minimised structure of **2.27** participating in intramolecular hydrogen bonding.

Molecular dynamics simulations of **2.27** strengthened the finding that the amido-squaramide prefers to maintain a planar conformation stabilised by H-bonding. Figure 2.12 shows a heat map of the conformational space of the system with regard to two parameters: the two torsional angles C-C-N-C(Phenyl) and C-C-N-C(=O), *i.e.* rotations around the bonds attached to the double bond of the cyclobut-3-ene ring of the squaramide. The heat map shows two minima (blue) of the amido-squaramide conformations, one where the amido-squaramide adopts an *anti*/*syn* conformation as it participates in intramolecular H-bonding and one where the amido-squaramide adopts an *anti*/*anti* conformation.

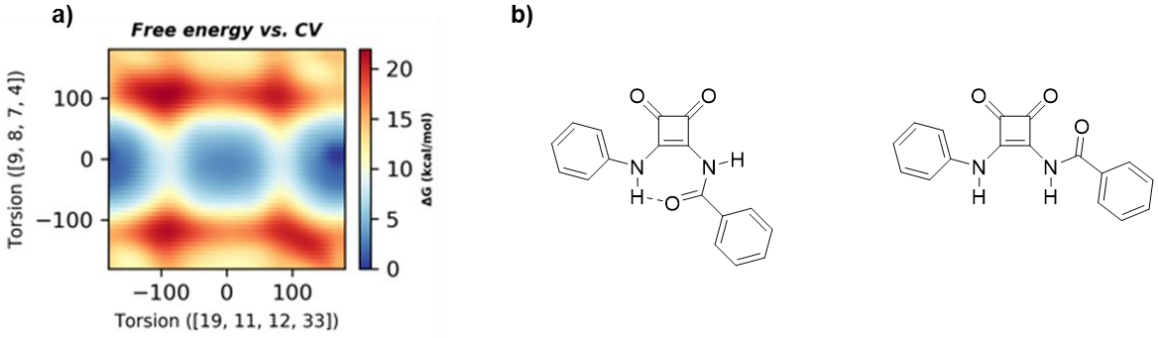

Figure 2.12 a) Heat map of conformational space of **2.27** illustrating two minima (blue). b) The two lowest energy conformations of **2.27**, *anti*/*syn* (left), *anti*/*anti* (right).

Given the observed propensity of amidosquaramides to possibly form an intramolecular H-bond, we expected that this may impact on the anion binding ability of this receptor. Indeed, we envisaged that it may cause an additional thermodynamic barrier to anion recognition where the intramolecular interaction would first need to be overcome before anion recognition could proceed.

2.6 Anion Binding Studies

Receptors **2.27** – **2.29** were selected to undergo ^{1}H NMR spectroscopic anion screening to assess their interaction in DMSO-d_6 (0.5% H_2O) with a range TBA salts of halides and oxoanions (Table 2.3).

Table 2.3 Summary of interaction of **2.27** – **2.34** and TBA salts of various anions and their association constants. [a] deprotonation occurred. [b] H-bonding indicated by a downfield shift of NH protons. [c] no interaction observed.

Receptor	F^-	Cl^-	Br^-	I^-	SO_4^{2-}	NO_3^-	AcO^-	$H_2PO_4^{2-}$
2.27	d.[a]	int.[b]	n.i[c].	n.i.	d.	n.i.	d.	d.
2.28	d.	int.	n.i.	n.i.	d.	n.i.	d.	d.
2.29	d.	int.	n.i.	n.i.	d.	n.i.	d.	d.

When treated with basic anions (F^-, SO_4^{2-}, AcO^- and $H_2PO_4^{2-}$) all receptors underwent deprotonation. This was observed in the ^{1}H NMR spectra with the disappearance of both NH peaks and in some cases, the coalescence of aromatic peaks (Figure 2.13). In the case of TBAF, the formation of HF_2^- can be seen by the characteristic peak at 16.15 ppm (Figure 2.13). No observable changes in the ^{1}H NMR spectra were observed when receptors were treated with 10 molar equivalents of Br^-, I^- or NO_3^- indicating that no interaction was taking place (Figure 2.13). When treated with 10 molar equivalents of Cl^-, a downfield shift of the amide NH was observed (Δ ppm $\approx$ 1) indicating hydrogen bond formation between the anion and receptor (Figure 2.13).

Based on the results of the anion screen, more detailed ^{1}H spectroscopic titrations were performed in DMSO-d_6 (0.5% H_2O) at 298 K, to determine the binding constants in the presence of chloride. All receptors displayed the same behaviour when treated with TBACl (see Appendix). Looking at **2.29** as an example (Figure 2.14), sequential additions of Cl^- resulted in the NH peak corresponding to the *N*-amide (blue) undergoing a downfield shift, while the NH peak corresponding to the *N*-phenyl (green) displayed a barely discernible downfield shift. Slight shifts in aromatic resonances could also be observed, indicating possibly weak C-H···anion interactions.

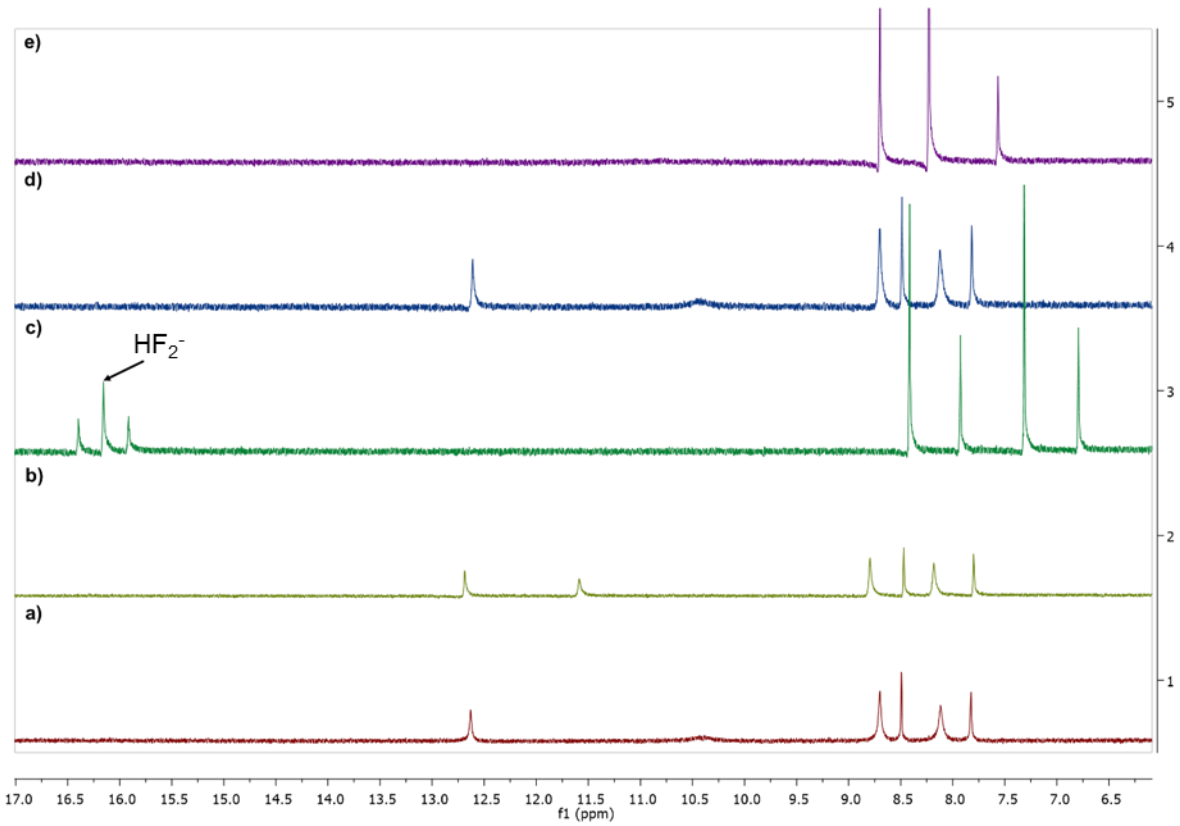

Figure 2.13 ^{1}H NMR stackplot of **2.29** (2.5 x 10^{-6} M) treated with different TBA salts of anions (10 equiv.). a) Blank spectra of **2.29** (no anion present). b) **2.29** + TBACl. c) **2.29** + TBAF. d) **2.29** + TBABr. e) **2.29** + TBAAcO.

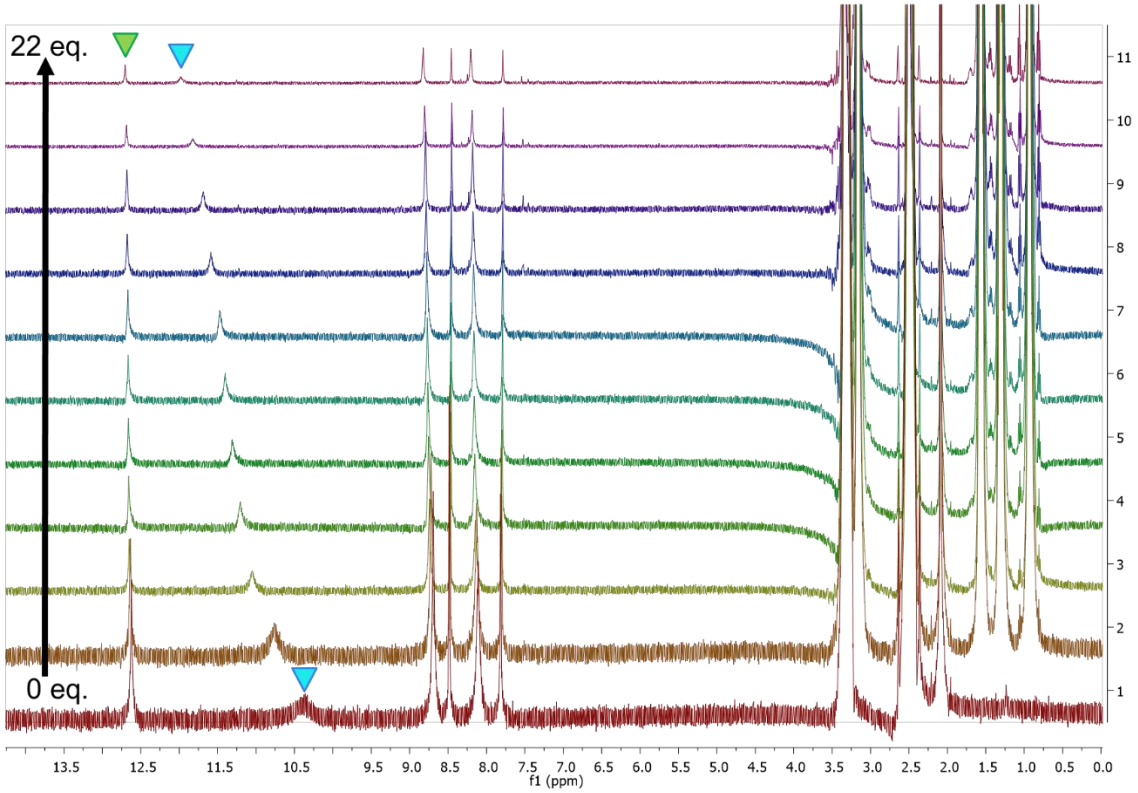

Figure 2.14 ^{1}H NMR stackplot of receptor **2.29** with 0.0 – 22.0 equiv. TBACl in DMSO-d_6/0.5% H_2O.

As the results of the geometry optimisation showed the amido-squaramides contain an intramolecular H-bond between the *N*-phenyl NH and the amide's oxygen atom, it is unsurprising that there was only a slight shift observed for the corresponding signal when treated with TBACl. We postulate that the stability afforded by the intramolecular H-bond results in the amido-squaramide being unwilling to break this intramolecular interaction, resulting in only one NH being available to bind to anionic guests.

Binding constants were determined by plotting the changes in chemical shift of the NH peaks against anion concentration and the resulting plots were analysed using the open access software BindFit (*e.g.* Figure 2.15), and fitted to a 1:1 binding model.[153] The results are summarised in Table 2.4. A 1:1 binding model was found to be the best fit the data for all receptors. This was validated by % error for each receptor < 5%, combined with their residuals plots displaying a random scatter centred around the x-axis, as seen in Figure 2.16.

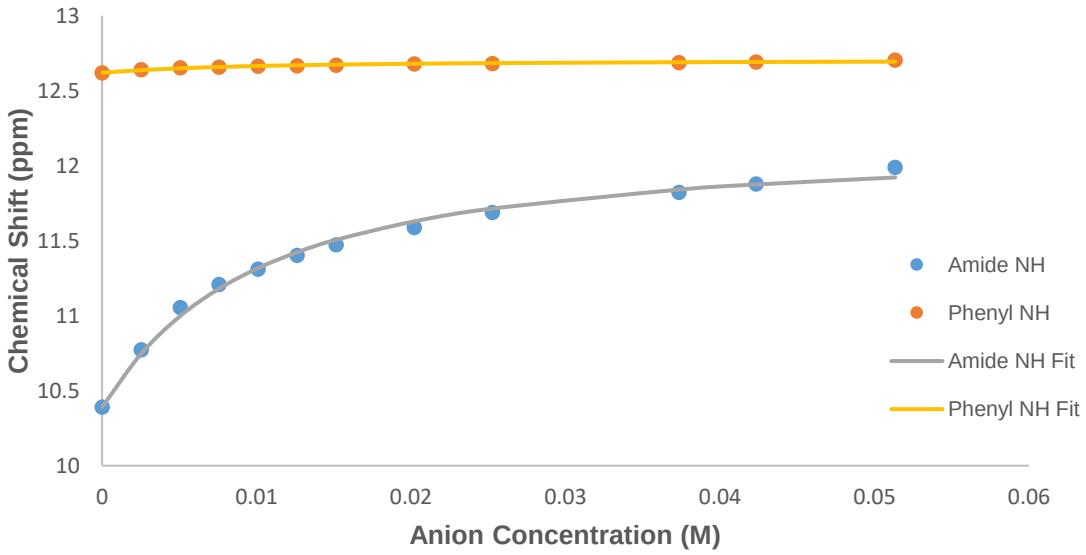

Figure 2.15 Fitted binding isotherm for the titration of **2.29** (2.5 X 10^{-6} M) in the presence of increasing concentrations of Cl^- in DMSO-d_6/0.5% H_2O). The data is fitted to a 1:1 binding model and shows the chemical shift of the NH signals throughout the titration.

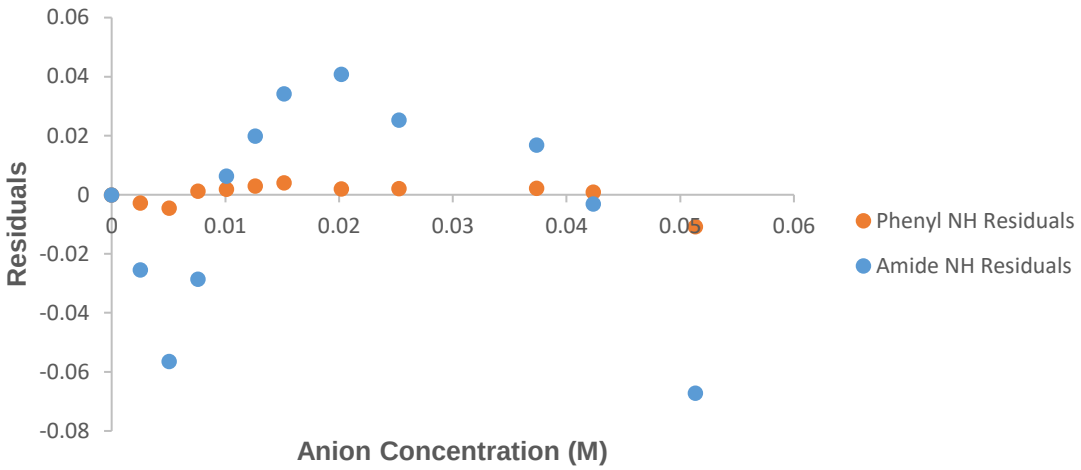

Figure 2.16 Residual plot of **2.29**

The binding affinity of the amido-squaramides were in the order of **2.29** > **2.28** > **2.76** > **2.33** > **2.34** > **2.30** ≈ **2.32** > **2.31**. Unsurprisingly, **2.29** displayed the highest binding constant of 123 K_a/M^{-1} due to the presence of the bis-3,5-(trifluoro)methyl substituents on both aromatic rings. This aligns with previously reported receptors decorated with CF_3 moieties displaying the highest binding constants.[128] **2.31** displayed the lowest binding constant of 6 k_a/M^{-1}. We postulate that this is a result of the 2-iodo substituent causing steric hindrance at the binding site, preventing Cl^- to come into proximity of the NH hydrogen bond donor. Due to the Hammett constants of the relevant substituents of **2.32** – **2.34** and their decreased pK_a, it was expected that there would be higher binding constants for these receptors compared to that of unsubstituted **2.27**, however, this was not the case. It remains unclear as to why **2.27** displays a higher anion binding constant than that of receptors bearing electron-withdrawing groups with lower pK_a values.

Table 2.4 Summary of the binding constants for Cl^- (K_a/M^{-1}) of receptors **2.27**–**2.34** in 0.5% H_2O in DMSO-d_6 at 298 K. Data fitted to 1:1 binding model.

Receptor	K_a / M^{-1}
2.27	76
2.28	97
2.29	123
2.30	54
2.31	6
2.32	52
2.33	69
2.34	58

When comparing amido-squaramides to analogous squaramides, ureas, and thioureas (Figure 2.17), we see that while amido-squaramides do not reach the anion binding ability of their analogous squaramides, they do, however, show anion binding abilities greater than that of their urea and thioureas analogues (Table 2.5).

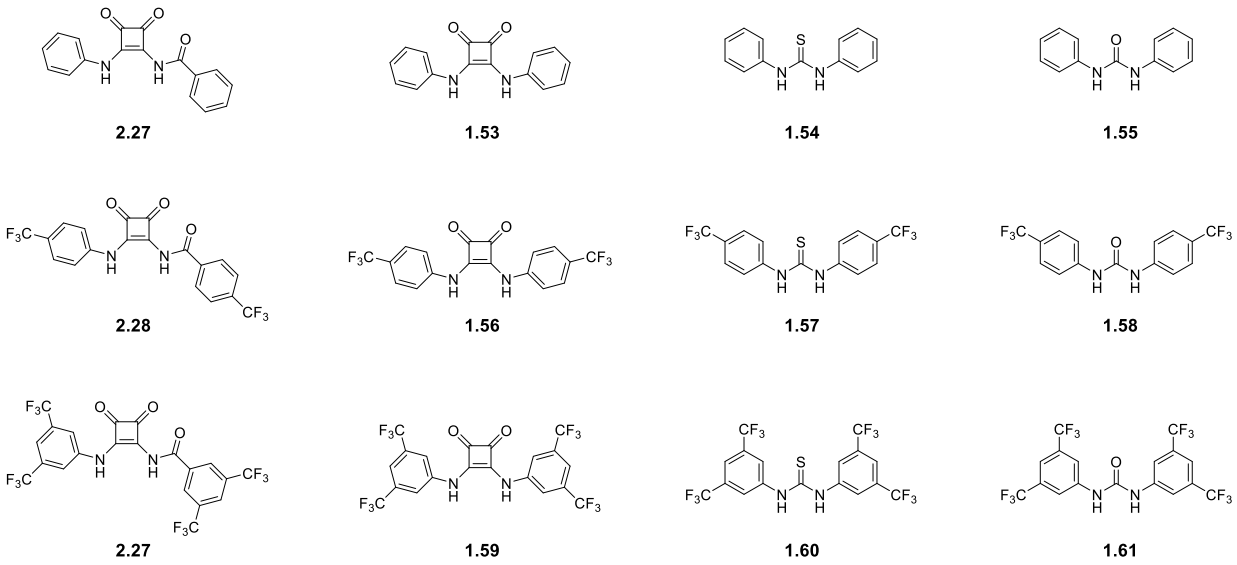

Figure 2.17 Structures of amido-squaramides and their analogous squaramides, thioureas and ureas.

Table 2.5 Comparison of binding constants (K_a/M^{-1}) of amido-squaramides and previously reported squaramide, thiourea and urea receptors.[128]

Amido-squaramide	K_a/M^{-1}	Squaramide	K_a/M^{-1}	Thiourea	K_a/M^{-1}	Urea	K_a/M^{-1}
2.27	76	**1.53**	260	**1.54**	15	**1.55**	31
2.28	97	**1.56**	458	**1.57**	43	**1.58**	75
2.29	123	**1.59**	643	**1.60**	41	**1.61**	88

We postulated that the *anti*/*syn* conformation of the receptors arising from the intramolecular H-bonding was a factor in the relatively low Cl^- binding constants, as only one hydrogen bond donor is available for H-bond formation with Cl^-, compared to the analogous squaramides which display two hydrogen bond donors.

We considered that acidic conditions might disturb the H-bond between the phenyl NH and the carbonyl oxygen, therefore switching the conformation to *anti/anti*, 'freeing' the *N*-phenyl NH, which would in turn facilitate superior anion binding. If acidic conditions could perturb this intramolecular interaction, we expected to observe a shift of the phenyl NH signal in the ^1H NMR spectrum,

where it would resonate more downfield, due to the NH no longer participating in H-bonding interactions.

To investigate this theory, we employed ^{1}H NMR spectroscopy to examine the effects of acidic conditions on the amido-squaramide and its chloride binding ability. Initially, a solution of **2.29** in DMSO-d_6 was made acidic by the addition of AcOH (1 µL, 11.6 equiv.). No visible changes in the spectrum were observed, indicating that the intramolecular H-bond was still intact (Figure 2.18). We had seen previously that addition of **2.29** with TBACl (10 equiv.) resulted in a downfield shift of one NH signal by approximately 1 ppm (Δ ppm ≈ 1). Upon addition of TBACl (10 equiv.) in the presence of AcOH, a shift of one NH signal was still observed, however, the shift downfield was not as significant, Δ ppm ≈ 0.4. Subsequent additions of AcOH (up to 5 µL) did not result in further changes to the spectrum.

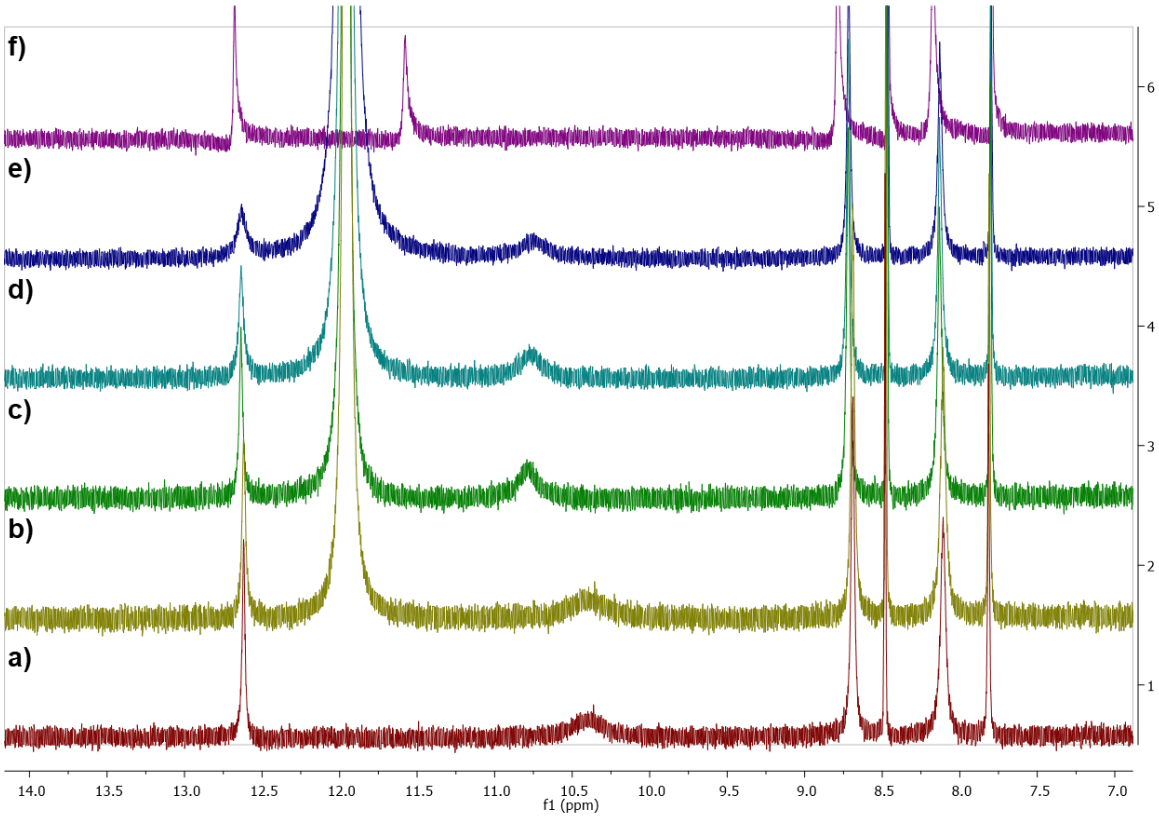

Figure 2.18 ^{1}H NMR stackplot of **2.29** (2.5 x 10^{-6} M) and TBACl (10 equiv.), treated with increasing additions of AcOH. a) **2.29** (no AcOH or TBACl). b) **2.29** + 1 µL AcOH. c) **2.29** + 1 µL AcOH + TBACl. d) **2.29** + 2 µL AcOH + TBACl e) **2.29** + 5 µL + TBACl. f) **2.29** + TBACl.

As AcOH failed to result in perturbation of the intramolecular H-bond, TFA was then employed as it displays a lower pK_a than AcOH (pK_a = 0.23; pK_a = 4.75, respectively) (Figure 2.19). Similar to AcOH, the addition of 1 µL of TFA did not

result in any visible change in the ^{1}H NMR spectrum. Addition of TBACl (10 equiv.) in the presence of TFA, again resulted in a lesser downfield shift, Δ ppm ≈ 0.4. Further additions of TFA to 5 µL resulted in a very slight upfield shift of the NH signal.

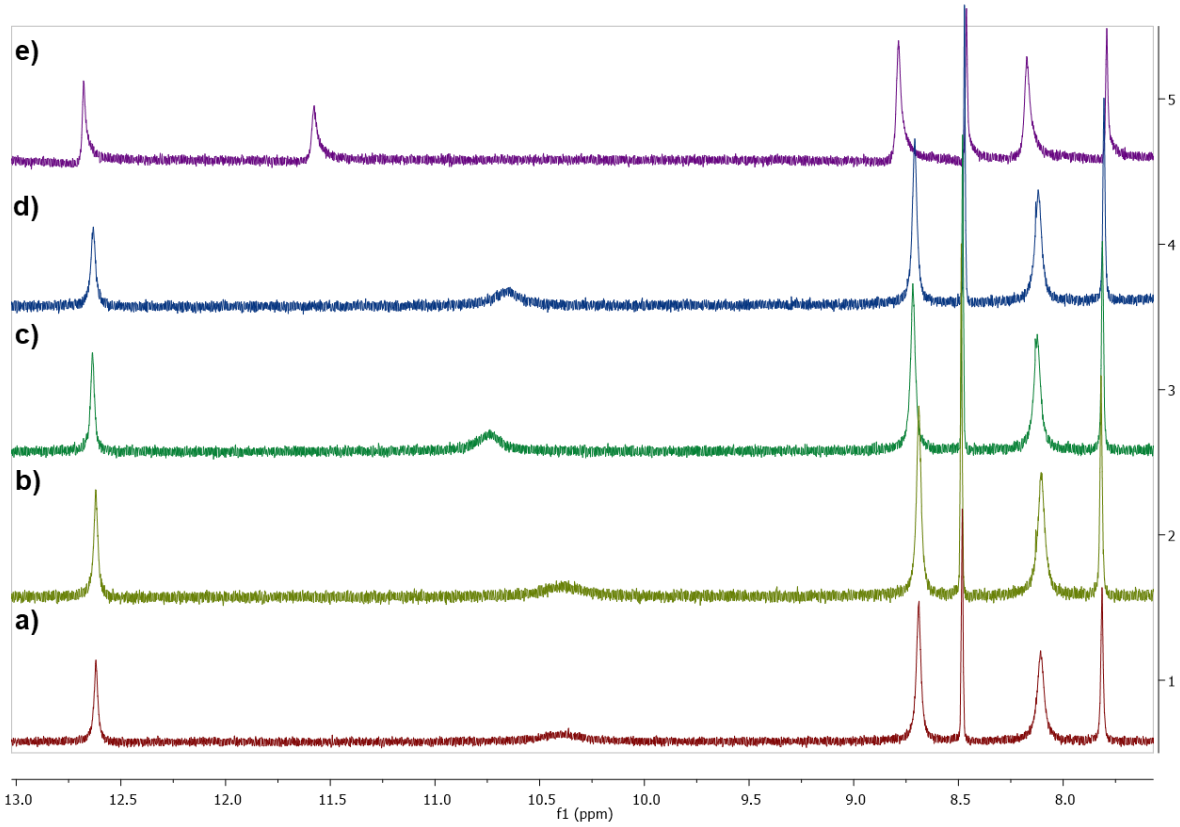

Figure 2.19 ^{1}H NMR stackplot of **2.29** (2.5 x 10^{-6} M) and TBACl (10 equiv.), treated with increasing additions of TFA. a) **2.29** (no TFA or TBACl). b) **2.29** + 1 µL TFA. c) **2.29** + 1 µL TFA + TBACl. d) **2.29** + 5 µL AcOH + TBACl. e) **2.29** + TBACl.

From these rudimentary experiments, it was apparent that under acidic conditions, the intramolecular H-bond of **2.29** was not disrupted, as the phenyl NH signal remained unchanged. It was also evident that the interactions between **2.29** and Cl^{-} were reduced compared to when no acid was present, as shown by a reduced downfield shift of the NH signal. While it is it not evident why exactly this is the case, it appears that AcOH and TFA introduce competition for interactions between **2.29** and Cl^{-}.

2.7 Anion Transport Assays

With just moderate Cl^{-} binding affinities, we expected that the amidosquaramides may not exhibit efficient anion transport as we had initially envisaged. Nevertheless, the anionophoric activity of receptors **2.27 - 2.34** was screened

using methods reported by Gale *et al*.[154] Unilamellar vesicles were created using a 7:3 molar ratio of 1-palmitoyl-2-oleoyl-sn-glycero-3-phosphocholine (POPC) and cholesterol by hydrating the lipid mixture using a solution of a NaCl solution (487 mM), buffered to pH 7.2 using a sodium phosphate buffer (5 mM)), known as the internal solution. The solution was then subjected to nine freeze-thaw cycles, followed by extrusion twenty-five times through a 200 nm polycarbonate membrane. The liposomes then underwent dialysis using a $NaNO_3$ solution (487 mM) buffered to pH 7.20 using a sodium phosphate buffer (5 mM)), known as the external solution, to remove unencapsulated chloride ions. Using the external solution, the liposomes were diluted to 0.5 mM before each run was performed. The efflux of chloride was measured using a chloride ion selective electrode (ISE). The amido-squaramides were added to the vesicles as DMSO solutions *via* micropipette (Figure 2.20). See Experimental Procedures for detailed assay conditions.

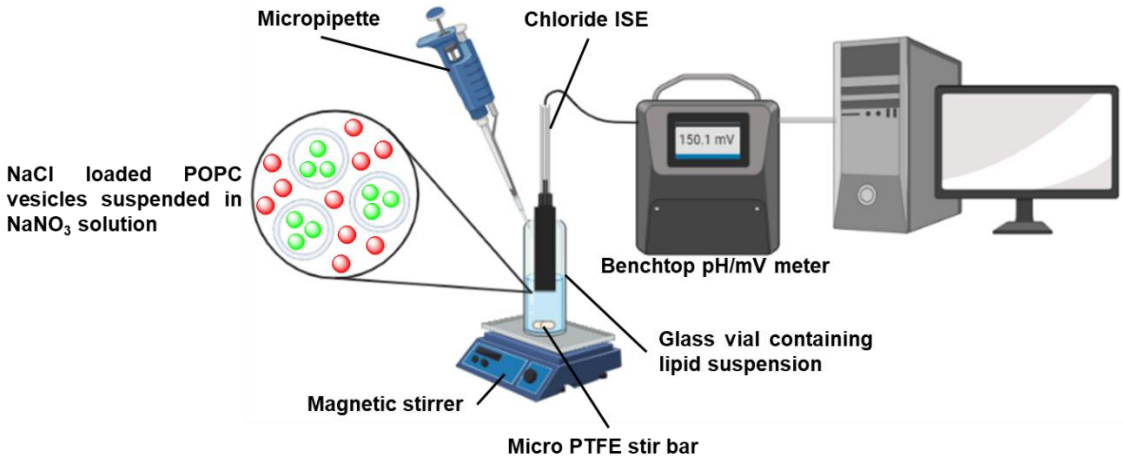

Scheme 2.20 Experimental setup used for Cl^-/NO_3^- exchange ISE assay.

Initially, the anionophoric activity of the amido-squaramides were assessed at pH 7.20 at a concentration of 5 mol% (with respect to POPC concentration), repeated in triplicate. The amido-squaramides were added at 0 seconds and the efflux was monitored for 300 seconds before the addition of a solution of Triton X-100 (11 wt% in H_2O:DMSO 7:1 v:v) in order to calibrate the 100% efflux value.

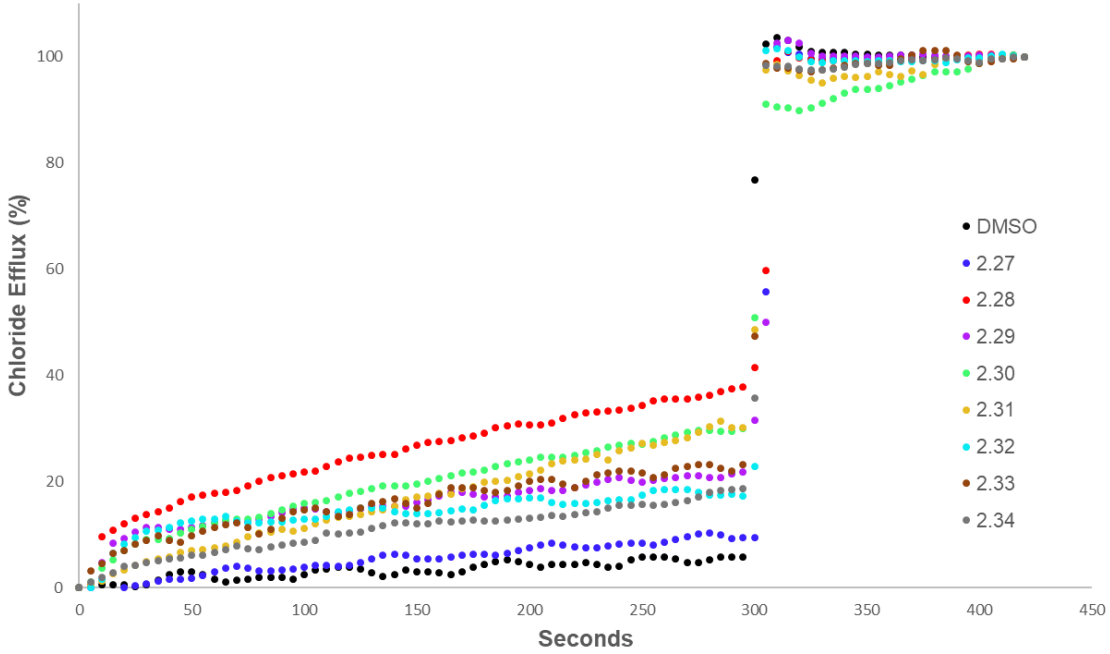

Figure 2.21 Chloride efflux facilitated by **2.27** – **2.34** (5 mol % receptor to lipid) from unilamellar POPC vesicles loaded with 487 mM NaCl buffered to pH 7.20 with 5 mM sodium phosphate salts, and suspended in 487 mM $NaNO_3$ buffered to pH 7.20 with 5 mM sodium phosphate salts. Each trace represents the average of three trials.

The results from the anion transport assays performed at pH 7.20 (Figure 2.21), revealed that the receptors displayed minimal transport at this pH. **2.28** demonstrated the most potent anionophoric activity, yet still failed to reach 50% efflux at 5 mol %. **2.30** and **2.31** also performed well in effluxing chloride from the vesicles compared to the remaining receptors, but to a lesser extent compared to **2.28**. The anionophoric activity of **2.28** can be attributed to their higher binding constants for Cl^- than the remaining receptors, in addition to enhanced lipophilicity granted to the receptor by the trifluoromethyl moieties. Surprisingly, **2.31** displayed higher anionophoric activity than receptors that displayed higher binding constants for Cl^-. While **2.29** displayed the highest binding constant and contained multiple trifluoromethyl moieties, which are known to increase lipophilicity and anion transport, the receptor was only able to facilitate approximately 20% Cl^- efflux.

The poor anion transport ability of **2.29**, and indeed, all of the receptors, can be ascribed to their pK_a values. The range pK_a values of the amido-squaramide amide NH were experimentally determined to be between 6.3 – 8.8. Thus, as the anion transport assays were performed at pH 7.20, a large proportion of the receptors would exist in their deprotonated state, and as only

the amide NH is available to participate in H-bonding to anionic species, this effectively limits their ability to transport Cl^- at neutral pH.

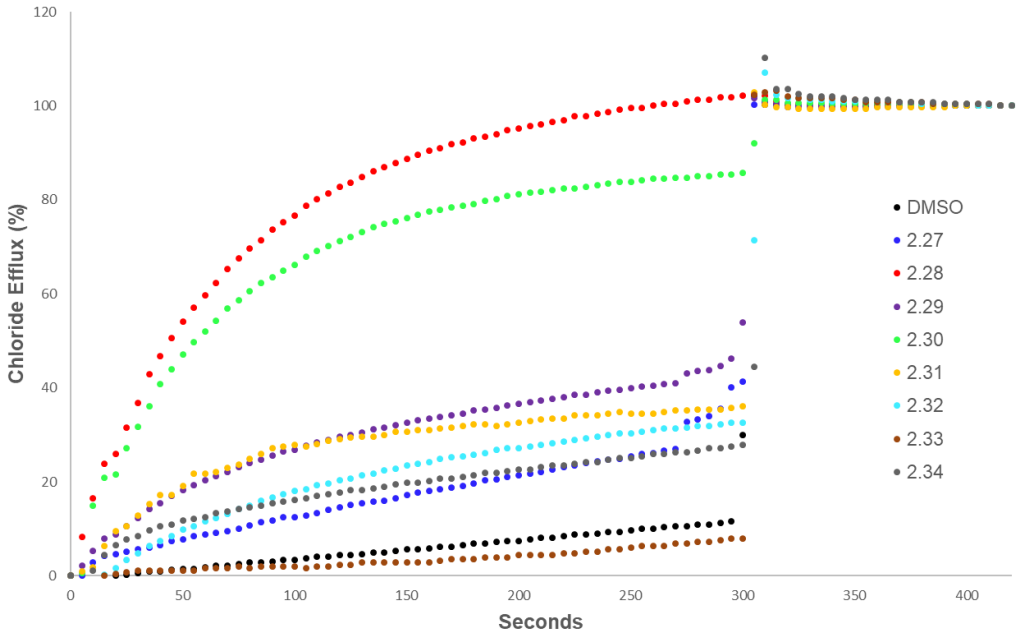

Figure 2.22 Chloride efflux facilitated by **2.27** – **2.34** (5 mol % receptor to lipid) from unilamellar POPC vesicles loaded with 487 mM NaCl buffered to pH 4.20 with 5 mM citric acid buffer, and suspended in 487 mM $NaNO_3$ buffered to pH 4.20 with 5 mM citric acid buffer. Each trace represents the average of three trials.

The anion transport assays were repeated at pH 4.20, using the method described previously, with the solutions buffered to pH 4.20 using a citrate buffer. At acidic pH, a considerable increase was observed in the anionophoric activity of the amido-squaramides (Figure 2.22). **2.28** facilitated 100% Cl^- efflux at 5 mol %, and **2.30** also demonstrated a stark increase from approximately 30% efflux to approximately 80% efflux. The remaining receptors did not manage to obtain 50% efflux of Cl^- after the 300 seconds, placing **2.28** and **2.30** as the most potent anionophores. This increase of anionophoric activity can be attributed to the receptors not being deprotonated at acidic pH, allowing for the receptor to bind and transport Cl^- across the vesicle membrane.

The results of the anion transport assays established that amido-squaramides can facilitate Cl^-/NO_3^- exchange across a lipid membrane, and display pH-switchable behaviour, where anion transport is 'switched on' at acidic pH. In depth analysis of the anionophoric activity of the amido-squaramides was unable to be performed due to time constraints of the project and the instability of the POPC liposomes at pH 4.20. Future work will focus on determining the EC_{50} values of the receptors using Hill analysis, and investigating other antiport

exchange processes and whether amido-squaramides can also facilitate symport processes.

2.8 Conclusion

In conclusion, we synthesised a novel family of amido-squaramide anion receptors, **2.27** – **2.34**, featuring an *N*-aryl linkage and an *N*-amide linkage to an aryl group, with both aryl moieties decorated with a range of substituents to tune anion binding and transport properties. These amido-squaramides were accessed through a facile four step synthetic pathway, employing well-established methods such as amide coupling reaction and nucleophilic substitution of the amido-squarate intermediate. The yields of these reactions ranged as low as 10% to as high as 71%, dependent on the strength of the electron-withdrawing substituents of the aryl rings. Novel structures were characterised by NMR and IR spectroscopy, and HRMS.

The pK_a of the receptors were determined both experimentally, using pH-spectrophotometric titrations, and theoretically, where the results were in good agreement with each other and with previously reported examples in the literature. The pK_a values correlated with the Hammett constants of the aryl substituents, with **2.29** displaying the lowest pK_a values and **2.27** displaying the lowest. Geometry optimisation and molecular dynamics simulations of **2.27** revealed that the amido-squaramide participates in an intramolecular H-bond between the phenyl NH and the amide carbonyl's oxygen, holding the receptor in an *anti/syn* conformation.

The amido-squaramides displayed deprotonation with basic anions such as F^-, SO_4^{2-}, AcO^-, and $H_2PO_4^{2-}$, and selective H-bond formation with Cl^-. ^1H NMR titrations were employed to determine anion binding constants, where a 1:1 binding model was found to have the best fit. The order of binding affinity for the receptors were in the order of **2.29** > **2.28** > **2.76** > **2.33** > **2.34** > **2.30** ≈ **2.32** > **2.31**. Upon comparison of binding constants of the amido-squaramides displayed higher binding affinities than their urea and thiourea analogues, however, they were less effective at binding Cl^- than squaramide analogues. This was attributed to the intramolecular H-bond of the amido-squaramides, resulting in only one NH hydrogen bond donor being available.

Anion transport studies performed at pH 7.20 revealed that only minimal anionophoric activity was observed. However, anionophoric activity of the receptors was observed to be 'switched on' when the assays were performed at pH 4.20. **2.28** was the most potent anionophore, were 100% efflux of Cl^- was observed at pH 4.20**,** at 5 mol % concentration of the receptor. In-depth analysis of the anionophoric activity of the amido-squaramides at this pH was unable to be performed due to time constraints of the project and the instability of the liposomes under acidic conditions. However, the preliminary results demonstrated the proof of principle that the amido-squaramides could act as pH-switchable Cl^-/NO_3^- exchangers.

Further work will further investigate the anion transport abilities of amido-squaramides at acidic pH, along studies to assess the capabilities of the transporters to perform other antiport exchanges and symport processes.

Chapter 3

Towards Stimuli-Responsive Anion Transport

3 Towards Stimuli-Responsive Anion Transport

3.1 Introduction

Anion transport across cellular membranes is controlled by specialised proteins embedded in the plasma membrane. Malfunction of these proteins and the consequent disruption of cellular and extracellular anion regulation leads to the onset of various diseases known as channelopathies, such as cystic fibrosis (as discussed in Chapter 1). Intense investigation in recent years has yielded several examples of small molecules that can facilitate anion transport across lipid membranes, displaying anti-cancer properties by disrupting the polarisation of intracellular compartments and triggering apoptosis.[155,156]

As controlled anion transport is intrinsic for healthy cells, anionophores that indiscriminately transport anions across membranes may have many adverse effects on normal cellular function. However, few examples in the literature exist of synthetic anionophores that exhibit the gating/switching behaviour seen in biological systems.

One example is the family of thiosquaramides reported by Jolliffe and Gale *et al*. which displayed switching behaviour of their anion transport activity in response to pH (Figure 3.1).[151] The presence of the sulfur atoms on receptors **3.1** – **3.3** led to a decrease in pK_a values compared to that of the oxosquaramide analogues, **1.53**, **1.56**, and **1.59**. Thiosquaramide receptors containing electron-withdrawing groups, **3.2** and **3.3**, displayed lower chloride binding constants than the corresponding oxosquaramides in DMSO-d_6. The authors attributed this to the thiosquaramides existing in a partially deprotonated form in DMSO, resulting in the loss of a hydrogen bond donor and a charge-repulsion between the anion and the partially deprotonated receptor. However, **3.1** and **3.4** showed higher or similar chloride binding constants compared to their oxosquaramide counterparts.

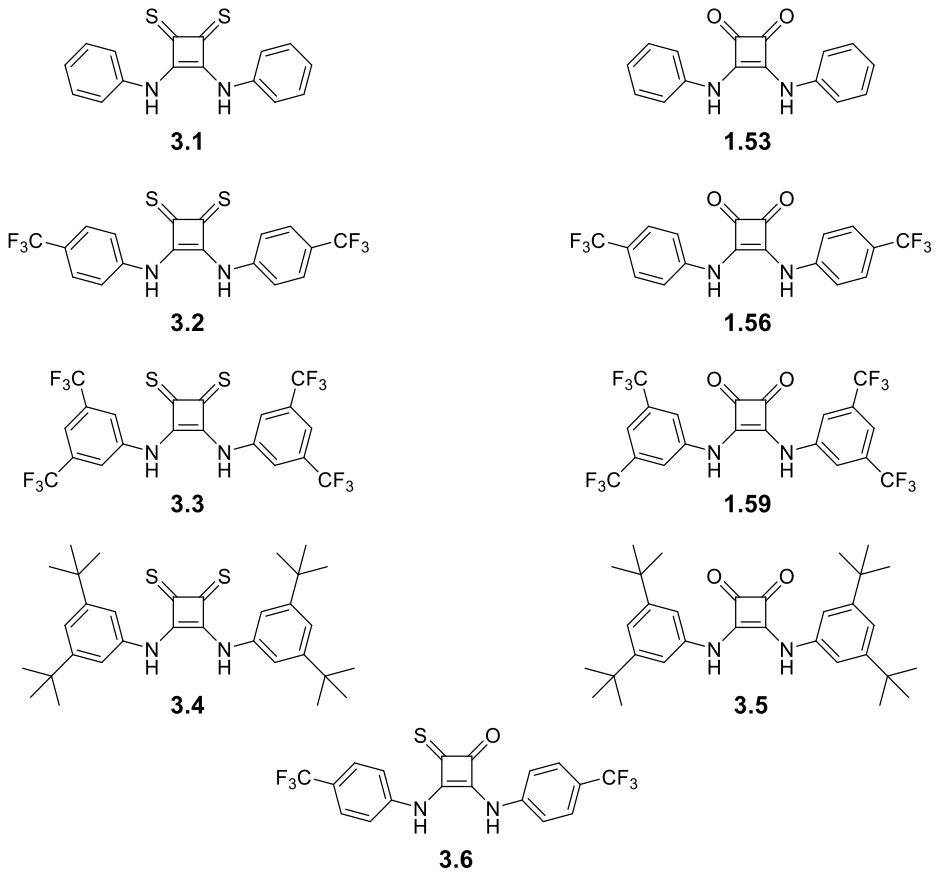

Figure 3.1. Chemical structures of thiosquaramide and oxothiosquaramide receptors investigated by Elmes and Busschaert *et al*. and their oxosquaramide analogues.

Anion transport studies showed that the anionophoric activity of thiosquaramides at pH 7 was greatly decreased. Again, the authors attributed this to the deprotonation of the thiosquaramides at neutral pH, and when anion transport studies were conducted at pH 4, the anionophoric activity of the thiosquaramides was 'switched on' (Figure 3.2). Receptors **3.1** and **3.2** displayed the lowest EC_{50} values at 0.0125 mol%, surpassing their analogous oxosquaramides at pH 4.

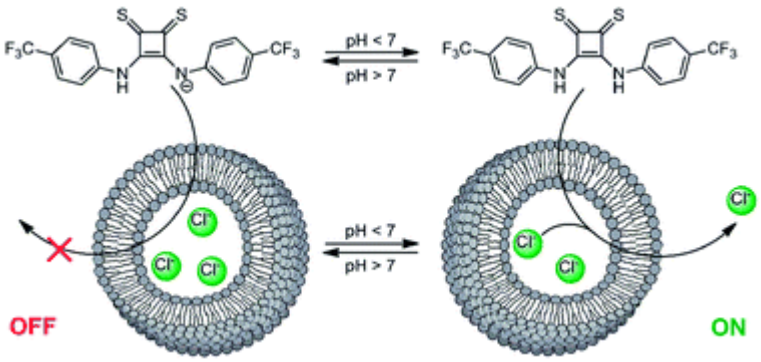

Figure 3.2. Schematic of Thiosquaramide **3.2** displaying switching behaviour in response to pH - when pH > 7, anionophoric activity is 'switched off' due to deprotonation, when pH < 7 anionophoric activity is restored.

The first example of 'mixed' oxothiosquaramide, **3.6**, was also synthesised by Jolliffe and Gale *et al*. (Figure 3.1).[157] The authors noted that the inclusion of just one sulfur atom to the squaramide was enough to sufficiently decrease the receptor's pK_a resulting in switching behaviour of anion transport in response to pH, mirroring the results of thiosquaramides. **3.6** displayed a much greater chloride binding affinity than the corresponding thiosquaramide but did not exhibit the same level of anionophoric activity. Other anion binding motifs have also been employed for pH-sensitive anion transport such as phenylthiosemicarbazones[158-159] and indole-based perenosins[160] that facilitate electroneutral transporf of H^+/Cl^- through a symport mechanism under slightly acidic conditions.

Other examples of stimuli-responsive anionophores include the photo-triggered anionophores reported by Langton *et al*.[161] These azo-benzene di-squaramides underwent reversible *E*-*Z* photo-isomerisation when irradiated with red and blue light (Figure 3.3). Anion binding constants for Cl^- in DMSO-d_6 were higher for the *Z*-isomer when compared to the *E*-isomer. Authors attributed this to the hydrogen bond donors of the squaramide motif being in more favourable positions to bind cooperatively to the anion as the *Z*- isomer.

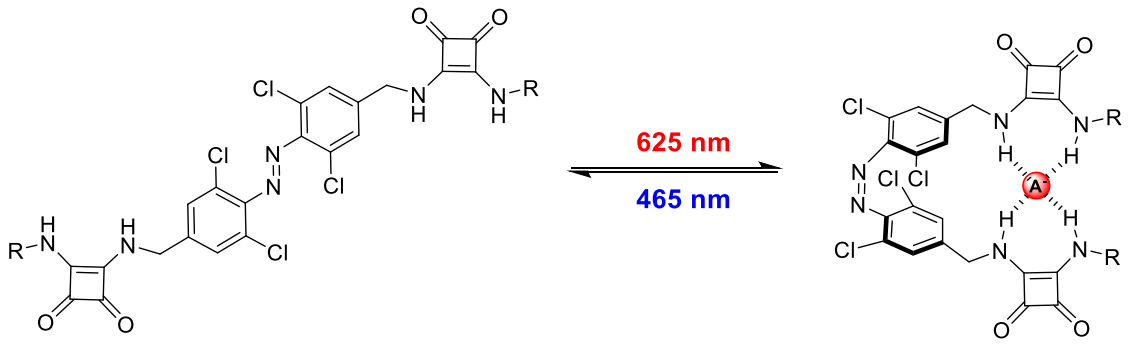

Figure 3.3 General structure of photo-activated anion transporters reported by Kerckhoffs *et al*., **3.7**, that undergoes reversible photo-isomerisation when irradiated with red and blue light.

Anionophoric activity was also increased post photo-isomerisation, marked by a decrease in EC_{50} values *e.g.* EC_{50}^{E} = 181 ± 16 nm and EC_{50}^{Z} = 22 ± 2 nm. *In situ* control of the anion transport activity was demonstrated when, during anion transport assays, the system was irradiated at 652 nm which led to

'turn on' of anionophoric activity (Figure 3.4). When irradiated at 455 nm, anion transport was 'turned off'.

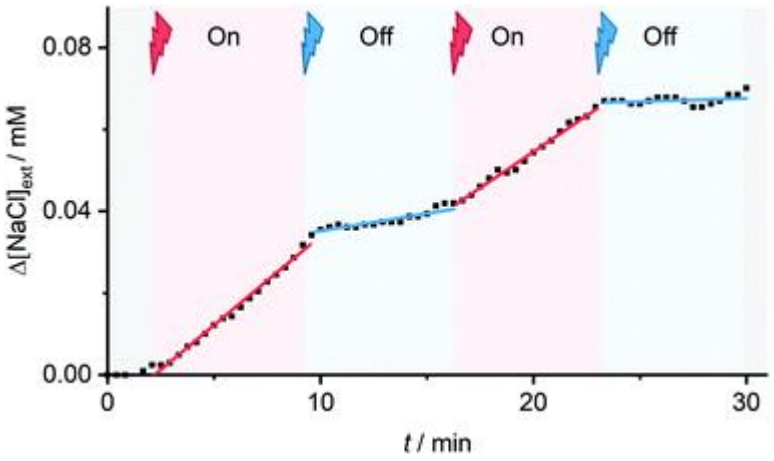

Figure 3.4 Photo-triggered anion transport facilitated by **3.7** from POPC vesicles. Red indicates irradiation of system using 625 nm, blue indicated irradiation of system using 455 nm.

Gale *et al*. have also investigated the application of photo-responsive anion transporters using stiff-stilbene based bis(thio)ureas, **3.8** (Figure 3.5).[162] Similar to the azo-benzene example above, irradiation of the receptors induces an *E*-*Z* isomeric interconversion. The *Z*-isomer displayed higher chloride binding affinity and transport activity than the *E*-isomer, due to the cooperative binding of the binding motifs. It was also reported that the thiourea-based receptors displayed higher anionophoric activity than the urea counterparts due to the increased lipophilicity of the sulfur atom; a trend previously reported by Gale *et al*.[128]

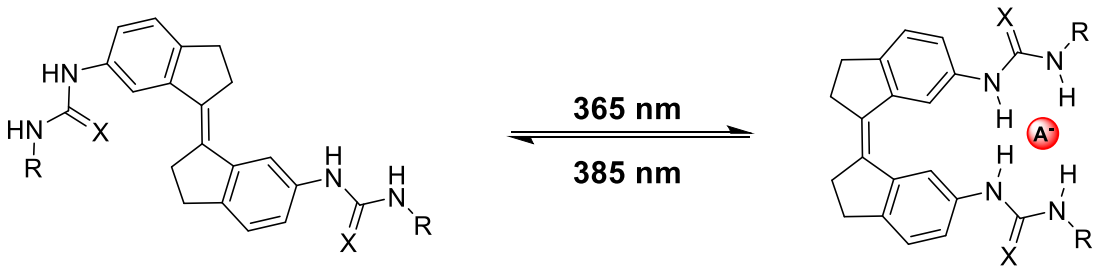

3.8 (*E*) **3.8 (*Z*)**

Figure 3.5 General structure of stiff-stilbene based bis(thio)ureas synthesised by Wezenberg *et al*. that display photomodulated anion transport activity.

The previous two examples demonstrated how an isomeric change can modulate anion transport. However, while an increase of anion transport was observed after photo-stimulation, some anion transport in the less active *E*-

isomers was still observed. An alternative strategy was used by Talukdar *et al*. who reported procarrier **3.9**. The procarrier remained inactive until light irradiation, which caused the molecule to fragment, releasing an active anion transporter (Figure 3.6).[163]

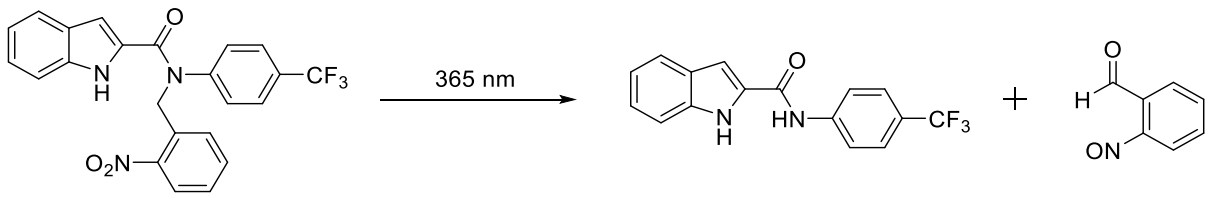

3.9 **3.10**

Figure 3.6 Indole-based procarrier that undergoes photo-cleavage reported by Salunke *et al*.

Procarrier **3.9** contains an *ortho*-nitrobenzyl moiety which acts as a 'blocking group', reducing the number of hydrogen bond donors available for anion recognition. This limits the anion transport activity, as evidenced by the lack of anion transport measured during transport assays. Upon irradiation at 365 nm, the *ortho*-nitrobenzyl moiety undergoes photo-cleavage, releasing the active anionophore, **3.10**, and an aldehyde by-product (Figure 3.6). **3.10** was shown to be an efficient anion transporter, with an EC_{50} value of 0.219 μM. *In vitro* studies using the MCF 7 cell line revealed that procarrier **3.9** displayed no cytotoxic effects. However, when irradiated at 365 nm, pronounced cell death was observed. This finding established stimuli-responsive anion transporters as viable targeted therapeutics for deep tissue cancers.

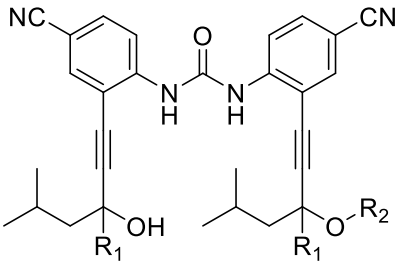

3.11: R_1 = H, R_2 = H

3.12: R_1 = H, R_2 = 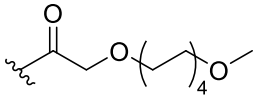

3.13: R_1 = H, R_2 = 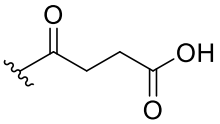

3.14: R_1 = H, R_2 = 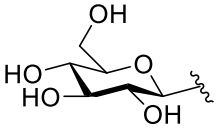

3.15: R_1 = H, R_2 = 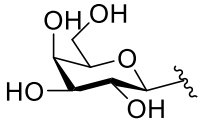

Figure 3.7 Chemical structure of active anion transporter **3.11**, and procarriers **3.12** – **3.15**

Biomolecules have also been employed in creating stimuli-responsive anion transporters. Jeong *et al*. synthesised a series of enzyme-responsive procarriers featuring a urea binding motif (Figure 3.7).[164] These procarriers contained hydrophilic appendages which rendered the transporter inactive due to their inability to partition into the lipophilic membranes. In the presence of specific enzymes, enzymatic hydrolysis occurred, releasing active anion transporter, **3.11**, thereby stimulating anion transport across lipid membranes.

Procarrier **3.12** was able to undergo enzymatic hydrolysis to produce the active anion transporter upon treatment with *Candida antarctica* lipase, *Candida* sp. lipase, and porcine pancreas lipase. **3.13** was more sluggish to react and was only activated by porcine pancreas lipase. **3.14**, bearing a glucose unit, displayed slow enzymatic conversion using a range of glycosylases at pH 7.2. However, when performed at pH 5.5, enzymatic conversion increased significantly. This was deemed advantageous as extracellular pH of tumour tissues is more acidic than normal.[165] Procarrier **3.15** bearing a galactosyl appendage did not encounter the same issues as the glucose counterpart, undergoing enzymatic conversion to **3.11** at pH 7.2 in the presence of *Aspergillus oryzae β*-galactosidase (AOG).

Using Fischer rat thyroid (FRT) epithelial cells inoculated with halide-selective sensor YFP-F46L/H148Q/I152L, the relevant enzymes, and the procarriers **3.12** and **3.15**, the *in vitro* activity was measured. A mixture of **3.15** and AOG proved to be a more effective facilitator of Cl^- influx to the FRT cells than **3.11** alone. This was suspected to be due to the hydrophilic nature of the appendages increasing water solubility, thereby increasing the deliverability of the procarrier.

With just a small number of reported examples, the concept of stimulated anion transport remains largely unexplored. Of these examples, pH-sensitive anionophores rely on a change in environmental conditions to modulate their activity and photo-sensitive procarriers must rely on the application of an external light source to achieve the desired effect. The employment of enzymes to act as triggers for anion transport has many advantages and represents a highly useful strategy that can be easily targeted towards various disease states and cell types.

Indeed, enzymes have been similarly exploited in both prodrug strategies,[166-167] and in the detection of tumour hypoxia in the recent past.[168-169]

3.2 Chapter Objectives

The objective of this chapter is to synthesise a series of stimuli-responsive anion transporters (SRATs), utilising a squaramide motif as the binding unit. (Figure 3.8). These SRATs feature what we term 'tertiary squaramides' that lack hydrogen bond donor groups, inactivating anion binding and transport. The *N*-phenyl substituents of the squaramide would be decorated with trifluoromethyl moieties to increase anion binding and transport activity. The squaramide NHs would be protected by benzyl functional groups with a varying trigger in the *para*-position.

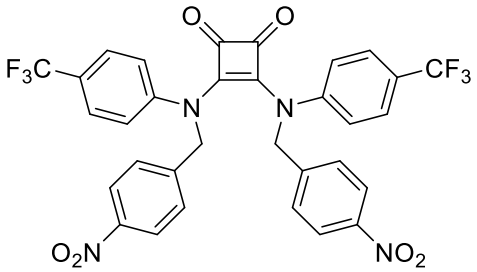

3.16

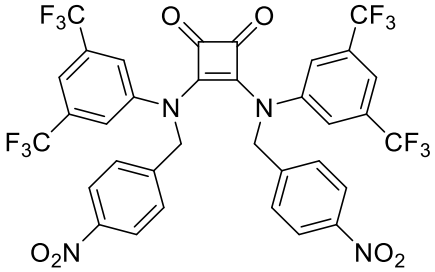

3.17

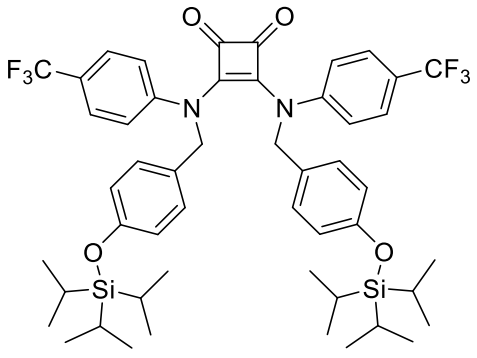

3.18

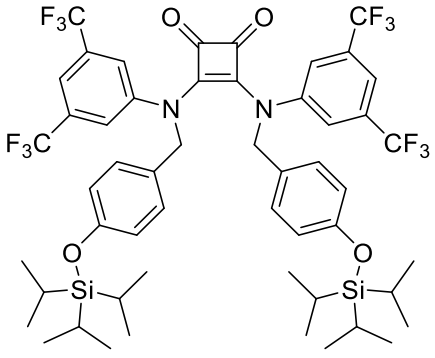

3.19

Figure 3.8 Chemical structures of SRATs. **3.16** and **3.17** bearing the *para*-nitrobenzyl trigger for nitroreductase, **3.18** and **3.19** bearing the triisopropylsilyl ether protecting group which acts as a trigger for fluoride.

Tertiary squaramides **3.16** and **3.17** contain a *para*-nitrobenzyl trigger. The *para*-nitrobenzyl moiety has been used as a trigger moiety in fluorescent probes for the detection of nitroreductase (NTR) as a marker for tumour hypoxia.[168] In the presence of nicotinamide adenine dinucleotide (NADH), NTR reduces nitro-

aromatics to aromatic amines. The conversion from an electron-withdrawing moiety to an electron-donating moiety can cause the molecule to fragment, as has been reported in previous literature examples.[170] We envisage that upon treatment of **3.16** and **3.17** with NTR, the *para*-nitrobenzyl will be reduced to *para*-aminobenzyl which will cause an electron cascade resulting in the fragmentation of the SRAT into active anion transporter **1.56** and **1.59**, respectively (Figure 3.9). However, the study of the behaviour of these SRATs were anticipated to be made difficult due to the requirement of performing enzyme studies in aqueous media.

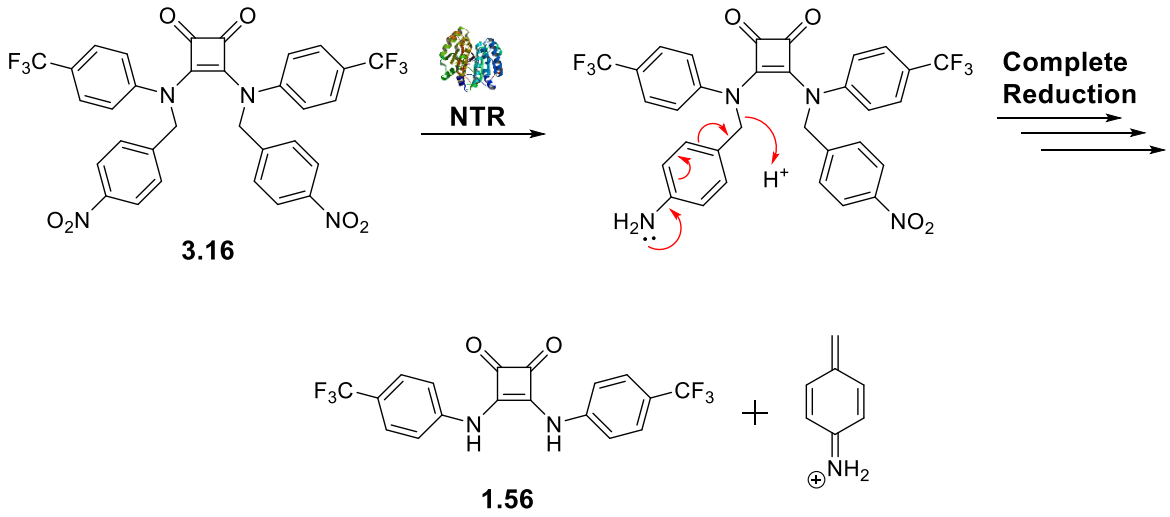

Figure 3.9 Proposed fragmentation mechanism of **3.16** *via* reduction by enzymatic activity to release active anion transporter **1.56**.

SRATs **3.18** and **3.19** contain a triisopropylsilyl ether protecting group, which can be removed in the presence of F^- or under acidic conditions. Upon deprotection, a hydroxyl group is revealed. As hydroxyl moieties are electron-donating, a similar process is expected to occur as depicted in Figure 3.9, causing the SRAT to fragment and produce an active anionophore. By creating a chemo-responsive anion transporter, it would allow analysis to be performed in organic media, facilitating in depth analysis of the fragmentation process.

After successful synthesis of the SRATs, investigation into the release mechanism would be performed to fully elucidate the fragmentation process, and the anion transport ability of the SRATs would be determined. In the following sections, the synthesis of tertiary squaramides will be discussed alongside preliminary results, followed by a change in design (due to unexpected synthetic issues) to create novel stimuli-responsive anion transporters.

3.3 Synthesis and Characterisation of Tertiary Squaramides

The synthetic pathway to tertiary squaramides is outlined in Scheme 3.1. **2.17**, the synthesis of which is described in Chapter 2, acts as the alkyl squarate precursor to the squaramide. For the formation of the secondary amines **3.20** – **3.23**, a one-pot reductive amination method was employed using an adapted method from Abdel-Magid *et al*.[171] Briefly, this involved the acid-catalysed formation of an imine, which is not isolated or purified, before undergoing a reduction using a mild reducing agent, sodium triacetoxyborohydride, to form the target secondary amine.

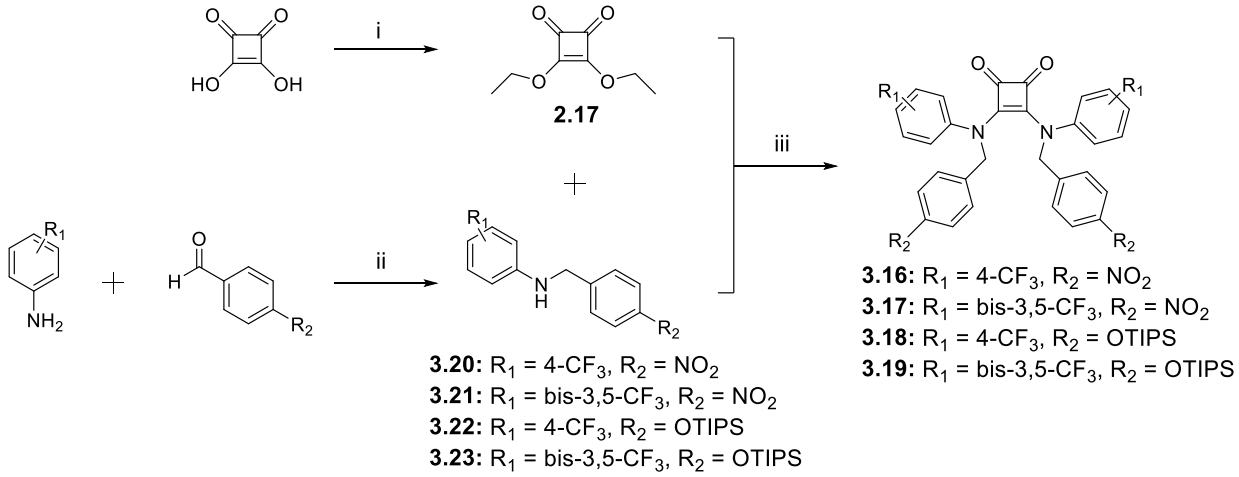

Scheme 3.1 Synthetic pathway to tertiary squaramides. *Reagents and conditions:* i) triethyl orthoformate, EtOH, 80℃, 72 h, 91%; ii) acetic acid, sodium triacetoxyborohydride, $MgSO_4$ (anhydrous), DCM (anhydrous), N_2, rt, 48 h, 45 – 59%; iii) $Zn(OTf)_2$, EtOH, 80℃, 18 h, 5%.

For the synthesis of **3.20** and **3.21**, commercially available 4-nitrobenzaldehyde was obtained. However, **3.22** and **3.23** required protection of 4-hydroxybenzaldehyde with triisopropylsilyl chloride (TIPS-Cl) before proceeding with the reductive amination (Scheme 3.2). 4-Hydroxybenzaldehyde was reacted with TIPS-Cl at room temperature in the presence of NEt_3 and DMAP, an adapted method reported by Lang *et al*.[172] No further purification was necessary after aqueous work-up to obtain the product in 90% yield.

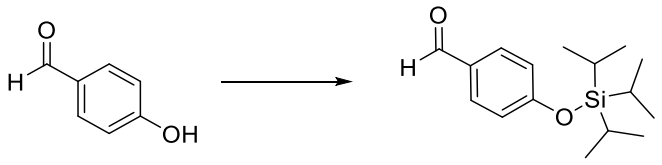

Scheme 3.2 Synthesis of TIPS protected 4-hydroxybenzaldehyde. *Reagents and conditions:* Triisopropylsilyl chloride, NEt_3, DMAP, DCM (anhydrous), N_2, rt, 18 h.

Successful synthesis of secondary amines **3.20** – **3.23** was achieved by way of a one-pot reductive amination (the mechanism for the synthesis of **3.20** as an example can be seen in Scheme 3.3). Acetic acid acts as a catalyst in imine formation, protonating the carbonyl of the benzaldehyde, increasing electrophilicity of the carbonyl carbon, allowing for nucleophilic attack of electron poor aniline. Upon formation of the hemiaminal intermediate, acetic acid is restored *via* deprotonation of the ammonium cation. The hydroxyl group is protonated by acetic acid, forming water, which acts as the leaving group upon formation of the imine bond. The acid-catalyst is regenerated by the deprotonation of the imine by the acetate. The iminium ion is then reduced by sodium triacetoxyborohydride as hydrogen is added across the C=N bond, forming the target secondary amine.

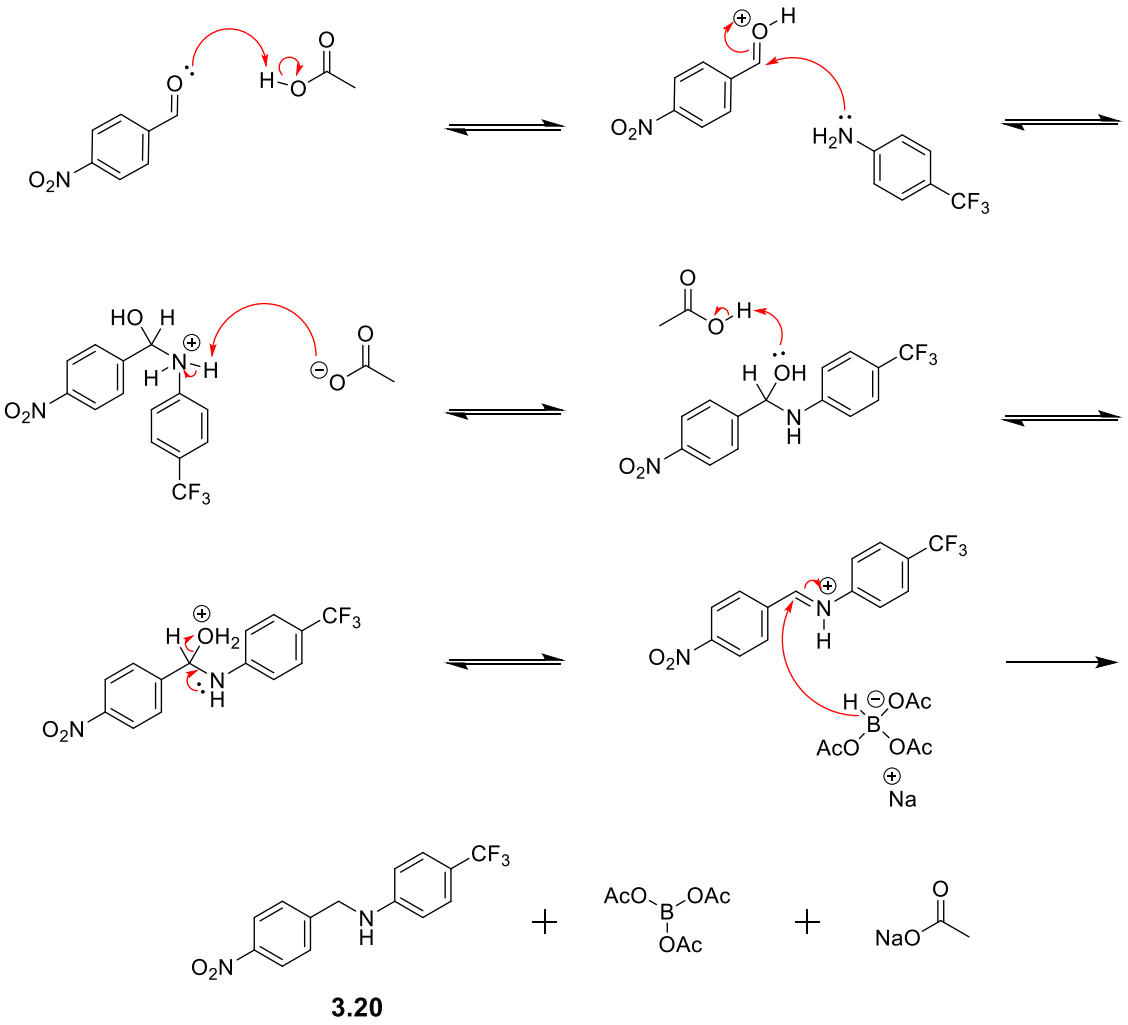

Scheme 3.3. Mechanism of reductive amination leading to the formation of **3.20**.

The reductive amination method was chosen to eliminate possible formation of tertiary or quaternary amines, while the one-pot method was chosen due to the possibility that the imine intermediate would be too unstable to isolate as a consequence of the electron-withdrawing groups on both sides of the molecule, increasing its susceptibility to nucleophilic attack. Sodium triacetoxyborohydride was employed as the reducing agent as it is less reactive than other borohydride-based reducing agents. This allowed for preferable reduction of the iminium ion to the amine, with minimal reduction of the aldehyde starting material.

Initial yields amines for **3.20** and **3.21** were 36% and 30%, respectively, while yields for **3.22** and **3.33** were 57% and 50%, respectively. We postulated that the low yields were due to slow formation of the imine intermediate and its instability. As imine formation is a condensation reaction, the H_2O released could act to hydrolyse the imine to its starting materials. To optimise the reaction, we sought to prolong the imine formation to 18 hours before the addition of the reducing agent. Anhydrous magnesium sulfate was added to the reaction mixture as a drying agent to sequester any water formed. This method saw an increase of yields across all amines, with **3.20** and **3.21** yields increased to 45% and 41%, respectively, and **3.22** and **3.33** increased to 65% and 59%, respectively. **3.20**

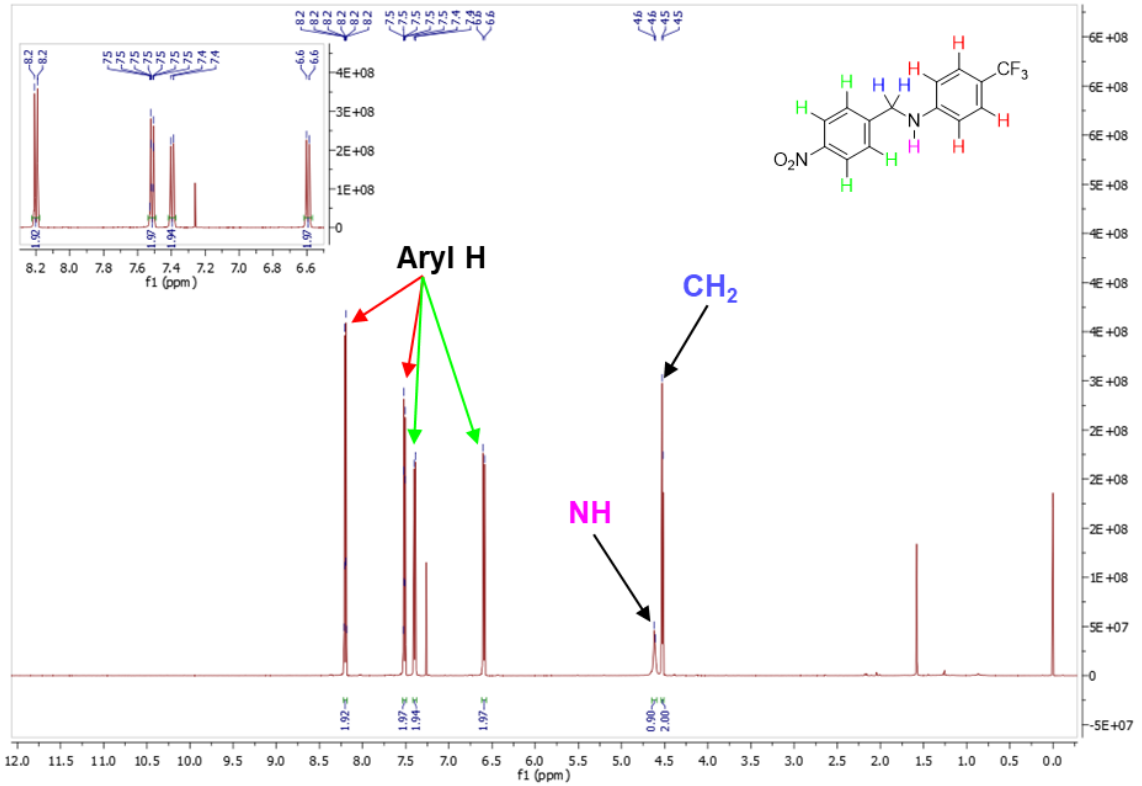

and **3.21** were purified *via* crystallisation using $CHCl_3$ while **3.22** and **3.23** were purified *via* flash chromatography.

Figure 3.10 ^{1}H NMR spectra of secondary amine **3.20** in $CDCl_3$.

The successful synthesis of the secondary amines was determined using ^{1}H and ^{13}C NMR, HRMS and IR (See Appendix). The ^{1}H NMR spectra above (Figure 3.10) shows the successful synthesis of **3.20**. The aromatic signals lie between 6.5 and 8.2 ppm, all integrating for 1H, with the protons on the phenyl ring containing the CF_3 moiety appearing as doublet of triplets while the protons of the phenyl ring containing the nitro group, appear as doublets. The methylene signal appears as a doublet at 4.5 ppm with an integration of 2H. The NH peak resonates at 4.6 ppm, appearing as a triplet with an integration of 1H.

The final step of the synthetic pathway to tertiary squaramides was the nucleophilic substitution involving the secondary amines and diethyl squarate. The reaction was performed at reflux in EtOH in the presence of zinc trifluoromethanesulfonate, acting as a lewis-acid catalyst to increase the electrophilicity of the squaramide and prevent squaraine formation (1,3 addition).

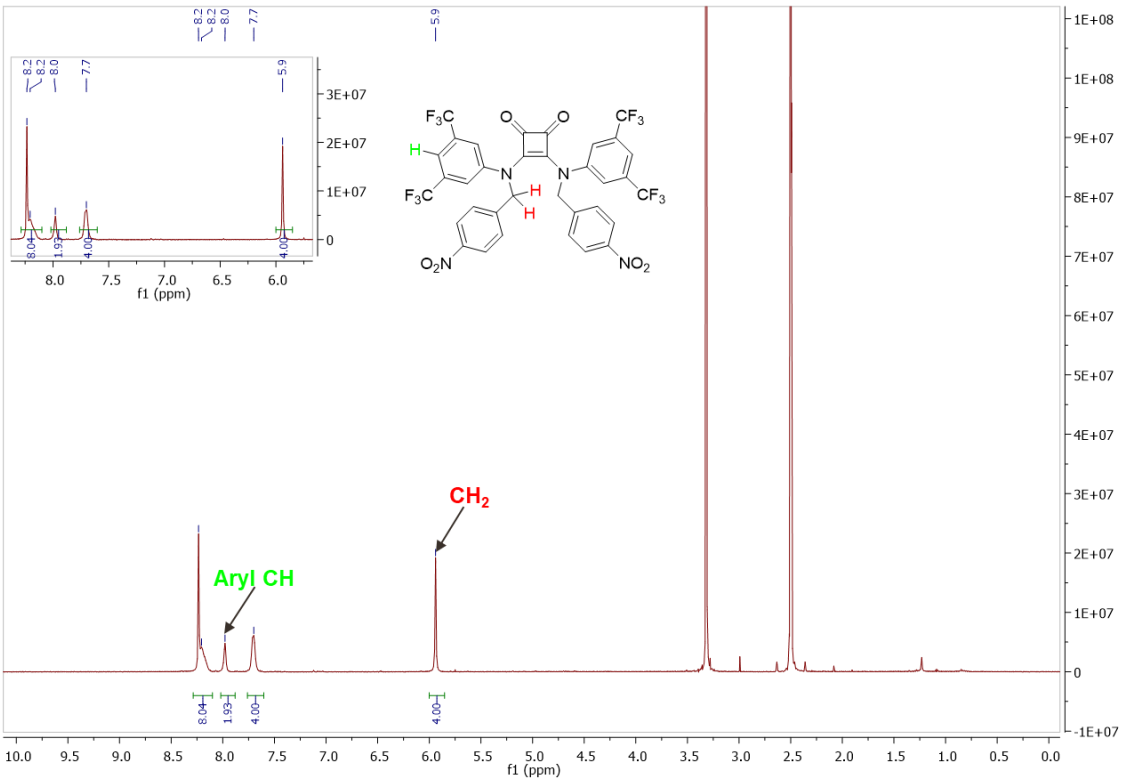

Figure 3.11 ^{1}H NMR spectra of **3.17** in DMSO-d_6.

This reaction proved to be troublesome, attributed to the poor reactivity of the secondary amine. After repeated attempts at synthesising the target tertiary

amines, only synthesis of **3.17** and **3.18** was achieved. The reaction proceeded with very poor yield of ~5% and the reproducibility of the reaction was also a cause of concern, as successful synthesis was only achieved intermittently. The ^{1}H NMR of **3.17** (Figure 3.11) was marked by the absence of NH peaks in the spectra; an indication that the tertiary squaramide had formed. All of the peaks presented as broad singlets, likely due to fast rotation of the compound on the NMR timescale. The methylene protons were present at 5.9 ppm with an integration of 4H, and the expected number of aromatic peaks were observed between 7.7 – 8.2 ppm with expected integration values. Mass spec data also supported the successful formation of the target compounds.

While synthetic issues prevailed at this point, enough material was obtained to perform preliminary analysis of the receptors and to evaluate if release of the active anion transporter occurred in the presence of the appropriate stimulus.

3.4 Preliminary Analysis

Preliminary tests were performed to investigate if **3.17** underwent a fragmentation after reduction of the nitro moiety *via* an enzymatic reduction, using NTR enzyme with NADH as a cofactor. A H_2O/DMSO (99.5/0.5; v/v) solution containing 10 µM of the receptor and 10 µg/mL of NTR and 500µM NADH was stirred at room temperature for 30 minutes. An aliquot of the solution was analysed via LC-MS to determine if fragmentation occurred. The UV trace (Figure 3.12, a) showed a complex mixture containing multiple peaks and due to the low concentration of the sample, baseline drift was also observed, obstructing a full analysis. However, it was evident due to the multiple peaks that a reaction had occurred.

The protonated mass of the **3.17** (807.5 amu) and the anionophore **1.59** (537 amu) were both observed in the extracted ion chromatogram (Figure 3.12, b) indicating that after enzymatic reduction of **3.17** *via* NTR, the SRAT underwent a fragmentation to release an active anion transporter, and that a full conversion of the **3.17** to **1.59** was not achieved. Full fragmentation and conversion to **1.59** could be attributed to the imperfect fit of the tertiary squaramide substrate to the NTR enzyme or due to slow kinetics of the enzymatic reduction.

Due to limited quantity of the SRAT and the irreproducible synthesis, further analysis could not be performed. While the evidence was not conclusive and the exact release mechanism was still to be elucidated, the preliminary results of **3.17** were promising in the journey to creating squaramide-based stimuli-responsive anionophores.

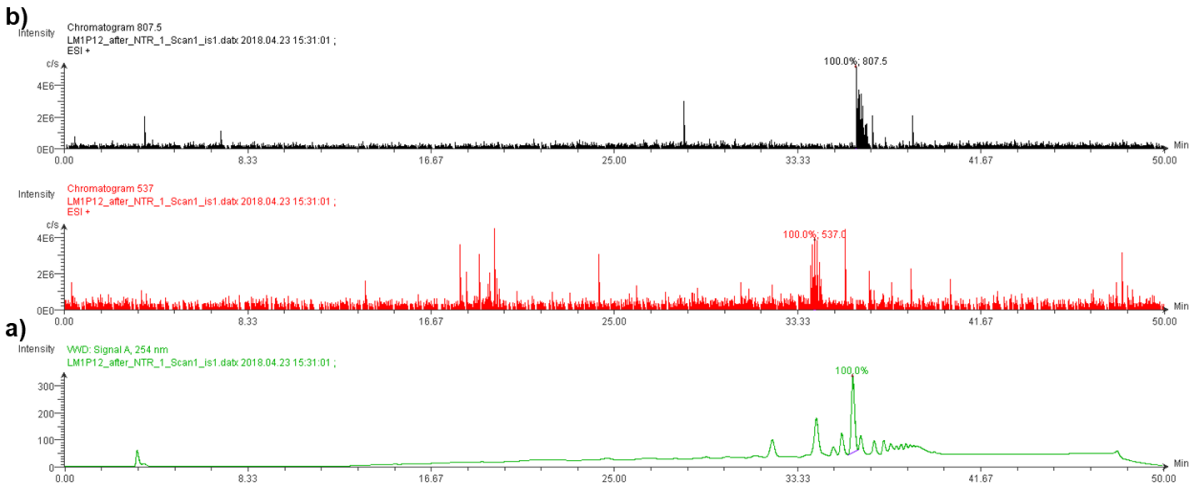

Figure 3.12 a) UV trace (254 nm) of **3.17** post-enzymatic treatment with NTR. b) Extracted ion chromatograph (XIC) of **3.17** post-enzymatic treatment with NTR. SRAT **3.17**, [M+H] 807.5 amu (red). Released anion transporter **1.59**, [M+H] 537 amu (green).

In a bid to further investigate the SRAT strategy, the efficacy of the OTIPS trigger's response to F^- was performed using a ^1H NMR titration in DMSO-d_6 (0.5% H_2O) where **3.18** was treated with TBAF in increasing equivalents. Upon addition of F^- to the solution containing the receptor, the signal corresponding to the methylene protons at ~5.6 ppm gradually reduced in intensity until it disappeared entirely. A large change in the aromatic region was observed with the reduction of intensity of some signals and the appearance of new ones. A triplet appearing at 16 ppm was observed after addition of five equivalents of F^-, indicating the formation of HF_2^-.

While the NMR data does not provide any definitive explanations as to what is occurring when **3.18** is exposed to F^-, it is apparent that the molecule is changing in response to F^-, as evidenced by the stark changes in the NMR spectra. It is possible that a deprotection of the TIPS moiety is occurring in the presence of TBAF without the SRAT fragmenting to release **1.56**, causing the formation of the phenol-derivative of **3.18**. This would account for the appearance of new peaks in the ^1H NMR spectra as two species, the protected and deprotected SRAT, were present in solution. The presence of the signal

corresponding to HF_2^- could be attributed to the deprotonation of the phenol hydrogen. It is also possible that **3.18**, was underwent fragmentation to release **1.59** after the deprotection of the TIPS moiety. This would also account for the appearance of additional peaks in the observed spectra, and the presence of HF_2^- could be attributed to the deprotonation of the released receptor, **1.59.** However, it is important to note that there is no conclusive evidence for either of these events in the ^{1}H NMR spectra.

While the preliminary analysis did not yield any definitive evidence of either the enzyme-responsive nor the chemo-responsive anion transporter releasing the desired anionophore after treatment with appropriate stimulus, the results were promising enough to pursue further. The irreproducibility and poor yield of the synthesis of the tertiary squaramides was the major hurdle in further analysing these compounds. Our attention then turned to the optimisation of the final step of the synthesis to produce a robust and reliable synthetic pathway to our target molecules.

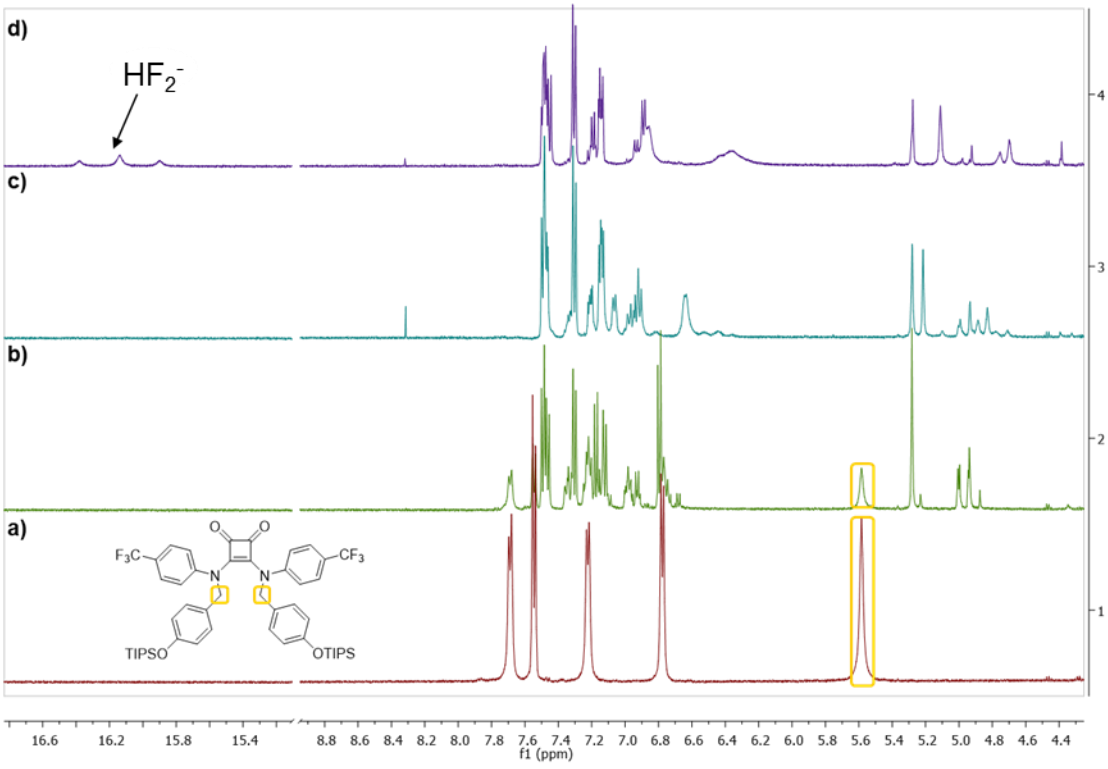

Figure 3.13 ^{1}H NMR stackplot of **3.18** (2.5 x 10^{-6} M) treated with TBAF. a) Blank spectra of **3.18** (no F^- present). b) **3.18** + 1 equiv. TBAF. c) **3.18** + 2 equiv. TBAF. d) **3.18** + 5 equiv. TBAF.

3.5 *Synthesis Optimisation of Tertiary Squaramides.*

We postulated that synthesis of the tertiary squaramides did not proceed due to the steric and electronic nature of the synthesised secondary amines. The secondary amines feature bulky phenyl and benzyl moieties, which could cause steric clash during the substitutions with diethyl squarate. Electronically, the amines are also deactivated due to the ability of the lone pairs of the nitrogen to donate into the phenyl ring bearing electron withdrawing substituents. It was decided to use a model reaction to investigate these effects in detail.

As the design of the stimuli-responsive anion transporters relied on the use of tertiary squaramides, reducing the possible steric hindrance of the secondary amines was not an avenue that could be explored. To create more favourable conditions for the nucleophilic substitution, it was decided to i) attempt to increase the electrophilicity of the squarate to compensate for the poor nucleophilicity of the secondary amines, and ii) perform a base screen to attempt to increase the nucleophilicity of the amines.

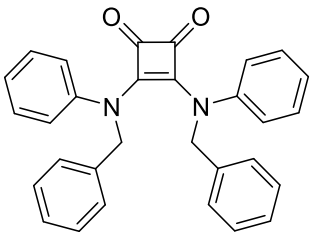

3.24

Figure 3.14 Chemical structure of model tertiary squaramide, **3.24**.

Tertiary squaramide **3.24** was used as a model target molecule for the synthesis optimisation (Figure 3.14), with *N*-benzylaniline being used as a model amine in the reaction.

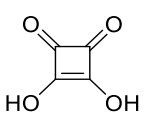

2.16

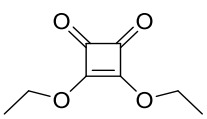

2.17

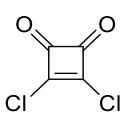

3.25

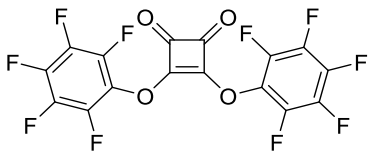

3.26

Figure 3.15 Four squarate starting materials in the synthesis optimisation of tertiary squaramides.

The first approach investigated was to increase the electrophilicity of the squarate starting material. After consultation with the literature, four squarate derivatives were chosen for trial in the synthesis optimisation (Figure 3.15). Diethyl squarate was chosen as the control starting material. Taking inspiration from amide-coupling chemistry, squaric acid, **2.16**, was selected as it was postulated that the hydroxyl groups could act as a nucleophile in the formation of an activated ester, which could then facilitate nucleophilic substitution. Squarate **3.26** was selected as pentafluorophenyl esters have been reported in literature as an intermediate in amide bond formation.[173] 3,4-dichlorocyclobut-3-ene-1,2-dione, **3.25**, has also been reported to have been used in the synthesis of squaramides.[150]

The control reaction (Scheme 3.3) of reacting *N*-benzylaniline and diethyl squarate in the presence of $Zn(OTf)_2$ yielded no product after reflux over 72 hours. LCMS analysis showed only unreacted starting materials present in the reaction mixture. This was not unexpected as it mirrored results seen previously for this reaction type.

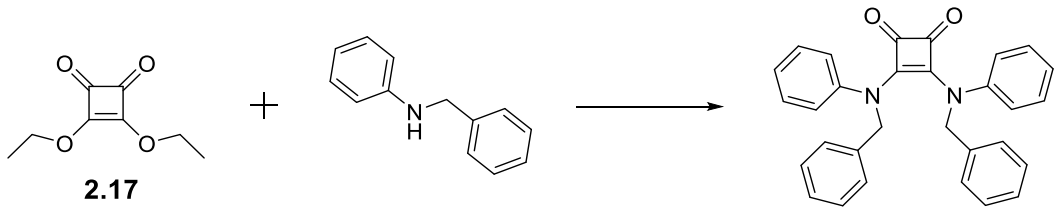

Scheme 3.3 Attempted synthesis of **3.24** *via* nucleophilic substitution of diethyl squarate. *Reagents and conditions:* $Zn(OTf)_2$, EtOH, 80℃, 72 h.

The next avenue explored was using squaric acid as a nucleophile in generating an activated ester intermediate, similar to amide-formation between a carboxylic acid and an amine (Scheme 3.4). Three coupling reagents were trialled, DCC, EDCI and PyBOP and each reagent yielded no product. LCMS analysis showed in each case, unreacted squaric acid and amine. It is likely that squaric acid cannot act as a nucleophile in the formation of an activated ester with the coupling reagents due to its low pKa.

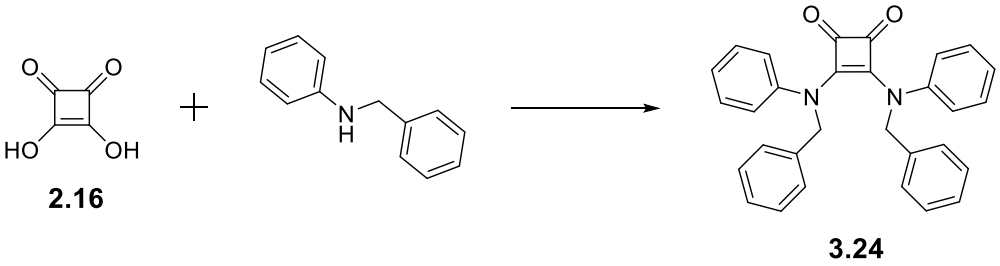

Scheme 3.4 Attempted synthesis of **3.24** *via* coupling reaction. *Reagents and conditions:* Coupling reagent: DCC/ EDCI/ PyBOP, DMAP, DCM (anhydrous), N_2, rt, 18 h.

3,4-dichloro-cyclobut-3-ene-1,2-dione seemed to be an attractive choice as an electrophile as the chloro substituents might act as a superior leaving group over the ethyl ester. Using an adapted procedure from Lunelli,[174] squaric acid was reacted with thionyl chloride to convert the squaric acid to squaric chloride (Scheme 3.5). Repeated attempts of this synthesis was met with failure, as the product failed to crystallise from solution. This method, while potentially promising, was ruled out due the inability of synthesising the desired intermediate.

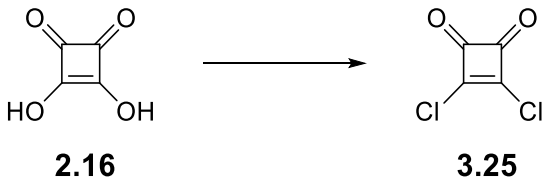

Scheme 3.5 Attempted synthesis of 3,4-dichlorocyclobut-3-ene-1,2-dione. *Reagents and conditions:* Thionyl chloride, $CHCl_3$, DMF, 50℃, 4 h.

Typically, pentafluorophenyl esters of carboxylic acids are generated using a coupling reagent and pentafluorophenol. However, as previous attempts of reacting squaric acid and various coupling reagents failed, a transesterification was attempted (Scheme 3.6). Diethyl squarate was stirred in THF in the presence of a vast excess of pentafluorophenol. The reaction was let proceed at room temperature and the temperature was subsequently increased to 70℃, however, LCMS analysis showed no evidence of transesterification.

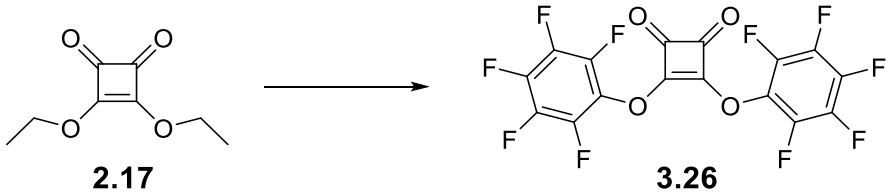

Scheme 3.6 Attempted synthesis of **3.26** *via* transesterification. *Reagents and conditions:* Pentafluorophenol, THF, rt - 70, 48 h.

Attempting to synthesise a more electrophilic squarate derivative yielded no success, despite numerous approaches and attempts. Our next approach was to attempt to use a base to increase the nucleophilicity of the amine.

DMAP, NEt_3, DIPEA, and NaH were the bases trialled, in conjunction with $Zn(OTf)_2$, in the attempted nucleophilic substitution using *N*-benzylaniline and diethyl squarate (Scheme 3.7). These bases were selected due to their non-nucleophilic nature, either due to steric hindrance or electronics, and display a range of base strength. Diethyl squarate was selected as the squarate starting material, as it was used when the reaction was previously successful.

The use of DMAP and DIPEA did not result in the formation of the tertiary squaramide, which was verified again by LCMS analysis. Surprisingly, even the strong base NaH did not encourage the reaction to proceed. When NEt_3 was employed, at reflux temperatures in EtOH over the period of one week, a precipitate was formed and isolated. ^{1}H NMR and HRMS analysis revealed we had synthesised **3.24**. However, the yield was still poor at 4% and the issues around reproducibility remained the same.

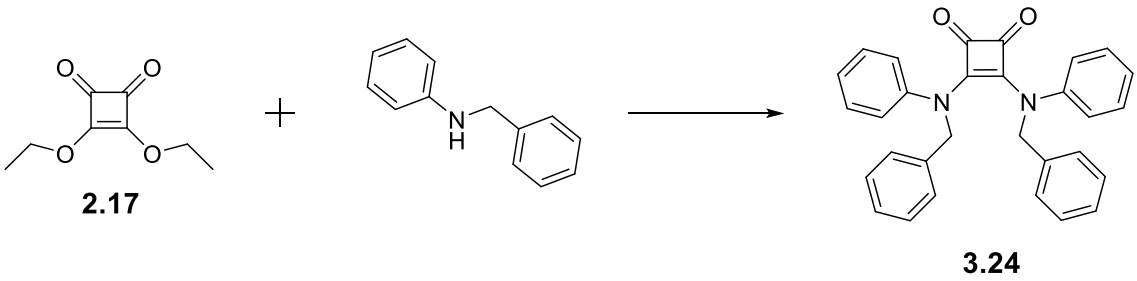

Scheme 3.7 Synthesis of model tertiary amine, **3.24**. *Reagents and conditions:* Base: DMAP/ NEt_3/ DIPEA/ NaH, EtOH/DCM, 80℃, 18 h – 1 week.

The ^{1}H NMR spectra of **3.24** (Figure 3.16), shows the formation of the model tertiary squaramide. Similar to the ^{1}H NMR spectra of **3.17** (Figure 3.11), all signals were broad singlets or poorly resolved multiplets. The methylene protons appeared at 5.6 ppm and the aromatic protons resonated between 7.2 – 7.3 ppm. The integration values were as expected and there was no apparent evidence of NH signals.

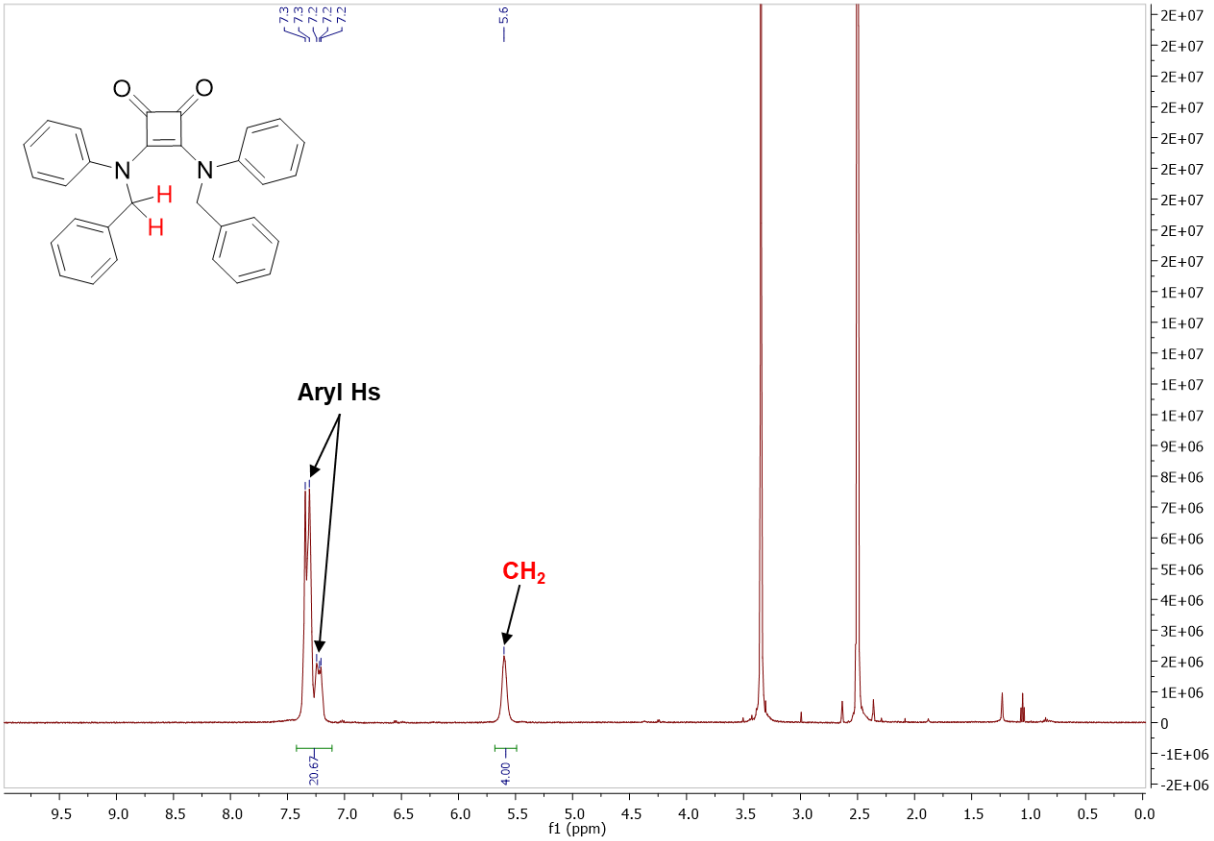

Figure 3.16 ^{1}H NMR spectra of **3.24** in DMSO-d_6.

A turning point in this project was reached when a crystal of **3.24** was obtained. X-ray crystal structure analysis (performed by Dr. Chris Hawes, The University of Keele, UK) revealed that a squaramide had not been synthesised but in fact, the reaction yielded squaraine **3.27**, resulting from a 1,3-disubstitution of the squarate (Figure 3.17). The bond lengths of the squaraine ring were all

equal at 1.461(2) Å as were the C-N bond lengths between the ring and the amino substituents 1.328(2) Å.

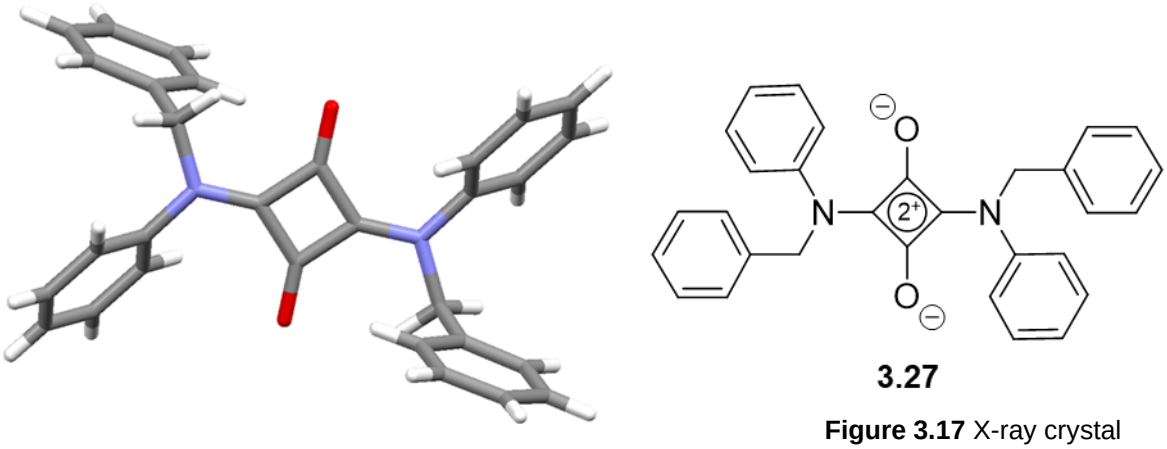

Figure 3.17 X-ray crystal structure of disubstituted squaraine (left). Chemical structure of squaraine **3.27** (right).

Squaraines are synthesised utilising squaric acid as a building block.[175] It is not fully understood how a squaraine was the product of our reaction when using diethyl squarate. We postulate that prolonged reflux could have resulted in the hydrolysis of diethyl squarate back to squaric acid where it then reacts to form a squaraine.

This was a vital result as it cast our previous preliminary data in regards to **3.17** and **3.18** into question. It cannot be said with certainty that our preliminary analysis was performed with squaramides or squaraines, as NMR and HRMS would not allow us to determine whether a squaramide or squaraine product had been isolated.

Given the persistent synthetic problems with these molecules, we chose not to further pursue this design for stimuli-responsive anion transporters. We turned our focus away from tertiary squaramides to tertiary ureas, instead. This slight change in design would eliminate the possibility of isomer formation and would allow us to employ the secondary amines we had developed thus far to prove the principle of SRATs.

3.6 *Synthesis and Characterisation of Tertiary Ureas*

Our new design approach features ureas as the anion-binding unit. While simple ureas do not display high anion binding affinities or anionophoric activity compared to squaramide analogues, their application in transmembrane anion transport is well documented, as discussed in Chapter 1. The chemical structure of the SRATs would remain largely the same, featuring an enzymatic-trigger masking the NH groups in the form of a *p*-nitrobenzyl moiety (Figure 3.18).

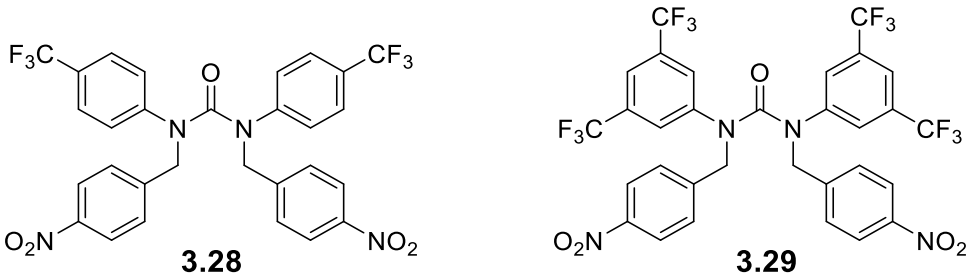

Figure 3.18 Chemical structure of tertiary urea SRATs.

The first step in this new direction was to explore the synthesis of tertiary ureas using a model reaction, similar to those performed previously when optimising the synthesis of tertiary squaramides (Scheme 3.8) *N*-benzylaniline was employed as a model amine. Triphosgene was chosen as the electrophilic reagent, as it is a safer alternative to phosgene. Using mild conditions and NEt_3 as a base, the reaction proceeded and gave tertiary urea, **3.30**, in a yield of 10%, after purification *via* flash chromatography. Successful synthesis was verified by NMR and HRMS analysis.

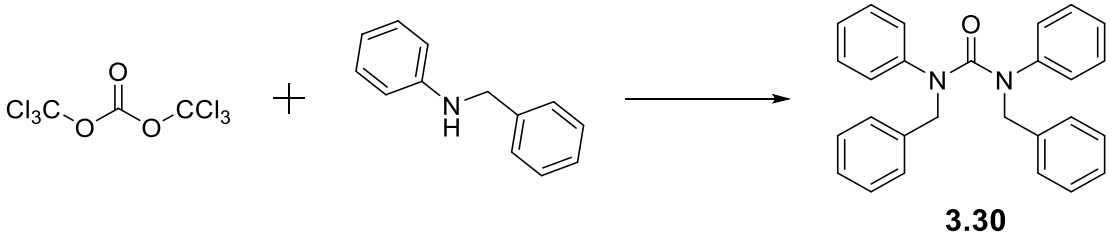

Scheme 3.8 Synthesis of model tertiary urea. *Reagents and Conditions:* NEt_3, DCM (anhydrous), N_2, rt, 18 h.

The ^1H NMR spectrum of **3.30** (Figure 3.19, a) showed a characteristic absence of a NH signal, indicating that a tertiary urea had been formed. The methylene protons resonated at 4.8 ppm, integrating for 4 H, and the aromatic protons appeared as complex multiplets between 6.6 and 7.3 ppm with a total

integration of 20 H. The ^{13}C NMR spectra (Figure 3.19, b) contained a peak at 161 ppm, indicating the presence of a carbonyl carbon, which added further evidence that a urea had been formed.

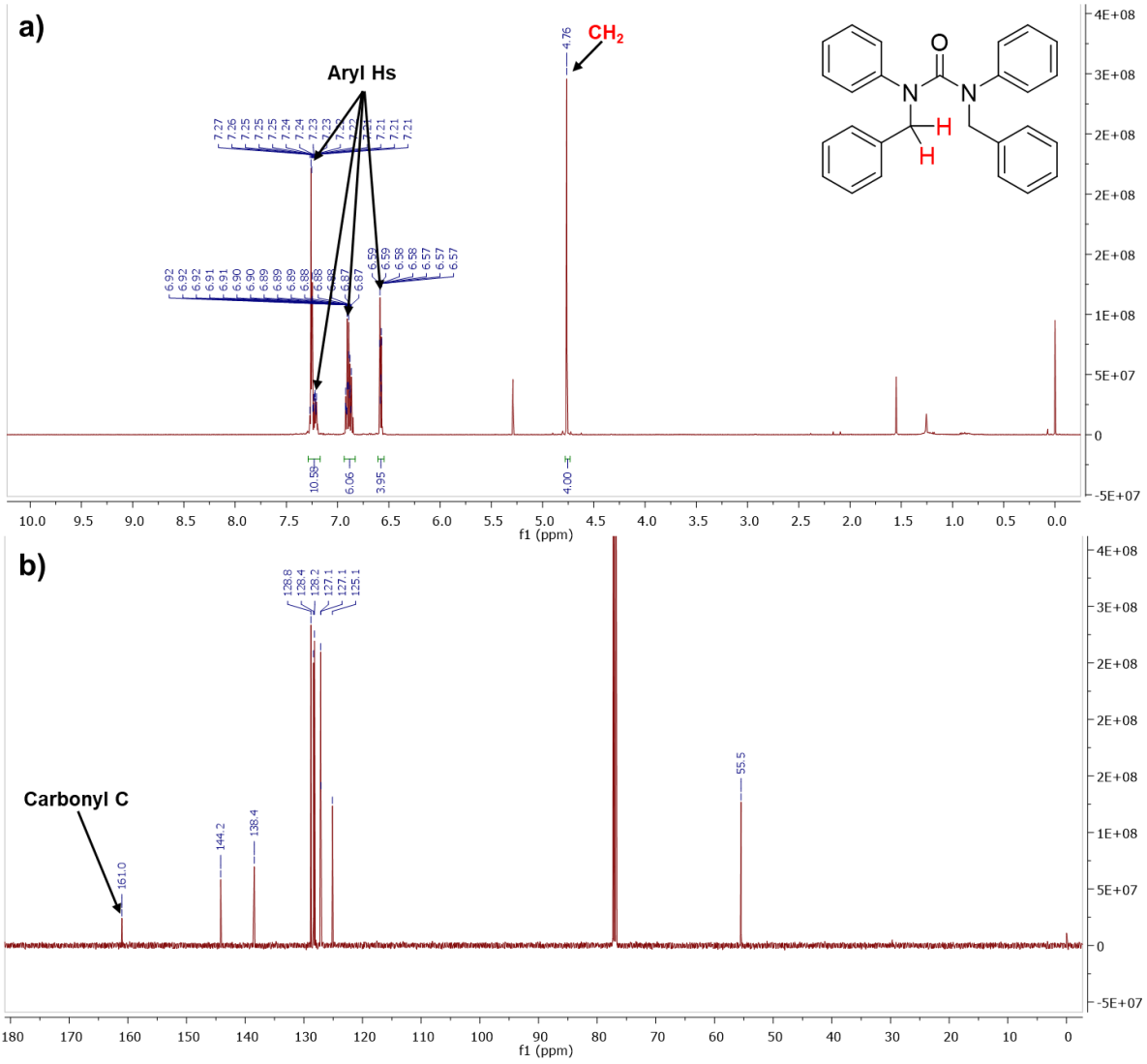

Figure 3.19 a) ^{1}H NMR spectrum of **3.30** in $CDCl_3$. b) ^{13}C NMR spectrum of **3.30** in $CDCl_3$.

A crystal of **3.30** was obtained *via* slow evaporation of a solution of **3.30** in $CHCl_3$. X-ray crystallographic analysis confirmed that we had successfully synthesised our target tertiary urea (Figure 3.20). The phenyl rings were pointing in parallel directions in the *anti*- orientation, while the benzyl moieties were in the were in the *syn*- orientation. While we expected the orientations to be reversed, we anticipated that once undergone fragmentation that the released NH hydrogen bond donor groups would be placed in the *anti*- orientation to facilitate anion binding. This result was confirmation that this avenue of exploration was feasible in our goal to create stimuli-responsive anion transporters.

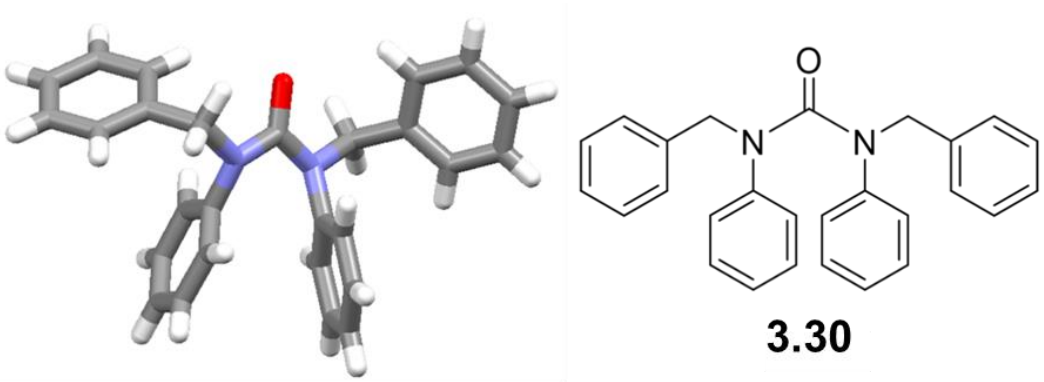

Figure 3.20 X-ray crystal structure of model tertiary urea, **3.30** (left). Chemical structure of tertiary urea **3.30** (right).

Following on the success of the synthesis of model tertiary urea, **3.30**, identical conditions were used in attempts to synthesise tertiary ureas bearing the nitrobenzyl trigger (Scheme 3.9). However, several attempts using these conditions were met with no success after ^{1}H NMR and LCMS analysis of the reaction mixture did not indicate any presence of the target compounds. We postulated that the presence of the electron-withdrawing trifluoromethyl moieties on the secondary amines were reducing its nucleophilicity. To overcome this obstacle, another base screen was performed with the aim to increase the nucleophilicity of the amine.

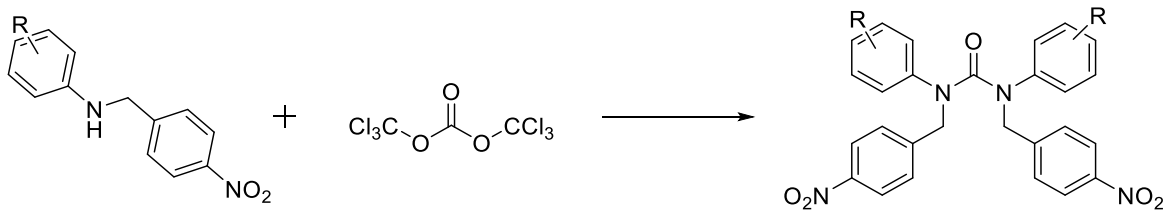

3.31: R = 4-CF_3
3.32: R = bis-3,5-CF_3

Scheme 3.9 Attempted synthesis of tertiary ureas, **3.31** and **3.32**, featuring nitrobenzyl trigger. *Reagents and Conditions:* DMAP/ NEt_3/ DIPEA/ DCM (anhydrous), N_2, rt, 18 h.

DMAP and DIPEA were again chosen for the base trial due to their non-nucleophilic nature. The base trial failed to yield any positive results, as no indication of product formation was found during ^{1}H NMR and LCMS analysis of reaction mixtures, after repeated attempts.

As unsubstituted urea, **3.30**, was able to be successfully synthesised, we postulate that the difficulty in synthesising **3.31** and **3.32** was due to the presence of the CF_3 and NO_2 moieties. As both moieties are electron-withdrawing, the electron density around the nitrogen atom could be severely reduced, resulting in

poor nucleophilicity. The steric bulk of these moieties could also be hindering reaction progress by preventing the amine approaching the electrophilic site at the Bürgi–Dunitz angle of 107°.[176]

3.7 *Conclusion*

Despite our best efforts, both the tertiary squaramides and the tertiary ureas we had envisaged as stimuli-responsive anion transporters, were not obtained. We synthesised four novel secondary amines, **3.16** – **3.19**, bearing a NTR-sensitive nitrobenzyl trigger and a fluoride-sensitive triisopropylsilyl ether trigger, which were characterised by NMR and IR spectroscopy and HRMS. Reaction of these secondary amines with diethyl squarate were met with mixed success, with what was thought to be **3.17** and **3.18** being the only target molecules synthesised and characterised.

Preliminary analysis of these compounds revealed a fragmentation process occurring upon treatment of the appropriate stimuli. Through LCMS analysis, **3.17** was shown to fragment in the presence of NTR and NADH, to release what was thought to be active anionophore **1.59**. Treatment of **3.18** with TBAF, led to dramatic changes in its ^{1}H NMR spectrum, where subsequent additions of excess TBAF led to the appearance of a H_2F triplet signal at ~16 ppm, possibly indicating the deprotonation of **1.59**. Full elucidation and in-depth analysis of these processes were unable to be performed due to the difficult, and unreliable, synthesis.

In our efforts to optimise the synthesis of the tertiary squaramides using a model amine and target model tertiary squaramide, **3.24**, X-ray crystal structure analysis revealed that we had in fact synthesised squaraine **3.27**. With the validity of our preliminary results questioned and, in order to move away from persistent synthetic problems with these molecules, we chose to modify our design to incorporate tertiary ureas.

Unfortunately, this new design was met with further synthetic problems as the target compounds failed to form under various conditions, due to possible deactivation of the nucleophile and steric hindrance caused by the substituents of the phenyl moieties.

Future work will be undertaken in attempts to create a viable synthetic pathway to **3.16** – **3.19**. Ullmann reactions, which utilises copper-catalysed aryl coupling[177] and Buchwald-Hartwig coupling reactions, which created C-N bonds through palladium-catalysed coupling between and aryl halide and aryl amine,[178] are promising avenues to explore in moving towards further examples of stimuli-responsive anion transporters.

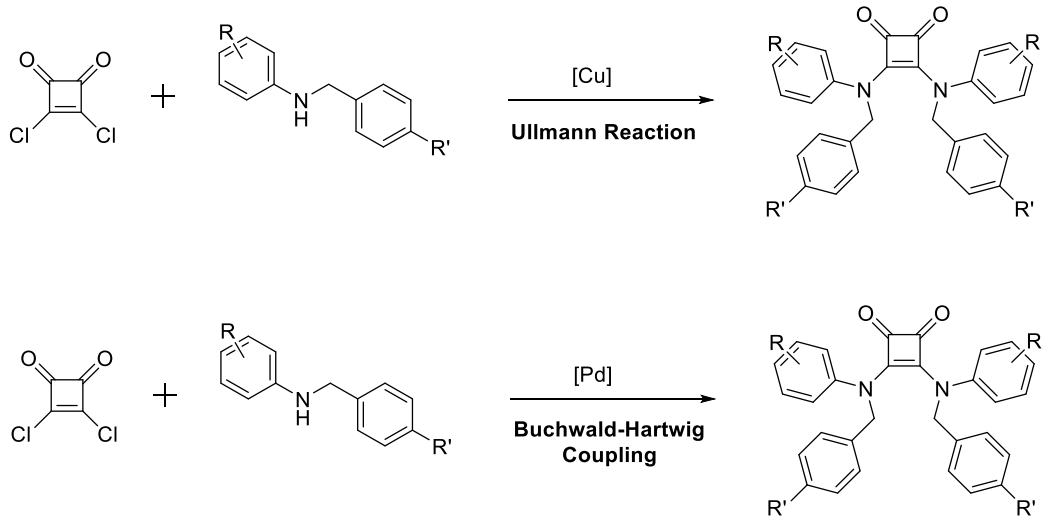

Scheme 3.10 Potential synthetic routes to tertiary squaramides employing the metal-based catalysed Ullmann and Buchwald-Hartwig coupling reactions, which couple aryl halides to amines, resulting in the formation of a C-N bond.

Chapter 4

Squaramidoquinoxalines as Anion Sensors

4 Squaramidoquinoxalines as Anion Sensors

4.1 Introduction

While anions play critical roles in biology, as outlined in Chapter 1, they can also act as environmental contaminants and cause both environmental and health concerns. For example, groundwater may become contaminated with sulphate from mining and excessive use of fertilisers, and while sulphate is not overtly toxic, it can cause dehydration, diarrhoea and catharsis if consumed in large amounts.[179] An abnormal level of sulfate in urine can be a marker for renal failure or cardiovascular disease.[180] Nitrate and phosphates are one of the most common contaminants of groundwater due to leaching of fertilisers, which can lead to eutrophication of rivers and lakes, resulting in of the death of aquatic animals and loss of biodiversity.[6]

Fluoride is a frequent groundwater contaminant due to weathering and leaching of fluoride-containing minerals from rocks. While fluoride is beneficial in dental health, excess consumption can lead to fluorosis.[181] Fluoride is also a hydrolytic degradation product of some nerve agents, and the its presence can be used to identify chemical warfare agents.[182] As such, the ability to selectively detect anions is a useful tool in environmental and health sciences.

Beyond their application in anion transport, squaramides have also been employed in anion sensing. There are numerous examples in the literature of squaramides acting as fluorescent or colourimetric sensing units for anions in solution, such as polymerisable squaramides, **4.1** – **4.6**, produced by Bollen *et al.* (Figure 4.1).[183]

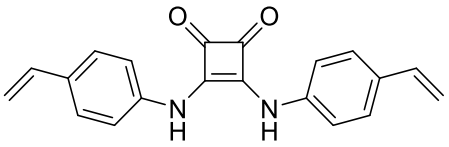

4.1

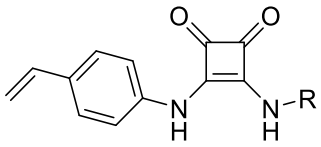

4.2: R = Phenyl
4.3: R = 3-nitrophenyl
4.4: R = 3,5-bis(trifluoromethyl)phenyl
4.5: R= Benzyl
4.6: R = 3,5-bis(trifluoromethyl)benzyl

Figure 4.1 Chemical structures of polymerisable squaramides synthesised by Manesiotis *et al*.

These squaramides were capable of forming molecularly imprinted polymers (MIPs) that increased their binding to a model anion. The monomeric units were also shown to bind to anions, which were evaluated using UV-vis spectroscopy, where the squaramides containing the most electron-withdrawing groups displayed the highest association values. Upon treatment of receptors **4.4** and **4.6** with excess fluoride, a colour change was observed, as evidenced by a corresponding appearance of an absorbance band at 470 nm, indicating a charge transfer between two species. A MIP created using **4.4**, templated with TBAF, resulted in polymeric particles that underwent a rapid and reversible association of TBAF causing colour changes observable by the naked eye.

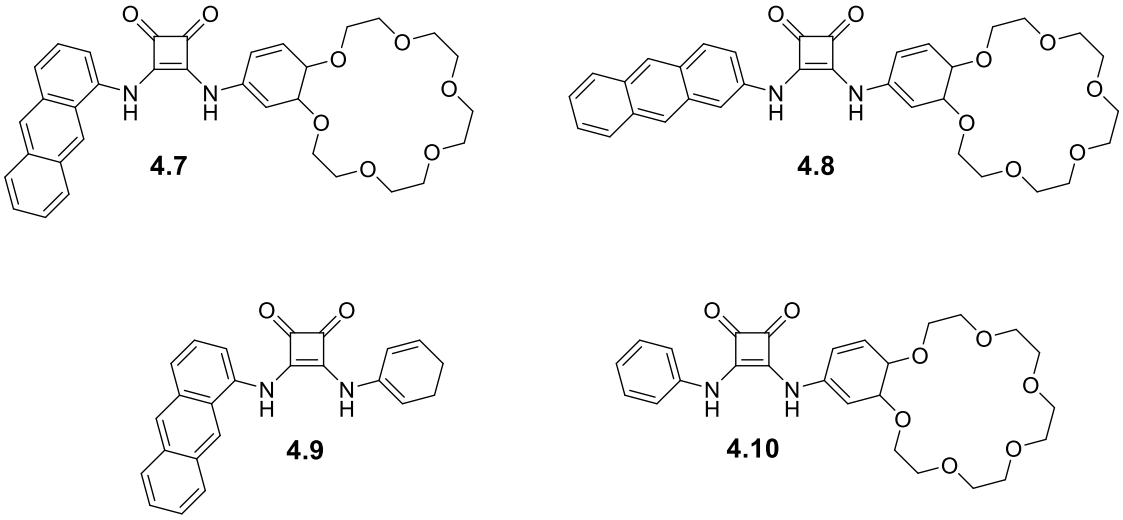

Figure 4.2 Family of squaramides synthesised by Zaleskaya-Hernik *et al.*

Romański *et al*. investigated the structure activity relationship of a family of ditopic squaramides, **4.7** – **4.10** (Figure 4.2).[184] Receptors **4.7** and **4.9** were found to bind more strongly to chloride than **4.8** and **4.10**, attributed to the close proximity of the aromatic protons of the 1-aminoanthracene moiety. Upon addition of potassium salts to receptors **4.7** and **4.8**, a decrease in fluorescence was observed, while addition of excess quantities of sulfate salts quenched the fluorescence. Deprotonation of the receptors was observed upon the treatment of the receptors with TBAF, marked by a fluorescence change from green to orange. By adding water to the solvent, different fluorogenic responses were observed. In dry solvents, addition of sulfate salts caused fluorescence quenching. However, in wet solvents the formation of receptor:sulfate complexes resulted in an increase in fluorescence intensity.

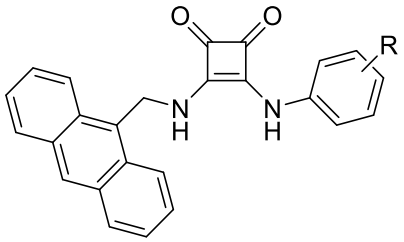

4.11: R = 3,5-bis(trifluoromethyl)phenyl
4.12: R = 4-trifluoromethylphenyl
4.13: R = 4-nitrophenyl
4.14: R = Phenyl

Figure 4.3 Squaramides synthesised by Elmes *et al*. that allow for selective sensing of chloride *via* H-bond formation

Detection of anions is not restricted to monitoring deprotonation events as shown by Jolliffe *et al*. where H-bond formation was also exploited.[185] The authors reported a family of colourimetric and luminescent anion sensors, **4.11** – **4.14**, by employing an anthracene moiety appended to a squaramide scaffold (Figure 4.3). Using UV-vis spectrometry, minimal interaction of the receptors with Br^-, I^- and NO_3^- was observed. However, upon addition of Cl^- to **4.11** and **4.12**, a hyperchromic shift at 393 nm and a hypochromic shift at 355 nm was recorded in their absorption spectra, resulting in a naked-eye colour change from colourless to yellow. **4.13** behaved similarly when treated with Cl^- with hyper- and hypochromic shifts with an additional hypsochromic shift of 5-10 nm, resulting in a colour change from orange to deep red, visible to the naked eye.

The fluorescence properties of these receptors were also found to be significantly affected upon treatment with Cl^-, as fluorescence excimer emission centred at 530 nm was significantly ‘‘switched off’’ by 66% for **4.11**. The authors postulated that the observed spectroscopic changes were caused by deprotonation of the squaramide, due to the increased acidity of the squaramide NH moieties due to the presence of the highly electron-withdrawing CF_3 substituents.

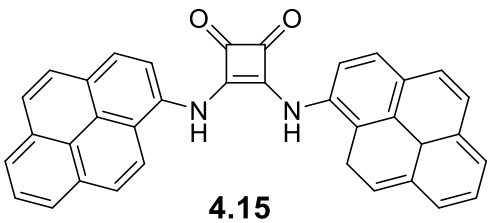

4.15

Figure 4.4 Chemical structure of *N*,*N’*-bis(1-pyrenyl) squaramide reported by Caltagirone *et al*.

Indeed, fluorescent moieties are often incorporated into chemosensors, as seen with the *N*,*N'*-bis(1-pyrenyl) squaramide reported by Caltagirone *et al* (Figure 4.4).[186] This squaramide, containing a 1-pryenyl fluorogenic moiety, through ^{1}H NMR analysis in DMSO-d_6, **4.15** was shown to interact with Cl^- *via* H-bonds formed from the squaramide NH groups in cooperation with weaker aromatic C-H hydrogen bonds. Although large shifts of the NH signals were observed during ^{1}H NMR titrations, the determined binding constants was relatively low at K_a = 98 ± 6 M^{-1}. This was attributed to possible competitive binding of DMSO to **4.15**, based on results from solid-state studies. Basic anions F^-, CN^-, and BzO^- resulted in a deprotonation of the NH groups, causing a colour change from colourless to yellow.

UV-vis studies were performed to further investigate this behaviour, which confirmed deprotonation of the sensor, as upon treatment of **4.15** with OH^- resulted in the disappearance of the absorbance band at 411 nm coinciding with the formation of two new absorbance bands centred at 348 and 465 nm. Similar results were obtained when the sensor was treated with F^- and CN^-.

Fluorescence studies with **4.15** showed that the receptor interacted strongly with F^- and CN^- before deprotonation occurs. Addition of less than one equivalent of these anions, resulted in an appearance of a new emission band at centred at 485 nm, and upon subsequent additions of F^- and CN^- of up to two equivalents, this new emission band disappeared due to deprotonation of the chemosensor. The utility of **4.15** extended beyond anion sensing, as upon treatment of the sensor with Cu^{2+}, the emission band at 425 nm was switched off as a new band centred at 480 nm formed. Binding analysis determined that **4.15** formed a 2:1 metal-to-ligand complex with Cu^{2+}.

Addition of four equivalents of F^-, CN^- and OH^- to the **4.15**:Cu^{2+} complex resulted in a bathochromic shift of the emission properties of the chemosensor, where a colour change from green to pale red was observed by the naked eye. Further addition of these basic anions up to 10 equivalents led to a decrease in the absorbance band at 380 nm, alongside the formation of a new absorbance band at 480 nm, suggesting deprotonation of the sensor.

While the above examples are just a flavour of the strategies employed in anion sensing, it is evident that squaramides are effective as selective anion sensors and are privileged structures due to the variability of NH acidities and H-bonding propensities. Thus, the possibilities that the squaramide motif presents for the rapid, naked-eye detection of potential anionic environmental pollutants and biomarkers make it particularly interesting for further exploration.

4.2 Chapter Objectives

In this chapter, we aim to develop a small family of squaramide-based anion sensors inspired by Chen *et al*. and their previously reported squaramidoquinoxaline (cyclobuta[b]quinoxaline1,2(3H,8H)-dione) moiety, **4.16** (Figure 4.5). This receptor demonstrated a ratiometric and colourimetric response to fluoride, undergoing a colour change from colourless to pale orange in the presence of F^- due to deprotonation of the NH.[187]

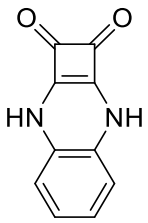

4.16

Figure 4.5 Structure of squaramidoquinoxaline reported by Chen *et al*.

We wished to investigate this motif further, by appending an electron-withdrawing group and an electron-donating group, NO_2 and OMe, respectively, onto the phenylene ring (Figure 4.6). We envisaged that substituents of the phenylene ring would result in variations of the NH acidities, which would allow for control over anion recognition selectivity. What follows are the results of the synthesis of these squaramidoquinoxalines, in depth structural characterisation and an investigation of their physical properties and anion sensing behaviour using a combination of NMR spectroscopy, UV-Vis spectrometry and computational analysis.

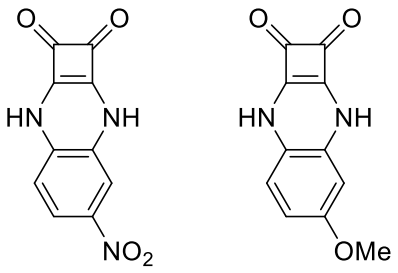

4.17 **4.18**

Figure 4.6 Structure of target squaramidoquinoxaline bearing electron-withdrawing and electron-donating moieties.

4.3 Synthesis and Characterisation of Squaramidoquinoxalines

The synthetic route to squaramidoquinoxalines was proposed as a simple two-step synthesis (Scheme 4.1). The first step being the synthesis of diethyl squarate, **2.17**, as discussed in Chapter 2. The second step involved the nucleophilic substitution of *o*-phenylenediamine derivatives with diethyl squarate in the presence of $Zn(OTf)_2$ to yield the desired products. The yields of **4.16** – **4.18** ranged from moderate to near quantitative, with **4.16** being obtained in 64% yield, **4.17** in 74% yield, and **4.18** in 97% yield. Sensors **4.16** – **4.18** were fully characterised using NMR, IR, HRMS and UV-Vis spectroscopy.

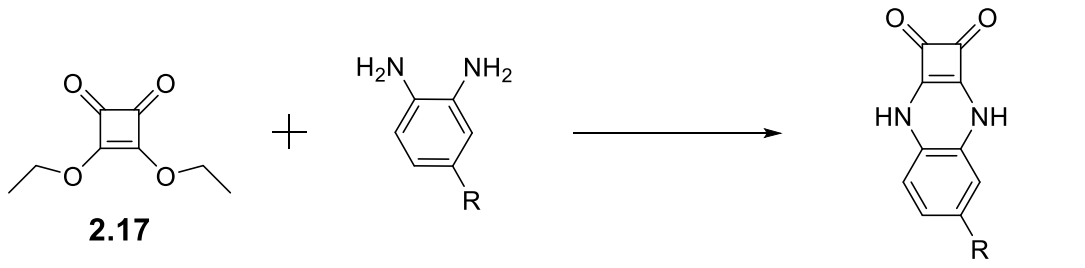

4.16: R = H
4.17: R = NO_2
4.18: R = OMe

Scheme 4.1 Synthesis of squaramidoquinoxalines, **4.16** – **4.18**. *Reagents and Conditions*: $Zn(OTf)_2$, EtOH, rt, 24 h, 64 – 97%.

The successful synthesis of the sensors was confirmed from their ^{1}H NMR spectra by the absence of the characteristic ethyl signals in the aliphatic region. ^{1}H NMR data for **4.16** was consistent with previously reported data.[187] The aromatic protons of **4.17** appeared between 6.4 – 7.6 ppm while the NH signals appeared as an apparent broad doublet further downfield at 10.4 ppm (Figure 4.7a). The methyl peak of the methoxy moiety of **4.18** appears at 3.6 ppm, with the rest of the signals mirroring those of **4.17** (Figure 4.6b).

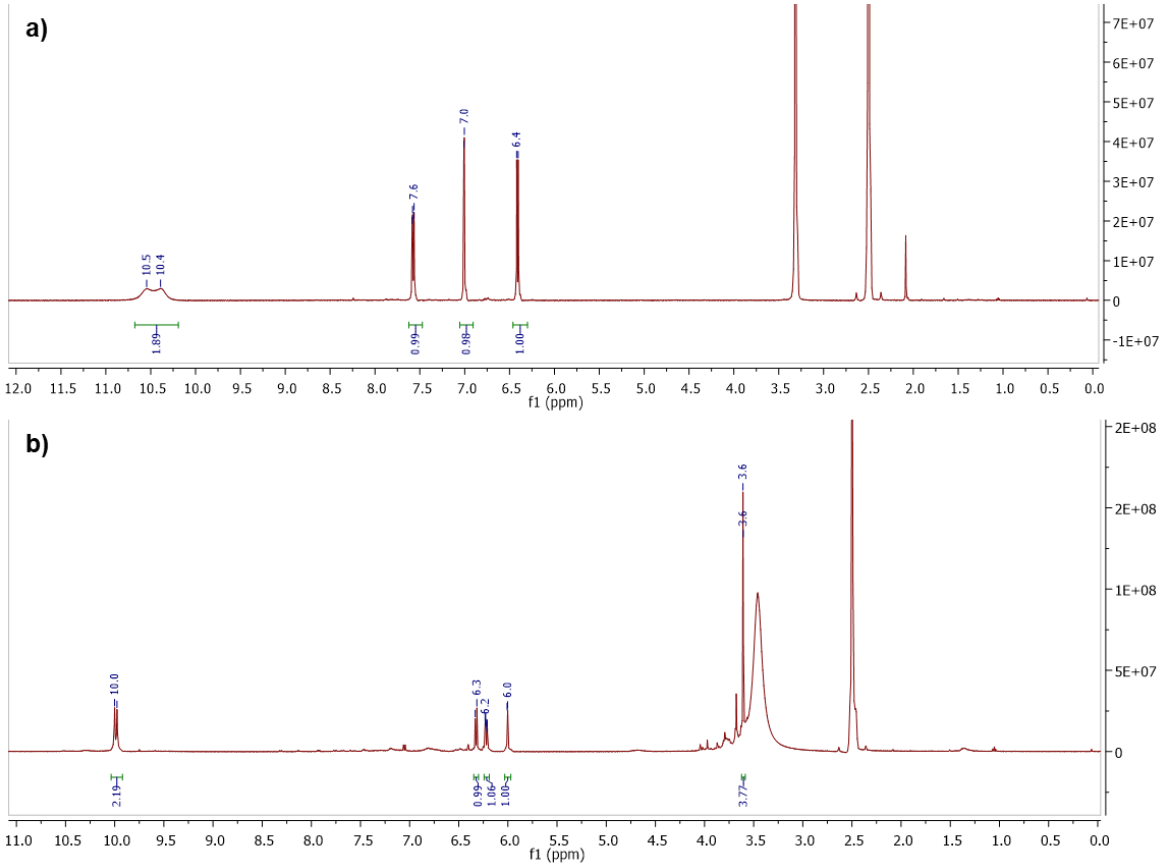

Figure 4.7 a) ^{1}H NMR spectrum of **4.17**. b) ^{1}H NMR spectrum of **4.18**.

Crystals of **4.17** were obtained through the slow evaporation of a DMSO solution. X-ray analysis of **4.17**·DMSO, performed by Dr. Jonathan A. Kitchen, Massey University, New Zealand, determined the low temperature (100K) molecular structure. **4.17**·DMSO crystallised in the triclinic space group *P*-1, and contained two crystallographically independent molecules of **4.17** in the asymmetric unit, as well as two interstitial DMSO molecules (Figure 4.8), that form strong H-bonds to one of the NH groups of each independent molecule of **4.17** [N2···O100 = 2.742(4) Å and <(NH···O) = 171°; N21···O200 = 2.728(4) Å and <(NH···O) = 176°].

The crystal structure displayed packing interactions classical H-bonding, aromatic C-H hydrogen bonding and π-π stacking. A zig-zag chain of **4.17** arises in the structure due to NH and aromatic C-H hydrogen bonding between neighbouring molecules, where the squaramide oxygen atoms act as hydrogen bond acceptors and the NH and CH groups of a neighbouring molecule acting as hydrogen bond donors [N1···O21 = 2.783(4) Å and <(NH···O) = 170°; C4···O22 = 3.248(5) Å and <(CH···O) = 171°; N22···O2 = 2.806 Å and <(NH···O) = 161°; C27···O1 = 3.240(5) Å and <(CH···O) = 173°] (Figure 4.9).

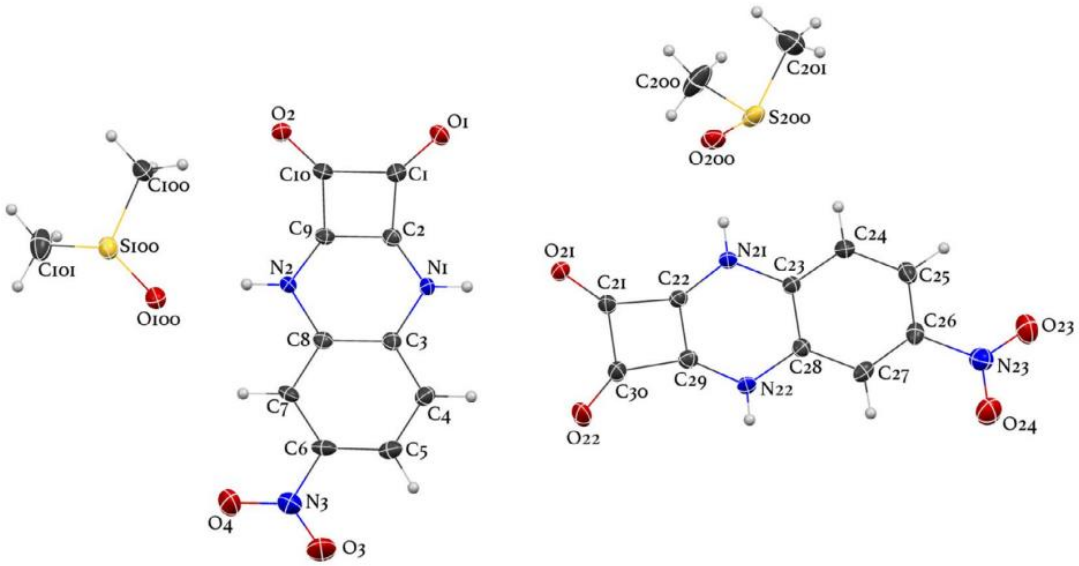

Figure 4.8 Molecular structure of **4.17**·DMSO with thermal elipsoids set at 50%.

These zig-zag chains are further linked into sheets *via* weak aromatic C-H hydrogen bonds between the NO_2 moiety's oxygen atoms and neighbouring CH groups [C25···O3 = 3.360(5) Å and <(CH···O) = 165° (Figure 4.10). Based on the observed self-assembly of these chains it was envisaged that disruption caused by competitive H-bonding species may lead to some modulation of the bulk photophysical properties. These properties are discussed in the following section.

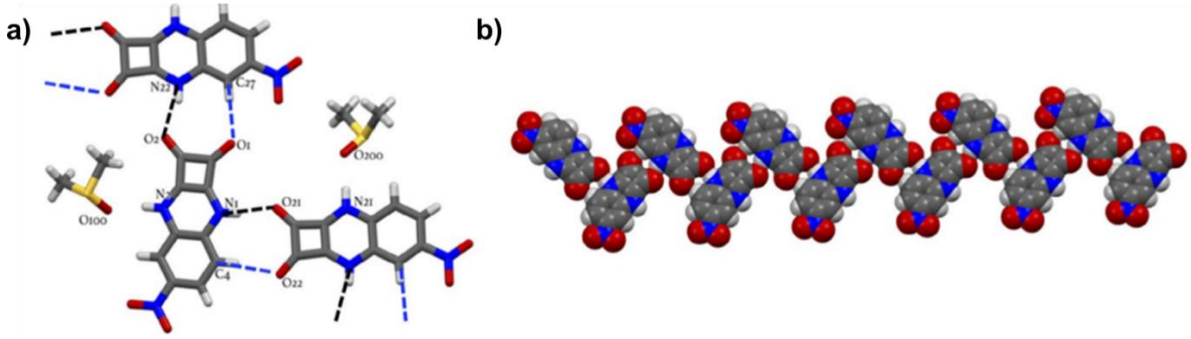

Figure 4.9 a) Hydrogen bonding interactions in **4.17**·DMSO that result in a zig-zag chain - [N1···O21 = 2.783(4) Å and <(NH···O) = 170°; C4···O22 = 3.248(5) Å and <(CH···O) = 171°; N22···O2 = 2.806 Å and <(NH···O) = 161°; C27···O1 = 3.240(5) Å and <(CH···O) = 173°]. b) space filling representation showing the long range ordering of the zig-zag H-bonded chain.

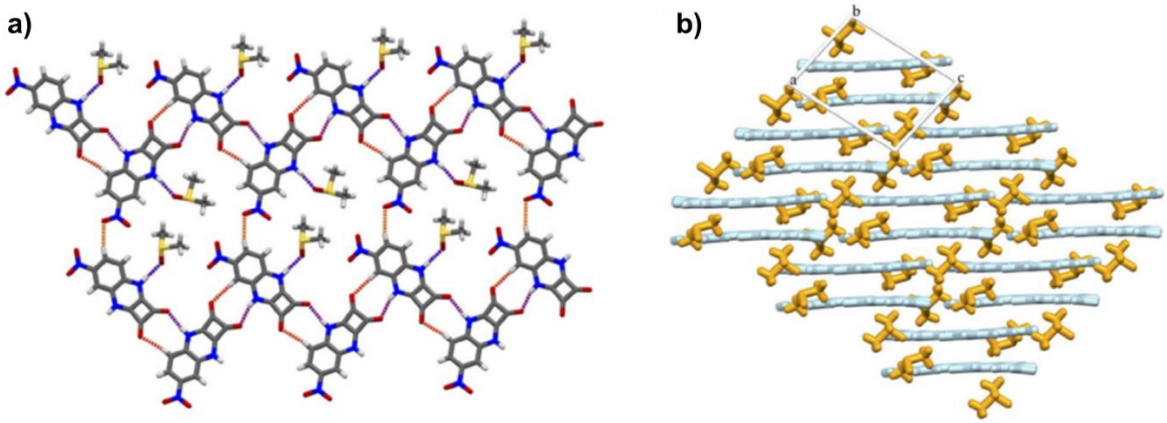

Figure 4.10 a) All hydrogen bonding interaction involved in the formation of 2D sheets of **4.17**·DMSO. Purple dashed lines signify NH H-bonds and orange dashed lines signify CH H-bonds. b) Side-view of the layers formed by π-π stacking between the 2D sheets of **4.17**·DMSO (blue) and the interstitial DMSO molecules (orange).

4.4 UV-Vis Absorption Properties

The absorption spectra of **4.16** – **4.18** were recorded in DMSO (0.5% H_2O). For **4.16**, broad absorption bands were centred at 312 nm and 347 nm, and 320 and 354 nm for **4.18**, which were attributed to π–π* transitions. The spectrum of **4.17** also displayed strong π–π* absorbance bands at 310 and 390 nm. A broad shoulder centred at 532 nm, attributed to a charge transfer within the molecule, was present, which was ascribed to the presence of the electron-withdrawing NO_2 moiety, alongside an additional long wavelength shoulder at 715 nm.

The addition of 1% acetic acid to a solution of **4.17** (10 µM) in DMSO (0.5% H_2O) resulted in the disappearance of the absorption band at 715 nm and a concomitant increase of the absorbance bands at 310, 390 and 532 nm. The addition of 1% NEt_3 resulted in an increase in the absorbance bands at 450 and 715 nm, and a colour change from pink-red to green, visible to the naked eye (Figure 4.11).

Treatment of **4.16** with 1% NEt_3 resulted in a colour change from colourless to pale orange, which was in agreement with behaviour reported by Liu *et al*.[187] Upon treatment of **4.18** with 1% NEt_3, no stark changes were observed like that of **4.17**. To gain further insight to the UV-vis spectral changes of **4.17**, TD-DFT calculations at the SMD-PCM/B3LYP/6-311G+(2p,d) level of theory, were performed by Dr. Tobias Kramer, Maynooth University.

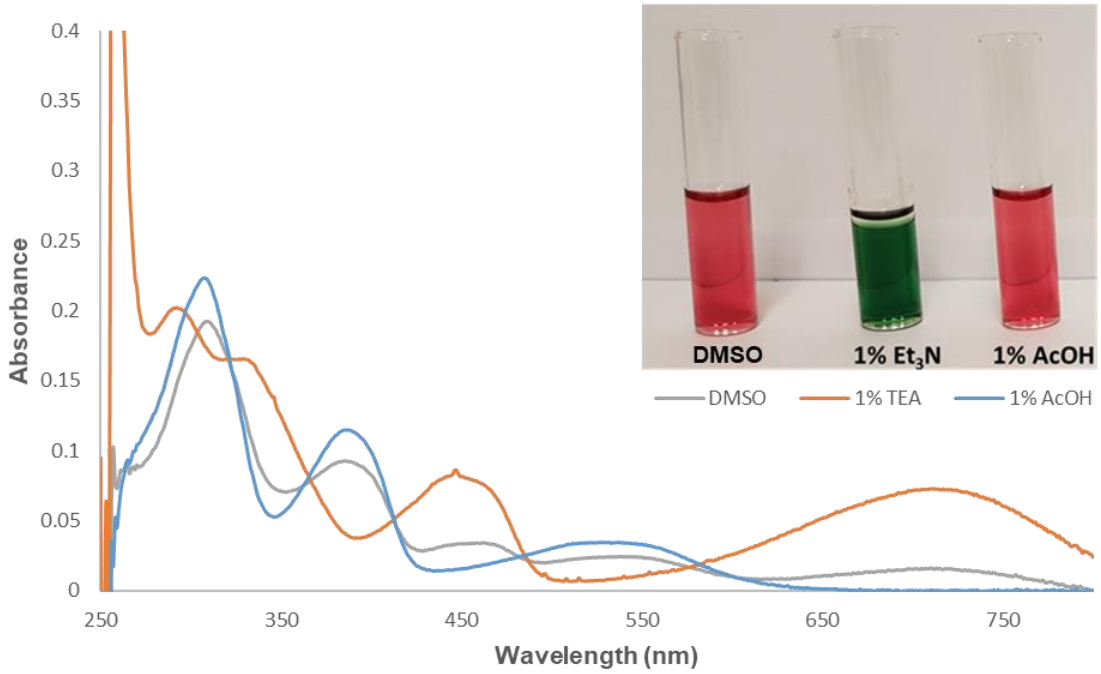

Figure 4.11 The absorption spectra of **4.17** (0.5 x 10^{-5} M) in DMSO, 1% NEt_3 in DMSO, and 1% AcOH in DMSO. *Inset*: The appearance of the corresponding solutions to the naked eye.

The calculated absorption spectrum of **4.17** was in close agreement with the experimentally obtained spectrum, with three peaks predicted at 301, 382 and 549 nm. Analysis of the Natural Transition Orbitals (NTO) revealed the π–π* transition type character of these peaks The peak at 549 nm corresponded to the HOMO-LUMO transition, which was dominated by an intramolecular charge transfer process between the NO_2 moiety and the squaramide ring (Figure 4.12).

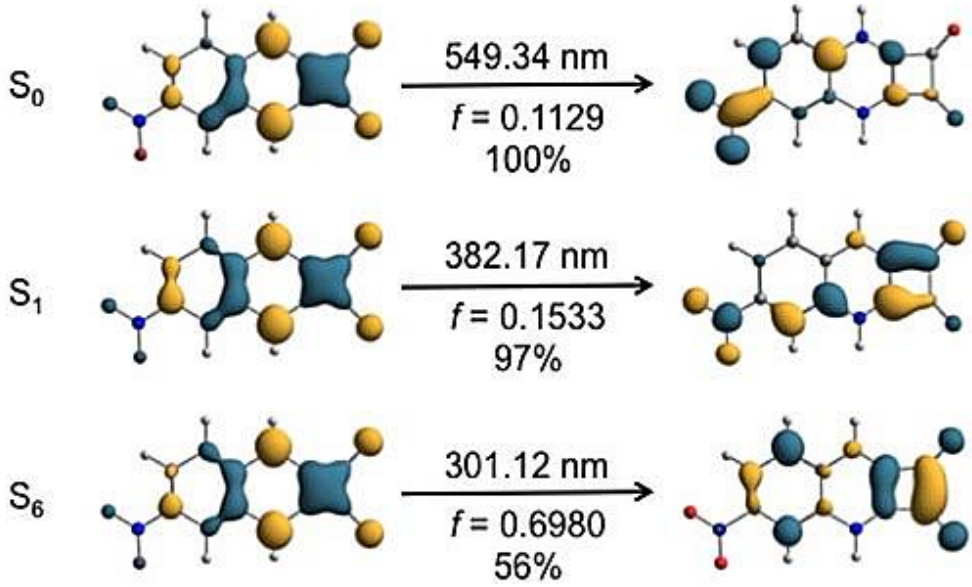

Figure 4.12 plots of NTOs s (isovalue = 0.05) for key electronic transitions in **4.17**. Excitation energies are given along with oscillator strengths and weights of NTO pairs.

Single deprotonation of **4.17** causes the bathochromic shift of the peak at 549 nm, regardless of which NH is deprotonated (See Appendix). The calculated peaks at 653 nm and 730 nm for each [**4.17-H**]$^-$ tautomer suggest a reduced HOMO-LUMO gap for these anionic species. The peak at 382 nm also undergoes a bathochromic shift to approximately 420 nm for both anionic tautomers.

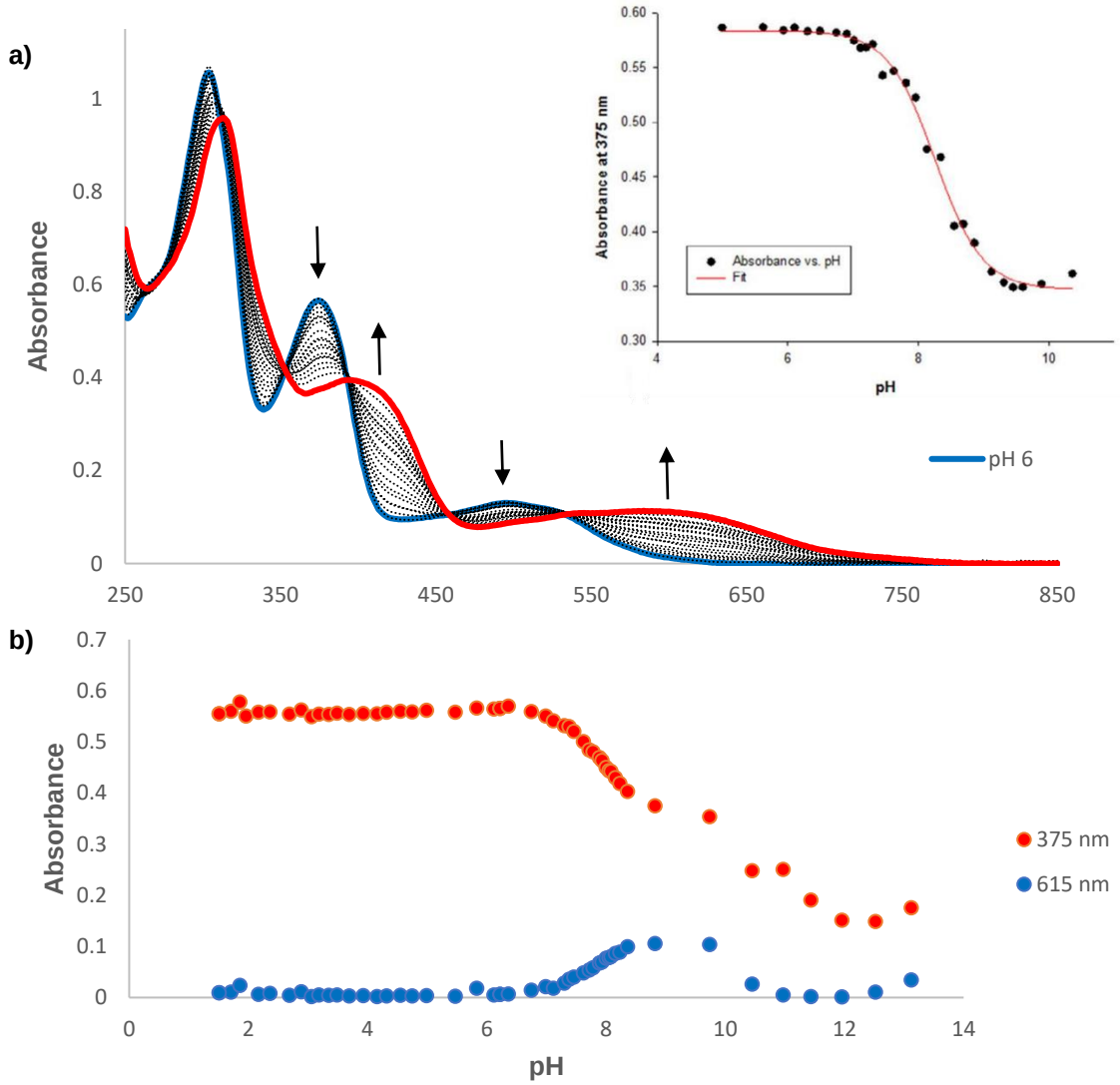

Figure 4.13 a) Absorption spectra taken over the course of the pH-spectrophotometric titration of **4.17** (1×10^{-5} M) from pH ≈ 6–9 in a MeCN–H_2O mixture (9/1 v/v; in presence of 0.1 M $TBAPF_6$). *Inset*: Four parameter sigmoid curve fit with the point of inflexion corresponding to the pKa value (b) Plots of absorbance vs. pH at 375 nm and 615 nm showing two distinct deprotonation events from pH 2 – pH 13.

The sum of the above results suggests that a proportion of **4.17** exists in its mono-deprotonated form, even in the absence of base. This behaviour has been reported previously for squaramides containing strongly electron-withdrawing substituents by Rostami *et al*.[120] To probe this observation further, a pH-spectrophotometric titration was undertaken in a mixture of MeCN/H_2O (9/1 v/v; in the presence of 0.1 M $TBAPF_6$) as described previously in Chapter 2.[151]

The titration was performed in MeCN/H_2O mixture due to precipitation of salts when performed in a DMSO/H_2O solution, which led to issues in recording the absorption spectra. The absorption spectrum of **4.17** was considerably shifted due to the change in solvent, however, two deprotonation events were observed for **4.17**, marked by a hypochromism centred at 415 and 615 nm between pH ≈ 6 – 9.5, followed by a second spectral change between pH ≈ 10.3 – 12, which involved hypochromism for the entire spectrum (Figure 4.13).

These spectral changes could be observed by the naked eye, as they resulted in a colour change from pink to green to yellow. The first deprotonation event (pink – green colour change) was shown to be reversible upon the addition of a protic solvent. However, the second deprotonation event (green – yellow) was not reversible as it appeared that [**4.17-2H**]$^{2-}$ underwent a time-dependent fragmentation (Figure 4.14).

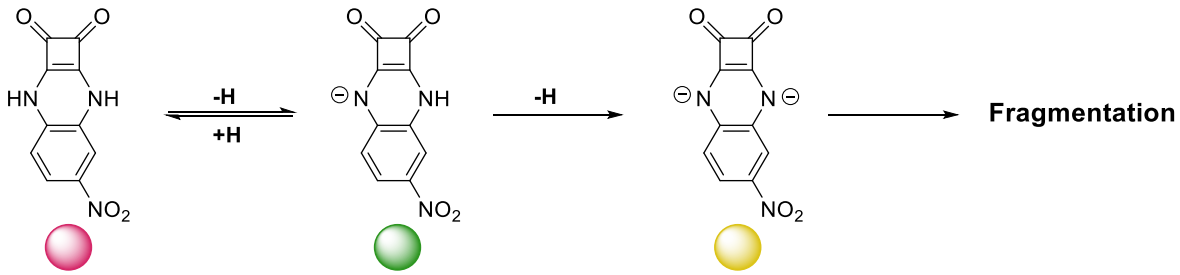

Figure 4.14 Proposed acid-base behaviour and corresponding colourimetric response of **4.17**.

4.5 UV-Vis Absorption Anion Titrations

We expected the behaviour of **4.17** to arise from the electron withdrawing effects of the NO_2 moiety increasing the acidity of the squaramide NH groups, thus increasing its propensity to be deprotonated. We wished to explore the possibility of **4.17** to act as a colourimetric halide sensor, where the selective detection of F^- could be achieved due to F^- being the most basic halide. The ability of **4.16** – **4.18** to detect halides in DMSO (0.5% H_2O) was examined by UV-vis titration of TBA halide salts. As **4.16** had already been studied by Chen *et al*., we focussed our efforts on **4.17** and **4.18**.

Upon addition of F^- to **4.17**, a colour change from pink-red to green was noted, similar to behaviour displayed upon addition of NEt_3. The absorption band at 310 nm underwent a bathochromic shift to 324 nm, and experienced a hypochromic effect along with the bands at 390 and 532 nm. Concomitantly, a

new absorbance band, centred at 450 nm, formed alongside an increase in the shoulder at 715 nm. (Figure 4.15). Four isosbestic points were observed at 364, 416, 484 and 597 nm were observed, suggesting that only two species exist at this equilibrium.

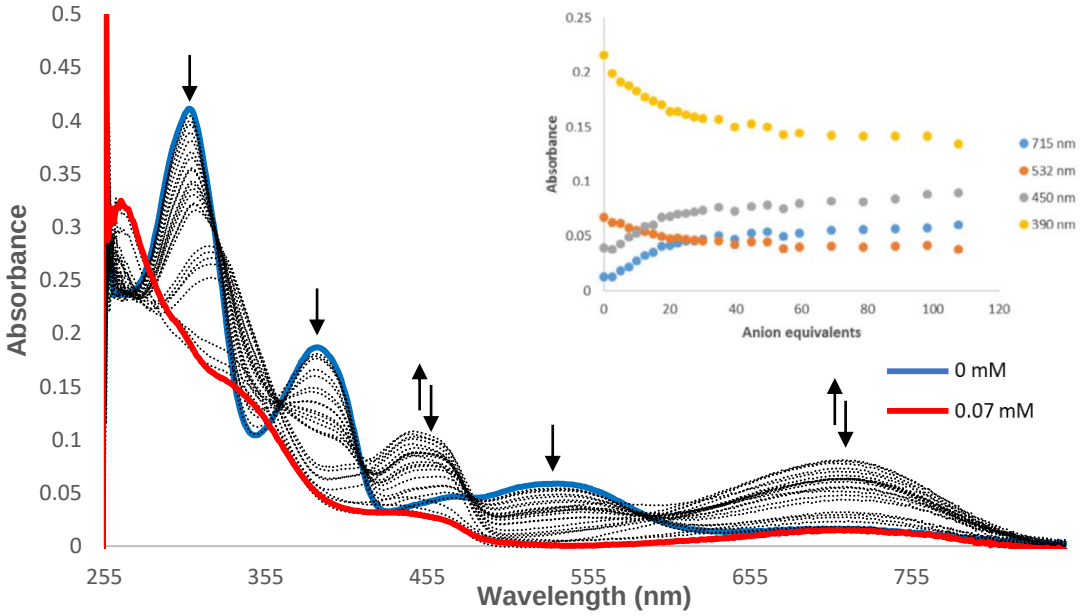

Figure 4.15 Uv-vis spectrum of titration of **4.17** (1×10^{-5} M) upon addition of TBAF (0–0.07 mM) in 0.5% H_2O in DMSO solution. *Inset*: Absorbance changes observed at 715, 532, 450 and 390 nm.

It appeared that **4.17** interacts with F^- in two well-defined steps, where further addition of F^- led to a sudden decrease in the absorbance bands at 324, 450 and 715 nm. We postulate that the addition of low concentrations of F^- causes mono-deprotonation of **4.17** [**4.17-H**]$^-$, resulting in a bathochromic shift of the charge-transfer bands. Further additions of excess F^- results in a second deprotonation of [**4.17-H**]$^-$ to form [**4.17-2H**]$^{2-}$, correlating to the second colour change from green to yellow. Similar behaviour has been previously reported with squaramide and urea derivatives containing electron-withdrawing substituents.[120,185]

Relatively minor changes in the UV-vis spectra was observed upon treatment of **4.17** with Cl^-, Br^- and I^-. Increases in the absorbance at 450 and 715 nm coinciding with a decrease in absorbance at 540 nm suggesting that the presence of Cl^-, Br^-, and I^- may promote the mono-deprotonation of **4.17** in DMSO (Figure 4.16). However, no colour change was observed upon addition of these halides to the solution. We also examined the interactions of basic oxoanions $H_2PO_4^-$, SO_4^{2-}, and CH_3COO^- with **4.17**. Similar results were observed with a

colour change from pink-red to green, confirming the susceptibility of **4.17** towards deprotonation in the presence of basic anions.

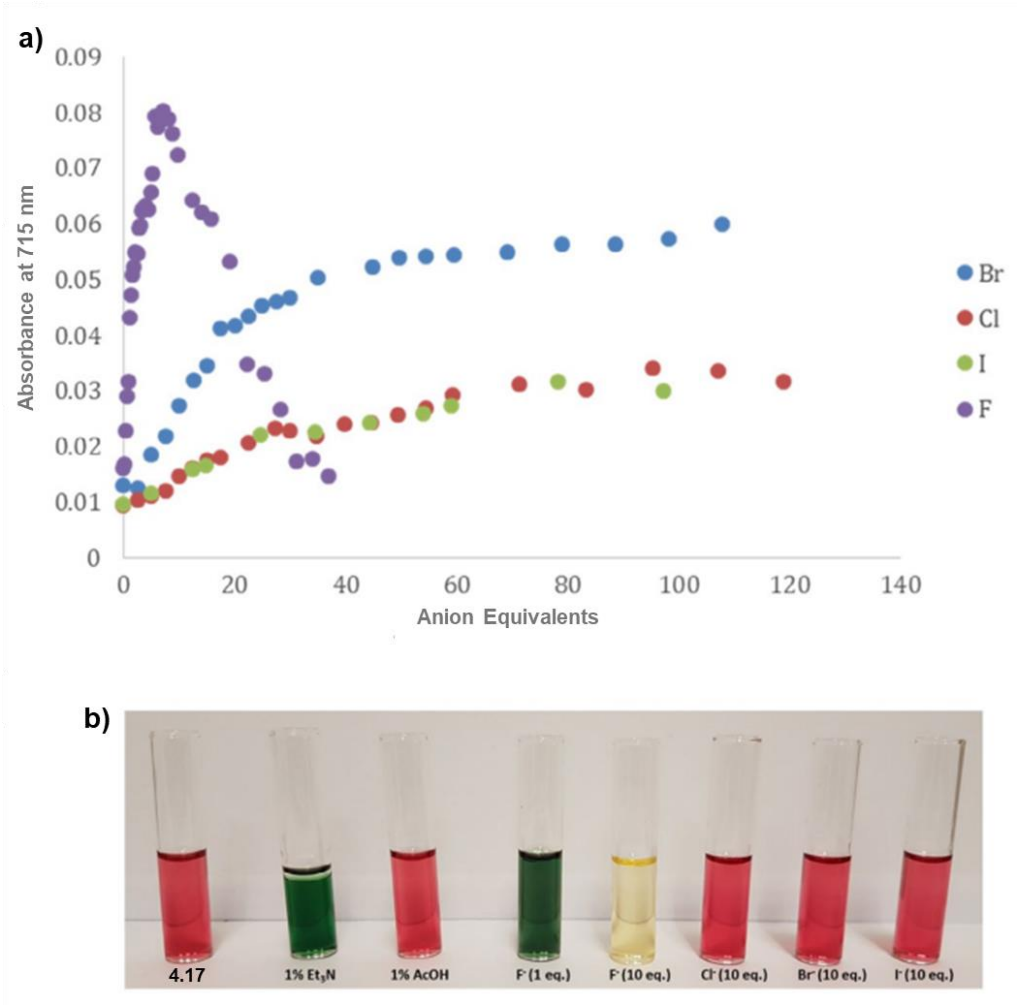

Figure 4.16 a) Comparison of the absorbance changes at 715 nm upon addition of TBAF (0–0.37 mM), TBAI (0–1.1 mM), TBACl (0–1.2 mM) and TBABr (0–1.1 mM) to a solution of **4.17** (1×10^{-5} M) in 0.5% H_2O in DMSO (0.5% H_2O). b) Colourimetric changes of **4.17** (1×10^{-3} M) under acidic conditions, basic conditions and in the presence of various halides in DMSO (0.5% H_2O) at 25 °C.

These titrations were repeated with **4.18**, where minor changes upon addition were observed upon the addition of the halide anions compared to the response of **4.17**. An additional absorbance band centred at 387 nm appeared upon the addition of F^-, which disappeared after subsequent additions (Figure 4.17), resulting in a colour change from pale orange to a slightly darker orange.

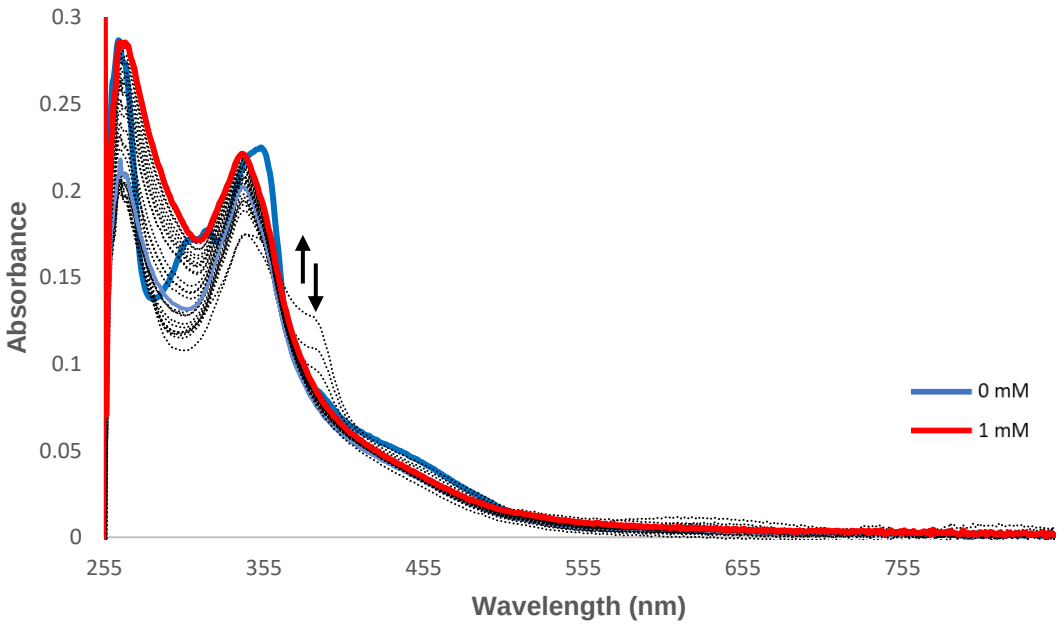

Figure 4.17 Changes observed in the absorption spectrum of **4.18** (1 x 10^{-5} M) upon addition of TBAF (0 – 1 mM) in 0.5% H_2O in DMSO solution.

4.6 ^{1}H NMR Titrations

To support our observations thus far, ^{1}H NMR studies of **4.17** were performed in DMSO-d_6 (0.5% H_2O), where a solution of **4.17** (2.5 x 10^{-3} M) was treated with TBA salts of halides up to 2 equivalents. When treated with Cl^-, Br^-, and I^-, a minimal response was observed, which involved a broadening and downfield shift of the NH signals (see Appendix). These findings suggest that these anions do not bind to **4.17** in a significant manner, and that there are, in fact, very little interactions between these anions and **4.17**. The responses observed during the UV-vis titrations are postulated to arise from the increase of susceptibility towards deprotonation of **4.17** in the presence of these anions. This was a surprising result, as we had expected the increase of acidity of the NH groups, due to the presence of the electron-withdrawing NO_2 moiety, would lead to strong hydrogen-bond donor abilities of the squaramide, as has been reported previously.[185]

Titration of **4.17** against F^- resulted in the NH signals broadening to a large extent and a upfield shift of the aromatic signals during the initial additions of F^- (0 – 0.6 equiv.), alongside a colour change from pink-red to green. We attributed this behaviour to mono-deprotonation of **4.17** seen previously in our UV-vis titrations. Further additions of F^- (0.8 – 2.0 equiv.) resulted in the disappearance

of the original aromatic peaks and the appearance of new aromatic peaks at 8.3, 8.5, 8.9 ppm, alongside a colour change from green to yellow (Figure 4.18). Again, this process was attributed to the second deprotonation of **4.17** in the presence of excess F^-. Subsequent additions of F^- (5 equiv.) saw the appearance of a triplet at 16.2 ppm, signalling the formation of H_2F as a by-product of the deprotonation of **4.17** and TBAF.

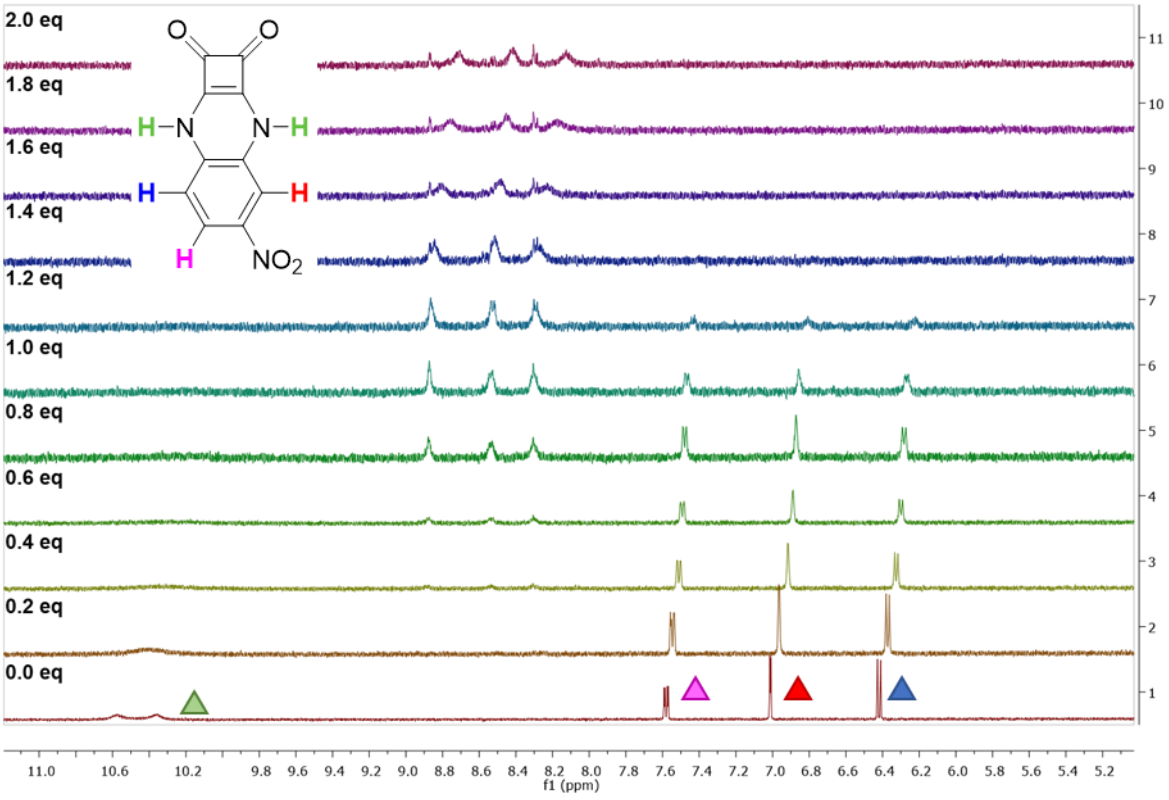

Figure 4.18 Stack plot of 1H NMR spectra of **4.17** (2.5×10^{-3} M) upon addition of TBAF (0 – 2 equiv.) in DMSO-d_6.

4.7 *Applications of Squaramidoquinoxalines*

Having studied in detail the anion sensing mechanism of **4.17**, we wished to move towards implementing the sensor for real-world applications. Filter paper was impregnated with **4.17** by immersing the paper into a DMSO solution of **4.17** (40.7 mM) and placing in an oven at 60°C for 12 hours. To investigate the efficacy of these test strips, 2 µL of DMSO solutions TBAF, TBACl, TBABr, and TBAI (0.445 M) were dropped onto the filter paper. The area of the filter paper that were treated with TBAF underwent an immediate colour change from pink to green,

while the remaining areas treated with the other halides remained unchanged (Figure 4.19).

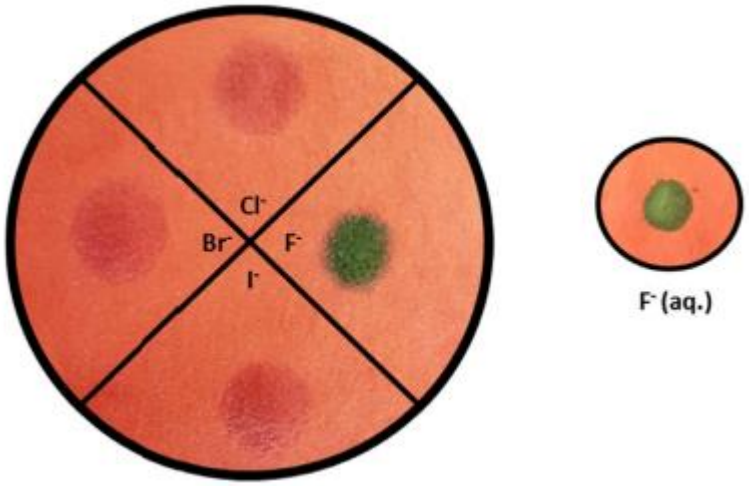

Figure 4.19 Photograph of filter paper impregnated with **4.17** (40.7 mM) and the colorimetric response observed upon addition of 2 μL of (a) TBAF, TBACl, TBABr and TBAI (0.445 M) in DMSO (0.5% H_2O) (left), and TBAF (0.445 M) in H_2O after gentle drying (right).

These tests were repeated at pH values ranging from pH 5 – 8, where **4.17** demonstrated the ability to detect the presence of F^-. An aqueous solution of TBAF (0.445 M) was additionally tested, where upon gentle heating, a colour change of pink to green was observed. We believe that these simple experiments, demonstrate the applicability of **4.17** in a practical setting for the detection of F^- in aqueous solutions.

4.8 *Conclusions*

In conclusion, we synthesised a small family of squaramidoquinoxalines, **4.16** – **4.18**, *via* a simple two-step synthesis with moderate to near quantitative yields. Novel structures were characterised by NMR and IR spectroscopy, HRMS, and where possible, X-ray crystallography. An interesting packing interaction in the crystal structure of **4.17** revealed the molecule to partake in classical hydrogen bonding, weaker aromatic CH-based hydrogen bonds and π-π stacking. Their UV-vis absorption properties were investigated, where **4.17** displayed a characteristic long wavelength absorption at 715 nm.

The halide sensing abilities of the squaramidoquinoxalines were examined, where **4.17** demonstrated a stark colourimetric change from pink-red to green upon addition of F^-, which consequently led to a large increase in the absorption at 715 nm, suggesting a deprotonation event. Further additions of F^-

resulted in a subsequent colourimetric change from green to yellow and a decrease in all absorbance bands in the UV-vis spectrum. **4.17** was found to be a selective halide sensor for F^-, as no such changes were observed for the other halides, as was the case for F^-. A combination of UV-vis, NMR and TD-DFT analysis allowed us to conclude that the observed colour change is likely due to a two distinct deprotonation events.

4.18 did not display any similar colourimetric changes in the presence of F^-, attributed to the decreased acidity of the NH groups due to the presence of the electron-donating methoxy substituent, as opposed to the electron-withdrawing NO_2 moiety present in **4.17**.

The use of **4.17** in rudimentary test strips was also demonstrated by impregnating filter paper with a DMSO solution of the chemosensor. Addition of F^- to the test strip resulted in a colour change of the treated paper from pink to green, while areas treated with the remaining halides were unchanged.

The results of this chapter demonstrate the use of the squaramide moiety in the field of anion recognition and sensing, and possibly supramolecular self-assembly formations. The results also illustrate how greatly the presence of electron-withdrawing and electron-donating aryl substituents can impact the recognition and sensing ability a molecule can possess.

Chapter 5

Thesis Summary

5.1 Thesis Summary

The selective recognition, sensing, and transport of anion has significance in both an environmental and biological context. The overarching aim of this research described in this thesis was to exploit the squaramide motif in developing novel anion receptors, sensors and transporters.

Chapter 2 details the synthesis of amido-squaramides, which feature a squaramide core containing an *N*-aryl substituent, and importantly an *N*-amido linkage to an aryl moiety with the aim to vary the pK_a of the corresponding NH. The aryl moieties were decorated with a range of electron-withdrawing groups to tune anion recognition and transport abilities of the receptors. The pK_a of the receptors were determined experimentally and computationally, where results showed that the *N*-amide linkage succeeded in lowering the pK_a of the NH. Molecular dynamics and geometry optimisation determined that the amido-squaramides exist in the *anti/syn* conformation due to an intramolecular H-bond between the phenyl NH and the amide carbonyl's oxygen atom.

The amido-squaramides were shown to selectively bind to Cl^- through H-bond formation and underwent deprotonation when treated with basic anions. The binding constants were determined using ^1H NMR spectroscopy, where **2.29** was determined to display the highest binding affinity for Cl^-. The amido-squaramides displayed higher binding affinities than their urea and thiourea analogues, but failed to reach binding affinities as high as those displayed by squaramide analogues. The receptors displayed minimal anionophoric activity at pH 7.20, and displayed a 'switching on' of anionophoric activity at pH 4.20, with **2.28** displaying the most potent anionophoric activity. These results established amido-squaramides as pH-switchable anion transporters.

Chapter 3 discusses the attempted synthesis of stimuli-responsive anion transporters. Four novel secondary amines displaying enzyme-sensitive and fluoride-sensitive triggers, were synthesised and characterised. Many attempts at synthesising tertiary squaramides with these secondary amines were met with limited success. However, after synthesis optimisation studies were performed using a model tertiary amine, it was found that squaraines had been synthesised as opposed to squaramides. A change in design led to the pursuit of tertiary ureas, where again, limited success was achieved. A model tertiary urea, featuring unsubstituted phenyl rings, was synthesised and characterised.

However, when synthesis was attempted with the novel secondary amines synthesised previously, no success was achieved. We attribute this lack of reactivity to the steric bulk of the secondary amines and the poor nucleophilicity owed to the presence of electron withdrawing groups.

Chapter 4 describes the synthesis and characterisation of a small family of squaramidoquinoxalines. X-ray crystallography of **4.17** revealed interesting packing interactions of the molecule in the solid-state, where classical H-bonding, aromatic CH-based H-bonds, and π-π stacking resulted in a zig-zag chains linked into sheets. **4.17** demonstrated a selectivity of F^- over other halide anions, where a colourimetric change from pink-red to green was observed, with a consequential significant increase in the absorption as 715 nm in the UV-vis spectrum, due to deprotonation.

In the presence of excess F^-, a second deprotonation event leads to a colourimetric change of green to yellow and a decrease in all absorbance bands in the UV-vis spectrum, followed by fragmentation of the molecule. **4.18** did not display any colourimetric responses in the presence of F^-, attributed to the decreased acidity of the NH groups, due to the presence of the electron-donating methoxy substituent. Rudimentary test strips were created using filter paper a solution of **4.17** in DMSO. These test strips demonstrated a colour change upon the addition of F^- from pink to green, mirroring the behaviour seen in solution.

Future work on amido-squaramides will focus on further investigating the anion transport capabilities of the receptors. Next to be determined are the effective transporter concentration values (EC_{50} values) of the amido-squaramides, to quantify the efficacy of the receptors to exchange Cl^-/NO_3^- at pH 7.20 and 4.20. Furthermore, antiport assays will be performed to assess the ability of the amido-squaramides to engage in the biologically relevant exchange of Cl^-/HCO_3^- across lipid membranes. The ability of the receptors to rectify a pH gradient across a membrane will also be examined using HPTS (8-hydroxypyrene-1,3,6-trisulfonic acid) assays. Cl^- uniport and H^+/Cl^- symport activities will be investigated using cationophore-coupled ISE assays developed by Gale and co-workers,[188] as well as to provide additional insight into electroneutral transport that could rate-limit the Cl^-/NO_3^- exchange process.[189]

As we postulate that the binding and transport abilities of amido-squaramides are hindered by the intramolecular interactions of the receptors, expanding the number of hydrogen bond donors available in the system could increase their anion binding abilities and anionophoric activities. As depicted in Scheme 5.1, the expansion of amido-squaramides to a squaramide directly conjugated to a urea, forming a *N*-carbamoyl squaramide, is a promising avenue of exploration. A previous example of such a molecule has been reported previously by Davis *et al*., however, these compounds were not screened for their anion binding affinity and were only investigated for their intermolecular interactions.[119] While the squaramide phenyl NH could likely still be participating in an intramolecular H-bond, the addition of the second NH bond donor could increase the anion affinity and transport ability of the receptor, while the amido-squaramide NH still receives the increased acidity, due to being linked to the squaramide core, and therefore increased anion binding potential.

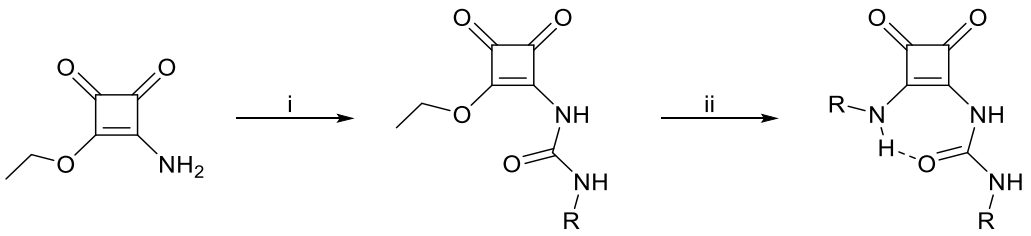

Scheme 5.1 Proposed synthetic route to *N*-carbamoyl squaramides for enhanced anion binding and transport. *Proposed reagents and conditions:* i) NH_3.EtOH, rt; ii) R-NCO, NEt_3, rt; iii) $Zn(OTf)_2$, aryl amine.

Further pursuit of stimuli-responsive anion transporters will be undertaken to achieve enzymatic or chemo-responsive control over anionophoric activity. Using metal-based catalysis, synthesis of tertiary squaramides will be attempted (Scheme 5.2). Ullmann reactions are often utilised to form new C-N bonds, coupling together an aryl halide and aryl amine using a copper catalyst. As squarates are known to be aromatic, we aim to trial this reaction using 3,4-dichloro-cyclobut-3-ene-1,2-dione and our secondary amines. Similarly, Buchwald-Hartwig coupling reactions employ a palladium catalyst to facilitate the formation of new C-N bonds between aryl halides and aryl amines. These methods may allow us to produce stimuli-responsive tertiary squaramides, and investigate their ability to release an active anion transporter upon treatment of the appropriate stimulus.

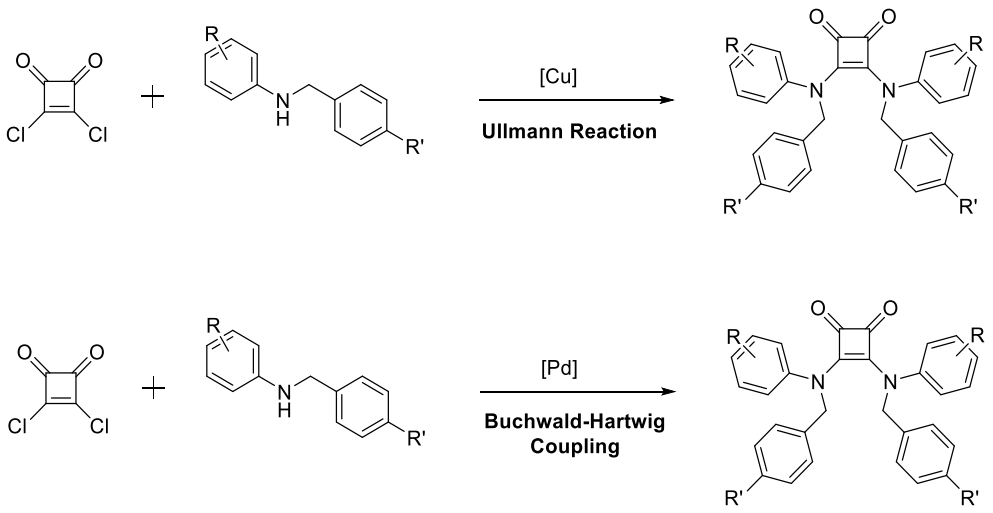

Scheme 5.2 Potential synthetic routes to tertiary squaramides employing the metal-based catalysed Ullmann and Buchwald-Hartwig coupling reactions, which couple aryl halides to amines, resulting in the formation of a C-N bond.

Reaction of our secondary amines with isocyanates is another possible route to explore in working towards stimuli-responsive anionophores (Scheme 5.3). With only one NH available, this urea could display little no anion transport. Similar to the tertiary ureas that were attempted to by synthesised in Chapter 3, the second NH H-bond donor is 'masked' by a trigger, that will cause the molecule to fragment and release an active urea-based anionophore upon interaction with appropriate stimuli.

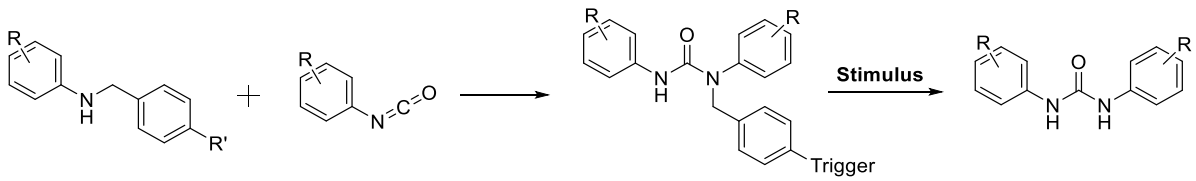

Scheme 5.3 Potential synthetic route to stimuli-responsive urea-based anionophore, featuring one 'free' NH hydrogen bond donor and another NH hydrogen bond donor 'masked' by a trigger.

Future work based on the results of Chapter 4 could examine the effects of varying the substituent and position of the aryl moiety (Figure 5.1). As the Hammett constants for aryl substituents vary depending on their position, varying the substituents and their substitution pattern may allow us to fine-tune the squaramidoquinoxaline's sensing ability. As the electron-donating OMe moiety of **4.18** did not yield any colourimetric response of the chemosensor, electron-withdrawing groups, such as halides, a cyano group, or a carboxylic acid, could yield chemosensors with different UV-visible properties, pK_a values, and subsequent selectivity towards different anions when compared to **4.17**. Future

work in this area could yield a family of squaramidoquinoxalines displaying selectivity over a range of biologically and environmentally relevant anions, which could further be implemented into test strips for the rapid, naked-eye detection of anionic contaminants in samples.

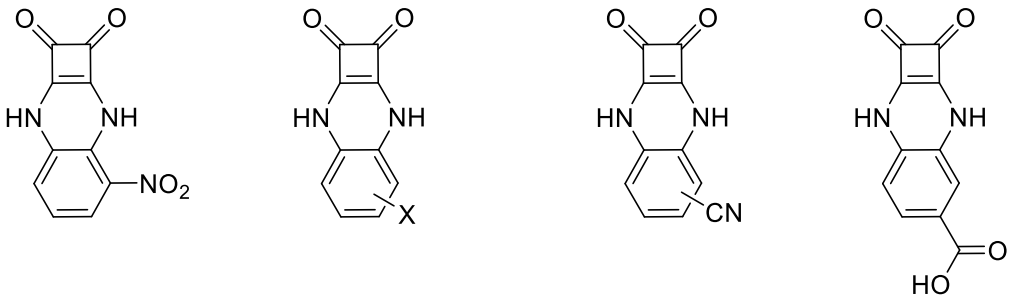

Figure 5.1 Chemical structures of potential squaramidoquinoxalines with fine-tuned anion sensing abilities due to variations of phenyl substituents.

5.2 Publications

Marchetti, L. A.; Mao, N.; Kramer, T.; Kitchen, J. A.; Elmes, R. B. P., *A long wavelength colourimetric chemosensor for fluoride*, Supramol. Chem., 2018, 30, 795–805.

Marchetti, L. A.; Kumawat, L. K.; Mao, N.; Stephens, J. C.; Elmes, R. B. P., *The Versatility of Squaramides: From Supramolecular Chemistry to Chemical Biology*, Chem, 2019, 5, 1398–1485.

Pérez-Calatrava, E.; **Marchetti, L. A.**; McManus, G. J., Lynch, D. M.; Elmes, R. B. P.; Clive Williams, D.; Gunnlaugsson, T.; Scanlan, E. M., *Real-Time Multi-Photon Tracking and Bioimaging of Glycosylated Theranostic Prodrugs upon Specific Enzyme Triggered Release*, Chem. Eur. J., 2022, 28, e202103858.

Chapter 6

Experimental Procedures

6 Experimental Procedures

6.1 General Procedures and Instrumentation

All chemicals purchased were obtained from commercial suppliers and used without further purification. DCM was distilled over CaH_2 and MeCN was dried over 3 Å molecular sieves. Anhydrous DMF was purchased from Sigma Aldrich. TLC was performed on Merck Silica Gel F_{254} plates and visualised under UV light (λ = 254 nm). Flash chromatography was performed with Merck Silica Gel 60. Compounds were lyophilised on a Labconco Freezone 1 Dry system. NMR spectrum were recorded on a Bruker Ascend 500 NMR spectrometer, operated at 500 MHz for ^{1}H NMR analysis and 126 MHz for ^{13}C analysis, both at 293 K. The residual solvent peak was used as an internal standard for DMSO-d_6 and $(CD_3)_2CO$ and TMS for $CDCl_3$. Chemical shifts (δ) were reported in ppm. NMR spectra were processed and stack plots produced using MestReNova 6.0.2 software. Proton and carbon signals were assigned with the aid of 2D NMR experiments (COSY, HSQC and HMBC). Multiplicity is given as s = singlet, bs = broad singlet, d = doublet, brd = broad doublet, dd = doublet of doublets, ddd= doublet of doublet of doublets, t = triplet, q = quartet, m = multiplet as appropriate, and *J* values are given in Hz. Infrared spectra were obtained *via* ATR as a solid on a zinc selenide crystal in the region of 4000 – 400 cm^{-1} on a Perkin Elmer Spectrum 100 FT-IR spectrophotometer. LC-MS was performed on an Agilent Technologies 1200 Series instrument consisting of a G1322A Quaternary pump and a G1314B UV detector (254 nm) coupled to an Advion Expression L Compact Mass spectrometer (ESI) operating in positive mode. High resolution ESI spectra were recorded on an Agilent 6310 LCMS TOF. UV-vis spectra were recorded on a Varian Cary 50 Scan UV-visible spectrophotometer using Cary WinUV software. pH measurements were recorded using a Jenway 350 pH meter. Conductivity measurements were performed using an Orion Star A211 Benchtop pH Meter and a Fisherbrand accumet chloride combination electrode.

6.2 Synthetic Procedures for Chapter 2

3,4-Diethoxy-3-cyclobutene-1,2-dione (2.17)

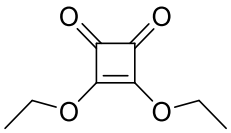

3,4-Dihydroxy-3-cyclobutene-1,2-dione (6 g, 53 mmol) was suspended in EtOH (150 mL). Triethyl orthoformate (21.5 mL, 145 mmol) was added to the suspension and refluxed for 72 hours. The solvent was removed *in vacuo* and the resulting oil was purified *via* column chromatography (DCM) to yield the product as a yellow oil (8.5 g, 94%). **^{1}H NMR** (500 MHz, DMSO-d_6) δ 4.63 (q, J = 7.1 Hz, 1H), 1.35 (t, J = 7.1 Hz, 2H). **^{13}C NMR** (126 MHz, DMSO-d_6) δ 189.6 (s), 184.2 (s), 70.8 (s), 15.7 (s). **IR** (ATR):): ν_{max} (cm^{-1}) = 2986, 1811, 1730, 1592, 1482, 1421, 1330, 1187 cm^{-1}. **HRMS** (ESI+): *m/z* calcd for 171.0652 $[M+H]^+$, found 171.0653.

3-Amino-4-ethoxy-3-cyclobutene-1,2-dione (2.18)

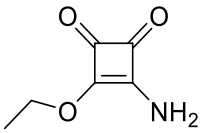

3,4-Diethoxy-3-cyclobutene-1,2-dione (4.5 g, 26.5 mmol) was dissolved in EtOH (100 mL). 2M Ammonia in ethanol solution (13.5 mL, 26.5 mmol) was added portion-wise over 6 hours Upon completion of the addition, the reaction was left to stir overnight (approx. 18 hours) at room temperature. The reaction mixture was filtered and the filtrate was concentrated *in vacuo* to yield a beige solid. Diethyl ether (100 mL) was added to the flask to create a suspension, after which the flask was sonicated for a period of 15 minutes. The suspension was then filtered, washed with diethyl ether and dried *via* vacuum filtration to yield the product as a pale yellow solid (2.6 g, 70%). **^{1}H NMR** (500 MHz, DMSO-d_6) δ 8.33 (brd, J = 68.0 Hz, 2H), 4.63 (q, J = 7.1 Hz, 2H), 1.36 (t, J = 7.1 Hz, 3H). **^{13}C NMR** (126 MHz, DMSO-d_6) δ 190.5, 183.5, 178.2, 174.8, 69.0, 16.1. **IR** (ATR): ν_{max} (cm^{-1}) = 3332, 3074,1810,1700, 1641, 1547,1435, 1350, 1261, 1032, 873, 773. **HRMS** (ESI+) *m/z* calcd for $C_6H_7NO_3$ 142.0499 $[M+H]^+$, found 142.0501.

N-(2-Ethoxy-3,4-dioxocyclobut-1-en-1-yl) benzamide (2.19)

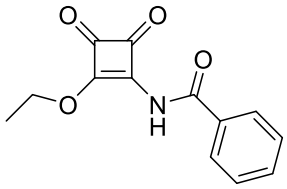

Benzoic acid (394 mg, 3.22 mmol), 4-dimethylaminopyridine (433 mg, 3.54 mmol) and 1-ethyl-3-(3-dimethylaminopropyl) carbodiimide (678 mg, 3.54 mmol) were placed under a N_2 atmosphere and dissolved in anhydrous MeCN (20 mL) and stirred for 15 minutes. 3-Amino-4-ethoxy-3-cyclobutene-1,2-dione (500 mg, 3.54 mmol) was placed under N_2 atmosphere and dissolved in anhydrous MeCN (20 mL) and transferred to the reaction flask *via* cannulation. The reaction was left to stir overnight (approx. 18 hours) at room temperature. The solvent was removed using a rotary evaporator and the obtained white solid was purified by column chromatography (SiO_2, 10% MeCN in DCM) to yield an off-white solid (600 mg, 76%). **^{1}H NMR** (500 MHz, $CDCl_3$) δ 9.88 (s, 1H), 8.03 (dd, *J* = 8.3, 1.1 Hz, 2H), 7.64 – 7.59 (m, 1H), 7.51 (dd, *J* = 11.6, 4.2 Hz, 2H), 4.95 (q, *J* = 7.1 Hz, 2H), 1.54 (t, *J* = 7.1 Hz, 3H). **^{13}C NMR** (126 MHz, $CDCl_3$) δ 188.7, 188.6, 184.9, 167.00, 163.50, 133.8, 131.1, 129.00, 128.5, 71.2, 15.9. **IR** (ATR): ν_{max} (cm^{-1}) = 3305, 3001,1814, 1707, 1581, 1519, 1340, 1250, 1125, 1060, 1006, 865. **HRMS** (ESI+) *m/z* calcd for $C_{13}H_{11}NO_4$ 246.0688 $[M+H]^+$, found 246.0764.

N-(2-Ethoxy-3,4-dioxocyclobut-1-en-1-yl)-4-(trifluoromethyl)benzamide (2.20)

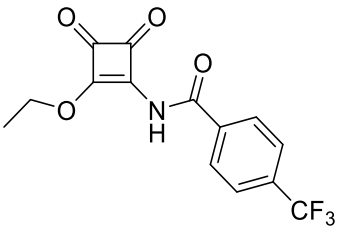

4-(Trifluoromethyl) benzoic acid (612 mg, 3.22 mmol), 4-dimethylaminopyridine (433 mg, 3.54 mmol) and 1-ethyl-3-(3-dimethylaminopropyl) carbodiimide (678 mg, 3.54 mmol) were placed under a N_2 atmosphere and dissolved in anhydrous MeCN (20 mL) and stirred for 15 minutes. 3-Amino-4-ethoxy-3-cyclobutene-1,2-dione (500 mg, 3.54 mmol) was placed under N_2 atmosphere and dissolved in anhydrous MeCN (20 mL) and transferred to the reaction flask *via* cannulation. The reaction was left to stir overnight (approx. 18 hours) at room temperature.

The solvent was removed using a rotary evaporator and the obtained white solid was purified by column chromatography (SiO_2,15% MeCN in DCM) to yield an off-white solid (540 mg, 54%). **^{1}H NMR** (500 MHz, DMSO-d_6) δ 12.17 (s, 1H), 8.19 (d, J = 8.1 Hz, 2H), 7.92 (d, J = 8.2 Hz, 2H), 4.82 (q, J = 7.1 Hz, 2H), 1.42 (t, J = 7.1 Hz, 3H). **^{13}C NMR** (126 MHz, DMSO) δ 190.6, 187.4, 185.0, 169.0, 163.4, 135.9, 133.00 (q, $^2J_{CF}$ = 32.0 Hz), 130.3, 125.9 (overlapping signals X 3), 124.2 (q, $^1J_{CF}$ = 273.4 Hz), 70.6, 16.0. **IR** (ATR): ν_{max} (cm^{-1}) = 3295, 2986, 1813, 1707, 1581, 1525, 1411, 1326, 1260, 1129, 1059, 1004, 854, 755. **HRMS** (ESI+) *m/z* calcd for $C_{14}H_{10}F_3NO_4$ $[M+H]^+$ 314.0562, found 314.0637.

N-(2-Ethoxy-3,4-dioxocyclobut-1-en-1-yl)-3,5-bis(trifluoromethyl)benzamide (2.21)

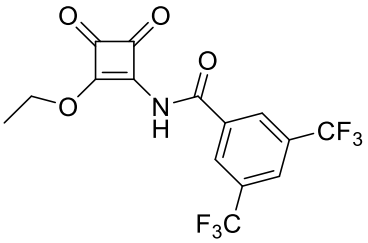

Bis-3,5-(trifluoromethyl) benzoic acid (831 mg, 3.22 mmol), 4-dimethylaminopyridine (433 mg, 3.54 mmol) and 1-ethyl-3-(3-dimethylaminopropyl) carbodiimide (678 mg, 3.54 mmol) were placed under a N_2 atmosphere and dissolved in anhydrous MeCN (30 mL) and stirred for 15 minutes. 3-Amino-4-ethoxy-3-cyclobutene-1,2-dione (500 mg, 3.54 mmol) was placed under N_2 atmosphere and dissolved in anhydrous MeCN (20 mL) and transferred to the reaction flask *via* cannulation. The reaction was left to stir overnight (approx. 18 hours) at room temperature. The solvent was removed using a rotary evaporator and the obtained white solid was purified by column chromatography (SiO_2, 20% MeCN in DCM) to yield an off-white solid (504 mg, 41%).**^{1}H NMR** (500 MHz, DMSO-d_6) δ 12.38 (s, 1H), 8.65 (s, 2H), 8.44 (s, 1H), 4.83 (q, J = 7.1 Hz, 2H), 1.42 (t, J = 7.1 Hz, 3H). **^{13}C NMR** (126 MHz, DMSO) δ 190.5, 187.4, 185.1, 168.6, 161.7, 131 (q, $^2J_{CF}$ = 33.5 Hz), 130.2 (overlapping C X 2), 126.7 (overlapping C X 2), 123.4 (q, $^1J_{CF}$ = 273.1 Hz), 70.8, 16.0. **IR** (ATR): ν_{max} (cm^{-1}) = 3282, 3195, 3037, 1807, 1736, 1601, 1530, 1353, 1272, 1131, 992, 901, 817, 757. **HRMS** (ESI+) *m/z* calcd for $C_{15}H_9F_6NO_4$ $[M+H]^+$ 382.0436, found 382.0510.

***N*-(2-Ethoxy-3,4-dioxocyclobut-1-en-1-yl)-4-nitrobenzamide (2.22)**

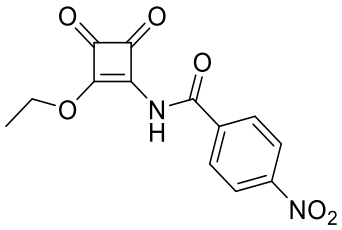

4-Nitrobenzoic acid (538 mg, 3.22 mmol), 4-dimethylaminopyridine (433 mg, 3.54 mmol) and 1-ethyl-3-(3-dimethylaminopropyl) carbodiimide (678 mg, 3.54 mmol) were placed under a N_2 atmosphere and dissolved in anhydrous DMF (40 mL) and stirred for 15 minutes. 3-Amino-4-ethoxy-3-cyclobutene-1,2-dione (500 mg, 3.54 mmol) was placed under N_2 atmosphere and dissolved in anhydrous MeCN (20 mL) and transferred to the reaction flask *via* cannulation. The reaction was left to stir overnight (approx. 18 hours) at room temperature. The solvent was removed using a rotary evaporator and the obtained yellow solid was purified by column chromatography (SiO_2, 20% MeCN in DCM) to yield a yellow solid (504 mg, 41%).**^{1}H NMR** (500 MHz, DMSO-d_6) δ 12.26 (s, 1H), 8.36 (d, J = 8.8 Hz, 2H), 8.22 (d, J = 8.7 Hz, 2H), 4.83 (q, J = 7.1 Hz, 2H), 1.42 (t, J = 7.1 Hz, 3H). **^{13}C NMR** (126 MHz, DMSO-d_6) δ 190.6, 187.4, 185.1, 168.9, 162.9, 150.4, 137.7, 130.9, 124.0, 70.7, 16.0. **IR** (ATR): $\mathbf{v}_{max}$ (cm^{-1}) = 3295, 1814, 1707, 1582, 1525, 1412, 1327, 1255, 1133, 980, 853, 775, 712. **HRMS** (ESI+) *m/z* calcd for $C_{13}H_{10}N_2O_6$ $[M+H]^+$ 291.0539, found 291.0613.

***N*-(2-Ethoxy-3,4-dioxocyclobut-1-en-1-yl)-2-iodobenzamide (2.23)**

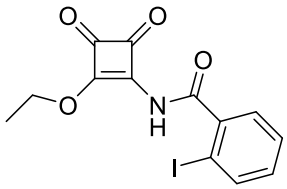

2-Iodoobenzoic acid (800 mg, 3.22 mmol), 4-dimethylaminopyridine (433 mg, 3.54 mmol) and 1-ethyl-3-(3-dimethylaminopropyl) carbodiimide (678 mg, 3.54 mmol) were placed under a N_2 atmosphere and dissolved in anhydrous MeCN (30 mL) and stirred for 15 minutes. 3-Amino-4-ethoxy-3-cyclobutene-1,2-dione (500 mg, 3.54 mmol) was placed under N_2 atmosphere and dissolved in anhydrous MeCN (20 mL) and transferred to the reaction flask *via* cannulation. The reaction was left to stir overnight (approx. 18 hours) at room temperature. The solvent was removed using a rotary evaporator and the obtained off-white solid was purified by column chromatography (SiO_2, 15% MeCN in DCM) to yield

a white solid (358 mg, 30%).**^{1}H NMR** (500 MHz, DMSO-d_6) δ 12.09 (s, 1H), 7.95 (dd, *J* = 7.9, 0.7 Hz, 1H), 7.57 – 7.46 (m, 3H), 7.27 (ddd, *J* = 7.9, 7.1, 2.0 Hz, 1H), 4.80 (q, *J* = 7.1 Hz, 2H), 1.41 (t, *J* = 7.1 Hz, 3H). **^{13}C NMR** (126 MHz, DMSO) δ 190.3, 187.2, 184.7, 168.4, 166.3, 140.3, 139.8, 132.6, 129.5, 128.5, 94.1, 70.6, 16.0. **IR** (ATR): $\mathbf{\nu}_{max}$ (cm^{-1}) = 3246, 3192, 1809, 1723, 1700, 1606, 1575, 1507, 1484, 1421, 1286, 1239, 1123, 1137, 1103, 957, 935, 901, 848, 784, 749, 703. **HRMS** (ESI+) *m/z* calcd for $C_{13}H_{10}INO_4$ $[M+H]^+$ 371.9655, found 371.9728.

***N*-(2-Ethoxy-3,4-dioxocyclobut-1-en-1-yl)-4-iodobenzamide (2.24)**

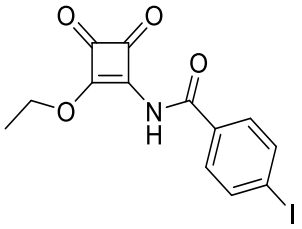

2-Iodoobenzoic acid (800 mg, 3.22 mmol), 4-dimethylaminopyridine (433 mg, 3.54 mmol) and 1-ethyl-3-(3-dimethylaminopropyl) carbodiimide (678 mg, 3.54 mmol) were placed under a N_2 atmosphere and dissolved in anhydrous MeCN (30 mL) and stirred for 15 minutes. 3-Amino-4-ethoxy-3-cyclobutene-1,2-dione (500 mg, 3.54 mmol) was placed under N_2 atmosphere and dissolved in anhydrous MeCN (20 mL) and transferred to the reaction flask *via* cannulation. The reaction was left to stir overnight (approx. 18 hours) at room temperature. The solvent was removed using a rotary evaporator and the obtained off-white solid was purified by column chromatography (SiO_2, 15% MeCN in DCM) to yield a white solid (600 mg, 50%). **^{1}H NMR** (500 MHz, DMSO-d_6) δ 11.99 (s, 1H), 11.99 (s, 1H), 7.95 – 7.91 (m, 2H), 7.79 – 7.75 (m, 2H), 4.81 (q, *J* = 7.1 Hz, 2H), 4.81 (q, *J* = 7.1 Hz, 2H), 1.41 (t, *J* = 7.1 Hz, 3H), 1.41 (t, *J* = 7.1 Hz, 3H). **^{13}C NMR** (126 MHz, DMSO-d_6) δ 190.5, 187.5, 184.9, 169.3, 163.8, 138.0, 131.5, 131.1, 102.1, 70.6, 161. **IR** (ATR): $\mathbf{\nu}_{max}$ (cm^{-1}) = 3296, 1812, 1732, 1707, 1576, 1515, 1480, 1408, 1377, 1328, 1256, 1058, 997, 836, 742. **HRMS** (ESI+) *m/z* calcd for $[M+H]^+$ 371.9655, found 371.9727.

3,4-Dichloro-*N*-(2-ethoxy-3,4-dioxocyclobut-1-en-1-yl)benzamide (2.25)

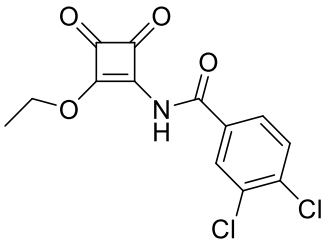

3,4-Dichlorobenzoic acid (612 mg, 3.22 mmol), 4-dimethylaminopyridine (433 mg, 3.54 mmol) and 1-ethyl-3-(3-dimethylaminopropyl) carbodiimide (678 mg, 3.54 mmol) were placed under a N_2 atmosphere and dissolved in anhydrous MeCN (30 mL) and stirred for 15 minutes. 3-Amino-4-ethoxy-3-cyclobutene-1,2-dione (500 mg, 3.54 mmol) was placed under N_2 atmosphere and dissolved in anhydrous MeCN (20 mL) and transferred to the reaction flask *via* cannulation. The reaction was left to stir overnight (approx. 18 hours) at room temperature. The solvent was removed using a rotary evaporator and the obtained yellow solid was purified by column chromatography (SiO_2, 15% MeCN in DCM) to yield an off-white solid (539 mg, 54%). **^{1}H NMR** (500 MHz, DMSO-d_6) δ 12.12 (s, 1H), 8.31 (d, *J* = 2.1 Hz, 1H), 7.96 (dd, *J* = 8.4, 2.1 Hz, 1H), 7.84 (d, *J* = 8.4 Hz, 1H), 4.82 (q, *J* = 7.1 Hz, 2H), 1.42 (t, *J* = 7.1 Hz, 3H). **^{13}C NMR** (126 MHz, DMSO-d_6) δ 190.5, 187.4, 185.0, 169.0, 162.2, 136.4, 132.5, 131.9, 131.4, 131.2, 129.6, 70.6, 16.0. **IR** (ATR): $\mathbf{v}_{max}$ (cm^{-1}) = 3293, 1807, 1702, 1580, 1517, 1468, 1406, 1334, 1256, 1132, 1064, 984, 907, 851, 750. **HRMS** (ESI+) *m/z* calcd for $C_{13}H_9Cl_2NO_4$ $[M+H]^+$ 313.9909, found 313.9982.

4-Chloro-*N*-(2-ethoxy-3,4-dioxocyclobut-1-en-1-yl)benzamide (2.26)

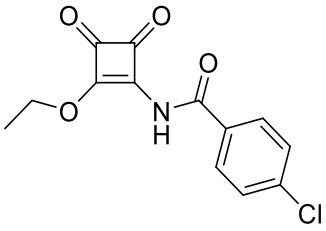

4-Chlorobenzoic acid (503 mg, 3.22 mmol), 4-dimethylaminopyridine (433 mg, 3.54 mmol) and 1-ethyl-3-(3-dimethylaminopropyl) carbodiimide (678 mg, 3.54 mmol) were placed under a N_2 atmosphere and dissolved in anhydrous MeCN (30 mL) and stirred for 15 minutes. 3-Amino-4-ethoxy-3-cyclobutene-1,2-dione (500 mg, 3.54 mmol) was placed under N_2 atmosphere and dissolved in anhydrous MeCN (20 mL) and transferred to the reaction flask *via* cannulation. The reaction was left to stir overnight (approx. 18 hours) at room temperature.

The solvent was removed using a rotary evaporator and the obtained off-white solid was purified by column chromatography (SiO_2, 15% MeCN in DCM) to yield a white solid (458 mg, 51%). **^{1}H NMR** (500 MHz, $CDCl_3$) δ 12.04 (s, 1H), 8.05 – 8.00 (m, 2H), 7.64 – 7.60 (m, 2H), 4.81 (q, *J* = 7.1 Hz, 2H), 1.41 (t, *J* = 7.1 Hz, 3H). **^{13}C NMR** (126 MHz, $CDCl_3$) δ 190.0, 187.1, 184.4, 168.8, 162.9, 138.1, 130.8, 130.4, 128.7, 70.1, 15.6. **IR** (ATR): $\mathbf{\nu}_{max}$ (cm^{-1}) = 3682, 3291, 2973, 2866, 1815, 1707, 1579, 1485, 1411, 1323, 1256, 1056, 855, 750. **HRMS** (ESI+) *m/z* calcd for $C_{13}H_{10}ClNO_4$ $[M+H]^+$ 280.0298, found 280.0370.

***N*-(3,4-Dioxo-2-(phenylamino)cyclobut-1-en-1-yl)benzamide (2.27)**

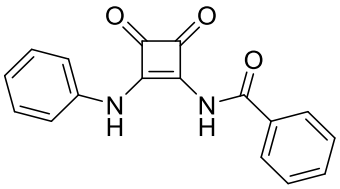

N-(2-Ethoxy-3,4-dioxocyclobut-1-en-1-yl) benzamide (200 mg, 0.82 mmol) and zinc trifluoromethanesulfonate (58 mg, 0.16 mmol) were dissolved in MeCN (40 mL) and stirred for 5 minutes. Aniline (90 µL, 0.98 mmol) was added to the solution and stirred for 1 hour at room temperature. The precipitate was filtered and washed with MeCN to yield the product as a pale yellow solid. **^{1}H NMR** (500 MHz, DMSO-d_6) δ 11.95 (s, 1H), 9.98 (s, 1H), 8.07 (d, *J* = 5.9 Hz, 2H), 7.68 (t, *J* = 7.4 Hz, 1H), 7.57 (t, *J* = 7.7 Hz, 2H), 7.42 (s, 2H), 7.38 (t, *J* = 7.1 Hz, 2H), 7.14 (t, *J* = 7.0 Hz, 1H). **^{13}C NMR** (126 MHz, DMSO-d_6) δ 188.0, 183.1, 171.0, 166.0, 163.7, 138.0, 133.7, 132.3, 129.5, 129.4, 129.1, 124.8, 120.67. **IR** (ATR): $\mathbf{\nu}_{max}$ (cm^{-1}) = 3227, 1809, 1724, 1588, 1504,1392,1275, 1155, 897, 751. **HRMS** (ESI+) *m/z* calcd for $C_{17}H_{12}N_2O_3$ $[M+H]^+$ 293.0848, found 293.0926.

***N*-(3,4-Dioxo-2-((4-(trifluoromethyl)phenyl)amino)cyclobut-1-en-1-yl)-4-(trifluoromethyl)benzamide (2.28)**

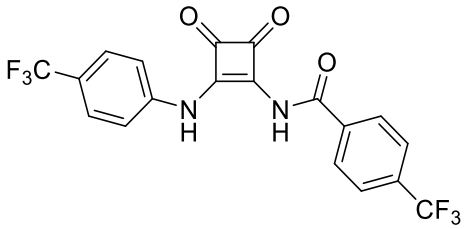

N-(2-Ethoxy-3,4-dioxocyclobut-1-en-1-yl)-4-(trifluoromethyl)benzamide (200 mg, 0.64 mmol) and zinc trifluoromethanesulfonate (48 mg, 0.13 mmol) were dissolved in MeCN (40 mL) and stirred for 5 minutes. 4-Trifluoroaniline (97 µL,

0.77 mmol) was added to the solution and refluxed overnight (approximately 18 hours). The solvent was removed *in vacuo* to yield a pale yellow solid. The crude product was purified using column chromatography (SiO_2, 10% MeCN in DCM) to yield a yellow solid (164 mg, 60%). **^{1}H NMR** (500 MHz, DMSO-d_6) δ 12.26 (s, 1H), 10.24 (s, 1H), 8.24 (d, J = 7.7 Hz, 2H), 7.96 (d, J = 7.9 Hz, 2H), 7.72 (d, J = 8.0 Hz, 2H), 7.60 (d, J = 7.2 Hz, 2H). **^{13}C NMR** (126 MHz, DMSO-d_6) δ 188.1, 183.8, 171.40, 164.7, 163.8, 141.5, 135.9, 133.1 (q, $^2J_{CF}$ = 32.2 Hz), 130.2, 126.7, 126.0, 124.8 (q, $^1J_{CF}$ = 277.2 Hz), 124.2 (q, $^1J_{CF}$ = 277.2 Hz) 120.8. **IR** (ATR): $\mathbf{v}_{max}$ (cm^{-1}) = 3234, 3196, 1811, 1727, 2581, 1545, 1382, 1319, 1273, 1112, 835, 700. **HRMS** (ESI+) *m/z* calcd for $C_{19}H_{10}F_6N_2O_3$ $[M+H]^+$ 428.0596, found 429.0926.

N-(2-((3,5-bis(trifluoromethyl)phenyl)amino)-3,4-dioxocyclobut-1-en-1-yl)-3,5-bis(trifluoromethyl)benzamide (**2.29)**

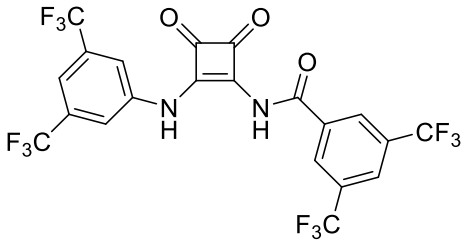

N-(2-ethoxy-3,4-dioxocyclobut-1-en-1-yl)-3,5-bis(trifluoromethyl)benzamide (250 mg, 0.66 mmol) and zinc trifluoromethanesulfonate (48 mg, 0.13 mmol) were dissolved in MeCN (40 mL) and stirred for 5 minutes. 4-Trifluoroaniline (123 µL, 0.78 mmol) was added to the solution and refluxed overnight (approximately 18 hours). The solvent was removed *in vacuo* to yield an off-white solid. The crude product was purified using column chromatography (SiO_2, 10% MeCN in DCM) to yield an off-white solid. (100mg, 33%). **^{1}H NMR** (500 MHz, Acetone-d_6) δ 11.56 (s, 1H), 10.21 (s, 1H), 8.80 (s, 2H), 8.43 (s, 1H), 8.28 (s, 2H), 7.80 (d, J = 0.5 Hz, 1H). **^{13}C NMR** (126 MHz, Acetone-d_6) δ 186.79, 182.58, 170.66, 164.20, 162.32, 139.62, 134.08, 131.9 (m/overlapping quartets X 2, $^2J_{CF}$ = 25 Hz), 129.5 (overlapping C X 2), 126.8 (m/overlapping quartets X 2, $^3J_{CF}$ = 4 Hz), 123.4 (q, $^1J_{CF}$ = 270 Hz), 123.1 (q, $^1J_{CF}$ = 271 Hz), 120.7 (overlapping C X 2), 170.1, 119.9 117.2 (m/overlapping quartets, $^3J_{CF}$ = 4 Hz). **IR** (ATR): $\mathbf{v}_{max}$ (cm^{-1}) = 3234, 1809, 1728, 1683, 1608 1585, 1530, 1477, 1376, 1290, 1273, 1233, 1135, 1033,856, 824, 129. **HRMS** (ESI+) *m/z* calcd for $C_{21}H_{18}F_{12}N_2O_3$ $[M+H]^+$ 428.0343, found 565.0414.

4-Nitro-*N*-(2-((4-nitrophenyl)amino)-3,4-dioxocyclobut-1-en-1-yl)benzamide (2.30)

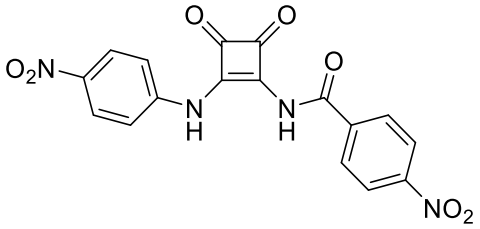

N-(2-Ethoxy-3,4-dioxocyclobut-1-en-1-yl)-4-nitrobenzamide (292 mg, 1 mmol) and zinc trifluoromethanesulfonate (72 mg, 0.2 mmol) were dissolved in MeCN (40 mL) and stirred for 5 minutes. 4-Nitroaniline (152 mg, 1.1 mmol) was added to the solution and refluxed overnight (approximately 18 hours). The precipitate was filtered and washed with hot MeCN to yield the product as a yellow solid (42 mg, 11%). **^{1}H NMR** (500 MHz, DMSO-d_6) δ 12.44 (s, 1H), 10.44 (s, 1H), 8.40 (d, *J* = 8.8 Hz, 2H), 8.26 (t, *J* = 8.6 Hz, 4H), 7.62 (d, *J* = 8.9 Hz, 2H). **^{13}C NMR** (126 MHz, DMSO) δ 188.1, 184.2, 171.3, 164.4, 164.2, 150.5, 144.1, 143.4, 137.6, 130.9, 125.6, 124.2, 120.4. **IR** (ATR): $\mathbf{\nu}_{max}$ (cm^{-1}) = 3234, 1809, 1728, 1683, 1608 1585, 1530, 1477, 1376, 1290, 1273, 1233, 1135, 1033, 856, 824, 729. . **HRMS** (ESI+) *m/z* calcd for $C_{17}H_{10}N_4O_7$ $[M+H]^+$ 382.0544, found 353.0626.

2-Iodo-*N*-(2-((2-iodophenyl)amino)-3,4-dioxocyclobut-1-en-1-yl)benzamide (2.31)

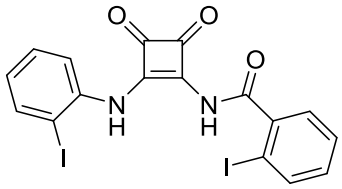

N-(2-Ethoxy-3,4-dioxocyclobut-1-en-1-yl)-2-iodobenzamide (200 mg, 0.54 mmol) and zinc trifluoromethanesulfonate (40 mg, 0.11 mmol) were dissolved in MeCN (40 mL) and stirred for 5 minutes. 2-Iodoaniline (130 mg, 0.59 mmol) was added to the solution and refluxed overnight (approximately 18 hours). The precipitate was filtered and washed with hot MeCN to yield the product as an off-white solid (106 mg, 36%). **^{1}H NMR** (500 MHz, DMSO) δ 12.48 (s, 1H), 9.88 (s, 1H), 7.98 (dd, *J* = 7.9, 0.8 Hz, 1H), 7.90 (dt, *J* = 3.4, 1.7 Hz, 1H), 7.66 – 7.60 (m, *J* = 11.5, 2.6 Hz, 2H), 7.54 (td, *J* = 7.5, 1.1 Hz, 1H), 7.46 – 7.41 (m, *J* = 8.1, 7.5, 1.4 Hz, 1H), 7.29 (td, 1H), 6.98 (td, 1H). **^{13}C NMR** (126 MHz, DMSO) δ 187.1, 183.3, 170.6, 169.2, 162.7, 140.0, 139.8, 139.5, 138.6, 132.7, 129.4, 128.5, 127.4, 123.2, 94.2, 91.9. **IR** (ATR): $\mathbf{\nu}_{max}$ (cm^{-1}) = 3246, 3192, 1809, 1723, 1700, 1606,

1575, 1507, 1484, 1421, 1286, 1239, 1153, 1137, 1103, 1017, 901, 750, 703. **HRMS** (ESI+) *m/z* calcd for $C_{17}H_{10}I_2N_2O_3$ $[M+H]^+$ 544.8781, found 544.8851.

4-Iodo-*N*-(2-((4-iodophenyl)amino)-3,4-dioxocyclobut-1-en-1-yl)benzamide (2.32)

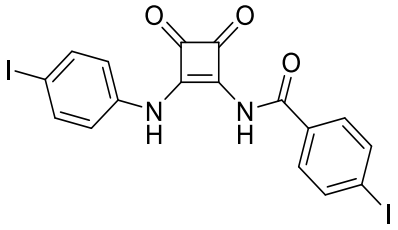

N-(2-Ethoxy-3,4-dioxocyclobut-1-en-1-yl)-4-iodobenzamide (200 mg, 0.72 mmol) and zinc trifluoromethanesulfonate (40 mg, 0.11 mmol) were dissolved in MeCN (40 mL) and stirred for 5 minutes. 4-Iodoaniline (130 mg, 0.59 mmol) was added to the reaction mixture and refluxed overnight (approximately 18 hours). The precipitate was filtered and washed with hot MeCN to yield the product as an off-white solid (150 mg, 51%). **^{1}H NMR** (500 MHz, DMSO-d_6) δ 12.03 (s, 1H), 9.95 (s, 1H), 7.97 (d, *J* = 8.5 Hz, 2H), 7.81 (d, *J* = 7.7 Hz, 2H), 7.70 (d, *J* = 8.3 Hz, 2H), 7.24 (s, 2H). **^{13}C NMR** (126 MHz, DMSO) δ 165.2, 138.1, 138.0, 137.9, 131.6, 131.1, 123.1, 102.2, 89.1. **IR** (ATR): $\mathbf{v}_{max}$ (cm^{-1}) = 3221, 3178, 1813, 1791, 1606, 1574, 1529, 1488, 1374, 1273, 1156, 1127, 1004, 899, 812, 733. **HRMS** (ESI+) *m/z* calcd for $C_{17}H_{10}I_2N_2O_3$ $[M+H]^+$ 544.8781, found 544.8851.

3,4-Dichloro-*N*-(2-((3,4-dichlorophenyl)amino)-3,4-dioxocyclobut-1-en-1-yl)benzamide (2.33)

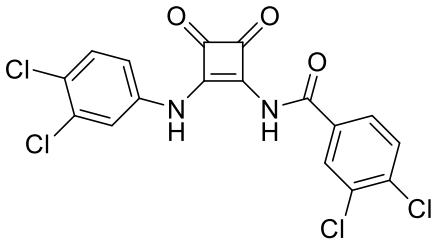

3,4-Dichloro-*N*-(2-ethoxy-3,4-dioxocyclobut-1-en-1-yl)benzamide (235 mg, 0.75 mmol) and zinc trifluoromethanesulfonate (55 mg, 0.15 mmol) were dissolved in MeCN (40 mL) and stirred for 5 minutes. 3,4-dichloroaniline (145 mg, 0.9 mmol) was added to the reaction mixture and refluxed overnight (approximately 18 hours). The precipitate was filtered and washed with hot MeCN to yield the product as a pale yellow solid (170 mg, 53%). **^{1}H NMR** (500 MHz, DMSO-d_6) δ 12.21 (s, 1H), 10.21 (s, 1H), 8.34 (s, 1H), 8.01 (d, *J* = 7.2 Hz, 1H), 7.86 (d, *J* = 8.4 Hz, 1H), 7.77 (s, 1H), 7.61 (d, *J* = 8.7 Hz, 1H), 7.39 (d, *J* = 7.6 Hz, 1H). **^{13}C**

NMR (126 MHz, DMSO-d_6) δ 131.9, 131.7, 131.4, 131.2, 129.5 **IR** (ATR): $\mathbf{v}_{max}$ (cm^{-1}) = 3168, 3113, 3078, 3057, 2990, 1813, 1738, 1619, 1575, 1517, 1374, 1325, 1270, 1106, 852, 748, 708. **HRMS** (ESI+) *m/z* calcd for $C_{17}H_8Cl_4N_2O_3$ $[M-H]^-$ 426.9289, found 426.9213.

4-Chloro-*N*-(2-((4-chlorophenyl)amino)-3,4-dioxocyclobut-1-en-1-yl)benzamide (2.34)

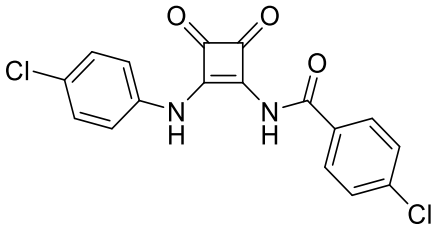

4-Chloro-*N*-(2-ethoxy-3,4-dioxocyclobut-1-en-1-yl)benzamide (200 mg, 0.72 mmol) and zinc trifluoromethanesulfonate (52 mg, 0.14 mmol) were dissolved in MeCN (40 mL) and stirred for 5 minutes. 4-chloroaniline (109 mg, 0.86 mmol) was added to the reaction mixture and refluxed overnight (approximately 18 hours). The precipitate was filtered and washed with hot MeCN to yield the product as a pale yellow solid (109 mg, 42%). **^{1}H NMR** (500 MHz, DMSO-d_6) δ 12.06 (s, 1H), 9.96 (s, 1H), 8.07 (d, *J* = 7.7 Hz, 2H), 7.65 (d, *J* = 8.6 Hz, 2H), 7.42 (s, 4H). **^{13}C NMR** (126 MHz, DMSO-d_6) δ 188.0, 183.4, 171.0 164.8, 163.3, 138.6, 137.0, 131.2, 131.0, 129.3, 129.2, 129.0, 122.6. **IR** (ATR): $\mathbf{v}_{max}$ (cm^{-1}) = 2973, 2950, 1809, 1724, 1579, 1487, 1455, 1371, 1265, 1057, 1034, 1011, 899, 841, 816, 745. **HRMS** (ESI+) *m/z* calcd for $C_{17}H_{10}Cl_2N_2O_3$ $[M + Na]^+$ 383.0068 , found 382.9960.

6.3 Synthetic Procedures for Chapter 3

4-((triisopropylsilyl)oxy) benzaldehyde

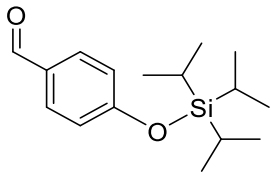

NEt_3 (1.7 mL, 12 mmol) was added to a solution of 4-hydroxybenzaldehyde (1.24 g, 10 mmol) and DMAP (0.12g, 1 mmol) in DCM (anhydrous, 20 mL), under an atmosphere of N_2, at 0°C. The solution was stirred for 10 minutes before the addition of triisopropylsilyl chloride (2.4 mL, 11 mmol). The reaction was allowed to reach room temperature and left to stir for 18 hours. The reaction mixture was diluted with DCM (10 mL) and washed with 1M HCl (2 x 30 mL) and brine (2 x 30m L). The organic layer was removed, dried over $MgSO_4$ and the solvent removed *in vacuo* to yield the product as an orange-red oil (2.5g, 90%). **^{1}H NMR** (500 MHz, $CDCl_3$) δ 9.88 (s, 1H), 7.83 – 7.70 (m, 2H), 7.03 – 6.91 (m, 2H), 1.29 (m, 3H), 1.11 (d, *J* = 7.4 Hz, 17H). **^{13}C NMR** (126 MHz, $CDCl_3$) δ 190.9, 162.1, 132.1, 130.4, 120.5, 18.0, 12.9.

The NMR data is in agreement with the data reported in the literature. 10.1055/s-2005-861863

3,4-bis((3,5-bis(trifluoromethyl)phenyl)(4-nitrobenzyl)amino)cyclobut-3-ene-1,2-dione (3.17)

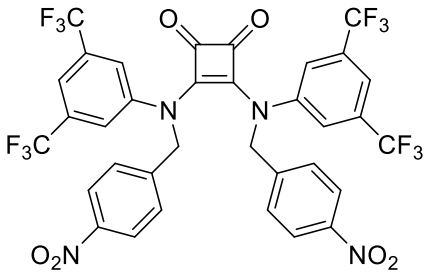

3,4-diethoxy-3-cyclobutene-1,2-dione (22 mg, 0.13 mmol) and N-(4-nitrobenzyl)-3,5-bis(trifluoromethyl)aniline (100 mg, 0.2 7 mmol) were dissolved in EtOH (5 mL) and stirred at room temperature for 5 minutes before the addition of zinc trifluoromethanesulfonate (9 mg, 25 mmol) in EtOH (5 mL). The reaction was refluxed at 120°C for 72 hours. The precipitate was collected *via* vacuum filtration and washed with cold EtOH and diethyl ether, to yield a yellow solid. (15mg,

15%). **^{1}H NMR** (500 MHz, DMSO-d_6) δ 8.23 (s, 4H), 8.21 (s, 2H), 7.98 (s, 4H), 7.70 (s, 4H), 5.94 (s, 4H). **^{13}C NMR** (126 MHz, DMSO-d_6) δ 147.8, 142.8, 131.3, 131.0, 126.6, 125.3, 124.4, 124.3, 122.2. **HRMS** (ESI+) *m/z* calcd for $C_{34}H_{18}F12N_4O_6$ $[M+H]^+$ 807.1035, found 807.1107.

3,4-bis((4-(trifluoromethyl)phenyl)(4-((triisopropylsilyl)oxy)benzyl)amino)cyclobut-3-ene-1,2-dione (3.18)

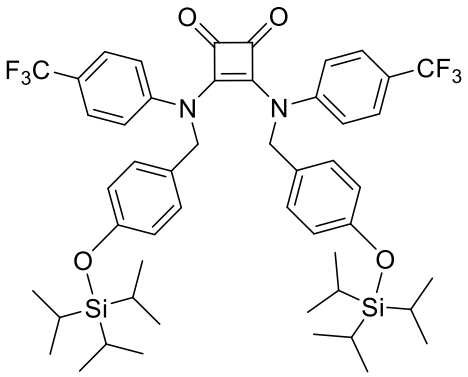

3,4-diethoxy-3-cyclobutene-1,2-dione (22 mg, 0.13 mmol) and 4-(trifluoromethyl)-N-(4-((triisopropylsilyl)oxy)benzyl)aniline (114 mg, 0.27 mmol) were dissolved in EtOH (5 mL) and stirred at room temperature for 5 minutes before the addition of zinc trifluoromethanesulfonate (9 mg, 25 mmol) in EtOH (5 mL). The reaction was refluxed at 120°C for 72 hours. The precipitate was collected *via* vacuum filtration and washed with cold EtOH and diethyl ether, to yield a pale orange solid. **^{1}H NMR** (500 MHz, $CDCl_3$) δ 7.58 (dd, *J* = 38.4, 7.4 Hz, 4H), 7.36 – 7.20 (m, 2H), 7.10 (dd, *J* = 22.0, 7.4 Hz, 4H), 6.79 (dd, *J* = 19.3, 7.5 Hz, 4H), 5.45 (d, *J* = 29.0 Hz, 4H), 1.29 – 1.15 (m, 6H), 1.05 (s, 36H). **^{13}C NMR** (126 MHz, $CDCl_3$) δ 177.9, 129.7, 129.5, 127.3, 126.1, 124.8, 120.4. **IR** (ATR): $\mathbf{v}_{max}$ (cm^{-1}) = 2945, 2867, 1603, 1509, 1464, 1435, 1409, 1360, 1322, 1262, 1204, 1164, 1122, 1107, 1065, 1013, 995, 975, 906, 882, 847, 815, 787. **HRMS** (ESI+) *m/z* calcd for $C_{50}H_{62}F_6N_2O_4Si_2$ $[M+H]^+$ 924.4512, found 413.2672.

N-(4-nitrobenzyl)-4-(trifluoromethyl)aniline (3.20)

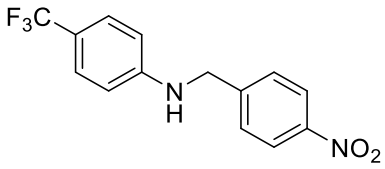

3,5-Bis(trifluoromethyl)aniline (2.16 mL, 13.8 mmol), 4-nitrobenzaldehyde (2.09 g, 13.8 mmol) and anhydrous MgSO4 (0.83 g, 6.9 mmol) were added to a round-bottom flask under N_2 and dissolved in anhydrous DCM (60 mL). The reaction mixture was stirred for 5 minutes before the addition of AcOH (1.17 mL, 6.5mmol) to the reaction mixture and stirred for 6 hours. Sodium triacetoxyborohydride (5.80g, 27.5 mmol) was then added to the reaction mixture and stirred overnight. The solvent was removed *in vacuo*, and the residue redissolved in EtOAc and sat. $NaHCO_3$. The organic layer was washed with $NaHCO_3$ (3 x 25 mL) and brine (3 x 25 mL). The organic layer was collected, dried over Na_2SO_4 and the solvent removed under reduced pressure to yield the crude product as a yellow oil. The product was purified *via* a hot recrystallization from $CHCl_3$ to afford the product as a yellow crystalline solid. (1.84 g, 45%). **^{1}H NMR** (500 MHz, $CDCl_3$) δ 8.29 – 8.12 (m, 1H), 7.55 – 7.43 (m, 1H), 7.39 (d, J = 8.4 Hz, 1H), 6.59 (d, J = 8.4 Hz, 1H), 4.61 (d, J = 5.4 Hz, 1H), 4.52 (d, J = 5.9 Hz, 1H). **^{13}C NMR** (126 MHz, $CDCl_3$) δ 149.8, 147.4, 146.4, 127.6, 126.77 (q, $^3J_{CF}$ = 3.8 Hz), 124.8 (q, $^1J_{CF}$ = 275 Hz), 124.1, 119.9 (q, $^2J_{CF}$ = 32.8 Hz), 47.1. **IR** (ATR): ν_{max} (cm^{-1}) = 3444, 1616, 1534, 1505, 1317, 1288, 1190, 1156, 1097, 1060, 994, 936, 860, 817, 786, 731. **HRMS** (ESI+) *m/z* calcd for $C_{14}H_{11}F_3N_2O_2$ $[M+H]^+$ 297.0845, found 297.0842.

N-(4-nitrobenzyl)-3,5-bis(trifluoromethyl)aniline (3.21)

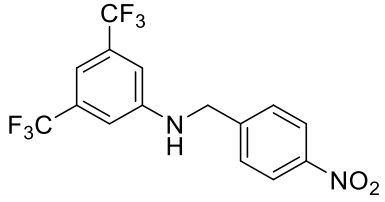

3,5-Bis(trifluoromethyl)aniline (2.16 mL, 13.8 mmol), 4-nitrobenzaldehyde (2.09 g, 13.8 mmol) and anhydrous $MgSO_4$ (0.83 g, 6.9 mmol) were added to a round-bottom flask under N_2 and dissolved in anhydrous DCM (60 mL). The reaction mixture was stirred for 5 minutes before the addition of AcOH (1.17 mL, 6.5 mmol) to the reaction mixture and stirred for 6 hours. Sodium triacetoxyborohydride

(5.80g, 27.5 mmol) was then added to the reaction mixture and stirred overnight. The solvent was removed *in vacuo*, and the residue redissolved in EtOAc and sat. $NaHCO_3$. The organic layer was washed with $NaHCO_3$ (3 x 25 mL) and brine (3 x 25 mL). The organic layer was collected, dried over Na_2SO_4 and the solvent removed under reduced pressure to yield the crude product as a yellow oil. The product was purified *via* a hot recrystallization from $CHCl_3$ to afford the product as a yellow crystalline solid. (2.06 g, 41%). **^{1}H NMR** (500 MHz, $CDCl_3$) δ 8.24 – 8.20 (m, 2H), 7.53 (dd, *J* = 8.3, 0.6 Hz, 2H), 7.21 (d, *J* = 0.6 Hz, 1H), 6.95 (s, 2H), 4.70 (t, *J* = 5.5 Hz, 1H), 4.55 (d, *J* = 5.8 Hz, 2H). **^{13}C NMR** (126 MHz, $CDCl_3$) δ 148.2, 147.7, 145.5, 132.82 (q, $^2J_{CF}$ = 32.9 Hz), 127.9, 124.3, 123.4 (q, $^1J_{CF}$ = 237 Hz) 112.26 (overlapping C X 2), 111.4 (m, $^3J_{CF}$ = 7.8, 3.9 Hz), 47.4. **IR** (ATR): $\boldsymbol{\nu}_{max}$ (cm^{-1}) = 3408, 1620, 1542, 1481, 1428, 1390, 1343, 1299, 1273, 1173, 1117, 1085, 1005, 903, 870, 847, 831, 788. **HRMS** (ESI+) *m/z* calcd for $C_{15}H_{10}F_6N_2O_2$ $[M+H]^+$ 365.0646, found 366.0719.

4-(trifluoromethyl)-N-(4-((triisopropylsilyl)oxy)benzyl)aniline (3.22)

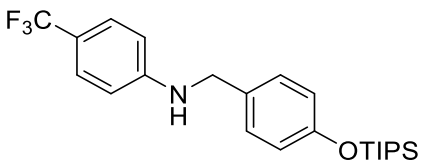

4-(trifluoromethyl)aniline (0.13 mL, 1 mmol) and 4-((triisopropylsilyl)oxy) benzaldehyde (0.28 g, 1 mmol) were dissolved in anhydrous DCM (20 mL) and stirred for 5 minutes under inert atmosphere. AcOH (0.10 mL, 1.5 mmol) was added to the reaction mixture and stirred for 6 hours. Sodium triacetoxyborohydride (0.32 g, 1.5 mmol) was then added to the reaction mixture and stirred for 48 hours. The solvent was removed *in vacuo*, and the residue redissolved in EtOAc and sat. $NaHCO_3$. The organic layer was washed with $NaHCO_3$ (3 x 25 mL) and brine (3 x 25 mL). The organic layer was dried over $MgSO_4$ and the solvent removed under reduced pressure to yield the crude product as a yellow oil. Column chromatography was used to purify the crude product (13:1 petroleum ether:ethyl acetate) to afford the product as an orange-pink oil. (275 mg, 65%). **^{1}H NMR** (500 MHz, $CDCl_3$) δ 7.41 (d, *J* = 8.5 Hz, 2H), 7.21 (d, *J* = 8.5 Hz, 2H), 6.89 (d, *J* = 8.5 Hz, 2H), 6.64 (d, *J* = 8.5 Hz, 2H), 4.28 (s, 2H), 1.34 – 1.23 (m, 3H), 1.13 (d, *J* = 7.4 Hz, 18H). **^{13}C NMR** (126 MHz, $CDCl_3$) δ 155.7, 150.7, 130.8, 128.8, 126.7 (q, $^3J_{CF}$ = 3.7 Hz), 123.0 (q, $^1J_{CF}$ = 269.6 Hz)

120.3, 119.1 (q, $^{2}J_{CF}$ = 32.6 Hz), 112.1, 47.6, 12.8. **IR** (ATR): $\mathbf{v}_{max}$ (cm^{-1}) = 3419, 2947, 2892, 2867, 1612, 1529, 1510, 1462, 1415, 1335, 1251, 1156, 1100, 1062, 998, 908, 882, 826. **HRMS** (ESI+) *m/z* calcd for $C_{23}H_{32}F_3NOSi$ $[M+Na]^+$ 446.2097, found 446.2113.

3,5-bis(trifluoromethyl)-N-(4-((triisopropylsilyl)oxy)benzyl)aniline (3.23)

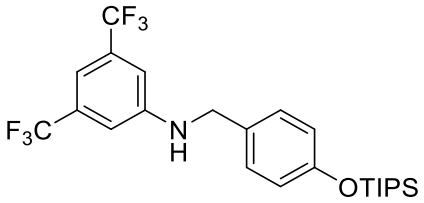

3,5-Bis(trifluoromethyl)aniline (0.26 mL, 1.68 mmol) and 4-((triisopropylsilyl)oxy) benzaldehyde (0.4 g, 1.4 mmol) were dissolved in anhydrous DCM (30 mL) and stirred for 5 minutes under inert atmosphere. AcOH (0.11 mL, 1.83 mmol) was added to the reaction mixture and stirred for 6 hours. Sodium triacetoxyborohydride (0.39 g, 1.82 mmol) was then added to the reaction mixture and stirred for 48 hours. The solvent was removed *in vacuo*, and the residue redissolved in EtOAc and sat. $NaHCO_3$. The organic layer was washed with $NaHCO_3$ (3 x 25mmL) and brine (3 x 25mmL). The organic layer was dried over $MgSO_4$ and the solvent removed under reduced pressure to yield the crude product as a yellow oil. Column chromatography was used to purify the crude product (13:1 petroleum ether:ethyl acetate) to afford the product as an orange-pink oil. (487 mg, 59%). **^{1}H NMR** (500 MHz, $CDCl_3$) δ 7.18 (dt, 2H), 7.12 (s, 1H), 6.95 (s, 2H), 6.86 (dt, 2H), 4.63 (t, *J* = 5.0 Hz, 1H), 4.27 (d, *J* = 5.2 Hz, 1H), 1.40 – 1.20 (m, 3H), 1.08 (d, *J* = 2.8 Hz, 18H). **^{13}C NMR** (126 MHz, $CDCl_3$) δ 171.4, 155.9, 148.9, 132.5 (q, *J* = 32.7 Hz), 130.1, 128.8, 123.7 (q, $^{1}J_{CF}$ = 272 Hz). 120.4, 112.0 (overlapping C X 2)), 110.31 – 110.05 (m/overlapping q), 17.8, 12.8, 12.0. **IR** (ATR): $\mathbf{v}_{max}$ (cm^{-1}) = 2946, 2868, 1621, 1509, 1470, 1430, 1391, 1355, 1274, 1169, 1127, 1079, 995, 952, 907, 860, 739. **HRMS** (ESI+) *m/z* calcd for $C_{24}H_{31}F_6NOSi$ $[M+Na]^+$ 514.1971, found 514.2081.

3,4-bis(benzyl(phenyl)amino)cyclobut-3-ene-1,2-dione (3.24)

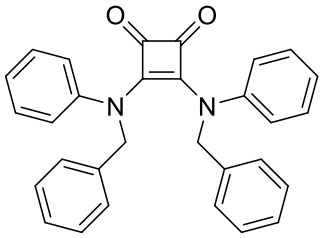

3,4-diethoxy-3-cyclobutene-1,2-dione (0.45 g, 2.65 mmol) and *N*-benzylaniline (1.02 g, 5.55 mmol) were dissolved in EtOH (30 mL) and stirred for 5 minutes before the addition of $Zn(OTf)_2$ (0.19 g, 0.53 mmol) and NEt_3 (773 µL, 5.55 mmol). The reaction was refluxed at 80°C for 96 hours. The reaction mixture was cooled to room temperature and the precipitate filtered and washed with cold EtOH and Et_2O to yield the product as a pale orange amorphous solid (12 mg, 10%). **^{1}H NMR** (500 MHz, DMSO-*d*$_6$) δ 7.36 (m, 4H), 7.31 (m, 4H), 7.25 – 7.16 (m, 2H), 7.09 – 6.99 (m, 4H), 6.63 (d, *J* = 7.8 Hz, 4H), 6.56 (t, *J* = 7.2 Hz, 2H), 4.27 (s, 4H). **^{13}C NMR** (126 MHz, DMSO) δ 148.3, 140.2, 129.3, 128.8, 127.8, 127.2, 117.0, 113.4, 47.4. **IR** (ATR): $\mathbf{\nu}_{max}$ (cm^{-1}) = 3057, 2923, 1610, 1470, 1428, 1358, 1324, 1297, 1272, 1209, 1154, 1099, 1074, 1027, 1002, 981, 927, 807, 761, 726. **HRMS** (ESI+) *m/z* calcd for $C_{30}H_{24}N_2O_2$ $[M+H]^+$ 444.1838, found 445.1913.

1,3-dibenzyl-1,3-diphenylurea (3.29)

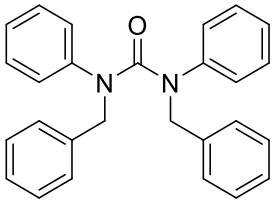

Triphosgene (114 mg, 0.388 mmol) was placed in a 50 mL round-bottomed flask under an atmosphere of N_2. *N*-benzylaniline (326 mg, 2.36 mmol) was placed in a 25 mL round-bottom flask, under an atmosphere of N_2, and dissolved in anhydrous DCM (10 mL). The solution of *N*-benzylaniline was transferred to the vessel containing triphosgene *via* cannulation. NEt_3 (329 µL, 2.36 mmol) was added to the reaction mixture and left to stir at room temperature for 18 hours. The solvent was removed *in vacuo* to yield a yellow solid, which was dissolved in EtOAc (20 mL) and washed with 0.1 M HCl (3 x 30 mL), water (3 x 30 mL), and brine (3 x 30 mL). The organic layer was dried over $MgSO_4$ and gravity filtered before the solvent was removed *in vacuo* to yield the crude product as a yellow

solid. The crude product was purified *via* flash chromatography (SiO_2, 4:1 petroleum ether:ethyl acetate) to yield the product as a pale brown amorphous solid (10 mg, 72%). **^{1}H NMR** (500 MHz, $CDCl_3$) δ 7.28 – 7.18 (m, 11H), 6.95 – 6.83 (m, 6H), 6.61 – 6.54 (m, 4H), 4.76 (s, 4H). **^{13}C NMR** (126 MHz, $CDCl_3$) δ 144.1, 138.4, 128.8, 128.4, 128.2, 127.1, 127.1, 125.1, 55.5. **IR** (ATR): $\mathbf{v}_{max}$ (cm^{-1}) = 3027, 2940, 1639, 1462, 1435, 1391, 1435, 1391, 1271, 1198, 1077, 1014, 924, 827. **HRMS** (ESI+) *m/z* calcd for $C_{27}H_{24}N_2O$ $[M+H]^+$ 392.1889, found 393.1964.

6.3 Synthetic Procedure for Chapter 4

General Synthetic Procedure

The appropriately substituted aromatic diamine (1.2 equiv) was added to a stirred solution of diethyl squarate (1.0 equiv) and $Zn(OTf)_2$ (0.2 equiv.) in ethanol (5 mL). The reaction mixture was stirred at room temperature for 24 hr before formation of a precipitate. The solid was collected by suction filtration and washed with EtOH and Et_2O before being allowed to dry at room temp.

cyclobuta[b]quinoxaline-1,2(3H,8H)-dione (4.16)

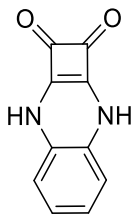

4.16 was collected as a beige solid. (0.708 g, 64%), m.p.≥300℃. **1H NMR** (500 MHz, DMSO-d_6) δ 9.99 (s, 2 NH), 6.65 (dd, *J* = 5.7/3.4 Hz, 2H), 6.36 (dd, *J* = 5.5/3.6 Hz, 2H); **^{13}C NMR** (126 MHz, DMSO-d_6) δ 178.7, 174.9, 132.2, 125.4, 116.9. **IR** (ATR): $\mathbf{v}_{max}$ (cm^{-1}) = 3123, 2955, 2017, 1913, 1805, 1790, 1657, 1614, 1558, 1478, 1458, 1358, 1304, 1245, 1213, 1180, 1129, 1075, 1041, 930, 900, 806, 777, 743, 666. HRMS (ESI+) *m/z* calcd for $C_{10}H_6O_2N_2$ $[M+H]^+$, expected: 186.0428, found 186.0429, PPM:-0.64.

5-nitrocyclobuta[b]quinoxaline-1,2(3H,8H)- dione (4.17)

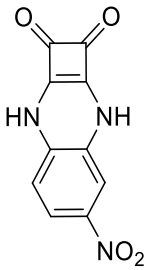

4.17 was collected as a purple solid. (1.004 g, 74%), m.p.≥300℃. **^{1}H NMR** (500 MHz, DMSO-*d*$_6$) δ 10.55 (s, NH), 10.39 (s, NH), 7.58 (dd J = 8.8/2.5 Hz, 1H), 7.01 (d, *J* = 2.5 Hz. 1H), 6.41 (d, *J* = 8.6 Hz, 1H); **13C NMR** (126 MHz, DMSO-*d*$_6$) δ 179.6, 178.5, 175.7, 174.8, 144.0, 139.8, 133.9, 122.7, 115.9, 110.4; **IR** (ATR): **ν**$_{max}$ (cm^{-1}) = 3572, 3141, 2974, 2020, 1870, 1794, 1665, 1632, 1583, 1529, 1487, 1419, 1322, 1267, 1247, 1218, 1202, 1092, 1073, 945, 883, 861, 837, 803, 788, 745, 670, 646. **HRMS** (ESI+) *m/z* calcd for $C_{10}H_5O_4N_3$ [M+H]+, expected: 231.0282, found: 231.028, PPM:0.71.

5-methoxycyclobuta[b]quinoxaline-1,2(3H,8H)- dione (4.18)

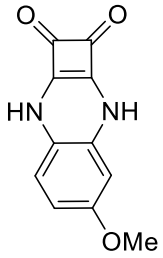

4.18 was collected as a brown solid. (0.646 g, 97%), m.p.≥300℃. **^{1}H NMR** (500 MHz, DMSO-*d*$_6$) δ 9.98 (s, NH), 9.96 (s, NH), 6.31 (d, *J* = 8.6 Hz, 1H), 6.2 (dd, *J* = 8.6/2.8 Hz, 1H), 6.00 (d, *J* = 2.7 Hz, 1H), 3.60 (s, 3H); **^{13}C NMR** (126 MHz, DMSO-*d*$_6$) 179.1, 178.2, 174.6, 173.7, 157.2, 133.1, 125.1, 117.2, 107.5, 104.9, 56.0.; **IR** (ATR): **ν**$_{max}$ (cm^{-1}) = 3123, 2944, 1797, 1660, 1351, 1315, 1279, 1217, 1160, 1123, 1084, 1067, 1032, 941, 854, 788, 718, 672. HRMS ESI+) *m/z* calcd for $C_{11}H_8O_3N_2$ [M+H]+, expected: 216.0547, found 216.0535, PPM:5.55.

6.4 Anion Binding Studies

Both the tetrabutylammonium halide salts (TBAX) and the receptors were lyophilised before use. Solutions of the TBA salts were made up in DMSO-d_6, which was dried over 3Å molecular sieves before use, to a concentration of 300 mM. An aliquot of stock solution of receptor in DMSO-d_6 was diluted to 1 mL (2.5 mM). 600 µL of this solution was added to an NMR and the ^{1}H NMR spectrum was recorded. Subsequent additions of aliquots of TBAX solutions were added to the NMR tube and shaken vigorously to ensure homogenisation. This process was repeated up to 22 equivalents of halide was reached.

The ^{1}H NMR spectra were analysed and processed, and stackplots were generated using MestReNova 6.0.2 software. A global fitting analysis assuming a 1:1 binding model was employed to provide the binding constant (K_a/M^{-1}), by fitting of the chemical shift changes of the NH signals as function of anion concentration using the open access BindFit software program.

6.5 UV-Vis pH-spectrophotometric titrations

pKa values were experimentally determined using the wavelength of macimum difference in absorbance between the UV-Vis spectra of the neutral and anionic species. The absorbance of each receptor was measured in a solution of DMSO/H_2O (9:1) containing 0.1 M $TBAPF_6$ between approximately pH 2.5 to 12.5. The solutions were initially acidified using HNO_3 and gradually basified by aliquots of either 1 M or 0.1 M NaOH. The absorbance values of maximal difference were plotted against pH values. A four parameter sigmoid curve using Sigma Plot was fitted through the data points with the point of inflexion corresponding to the pK_a value.

6.6 Cl^-/NO_3^- exchange assays

Preparation of POPC vesicles

The internal solution (NaCl 487 mM, sodium phosphate 5 mM) and external solution ($NaNO_3$ 487 mM, sodium phosphate 5 mM) were prepared using Milli-Q water to prevent ion contamination and buffered to pH 7.20. 1-palmitoyl-2-oleoyl-sn-glycero-3-phosphocholine (POPC) (118 mg) and cholesterol (26 mg) were dissolved in $CHCl_3$ (5 mL) in a 25 mL round-bottomed flask. The $CHCl_3$ was slowly gently removed using a rotary evaporator to form a thin lipid film, which

was then dried under vacuum overnight. The lipid film was rehydrated by vortexing with 5 mL of the internal solution for 5 minutes before brief sonication to ensure no lipid was remaining on the interior wall of the flask. The lipid solution was subjected to nine freeze-thaw cycles by submerging the flask in liquid N_2 and lukewarm water, followed by allowing the solution to rest for 30 minutes. Every 1 mL of the lipid solution was then extruded 27 times through a 200 nm polycarbonate membrane to form unilamellar vesicles. The vesicles were then dialysed against the external solution overnight to remove unencapsulated NaCl. The vesicles were then diluted to 10 mL with the external solution to obtain a stock solution of lipid.

For preparation of POPC vesicles at pH 4.20, the procedure is largely the same. Internal and external solutions are buffered with a citrate buffer to pH 4.20 (5 mM) instead of sodium phosphate. The dialysis of the lipid vesicles to remove unencapsulated NaCl lasts for 2 hours, as opposed to overnight.

Cl^-/NO_3^- exchange assays.

In a glass vial, an aliquot of the vesicle solution was diluted to 5 mL using the external solution to obtain a solution of 0.5 mM lipid. A micro PTFE stirring bar was added to the vial and set to stir at a moderate rate. The chloride ion selective electrode (ISE) was calibrated against standard solution of NaCl before using the ISE to monitor Cl^- efflux. The readings from the electrode reader were allowed to stabilise before initiating the experiment. A negative control using DMSO was added to the lipid solution as to ensure that the vesicles displayed no leakage. At t=0, a DMSO solution of the receptor was added to give a 5 mol % (concentration of the receptor with respect to the lipid) solution. The electrode reader was set to record the mV at 5 second intervals. At t=300, a solution of Triton X-100 (11 wt% in H_2O:DMSO 7:1 v:v) was added to lyse the vesicles to determine 100% Cl^- efflux. Experiments were each repeated in triplicate, and all traces are the average of three trials.

6.7 Computational Methods

All electronic structure calculations were carried out using the Gaussian 09 (revision E.01) and ORCA (version 4.2.1) program packages. Unconstrained optimizations of ground-state geometries and subsequent analytical frequency calculations were carried out at DFT level using the M06-2X functional in

conjunction with Pople's 6-31+G(d) basis set on all atoms except iodine. The Stuttgart-Dresden SDD effective core potential and associate basis sets were chosen to describe iodine, with an added polarization function (ζ_d = 0.289). A ultrafine integration grid, corresponding to a pruned grid of 99 radial shells and 590 angular points per shell, was used for all calculations. All stationary points were confirmed to be minima by the absence of imaginary modes in their vibrational spectra. Thermal and entropic corrections to the SCF energies (T = 298.15 K and p = 1 atm) were also extracted from the vibrational gas phase calculations. Effects due to the presence of solvent were included by means of the Polarizable Continuum Model (IEF-PCM), with parameters corresponding to those of dimethylsulfoxide (ε = 46.8). Non-electrostatic terms to solvation were calculated by invoking the SMD option. To this end, all geometries were again optimised in solution phase. The free energies of solvation (at fixed concentrations) for each compound was then obtained from the electronic energy difference of the species optimised in solution and gas phase:

$$\Delta G^{\ominus}_{solv} = E_{SCRF}(\boldsymbol{R}_s) - E_{SCF}(\boldsymbol{R}_g)$$

The "$\ominus$" superscript indicates that the quantities are calculated with respect to standard states of 1 mol L^{-1} (a correction of 1.9 kcal mol^{-1}). The variables $\boldsymbol{R}_g$ and $\boldsymbol{R}_s$ imply dependence of the energy on the gas phase and solution phase optimized geometries, respectively. High-level gas phase calculations were carried out at the DLPNO-CCSD(T) level of theory as single-point calculations on the M06-2X-optimised geometries. Automatic basis set extrapolation (involving cardinal numbers n = 3 and 4 within the def2-nZVP basis set family) was used to converge both HF and correlation energies to the complete basis set limit. The RIJCOSX approimxation and …. was used to speed up integral solvation, with the def2/J and autoaux auxiliary basis sets. These calculations were performed with ORCA.

All pK_a values were calculated using a direct method via the thermodynamic cycle depicted in Scheme 1, utilising a proton solvation free energy of –273.30 kcal mol^{-1} in DMSO:

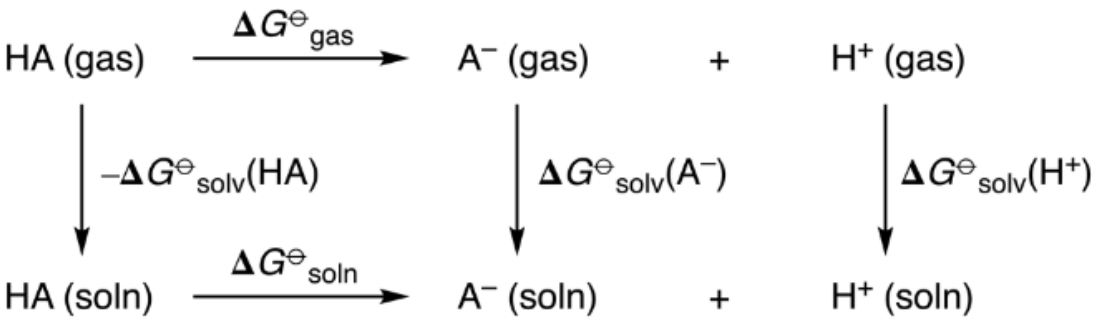

$$\Delta G^{\ominus}_{soln} = \Delta G^{\ominus}_{gas} + \Delta G^{\ominus}_{solv}(H^+) + \Delta G^{\ominus}_{solv}(A^-) - \Delta G^{\ominus}_{solv}(HA)$$

$$pK_a(HA) = \Delta G^{\ominus}_{soln} / RT\ln(10)$$

Bibliography

1. Dutzler, R.; Campbell, E. B.; Cadene, M.; Chait, B. T.; MacKinnon, R., X-ray structure of a ClC chloride channel at 3.0 Å reveals the molecular basis of anion selectivity. *Nature* **2002,** *415* (6869), 287-294.
2. Macknight, A. D. C., The role of anions in cellular volume regulation. *Pflügers Archiv* **1985,** *405* (1), S12-S16.
3. Welsh, M. J.; Smith, A. E., Molecular mechanisms of CFTR chloride channel dysfunction in cystic fibrosis. *Cell* **1993,** *73* (7), 1251-1254.
4. Duan, D.-y.; Liu, L. L. H.; Bozeat, N.; Huang, Z. M.; Xiang, S. Y.; Wang, G.-l.; Ye, L.; Hume, J. R., Functional role of anion channels in cardiac diseases. *Acta Pharmacologica Sinica* **2005,** *26* (3), 265-278.
5. Goraya, N.; Wesson, D. E., Management of the Metabolic Acidosis of Chronic Kidney Disease. *Advances in Chronic Kidney Disease* **2017,** *24* (5), 298-304.
6. Correll, D. L., The Role of Phosphorus in the Eutrophication of Receiving Waters: A Review. *Journal of Environmental Quality* **1998,** *27* (2), 261-266.
7. Qin, L.; Vervuurt, S. J. N.; Elmes, R. B. P.; Berry, S. N.; Proschogo, N.; Jolliffe, K. A., Extraction and transport of sulfate using macrocyclic squaramide receptors. *Chemical Science* **2020,** *11* (1), 201-207.
8. Mishra, R. K.; Sudarsan, K. V.; Sengupta, P.; Vatsa, R. K.; Tyagi, A. K.; Kaushik, C. P.; Das, D.; Raj, K., Role of Sulfate in Structural Modifications of Sodium Barium Borosilicate Glasses Developed for Nuclear Waste Immobilization. *Journal of the American Ceramic Society* **2008,** *91* (12), 3903-3907.
9. (a) Amendola, V.; Fabbrizzi, L.; Mosca, L., Anion recognition by hydrogen bonding: urea-based receptors. *Chemical Society Reviews* **2010,** *39* (10), 3889-3915; (b) Gale, P. A.; Caltagirone, C., Fluorescent and colorimetric sensors for anionic species. *Coordination Chemistry Reviews* **2018,** *354*, 2-27; (c) Gale, P. A.; Pérez-Tomás, R.; Quesada, R., Anion Transporters and Biological Systems. *Accounts of Chemical Research* **2013,** *46* (12), 2801-2813; (d) Gale, P. A.; Davis, J. T.; Quesada, R., Anion transport and supramolecular medicinal chemistry. *Chemical Society Reviews* **2017,** *46* (9), 2497-2519; (e) Busschaert, N.; Caltagirone, C.; Van Rossom, W.; Gale, P. A., Applications of Supramolecular Anion Recognition. *Chemical Reviews* **2015,** *115* (15), 8038-8155; (f) Gunnlaugsson, T.; Glynn, M.; Tocci, G. M.; Kruger, P. E.; Pfeffer, F. M., Anion recognition and sensing in organic and aqueous media using luminescent and colorimetric sensors. *Coordination Chemistry Reviews* **2006,** *250* (23), 3094-3117; (g) Snowden, T. S.; Anslyn, E. V., Anion recognition: synthetic receptors for anions and their application in sensors. *Current Opinion in Chemical Biology* **1999,** *3* (6), 740-746; (h) Davis, A. P., Anion binding and transport by steroid-based receptors. *Coordination Chemistry Reviews* **2006,** *250* (23), 2939-2951.
10. Prange, H. D.; J. L. Shoemaker, J.; Westen, E. A.; Horstkotte, D. G.; Pinshow, B., Physiological consequences of oxygen-dependent chloride binding to hemoglobin. *Journal of Applied Physiology* **2001,** *91* (1), 33-38.
11. Edward A. Westen; Henry D. Prange, A Reexamination of the Mechanisms Underlying the Arteriovenous Chloride Shift. *Physiological and Biochemical Zoology* **2003,** *76* (5), 603-614.
12. Linsdell, P., Mechanism of chloride permeation in the cystic fibrosis transmembrane conductance regulator chloride channel. *Experimental Physiology* **2006,** *91* (1), 123-129.
13. Markovich, D., Physiological Roles and Regulation of Mammalian Sulfate Transporters. *Physiological Reviews* **2001,** *81* (4), 1499-1533.

14. Nieuw Amerongen, A. V.; Bolscher, J. G. M.; Bloemena, E.; Veerman, E. C. I., Sulfomucins in the Human Body. *Biological Chemistry* **1998,** *379* (1), 1.
15. Xia, B.; Royall, J. A.; Damera, G.; Sachdev, G. P.; Cummings, R. D., Altered O-glycosylation and sulfation of airway mucins associated with cystic fibrosis. *Glycobiology* **2005,** *15* (8), 747-775.
16. Takeda, E.; Yamamoto, H.; Nashiki, K.; Sato, T.; Arai, H.; Taketani, Y., Inorganic phosphate homeostasis and the role of dietary phosphorus. *Journal of Cellular and Molecular Medicine* **2004,** *8* (2), 191-200.
17. Michigami, T.; Ozono, K., Roles of Phosphate in Skeleton. *Frontiers in Endocrinology* **2019,** *10* (180).
18. Conrads, K. A.; Yi, M.; Simpson, K. A.; Lucas, D. A.; Camalier, C. E.; Yu, L.-R.; Veenstra, T. D.; Stephens, R. M.; Conrads, T. P.; Beck, G. R., A Combined Proteome and Microarray Investigation of Inorganic Phosphate-induced Pre-osteoblast Cells*S. *Molecular & Cellular Proteomics* **2005,** *4* (9), 1284-1296.
19. Nishino, J.; Yamazaki, M.; Kawai, M.; Tachikawa, K.; Yamamoto, K.; Miyagawa, K.; Kogo, M.; Ozono, K.; Michigami, T., Extracellular Phosphate Induces the Expression of Dentin Matrix Protein 1 Through the FGF Receptor in Osteoblasts. *Journal of Cellular Biochemistry* **2017,** *118* (5), 1151-1163.
20. Fukumoto, S.; Ozono, K.; Michigami, T.; Minagawa, M.; Okazaki, R.; Sugimoto, T.; Takeuchi, Y.; Matsumoto, T., Pathogenesis and diagnostic criteria for rickets and osteomalacia--proposal by an expert panel supported by the Ministry of Health, Labour and Welfare, Japan, the Japanese Society for Bone and Mineral Research, and the Japan Endocrine Society. *Journal of bone and mineral metabolism* **2015,** *33* (5), 467-73.
21. M, C. G., *The Cell: A Molecular Approach. 2nd edition*. 2000.
22. Chapter 13 - Membrane Structure and Dynamics. In *Cell Biology (Third Edition)*, Pollard, T. D.; Earnshaw, W. C.; Lippincott-Schwartz, J.; Johnson, G. T., Eds. Elsevier: 2017; pp 227-239.
23. Riordan, J. F., Arginyl residues and anion binding sites in proteins. *Molecular and Cellular Biochemistry* **1979,** *26* (2), 71-92.
24. Chavali, S. S.; Cavender, C. E.; Mathews, D. H.; Wedekind, J. E., Arginine Forks Are a Widespread Motif to Recognize Phosphate Backbones and Guanine Nucleobases in the RNA Major Groove. *Journal of the American Chemical Society* **2020,** *142* (47), 19835-19839.
25. CRICHTON, R. R.; CHARLOTEAUX-WAUTERS, M., Iron transport and storage. *European Journal of Biochemistry* **1987,** *164* (3), 485-506.
26. Harris, W. R.; Nesset-Tollefson, D.; Stenback, J. Z.; Mohamed-Hani, N., Site selectivity in the binding of inorganic anions to serum transferrin. *Journal of Inorganic Biochemistry* **1990,** *38* (3), 175-183.
27. Baker, E. N.; Lindley, P. F., New perspectives on the structure and function of transferrins. *Journal of Inorganic Biochemistry* **1992,** *47* (1), 147-160.
28. Baker, E. N.; Anderson, B. F.; Baker, H. M.; Haridas, G.; Norris, E.; Rumball, S. V.; Smith, C. A., Metal and anion binding sites in lactoferrin and related proteins. *Pure and Applied Chemistry* **1990,** *62* (6), 1067-1070.
29. Langridge, R.; Shinagawa, H.; Pardee, A. B., Sulfate-binding protein from Salmonella typhimurium: physical properties. *Science (New York, N.Y.)* **1970,** *169* (3940), 59-61.
30. Pflugrath, J. W.; Quiocho, F. A., The 2 Å resolution structure of the sulfate-binding protein involved in active transport in Salmonella typhimurium. *Journal of Molecular Biology* **1988,** *200* (1), 163-180.
31. Kubik, S., Amino acid containing anion receptors. *Chemical Society Reviews* **2009,** *38* (2), 585-605.

32. Jentsch, T. J.; Steinmeyer, K.; Schwarz, G., Primary structure of Torpedo marmorata chloride channel isolated by expression cloning in Xenopus oocytes. *Nature* **1990,** *348* (6301), 510-514.
33. Fahlke, C.; Dürr, C.; George, A. L., Jr., Mechanism of Ion Permeation in Skeletal Muscle Chloride Channels. *Journal of General Physiology* **1997,** *110* (5), 551-564.
34. Picollo, A.; Pusch, M., Chloride/proton antiporter activity of mammalian CLC proteins ClC-4 and ClC-5. *Nature* **2005,** *436* (7049), 420-423.
35. Accardi, A.; Miller, C., Secondary active transport mediated by a prokaryotic homologue of ClC Cl- channels. *Nature* **2004,** *427* (6977), 803-807.
36. Poroca, D. R.; Pelis, R. M.; Chappe, V. M., ClC Channels and Transporters: Structure, Physiological Functions, and Implications in Human Chloride Channelopathies. *Frontiers in Pharmacology* **2017,** *8* (151).
37. Park, E.; MacKinnon, R., Structure of the CLC-1 chloride channel from Homo sapiens. *eLife* **2018**.
38. Jayaram, H.; Robertson, J. L.; Wu, F.; Williams, C.; Miller, C., Structure of a Slow CLC Cl−/H+ Antiporter from a Cyanobacterium. *Biochemistry* **2011,** *50* (5), 788-794.
39. Accardi , A.; Kolmakova-Partensky , L.; Williams , C.; Miller , C., Ionic Currents Mediated by a Prokaryotic Homologue of CLC Cl− Channels. *Journal of General Physiology* **2004,** *123* (2), 109-119.
40. Feng, L.; Campbell, E. B.; MacKinnon, R., Molecular mechanism of proton transport in CLC Cl⁻/H⁺ exchange transporters. *Proceedings of the National Academy of Sciences* **2012**.
41. Dutzler, R.; Campbell, E. B.; MacKinnon, R., Gating the selectivity filter in ClC chloride channels. *Science (New York, N.Y.)* **2003,** *300* (5616), 108-12.
42. Feng, L.; Campbell, E. B.; Hsiung, Y.; MacKinnon, R., Structure of a eukaryotic CLC transporter defines an intermediate state in the transport cycle. *Science (New York, N.Y.)* **2010,** *330* (6004), 635-41.
43. Friedrich, T.; Breiderhoff, T.; Jentsch, T. J., Mutational analysis demonstrates that ClC-4 and ClC-5 directly mediate plasma membrane currents. *The Journal of biological chemistry* **1999,** *274* (2), 896-902.
44. Scheel, O.; Zdebik, A. A.; Lourdel, S.; Jentsch, T. J., Voltage-dependent electrogenic chloride/proton exchange by endosomal CLC proteins. *Nature* **2005,** *436* (7049), 424-427.
45. Steinmeyer, K.; Klocke, R.; Ortland, C.; Gronemeier, M.; Jockusch, H.; GrÜnder, S.; Jentsch, T. J., Inactivation of muscle chloride channel by transposon insertion in myotonic mice. *Nature* **1991,** *354* (6351), 304-308.
46. Thomsen, J., Tonische Krämpfe in willkürlich beweglichen Muskeln in Folge von ererbter psychischer Disposition. *Archiv für Psychiatrie und Nervenkrankheiten* **1876,** *6* (3), 702-718.
47. Uchida, S.; Sasaki, S.; Nitta, K.; Uchida, K.; Horita, S.; Nihei, H.; Marumo, F., Localization and functional characterization of rat kidney-specific chloride channel, ClC-K1. *The Journal of Clinical Investigation* **1995,** *95* (1), 104-113.
48. Estévez, R.; Pusch, M.; Ferrer-Costa, C.; Orozco, M.; Jentsch, T. J., Functional and structural conservation of CBS domains from CLC chloride channels. *The Journal of physiology* **2004,** *557* (Pt 2), 363-78.
49. Adachi, S.; Uchida, S.; Ito, H.; Marumo, F.; Sasaki, S., Two isoforms of a chloride channel predominantly expressed in thick ascending limb of Henle's loop and collecting ducts of rat kidney. *Journal of Biological Chemistry* **1884,** *269* (26), 17677-17683.

50. Kawasaki, M.; Uchida, S.; Monkawa, T.; Miyawaki, A.; Mikoshiba, K.; Marumo, F.; Sasaki, S., Cloning and expression of a protein kinase C-regulated chloride channel abundantly expressed in rat brain neuronal cells. *Neuron* **1994,** *12* (3), 597-604.
51. Maritzen, T.; Keating, D. J.; Neagoe, I.; Zdebik, A. A.; Jentsch, T. J., Role of the Vesicular Chloride Transporter ClC-3 in Neuroendocrine Tissue. *The Journal of Neuroscience* **2008,** *28* (42), 10587-10598.
52. Huang, L.-Y.; He, Q.; Liang, S.-J.; Su, Y.-X.; Xiong, L.-X.; Wu, Q.-Q.; Wu, Q.-Y.; Tao, J.; Wang, J.-P.; Tang, Y.-B.; Lv, X.-F.; Liu, J.; Guan, Y.-Y.; Pang, R.-P.; Zhou, J.-G., ClC-3 chloride channel/antiporter defect contributes to inflammatory bowel disease in humans and mice. *Gut* **2014,** *63* (10), 1587-1595.
53. Tao, J.; Liu, C. Z.; Yang, J.; Xie, Z. Z.; Ma, M. M.; Li, X. Y.; Li, F. Y.; Wang, G. L.; Zhou, J. G.; Du, Y. H.; Guan, Y. Y., ClC-3 deficiency prevents atherosclerotic lesion development in ApoE-/- mice. *Journal of molecular and cellular cardiology* **2015,** *87*, 237-47.
54. Steinmeyer, K.; Schwappach, B.; Bens, M.; Vandewalle, A.; Jentsch, T. J., Cloning and functional expression of rat CLC-5, a chloride channel related to kidney disease. *The Journal of biological chemistry* **1995,** *270* (52), 31172-7.
55. Kornak, U.; Kasper, D.; Bösl, M. R.; Kaiser, E.; Schweizer, M.; Schulz, A.; Friedrich, W.; Delling, G.; Jentsch, T. J., Loss of the ClC-7 Chloride Channel Leads to Osteopetrosis in Mice and Man. *Cell* **2001,** *104* (2), 205-215.
56. Stölting, G.; Fischer, M.; Fahlke, C., CLC channel function and dysfunction in health and disease. *Frontiers in Physiology* **2014,** *5* (378).
57. Saviane, C.; Conti, F.; Pusch, M., The Muscle Chloride Channel ClC-1 Has a Double-Barreled Appearance that Is Differentially Affected in Dominant and Recessive Myotonia. *Journal of General Physiology* **1999,** *113* (3), 457-468.
58. Depienne, C.; Bugiani, M.; Dupuits, C.; Galanaud, D.; Touitou, V.; Postma, N.; van Berkel, C.; Polder, E.; Tollard, E.; Darios, F.; Brice, A.; de Die-Smulders, C. E.; Vles, J. S.; Vanderver, A.; Uziel, G.; Yalcinkaya, C.; Frints, S. G.; Kalscheuer, V. M.; Klooster, J.; Kamermans, M.; Abbink, T. E.; Wolf, N. I.; Sedel, F.; van der Knaap, M. S., Brain white matter oedema due to ClC-2 chloride channel deficiency: an observational analytical study. *The Lancet. Neurology* **2013,** *12* (7), 659-68.
59. Rickheit, G.; Maier, H.; Strenzke, N.; Andreescu, C. E.; De Zeeuw, C. I.; Muenscher, A.; Zdebik, A. A.; Jentsch, T. J., Endocochlear potential depends on Cl− channels: mechanism underlying deafness in Bartter syndrome IV. *The EMBO Journal* **2008,** *27* (21), 2907-2917.
60. Birkenhäger, R.; Otto, E.; Schürmann, M. J.; Vollmer, M.; Ruf, E. M.; Maier-Lutz, I.; Beekmann, F.; Fekete, A.; Omran, H.; Feldmann, D.; Milford, D. V.; Jeck, N.; Konrad, M.; Landau, D.; Knoers, N. V.; Antignac, C.; Sudbrak, R.; Kispert, A.; Hildebrandt, F., Mutation of BSND causes Bartter syndrome with sensorineural deafness and kidney failure. *Nature genetics* **2001,** *29* (3), 310-4.
61. Lloyd, S. E.; Günther, W.; Pearce, S. H. S.; Thomson, A.; Bianchi, M. L.; Bosio, M.; Craig, I. W.; Fisher, S. E.; Scheinman, S. J.; Wrong, O.; Jentsch, T. J.; Thakker, R. V., Characterisation of Renal Chloride Channel, CLCN5, Mutations in Hypercalciuric Nephrolithiasis (Kidney Stones) Disorders. *Human Molecular Genetics* **1997,** *6* (8), 1233-1239.
62. Alekov, A. K., Mutations associated with Dent's disease affect gating and voltage dependence of the human anion/proton exchanger ClC-5. *Frontiers in Physiology* **2015,** *6* (159).

63. Piwon, N.; Günther, W.; Schwake, M.; Bösl, M. R.; Jentsch, T. J., ClC-5 Cl--channel disruption impairs endocytosis in a mouse model for Dent's disease. *Nature* **2000,** *408* (6810), 369-373.
64. Liu, F.; Zhang, Z.; Csanády, L.; Gadsby, D. C.; Chen, J., Molecular Structure of the Human CFTR Ion Channel. *Cell* **2017,** *169* (1), 85-95.e8.
65. von Heijne, G., The distribution of positively charged residues in bacterial inner membrane proteins correlates with the trans-membrane topology. *The EMBO Journal* **1986,** *5* (11), 3021-3027.
66. SHEPPARD, D. N.; WELSH, M. J., Structure and Function of the CFTR Chloride Channel. *Physiological Reviews* **1999,** *79* (1), S23-S45.
67. Linsdell, P., Architecture and functional properties of the CFTR channel pore. *Cellular and Molecular Life Sciences* **2017,** *74* (1), 67-83.
68. Stutts, M. J.; Canessa, C. M.; Olsen, J. C.; Hamrick, M.; Cohn, J. A.; Rossier, B. C.; Boucher, R. C., CFTR as a cAMP-dependent regulator of sodium channels. *Science (New York, N.Y.)* **1995,** *269* (5225), 847-50.
69. Lu, M.; Leng, Q.; Egan, M. E.; Caplan, M. J.; Boulpaep, E. L.; Giebisch, G. H.; Hebert, S. C., CFTR is required for PKA-regulated ATP sensitivity of Kir1.1 potassium channels in mouse kidney. *The Journal of Clinical Investigation* **2006,** *116* (3), 797-807.
70. Fischbarg, J., Fluid Transport Across Leaky Epithelia: Central Role of the Tight Junction and Supporting Role of Aquaporins. *Physiological Reviews* **2010,** *90* (4), 1271-1290.
71. Ballard, S. T.; Trout, L.; Bebök, Z.; Sorscher, E. J.; Crews, A., CFTR involvement in chloride, bicarbonate, and liquid secretion by airway submucosal glands. *American Journal of Physiology-Lung Cellular and Molecular Physiology* **1999,** *277* (4), L694-L699.
72. Saint-Criq, V.; Gray, M. A., Role of CFTR in epithelial physiology. *Cellular and Molecular Life Sciences* **2017,** *74* (1), 93-115.
73. Roum, J. H.; Buhl, R.; McElvaney, N. G.; Borok, Z.; Crystal, R. G., Systemic deficiency of glutathione in cystic fibrosis. *Journal of Applied Physiology* **1993,** *75* (6), 2419-2424.
74. cfireland.ie.
75. Sosnay, P. R.; Siklosi, K. R.; Van Goor, F.; Kaniecki, K.; Yu, H.; Sharma, N.; Ramalho, A. S.; Amaral, M. D.; Dorfman, R.; Zielenski, J.; Masica, D. L.; Karchin, R.; Millen, L.; Thomas, P. J.; Patrinos, G. P.; Corey, M.; Lewis, M. H.; Rommens, J. M.; Castellani, C.; Penland, C. M.; Cutting, G. R., Defining the disease liability of variants in the cystic fibrosis transmembrane conductance regulator gene. *Nature genetics* **2013,** *45* (10), 1160-1167.
76. Liou, T. G., The Clinical Biology of Cystic Fibrosis Transmembrane Regulator Protein: Its Role and Function in Extrapulmonary Disease. *Chest* **2019,** *155* (3), 605-616.
77. Borowitz, D., CFTR, bicarbonate, and the pathophysiology of cystic fibrosis. *Pediatric pulmonology* **2015,** *50 Suppl 40*, S24-s30.
78. Shandro, H. J.; Casey, J. R., Chapter 11 - Plasma Membrane Cl−/HCO3− Exchange Proteins. In *Advances in Molecular and Cell Biology*, Bittar, E. E.; Pusch, M., Eds. Elsevier: 2006; Vol. 38, pp 279-328.
79. Jennings, M. L., Structure and Function of the Red Blood Cell Anion Transport Protein. *Annual Review of Biophysics and Biophysical Chemistry* **1989,** *18* (1), 397-430.
80. Sterling, D.; Casey, J. R., Bicarbonate transport proteins. *Biochemistry and Cell Biology* **2002,** *80* (5), 483-497.

81. Stuart-Tilley, A.; Sardet, C.; Pouyssegur, J.; Schwartz, M. A.; Brown, D.; Alper, S. L., Immunolocalization of anion exchanger AE2 and cation exchanger NHE-1 in distinct adjacent cells of gastric mucosa. *American Journal of Physiology-Cell Physiology* **1994,** *266* (2), C559-C568.
82. Thomas, H. A.; Machen, T. E., Regulation of Cl/HCO3 exchange in gastric parietal cells. *Cell regulation* **1991,** *2* (9), 727-37.
83. Blair, H. C.; Teitelbaum, S. L.; Ghiselli, R.; Gluck, S., Osteoclastic bone resorption by a polarized vacuolar proton pump. *Science (New York, N.Y.)* **1989,** *245* (4920), 855-7.
84. Cingolani, H. E.; Chiappe, G. E.; Ennis, I. L.; Morgan, P. G.; Alvarez, B. V.; Casey, J. R.; Dulce, R. A.; Pérez, N. G.; Hurtado, M. C. C. d., Influence of Na⁺-Independent Cl[−]-HCO₃[−] Exchange on the Slow Force Response to Myocardial Stretch. *Circulation Research* **2003,** *93* (11), 1082-1088.
85. Sohma, Y.; Gray, M. A.; Imai, Y.; Argent, B. E., A Mathematical Model of the Pancreatic Ductal Epithelium. *The Journal of Membrane Biology* **1996,** *154* (1), 53-67.
86. Rajendran, V. M.; Black, J.; Ardito, T. A.; Sangan, P.; Alper, S. L.; Schweinfest, C.; Kashgarian, M.; Binder, H. J., Regulation of DRA and AE1 in rat colon by dietary Na depletion. *American journal of physiology. Gastrointestinal and liver physiology* **2000,** *279* (5), G931-42.
87. Alvarez, B. V.; Kieller, D. M.; Quon, A. L.; Markovich, D.; Casey, J. R., Slc26a6: a cardiac chloride-hydroxyl exchanger and predominant chloride-bicarbonate exchanger of the mouse heart. *The Journal of physiology* **2004,** *561* (Pt 3), 721-34.
88. Petrovic, S.; Ju, X.; Barone, S.; Seidler, U.; Alper, S. L.; Lohi, H.; Kere, J.; Soleimani, M., Identification of a basolateral Cl−/HCO 3 − exchanger specific to gastric parietal cells. *American Journal of Physiology-Gastrointestinal and Liver Physiology* **2003,** *284* (6), G1093-G1103.
89. Maritzen, T.; Blanz, J.; Jentsch, T., Chapter 2 - Physiological Functions of the CLC Chloride Transport Proteins. In *Advances in Molecular and Cell Biology*, Bittar, E. E.; Pusch, M., Eds. Elsevier: 2006; Vol. 38, pp 9-57.
90. Park, C. H.; Simmons, H. E., Macrobicyclic amines. III. Encapsulation of halide ions by in,in-1,(k + 2)-diazabicyclo[k.l.m.]alkane ammonium ions. *Journal of the American Chemical Society* **1968,** *90* (9), 2431-2432.
91. Graf, E.; Kintzinger, J. P.; Lehn, J. M.; LeMoigne, J., Molecular recognition. Selective ammonium cryptates of synthetic receptor molecules possessing a tetrahedral recognition site. *Journal of the American Chemical Society* **1982,** *104* (6), 1672-1678.
92. Schmidtchen, F. P., Inclusion of Anions in Macrotricyclic Quaternary Ammonium Salts. *Angewandte Chemie International Edition in English* **1977,** *16* (10), 720-721.
93. Desiraju, G. R., Hydrogen Bridges in Crystal Engineering: Interactions without Borders. *Accounts of Chemical Research* **2002,** *35* (7), 565-573.
94. Mahadevi, A. S.; Sastry, G. N., Cation−π Interaction: Its Role and Relevance in Chemistry, Biology, and Material Science. *Chemical Reviews* **2013,** *113* (3), 2100-2138.
95. Rosokha, Y. S.; Lindeman, S. V.; Rosokha, S. V.; Kochi, J. K., Halide Recognition through Diagnostic “Anion–π” Interactions: Molecular Complexes of Cl−, Br−, and I− with Olefinic and Aromatic π Receptors. *Angewandte Chemie International Edition* **2004,** *43* (35), 4650-4652.

96. Brown, A.; Beer, P. D., Halogen bonding anion recognition. *Chemical Communications* **2016,** *52* (56), 8645-8658.
97. Bickerton, L. E.; Docker, A.; Sterling, A. J.; Kuhn, H.; Duarte, F.; Beer, P. D.; Langton, M. J., Highly Active Halogen Bonding and Chalcogen Bonding Chloride Transporters with Non-Protonophoric Activity. *Chemistry – A European Journal* **2021,** *27* (45), 11738-11745.
98. Gilli, P.; Pretto, L.; Bertolasi, V.; Gilli, G., Predicting Hydrogen-Bond Strengths from Acid−Base Molecular Properties. The pKa Slide Rule: Toward the Solution of a Long-Lasting Problem. *Accounts of Chemical Research* **2009,** *42* (1), 33-44.
99. Camiolo, S.; Gale, P. A.; Hursthouse, M. B.; Light, M. E.; Shi, A. J., Solution and solid-state studies of 3,4-dichloro-2,5-diamidopyrroles: formation of an unusual anionic narcissistic dimer. *Chemical Communications* **2002,** (7), 758-759.
100. Caltagirone, C.; Bates, G. W.; Gale, P. A.; Light, M. E., Anion binding vs.sulfonamide deprotonation in functionalised ureas. *Chemical Communications* **2008,** (1), 61-63.
101. Berry, S. N.; Qin, L.; Lewis, W.; Jolliffe, K. A., Conformationally adaptable macrocyclic receptors for ditopic anions: analysis of chelate cooperativity in aqueous containing media. *Chemical Science* **2020,** *11* (27), 7015-7022.
102. Alunni, S.; Pero, A.; Reichenbach, G., Reactivity of ions and ion pairs in the nucleophilic substitution reaction on methyl p-nitrobenzenesulfonate. *Journal of the Chemical Society, Perkin Transactions 2* **1998,** (8), 1747-1750.
103. Kang, B.; Tang, H.; Zhao, Z.; Song, S., Hofmeister Series: Insights of Ion Specificity from Amphiphilic Assembly and Interface Property. *ACS Omega* **2020,** *5* (12), 6229-6239.
104. Blažek Bregović, V.; Basarić, N.; Mlinarić-Majerski, K., Anion binding with urea and thiourea derivatives. *Coordination Chemistry Reviews* **2015,** *295*, 80-124.
105. Li, A.-F.; Wang, J.-H.; Wang, F.; Jiang, Y.-B., Anion complexation and sensing using modified urea and thiourea-based receptors. *Chemical Society Reviews* **2010,** *39* (10), 3729-3745.
106. Sijbesma, R. P.; Beijer, F. H.; Brunsveld, L.; Folmer, B. J. B.; Hirschberg, J. H. K. K.; Lange, R. F. M.; Lowe, J. K. L.; Meijer, E. W., Reversible Polymers Formed from Self-Complementary Monomers Using Quadruple Hydrogen Bonding. *Science (New York, N.Y.)* **1997,** *278* (5343), 1601-1604.
107. Spargo, P. L., Phosgenations - A Handbook By Livius Cotarca and Heiner Eckert. Wiley-VCH: Weinheim. 2004. 656 pp. £217.50. ISBN 3-527-29823-1. *Organic Process Research & Development* **2004,** *8* (6), 1085-1086.
108. Eckert, H.; Forster, B., Triphosgene, a Crystalline Phosgene Substitute. *Angewandte Chemie International Edition in English* **1987,** *26* (9), 894-895.
109. Clare, J. P.; Ayling, A. J.; Joos, J.-B.; Sisson, A. L.; Magro, G.; Pérez-Payán, M. N.; Lambert, T. N.; Shukla, R.; Smith, B. D.; Davis, A. P., Substrate Discrimination by Cholapod Anion Receptors: Geometric Effects and the "Affinity−Selectivity Principle". *Journal of the American Chemical Society* **2005,** *127* (30), 10739-10746.
110. Babu, J. N.; Bhalla, V.; Kumar, M.; Mahajan, R. K.; Puri, R. K., A chloride selective sensor based on a calix[4]arene possessing a urea moiety. *Tetrahedron Letters* **2008,** *49* (17), 2772-2775.
111. Emami Khansari, M.; Johnson, C. R.; Basaran, I.; Nafis, A.; Wang, J.; Leszczynski, J.; Hossain, M. A., Synthesis and anion binding studies of tris(3-aminopropyl)amine-based tripodal urea and thiourea receptors: proton transfer-

induced selectivity for hydrogen sulfate over sulfate. *RSC Advances* **2015,** *5* (23), 17606-17614.
112. Wurm, F. R.; Klok, H.-A., Be squared: expanding the horizon of squaric acid-mediated conjugations. *Chemical Society Reviews* **2013,** *42* (21), 8220-8236.
113. Ian Storer, R.; Aciro, C.; Jones, L. H., Squaramides: physical properties, synthesis and applications. *Chemical Society Reviews* **2011,** *40* (5), 2330-2346.
114. Marchetti, L. A.; Kumawat, L. K.; Mao, N.; Stephens, J. C.; Elmes, R. B. P., The Versatility of Squaramides: From Supramolecular Chemistry to Chemical Biology. *Chem* **2019,** *5* (6), 1398-1485.
115. Cohen, S.; Cohen, S. G., Preparation and Reactions of Derivatives of Squaric Acid. Alkoxy-, Hydroxy-, and Aminocyclobutenediones1. *Journal of the American Chemical Society* **1966,** *88* (7), 1533-1536.
116. Ito, M.; West, R., New Aromatic Anions. IV. Vibrational Spectra and Force Constants for C4O4-2 and C5O5-2. *Journal of the American Chemical Society* **1963,** *85* (17), 2580-2584.
117. Quiñonero, D.; Frontera, A.; Suñer, G. A.; Morey, J.; Costa, A.; Ballester, P.; Deyà, P. M., Squaramide as a binding unit in molecular recognition. *Chemical Physics Letters* **2000,** *326* (3), 247-254.
118. Tomàs, S.; Prohens, R.; Vega, M.; Rotger, M. C.; Deyà, P. M.; Ballester, P.; Costa, A., Squaramido-Based Receptors: Design, Synthesis, and Application to the Recognition of Tetraalkylammonium Compounds. *The Journal of Organic Chemistry* **1996,** *61* (26), 9394-9401.
119. P. Davis, A.; M. Draper, S.; Dunne, G.; Ashton, P., The N-carbamoyl squaramide dimer: a compact, strongly associated H-bonding motif. *Chemical Communications* **1999,** (22), 2265-2266.
120. Rostami, A.; Colin, A.; Li, X. Y.; Chudzinski, M. G.; Lough, A. J.; Taylor, M. S., N,N′-Diarylsquaramides: General, High-Yielding Synthesis and Applications in Colorimetric Anion Sensing. *The Journal of Organic Chemistry* **2010,** *75* (12), 3983-3992.
121. Prohens, R.; Martorell, G.; Ballester, P.; Costa, A., A squaramide fluorescent ensemble for monitoring sulfate in water. *Chemical Communications* **2001,** (16), 1456-1457.
122. Prohens, R.; Tomàs, S.; Morey, J.; Deyà, P. M.; Ballester, P.; Costa, A., Squaramido-based receptors: Molecular recognition of carboxylate anions in highly competitive media. *Tetrahedron Letters* **1998,** *39* (9), 1063-1066.
123. Tzioumis, N. A.; Yuen, K. K. Y.; Jolliffe, K. A., Investigating the effects of structure on sulfate recognition by neutral dipeptide receptors. *Supramolecular Chemistry* **2018,** *30* (8), 667-673.
124. Edwards, S. J.; Valkenier, H.; Busschaert, N.; Gale, P. A.; Davis, A. P., High-Affinity Anion Binding by Steroidal Squaramide Receptors. *Angewandte Chemie International Edition* **2015,** *54* (15), 4592-4596.
125. (a) Koulov, A. V.; Lambert, T. N.; Shukla, R.; Jain, M.; Boon, J. M.; Smith, B. D.; Li, H.; Sheppard, D. N.; Joos, J.-B.; Clare, J. P.; Davis, A. P., Chloride Transport Across Vesicle and Cell Membranes by Steroid-Based Receptors. *Angewandte Chemie International Edition* **2003,** *42* (40), 4931-4933; (b) Hussain, S.; Brotherhood, P. R.; Judd, L. W.; Davis, A. P., Diaxial Diureido Decalins as Compact, Efficient, and Tunable Anion Transporters. *Journal of the American Chemical Society* **2011,** *133* (6), 1614-1617; (c) Valkenier, H.; Judd, L. W.; Li, H.; Hussain, S.; Sheppard, D. N.; Davis, A. P., Preorganized Bis-Thioureas as Powerful Anion Carriers: Chloride Transport by Single Molecules in Large

Unilamellar Vesicles. *Journal of the American Chemical Society* **2014,** *136* (35), 12507-12512.
126. Amendola, V.; Bergamaschi, G.; Boiocchi, M.; Fabbrizzi, L.; Milani, M., The Squaramide versus Urea Contest for Anion Recognition. *Chemistry – A European Journal* **2010,** *16* (14), 4368-4380.
127. Elmes, R. B. P.; K. Y. Yuen, K.; Jolliffe, K. A., Sulfate-Selective Recognition by Using Neutral Dipeptide Anion Receptors in Aqueous Solution. *Chemistry – A European Journal* **2014,** *20* (24), 7373-7380.
128. Busschaert, N.; Kirby, I. L.; Young, S.; Coles, S. J.; Horton, P. N.; Light, M. E.; Gale, P. A., Squaramides as Potent Transmembrane Anion Transporters. *Angewandte Chemie International Edition* **2012,** *51* (18), 4426-4430.
129. Busschaert, N.; Bradberry, S. J.; Wenzel, M.; Haynes, C. J. E.; Hiscock, J. R.; Kirby, I. L.; Karagiannidis, L. E.; Moore, S. J.; Wells, N. J.; Herniman, J.; Langley, G. J.; Horton, P. N.; Light, M. E.; Marques, I.; Costa, P. J.; Félix, V.; Frey, J. G.; Gale, P. A., Towards predictable transmembrane transport: QSAR analysis of anion binding and transport. *Chemical Science* **2013,** *4* (8), 3036-3045.
130. Saggiomo, V.; Otto, S.; Marques, I.; Félix, V.; Torroba, T.; Quesada, R., The role of lipophilicity in transmembrane anion transport. *Chemical Communications* **2012,** *48* (43), 5274-5276.
131. Knight, N. J.; Hernando, E.; Haynes, C. J. E.; Busschaert, N.; Clarke, H. J.; Takimoto, K.; García-Valverde, M.; Frey, J. G.; Quesada, R.; Gale, P. A., QSAR analysis of substituent effects on tambjamine anion transporters. *Chemical Science* **2016,** *7* (2), 1600-1608.
132. McNally, B. A.; Koulov, A. V.; Lambert, T. N.; Smith, B. D.; Joos, J. B.; Sisson, A. L.; Clare, J. P.; Sgarlata, V.; Judd, L. W.; Magro, G.; Davis, A. P., Structure-activity relationships in cholapod anion carriers: enhanced transmembrane chloride transport through substituent tuning. *Chemistry (Weinheim an der Bergstrasse, Germany)* **2008,** *14* (31), 9599-606.
133. Hansch, C.; Leo, A.; Taft, R. W., A survey of Hammett substituent constants and resonance and field parameters. *Chemical Reviews* **1991,** *91* (2), 165-195.
134. Beer, P. D.; Hazlewood, C.; Hesek, D.; Hodacova, J.; Stokes, S. E., Anion recognition by acyclic redox-responsive amide-linked cobaltocenium receptors. *Journal of the Chemical Society, Dalton Transactions* **1993,** (8), 1327-1332.
135. Schneider, H.-J., Binding Mechanisms in Supramolecular Complexes. *Angewandte Chemie International Edition* **2009,** *48* (22), 3924-3977.
136. Wu, X.; Busschaert, N.; Wells, N. J.; Jiang, Y.-B.; Gale, P. A., Dynamic Covalent Transport of Amino Acids across Lipid Bilayers. *Journal of the American Chemical Society* **2015,** *137* (4), 1476-1484.
137. Marshall, S. R.; Singh, A.; Wagner, J. N.; Busschaert, N., Enhancing the selectivity of optical sensors using synthetic transmembrane ion transporters. *Chemical Communications* **2020,** *56* (92), 14455-14458.
138. Akhtar, N.; Biswas, O.; Manna, D., Biological applications of synthetic anion transporters. *Chemical Communications* **2020,** *56* (91), 14137-14153.
139. Wu, X.; Gilchrist, A. M.; Gale, P. A., Prospects and Challenges in Anion Recognition and Transport. *Chem* **2020,** *6* (6), 1296-1309.
140. Busschaert, N.; Park, S.-H.; Baek, K.-H.; Choi, Y. P.; Park, J.; Howe, E. N. W.; Hiscock, J. R.; Karagiannidis, L. E.; Marques, I.; Félix, V.; Namkung, W.; Sessler, J. L.; Gale, P. A.; Shin, I., A synthetic ion transporter that disrupts autophagy and induces apoptosis by perturbing cellular chloride concentrations. *Nature Chemistry* **2017,** *9* (7), 667-675.

141. Karagiannidis, L. E.; Haynes, C. J. E.; Holder, K. J.; Kirby, I. L.; Moore, S. J.; Wells, N. J.; Gale, P. A., Highly effective yet simple transmembrane anion transporters based upon ortho-phenylenediamine bis-ureas. *Chemical Communications* **2014,** *50* (81), 12050-12053.
142. Jin, C.; Zhang, M.; Wu, L.; Guan, Y.; Pan, Y.; Jiang, J.; Lin, C.; Wang, L., Squaramide-based tripodal receptors for selective recognition of sulfate anion. *Chemical Communications* **2013,** *49* (20), 2025-2027.
143. Picci, G.; Kubicki, M.; Garau, A.; Lippolis, V.; Mocci, R.; Porcheddu, A.; Quesada, R.; Ricci, P. C.; Scorciapino, M. A.; Caltagirone, C., Simple squaramide receptors for highly efficient anion binding in aqueous media and transmembrane transport. *Chemical Communications* **2020,** *56* (75), 11066-11069.
144. Caltagirone, C.; Gale, P. A.; Hiscock, J. R.; Brooks, S. J.; Hursthouse, M. B.; Light, M. E., 1,3-Diindolylureas: high affinity dihydrogen phosphate receptors. *Chemical Communications* **2008,** (26), 3007-3009.
145. Deng, L.-Q.; Lu, Y.-M.; Zhou, C.-Q.; Chen, J.-X.; Wang, B.; Chen, W.-H., Synthesis and potent ionophoric activity of a squaramide-linked bis(choloyl) conjugate. *Bioorganic & Medicinal Chemistry Letters* **2014,** *24* (13), 2859-2862.
146. Bao, X.; Wu, X.; Berry, S. N.; Howe, E. N. W.; Chang, Y.-T.; Gale, P. A., Fluorescent squaramides as anion receptors and transmembrane anion transporters. *Chemical Communications* **2018,** *54* (11), 1363-1366.
147. Berry, S. N.; Soto-Cerrato, V.; Howe, E. N. W.; Clarke, H. J.; Mistry, I.; Tavassoli, A.; Chang, Y. T.; Pérez-Tomás, R.; Gale, P. A., Fluorescent transmembrane anion transporters: shedding light on anionophoric activity in cells. **2016,** *7* (8), 5069-5077.
148. Li, Y.; Yang, G.-H.; Shen, Y.-Y.; Xue, X.-S.; Li, X.; Cheng, J.-P., N-tert-Butyl Sulfinyl Squaramide Receptors for Anion Recognition through Assisted tert-Butyl C–H Hydrogen Bonding. *The Journal of Organic Chemistry* **2017,** *82* (16), 8662-8667.
149. Liu, H.; Tomooka, C. S.; Moore, H. W., An Efficient General Synthesis of Squarate Esters. *Synthetic Communications* **1997,** *27* (12), 2177-2180.
150. Amendola, V.; Fabbrizzi, L.; Mosca, L.; Schmidtchen, F.-P., Urea-, Squaramide-, and Sulfonamide-Based Anion Receptors: A Thermodynamic Study. *Chemistry – A European Journal* **2011,** *17* (21), 5972-5981.
151. Busschaert, N.; Elmes, R. B. P.; Czech, D. D.; Wu, X.; Kirby, I. L.; Peck, E. M.; Hendzel, K. D.; Shaw, S. K.; Chan, B.; Smith, B. D.; Jolliffe, K. A.; Gale, P. A., Thiosquaramides: pH switchable anion transporters. *Chemical Science* **2014,** *5* (9), 3617-3626.
152. Ni, X.; Li, X.; Wang, Z.; Cheng, J.-P., Squaramide Equilibrium Acidities in DMSO. *Organic Letters* **2014,** *16* (6), 1786-1789.
153. (a) Brynn Hibbert, D.; Thordarson, P., The death of the Job plot, transparency, open science and online tools, uncertainty estimation methods and other developments in supramolecular chemistry data analysis. *Chemical Communications* **2016,** *52* (87), 12792-12805; (b) Thordarson, P.
154. Jowett, L. A.; Gale, P. A., Supramolecular methods: the chloride/nitrate transmembrane exchange assay. *Supramolecular Chemistry* **2019,** *31* (5), 297-312.
155. Sessler, J. L.; Eller, L. R.; Cho, W. S.; Nicolaou, S.; Aguilar, A.; Lee, J. T.; Lynch, V. M.; Magda, D. J., Synthesis, anion-binding properties, and in vitro anticancer activity of prodigiosin analogues. *Angewandte Chemie (International ed. in English)* **2005,** *44* (37), 5989-92.
156. OHKUMA, S.; SATO, T.; OKAMOTO, M.; MATSUYA, H.; ARAI, K.; KATAOKA, T.; NAGAI, K.; WASSERMAN, H. H., Prodigiosins uncouple

lysosomal vacuolar-type ATPase through promotion of H+/Cl− symport. *Biochemical Journal* **1998,** *334* (3), 731-741.
157. Elmes, R. B. P.; Busschaert, N.; Czech, D. D.; Gale, P. A.; Jolliffe, K. A., pH switchable anion transport by an oxothiosquaramide. *Chemical Communications* **2015,** *51* (50), 10107-10110.
158. Howe, E. N. W.; Busschaert, N.; Wu, X.; Berry, S. N.; Ho, J.; Light, M. E.; Czech, D. D.; Klein, H. A.; Kitchen, J. A.; Gale, P. A., pH-Regulated Nonelectrogenic Anion Transport by Phenylthiosemicarbazones. *Journal of the American Chemical Society* **2016,** *138* (26), 8301-8308.
159. Howe, E. N. W.; Chang, V.-V. T.; Wu, X.; Fares, M.; Lewis, W.; Macreadie, L. K.; Gale, P. A., Halide-selective, proton-coupled anion transport by phenylthiosemicarbazones. *Biochimica et Biophysica Acta (BBA) - Biomembranes* **2022,** *1864* (2), 183828.
160. Jowett, L. A.; Howe, E. N. W.; Soto-Cerrato, V.; Van Rossom, W.; Pérez-Tomás, R.; Gale, P. A., Indole-based perenosins as highly potent HCl transporters and potential anti-cancer agents. *Scientific Reports* **2017,** *7* (1), 9397.
161. Kerckhoffs, A.; Langton, M. J., Reversible photo-control over transmembrane anion transport using visible-light responsive supramolecular carriers. *Chemical Science* **2020,** *11* (24), 6325-6331.
162. Wezenberg, S. J.; Chen, L.-J.; Bos, J. E.; Feringa, B. L.; Howe, E. N. W.; Wu, X.; Siegler, M. A.; Gale, P. A., Photomodulation of Transmembrane Transport and Potential by Stiff-Stilbene Based Bis(thio)ureas. *Journal of the American Chemical Society* **2021**.
163. Salunke, S. B.; Malla, J. A.; Talukdar, P., Phototriggered Release of a Transmembrane Chloride Carrier from an o-Nitrobenzyl-Linked Procarrier. *Angewandte Chemie International Edition* **2019,** *58* (16), 5354-5358.
164. Choi, Y. R.; Lee, B.; Park, J.; Namkung, W.; Jeong, K.-S., Enzyme-Responsive Procarriers Capable of Transporting Chloride Ions across Lipid and Cellular Membranes. *Journal of the American Chemical Society* **2016,** *138* (47), 15319-15322.
165. Kato, Y.; Ozawa, S.; Miyamoto, C.; Maehata, Y.; Suzuki, A.; Maeda, T.; Baba, Y., Acidic extracellular microenvironment and cancer. *Cancer Cell International* **2013,** *13* (1), 89.
166. Denny, W. A., Hypoxia-activated prodrugs in cancer therapy: progress to the clinic. *Future Oncology* **2010,** *6* (3), 419-428.
167. Kling, J., Hypoxia-activated prodrugs forge ahead in cancer. *Nature Biotechnology* **2012,** *30* (5), 381-381.
168. Elmes, R. B. P., Bioreductive fluorescent imaging agents: applications to tumour hypoxia. *Chemical Communications* **2016,** *52* (58), 8935-8956.
169. Pacheco-Torres, J.; López-Larrubia, P.; Ballesteros, P.; Cerdán, S., Imaging tumor hypoxia by magnetic resonance methods. *NMR in Biomedicine* **2011,** *24* (1), 1-16.
170. Sedgwick, A. C.; Hayden, A.; Hill, B.; Bull, S. D.; Elmes, R. B. P.; James, T. D., A simple umbelliferone based fluorescent probe for the detection of nitroreductase. *Frontiers of Chemical Science and Engineering* **2018,** *12* (2), 311-314.
171. Abdel-Magid, A. F.; Carson, K. G.; Harris, B. D.; Maryanoff, C. A.; Shah, R. D., Reductive Amination of Aldehydes and Ketones with Sodium Triacetoxyborohydride. Studies on Direct and Indirect Reductive Amination Procedures1. *The Journal of Organic Chemistry* **1996,** *61* (11), 3849-3862.

172. Lang, M. S., Wolfgang, An Effective Method for the Synthesis of 13C-Labeled Polyprenylhydroxybenzoic Acids. *Synthesis* **2005,** *9*, 1019-1027.
173. Davis, A. P.; Walsh, J. J., Amide bond formation via pentafluorothiophenyl active esters. *Tetrahedron Letters* **1994,** *35* (27), 4865-4868.
174. Lunelli, B., New, optimized preparation of 1,2-dichlorocyclobuten-3,4-dione (C4O2Cl2) from squaric acid and oxalyl chloride. *Tetrahedron Letters* **2007,** *48* (20), 3595-3597.
175. Tatarets, A. L.; Fedyunyaeva, I. A.; Terpetschnig, E.; Patsenker, L. D., Synthesis of novel squaraine dyes and their intermediates. *Dyes and Pigments* **2005,** *64* (2), 125-134.
176. B:urgi, H. B.; Dunitz, J. D.; Lehn, J. M.; Wipff, G., Stereochemistry of reaction paths at carbonyl centres. *Tetrahedron* **1974,** *30* (12), 1563-1572.
177. Ma, D.; Cai, Q.; Zhang, H., Mild Method for Ullmann Coupling Reaction of Amines and Aryl Halides. *Organic Letters* **2003,** *5* (14), 2453-2455.
178. Forero-Cortés, P. A.; Haydl, A. M., The 25th Anniversary of the Buchwald–Hartwig Amination: Development, Applications, and Outlook. *Organic Process Research & Development* **2019,** *23* (8), 1478-1483.
179. Sharma, M. K.; Kumar, M., Sulphate contamination in groundwater and its remediation: an overview. *Environmental Monitoring and Assessment* **2020,** *192* (2), 74.
180. Nakanishi, T.; Otaki, Y.; Hasuike, Y.; Nanami, M.; Itahana, R.; Miyagawa, K.; Nishikage, H.; Izumi, M.; Takamitsu, Y., Association of hyperhomocysteinemia with plasma sulfate and urine sulfate excretion in patients with progressive renal disease. *American Journal of Kidney Diseases* **2002,** *40* (5), 909-915.
181. Jha, S. K.; Singh, R. K.; Damodaran, T.; Mishra, V. K.; Sharma, D. K.; Rai, D., Fluoride in Groundwater: Toxicological Exposure and Remedies. *Journal of Toxicology and Environmental Health, Part B* **2013,** *16* (1), 52-66.
182. Pardasani, D.; Mazumder, A.; Gupta, A. K.; Kanaujia, P. K.; Tak, V.; Dubey, D. K., Determination of hydrolytic degradation products of nerve agents by injection port fluorination in gas chromatography/mass spectrometry for the verification of the Chemical Weapons Convention. *Rapid Communications in Mass Spectrometry* **2007,** *21* (18), 3109-3114.
183. Manesiotis, P.; Riley, A.; Bollen, B., Polymerisable squaramide receptors for anion binding and sensing. *Journal of Materials Chemistry C* **2014,** *2* (42), 8990-8995.
184. Zaleskaya-Hernik, M.; Dobrzycki, Ł.; Karbarz, M.; Romański, J., Fluorescence Recognition of Anions Using a Heteroditopic Receptor: Homogenous and Two-Phase Sensing. *International Journal of Molecular Sciences* **2021,** *22* (24), 13396.
185. Elmes, R. B. P.; Turner, P.; Jolliffe, K. A., Colorimetric and Luminescent Sensors for Chloride: Hydrogen Bonding vs Deprotonation. *Organic Letters* **2013,** *15* (22), 5638-5641.
186. Picci, G.; Milia, J.; Aragoni, M. C.; Arca, M.; Coles, S. J.; Garau, A.; Lippolis, V.; Montis, R.; Orton, J. B.; Caltagirone, C., Switching-On Fluorescence by Copper (II) and Basic Anions: A Case Study with a Pyrene-Functionalized Squaramide. *Molecules* **2021,** *26* (5), 1301.
187. Niu, H.; Shu, Q.; Jin, S.; Li, B.; Zhu, J.; Li, L.; Chen, S., A simple ratiometric and colorimetric chemosensor for the selective detection of fluoride in DMSO buffered solution. *Spectrochimica Acta Part A: Molecular and Biomolecular Spectroscopy* **2016,** *153*, 194-198.

188. Wu, X.; Howe, E. N. W.; Gale, P. A., Supramolecular Transmembrane Anion Transport: New Assays and Insights. *Accounts of Chemical Research* **2018,** *51* (8), 1870-1879.
189. Yang, Y.; Wu, X.; Busschaert, N.; Furuta, H.; Gale, P. A., Dissecting the chloride–nitrate anion transport assay. *Chemical Communications* **2017,** *53* (66), 9230-9233.

Appendix

A. Chapter 2 Characterisation Data

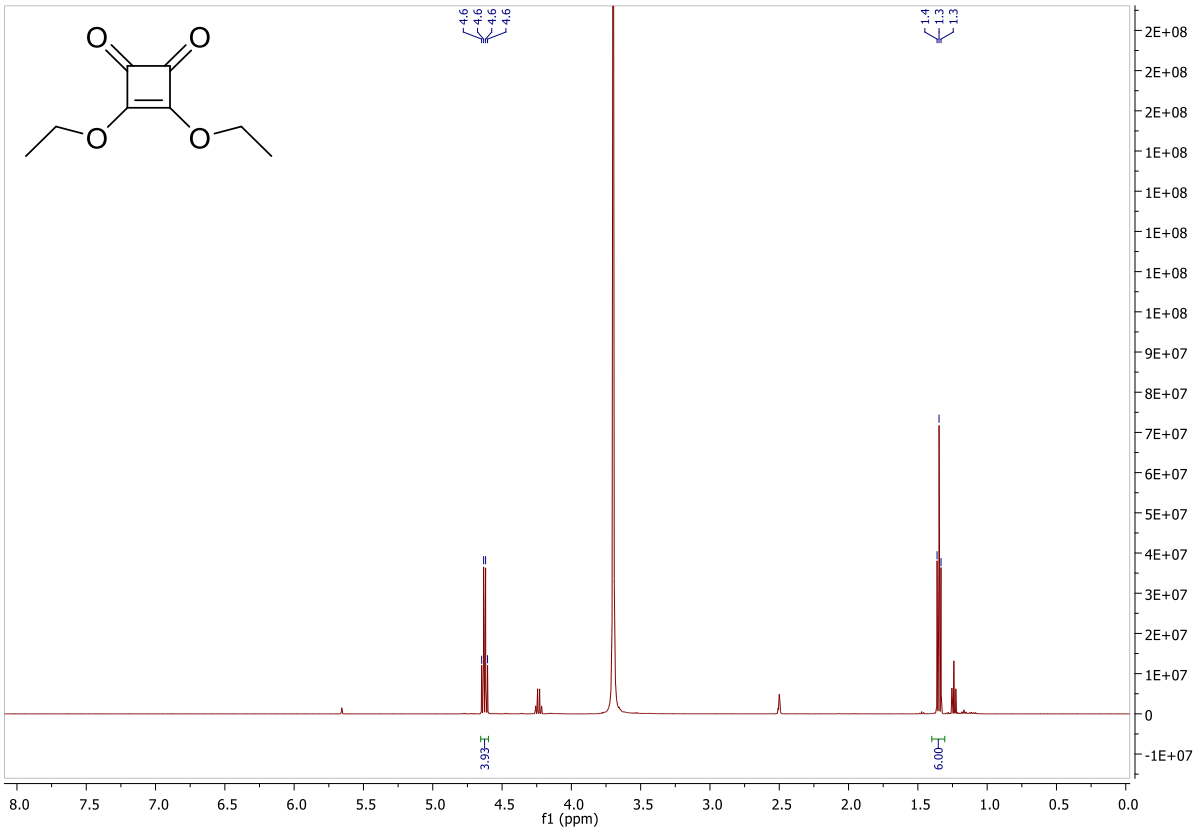

Figure A1. *^{1}H NMR (DMSO-d_6, 500 MHz) spectrum of* ***2.17****.*

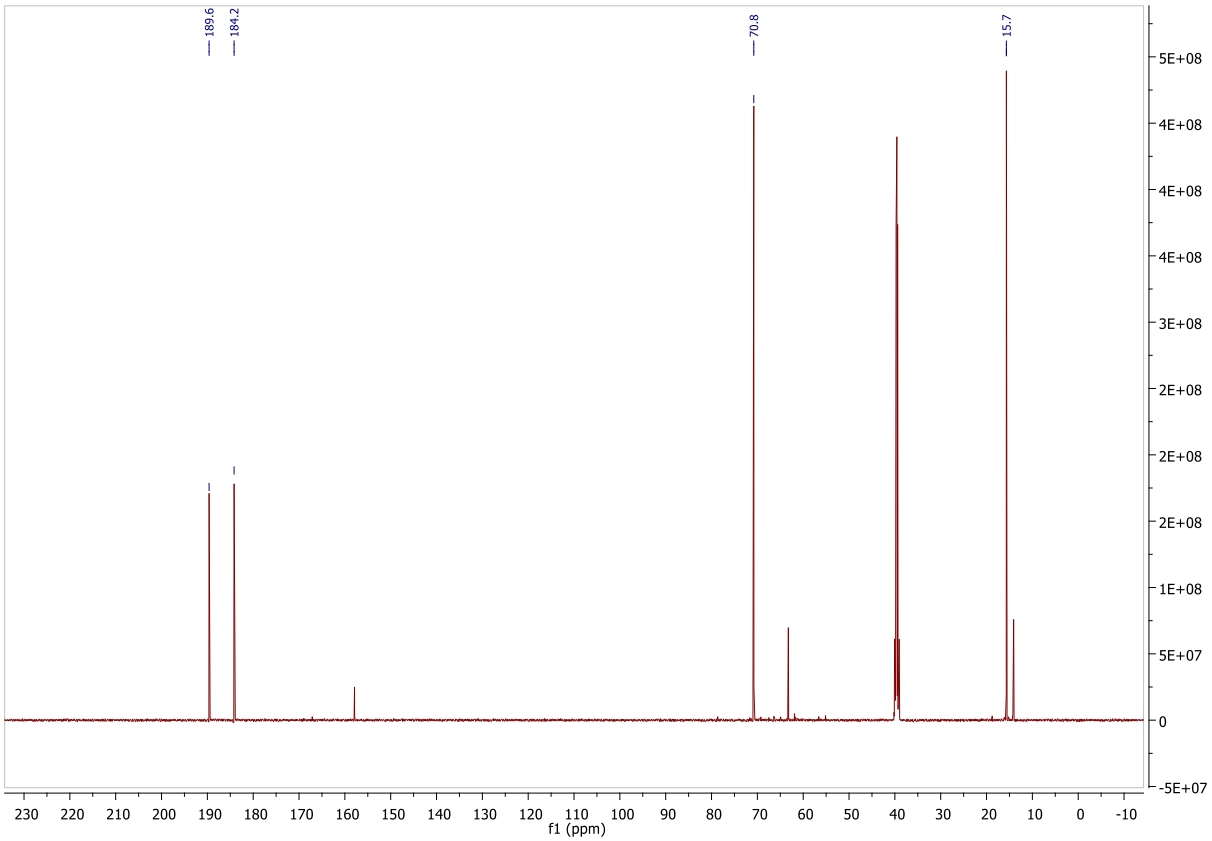

Figure A2. *^{13}C NMR (DMSO-d_6, 500 MHz) spectrum of* ***2.17****.*

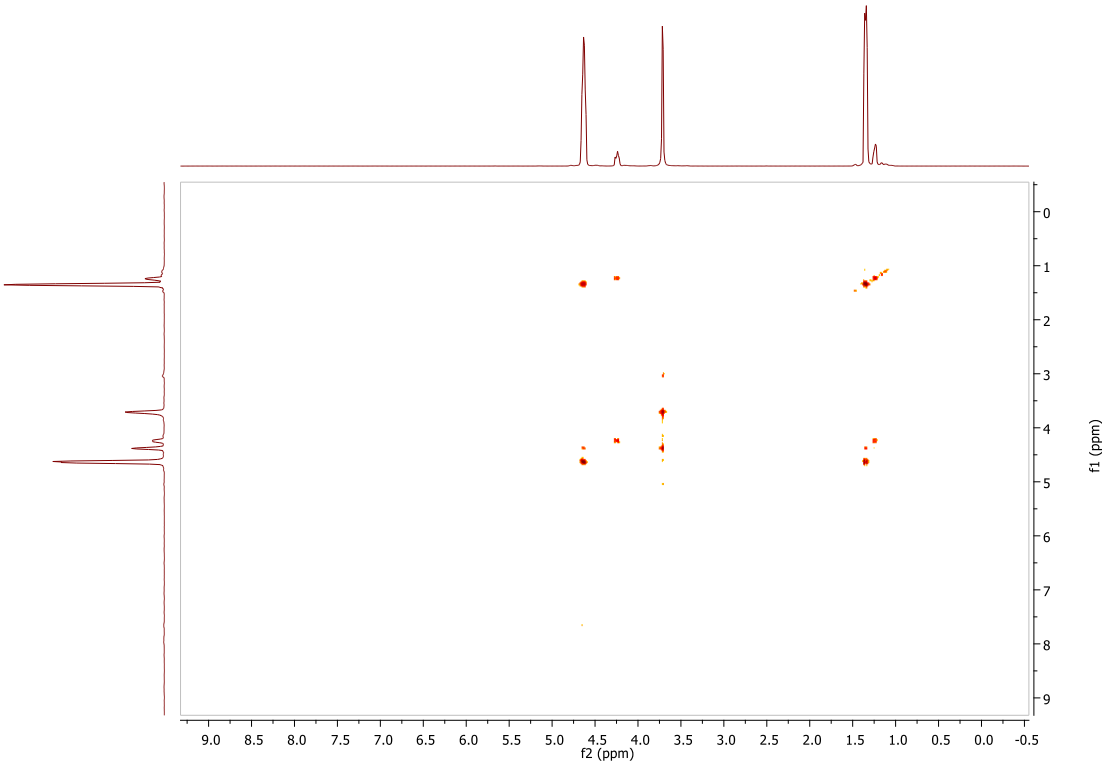

Figure A3. *^{1}H-^{1}H COSY spectrum of* ***2.17****.*

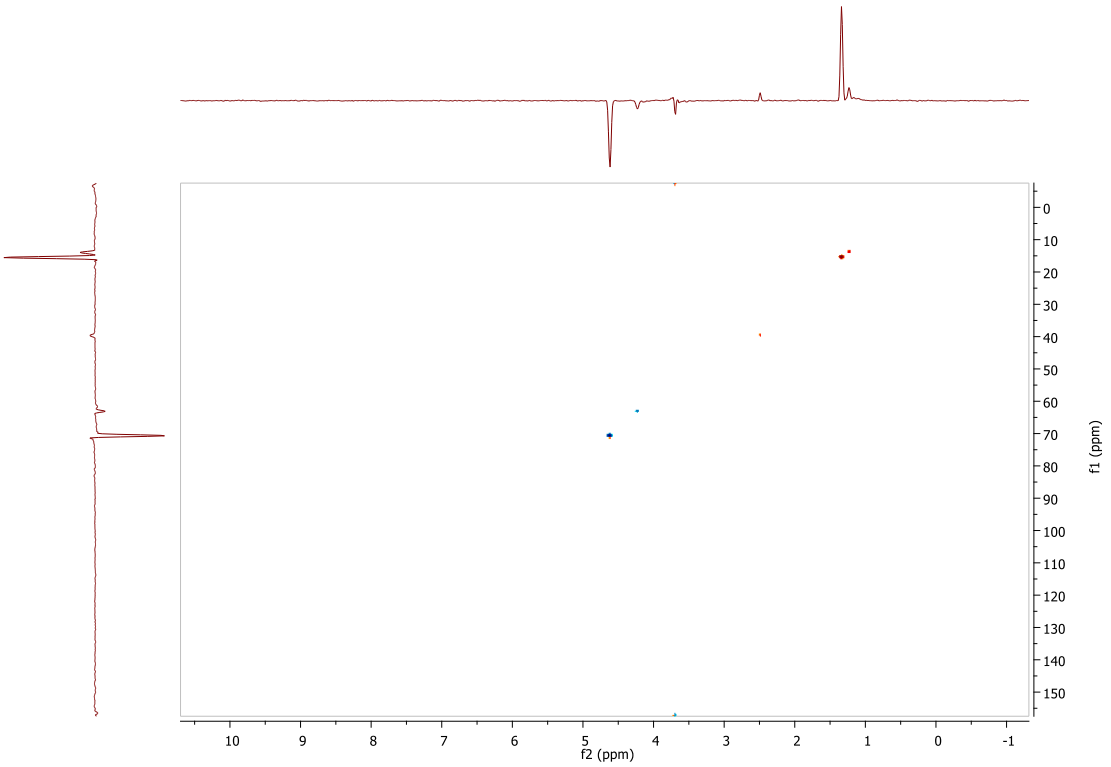

Figure A4. *HSQC spectrum of* ***2.17****.*

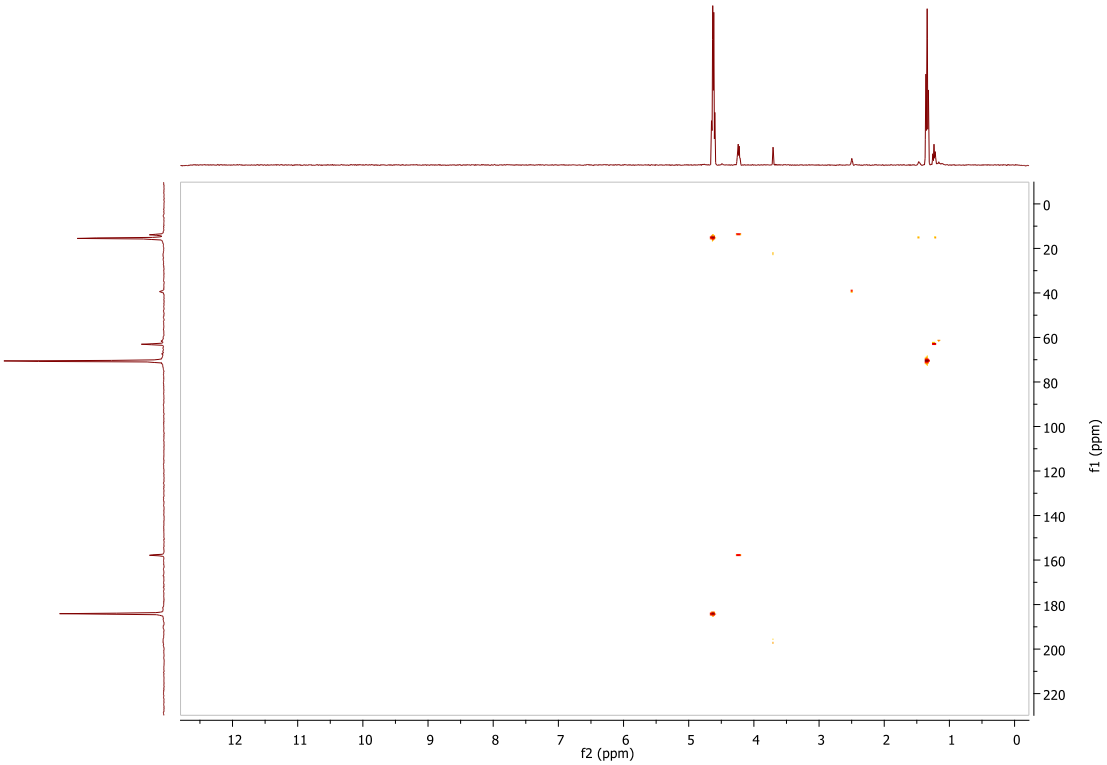

Figure A5. *HMBC spectrum of* ***2.17****.*

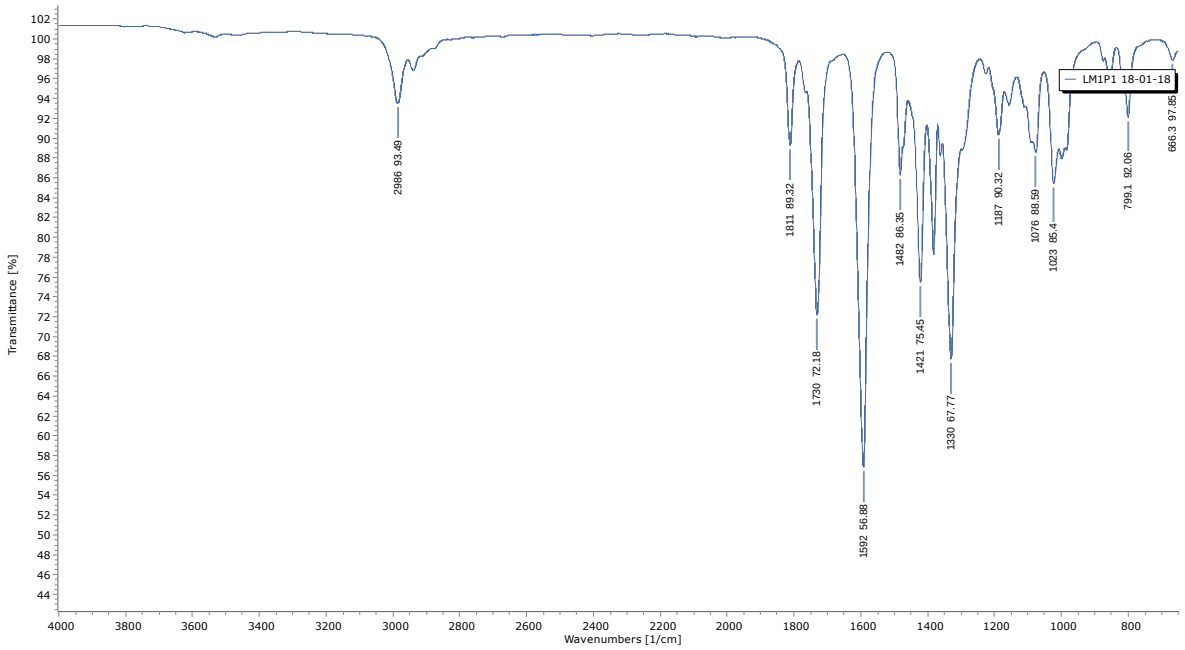

Figure A6. *IR spectrum of* ***2.17****.*

+MS, 1.0-1.3min #(119-153), -Spectral Bkgrnd

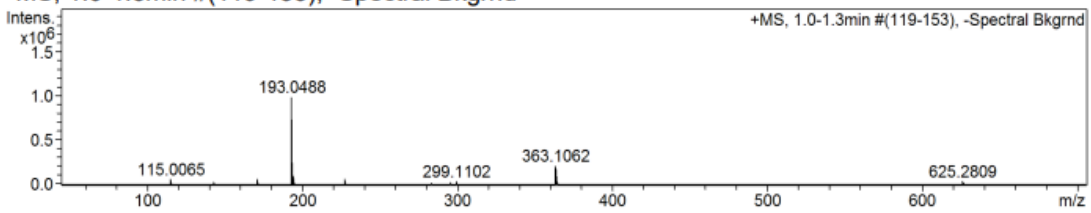

#	m/z	I	I %	Area	S/N
1	115.0065	55950	5.7	1041	3998.3
2	171.0653	60124	6.1	1824	1852.8
3	193.0488	987338	100.0	39236	18352.4
4	194.0501	91896	9.3	3202	1677.7
5	227.0885	61454	6.2	2490	1909.0
6	295.1497	32601	3.3	1674	1013.4
7	299.1102	35754	3.6	1787	1150.1
8	363.1062	212150	21.5	13058	4895.7
9	364.1089	34991	3.5	2097	795.5
10	625.2809	36818	3.7	3708	3178.1

Generate Molecular Formula Parameters

Charge	Tolerance	SearchRadius	H/C Ratio min.	H/C Ratio max.	Electron Conf.	Nitrogen Rule	sigma limit
positive	50 ppm	0.05 m/z	0	3	both	true	0.05

Expected Formula C8H10O4 **Adduct(s):** H, Na

#	meas. m/z	theo. m/z	Err[ppm]	Sigma	Formula
1	171.0653	171.0652	0.70	0.0134	C 8 H 11 O 4
1	193.0488	193.0471	8.80	0.0040	C 8 H 10 Na 1 O 4

Note: Sigma fits < 0.05 indicates high probability of correct MF.

Figure A7. *HRMS of* ***2.17****.*

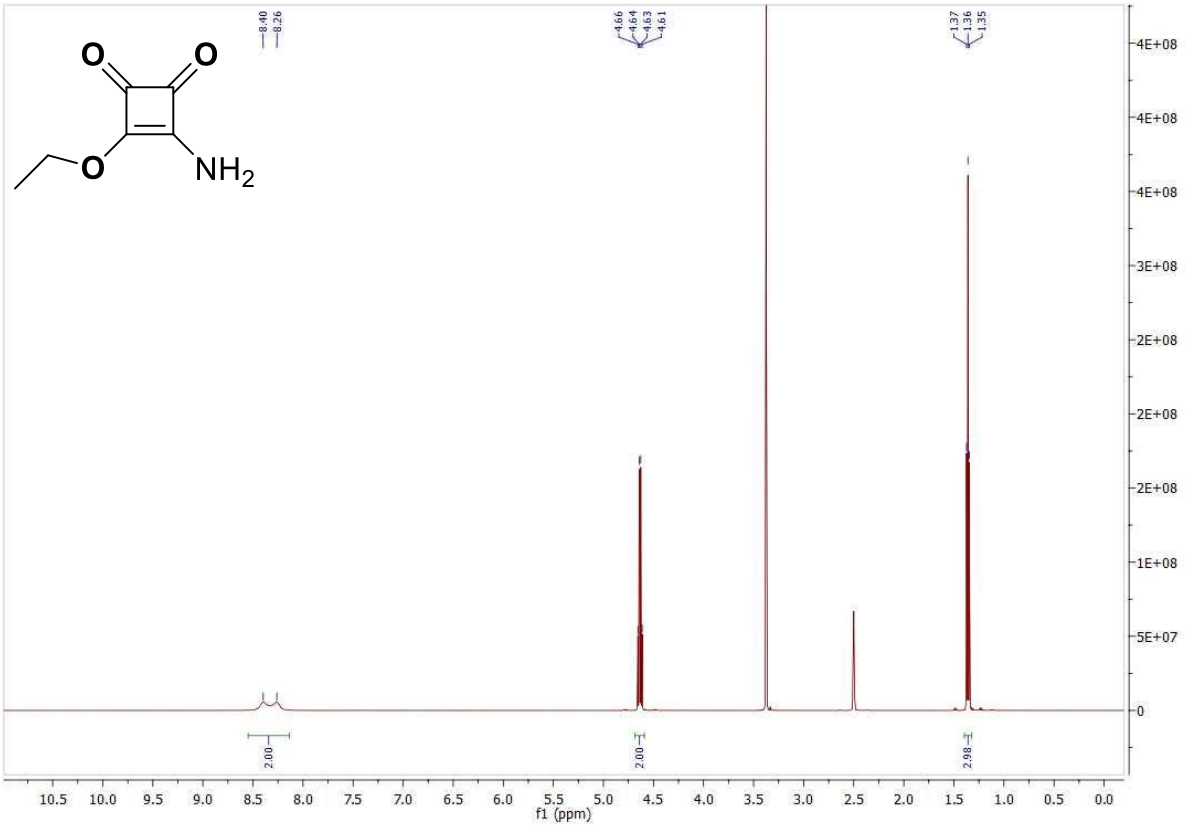

Figure A8. ^{1}H NMR (DMSO-d_6, 500 MHz) spectrum of **2.18**.

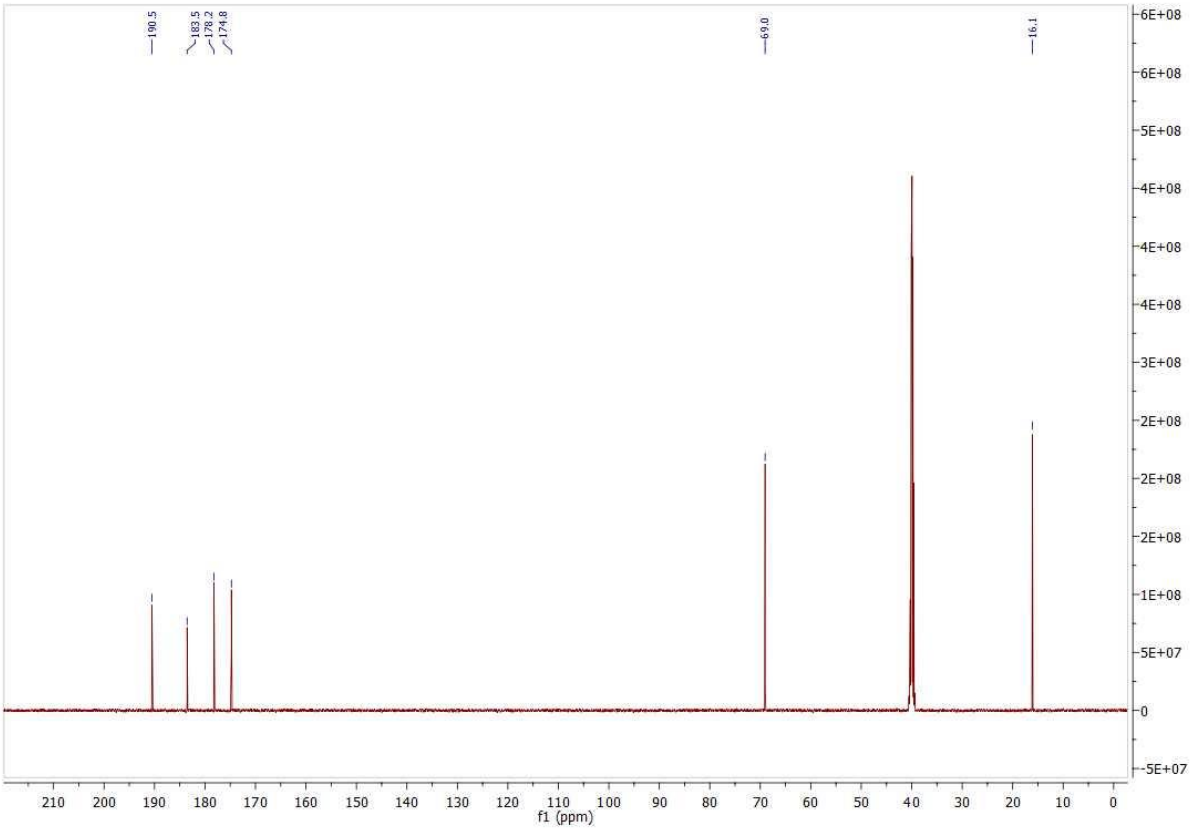

Figure A9. ^{13}C NMR (DMSO-d_6, 126 MHz) spectrum of **2.18**.

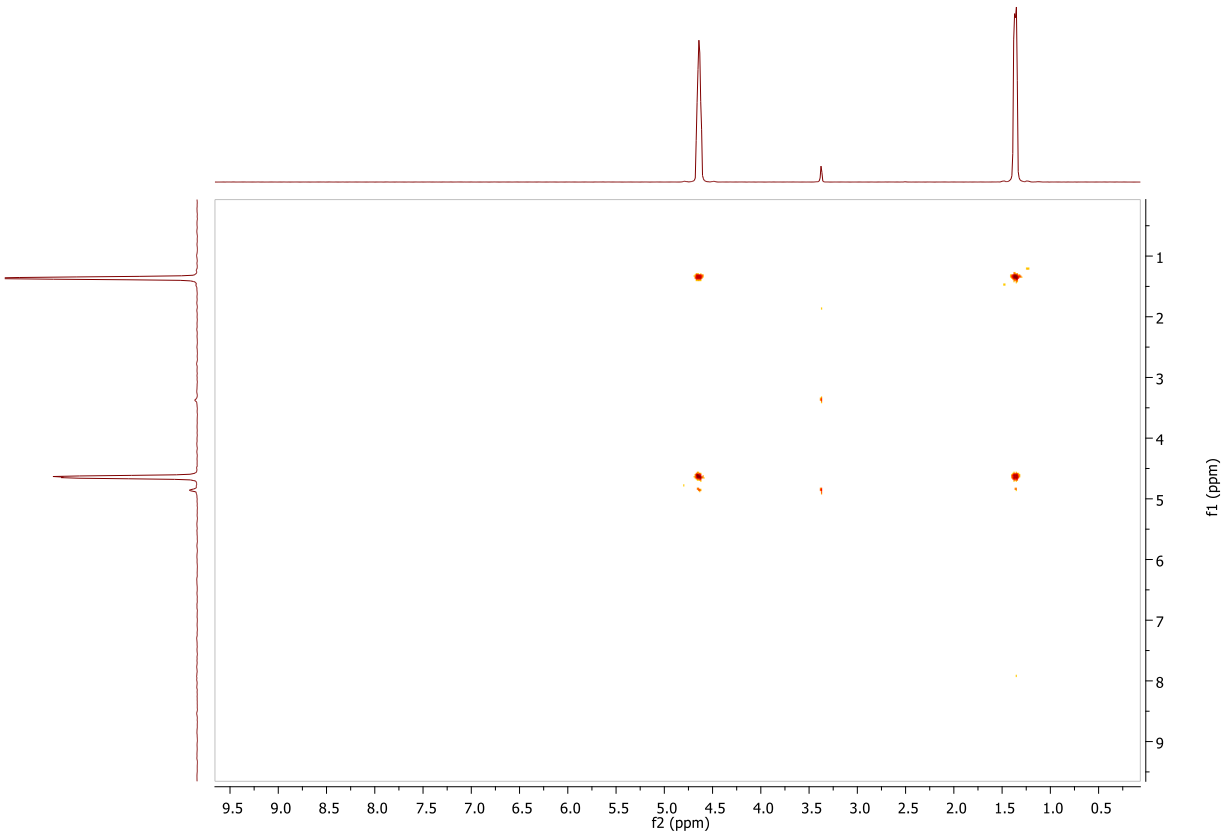

Figure A10. ^{1}H-^{1}H COSY spectrum of **2.18**

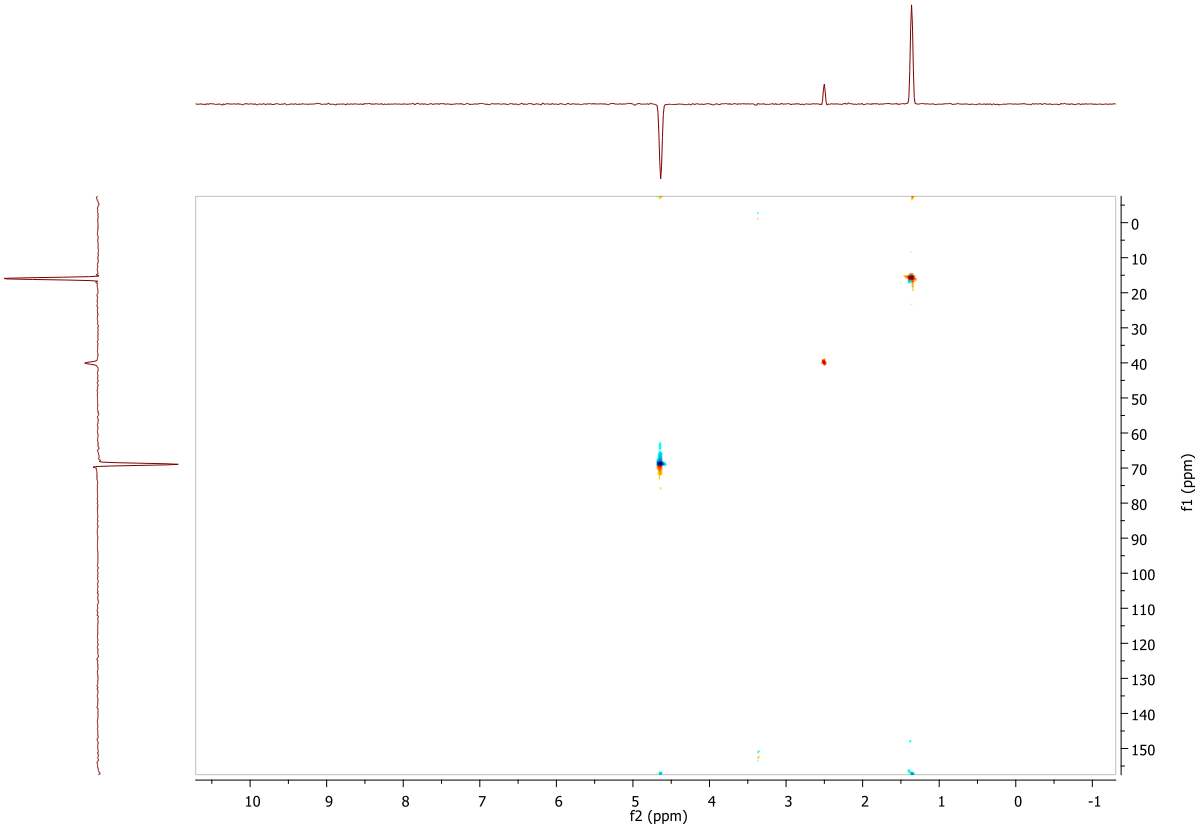

Figure A11. HSQC spectrum of **2.18**

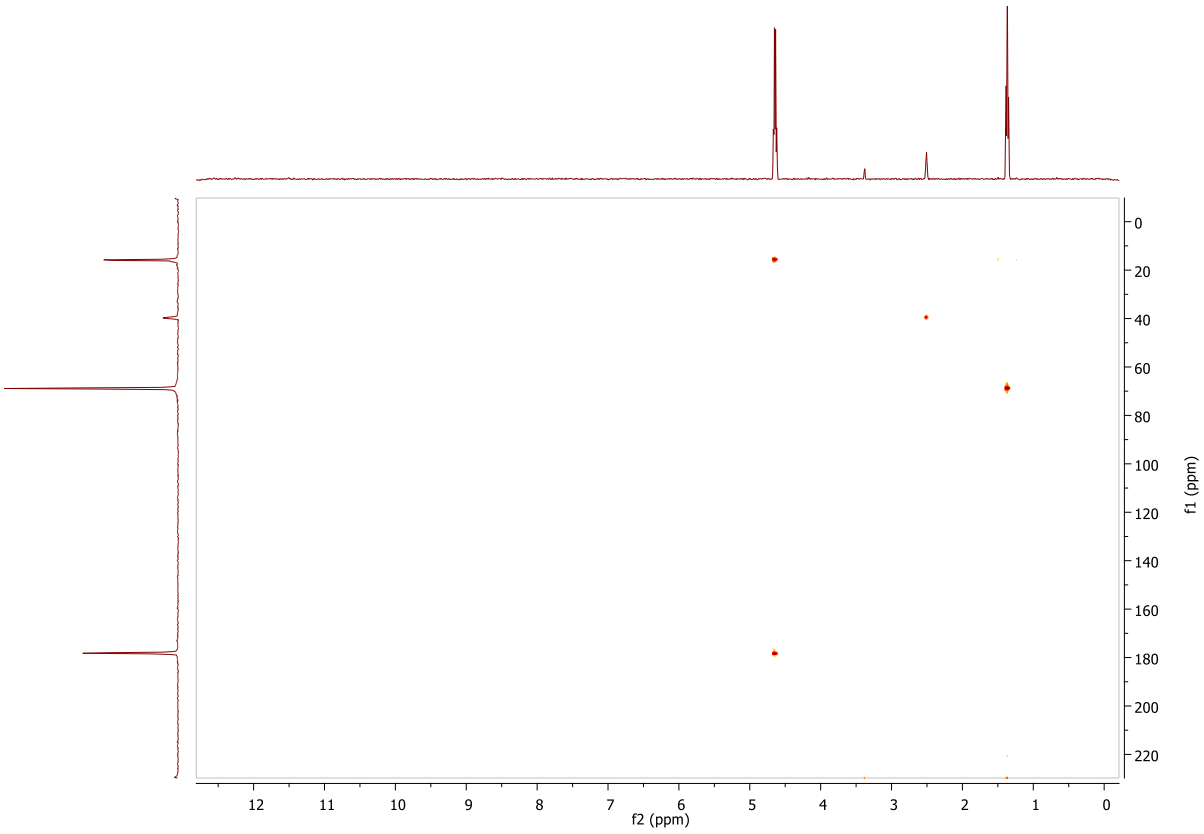

Figure 12. HMBC spectrum of **2.18**

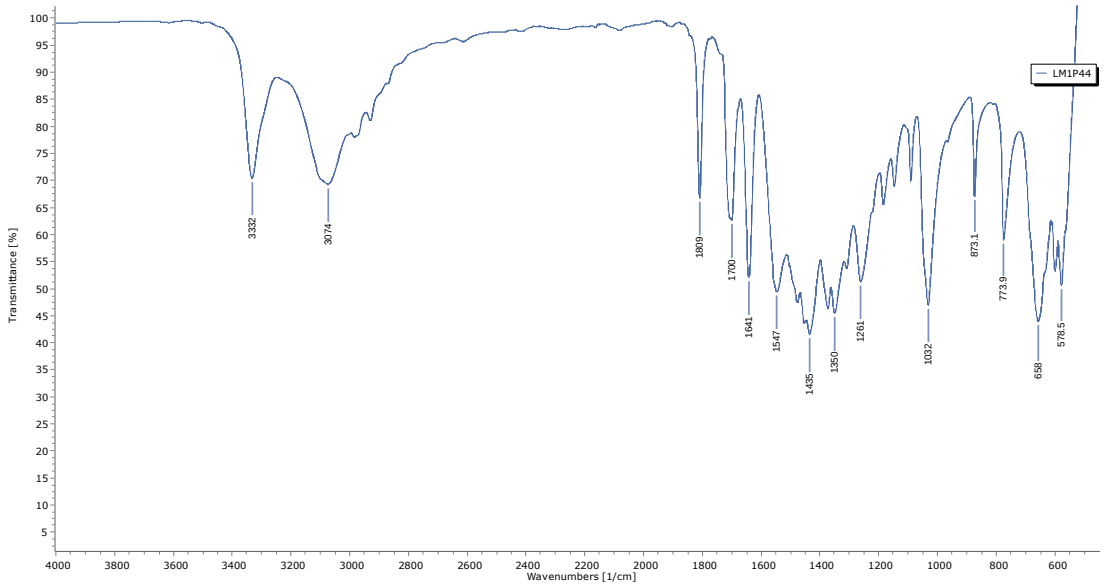

Figure A13. IR spectrum of **2.18**

Compounds

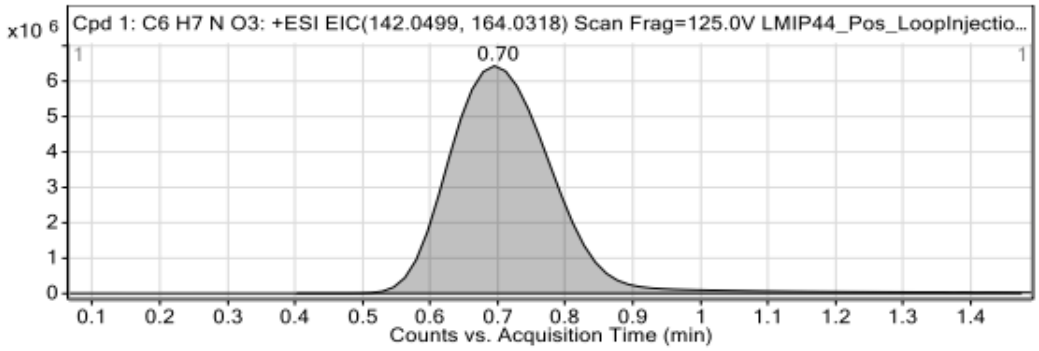

Integration Peak List

Start	RT	End	Height	Area
0.4	0.7	1.47	6234920	68646404

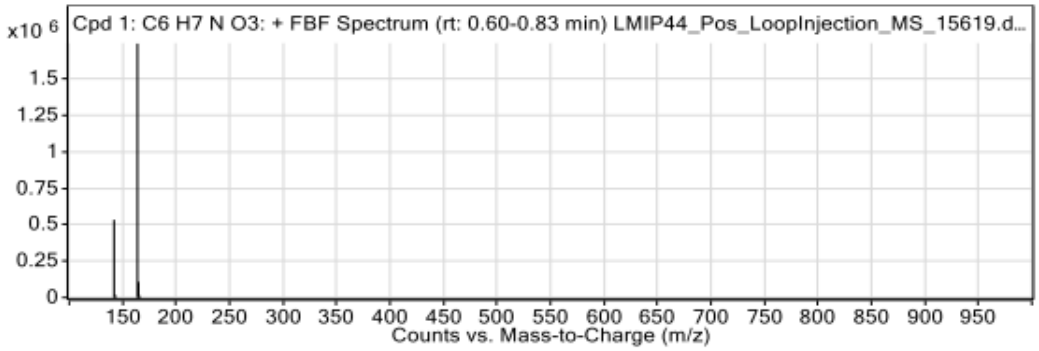

Peak List

m/z	z	Abund	Formula	Ion
142.0501	1	533324.88	C6H7NO3	(M+H)+
143.0343	1	19225.4	C6H7NO3	(M+H)+
144.033	1	2734.74	C6H7NO3	(M+H)+
164.032	1	1746564	C6H7NO3	(M+Na)+
165.0353	1	107480.85	C6H7NO3	(M+Na)+
166.0368	1	12796.33	C6H7NO3	(M+Na)+

--- End Of Report ---

Figure A14. HRMS of **2.18**

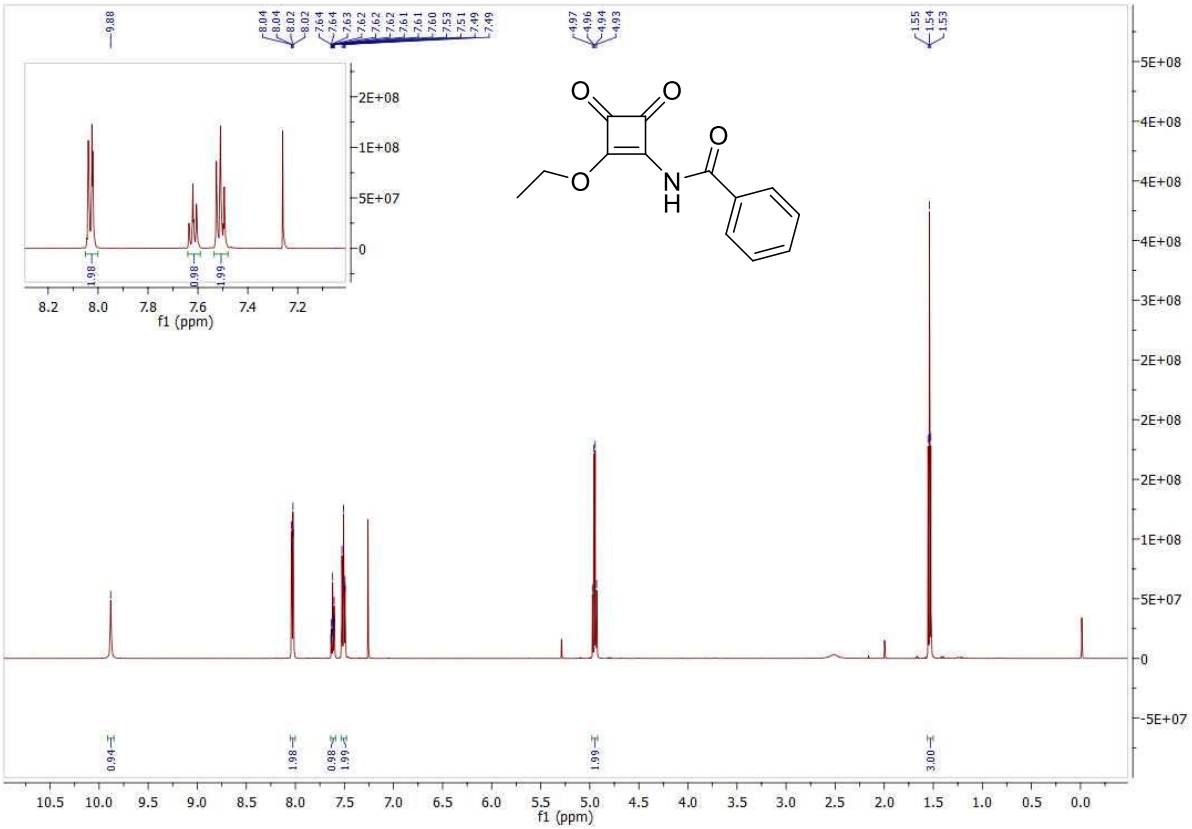

Figure A15. ^{1}H NMR ($CDCl_3$, 500 MHz) spectrum of **2.19**.

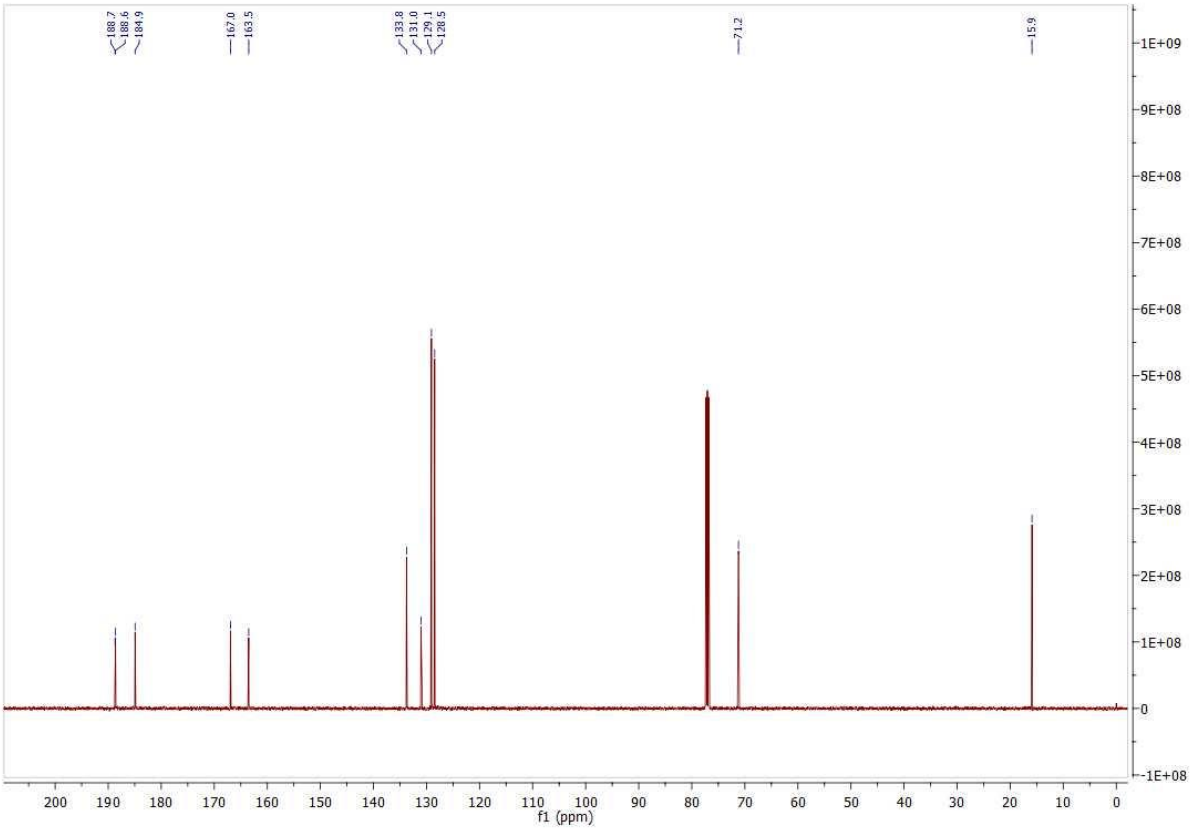

Figure A16. ^{13}C NMR (DMSO-d_6, 126 MHz) spectrum of **2.19**.

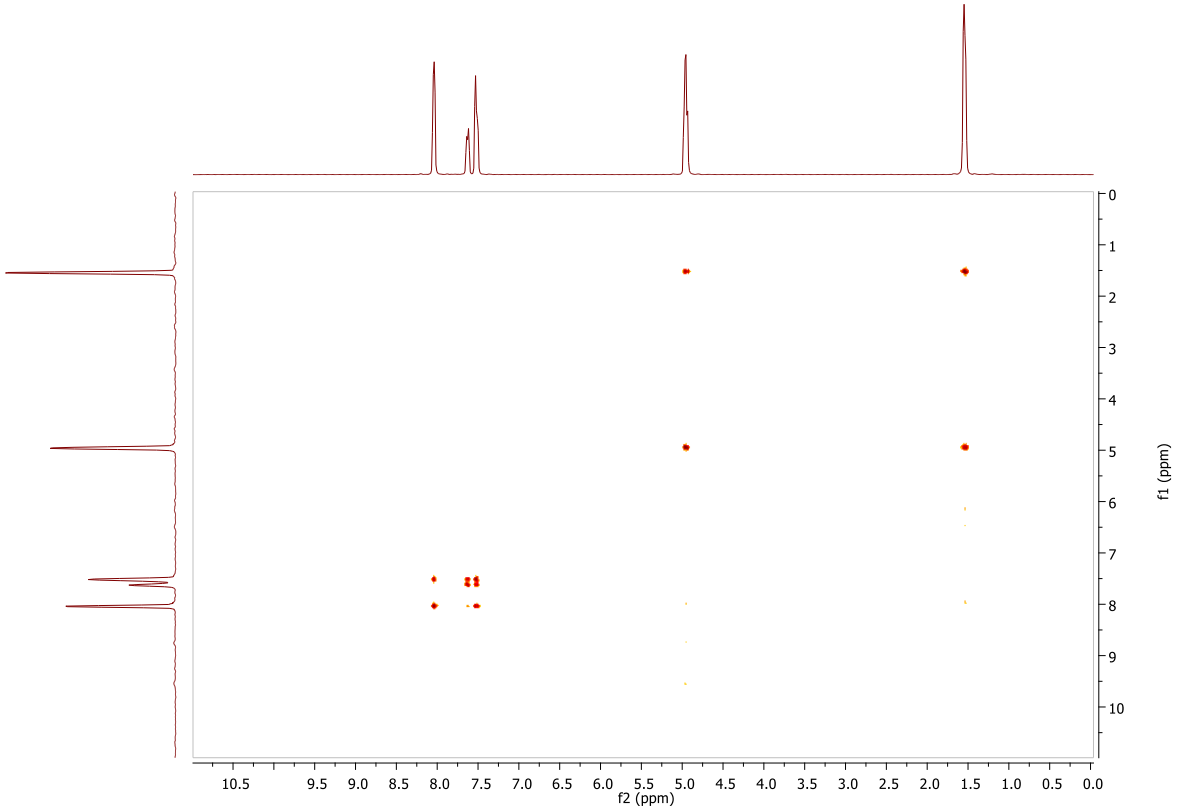

Figure A17. ^{1}H-^{1}H COSY spectrum of **2.19**

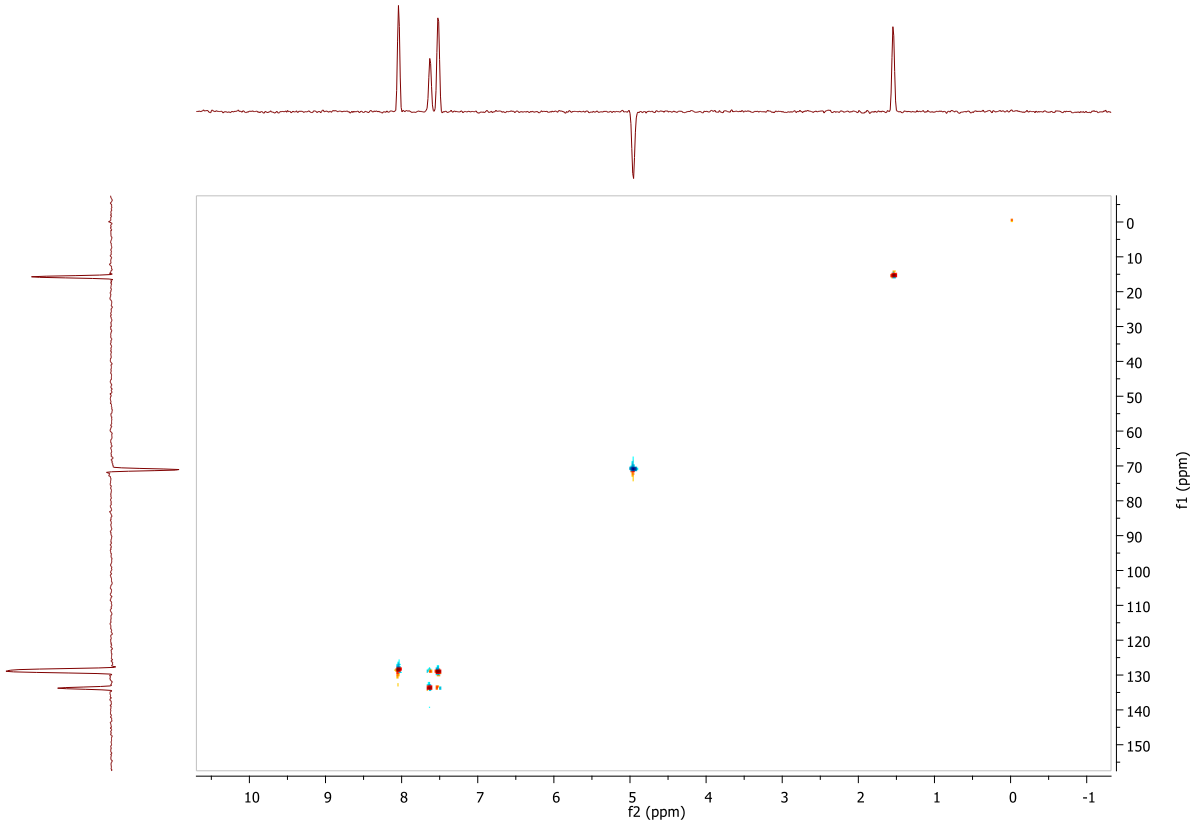

Figure A18. HSQC spectrum of **2.19**

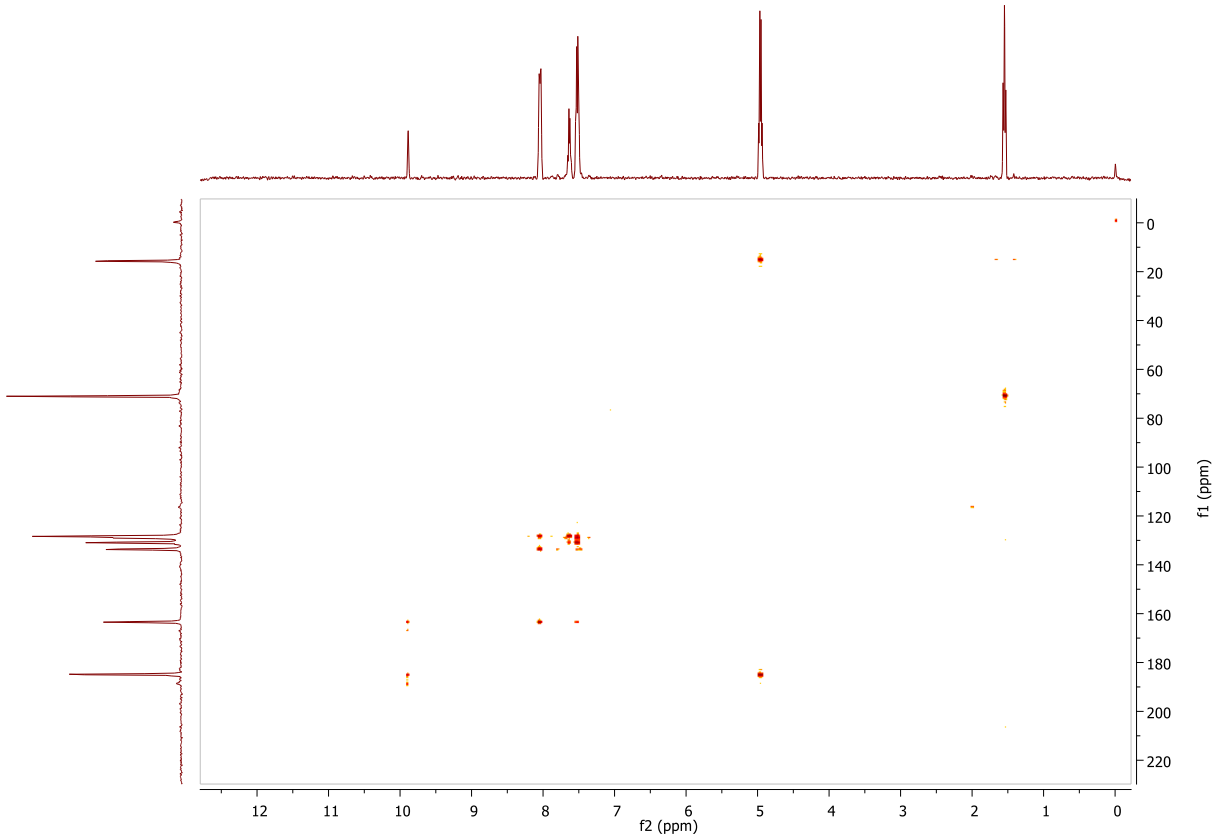

Figure A19. HMBC spectrum of **2.19**

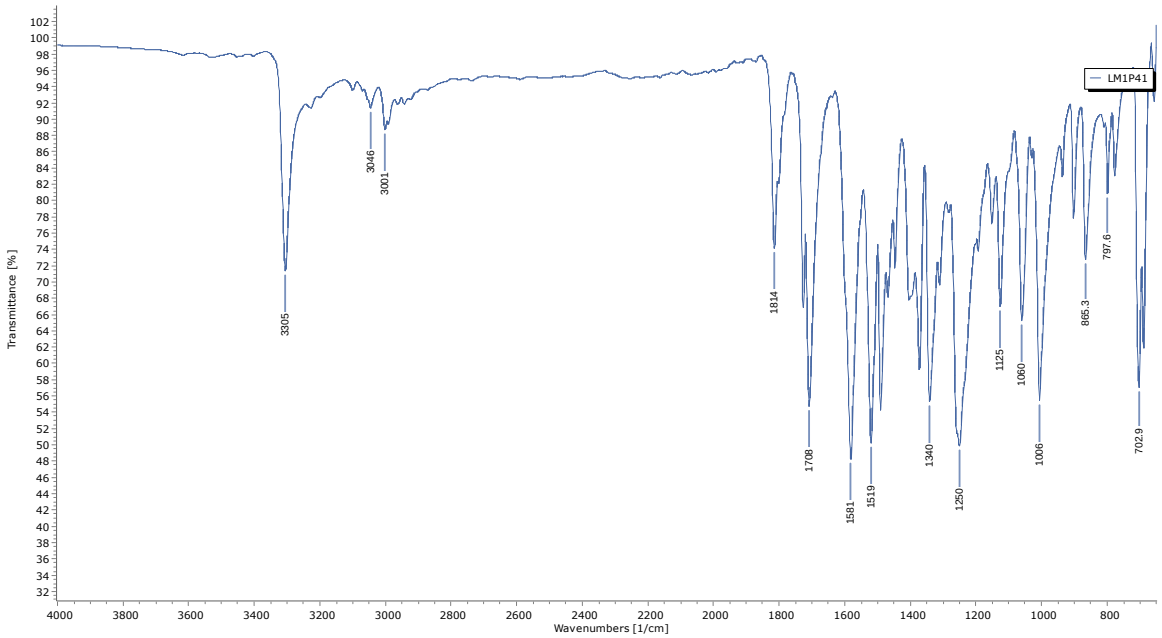

Figure A20. IR spectrum of **2.19**

Compounds

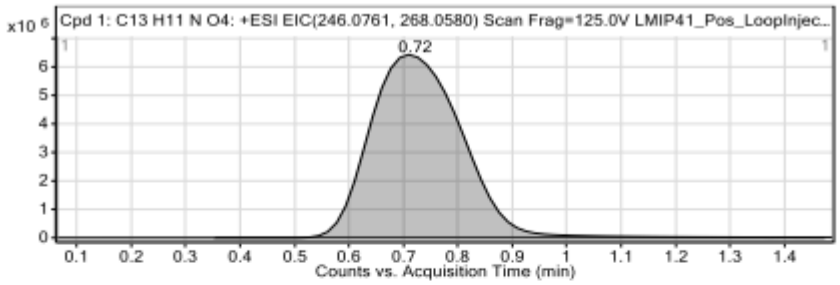

Integration Peak List

Start	RT	End	Height	Area
0.35	0.72	1.47	5992320	75718831

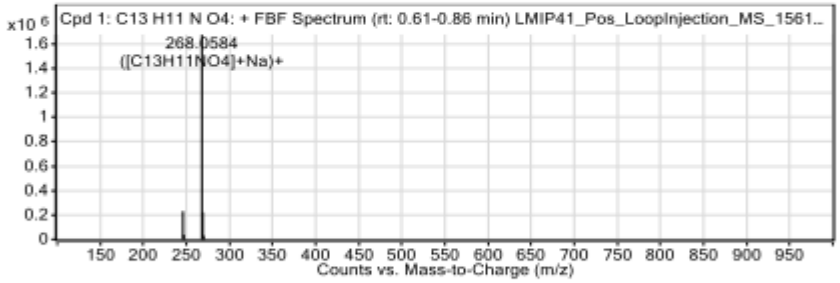

Peak List

m/z	z	Abund	Formula	Ion
246.0764	1	230198.02	C13H11NO4	(M+H)+
247.0794	1	36925.43	C13H11NO4	(M+H)+
248.081	1	4828.54	C13H11NO4	(M+H)+
268.0584	1	1675168.63	C13H11NO4	(M+Na)+
269.0617	1	222764.42	C13H11NO4	(M+Na)+
270.0638	1	29288.15	C13H11NO4	(M+Na)+
271.0669	1	3066.31	C13H11NO4	(M+Na)+

--- End Of Report ---

Figure A21. HRMS of **2.19**

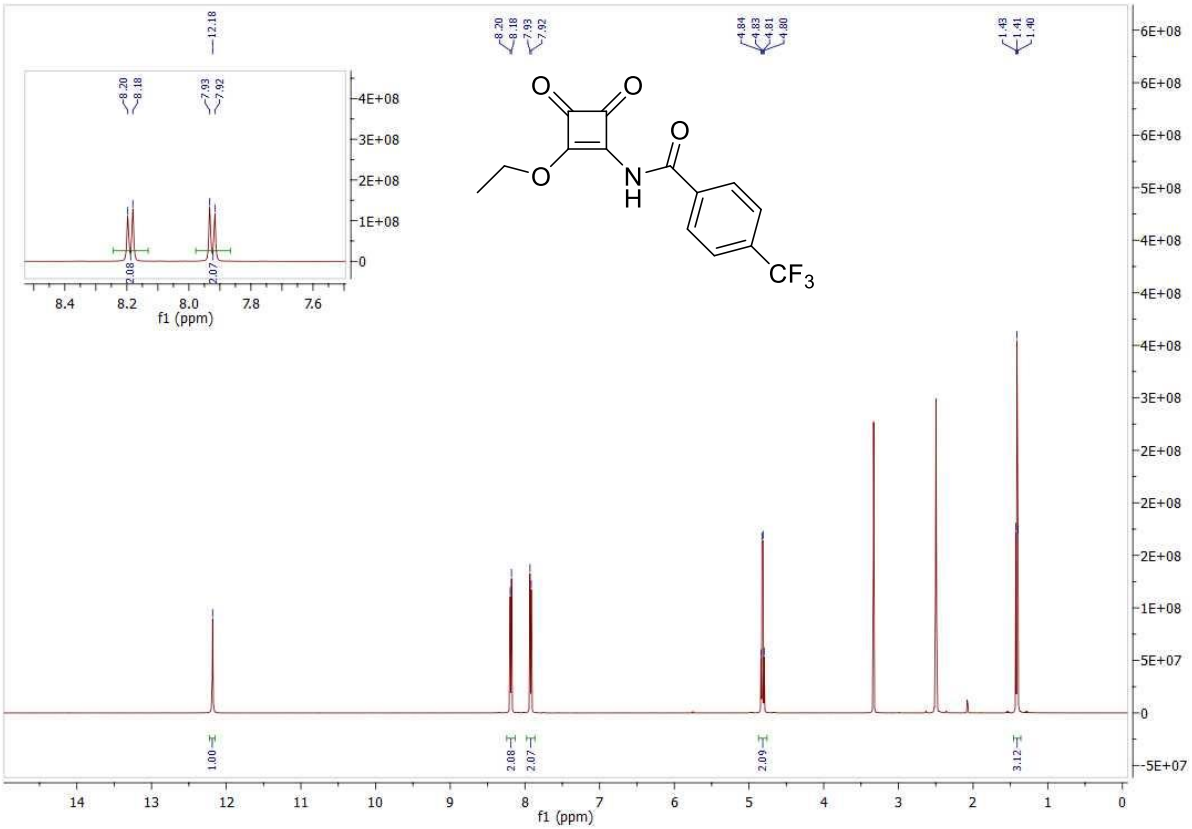

Figure A22. ^{1}H NMR (DMSO-d_6, 500 MHz) spectrum of **2.20**.

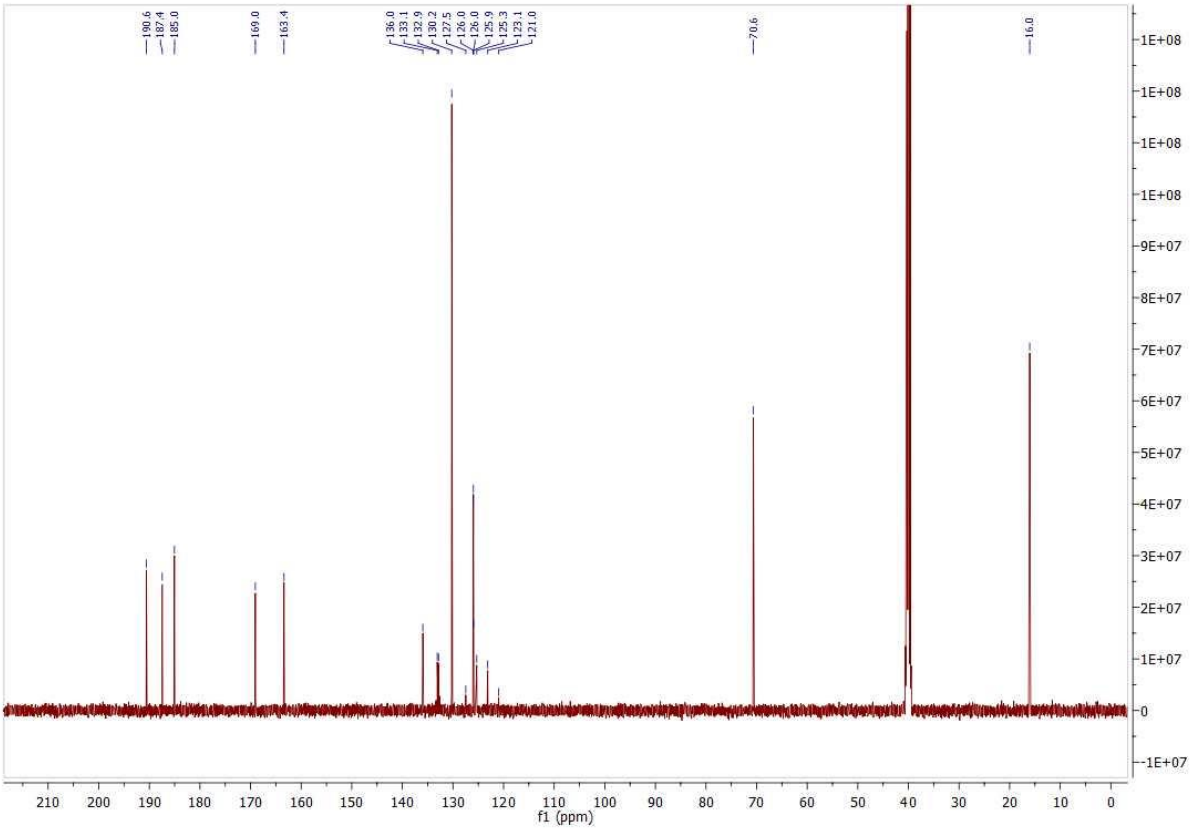

Figure A23. ^{13}C NMR (DMSO-d_6, 126 MHz) spectrum of **2.20**.

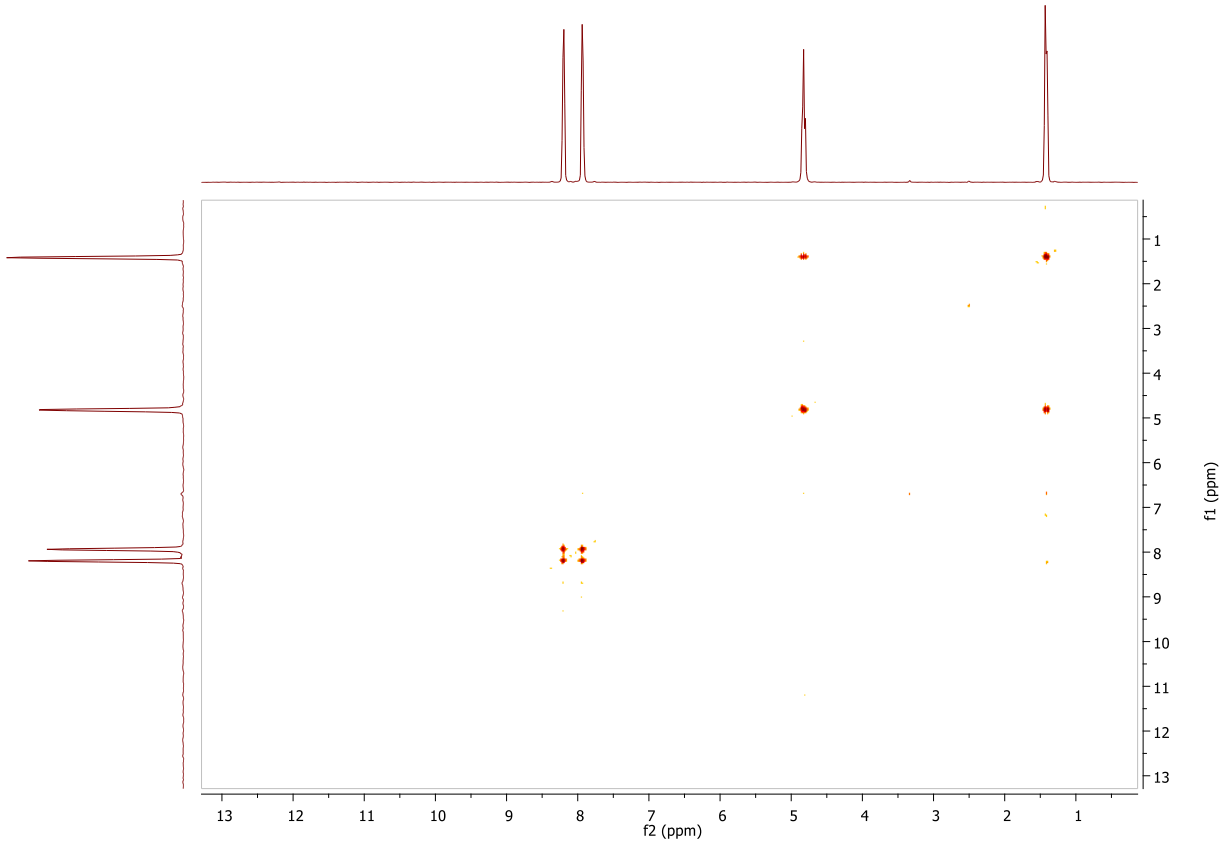

Figure A24. ^{1}H-^{1}H COSY spectrum of **2.20**

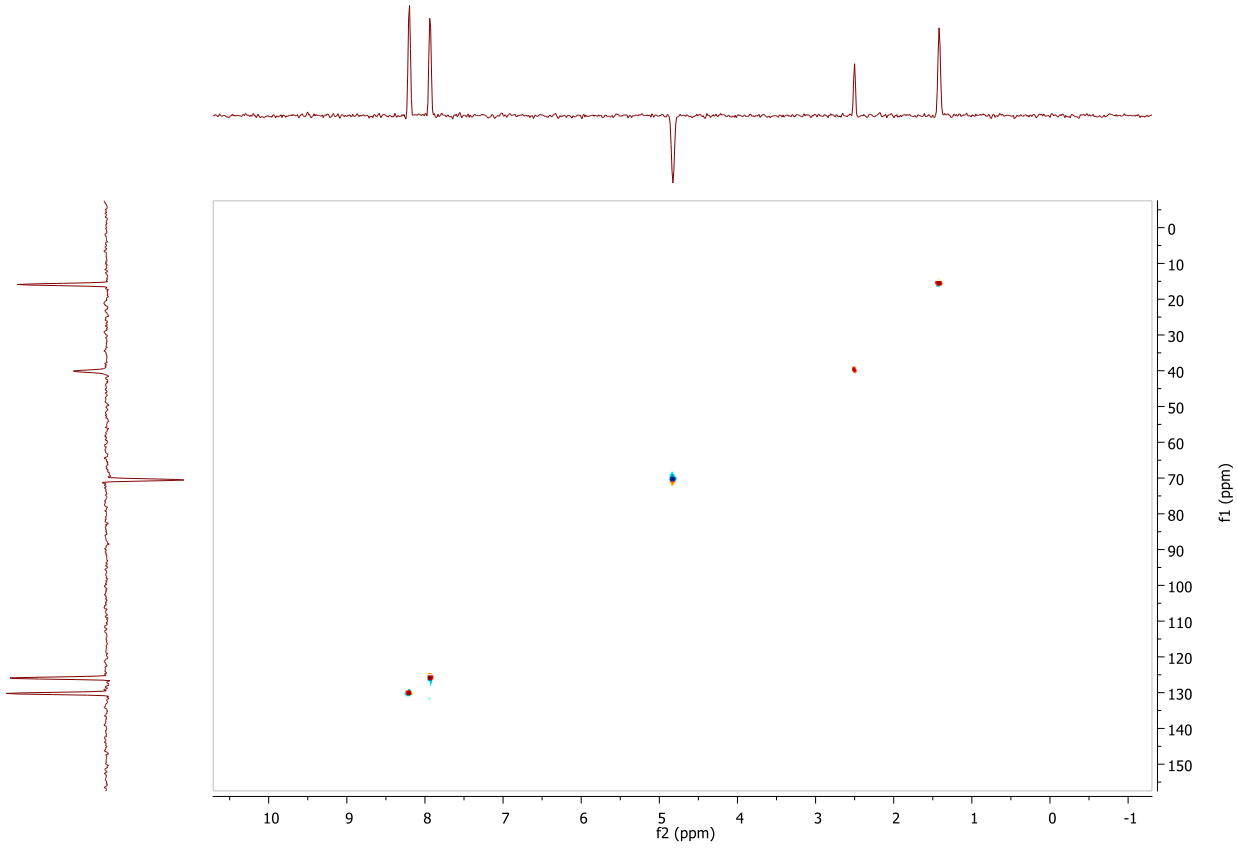

Figure A25. HSQC spectrum of **2.20**

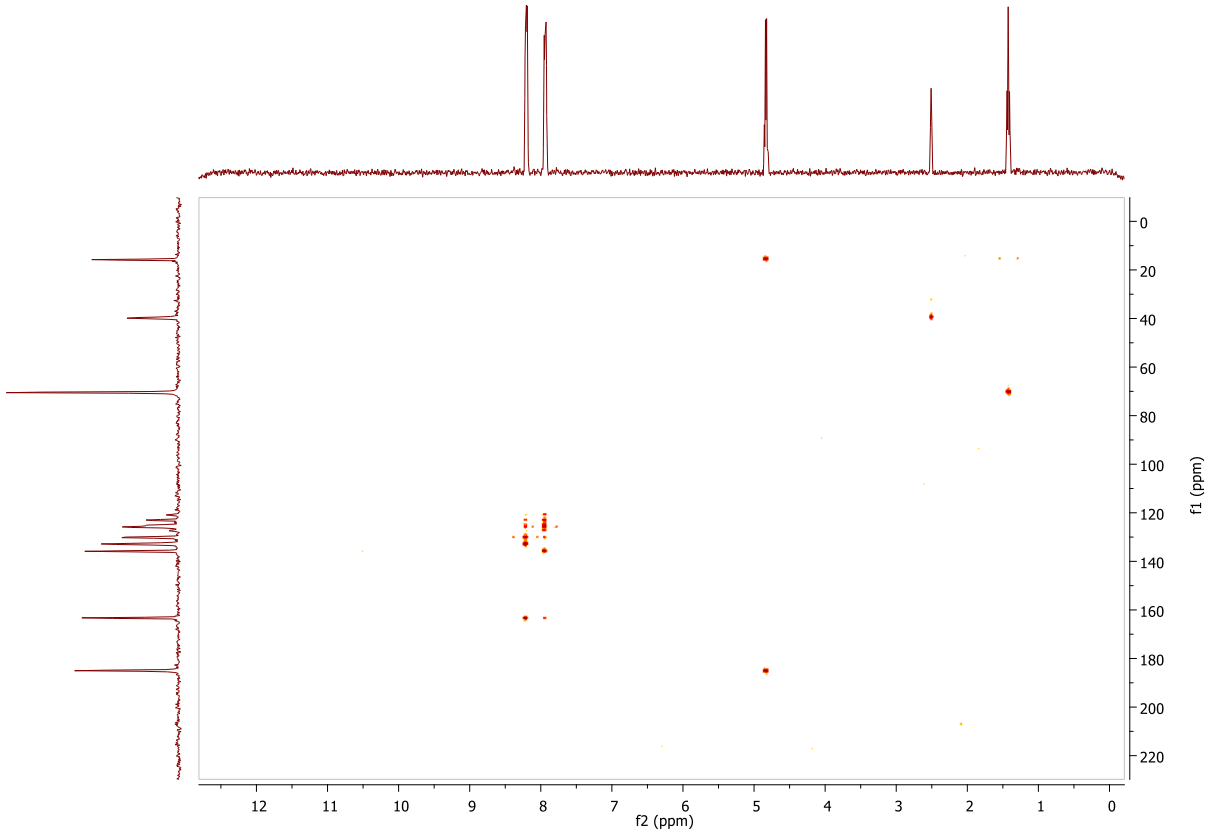

Figure A26. HMBC spectrum of **2.20**

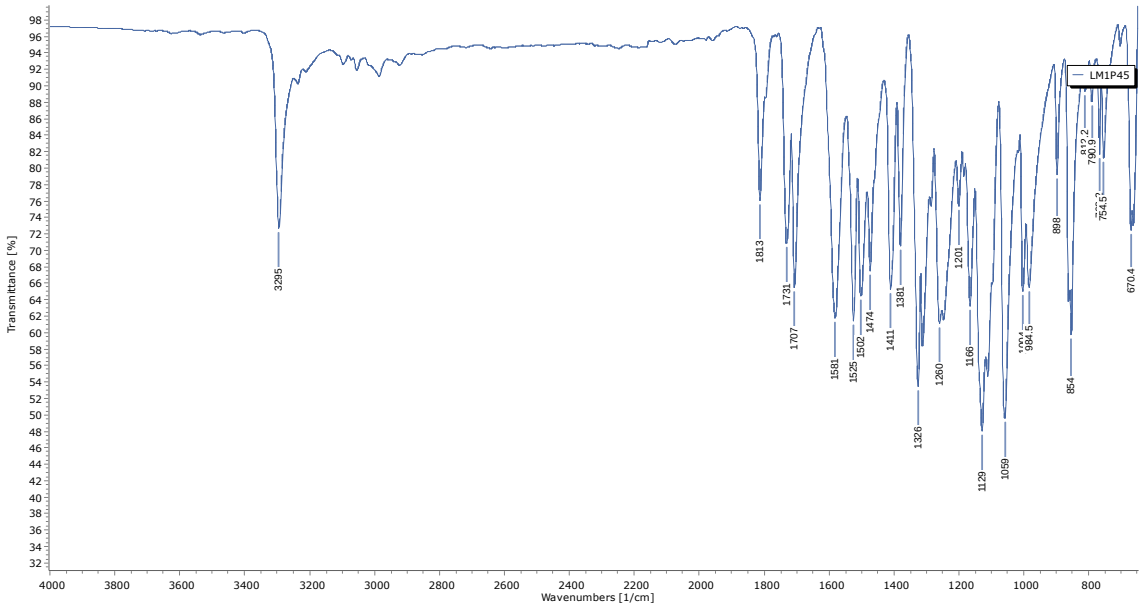

Figure A27. IR spectrum of **2.20**

Compounds

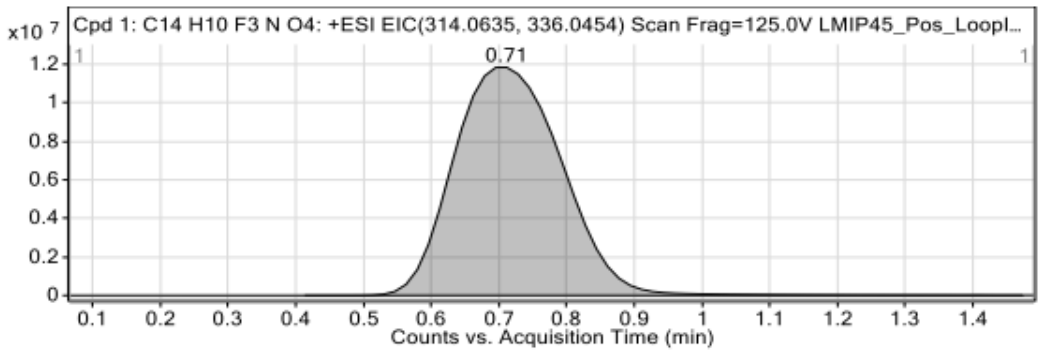

Integration Peak List

Start	RT	End	Height	Area
0.41	0.71	1.47	11649459	132314563

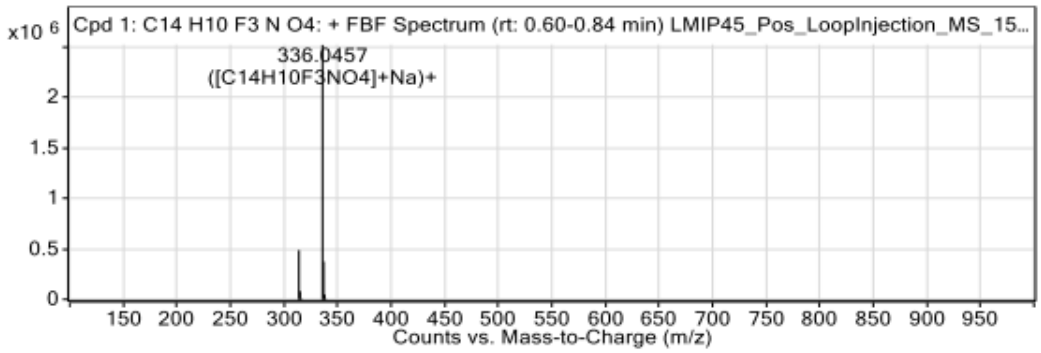

Peak List

m/z	z	Abund	Formula	Ion
314.0637	1	486639.28	C14H10F3NO4	(M+H)+
315.0676	1	80786.87	C14H10F3NO4	(M+H)+
316.0704	1	9808.21	C14H10F3NO4	(M+H)+
336.0457	1	2520331.75	C14H10F3NO4	(M+Na)+
337.0492	1	374240.66	C14H10F3NO4	(M+Na)+
338.0514	1	46300.03	C14H10F3NO4	(M+Na)+
339.0548	1	4834.05	C14H10F3NO4	(M+Na)+

--- End Of Report ---

Figure A28. HRMS of **2.20**

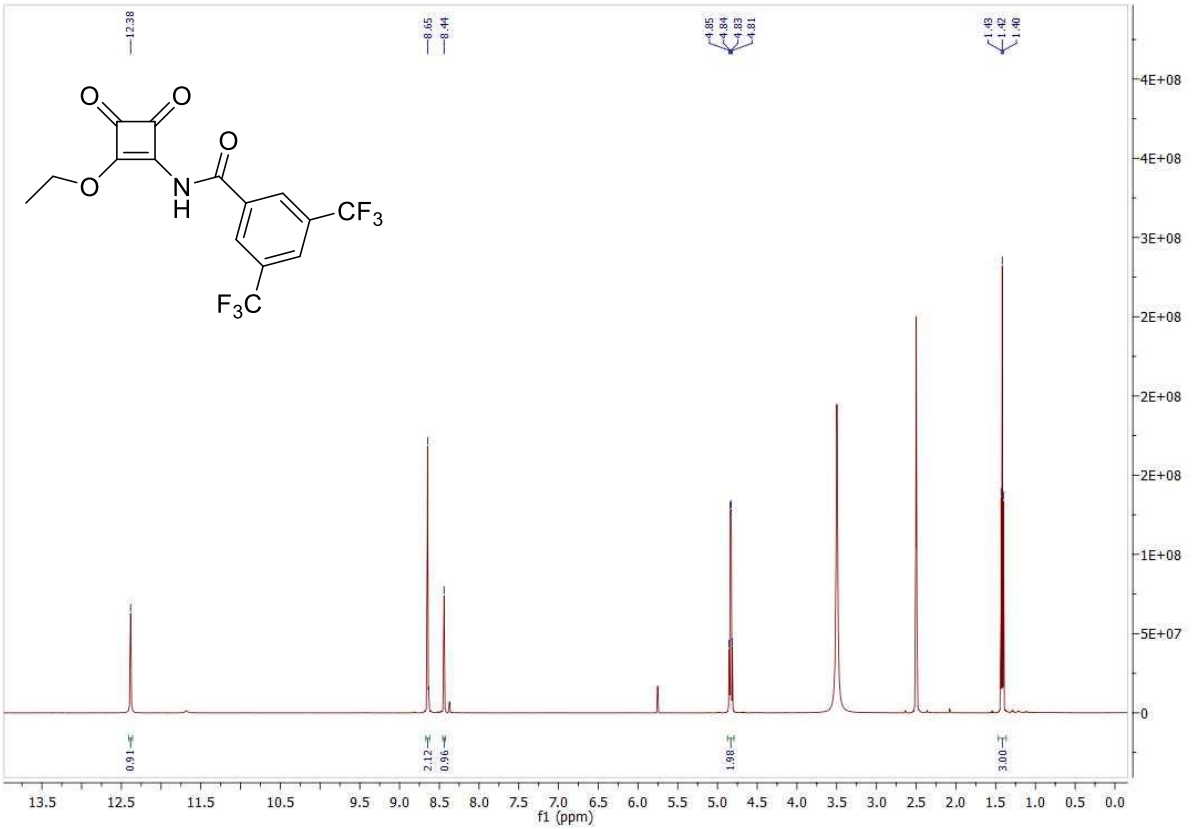

Figure A29. ^{1}H NMR (DMSO-d_6, 500 MHz) spectrum of **2.21**.

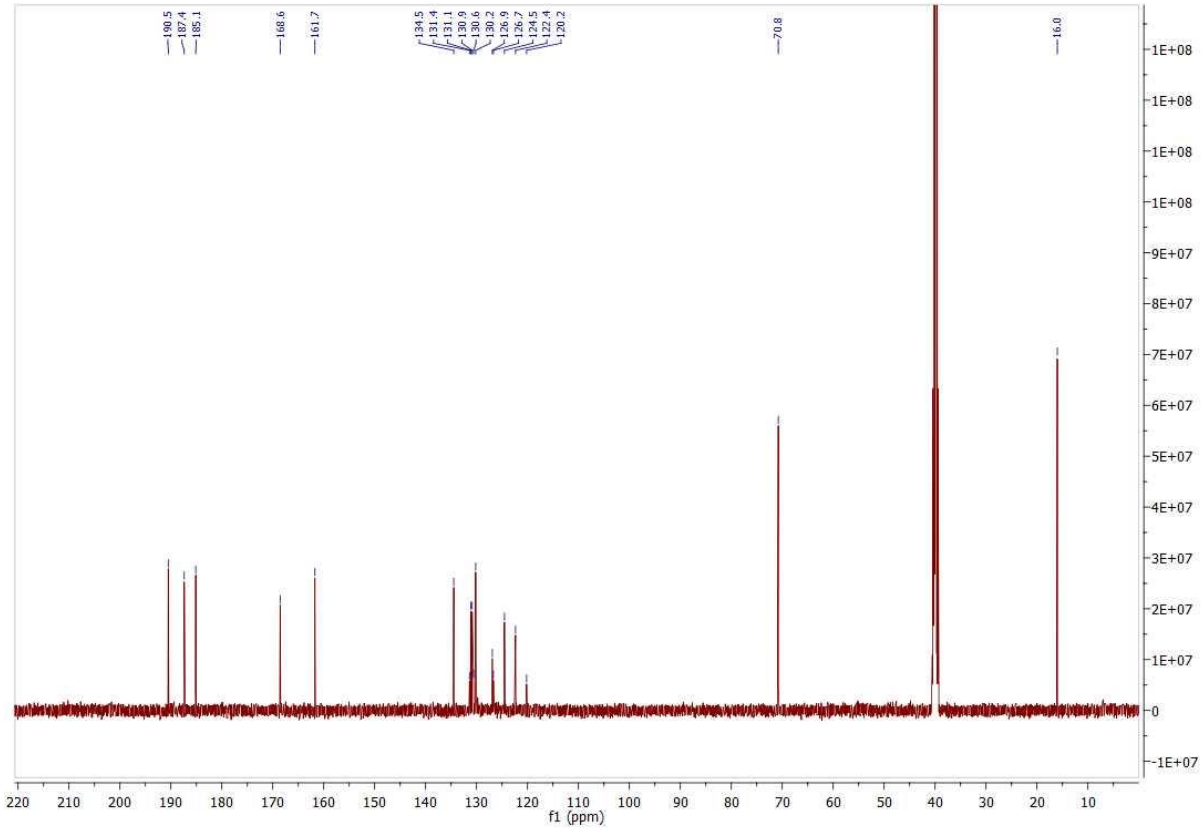

Figure A30. ^{13}C NMR (DMSO-d_6, 126 MHz) spectrum of **2.21**.

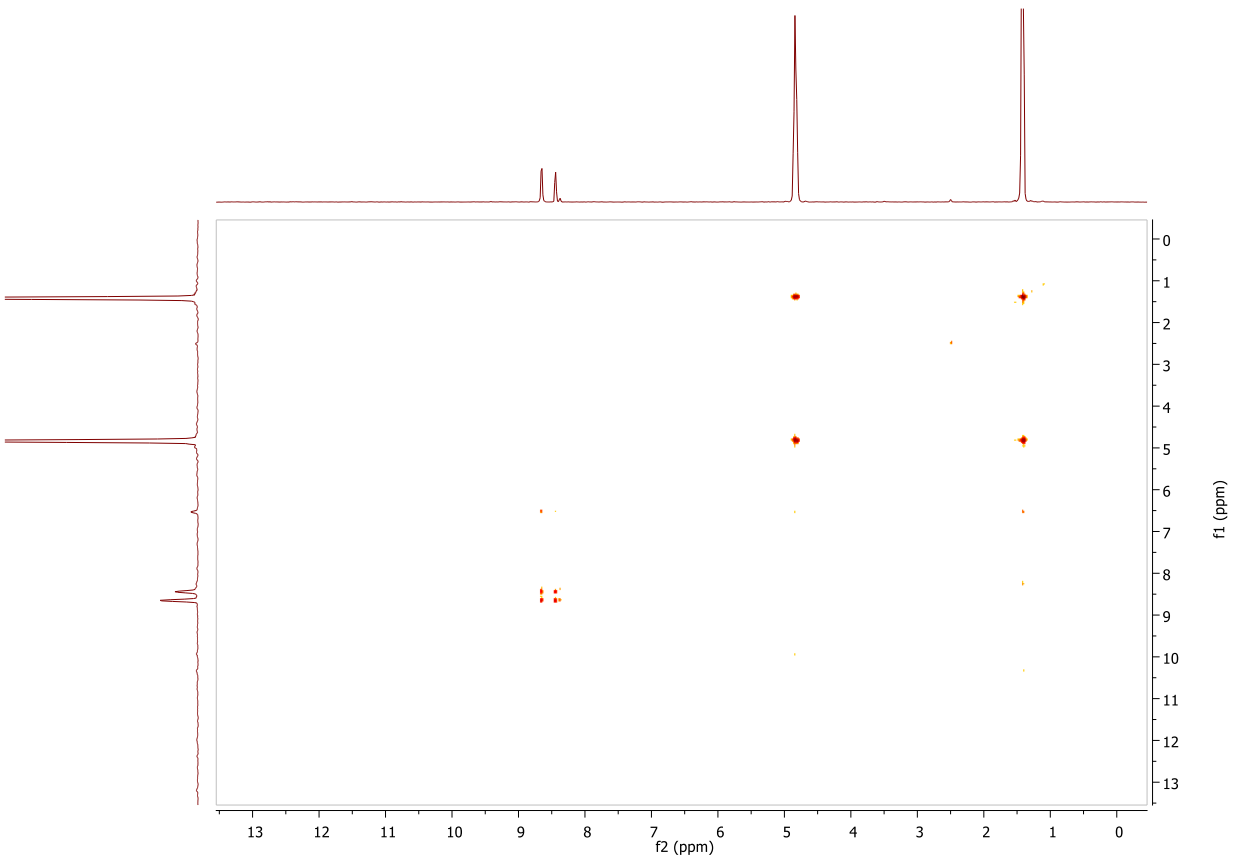

Figure A31. ^{1}H-^{1}H COSY spectrum of **2.21**

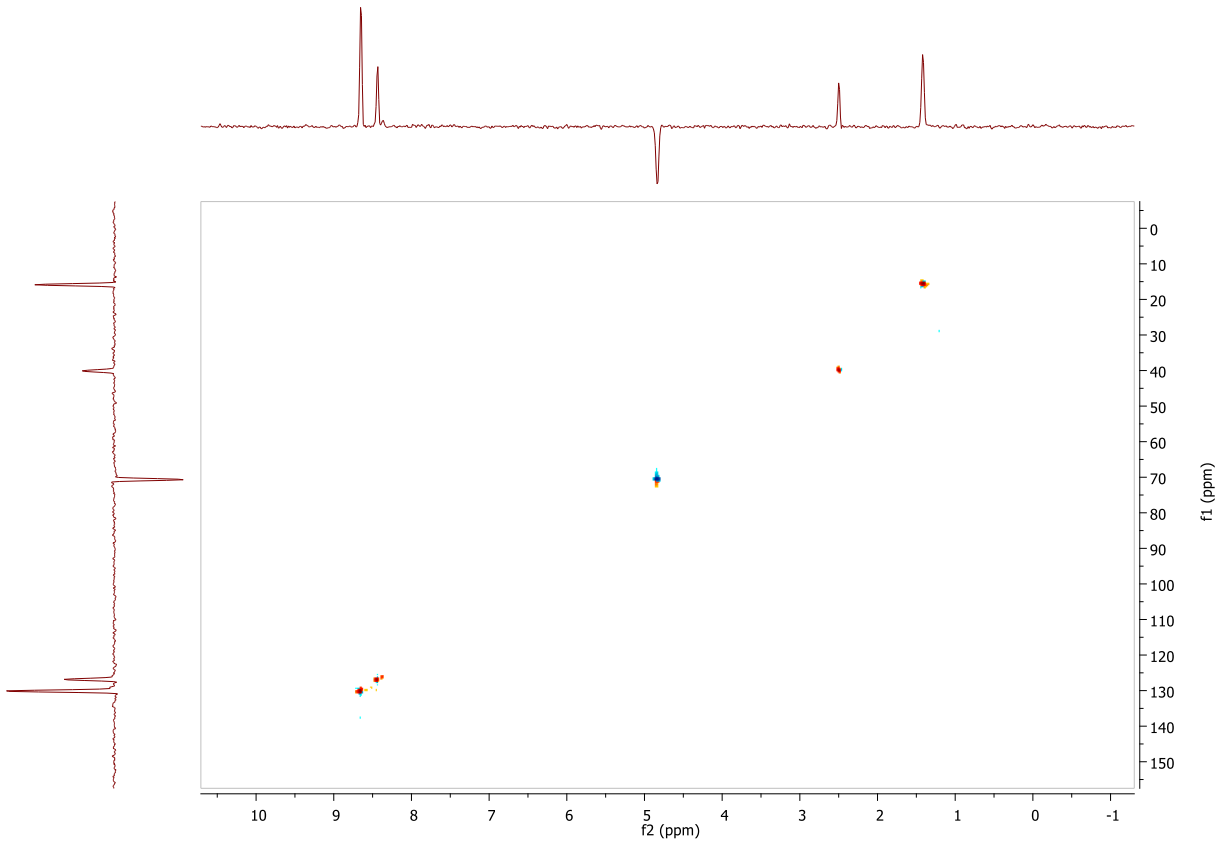

Figure A32. HSQC spectrum of **2.21**

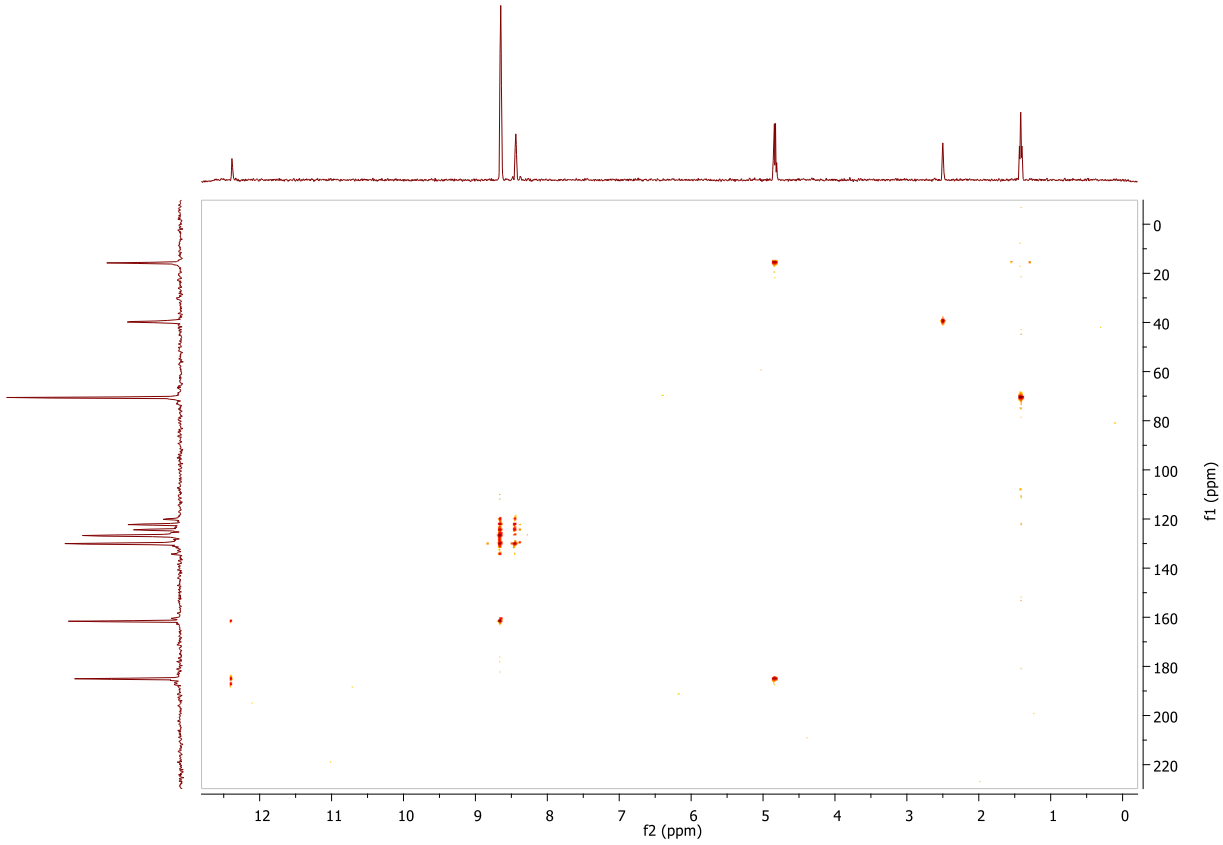

Figure A33. HMBC spectrum of **2.21**

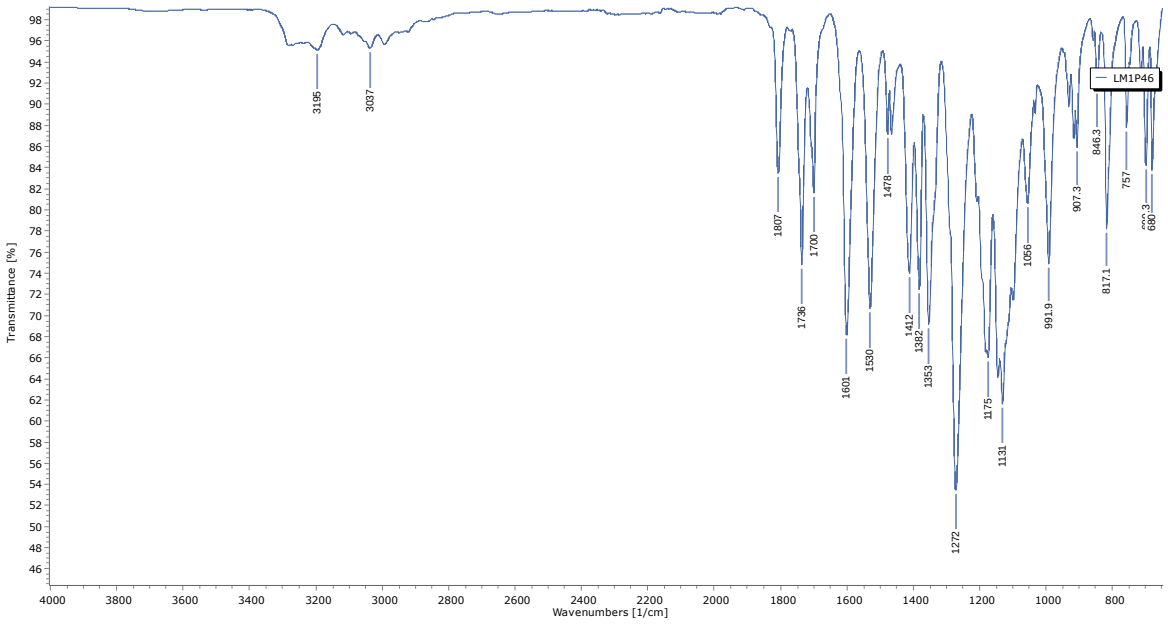

Figure A34. IR spectrum of **2.21**

Compounds

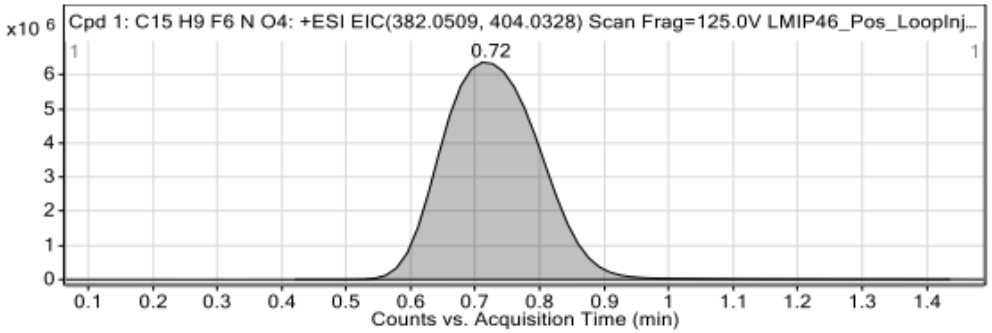

Integration Peak List

Start	RT	End	Height	Area
0.42	0.72	1.44	5957134	69029552

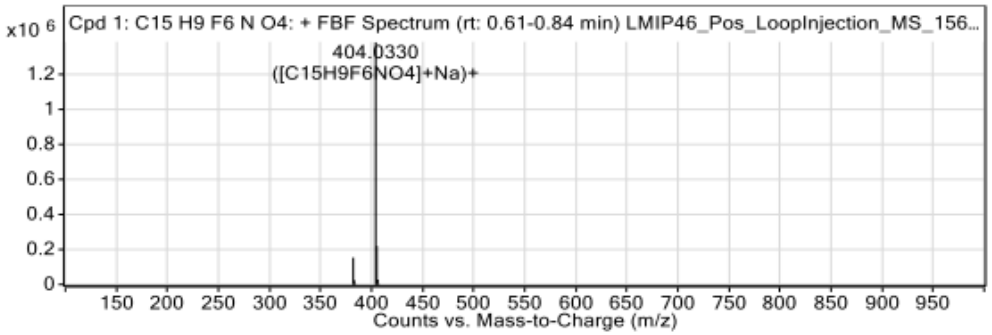

Peak List

m/z	z	Abund	Formula	Ion
382.051	1	153784.44	C15H9F6NO4	(M+H)+
383.0541	1	23695.58	C15H9F6NO4	(M+H)+
384.0563	1	3103.73	C15H9F6NO4	(M+H)+
404.033	1	1386279.25	C15H9F6NO4	(M+Na)+
405.0365	1	220258.97	C15H9F6NO4	(M+Na)+
406.0385	1	27570.79	C15H9F6NO4	(M+Na)+
407.0411	1	2809.82	C15H9F6NO4	(M+Na)+

--- End Of Report ---

Figure A35. HRMS of **2.21**

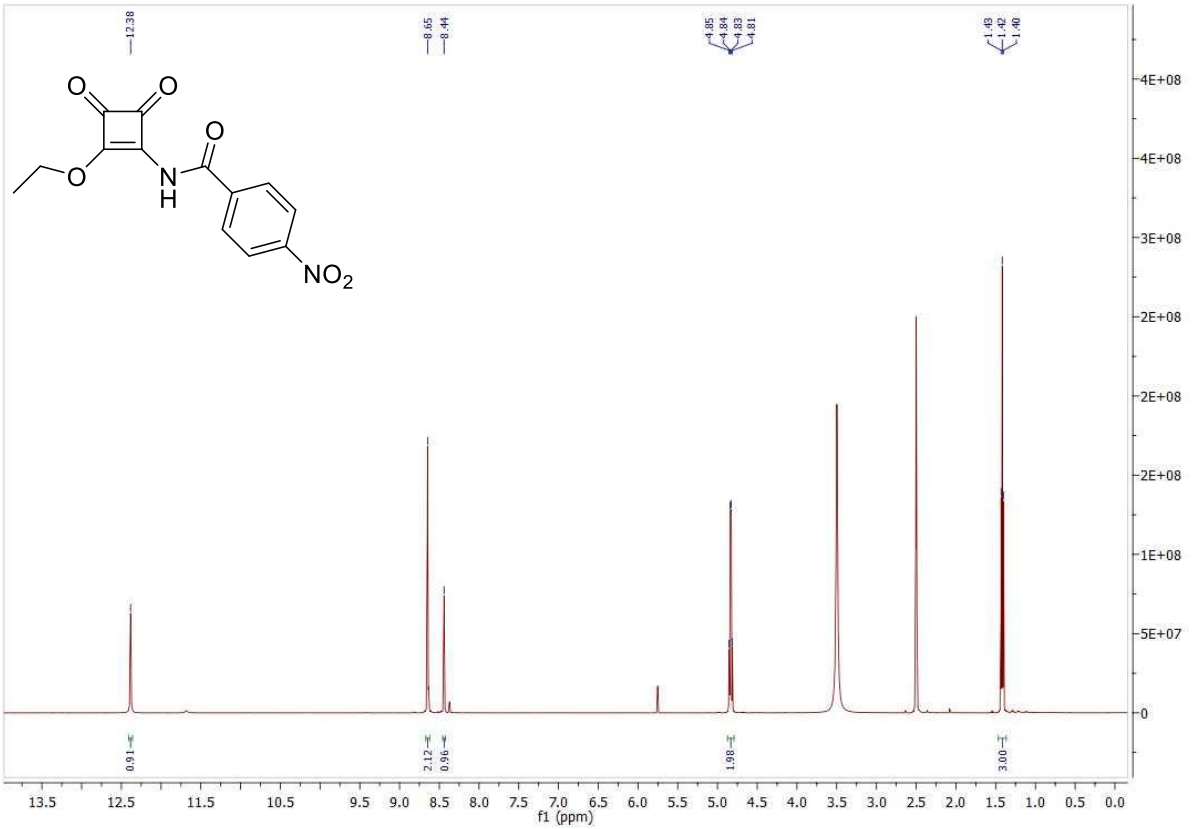

Figure A36. ^{1}H NMR (DMSO-d_6, 500 MHz) spectrum of **2.22**.

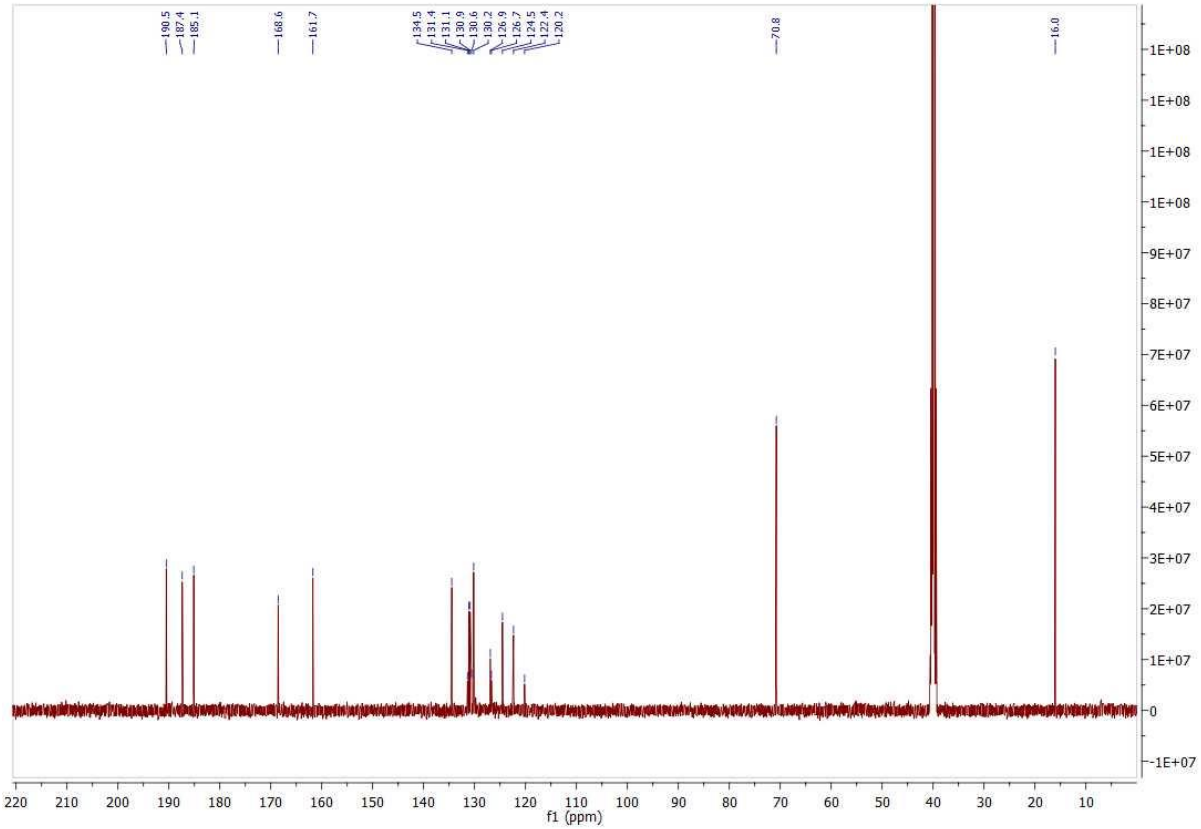

Figure A37. ^{13}C NMR (DMSO-d_6, 126 MHz) spectrum of **2.22**.

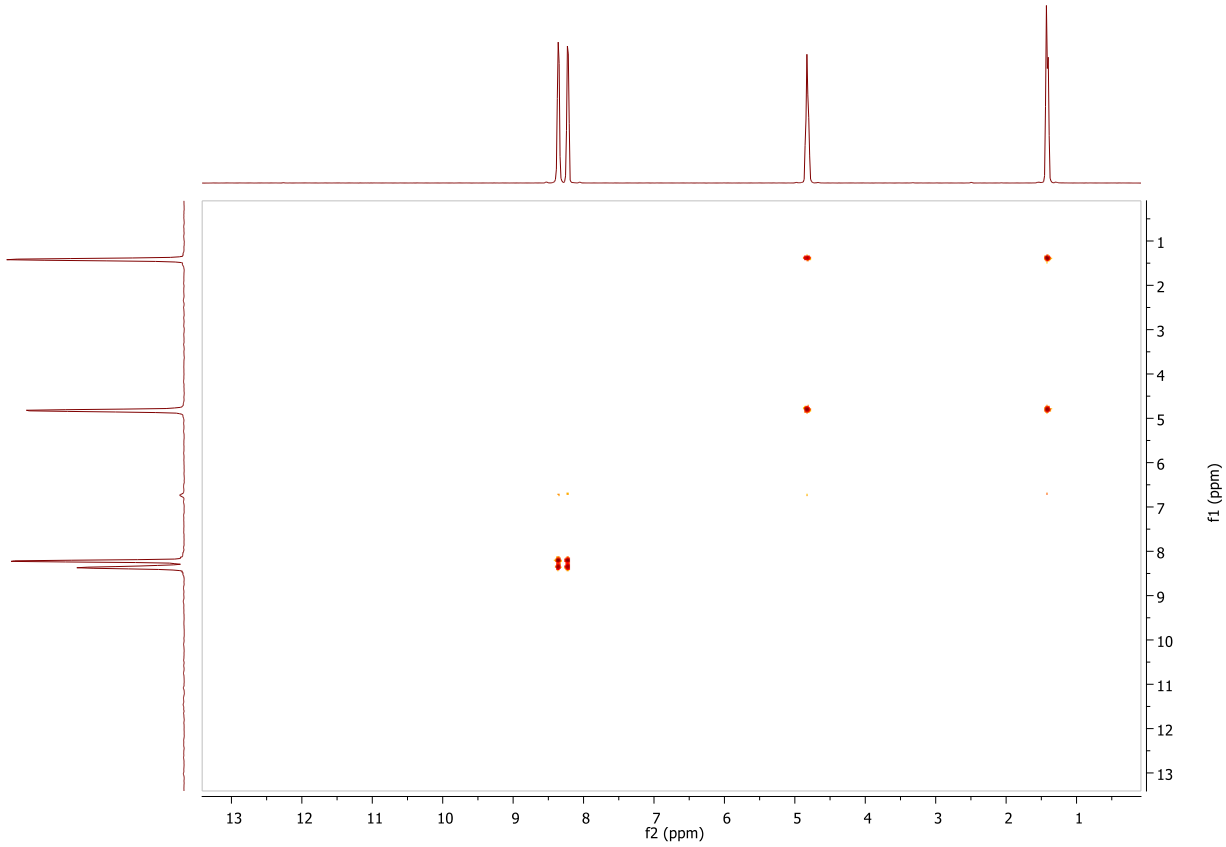

Figure A38. ^{1}H-^{1}H COSY spectrum of **2.22**

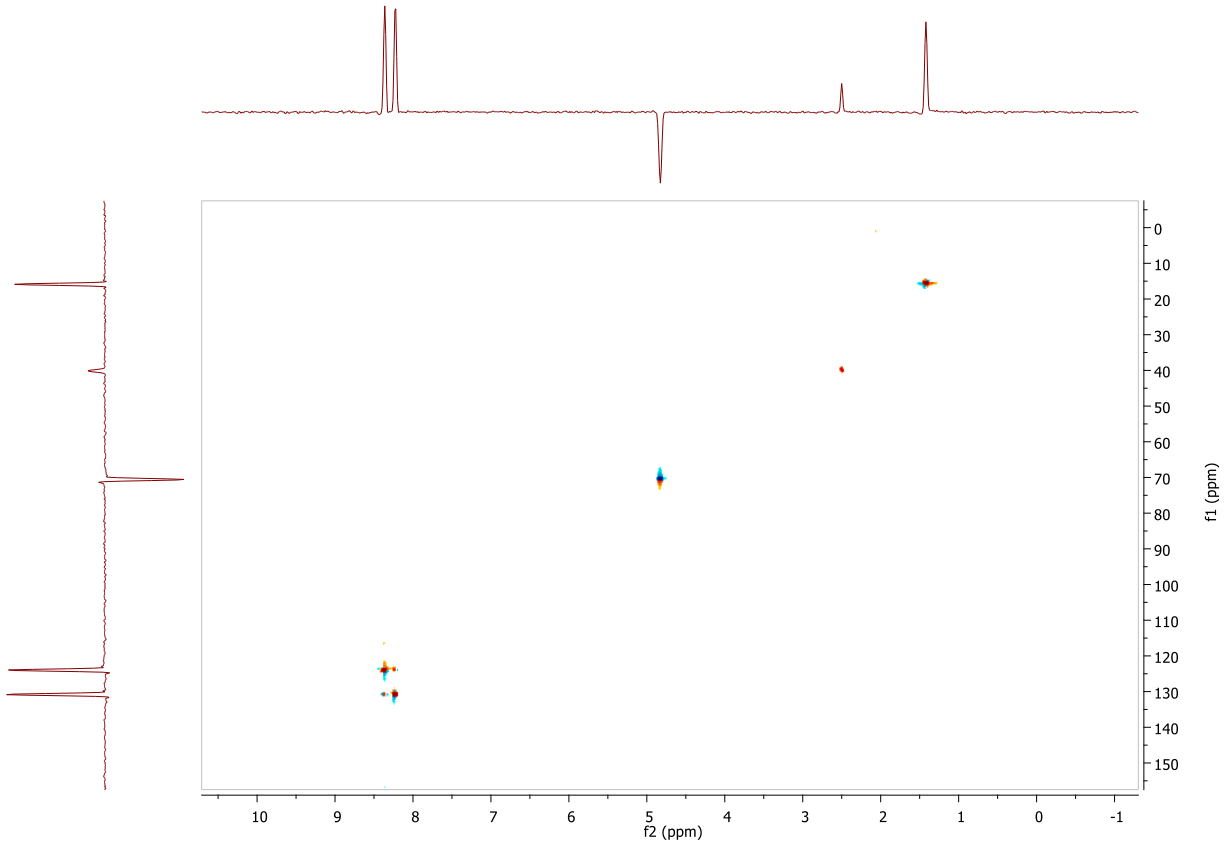

Figure A39. HSQC spectrum of **2.22**

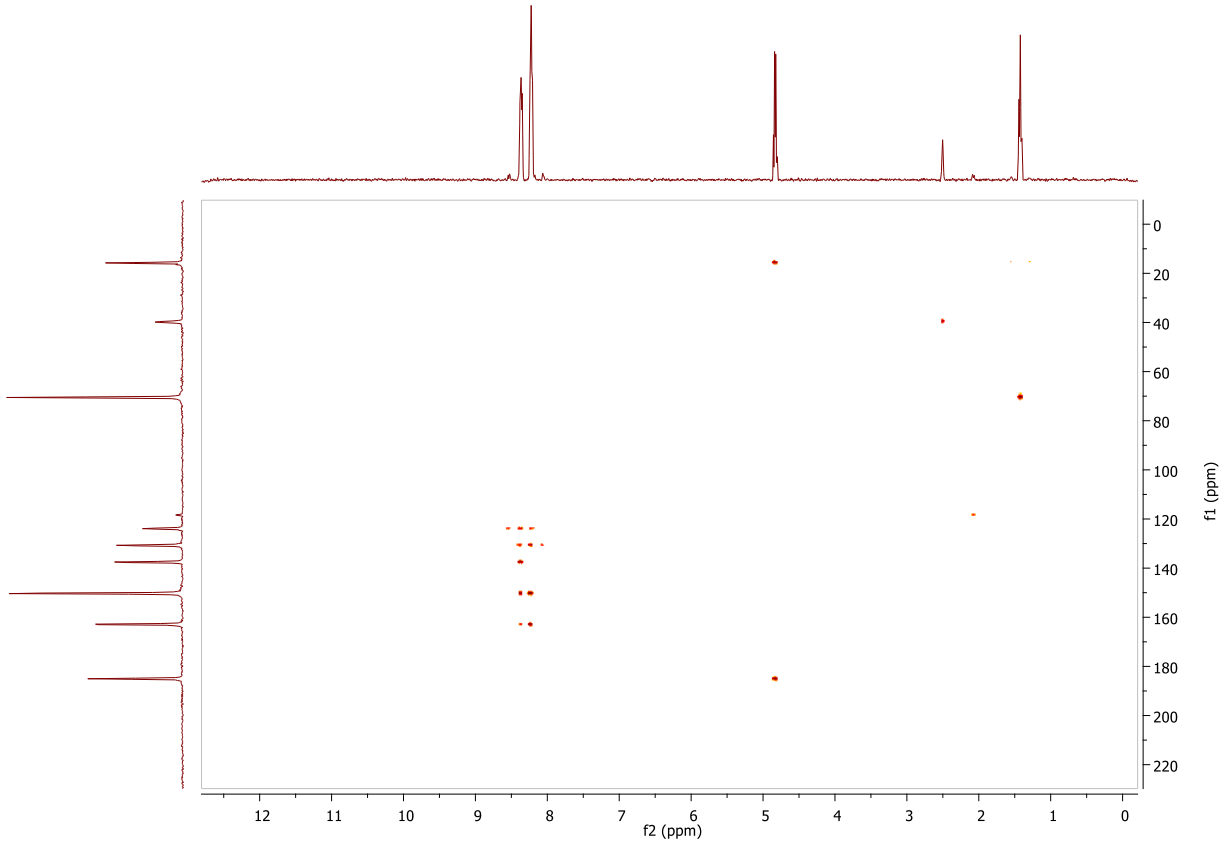

Figure A40. HMBC spectrum of **2.22**

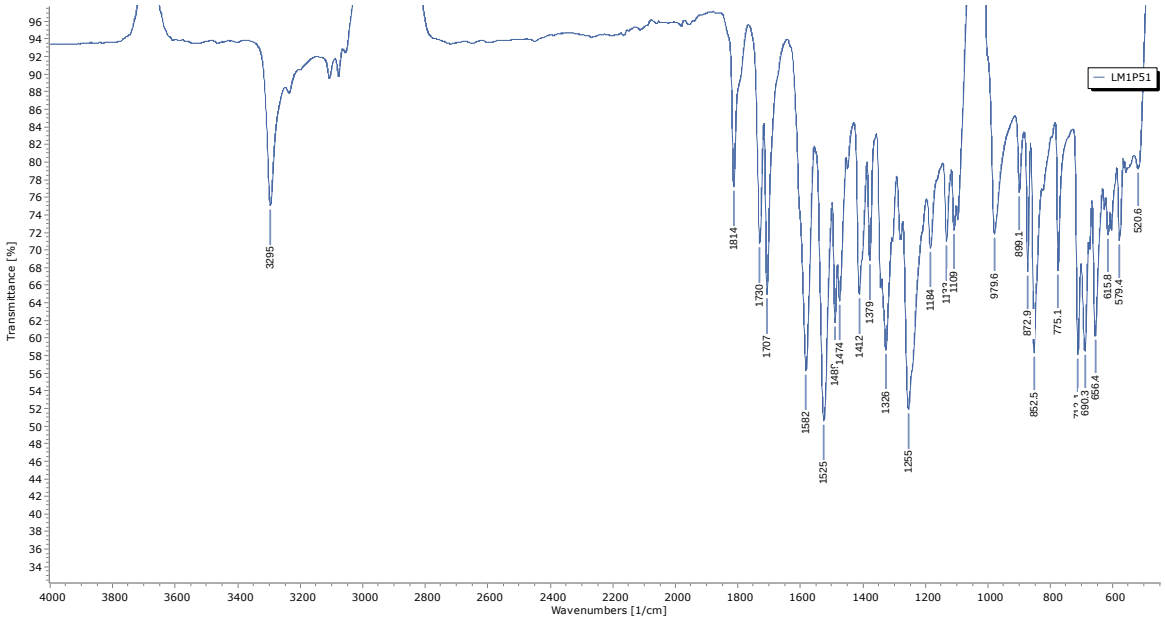

Figure A41. IR spectrum of **2.22**

Compounds

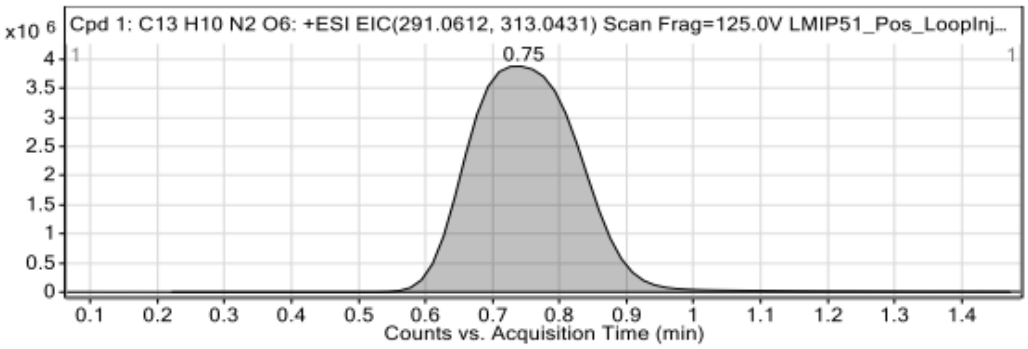

Integration Peak List

Start	RT	End	Height	Area
0.22	0.75	1.47	3822997	46311078

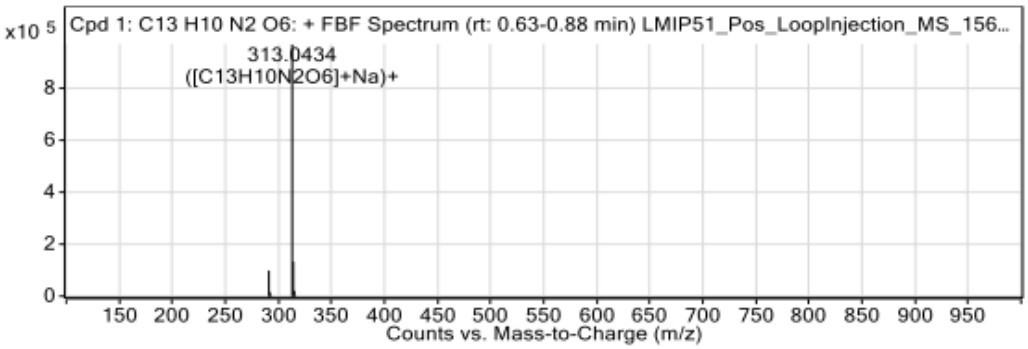

Peak List

m/z	z	Abund	Formula	Ion
291.0613	1	98875.48	C13H10N2O6	(M+H)+
292.0647	1	15112.59	C13H10N2O6	(M+H)+
293.0672	1	2379.04	C13H10N2O6	(M+H)+
313.0434	1	972596.19	C13H10N2O6	(M+Na)+
314.0467	1	133088.45	C13H10N2O6	(M+Na)+
315.049	1	20580.38	C13H10N2O6	(M+Na)+
316.0516	1	2236.74	C13H10N2O6	(M+Na)+

--- End Of Report ---

Figure A42. HRMS of **2.22**

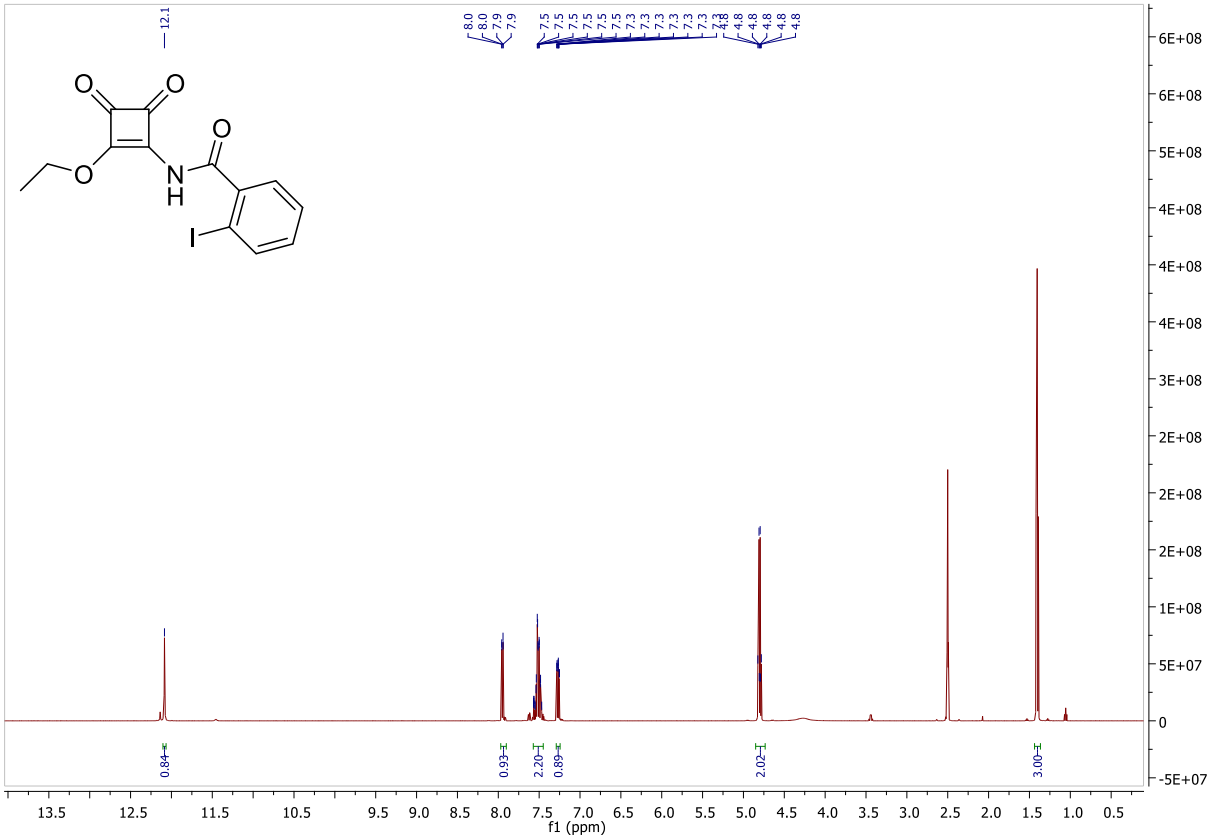

Figure A43. ^{1}H NMR (DMSO-d_6, 500 MHz) spectrum of **2.23**.

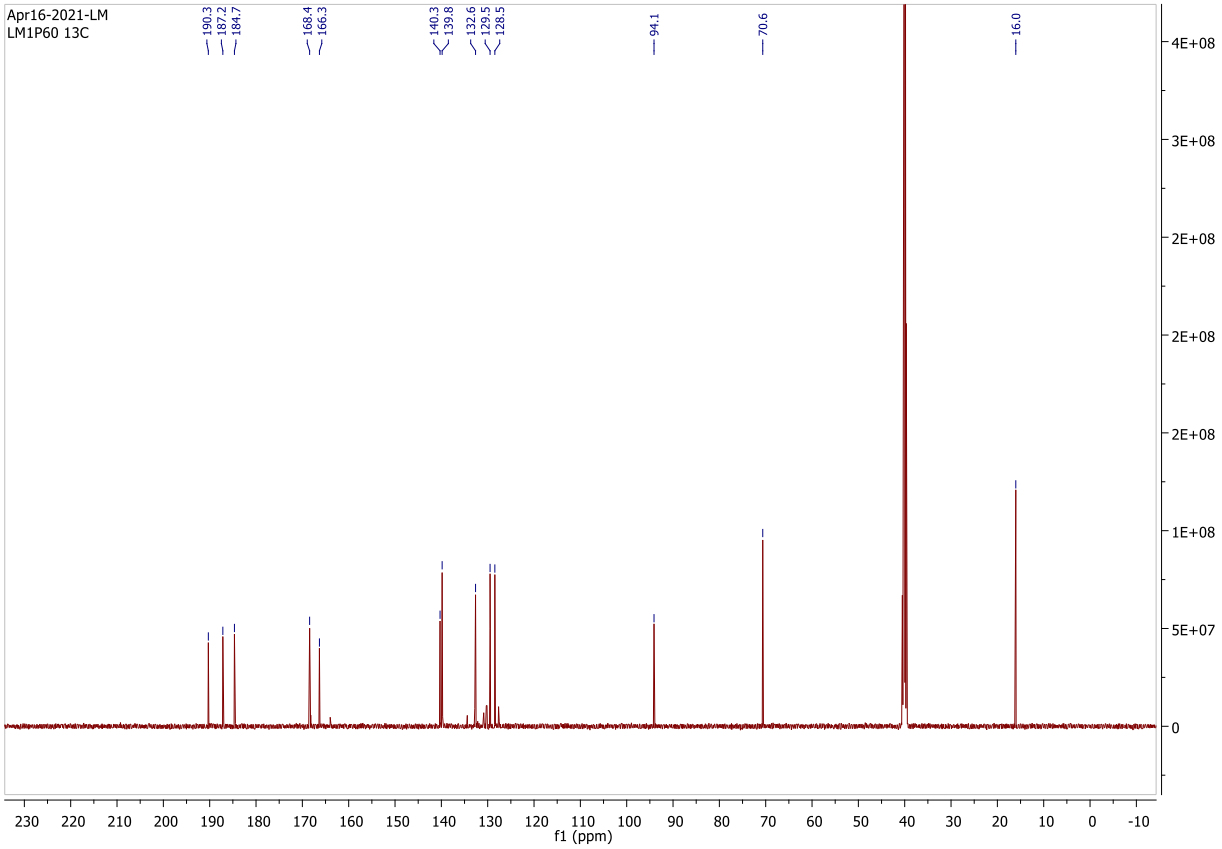

Figure A44. ^{13}C NMR (DMSO-d_6, 126 MHz) spectrum of **2.23**.

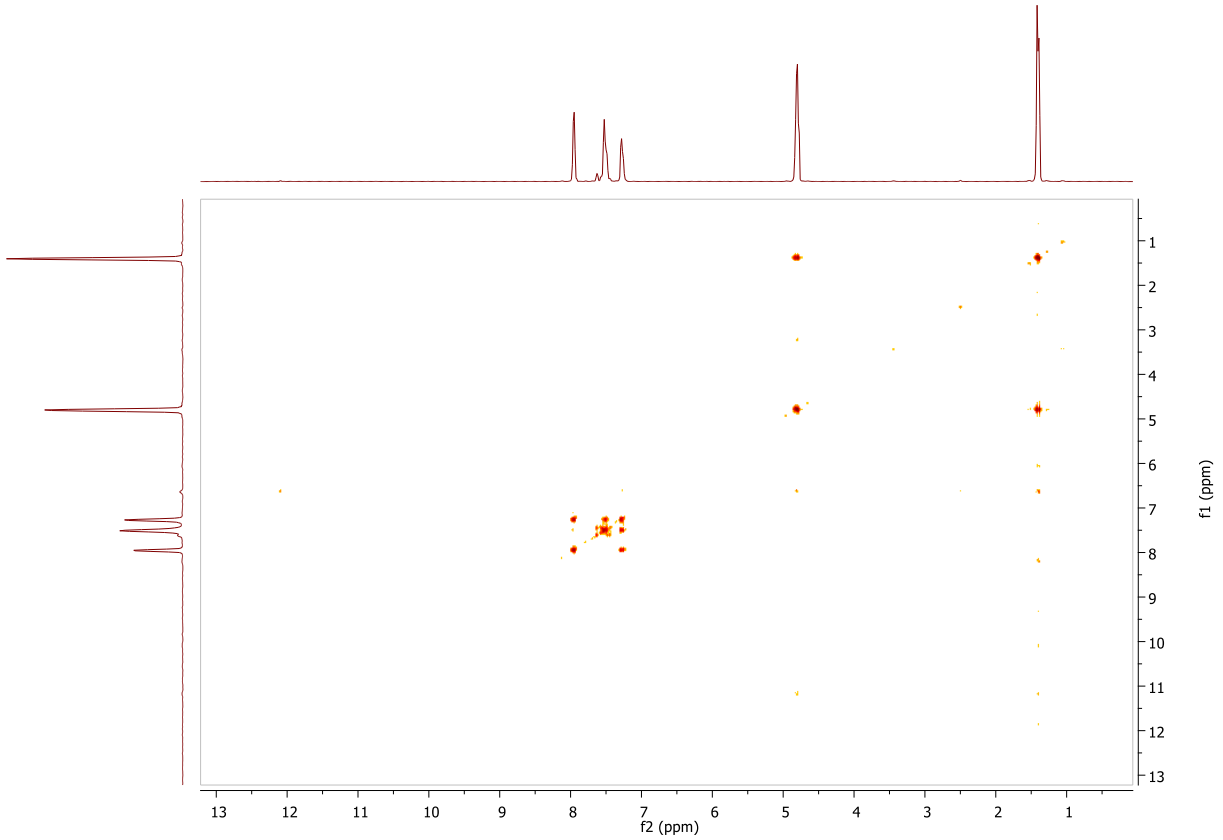

Figure A45. ^{1}H-^{1}H COSY NMR spectrum of **2.23**

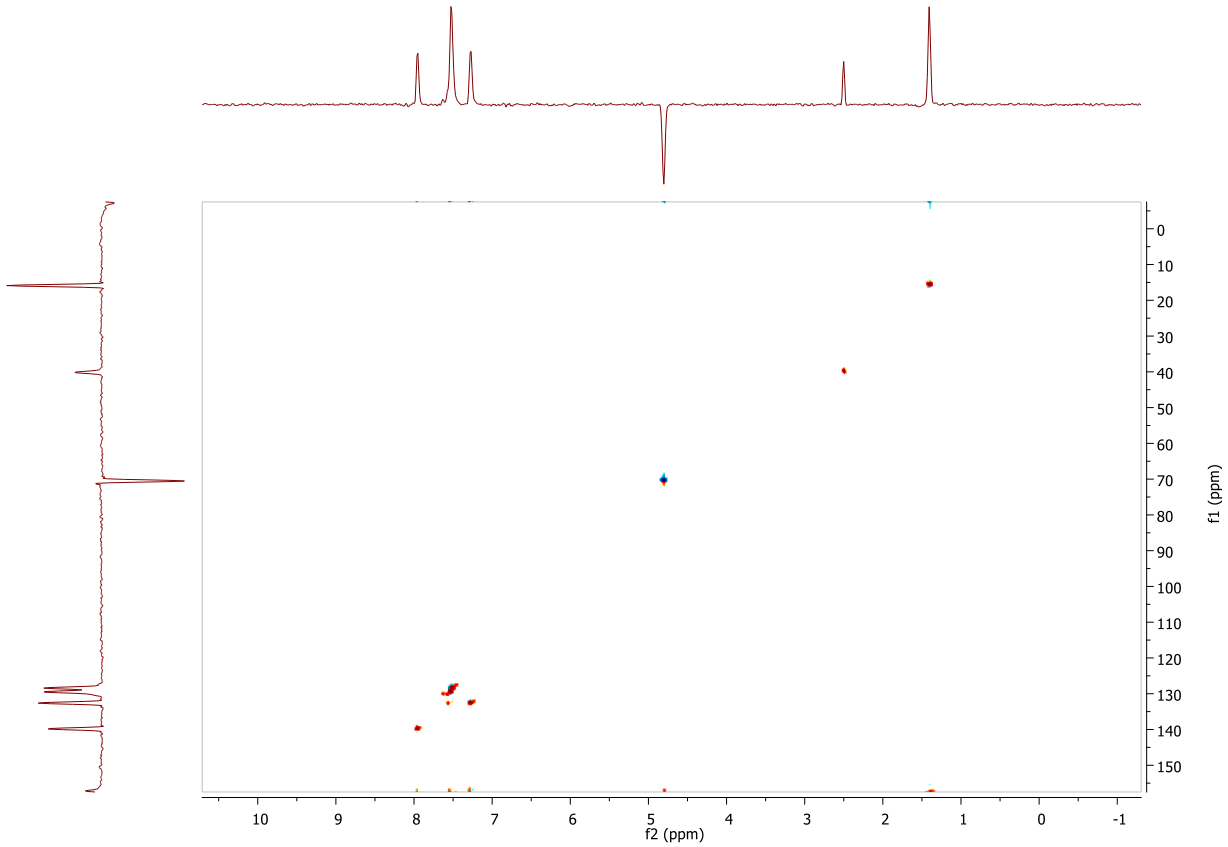

Figure A46. HSQC spectrum of **2.23**

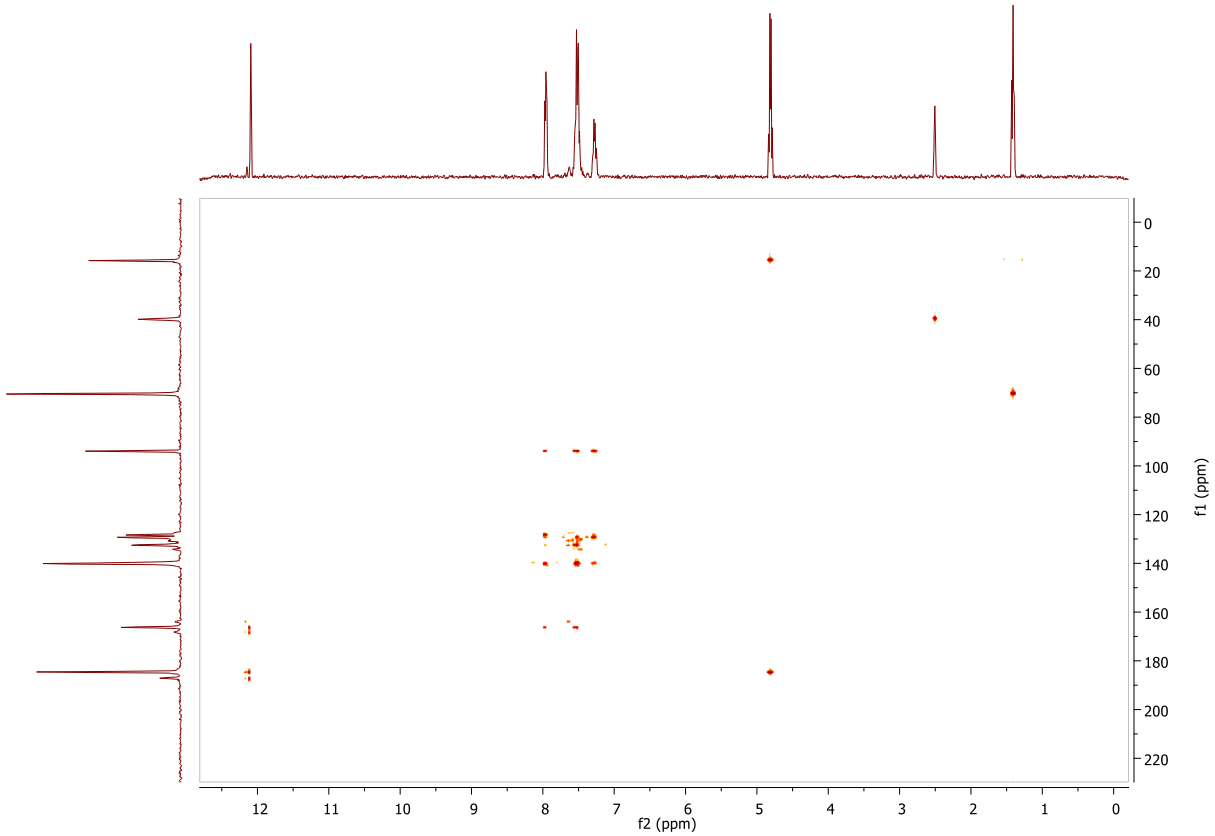

Figure A47. HMBC spectrum of **2.23**

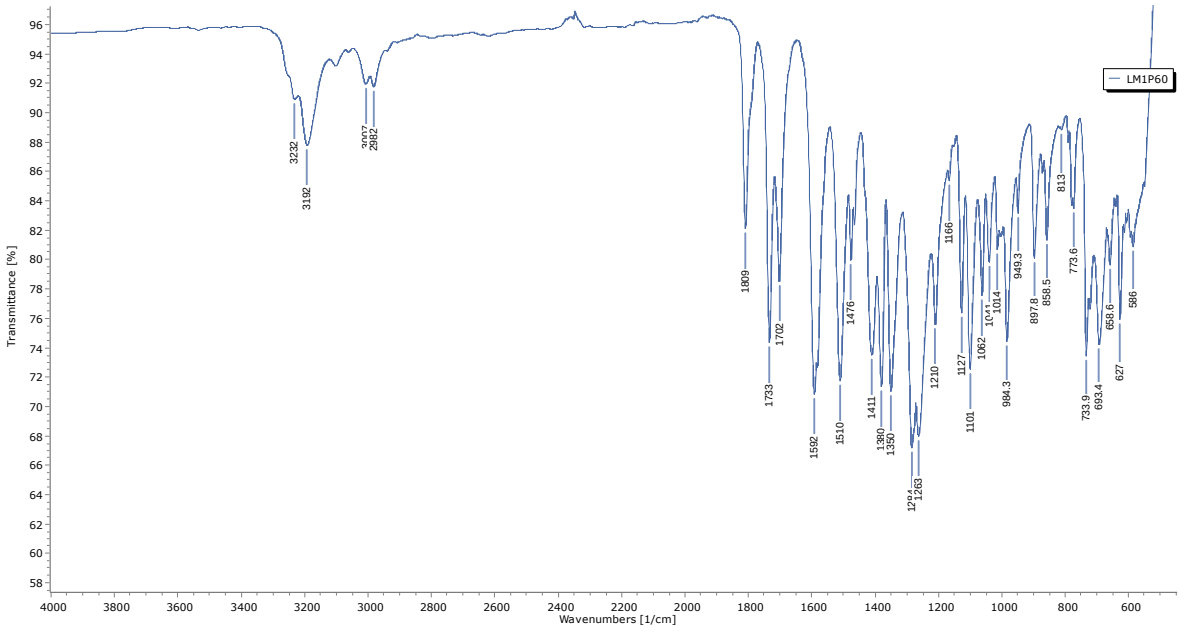

Figure A48. IR spectrum of **2.23**

Compounds

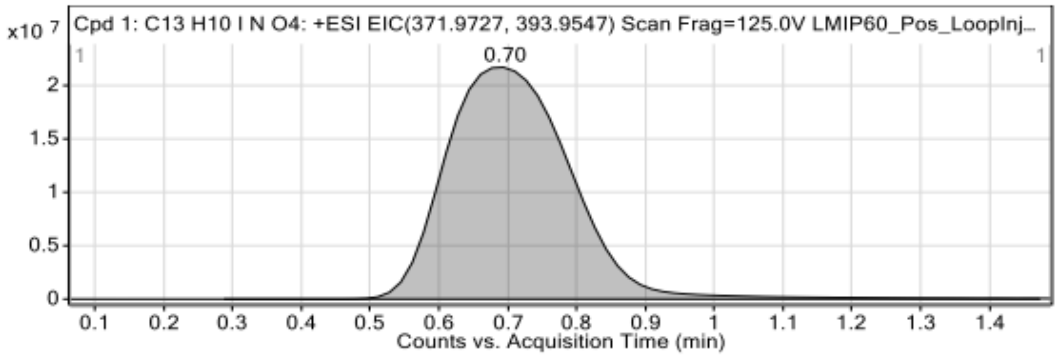

Integration Peak List

Start	RT	End	Height	Area
0.29	0.7	1.47	21498565	273497514

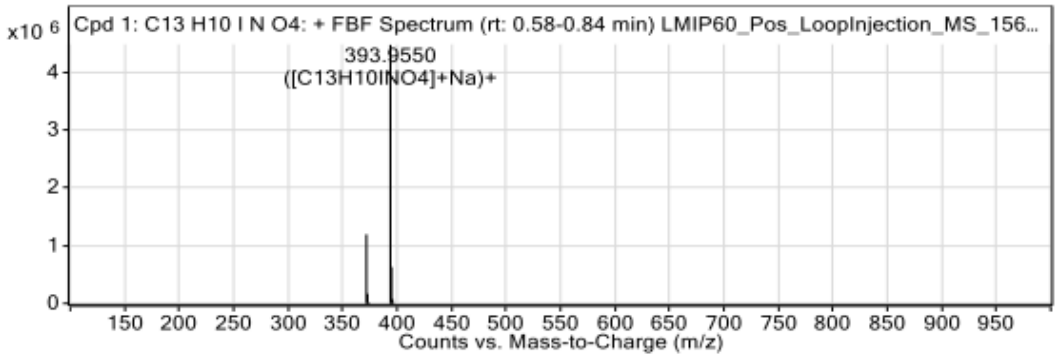

Peak List

m/z	z	Abund	Formula	Ion
371.9728	1	1196103.25	C13H10INO4	(M+H)+
372.9761	1	167462.86	C13H10INO4	(M+H)+
373.9784	1	20403.75	C13H10INO4	(M+H)+
393.955	1	4484876.5	C13H10INO4	(M+Na)+
394.9583	1	630267.38	C13H10INO4	(M+Na)+
395.9603	1	72445.63	C13H10INO4	(M+Na)+
396.9626	1	6382.16	C13H10INO4	(M+Na)+

--- End Of Report ---

Figure A49. HRMS of **2.23**

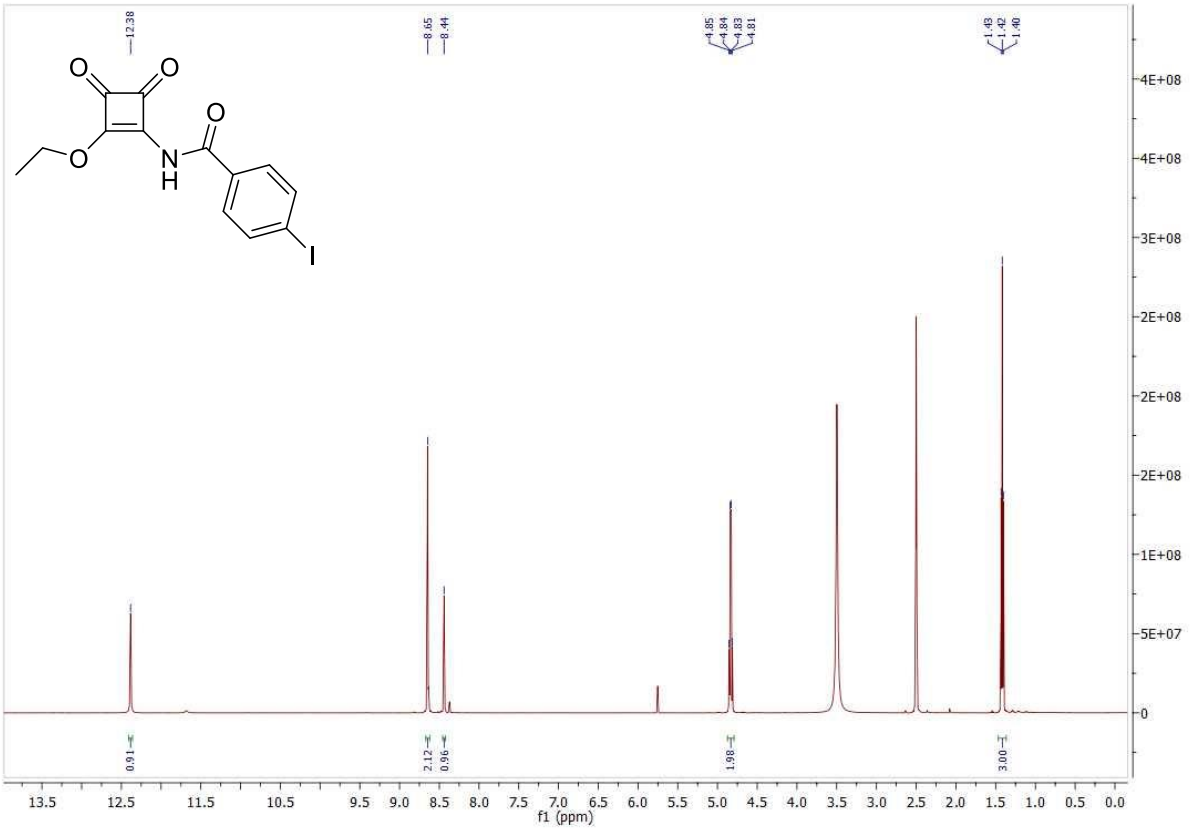

Figure A50. ^{1}H NMR (DMSO-d_6, 500 MHz) spectrum of **2.24**.

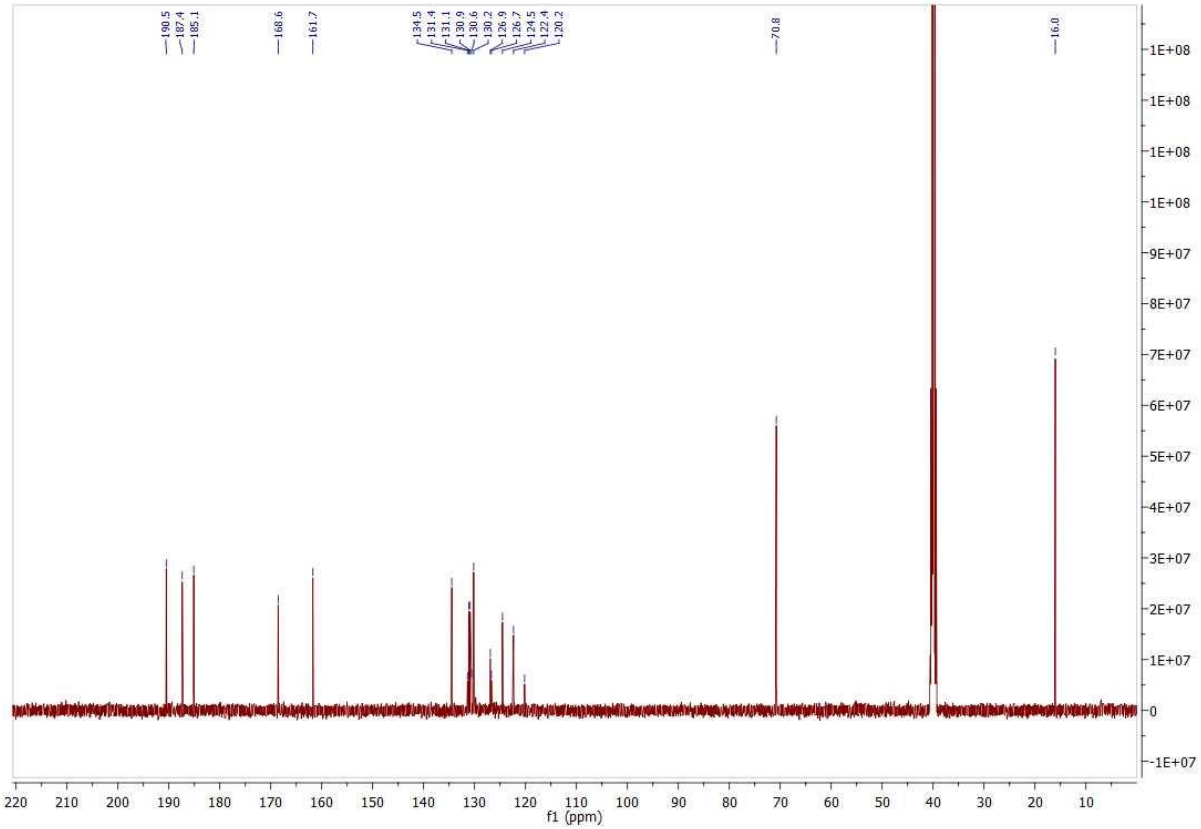

Figure A51. ^{13}C NMR (DMSO-d_6, 126 MHz) spectrum of **2.24**.

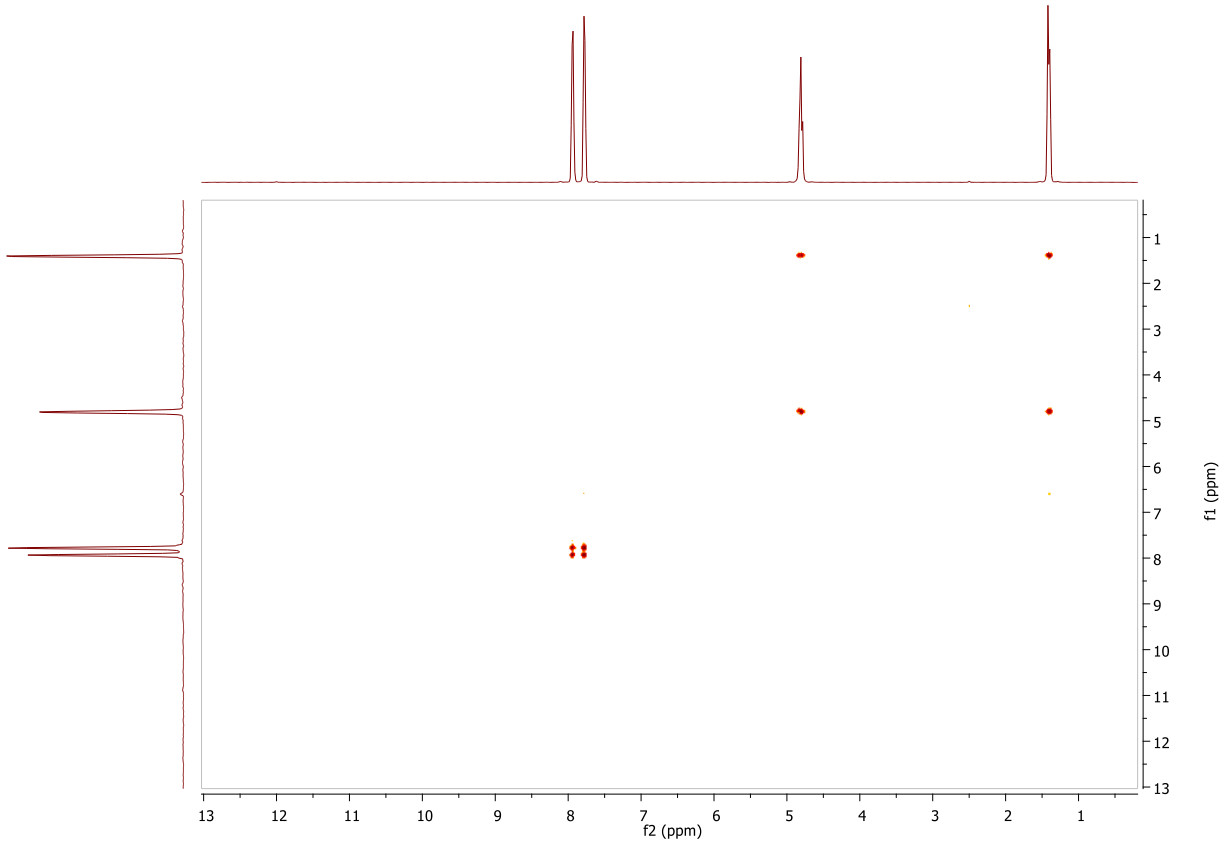

Figure A52. ^{1}H-^{1}H COSY spectrum of **2.24**

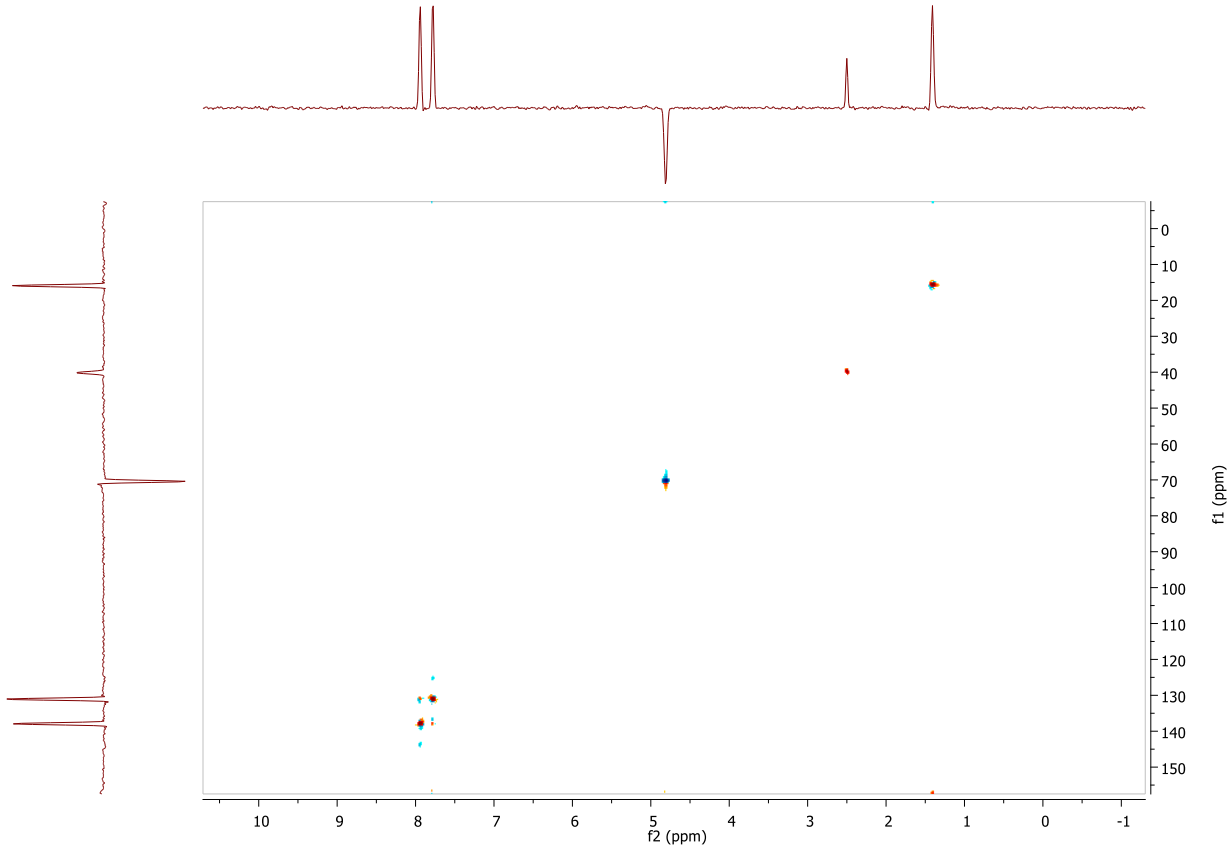

Figure A53. HSQC spectrum of **2.24**

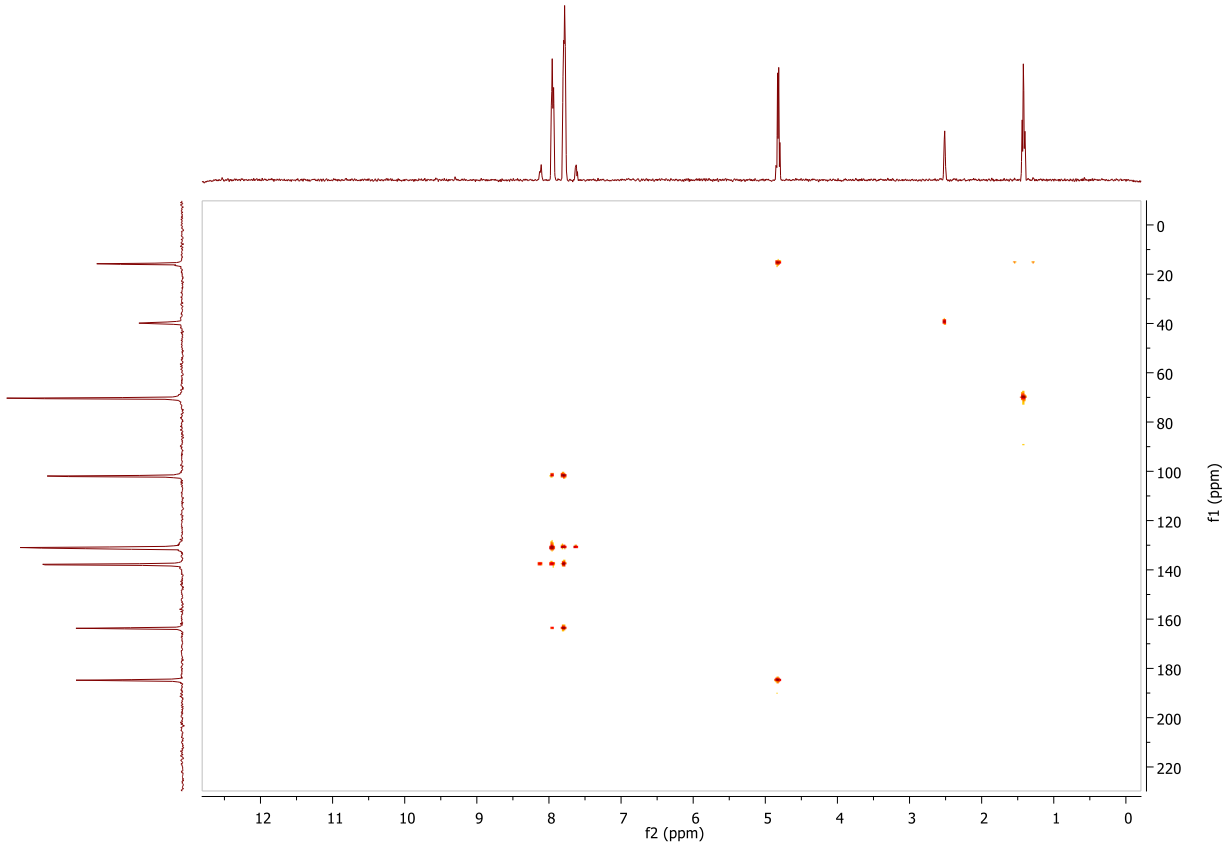

Figure A54. HMBC spectrum of **2.24**

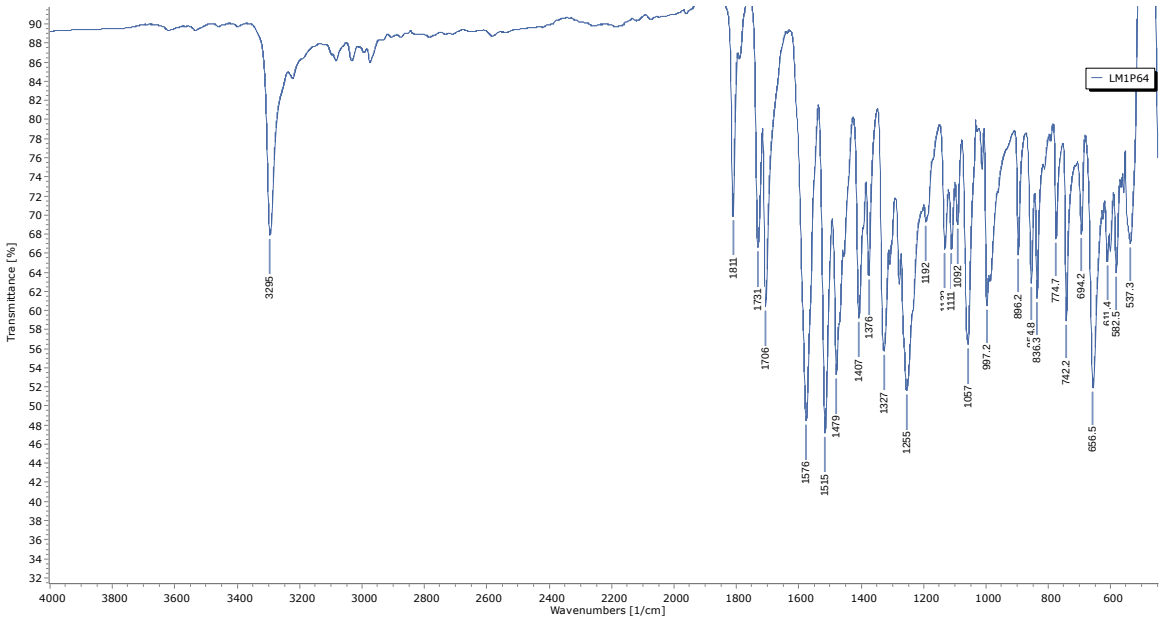

Figure A55. IR spectrum of **2.24**

Compounds

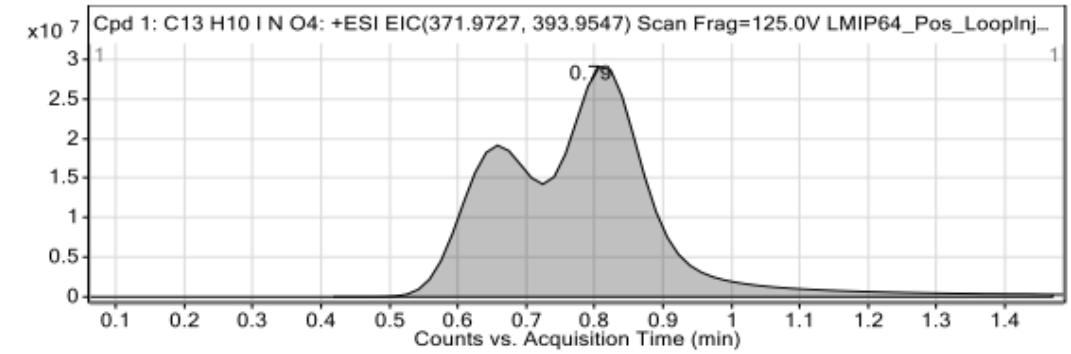

Integration Peak List

Start	RT	End	Height	Area
0.42	0.79	1.47	27848282	399393219

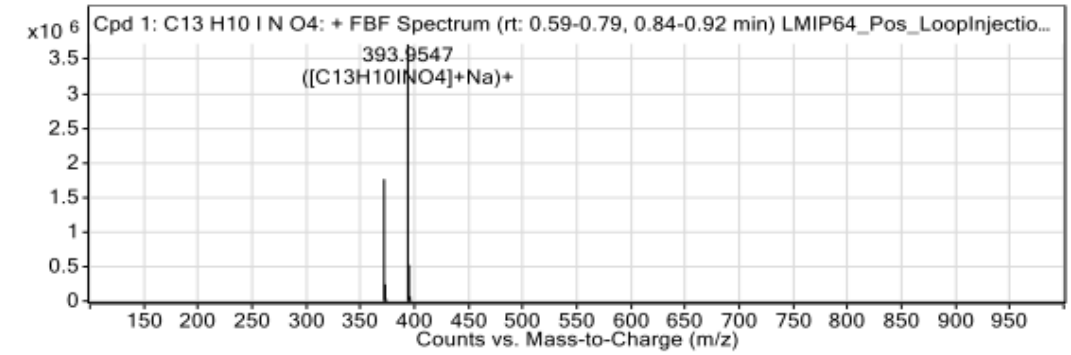

Peak List

m/z	z	Abund	Formula	Ion
371.9727	1	1764381.38	C13H10INO4	(M+H)+
372.9758	1	242278.47	C13H10INO4	(M+H)+
373.9779	1	28882.52	C13H10INO4	(M+H)+
393.9547	1	3720356.25	C13H10INO4	(M+Na)+
394.9579	1	522127.16	C13H10INO4	(M+Na)+
395.96	1	66019.08	C13H10INO4	(M+Na)+
396.9621	1	5653.62	C13H10INO4	(M+Na)+

--- End Of Report ---

Figure A56. HRMS of **2.24**

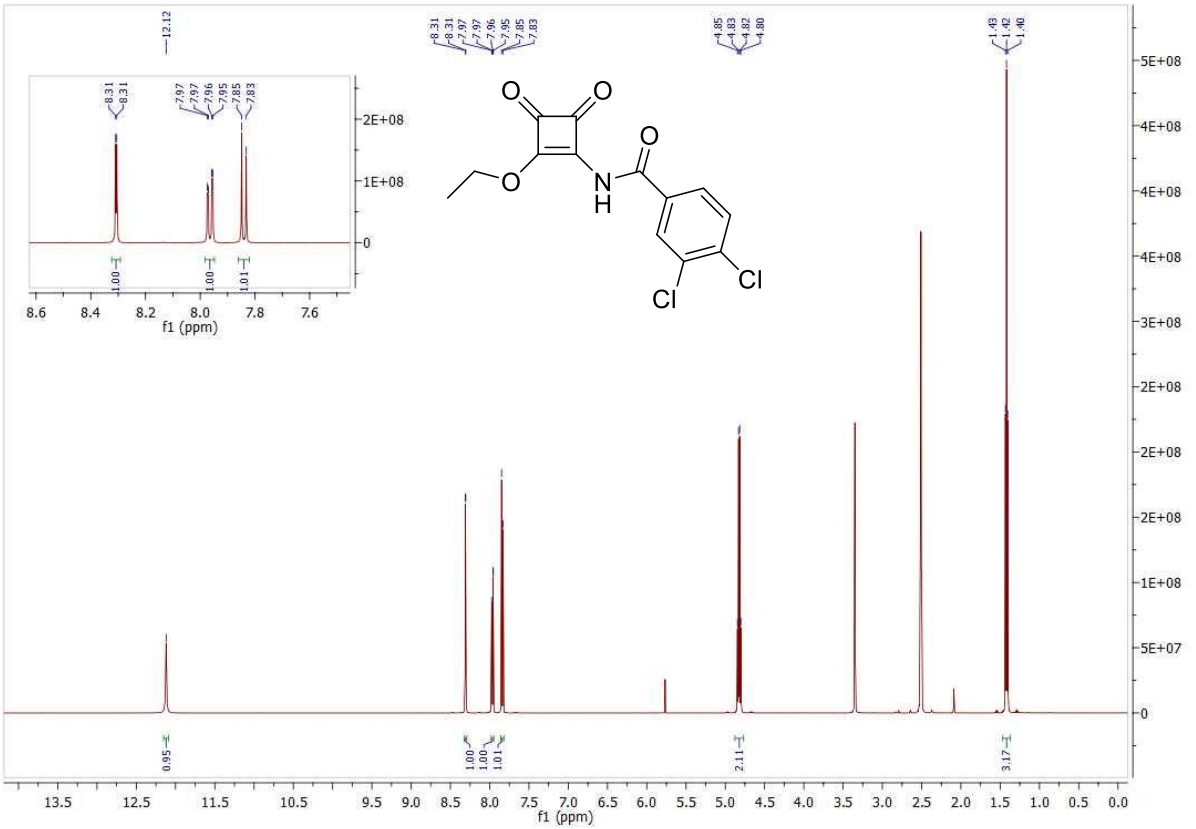

Figure A57. ^{1}H NMR (DMSO-d_6, 500 MHz) spectrum of **2.25**.

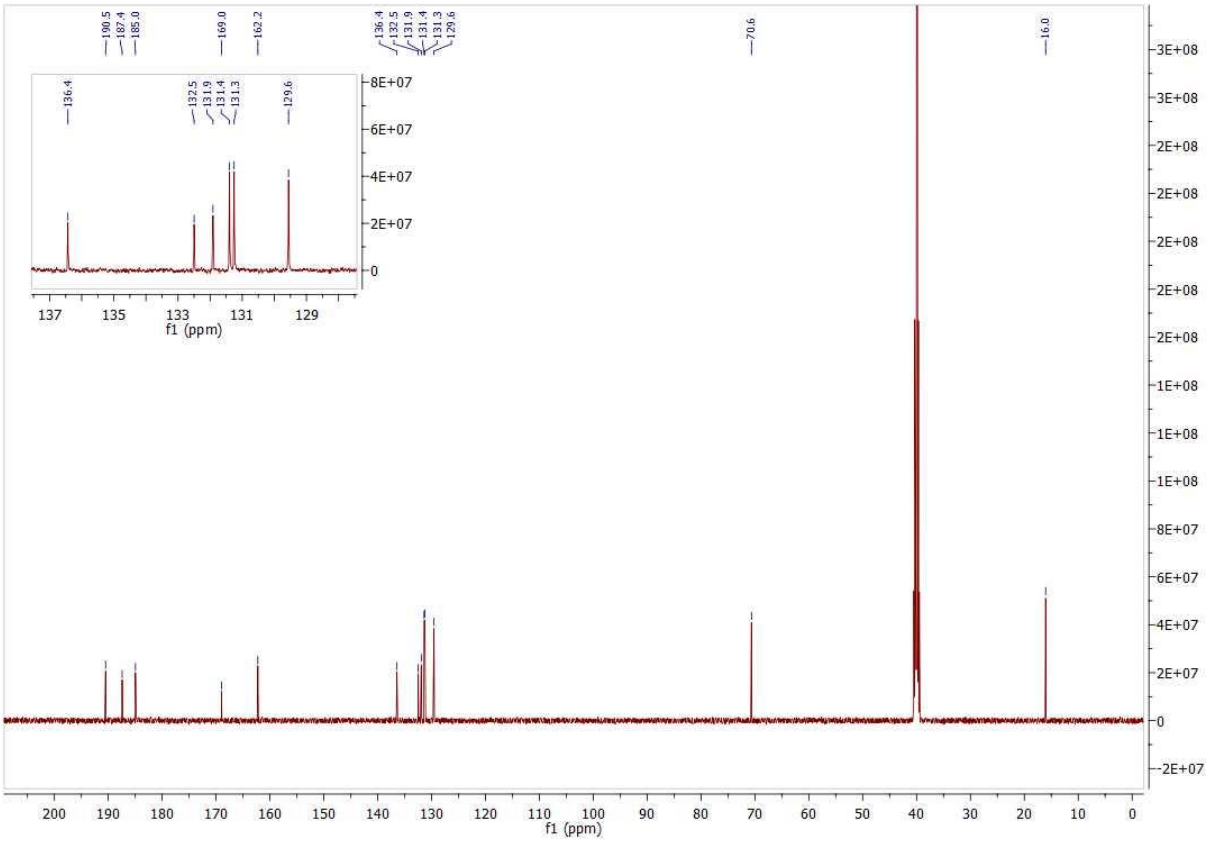

Figure A58. ^{13}C NMR (DMSO-d_6, 126 MHz) spectrum of **2.25**.

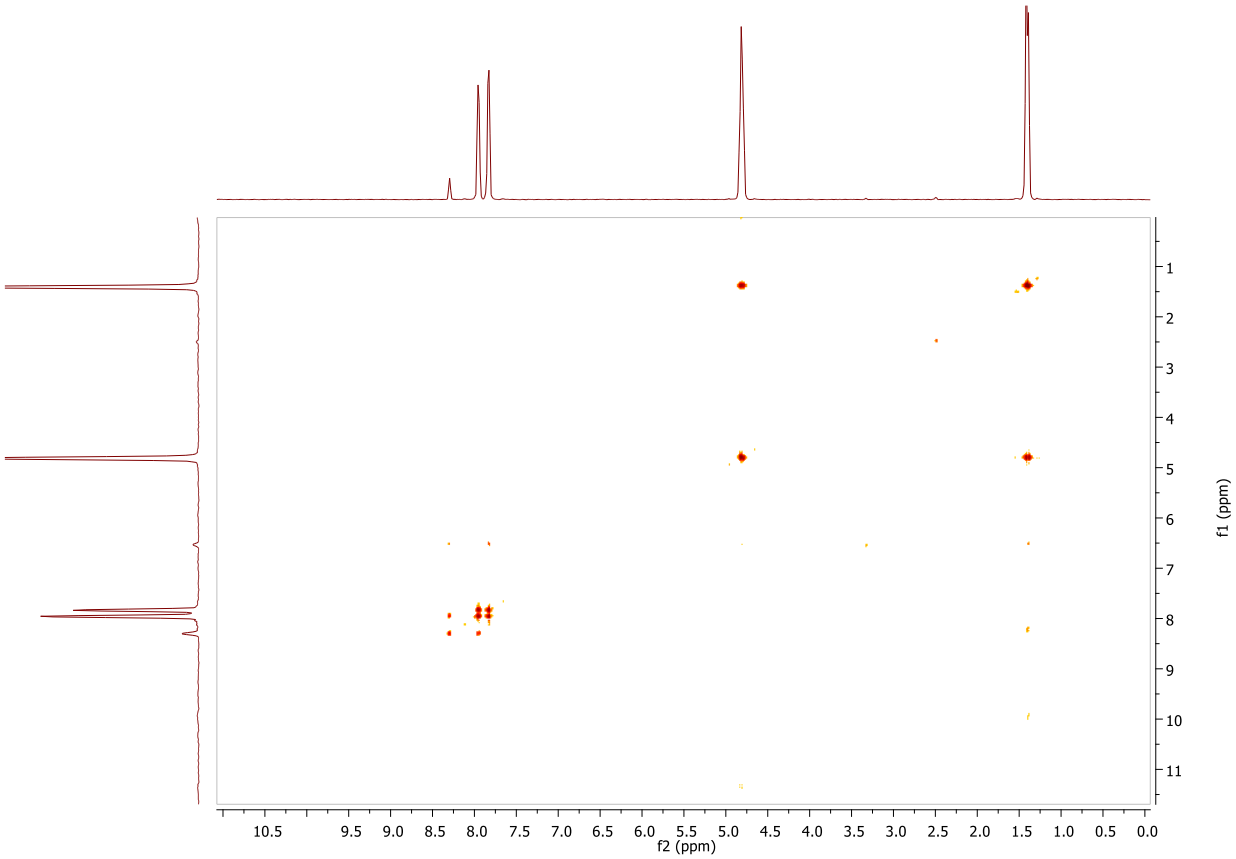

Figure A59. ^{1}H-^{1}H COSY spectrum of **2.25**

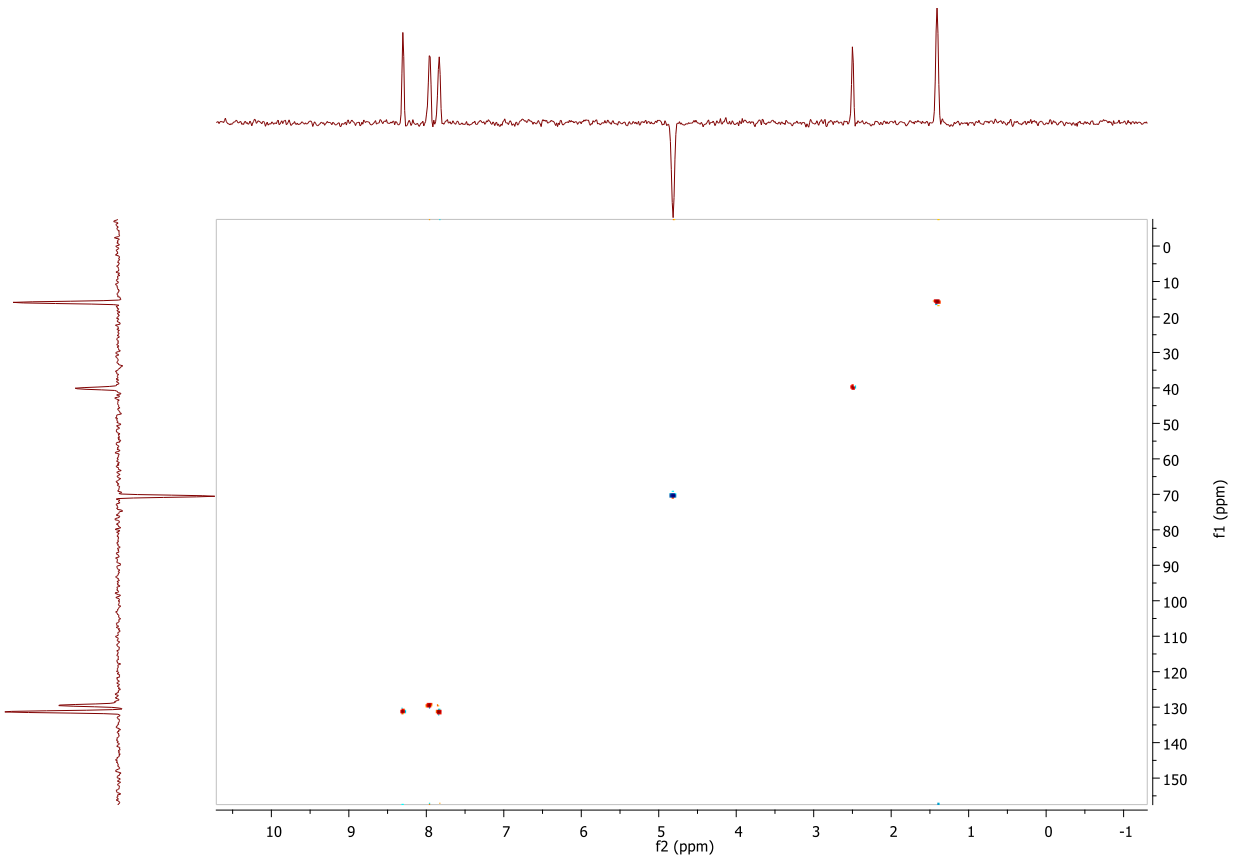

Figure A60. HSQC spectrum of **2.25**

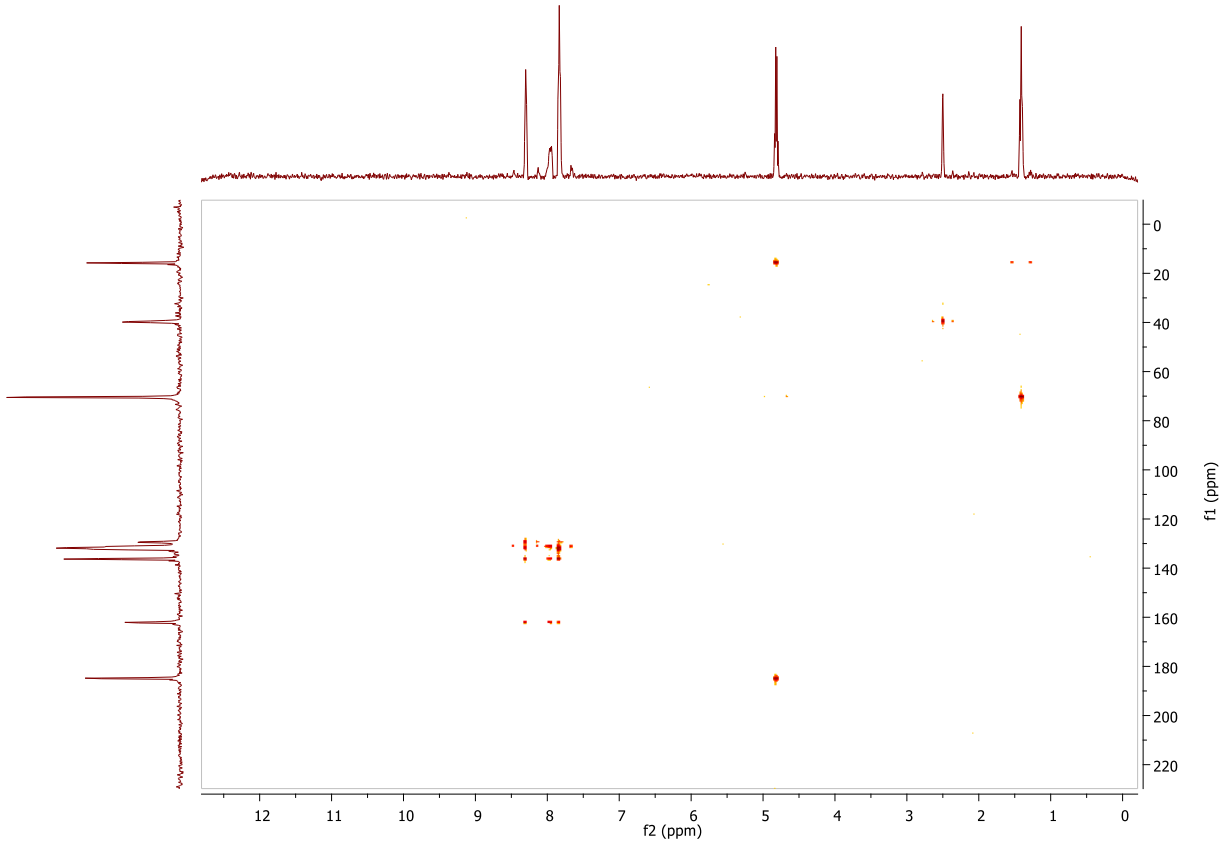

Figure A61. HMBC spectrum of **2.25**

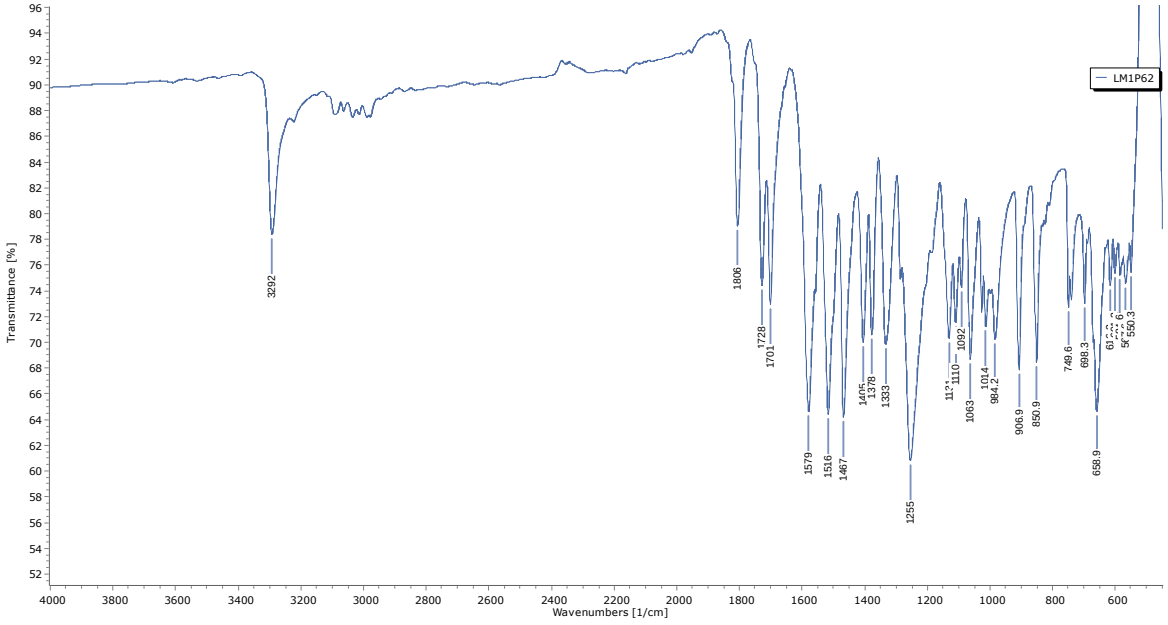

Figure A62. IR spectrum of **2.25**

Compounds

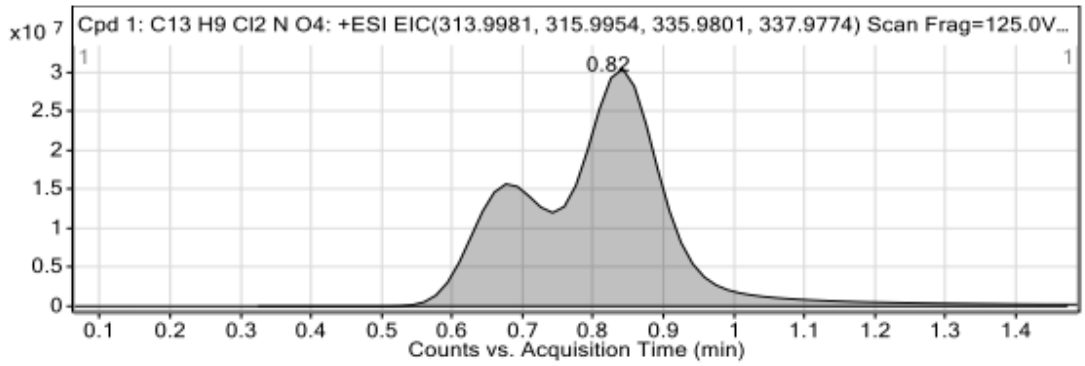

Integration Peak List

Start	RT	End	Height	Area
0.32	0.82	1.47	26273803	367928171

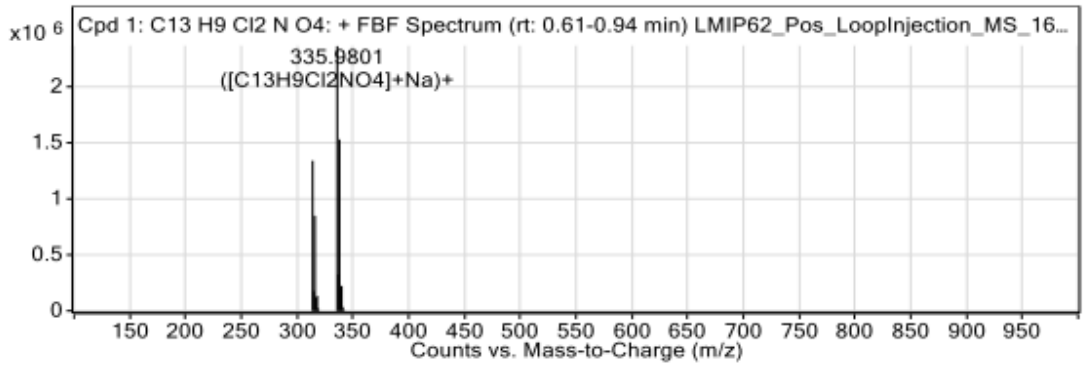

Peak List

m/z	z	Abund	Formula	Ion
313.9982	1	1337021.75	C13H9Cl2NO4	(M+H)+
315.0014	1	176449.2	C13H9Cl2NO4	(M+H)+
315.9953	1	846996.31	C13H9Cl2NO4	(M+H)+
316.9993	1	116364.72	C13H9Cl2NO4	(M+H)+
317.9932	1	134404.78	C13H9Cl2NO4	(M+H)+
335.9801	1	2360401	C13H9Cl2NO4	(M+Na)+
336.9834	1	323599.44	C13H9Cl2NO4	(M+Na)+
337.9774	1	1525534.63	C13H9Cl2NO4	(M+Na)+
338.9806	1	194775.28	C13H9Cl2NO4	(M+Na)+
339.9752	1	222677.34	C13H9Cl2NO4	(M+Na)+

--- End Of Report ---

Figure A63. HRMS of **2.25**

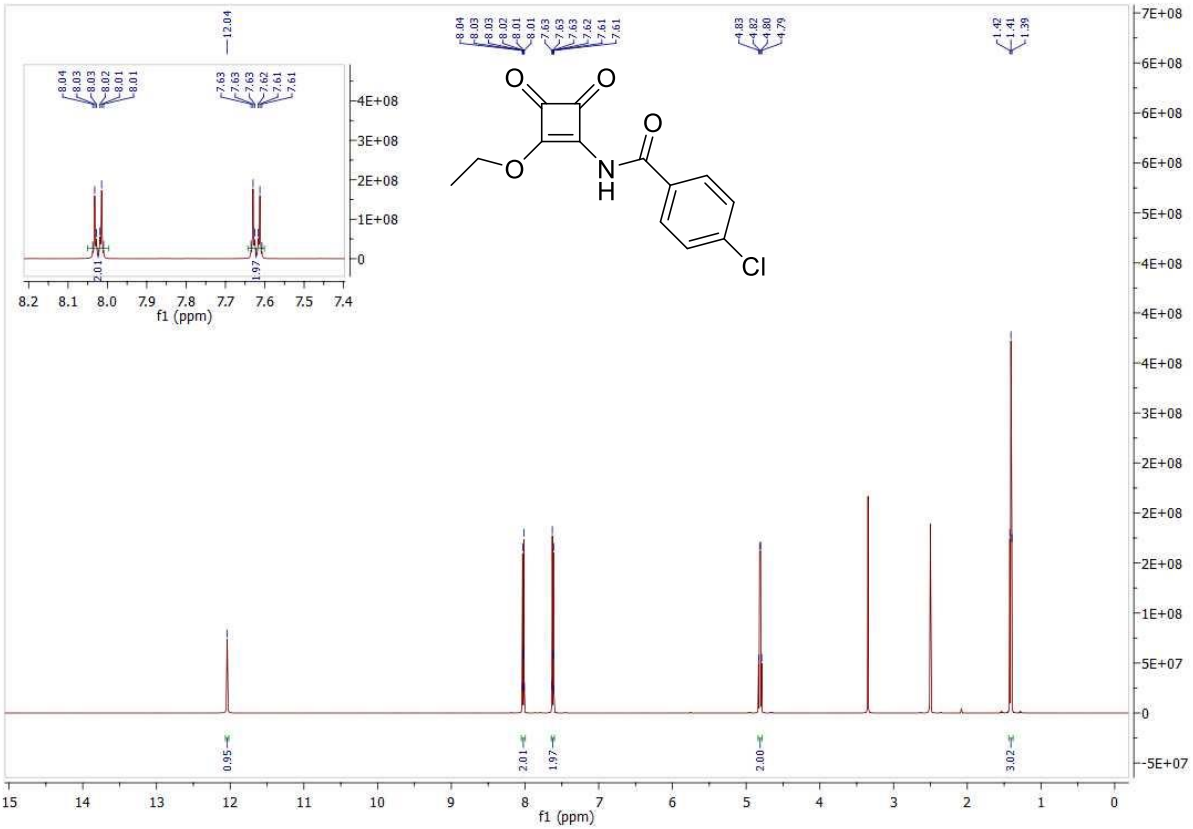

Figure A64. ^{1}H NMR (DMSO-d_6, 500 MHz) spectrum of **2.26**.

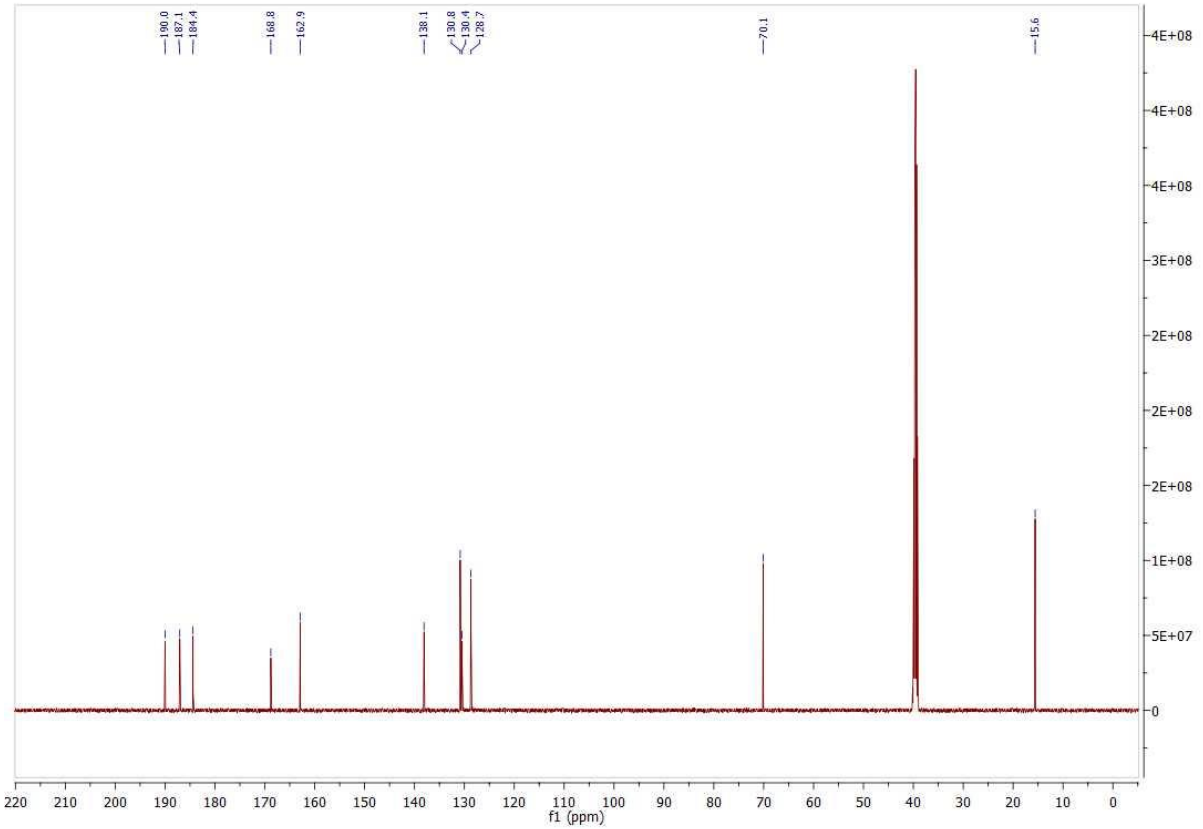

Figure A65. ^{13}C NMR (DMSO-d_6, 126 MHz) spectrum of **2.26**.

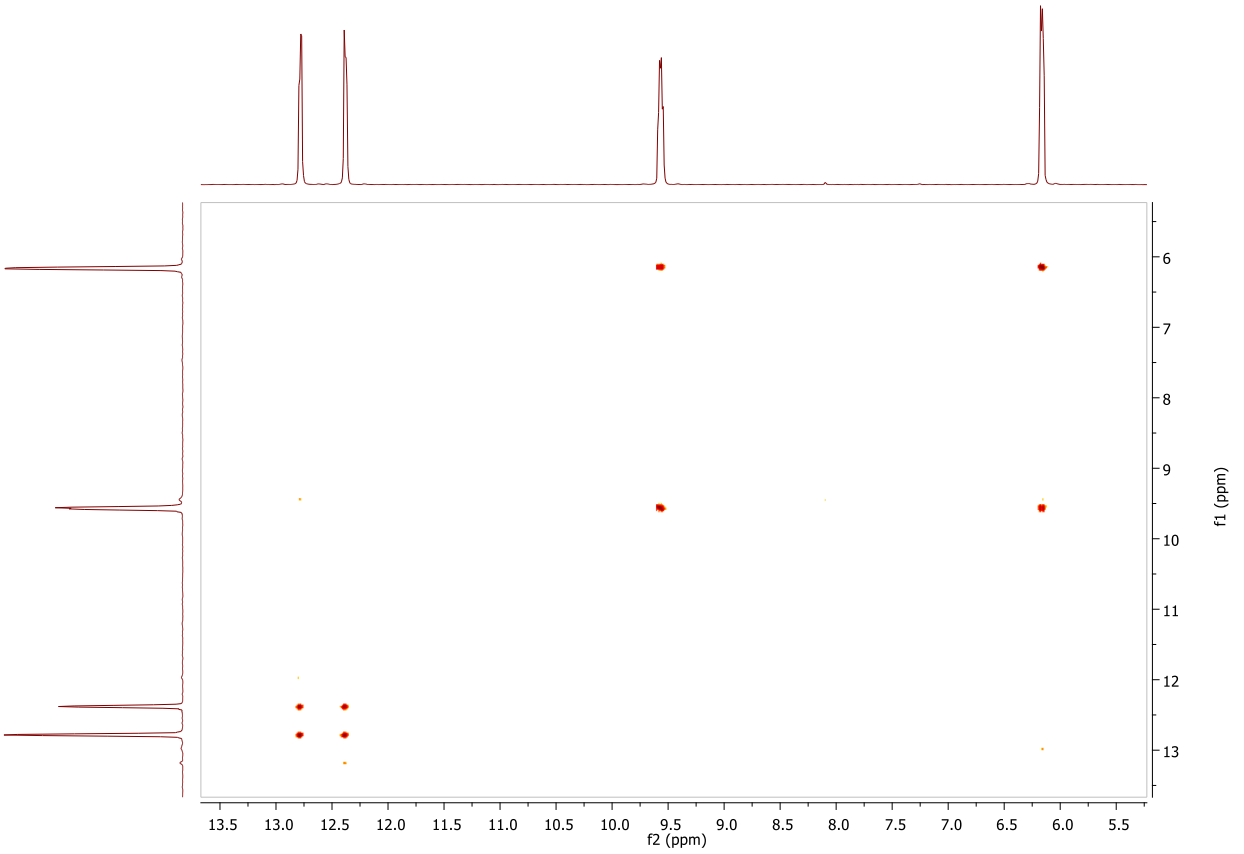

Figure A66. ^{1}H-^{1}H COSY spectrum of **2.26**

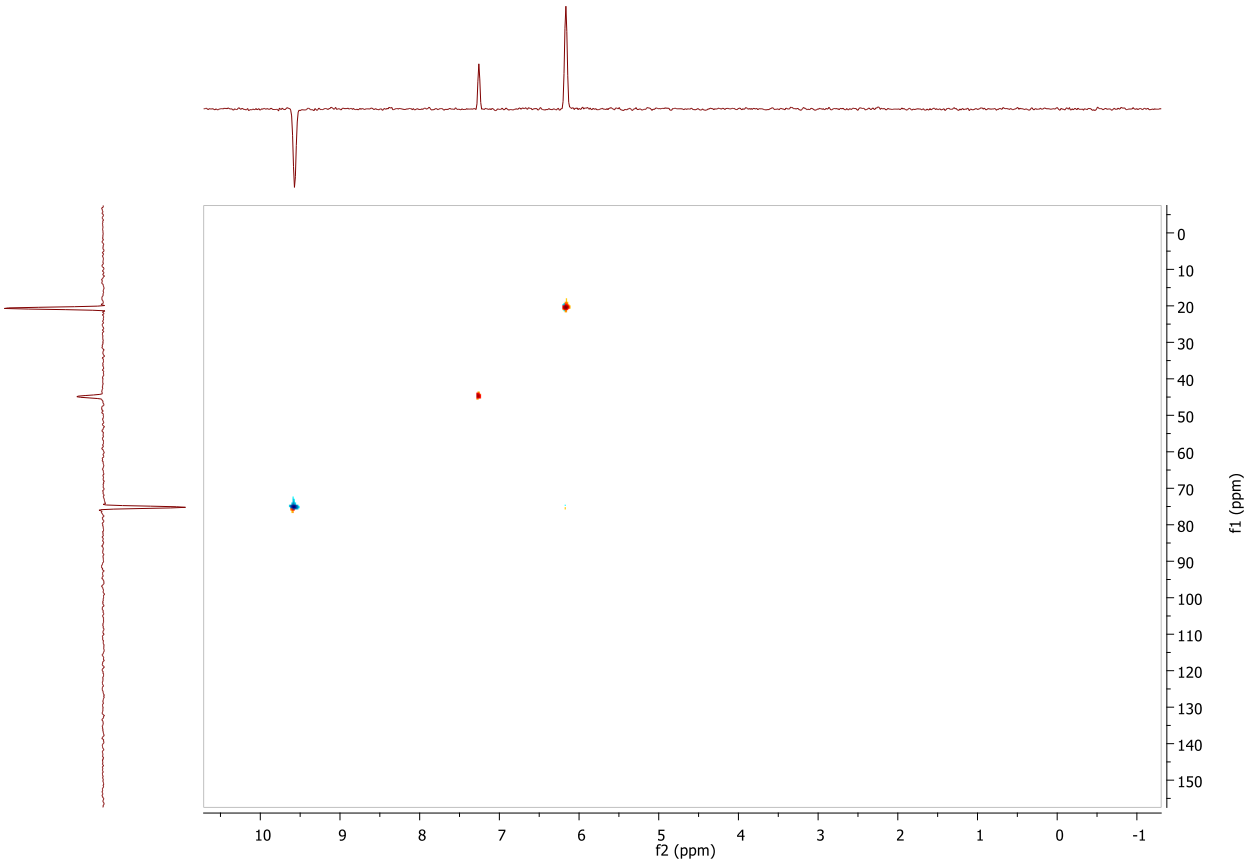

Figure A67. HSQC spectrum of **2.26**

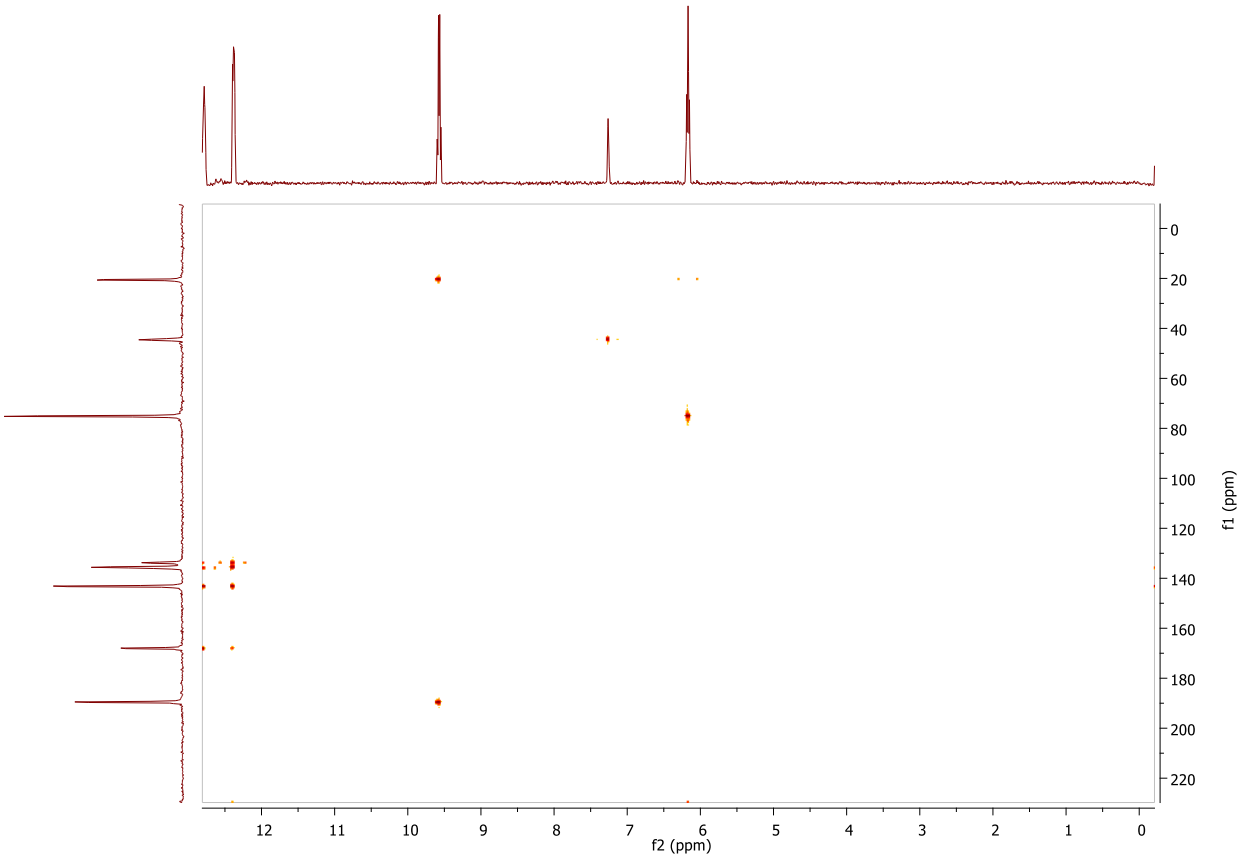

Figure A68. HMBC spectrum of **2.26**

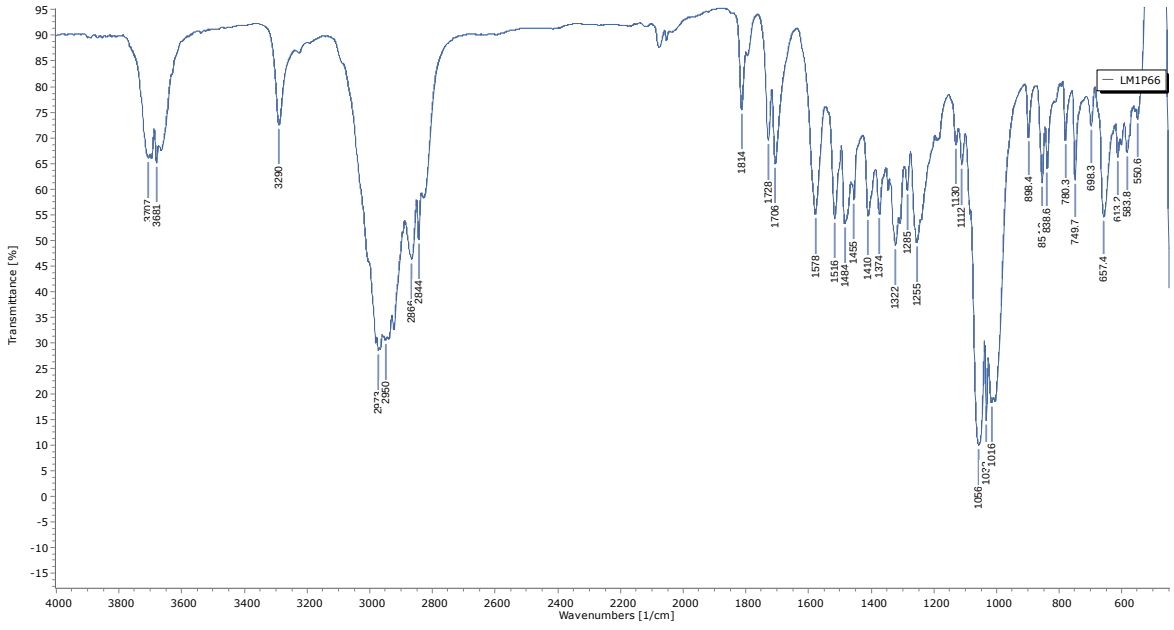

Figure A69. IR spectrum of **2.26**

Compounds

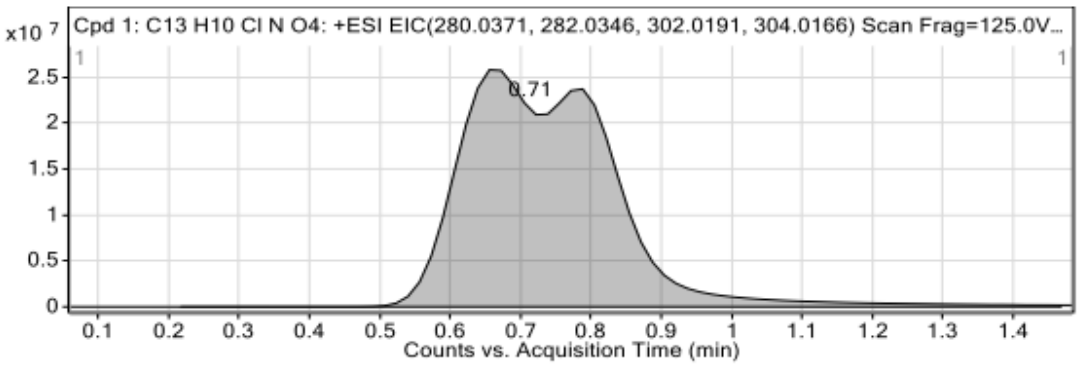

Integration Peak List

Start	RT	End	Height	Area
0.22	0.71	1.47	25315312	386370120

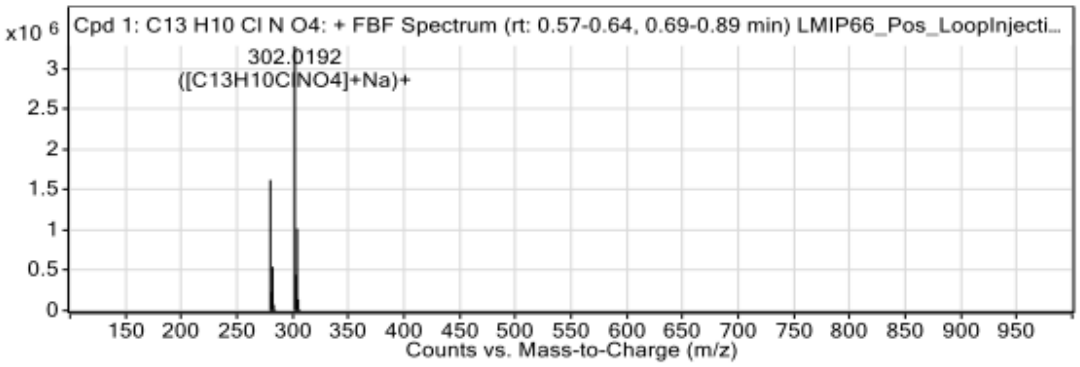

Peak List

m/z	z	Abund	Formula	Ion
280.037	1	1620053	C13H10ClNO4	(M+H)+
281.0405	1	228181.17	C13H10ClNO4	(M+H)+
282.0346	1	543549.5	C13H10ClNO4	(M+H)+
283.0382	1	73518.92	C13H10ClNO4	(M+H)+
284.039	1	10691.38	C13H10ClNO4	(M+H)+
302.0192	1	3282117.5	C13H10ClNO4	(M+Na)+
303.0224	1	444767.75	C13H10ClNO4	(M+Na)+
304.0164	1	1017450.31	C13H10ClNO4	(M+Na)+
305.0197	1	139950.11	C13H10ClNO4	(M+Na)+
306.0213	1	17136.4	C13H10ClNO4	(M+Na)+

--- End Of Report ---

Figure A70. HRMS of **2.26**

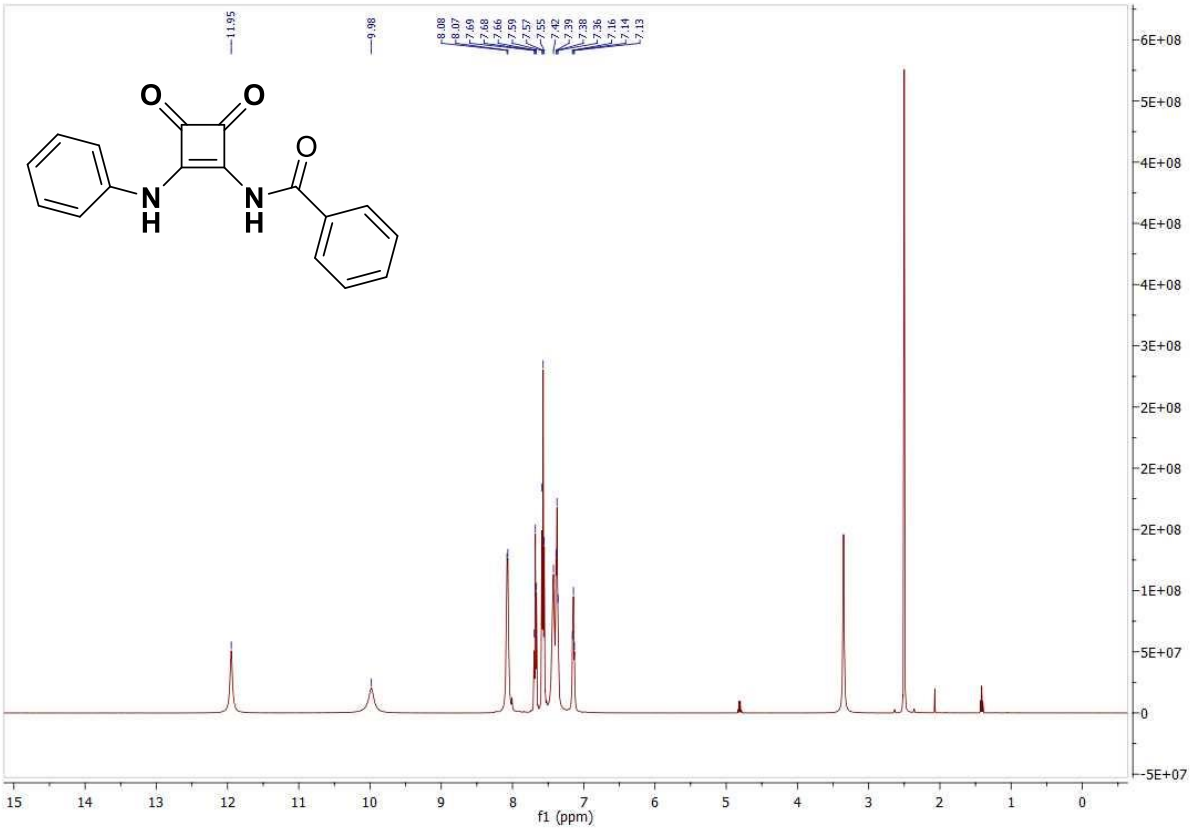

Figure A71. ^{1}H NMR (DMSO-d_6, 500 MHz) spectrum of **2.27**.

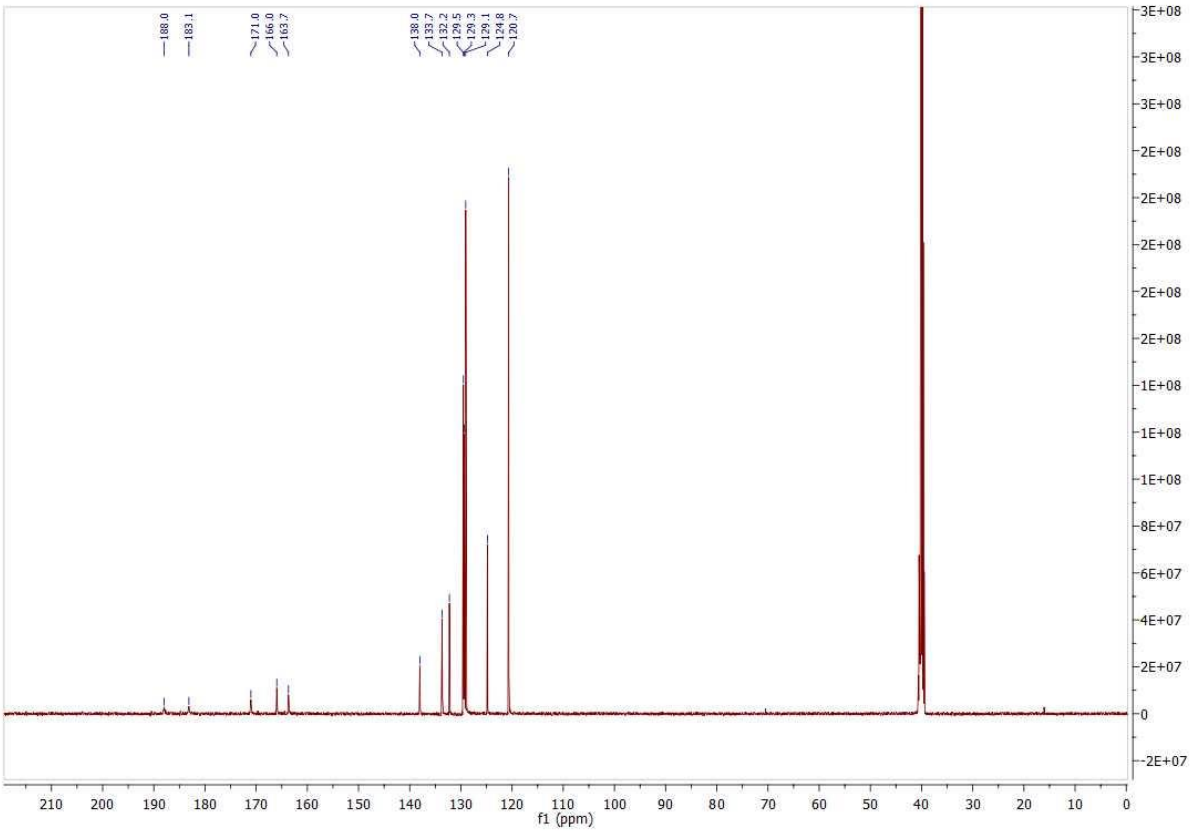

Figure A72. ^{13}C NMR (DMSO-d_6, 126 MHz) spectrum of **2.27**.

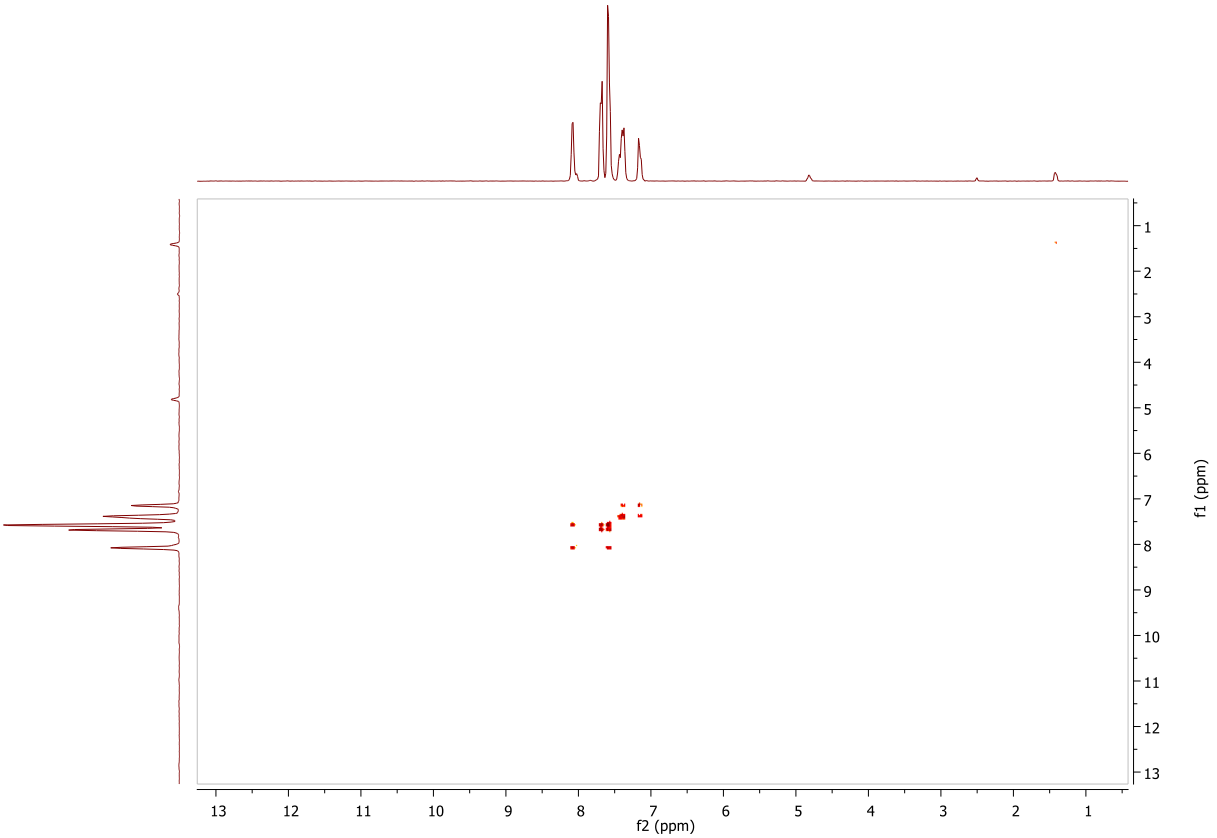

Figure A73. ^{1}H-^{1}H COSY spectrum of **2.27**

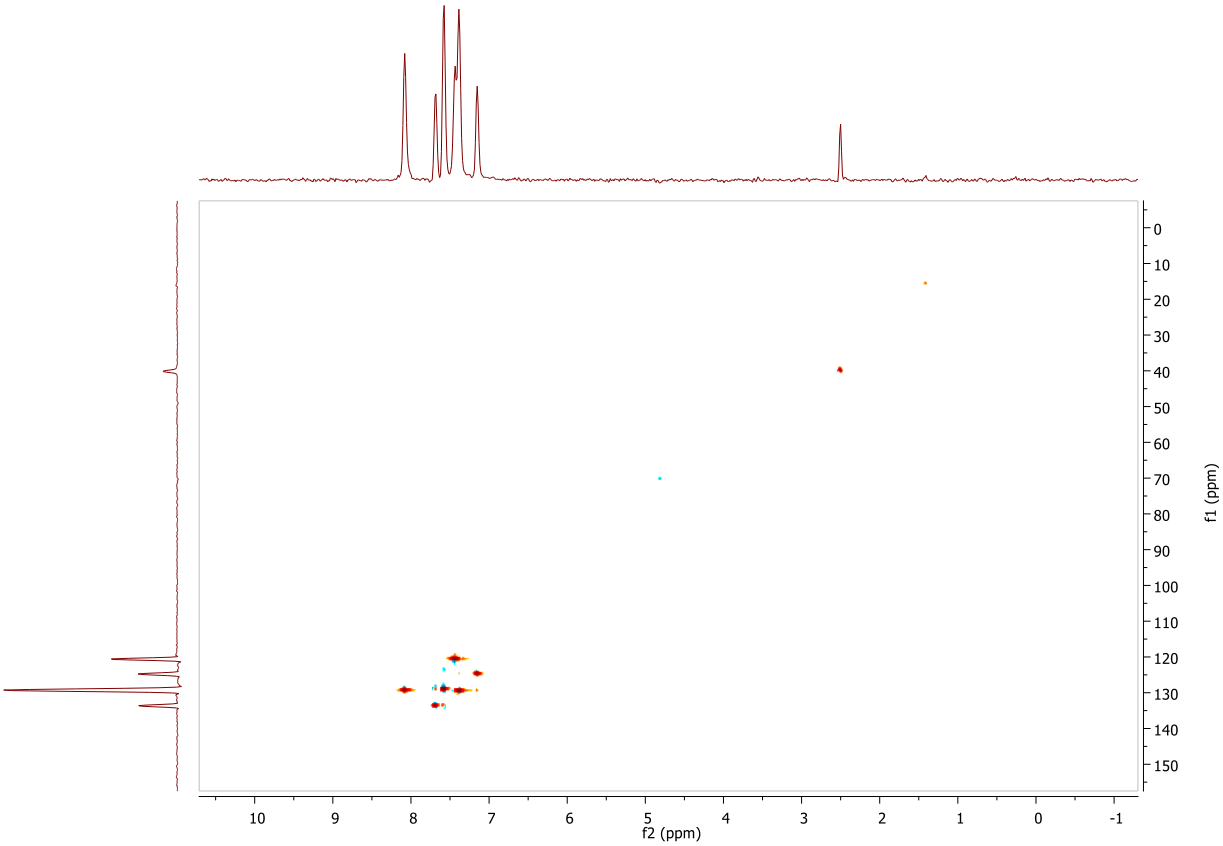

Figure A74. HSQC spectrum of **2.27**

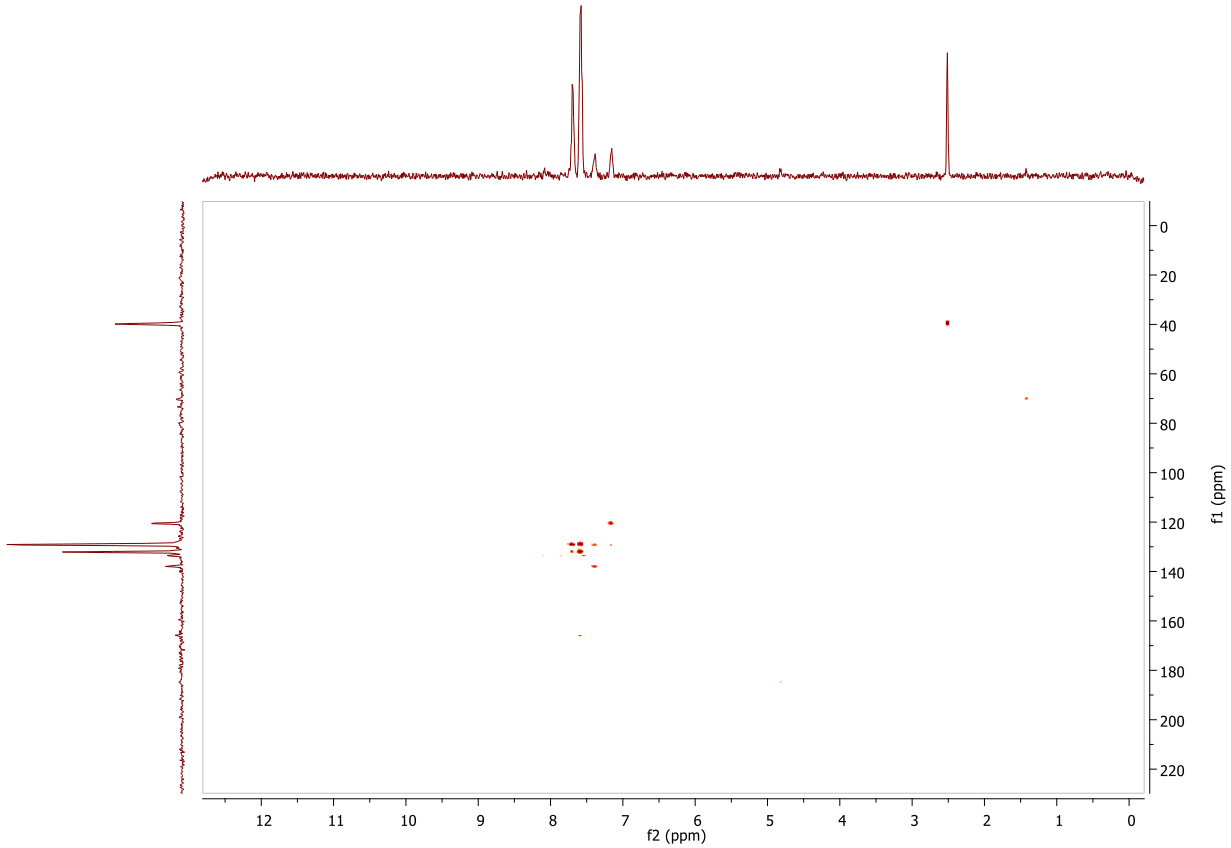

Figure A75. HMBC spectrum of **2.27**

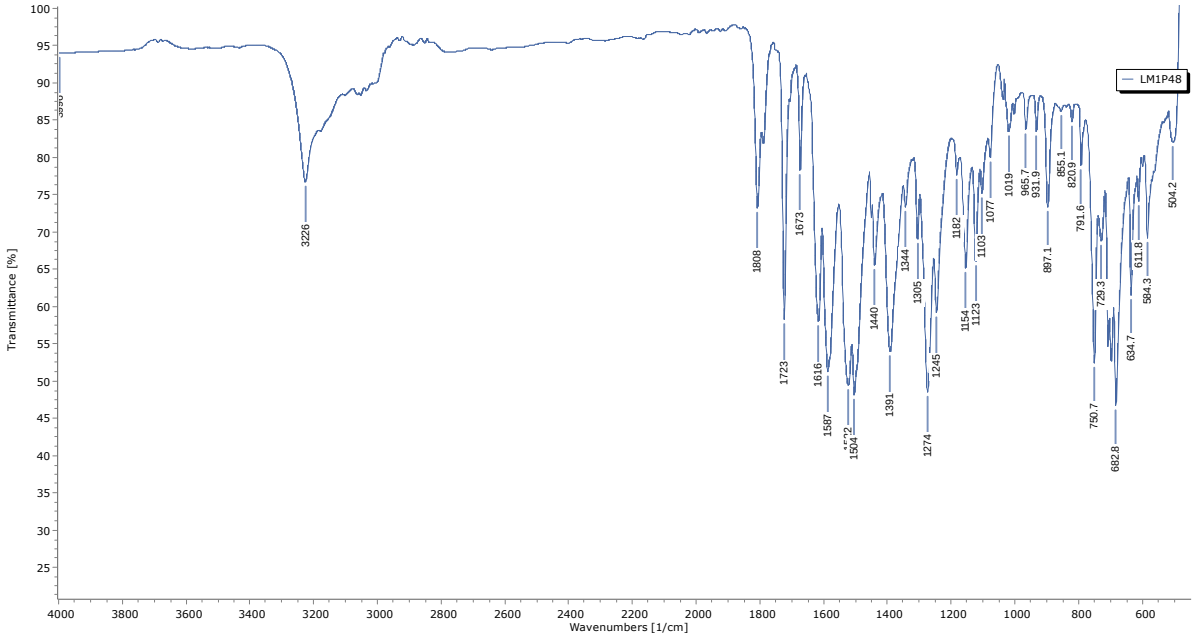

Figure A76. IR spectrum of **2.27**

Compounds

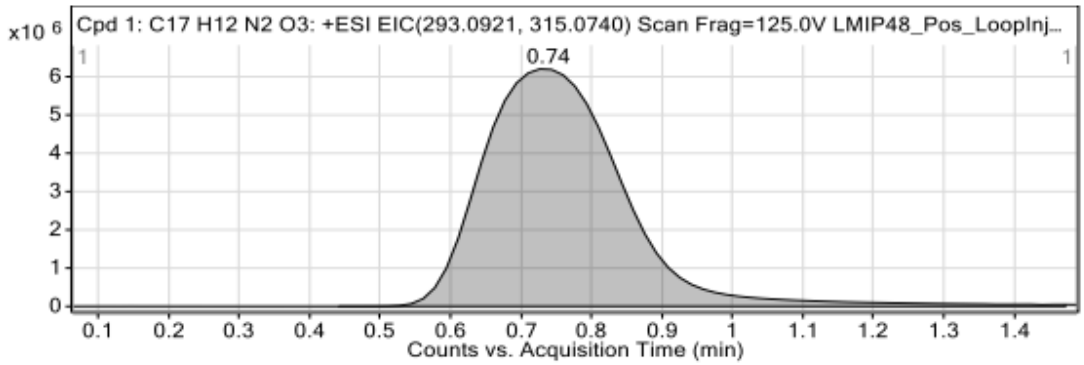

Integration Peak List

Start	RT	End	Height	Area
0.44	0.74	1.47	6065743	84953217

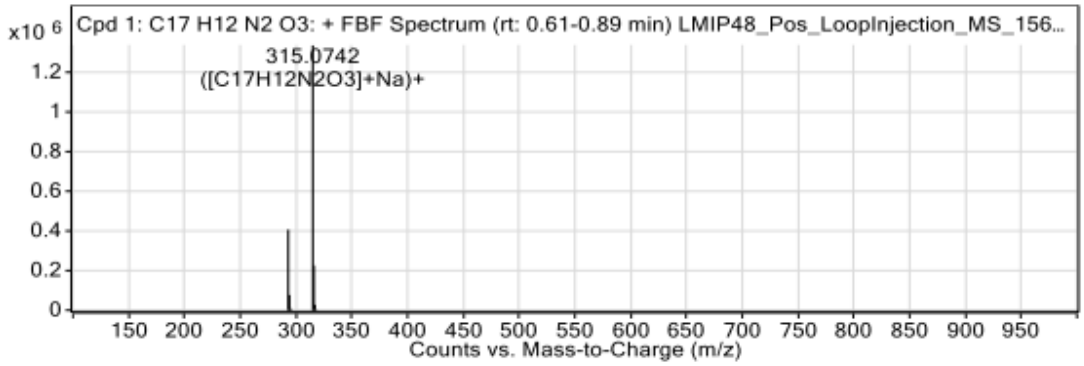

Peak List

m/z	z	Abund	Formula	Ion
293.0926	1	407026.53	C17H12N2O3	(M+H)+
294.0955	1	76758.41	C17H12N2O3	(M+H)+
295.0992	1	9511.4	C17H12N2O3	(M+H)+
296.1039	1	895.61	C17H12N2O3	(M+H)+
315.0742	1	1339016.38	C17H12N2O3	(M+Na)+
316.0776	1	226085.53	C17H12N2O3	(M+Na)+
317.0805	1	27438.29	C17H12N2O3	(M+Na)+
318.0829	1	2875.02	C17H12N2O3	(M+Na)+

--- End Of Report ---

Figure A77. HRMS of **2.27**

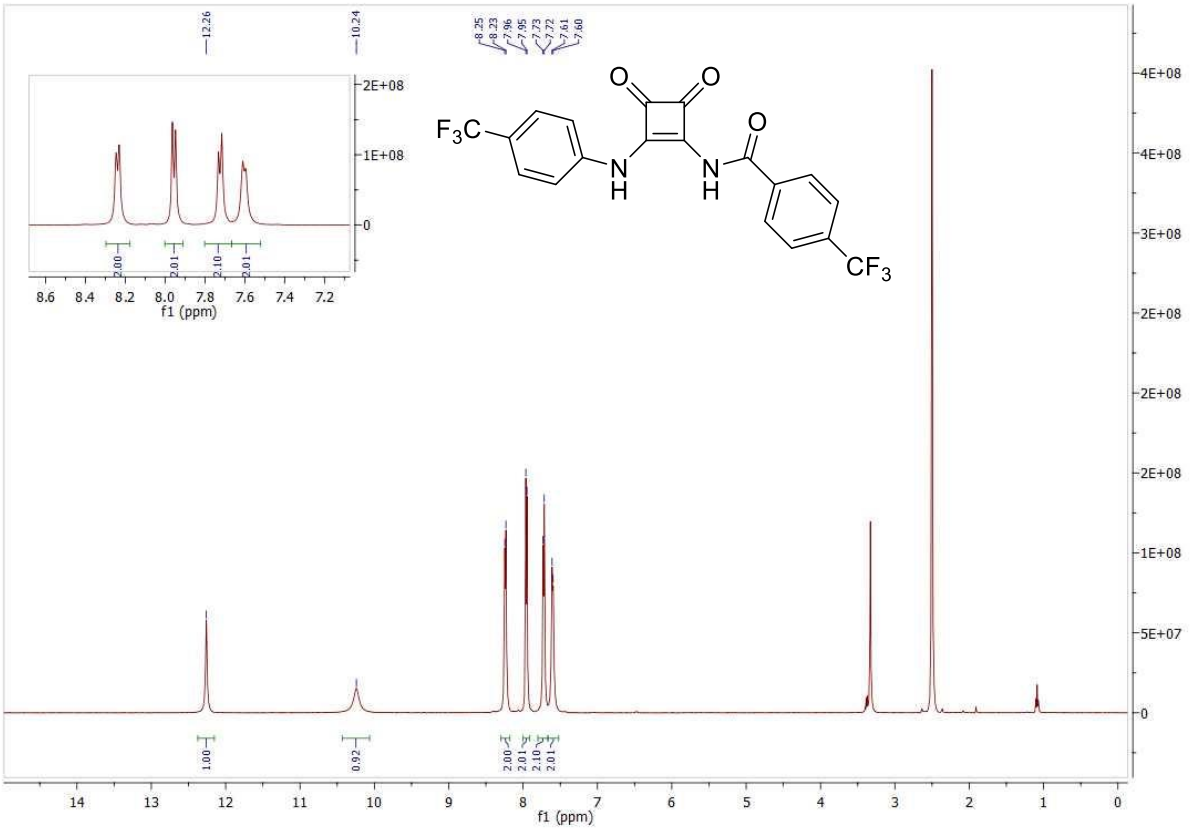

Figure A78. ^{1}H NMR (DMSO-d_6, 500 MHz) spectrum of **2.28**.

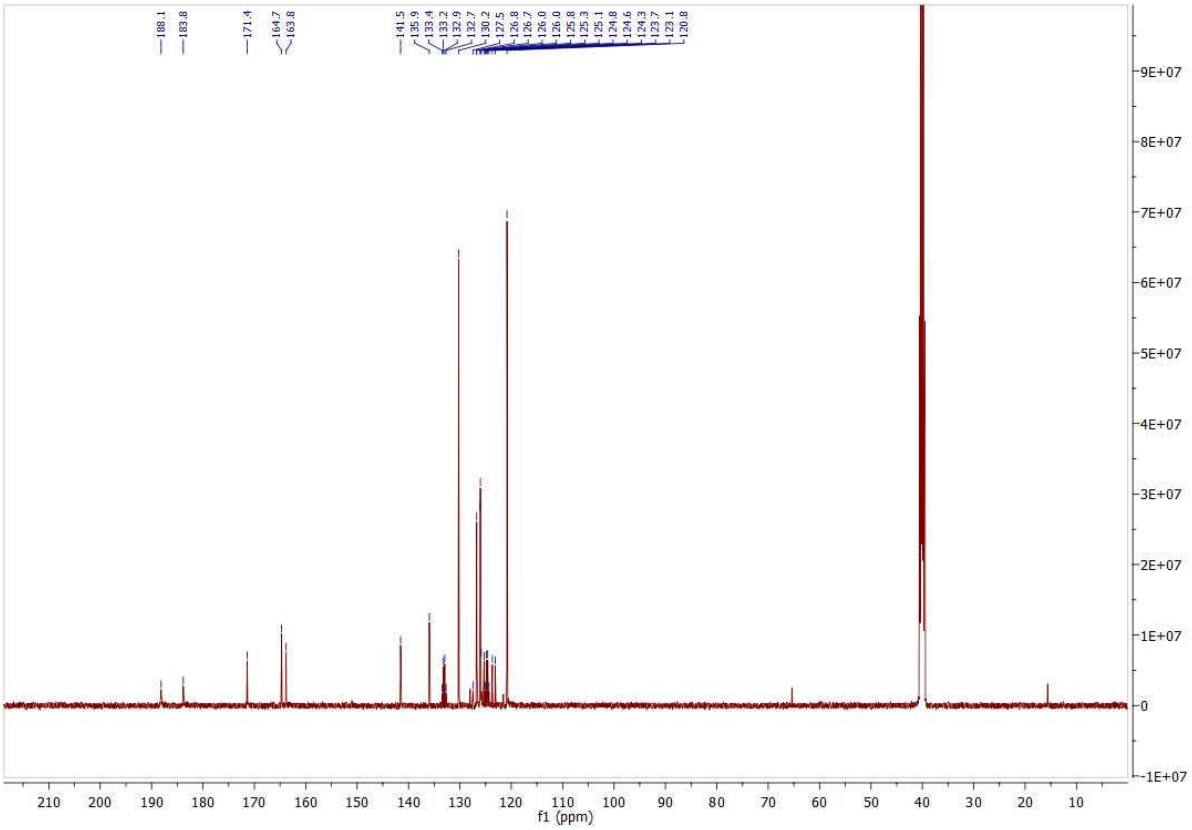

Figure A79. ^{13}C NMR (DMSO-d_6, 126 MHz) spectrum of **2.28**.

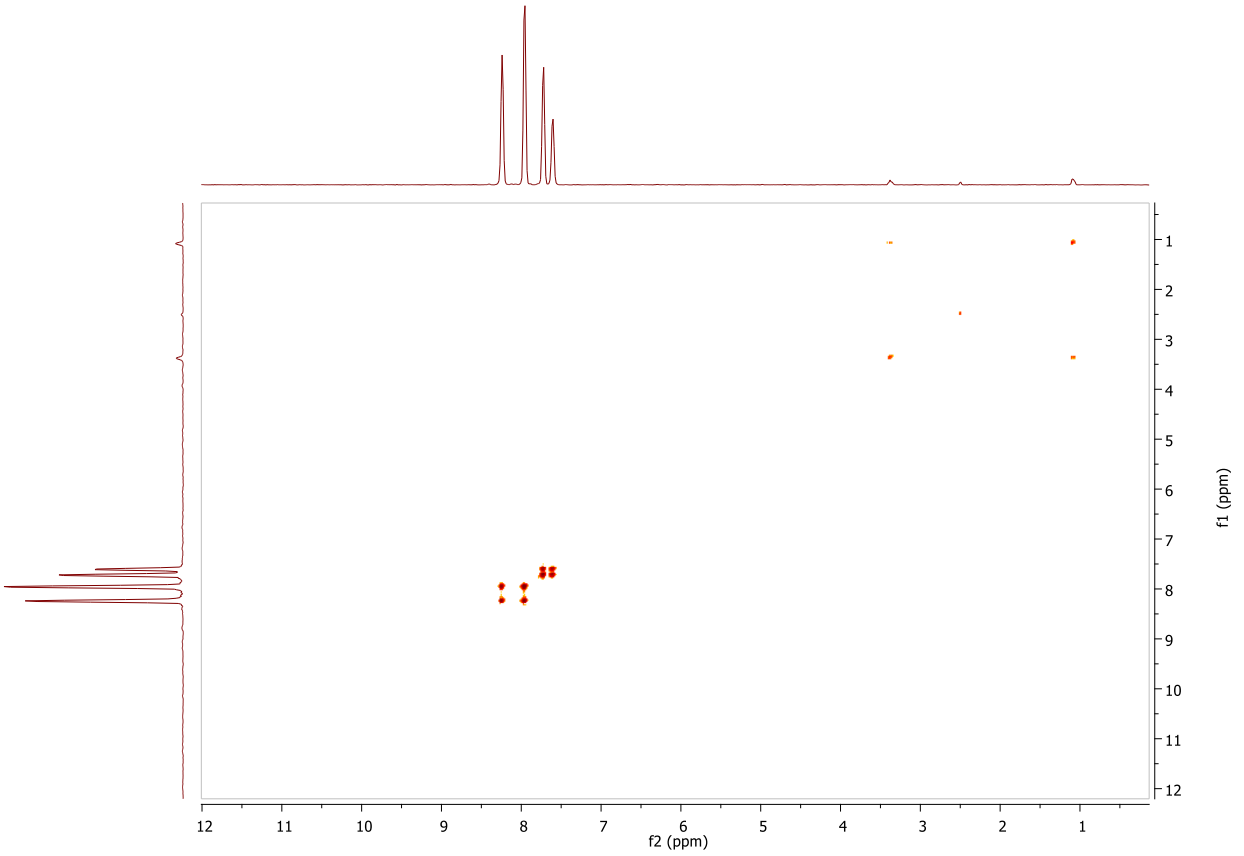

Figure A80. ^{1}H-^{1}H COSY spectrum of **2.28**

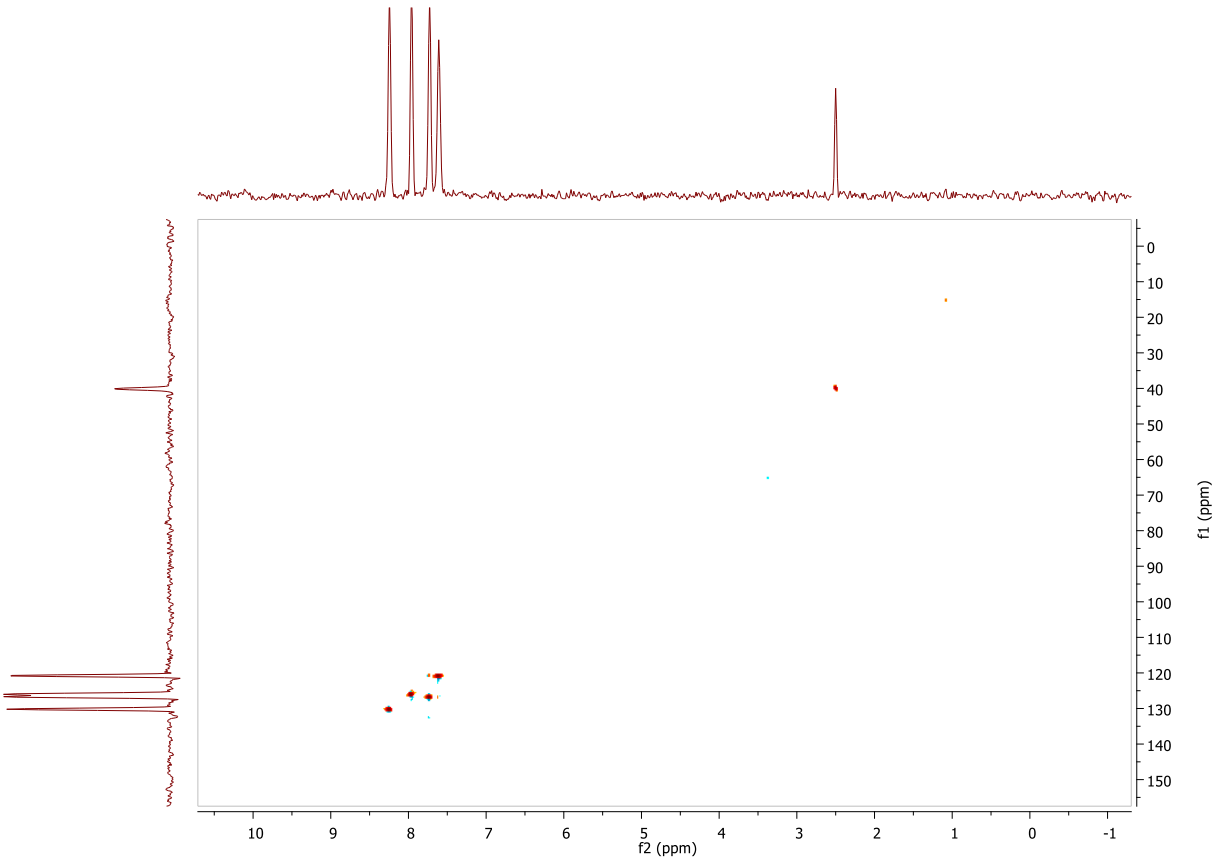

Figure A81. HSQC spectrum of **2.28**

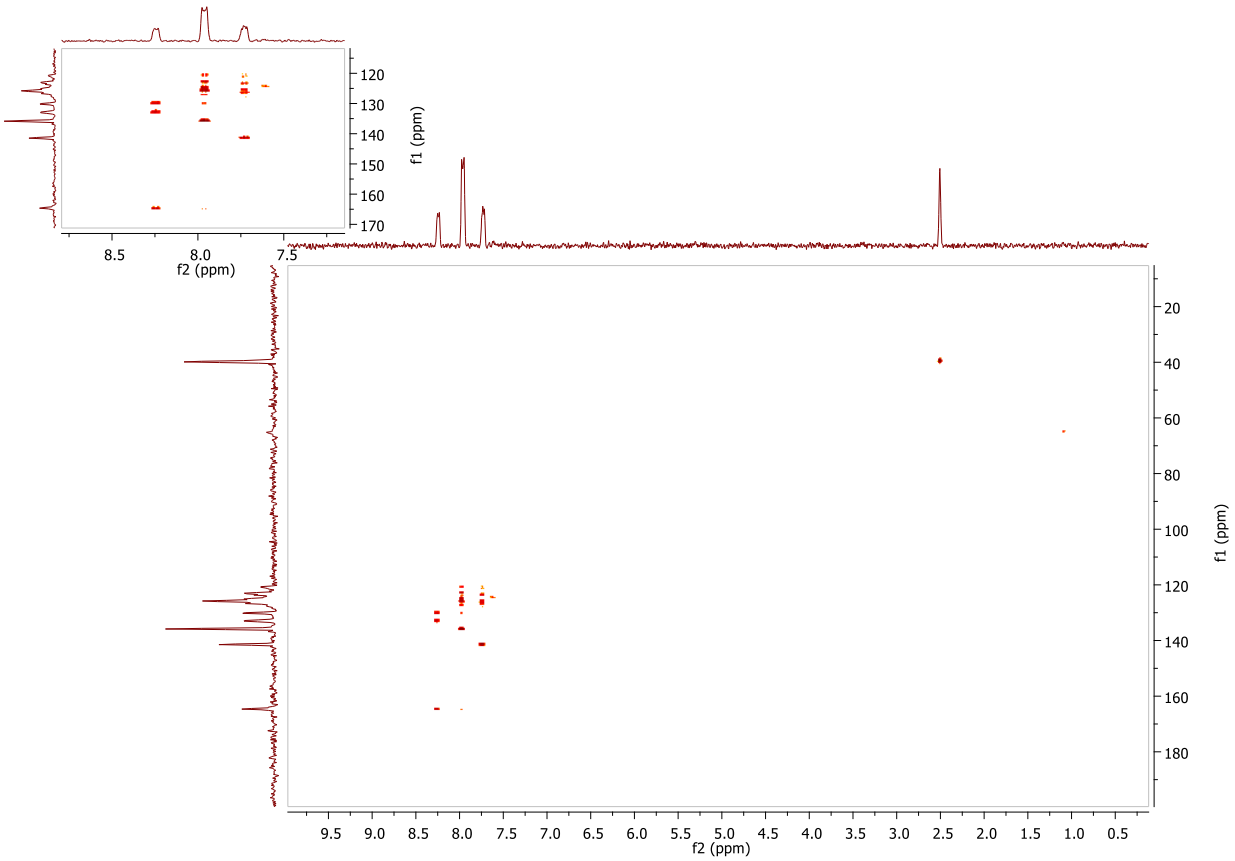

Figure A82. HMBC spectrum of **2.28**

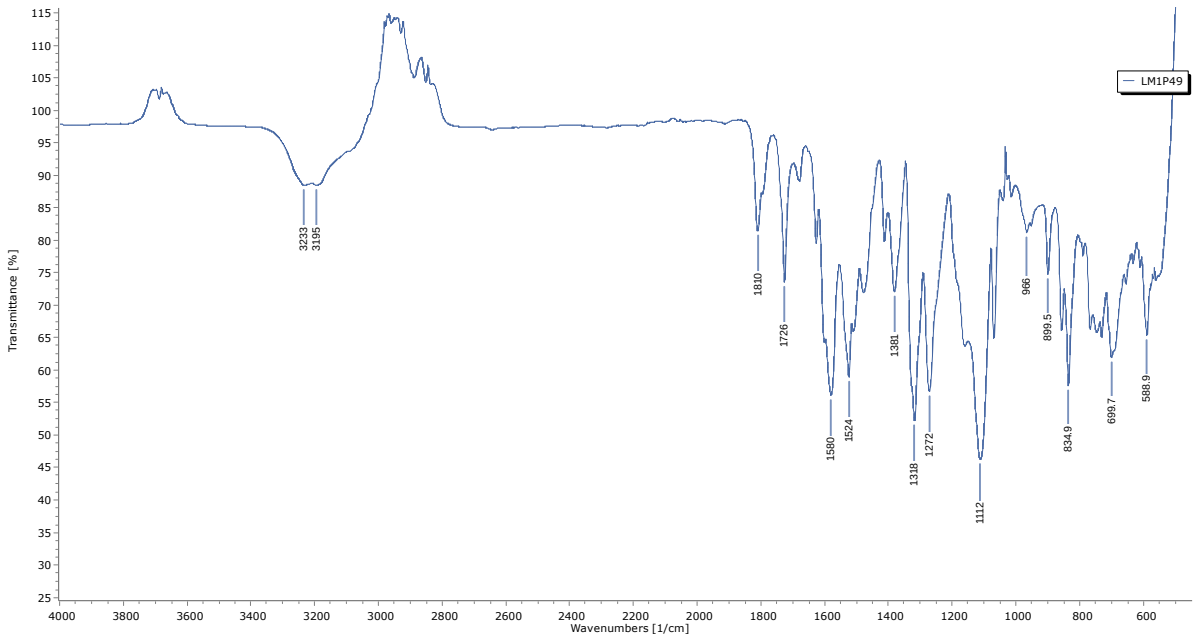

Figure A83. IR spectrum of **2.28**

Compounds

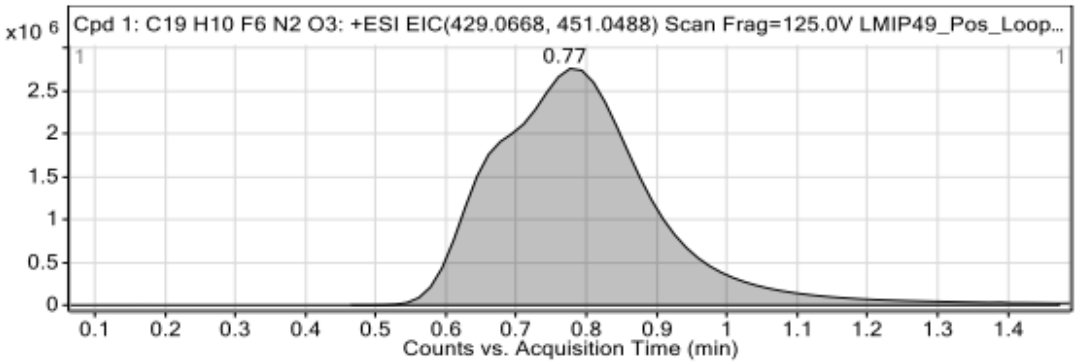

Integration Peak List

Start	RT	End	Height	Area
0.46	0.77	1.47	2565745	42556804

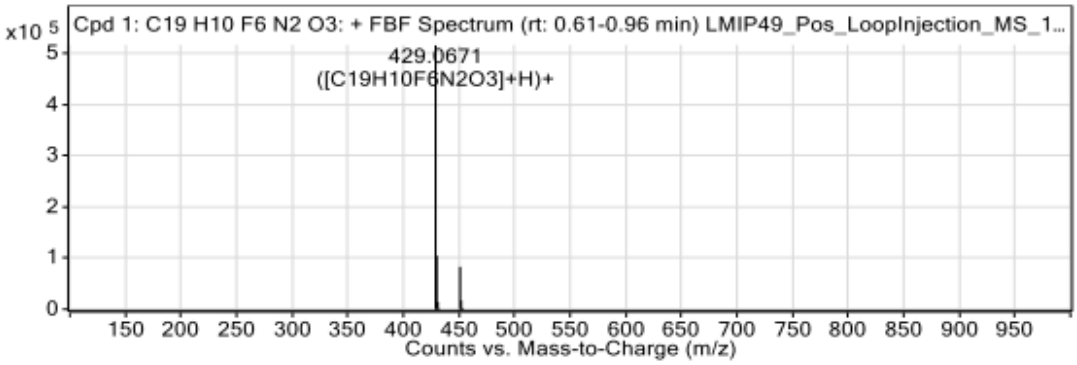

Peak List

m/z	z	Abund	Formula	Ion
429.0671	1	516063.66	C19H10F6N2O3	(M+H)+
430.0702	1	104402.95	C19H10F6N2O3	(M+H)+
431.0725	1	14208.69	C19H10F6N2O3	(M+H)+
432.0748	1	1429.52	C19H10F6N2O3	(M+H)+
451.0488	1	82831.23	C19H10F6N2O3	(M+Na)+
452.0518	1	17284.08	C19H10F6N2O3	(M+Na)+
453.0548	1	2438.04	C19H10F6N2O3	(M+Na)+
454.0573	1	228.05	C19H10F6N2O3	(M+Na)+

--- End Of Report ---

Figure A84. HRMS of **2.28**

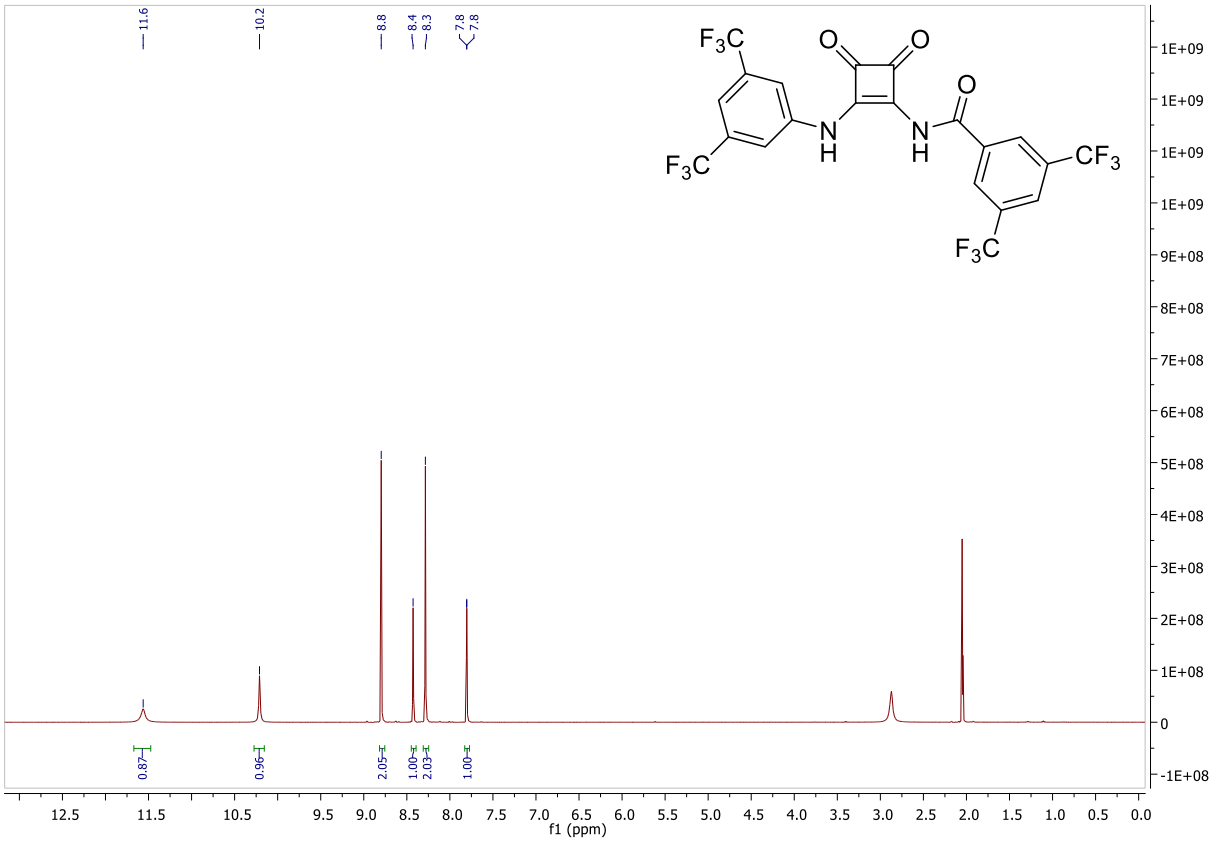

Figure A85. ^{1}H NMR ((CD$_3$)$_2$CO-*d*$_6$, 500 MHz) spectrum of **2.29**.

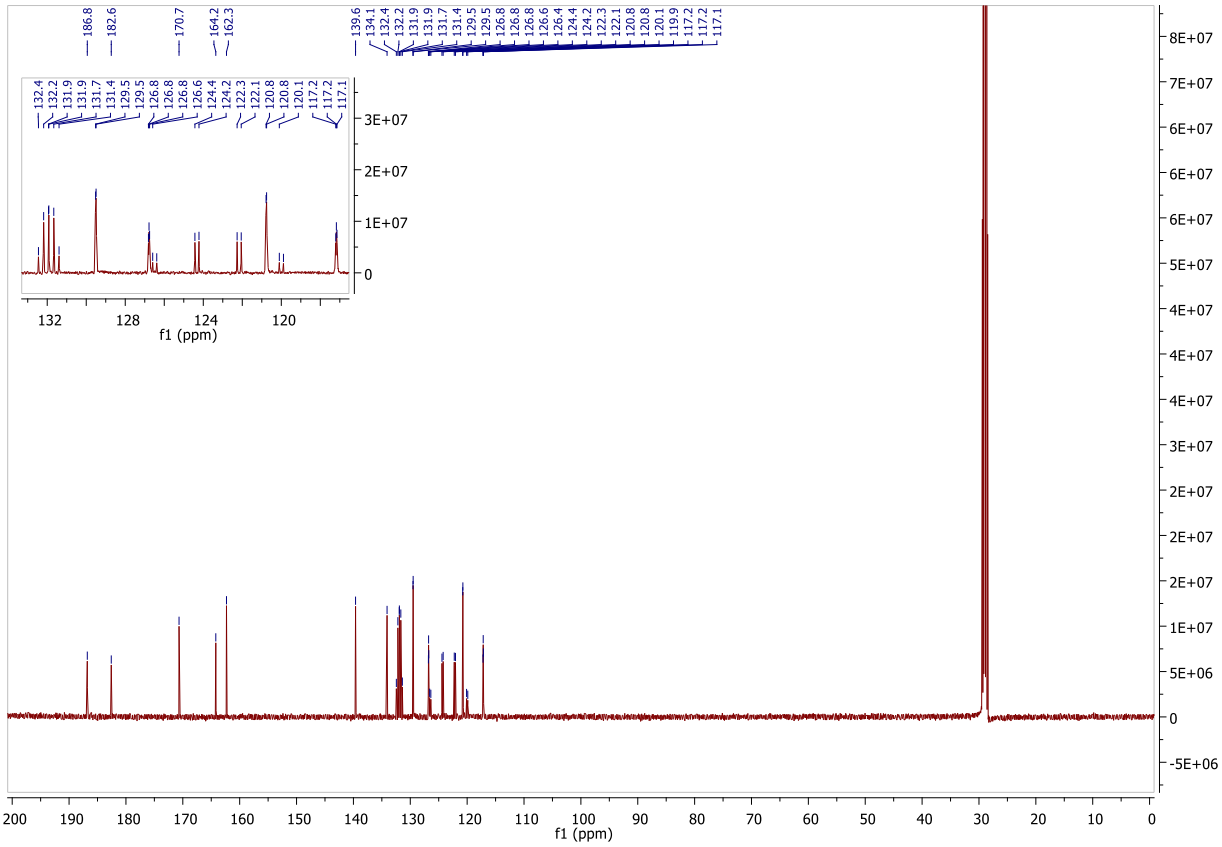

Figure A86. ^{13}C NMR ((CD$_3$)$_2$CO-*d*$_6$, 126 MHz) spectrum of **2.29**.

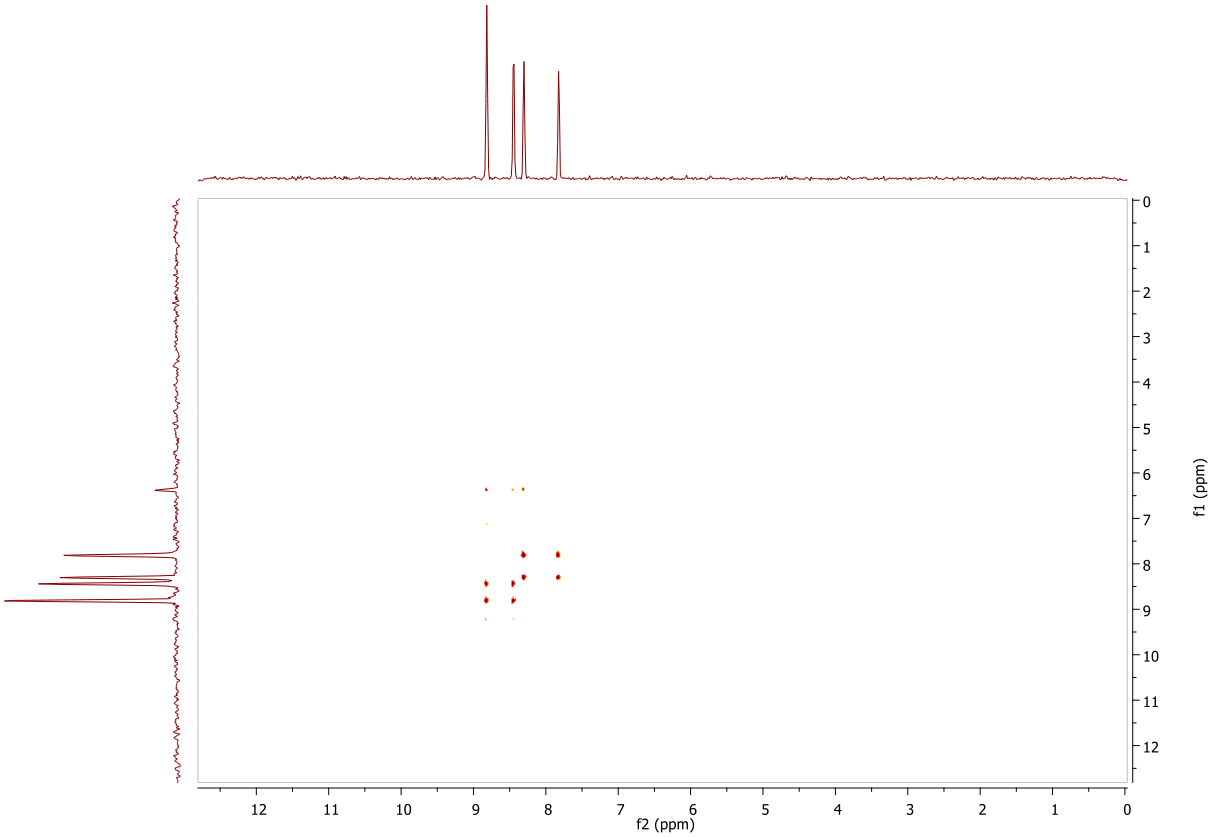

Figure A87. ^{1}H-^{1}H COSY spectrum of **2.29**

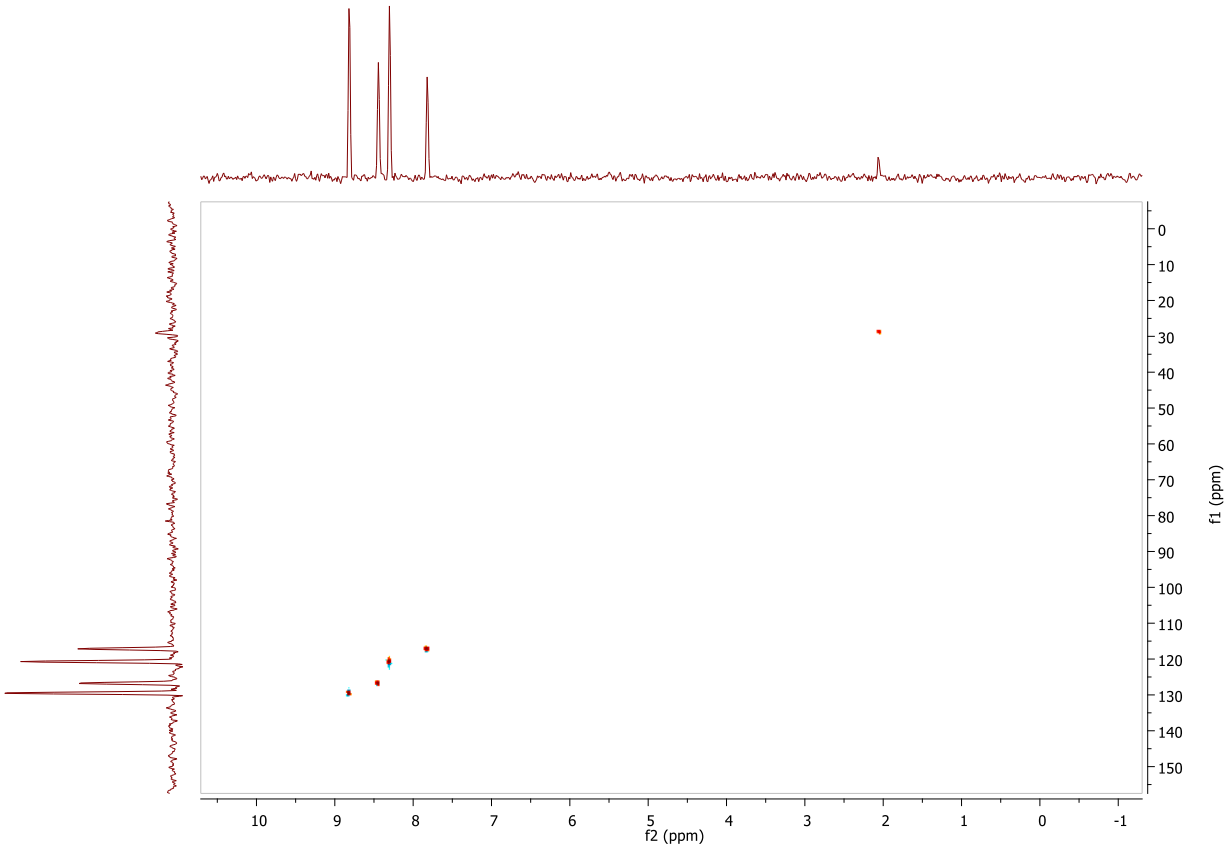

Figure A88. HSQC spectrum of **2.29**

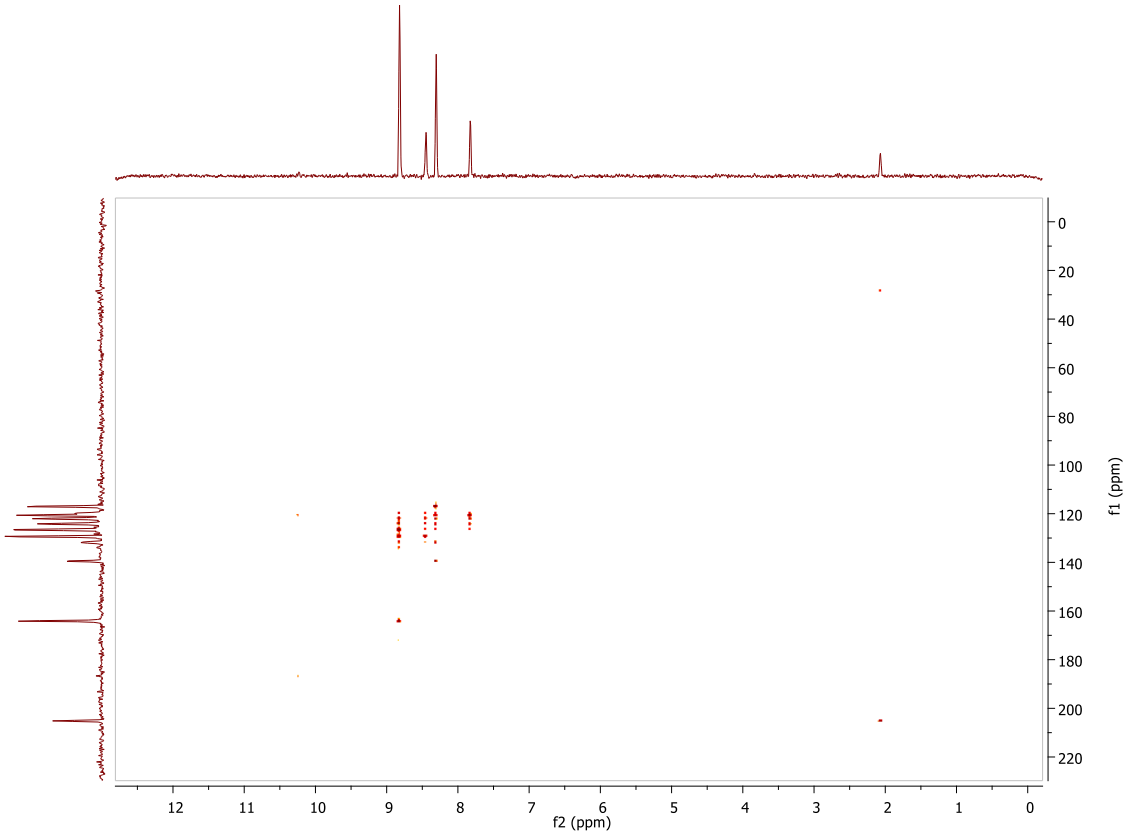

Figure A89. HMBC spectrum of **2.29**

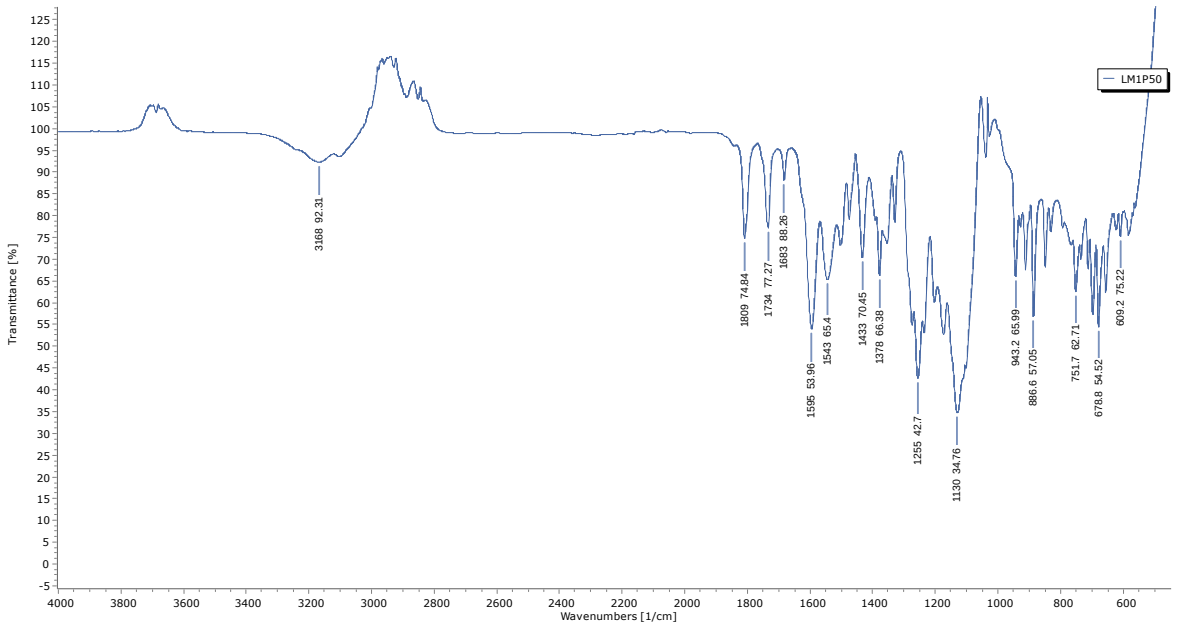

Figure A90. IR spectrum of **2.29**

Compounds

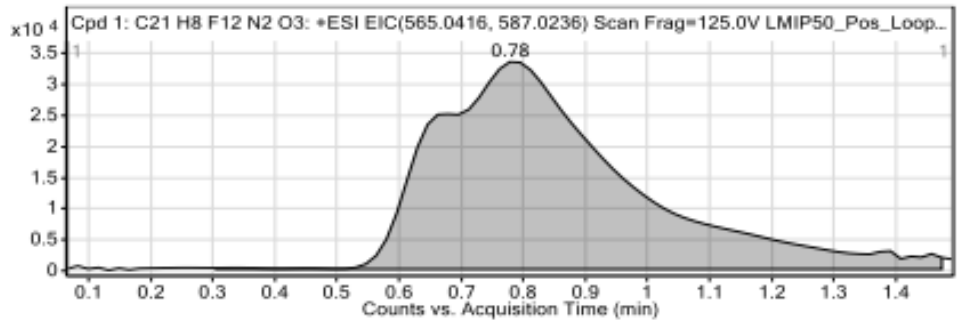

Integration Peak List

Start	RT	End	Height	Area
0.3	0.78	1.47	31268	718740

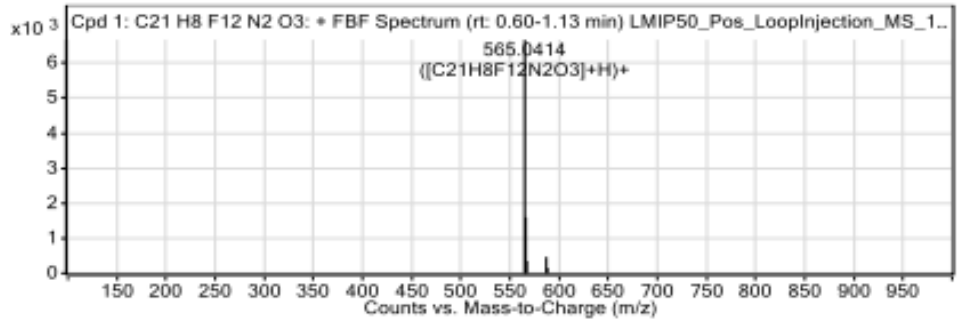

Peak List

m/z	z	Abund	Formula	Ion
565.0414	1	6662.23	C21H8F12N2O3	(M+H)+
566.0449	1	1596.42	C21H8F12N2O3	(M+H)+
567.0472	1	348.42	C21H8F12N2O3	(M+H)+
587.023	1	464.75	C21H8F12N2O3	(M+Na)+
588.0256	1	152.73	C21H8F12N2O3	(M+Na)+

--- End Of Report ---

Figure A91. HRMS of **2.29**

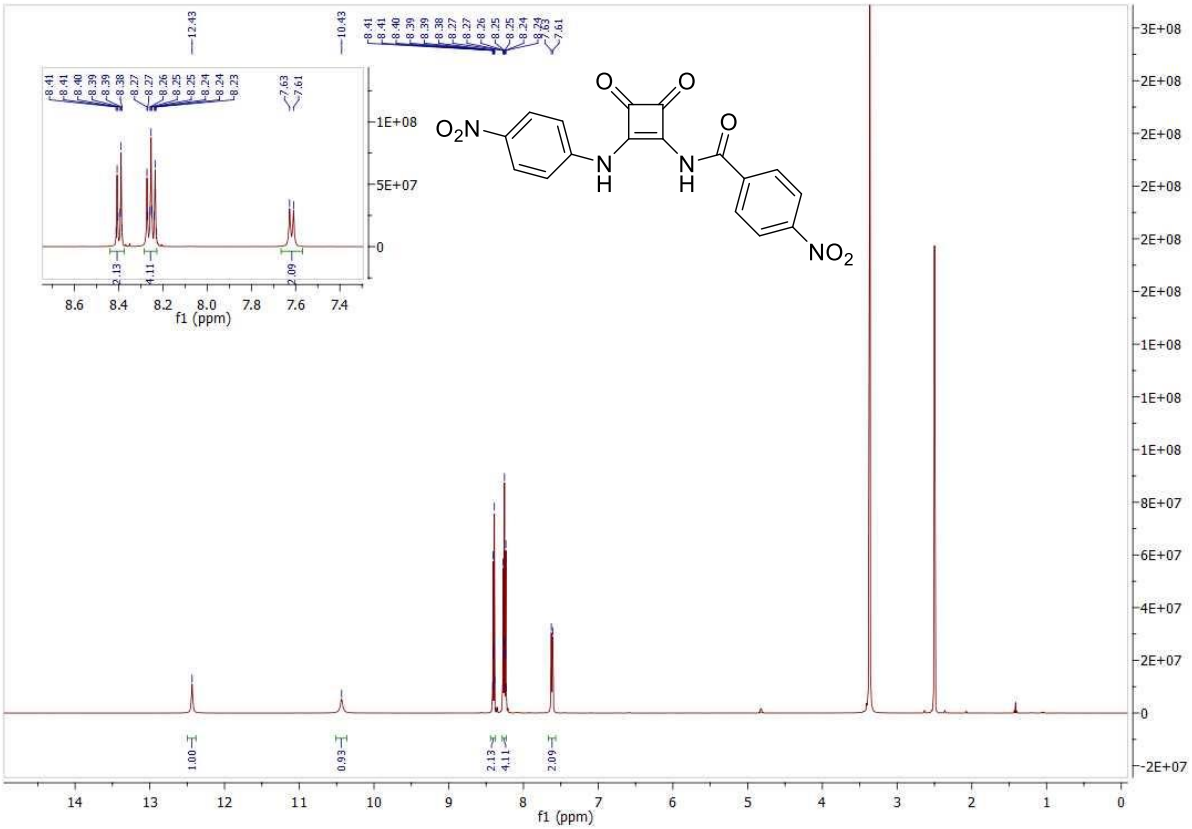

Figure A92. ^{1}H NMR (DMSO-d_6, 500 MHz) spectrum of **2.30**.

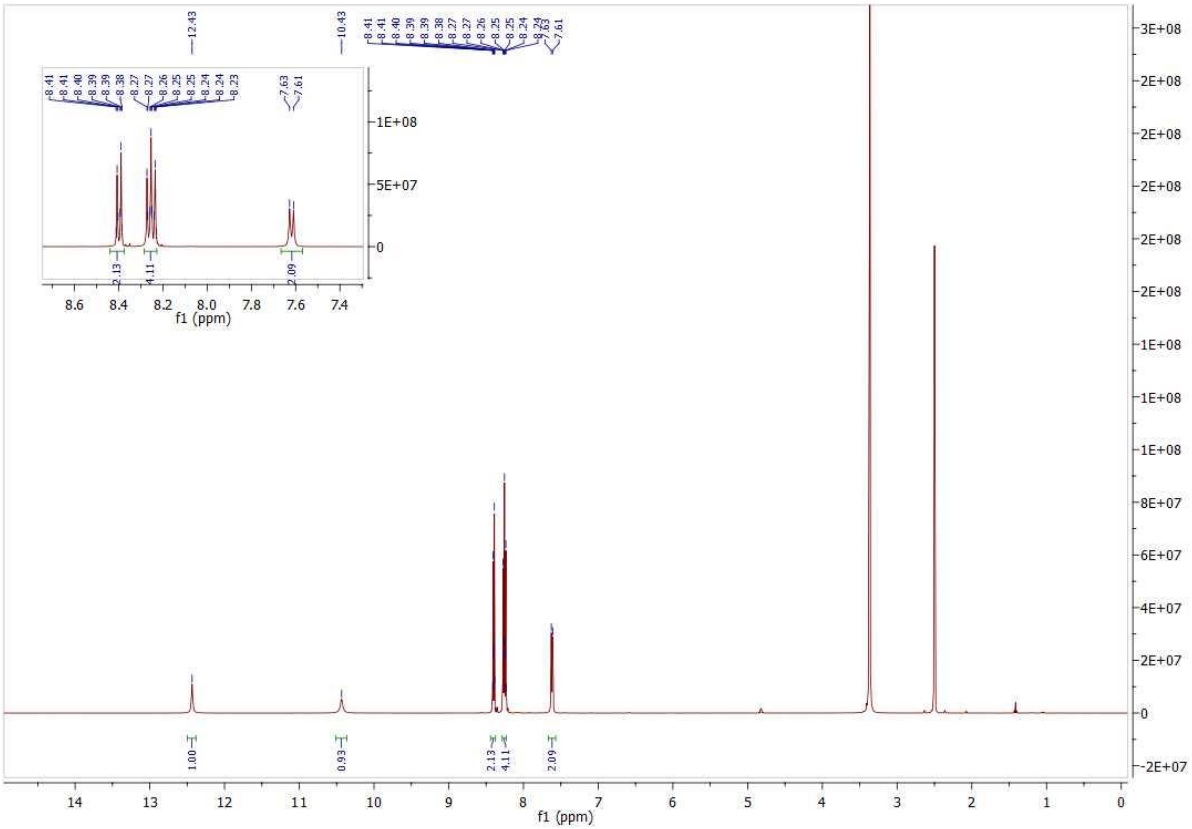

Figure A93. ^{13}C NMR (DMSO-d_6, 126 MHz) spectrum of **2.30**.

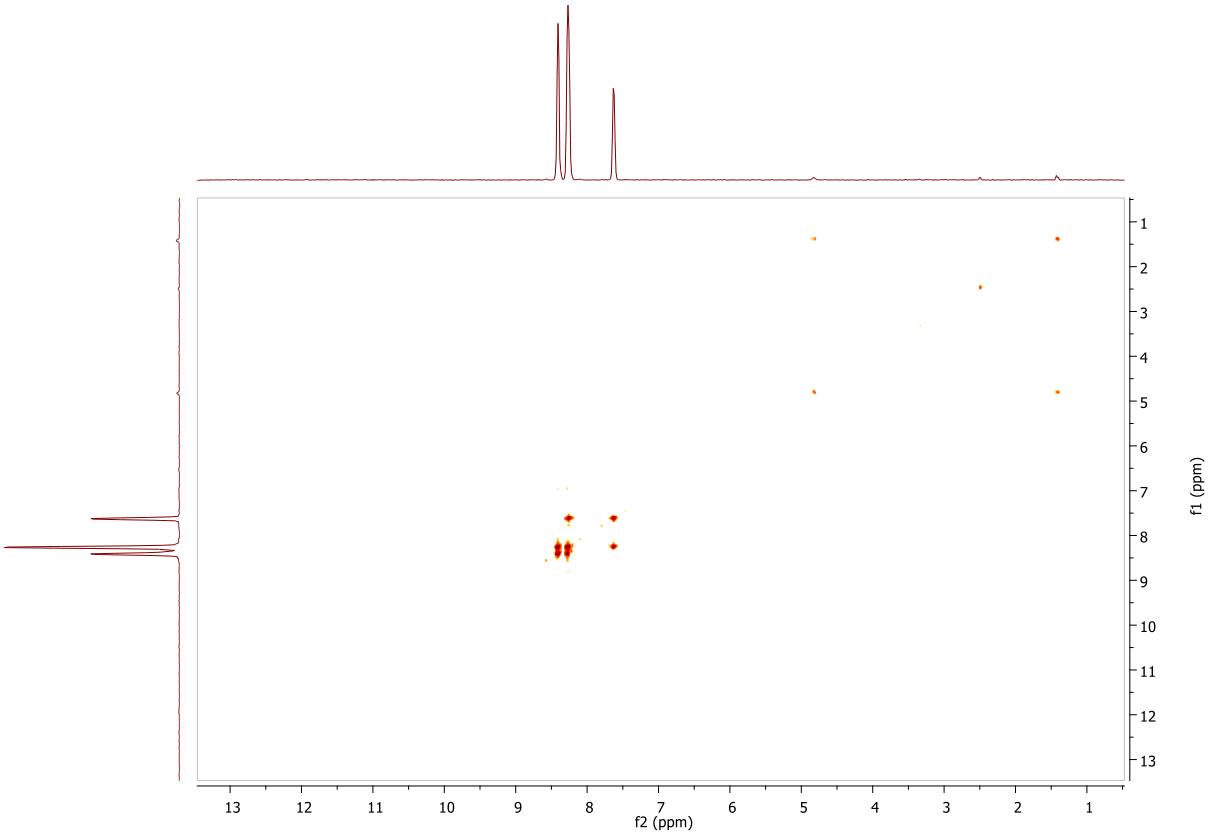

Figure A94. ^{1}H-^{1}H COSY spectrum of **2.30**

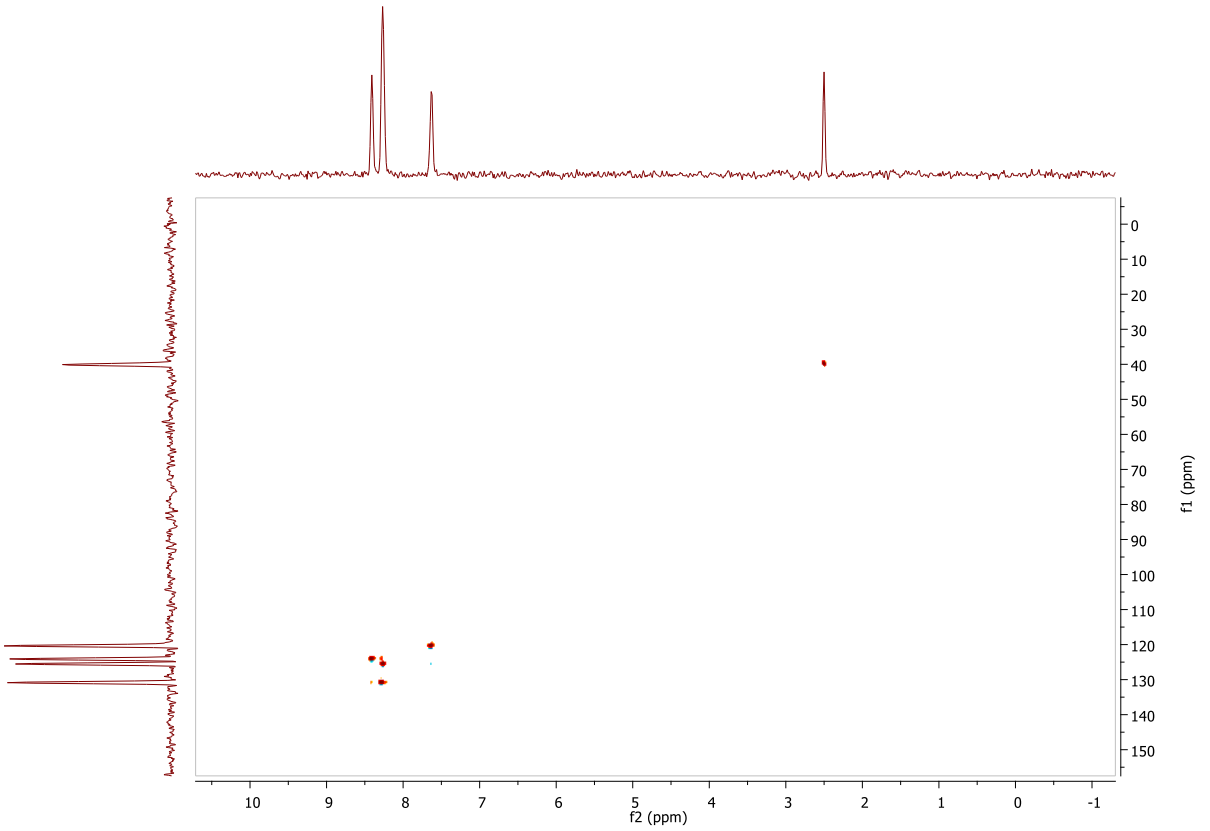

Figure A95. HSQC spectrum of **2.30**

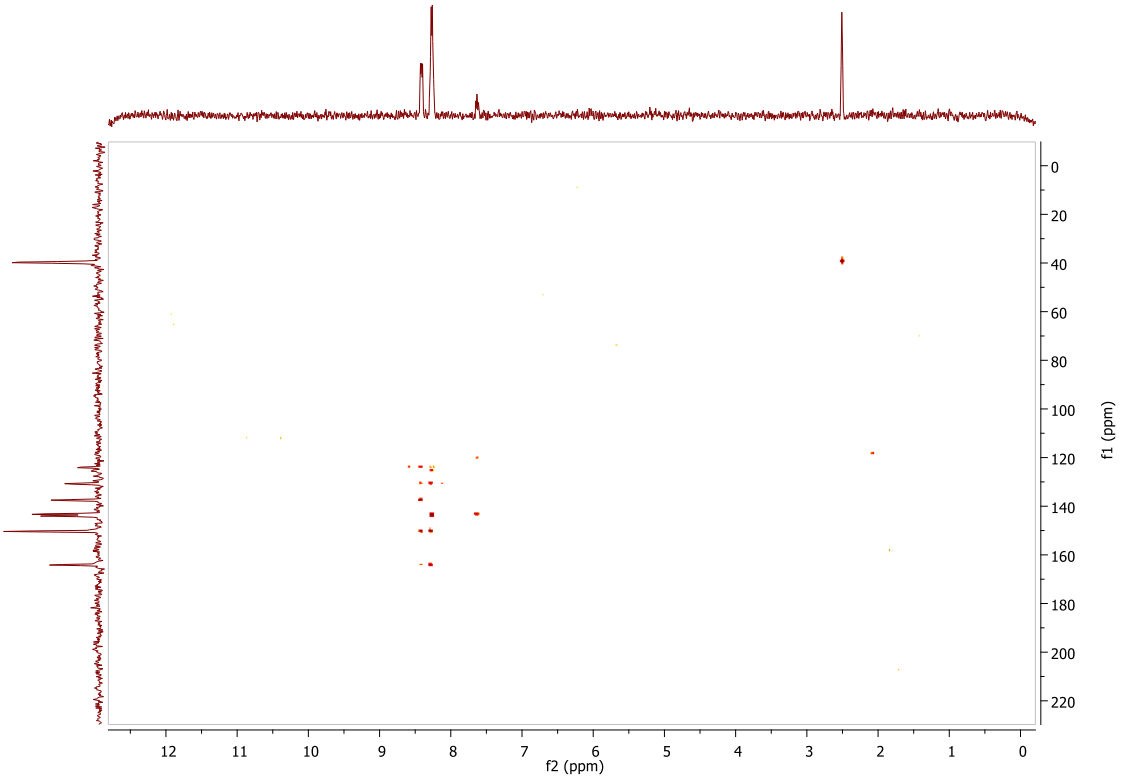

Figure A96. HMBC spectrum of **2.30**

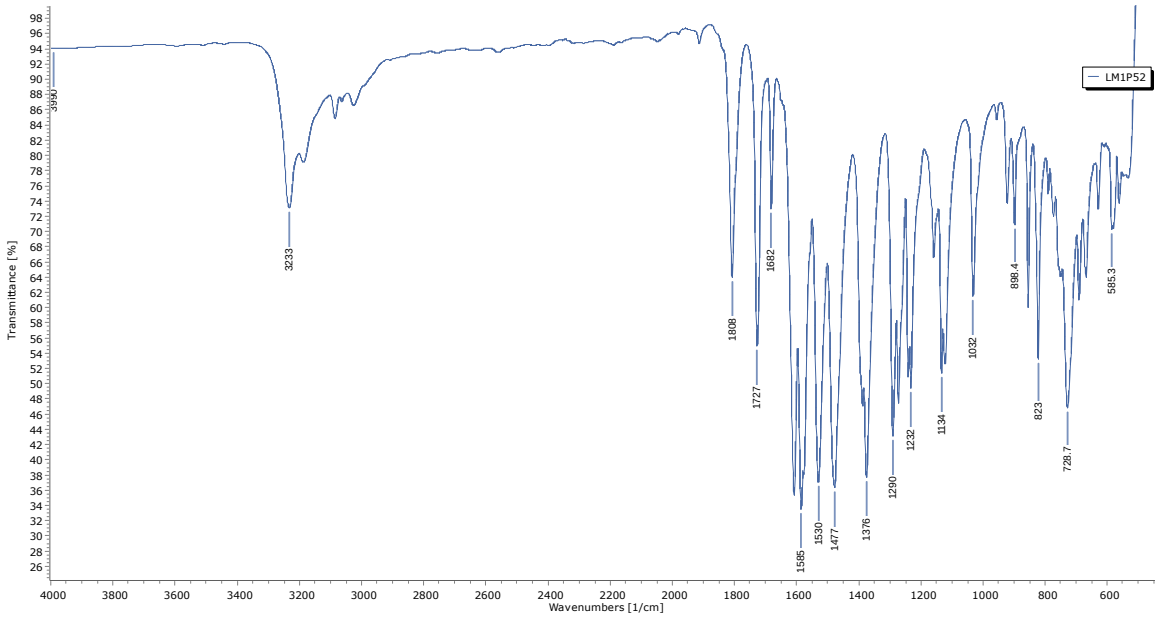

Figure A97. IR spectrum of **2.30**

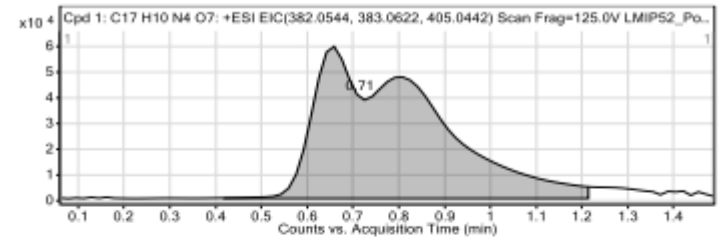

Integration Peak List

Start	RT	End	Height	Area
0.42	0.71	1.21	51518	1056805

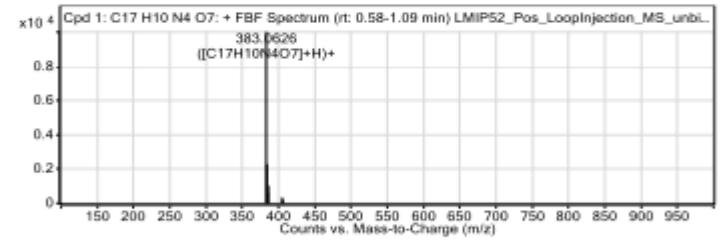

Peak List

m/z	z	Abund	Formula	Ion
383.0626	1	10051.52	C17H10N4O7	(M+H)+
384.0661	1	2283.79	C17H10N4O7	(M+H)+
385.0708	1	617.55	C17H10N4O7	(M+H)+
386.0813	1	1026.47	C17H10N4O7	(M+H)+
405.0449	1	334.57	C17H10N4O7	(M+Na)+
406.0365	1	213.53	C17H10N4O7	(M+Na)+

--- End Of Report ---

Figure A98. HRMS of **2.30**

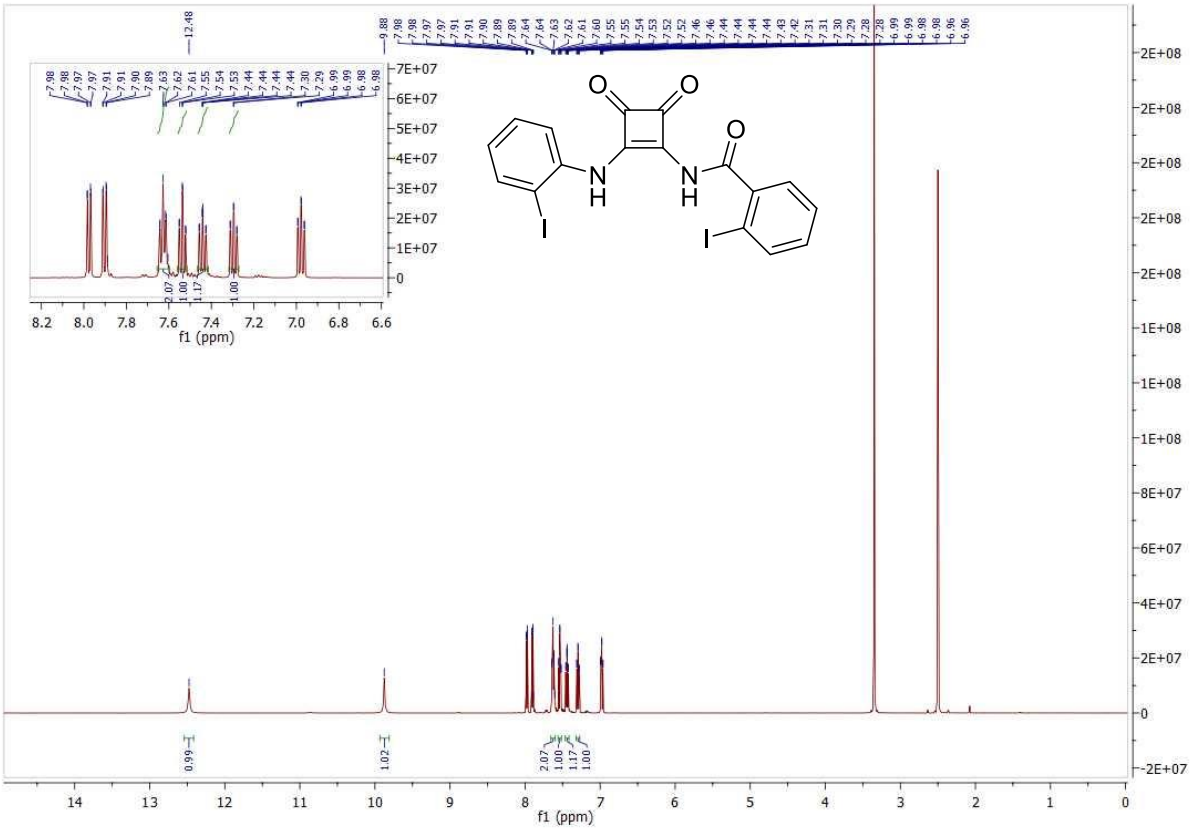

Figure A99. ^{1}H NMR (DMSO-d_6, 500 MHz) spectrum of **2.31**.

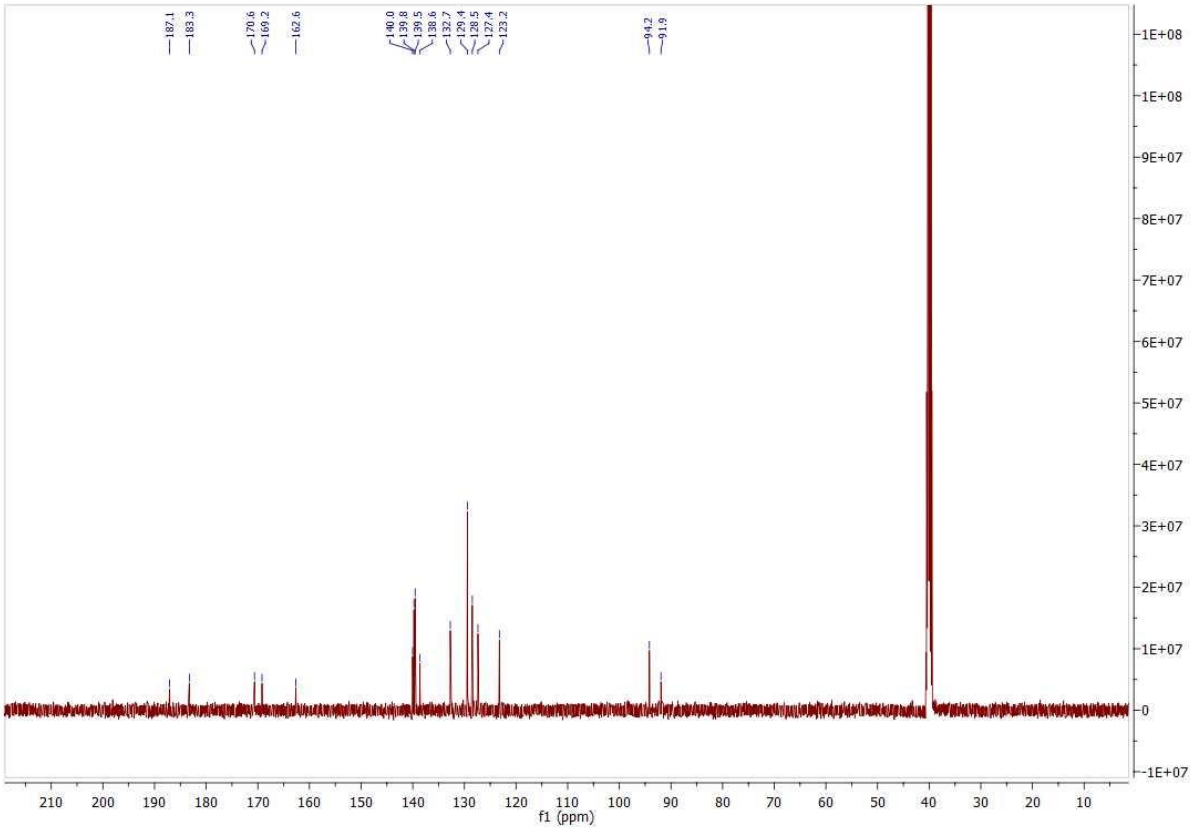

Figure A100. ^{13}C NMR (DMSO-d_6, 126 MHz) spectrum of **2.31**.

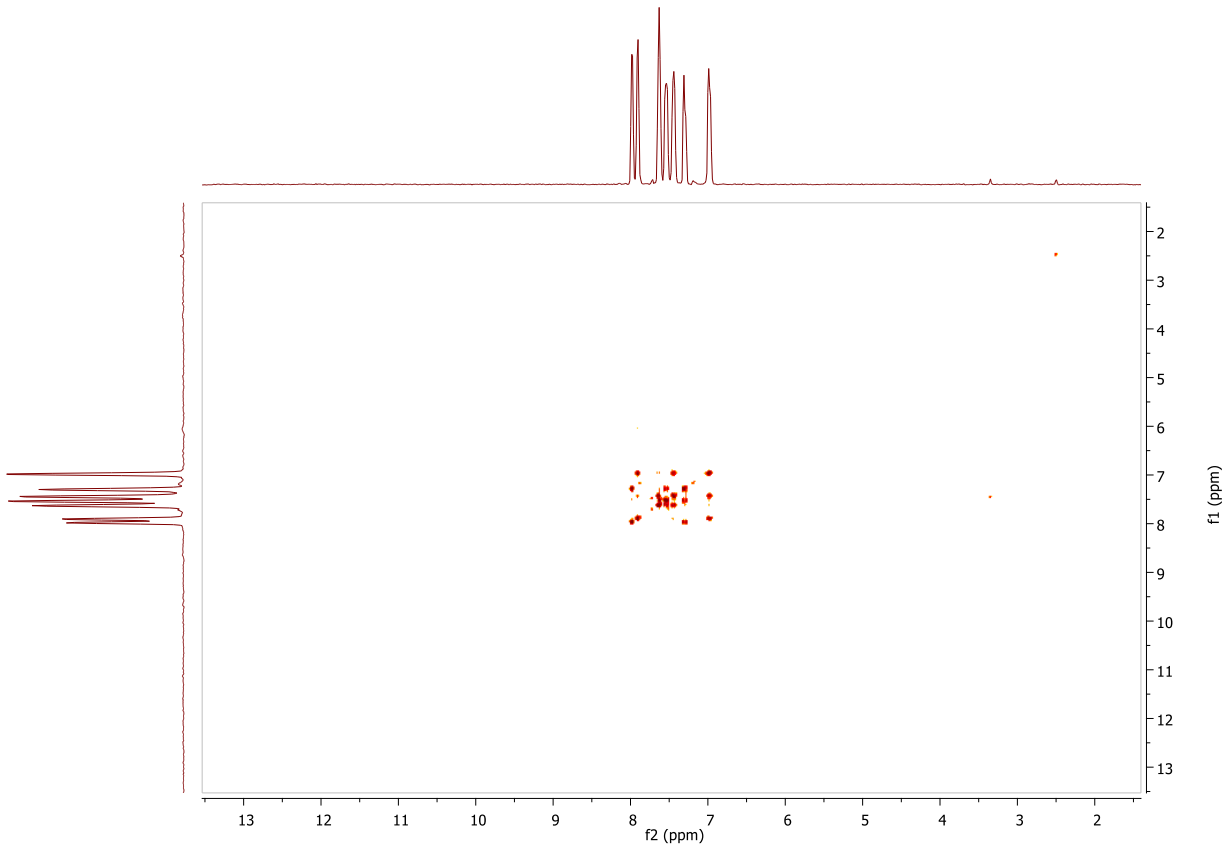

Figure A101. ^{1}H-^{1}H COSY spectrum of **2.31**

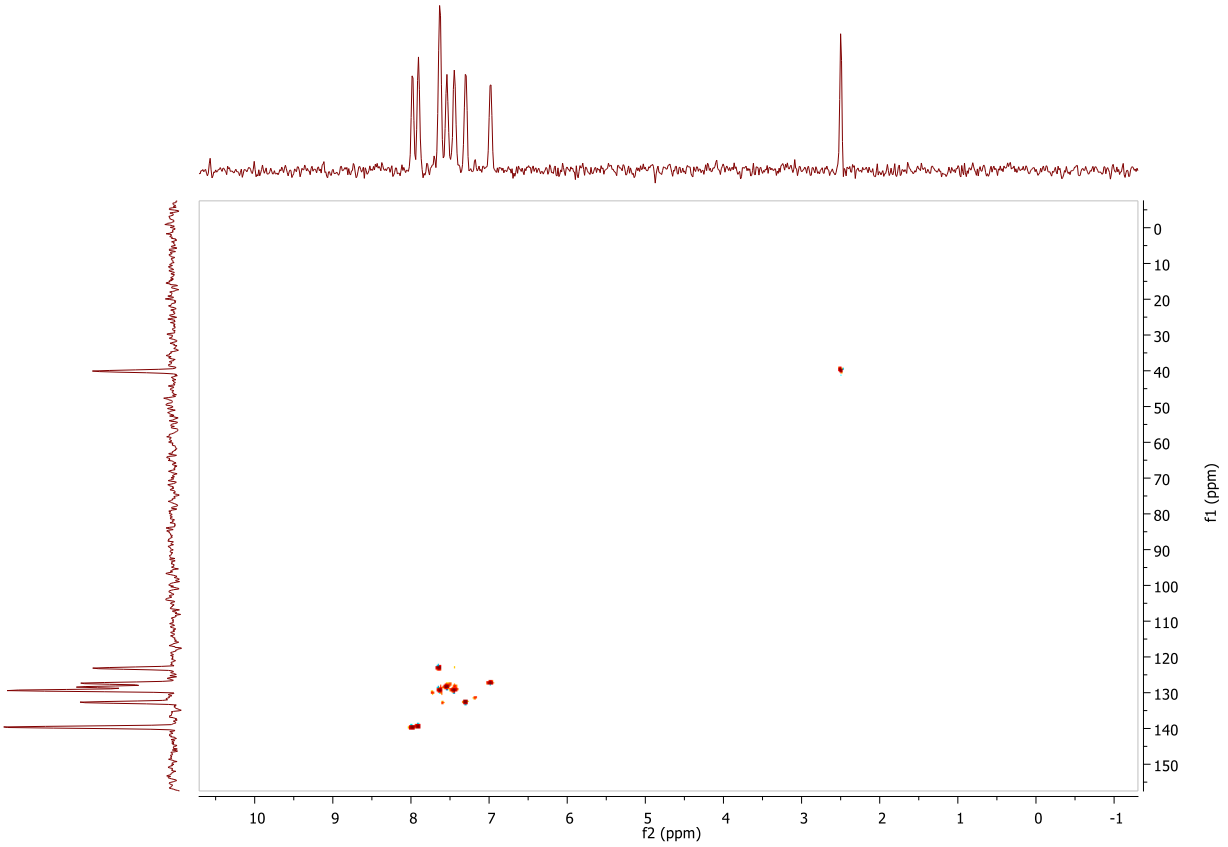

Figure A102. HSQC spectrum of **2.31**

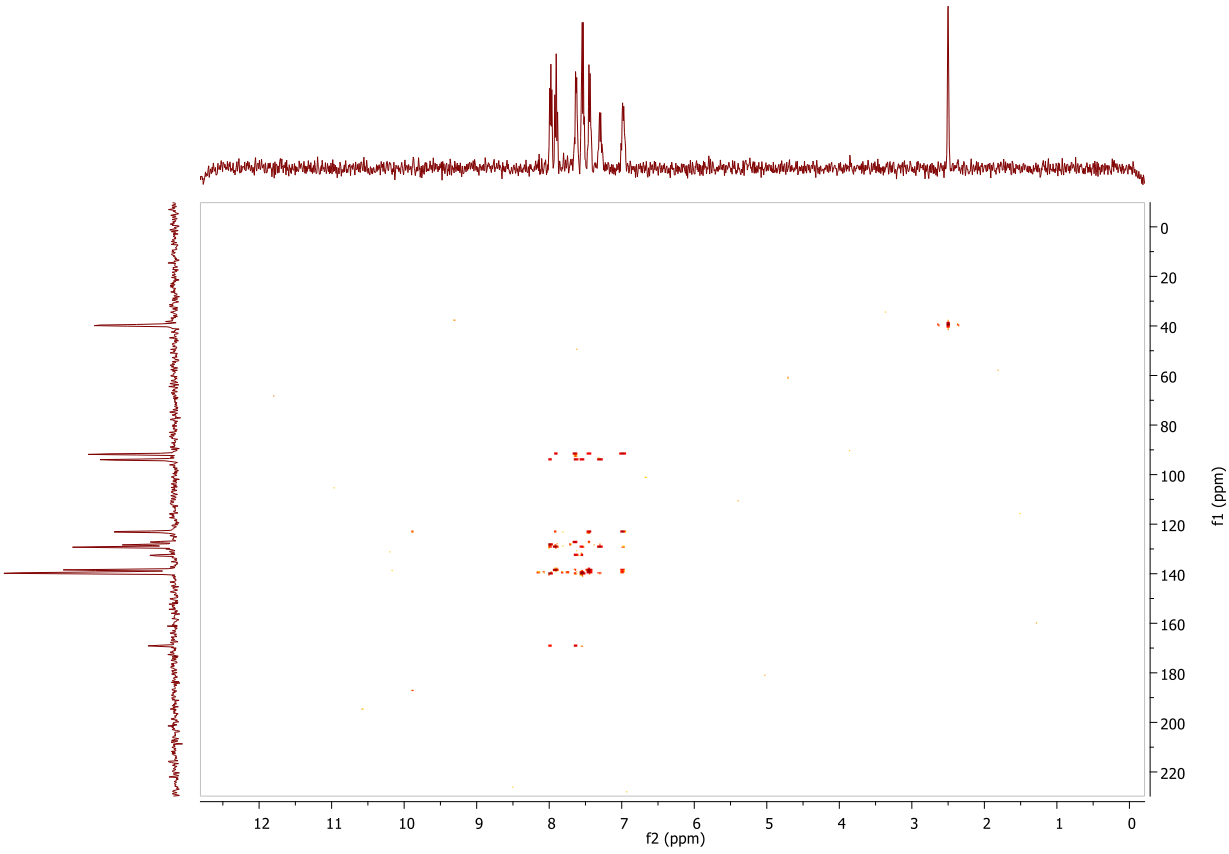

Figure A103. HMBC spectrum of **2.31**

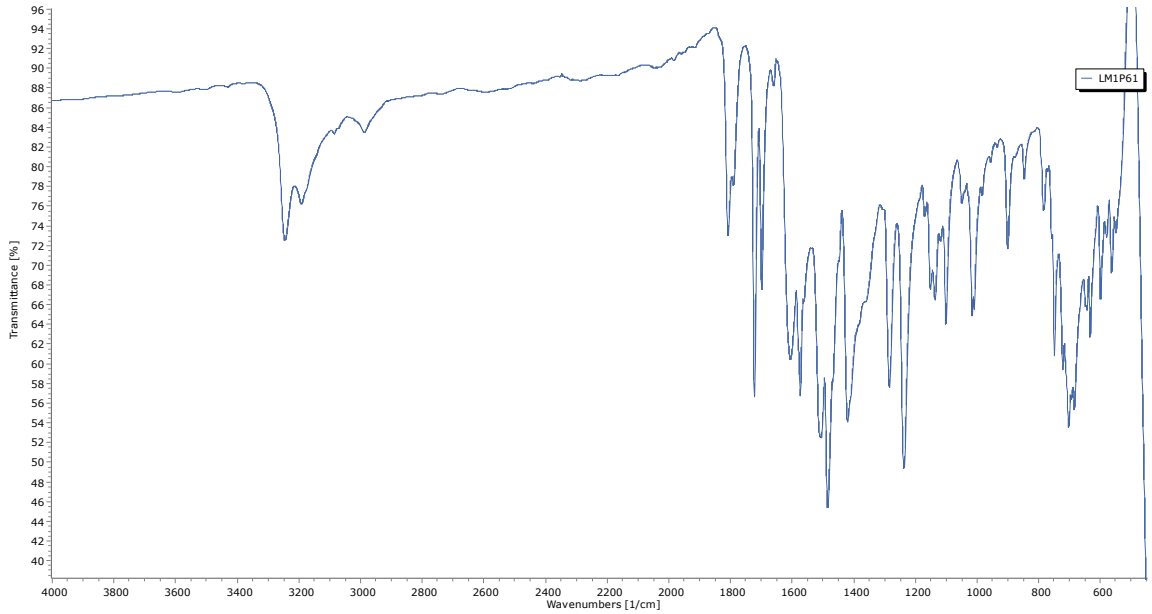

Figure A104. IR spectrum of **2.31**

Compounds

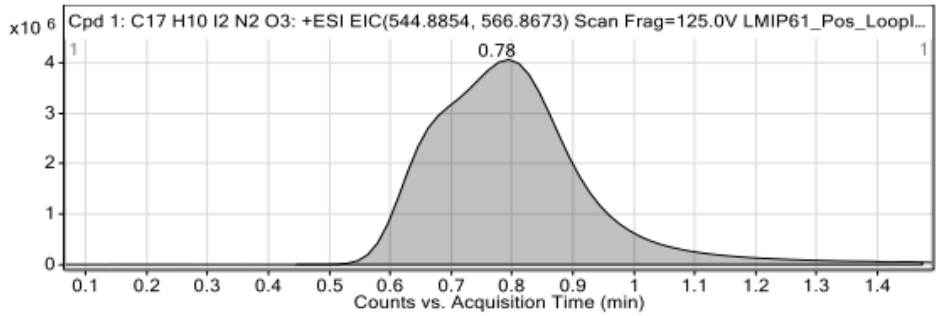

Integration Peak List

Start	RT	End	Height	Area
0.45	0.78	1.47	3793140	68013276

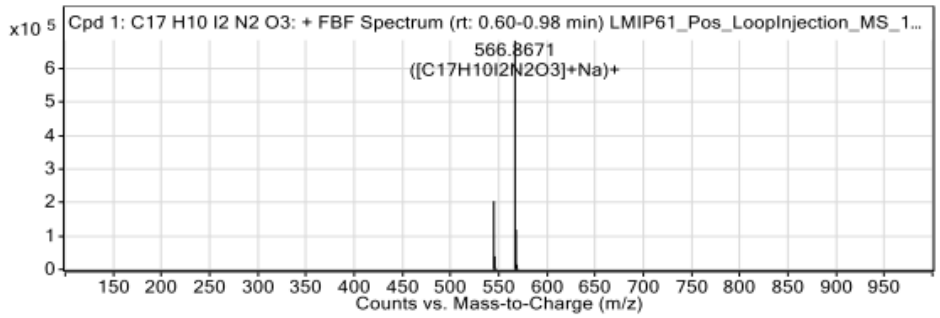

Peak List

m/z	z	Abund	Formula	Ion
544.8851	1	204029.7	C17H10I2N2O3	(M+H)+
545.888	1	39219.65	C17H10I2N2O3	(M+H)+
546.8907	1	4593.09	C17H10I2N2O3	(M+H)+
547.8918	1	444.34	C17H10I2N2O3	(M+H)+
566.8671	1	684266.06	C17H10I2N2O3	(M+Na)+
567.8701	1	118774.71	C17H10I2N2O3	(M+Na)+
568.8724	1	14634.17	C17H10I2N2O3	(M+Na)+
569.8749	1	1514.81	C17H10I2N2O3	(M+Na)+

--- End Of Report ---

Figure A105. HRMS of **2.31**

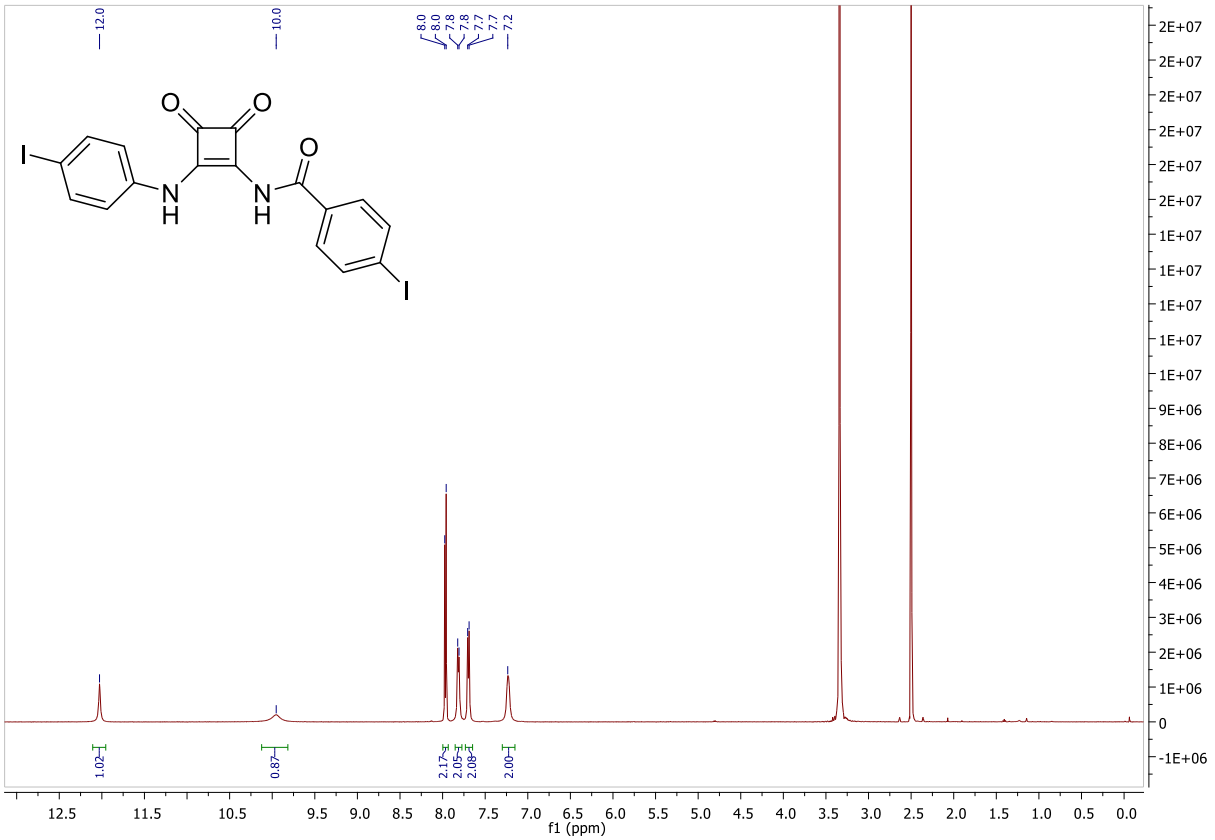

Figure A106. ^{1}H NMR (DMSO-d_6, 500 MHz) spectrum of **2.32**.

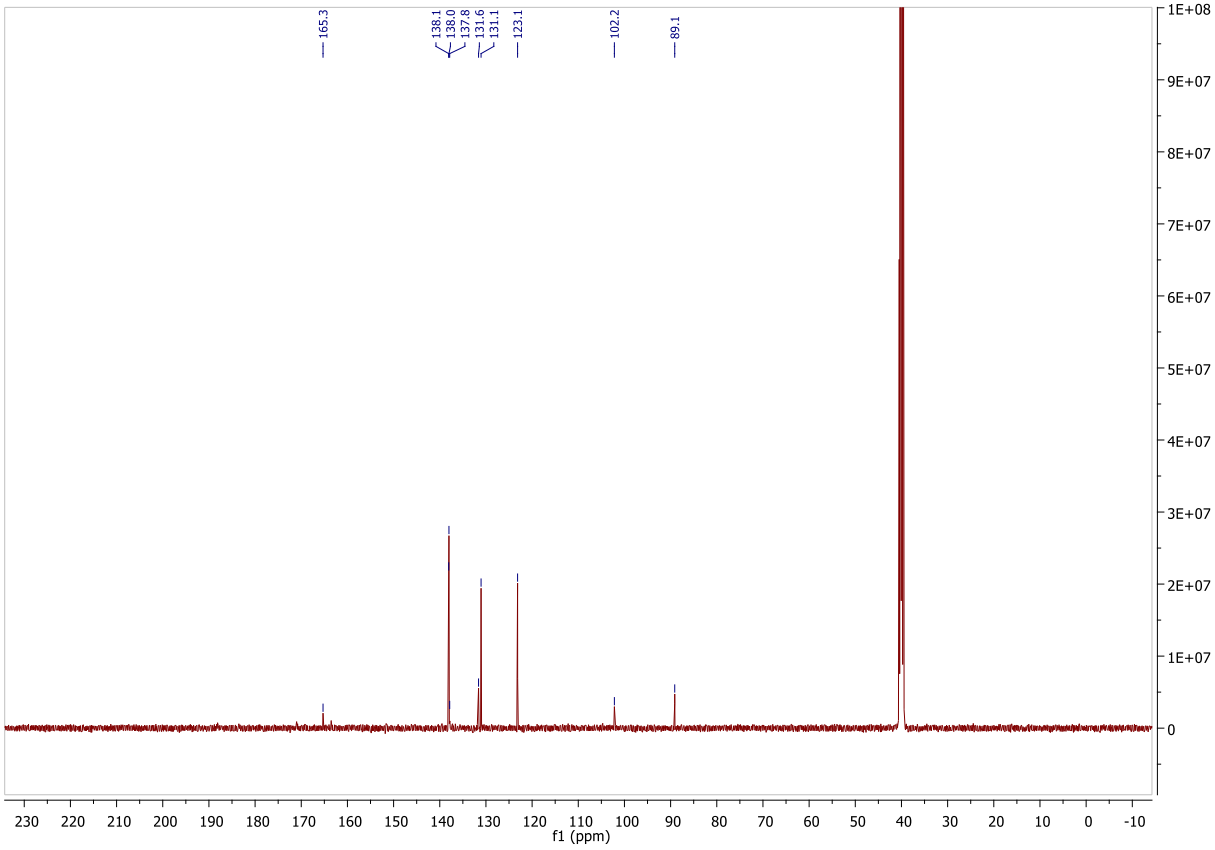

Figure A107. ^{13}C NMR (DMSO-d_6, 126 MHz) spectrum of **2.32**.

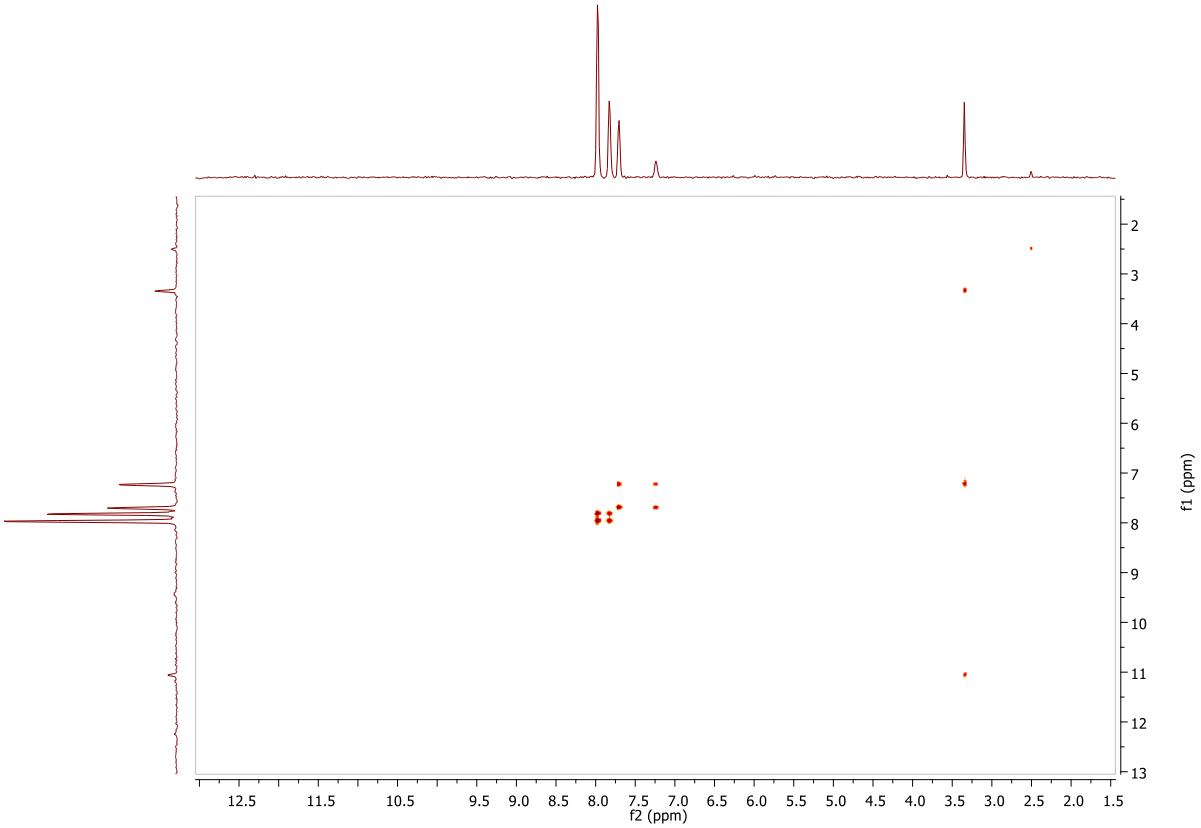

Figure A108. ^{1}H-^{1}H COSY spectrum of **2.32**

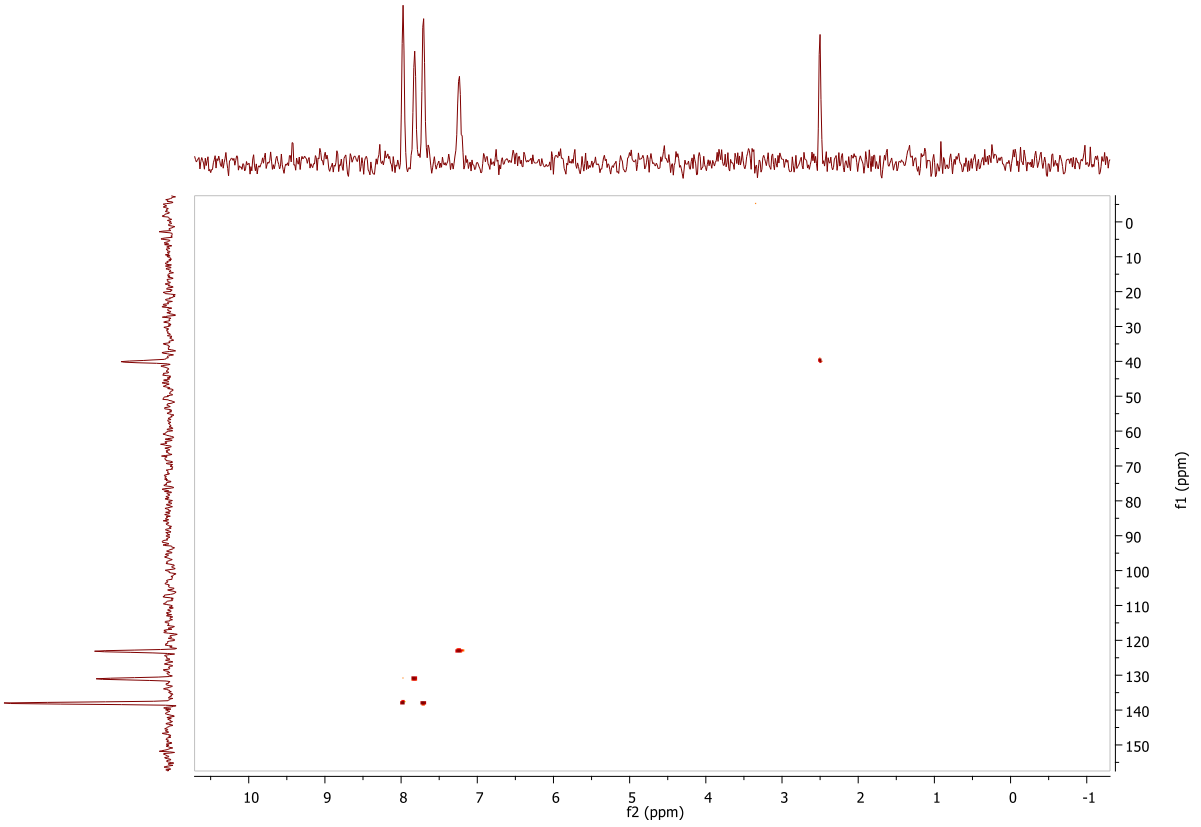

Figure A109. HSQC spectrum of **2.32**

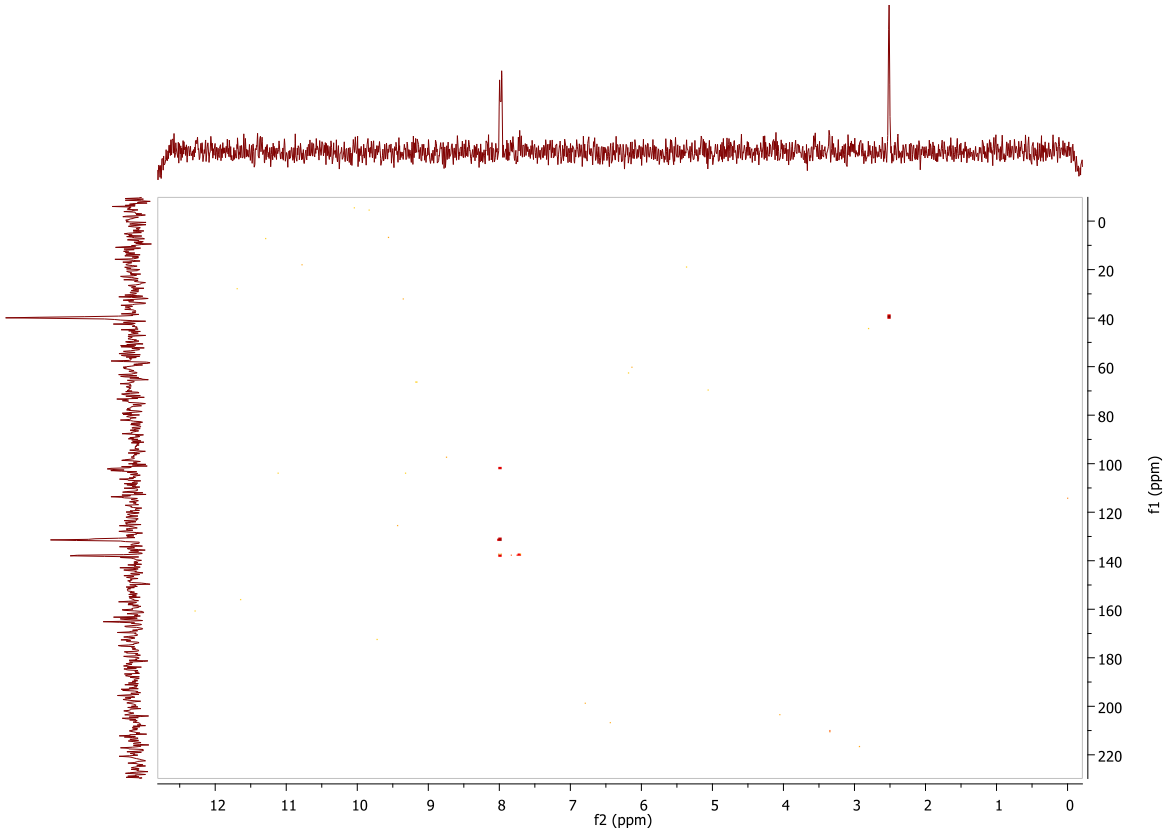

Figure A110. HMBC spectrum of **2.32**

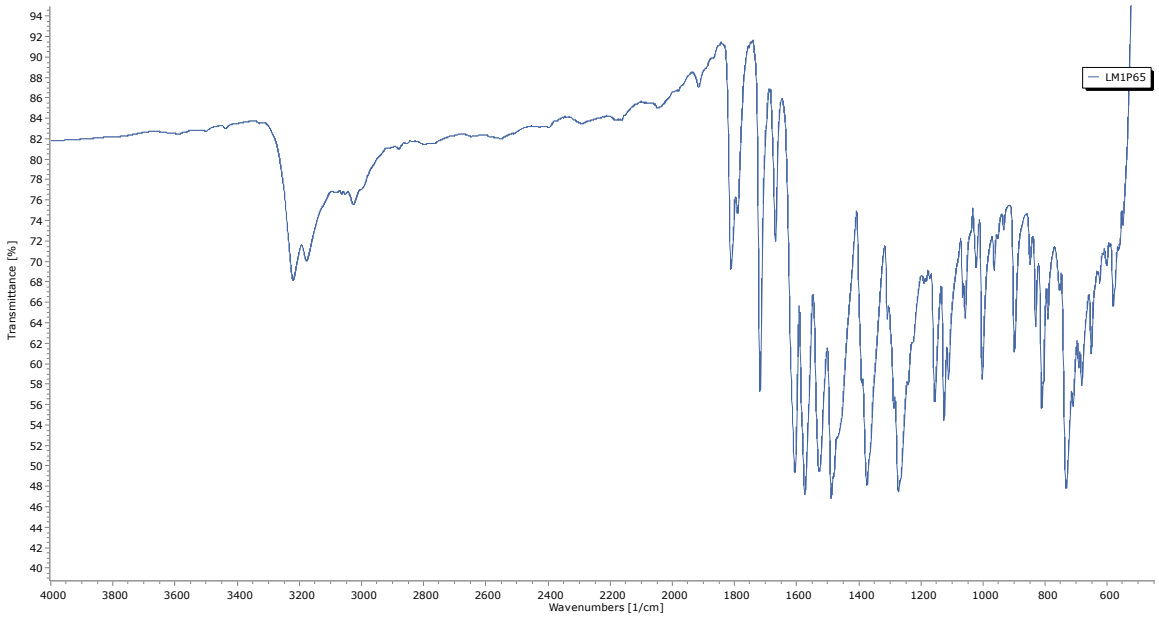

Figure A111. IR spectrum of **2.32**

Compounds

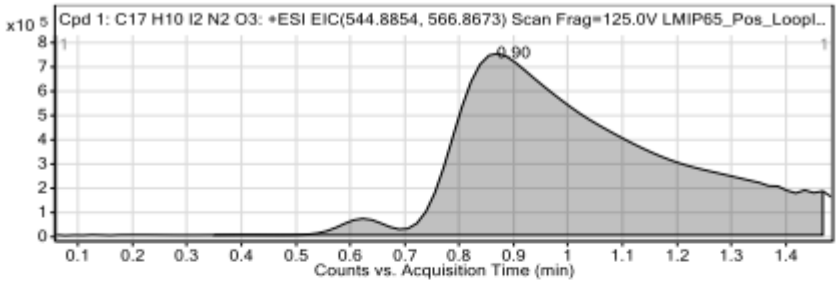

Integration Peak List

Start	RT	End	Height	Area
0.35	0.9	1.47	742996	17890863

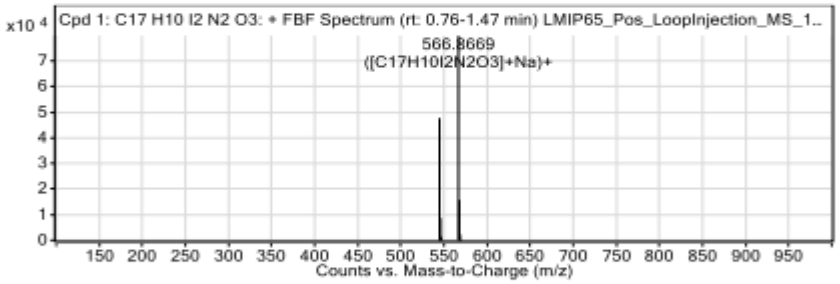

Peak List

m/z	z	Abund	Formula	Ion
544.8846	1	47712.78	C17H10I2N2O3	(M+H)+
545.8878	1	8701.18	C17H10I2N2O3	(M+H)+
546.8899	1	1333.92	C17H10I2N2O3	(M+H)+
547.8885	1	163.43	C17H10I2N2O3	(M+H)+
566.8669	1	79898.44	C17H10I2N2O3	(M+Na)+
567.8698	1	15761.88	C17H10I2N2O3	(M+Na)+
568.8725	1	2281.32	C17H10I2N2O3	(M+Na)+
569.8507	1	322.66	C17H10I2N2O3	(M+Na)+

--- End Of Report ---

Figure A112. HRMS of **2.32**

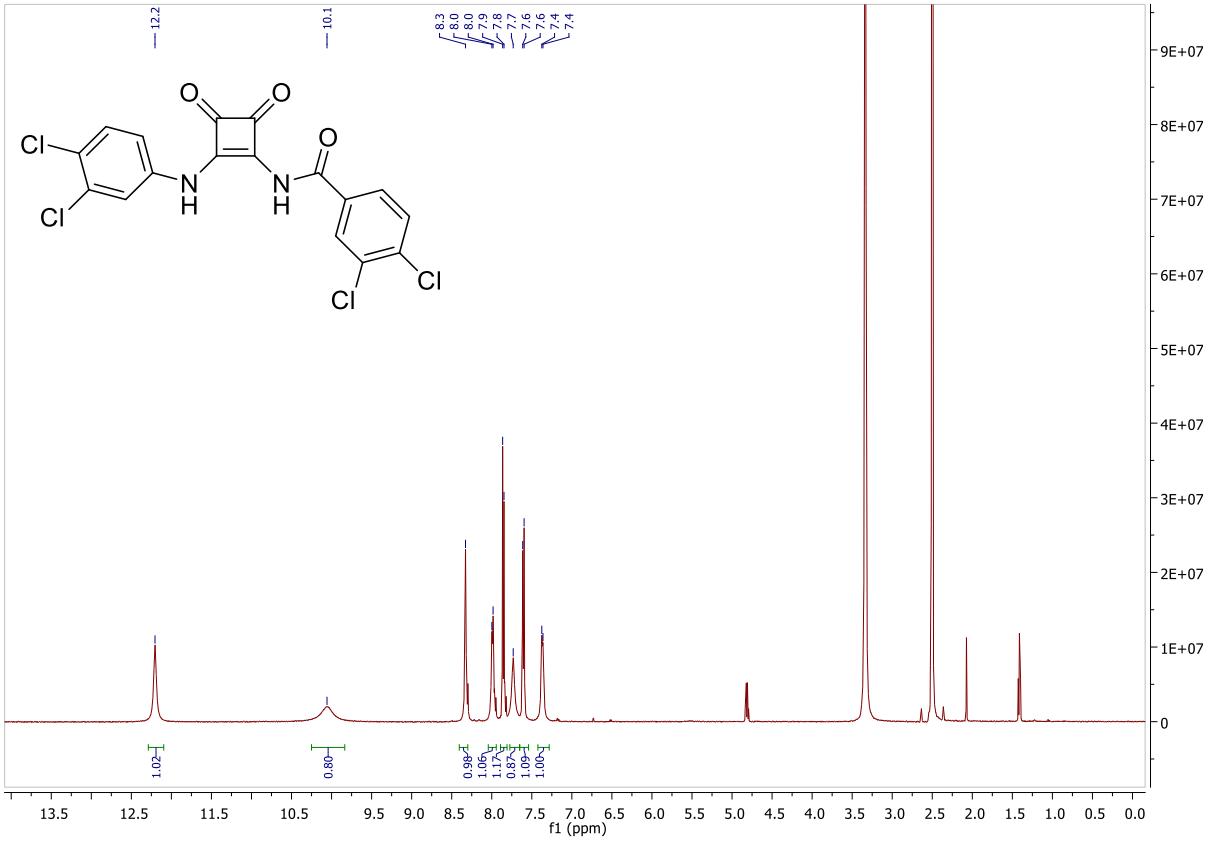

Figure A113. ^{1}H NMR (DMSO-d_6, 500 MHz) spectrum of **2.33**.

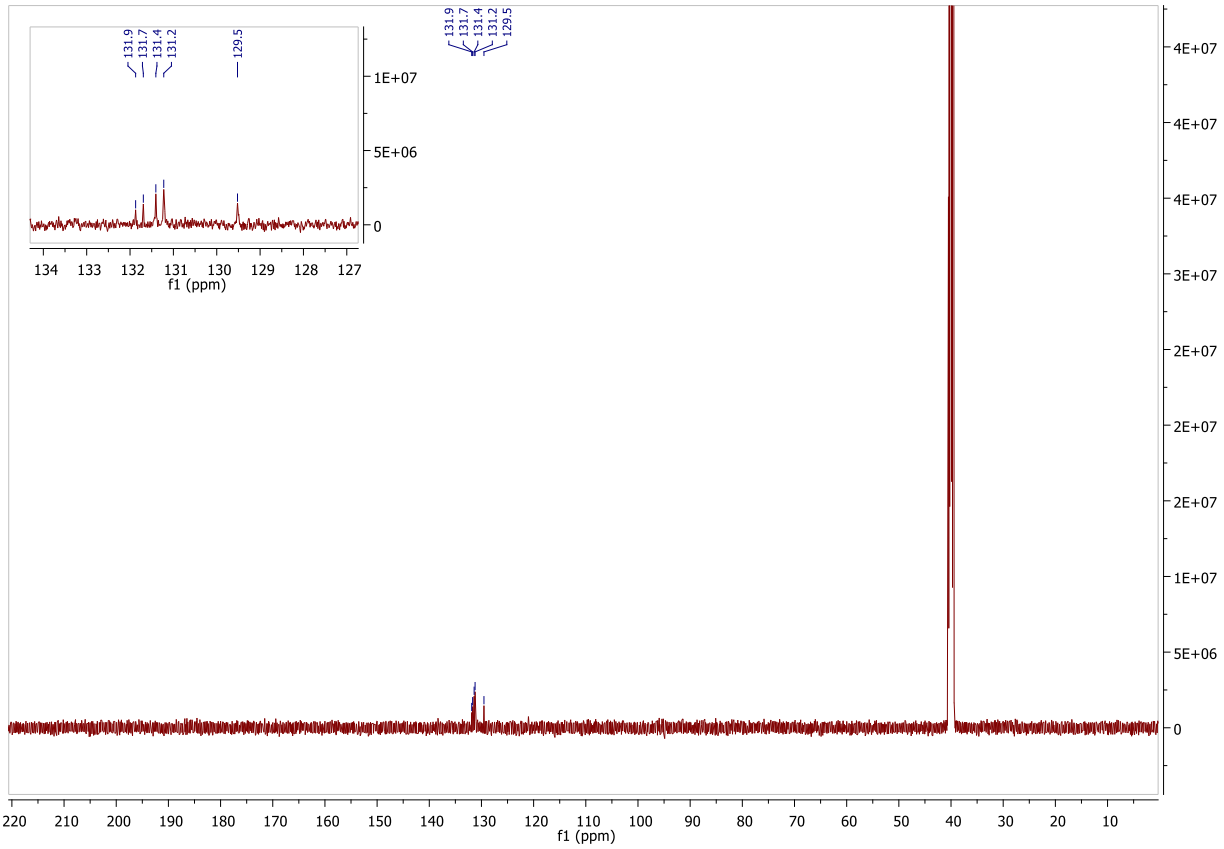

Figure A114. ^{13}C NMR (DMSO-d_6, 126 MHz) spectrum of **2.33**.

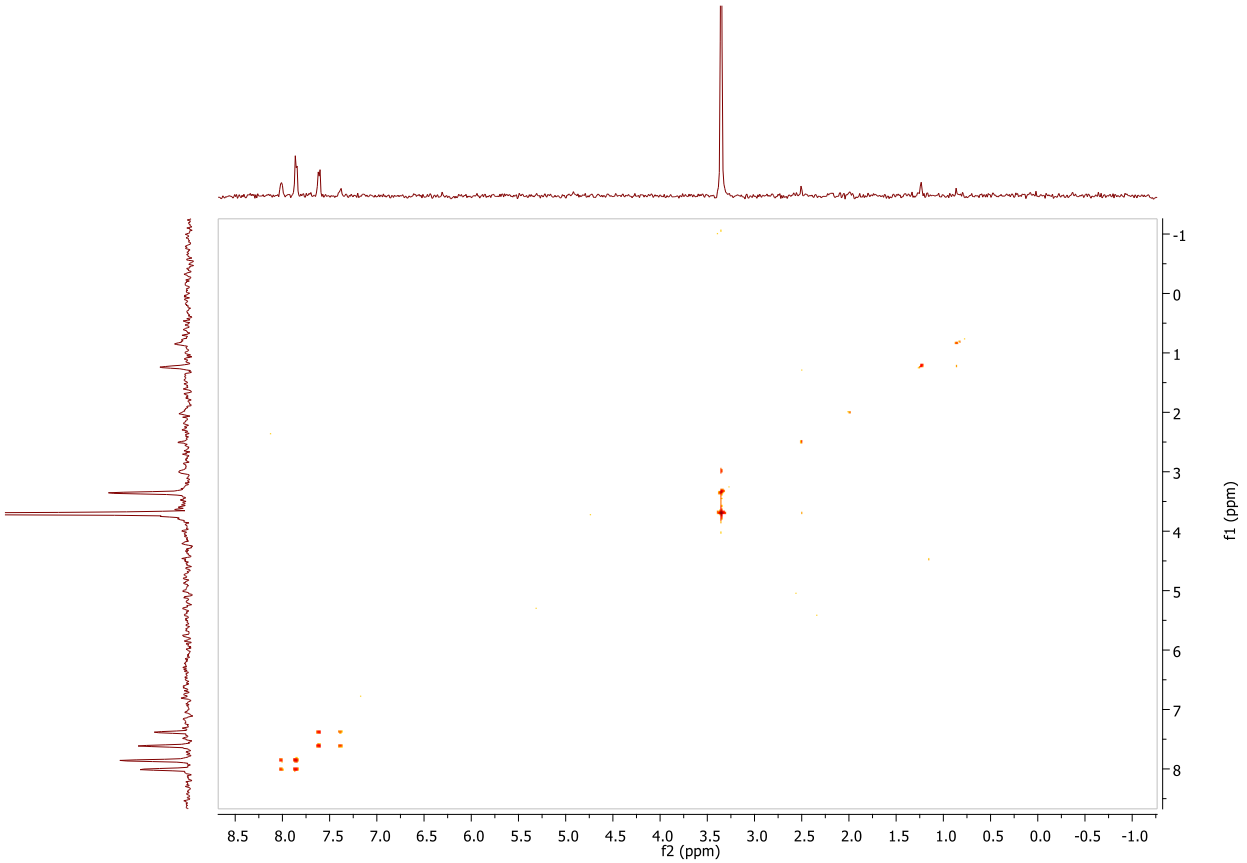

Figure A115. ^{1}H-^{1}H COSY spectrum of **2.33**

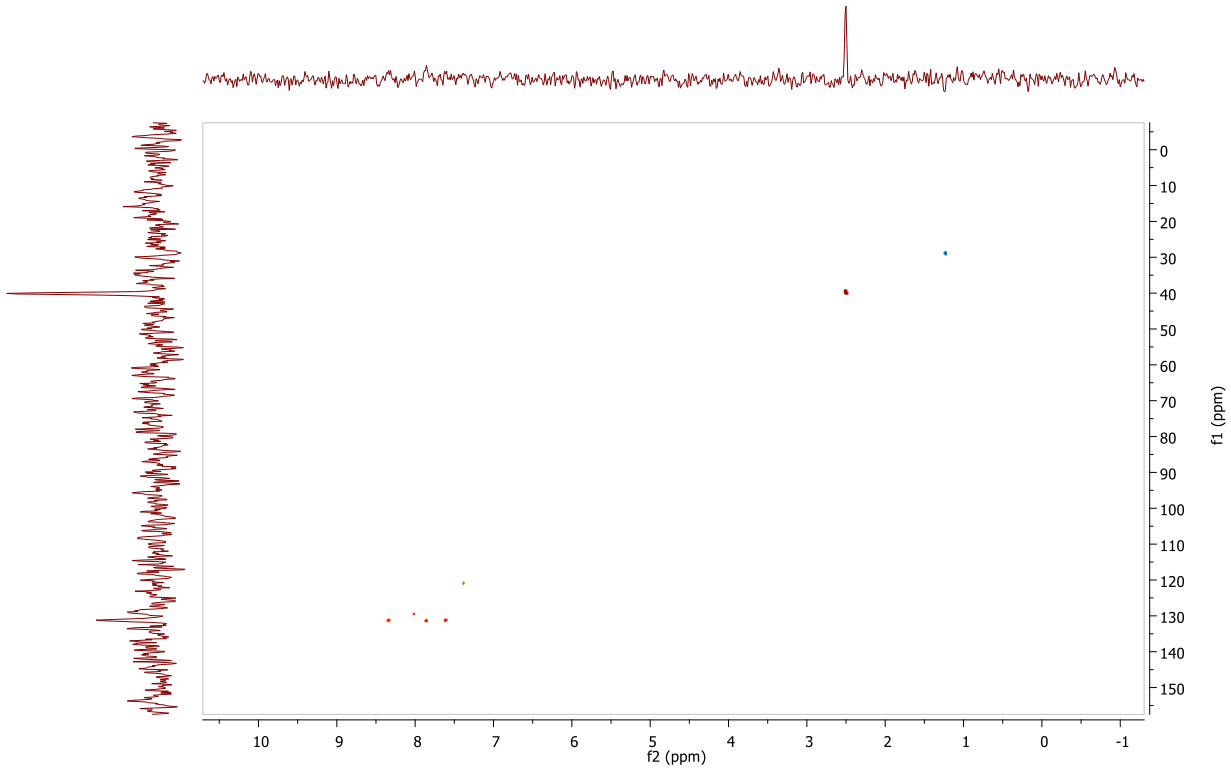

Figure A116. HSQC spectrum of **2.33**

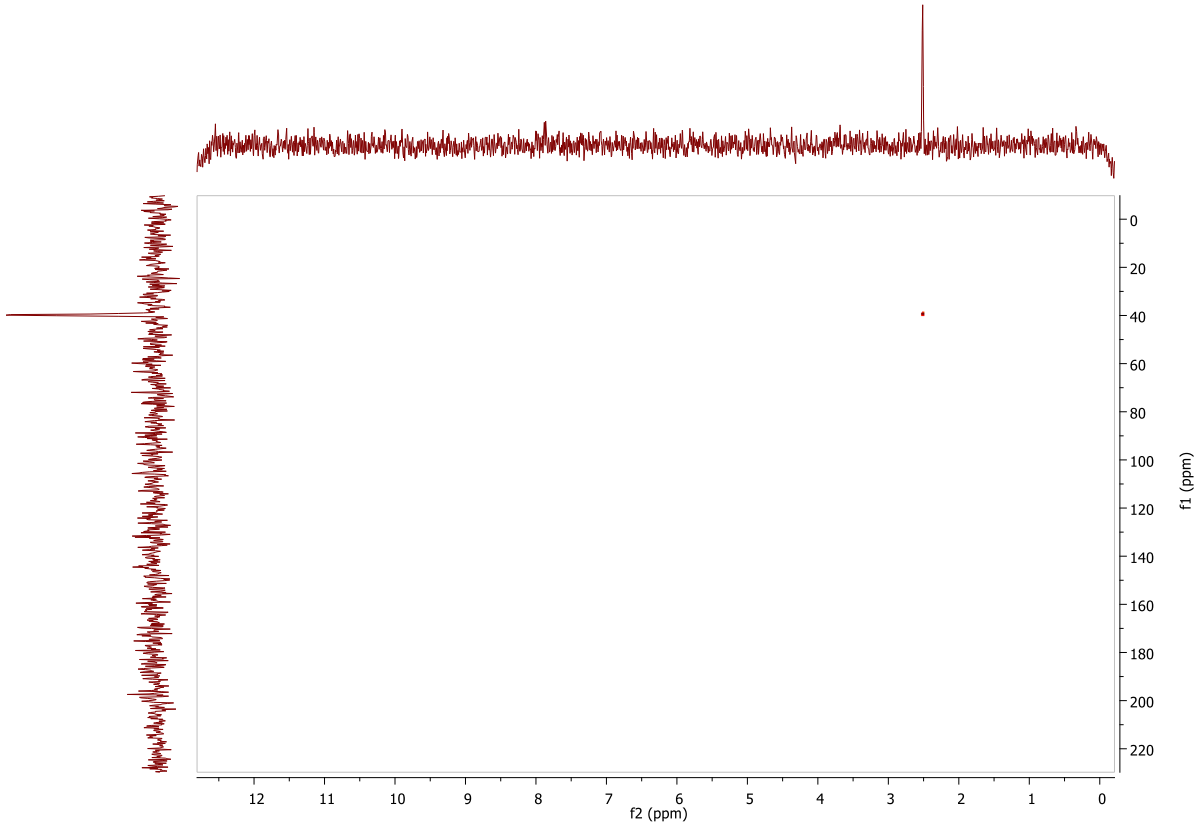

Figure A117. HMBC spectrum of **2.33**

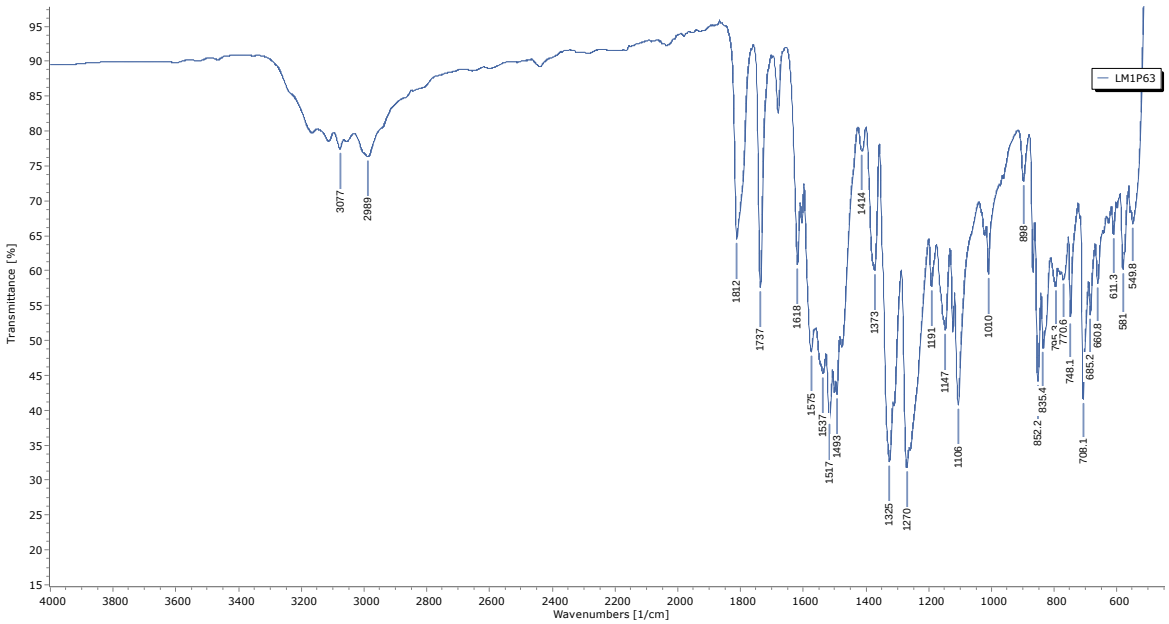

Figure A118. IR spectrum of **2.33**

Compounds

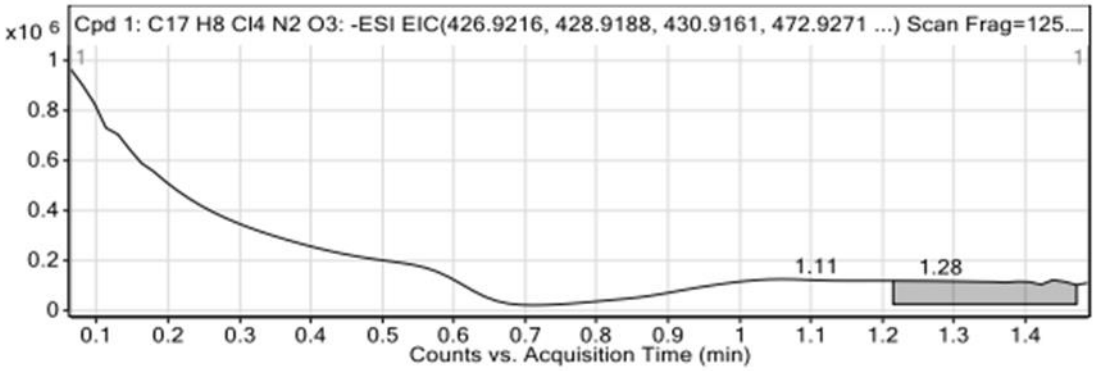

Integration Peak List

Start	RT	End	Height	Area
0.75	1.11	1.22	98506	1811788
1.22	1.28	1.47	91992	1385531

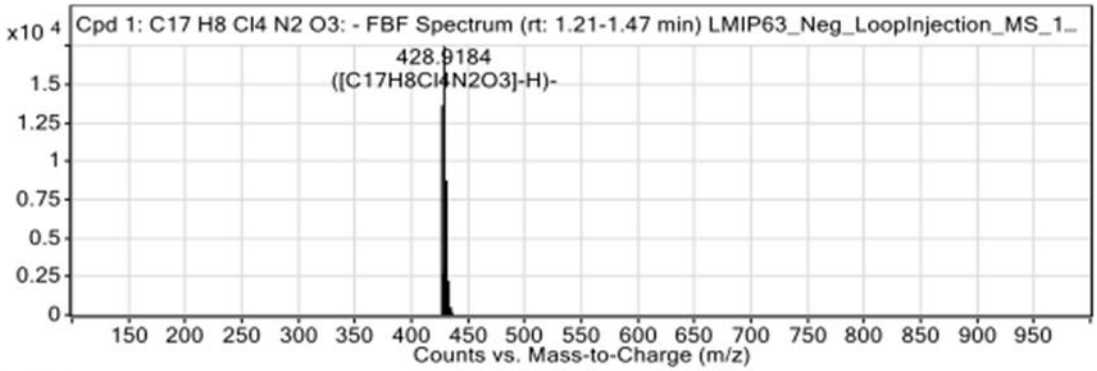

Peak List

m/z	z	Abund	Formula	Ion
426.9213	1	13656.46	C17H8Cl4N2O3	(M-H)-
427.9245	1	2656.83	C17H8Cl4N2O3	(M-H)-
428.9184	1	17543.08	C17H8Cl4N2O3	(M-H)-
429.9218	1	3160.57	C17H8Cl4N2O3	(M-H)-
430.9172	1	8763.45	C17H8Cl4N2O3	(M-H)-
431.92	1	1753.84	C17H8Cl4N2O3	(M-H)-
432.9138	1	2221.39	C17H8Cl4N2O3	(M-H)-
433.9161	1	420.11	C17H8Cl4N2O3	(M-H)-
434.8979	1	514.83	C17H8Cl4N2O3	(M-H)-
435.9007	1	176.8	C17H8Cl4N2O3	(M-H)-

--- End Of Report ---

Figure A119. HRMS of **2.33**

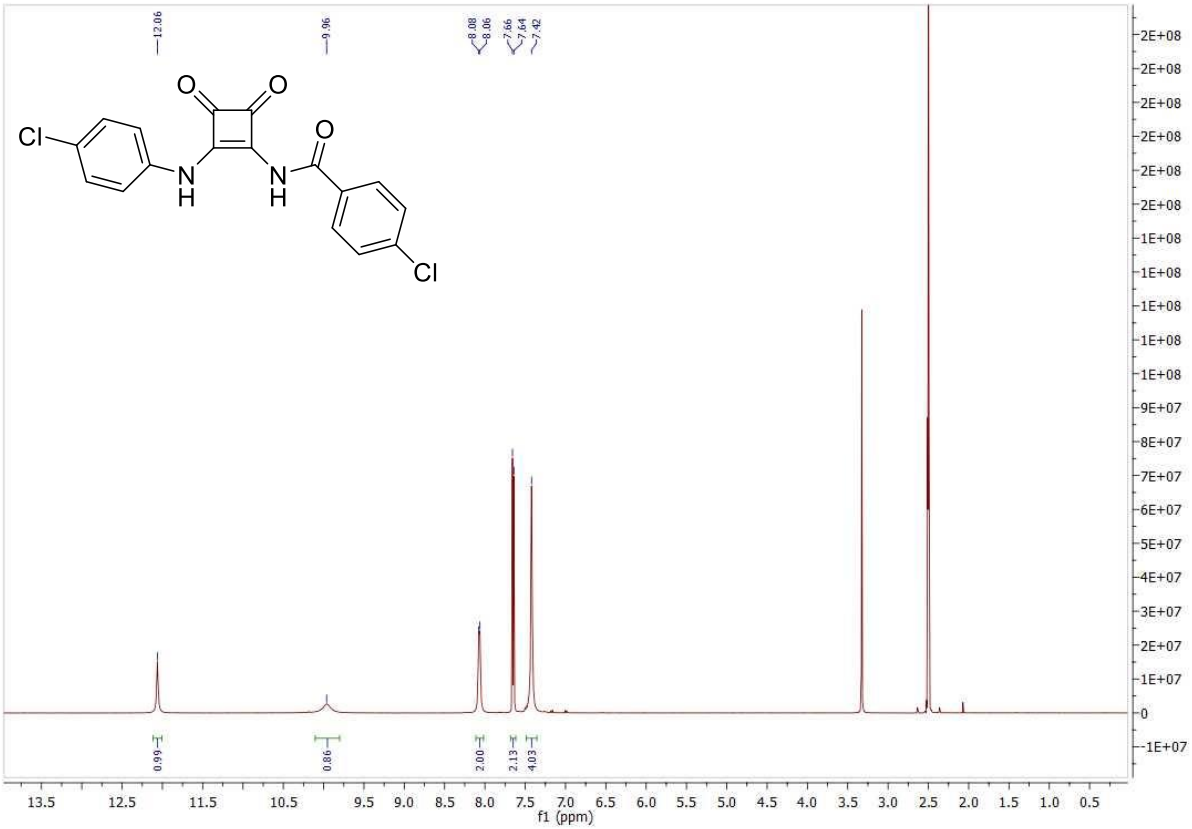

Figure A120. ^{1}H NMR (DMSO-d_6, 500 MHz) spectrum of **2.34**.

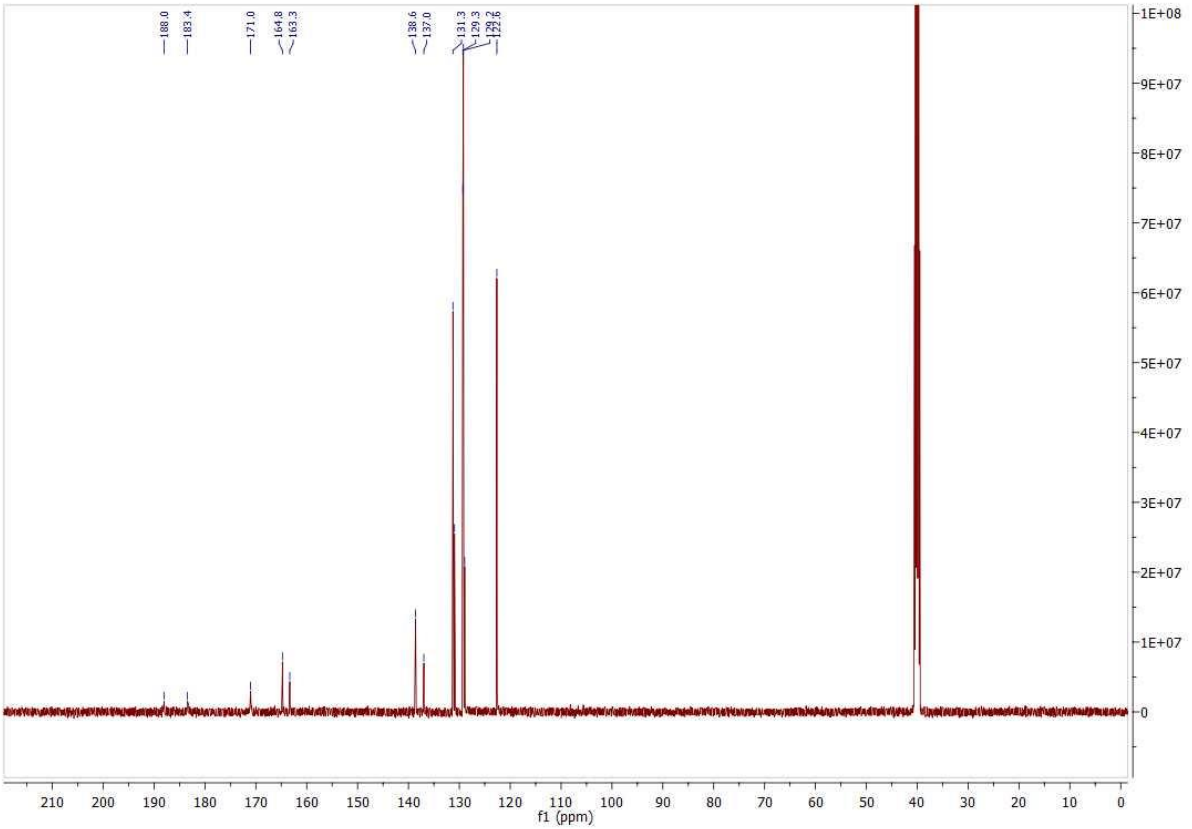

Figure A121. ^{13}C NMR (DMSO-d_6, 126 MHz) spectrum of **2.34**.

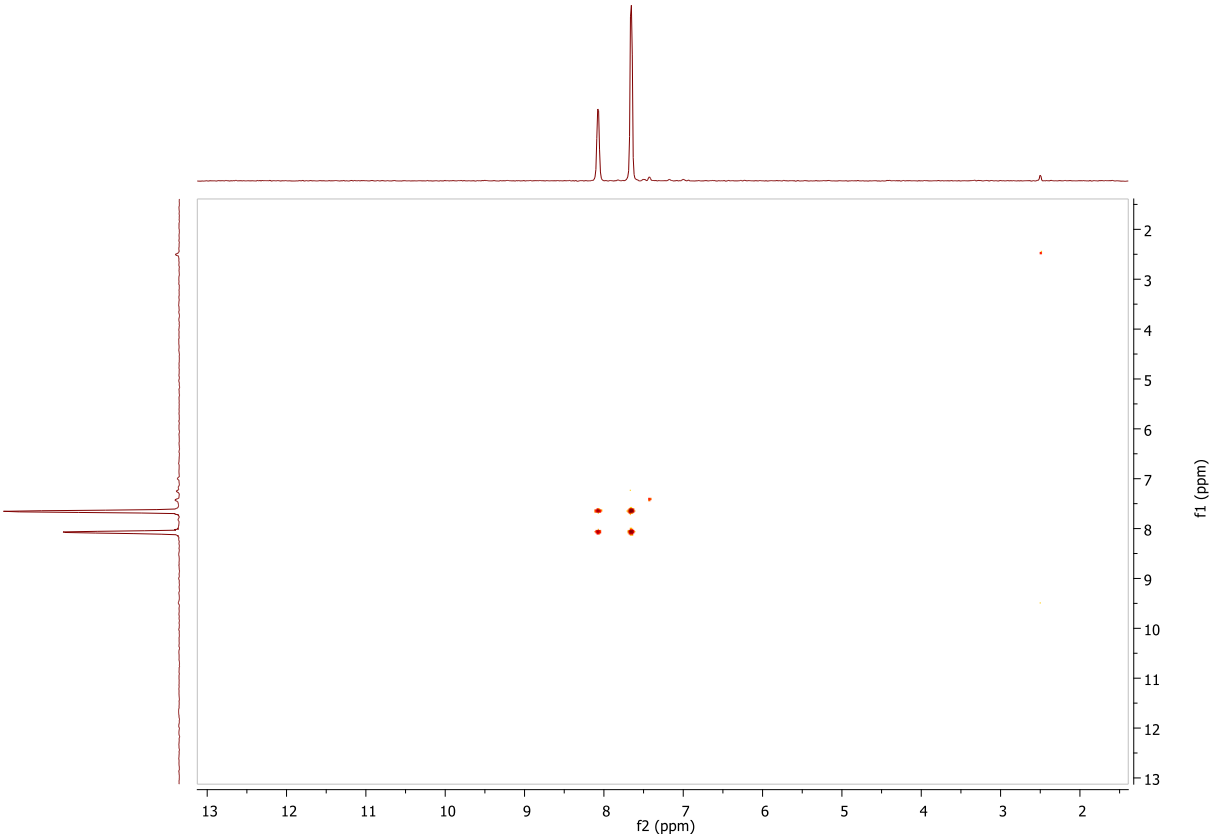

Figure A122. ^{1}H-^{1}H COSY spectrum of **2.34**

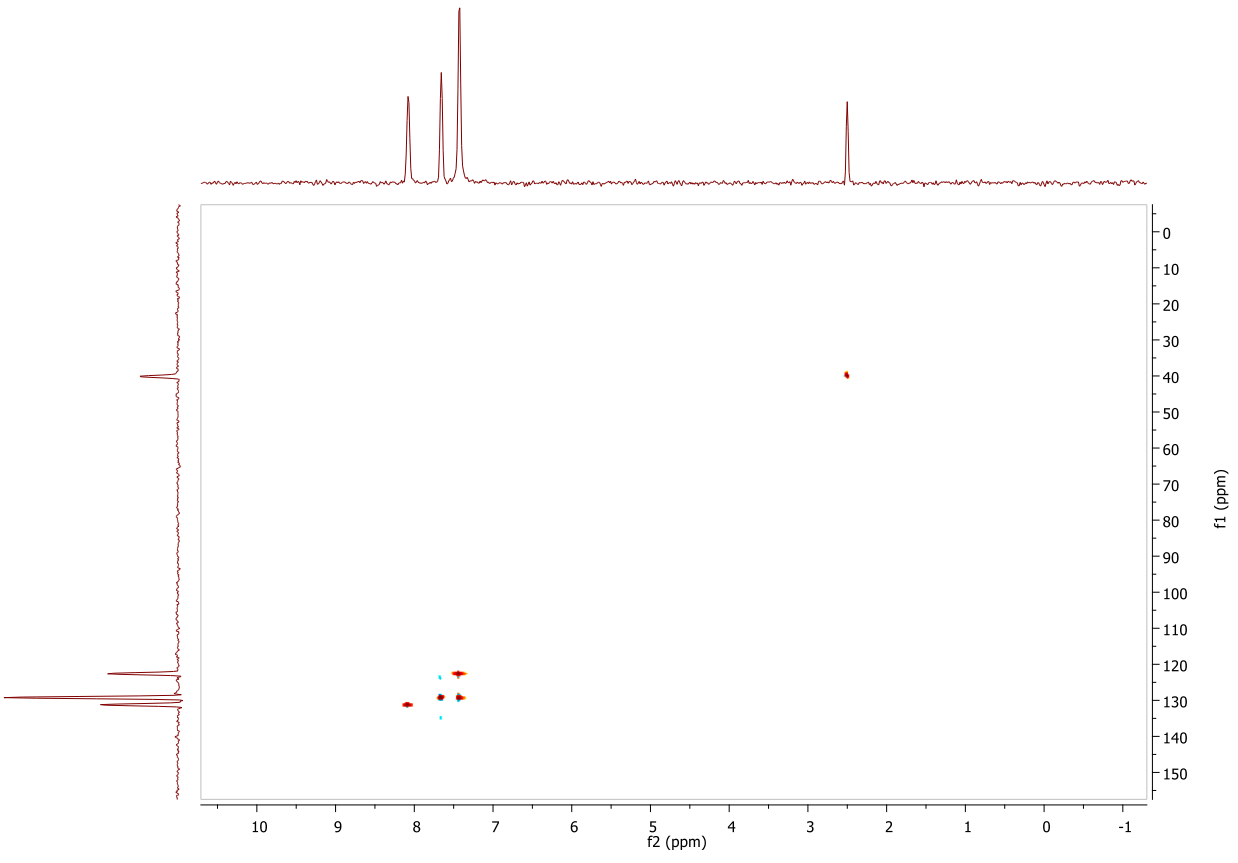

Figure A123. HSQC spectrum of **2.34**

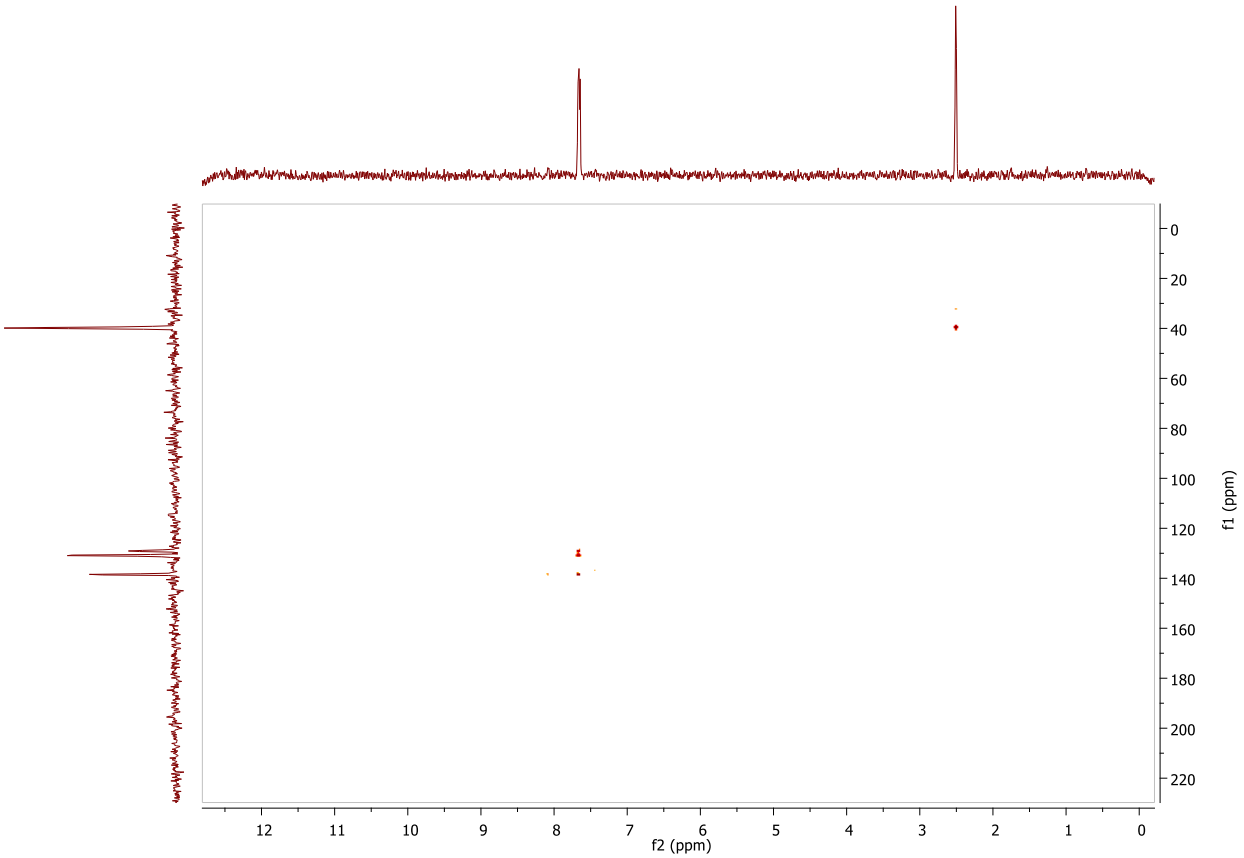

Figure A124. HMBC spectrum of **2.34**

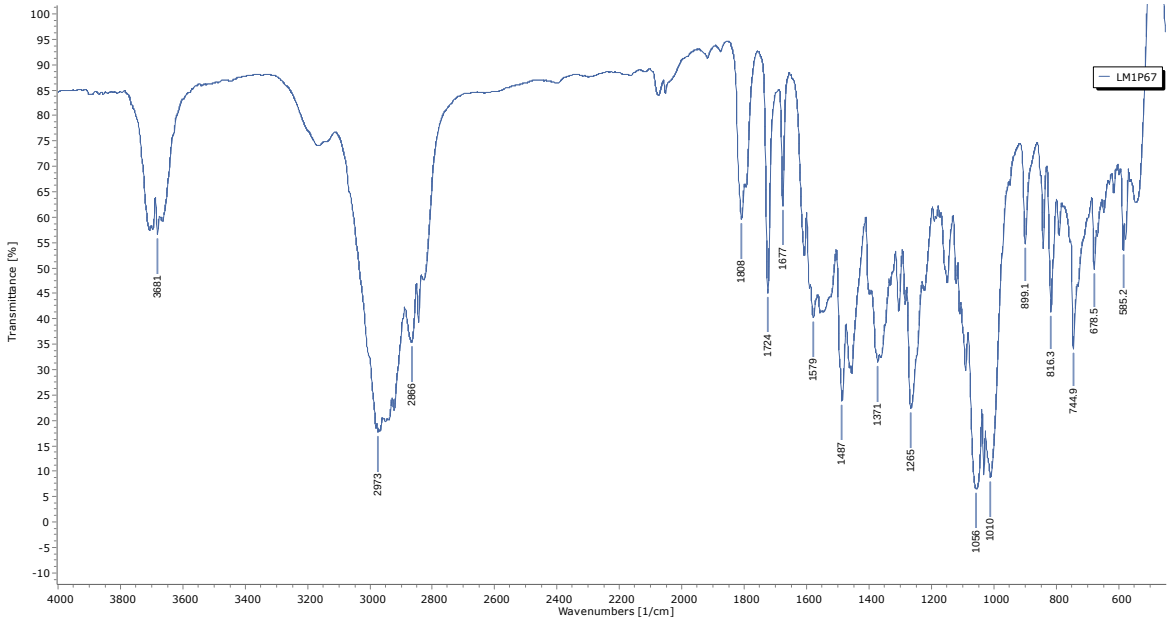

Figure A125. IR spectrum of **2.34**

Compounds

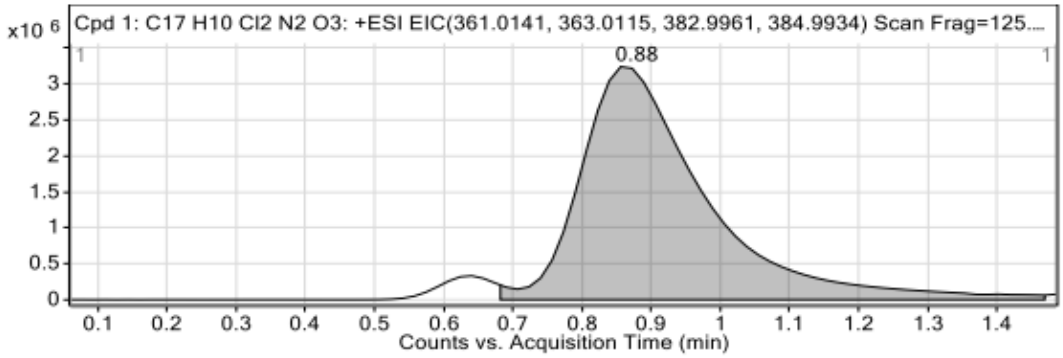

Integration Peak List

Start	RT	End	Height	Area
0.68	0.88	1.47	3052489	40426406

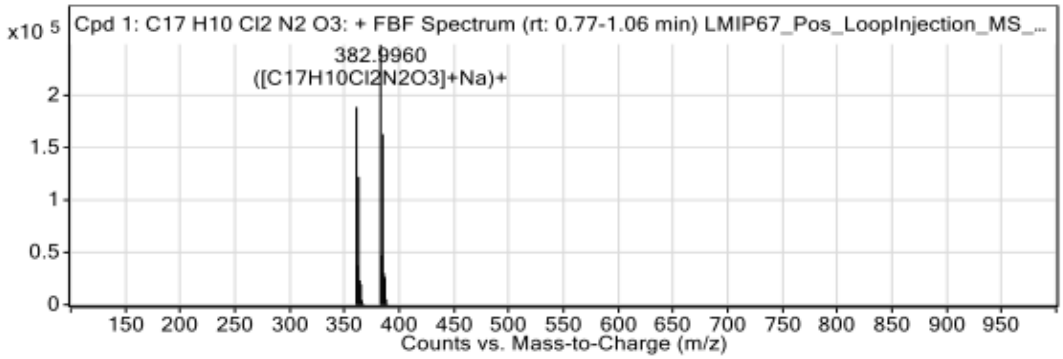

Peak List

m/z	z	Abund	Formula	Ion
361.014	1	188503.16	C17H10Cl2N2O3	(M+H)+
362.0172	1	37399.45	C17H10Cl2N2O3	(M+H)+
363.0113	1	121920.34	C17H10Cl2N2O3	(M+H)+
364.0142	1	23217.99	C17H10Cl2N2O3	(M+H)+
365.009	1	19490.81	C17H10Cl2N2O3	(M+H)+
382.996	1	248171.25	C17H10Cl2N2O3	(M+Na)+
383.9989	1	47022.43	C17H10Cl2N2O3	(M+Na)+
384.9934	1	162578.2	C17H10Cl2N2O3	(M+Na)+
385.9962	1	30132.79	C17H10Cl2N2O3	(M+Na)+
386.991	1	26273.02	C17H10Cl2N2O3	(M+Na)+

--- End Of Report ---

Figure A126. HRMS of **2.34**

B. Chapter 2 UV-Vis Data

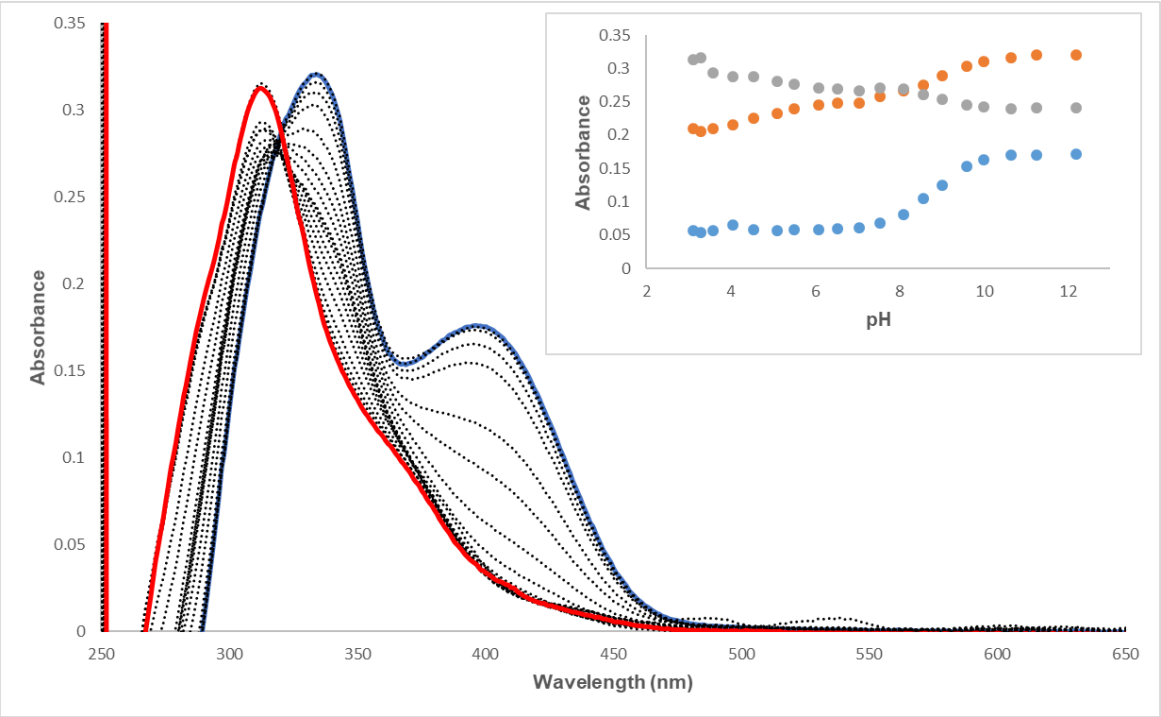

Figure B1. Absorption spectra taken over the course of a pH-spectrophotometric titration of **2.27** (10 µM) in an DMSO–water mixture (9/1 v/v; in presence of 0.1 M TBAPF6) pH 3.29 (red), pH 12.18 (blue). *Inset*: Comparison plots of absorbance at 312 nm (grey), 332 nm (orange), 312 nm (blue) vs. pH.

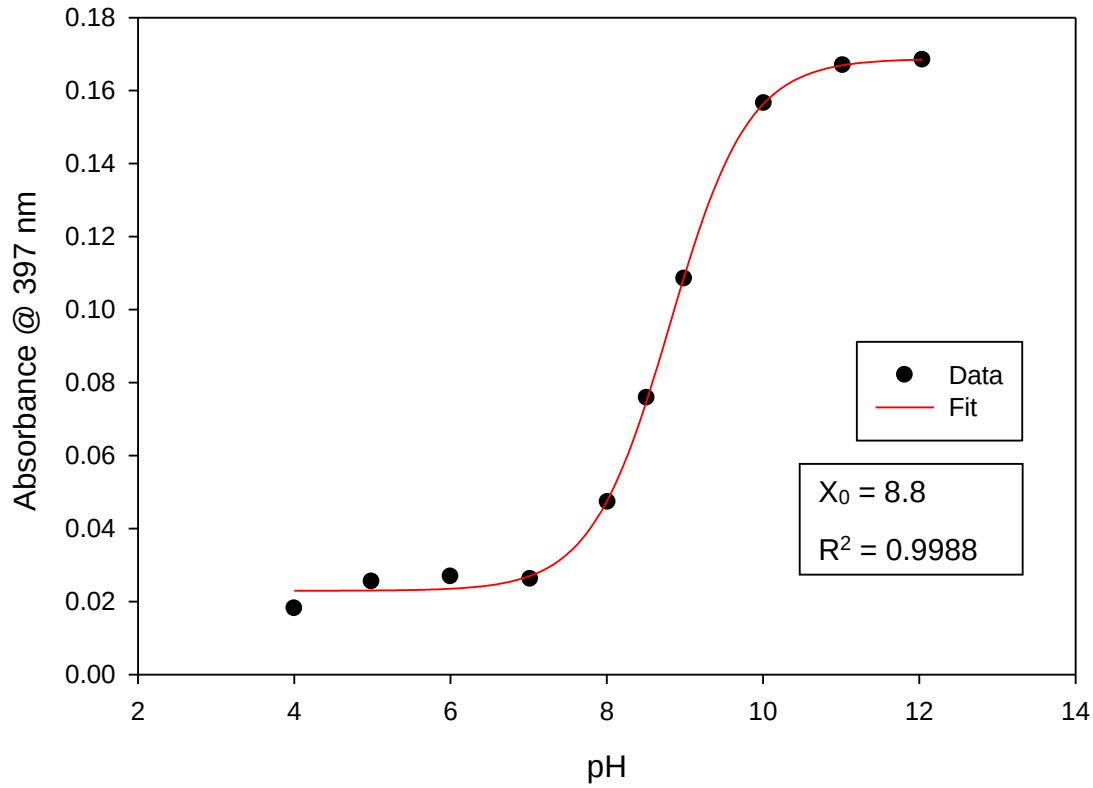

Figure B2. Four parameter sigmoid curve fit with the point of inflexion (X_0) corresponding to the pK_a value for **2.27**.

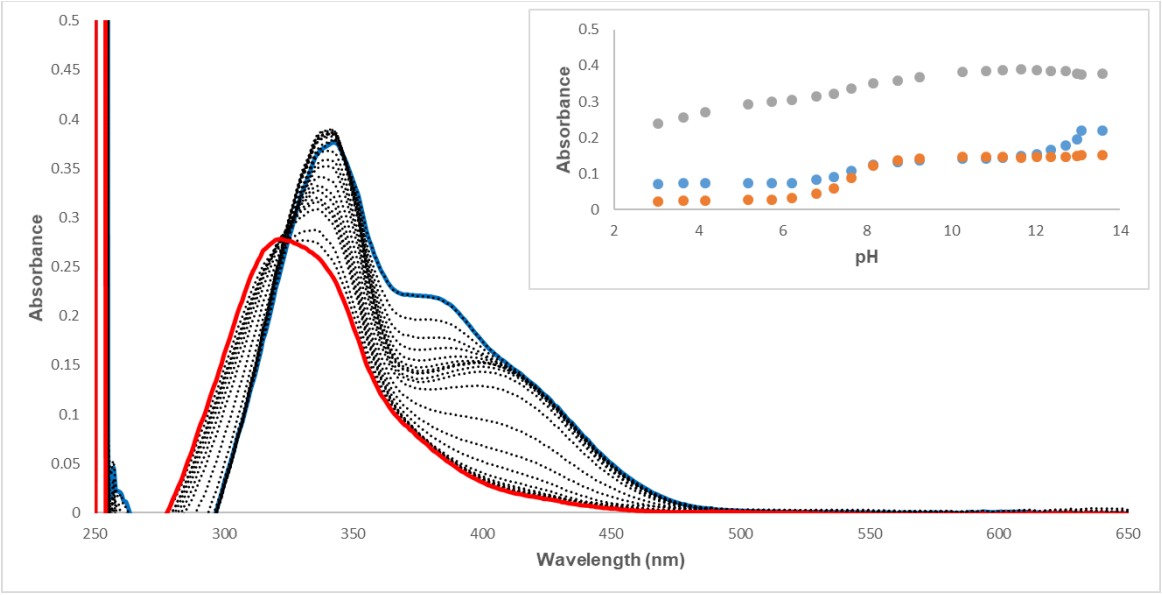

Figure B3. Absorption spectra taken over the course of a pH-spectrophotometric titration of **2.28** (10 µM) in an DMSO–water mixture (9/1 v/v; in presence of 0.1 M TBAPF6) pH 3.04 (red), pH 13.08 (blue). *Inset*: Comparison plots of absorbance at 342 nm (grey), 410 nm (orange), 378 nm (blue) vs. pH.

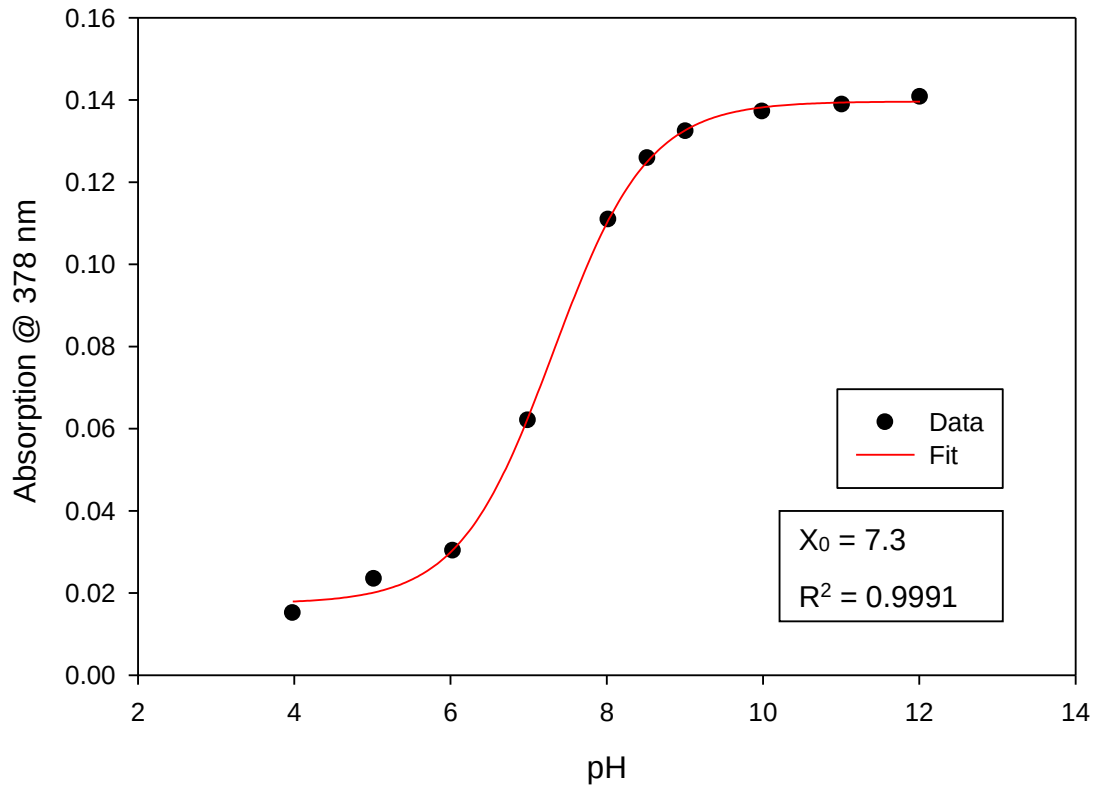

Figure B4. Four parameter sigmoid curve fit with the point of inflexion (X_0) corresponding to the pK_a value for **2.28**.

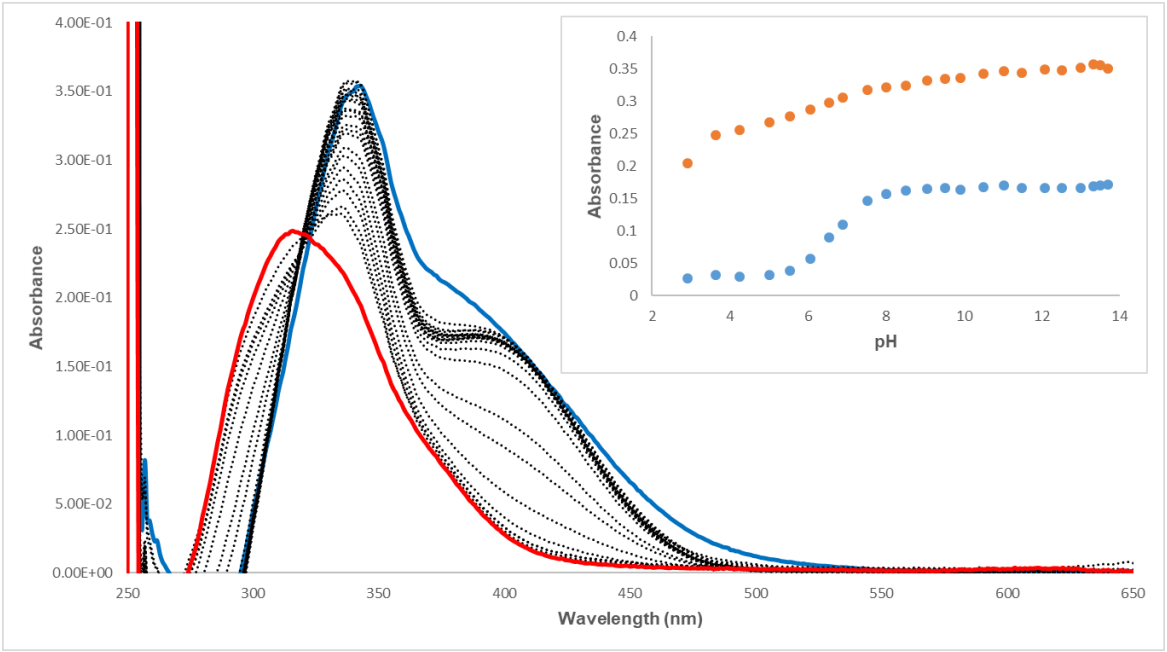

Figure B5. Absorption spectra taken over the course of a pH-spectrophotometric titration of **2.29** (10 µM) in an DMSO–water mixture (9/1 v/v; in presence of 0.1 M TBAPF6) pH 2.90 (red), pH 12.46 (blue). *Inset*: Comparison plots of absorbance at 340 nm (orange) and 401 nm (blue) vs. pH.

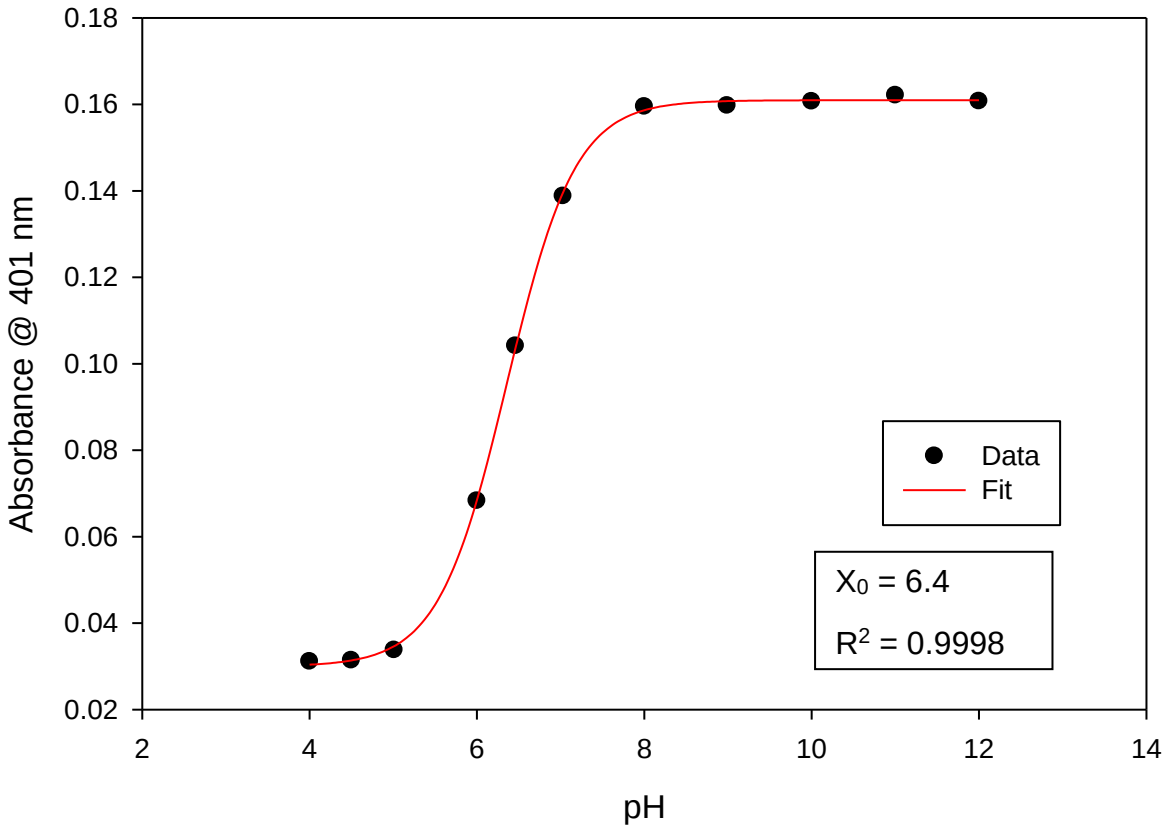

Figure B6. Four parameter sigmoid curve fit with the point of inflexion (X_0) corresponding to the pK_a value for **2.29**.

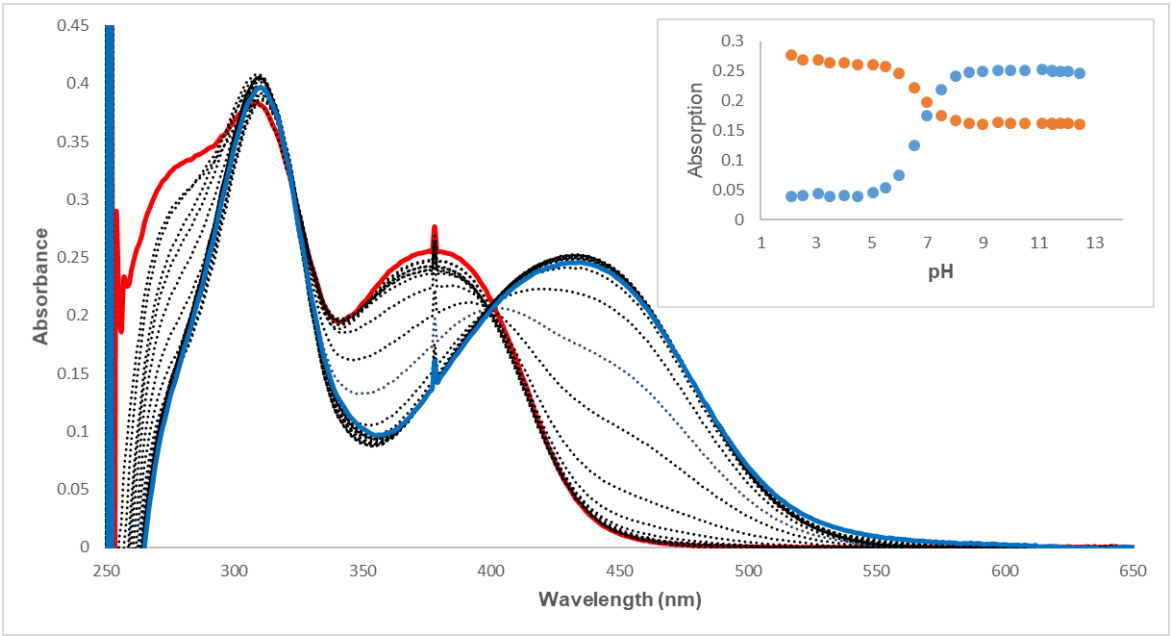

Figure B7. Absorption spectra taken over the course of a pH-spectrophotometric titration of **2.30** (10 µM) in an DMSO–water mixture (9/1 v/v; in presence of 0.1 M TBAPF6) pH 2.08 (red), pH 13.70 (blue). *Inset*: Comparison plots of absorbance at 378 nm (orange) and 434 nm (blue) vs. pH.

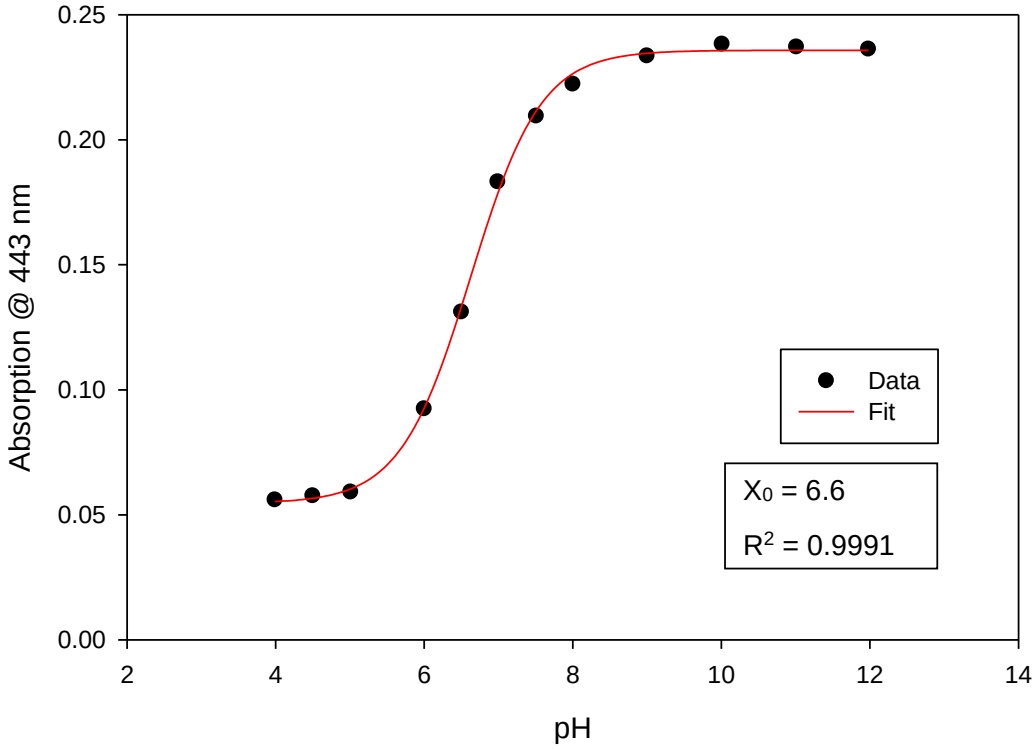

Figure B8. Four parameter sigmoid curve fit with the point of inflexion (X_0) corresponding to the pK_a value for **2.30**.

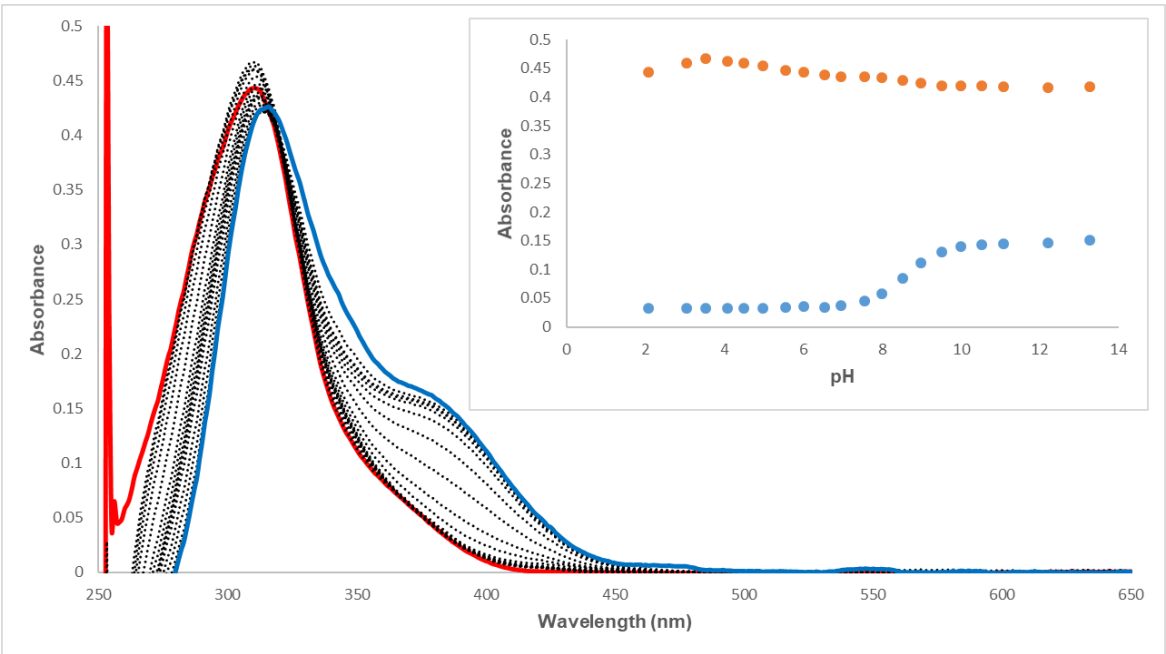

Figure B9. Absorption spectra taken over the course of a pH-spectrophotometric titration of **2.31** (10 µM) in an DMSO–water mixture (9/1 v/v; in presence of 0.1 M TBAPF6) pH 2.08 (red), pH 13.27 (blue). *Inset*: Comparison plots of absorbance at 311 nm (orange) and 385 nm (blue) vs. pH.

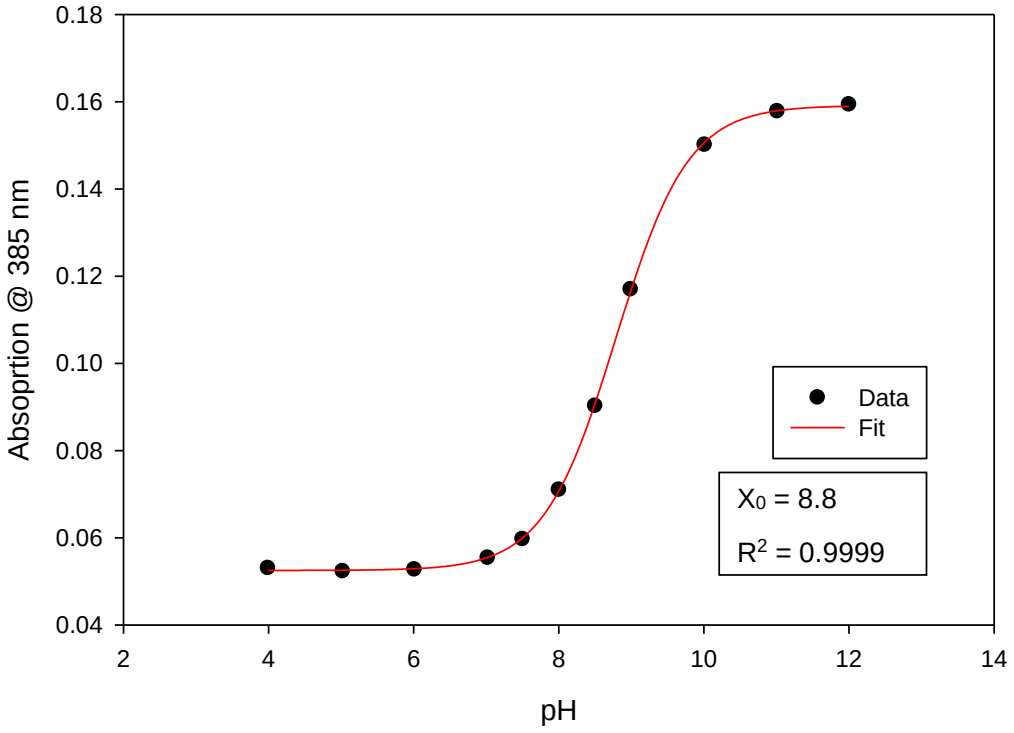

Figure B10. Four parameter sigmoid curve fit with the point of inflexion (X_0) corresponding to the pK_a value for **2.31**.

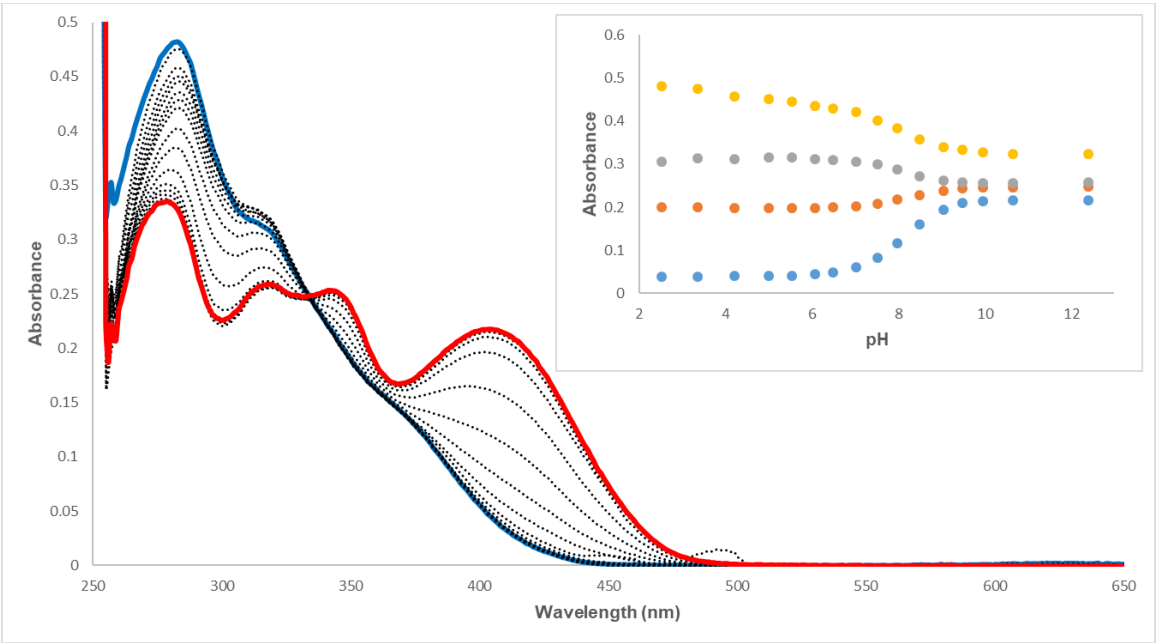

Figure B11. Absorption spectra taken over the course of a pH-spectrophotometric titration of **2.32** (10 µM) in an DMSO–water mixture (9/1 v/v; in presence of 0.1 M TBAPF6) pH 2.52 (red), pH 12.40 (blue). *Inset*: Comparison plots of absorbance at 284 nm (yellow), 320 nm (grey), 347 nm (orange), and 407 nm (blue) vs. pH.

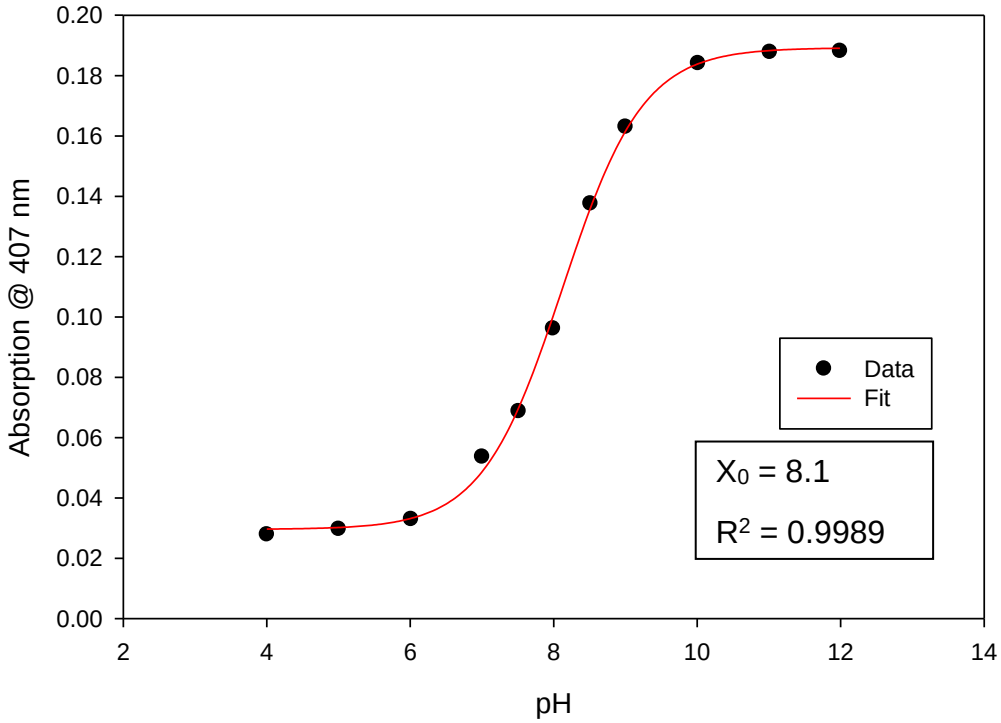

Figure B12. Four parameter sigmoid curve fit with the point of inflexion (X_0) corresponding to the pK_a value for **2.32**.

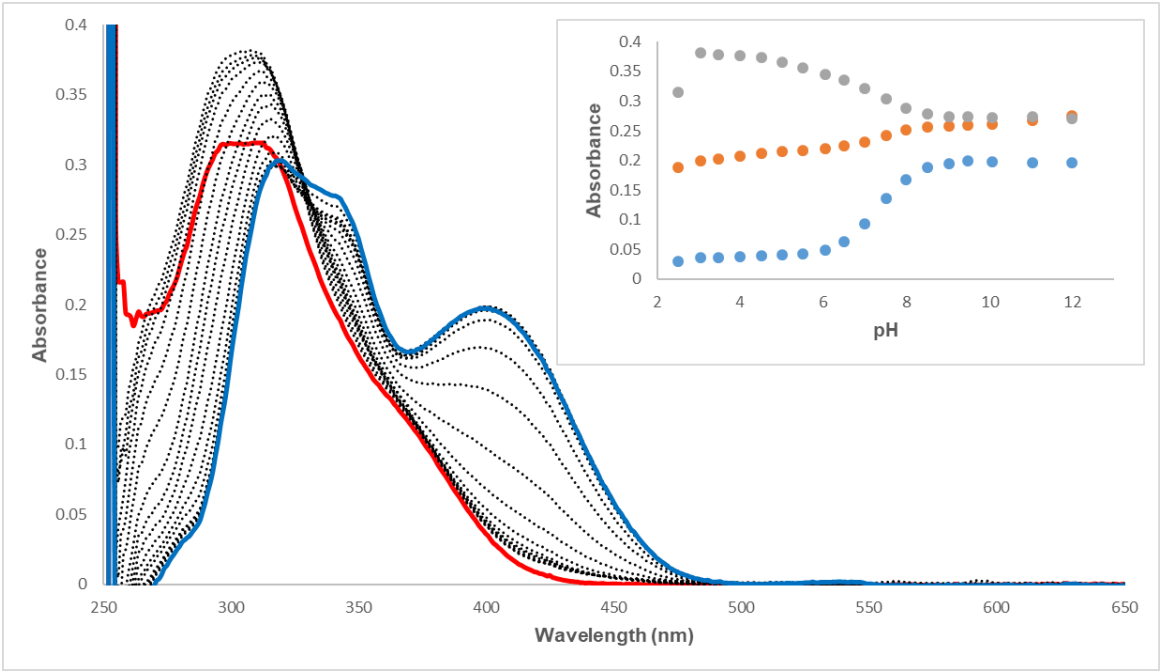

Figure B13. Absorption spectra taken over the course of a pH-spectrophotometric titration of **2.33** (10 µM) in an DMSO–water mixture (9/1 v/v; in presence of 0.1 M TBAPF6) pH 2.50 (red), pH 11.98 (blue). *Inset*: Comparison plots of absorbance at 310 nm (grey), 343 nm (orange), and 403 nm (blue) vs. pH.

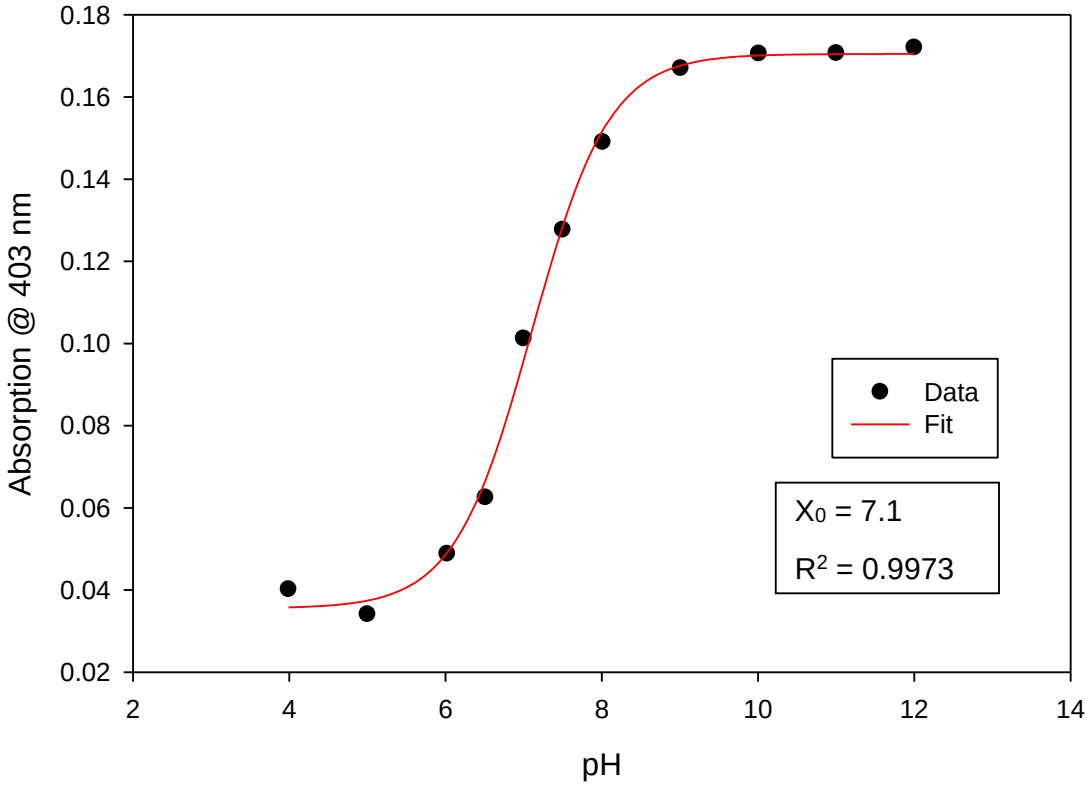

Figure B14. Four parameter sigmoid curve fit with the point of inflexion (X_0) corresponding to the pK_a value for **2.33**.

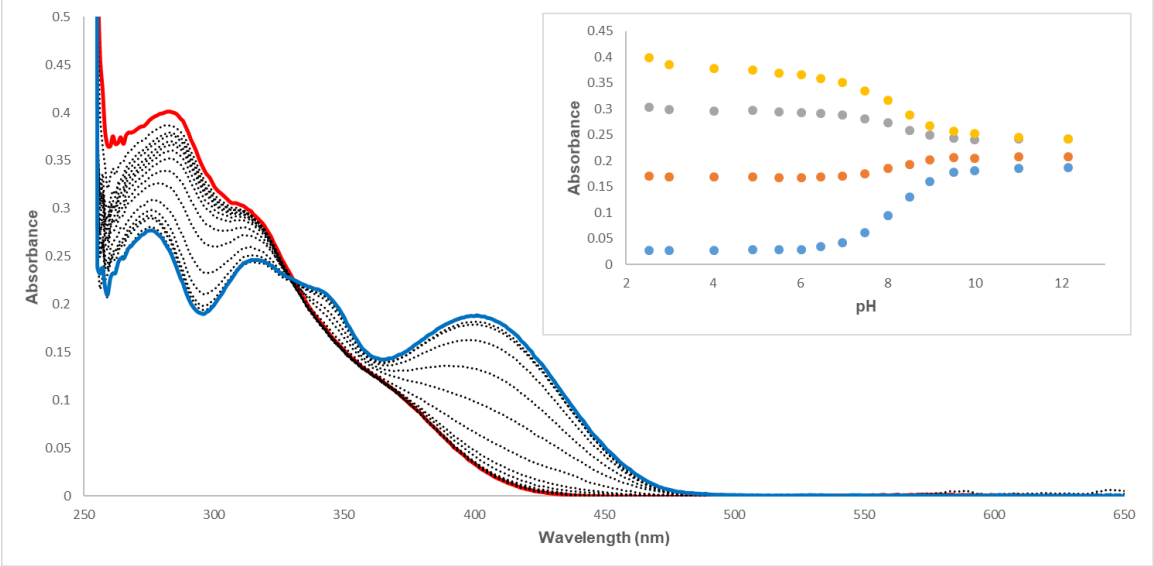

Figure B15. Absorption spectra taken over the course of a pH-spectrophotometric titration of **2.34** (10 µM) in an DMSO–water mixture (9/1 v/v; in presence of 0.1 M TBAPF6) pH 2.53 (red), pH 12.14 (blue). *Inset*: Comparison plots of absorbance at 285 nm (yellow), 311 nm (grey), 344 nm (orange), and 404 nm (blue) vs. pH.

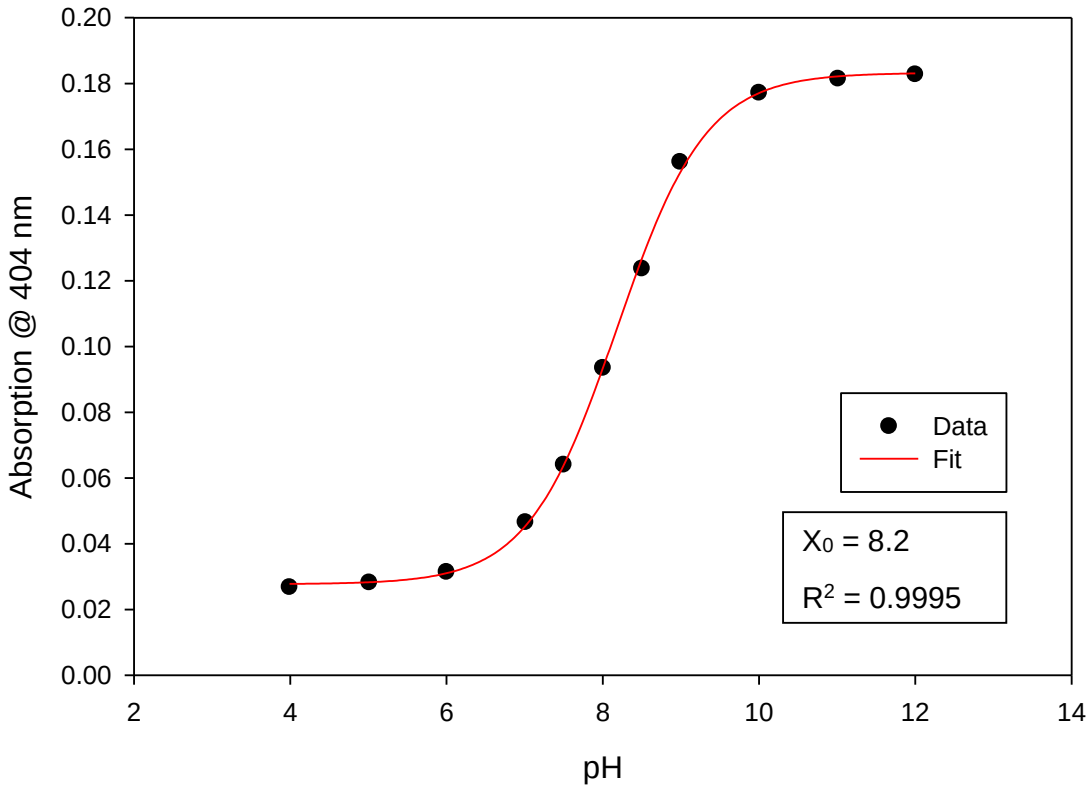

Figure B16. Four parameter sigmoid curve fit with the point of inflexion (X_0) corresponding to the pK_a value for **2.34**.

C. Chapter 2 ^{1}H NMR Anion Titration and Binding Data

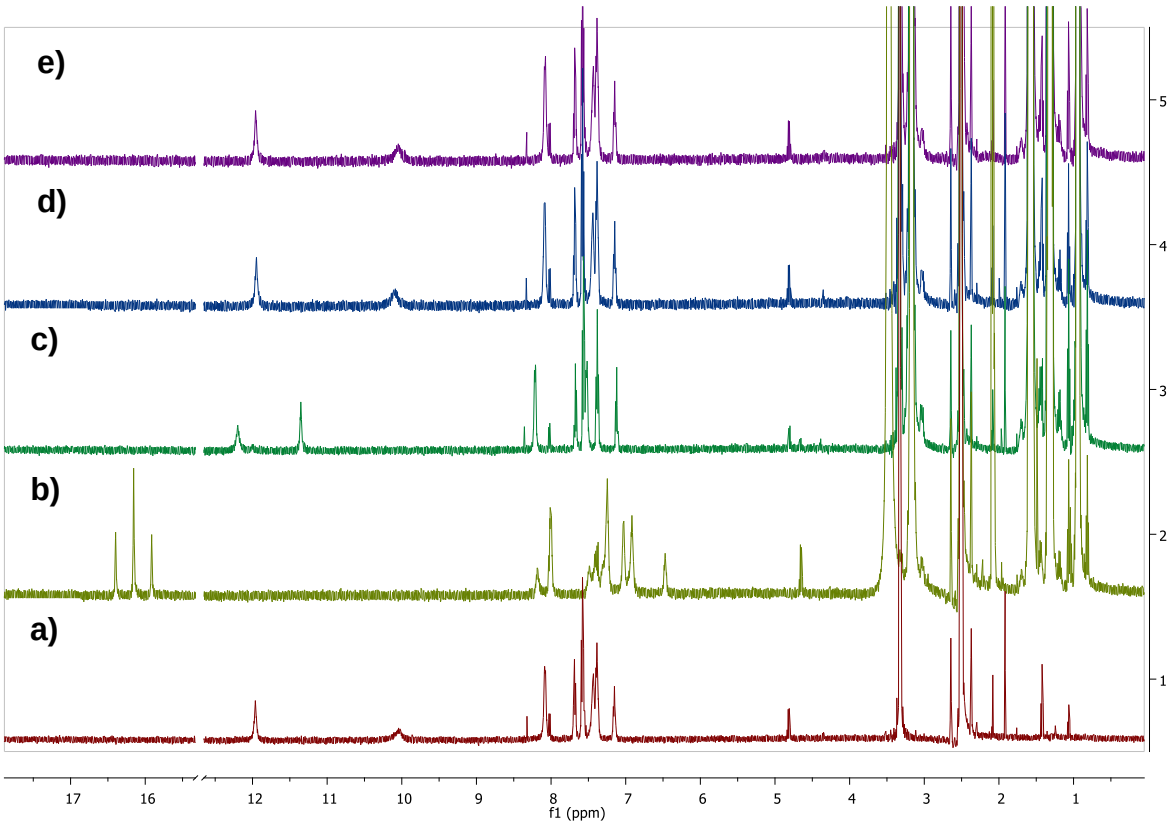

Figure C1. ^{1}H NMR stackplot of **2.27** (2.5 x 10^{-6} M) treated with different TBA salts of anions (10 equiv.). a) Blank spectra of **2.27** (no anion present). b) **2.27** + TBAF. c) **2.27** + TBACl. d) **2.27** + TBABr. e) **2.27** + TBAI.

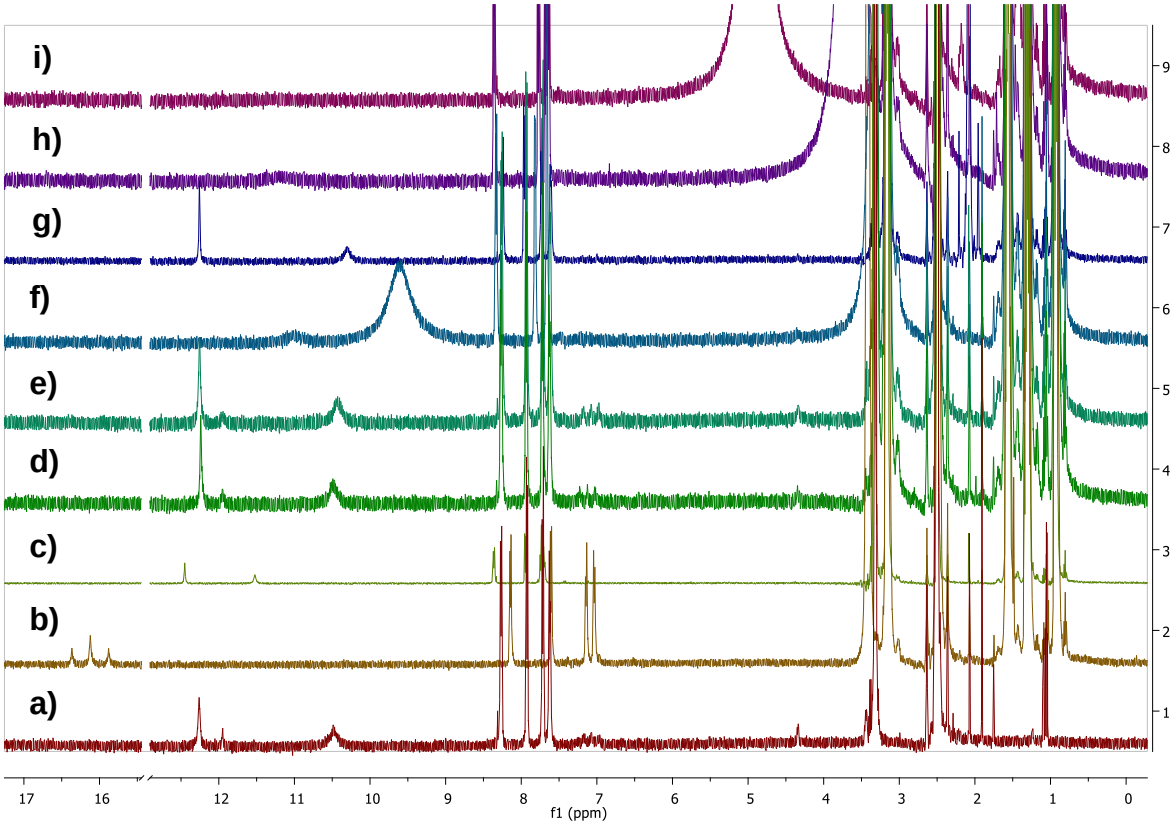

Figure C2. ^{1}H NMR stackplot of **2.28** (2.5 x 10^{-6} M) treated with different TBA salts of anions (10 equiv.). a) Blank spectra of **2.28** (no anion present). b) **2.28** + TBAF. c) **2.28** + TBACl. d) **2.28** + TBABr. e) **2.28** + TBAI, f) **2.28** + TBA_2SO_4, g) **2.28** + $TBANO_3$, h) **2.28** + TBAOAc, i) **2.28** + $TBA_2H_2PO_4$.

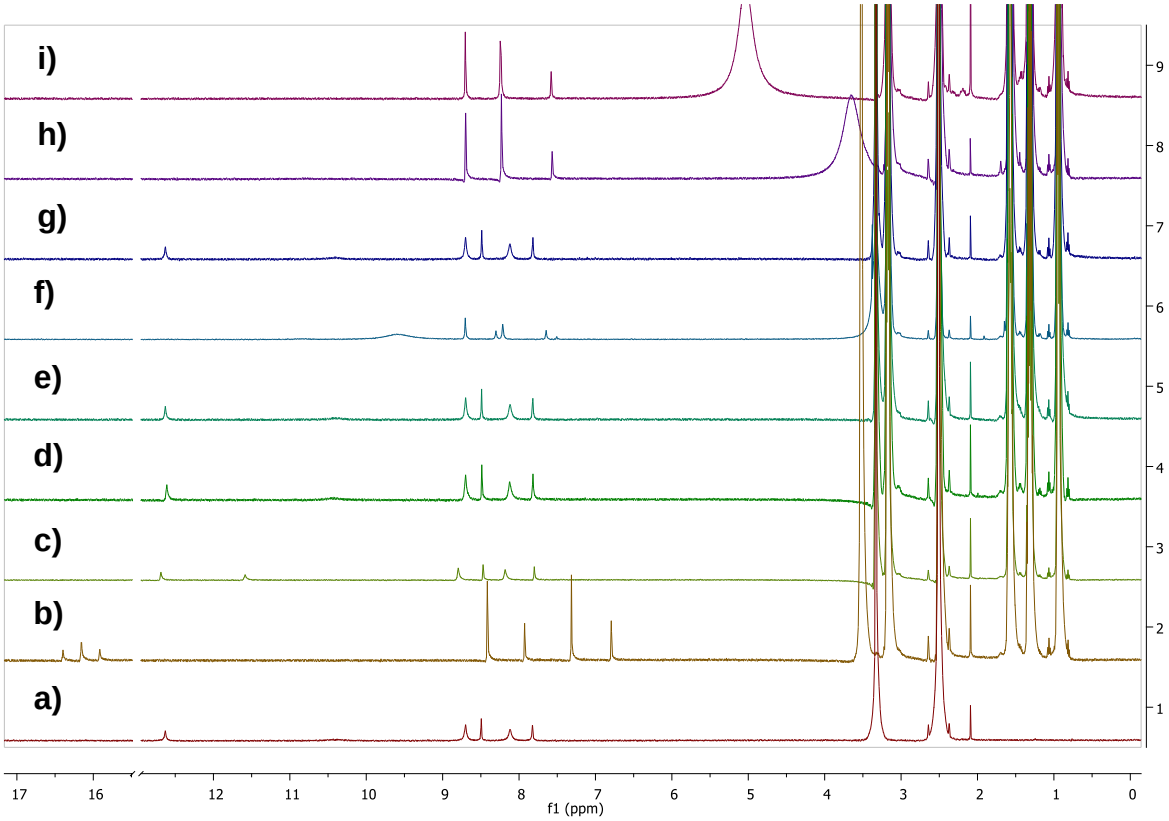

Figure C3 ^{1}H NMR stackplot of **2.29** (2.5 x 10^{-6} M) treated with different TBA salts of anions (10 equiv.). a) Blank spectra of **2.29** (no anion present). b) **2.29** + TBAF. c) **2.29** + TBACl. d) **2.29** + TBABr. e) **2.29** + TBAI, f) **2.29** + TBA_2SO_4, g) **2.29** + $TBANO_3$, h) **2.29** + TBAOAc, i) **2.29** + $TBA_2H_2PO_4$.

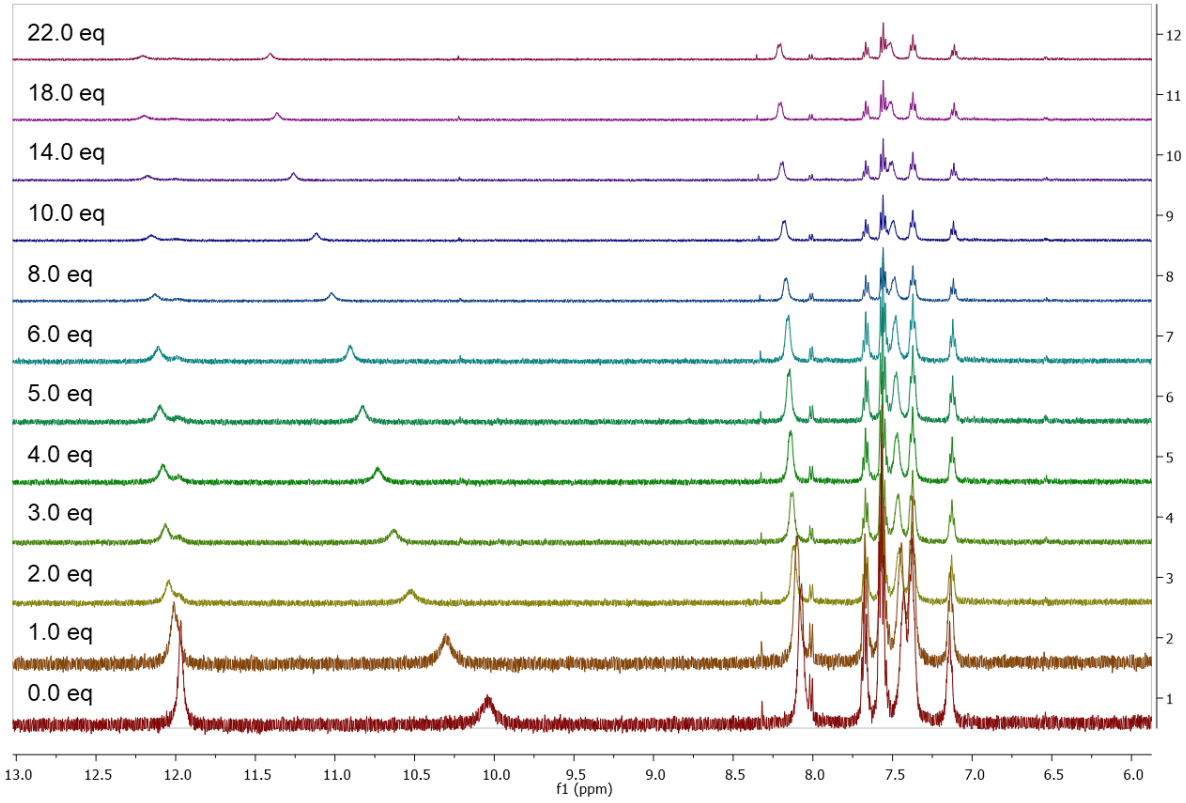

Figure C4. ^{1}H NMR stackplot, 6.0 ppm – 13.0 ppm, of receptor **2.27** with 0.0 – 22.0 equiv. TBACl in DMSO-*d*$_6$/0.5% H_2O.

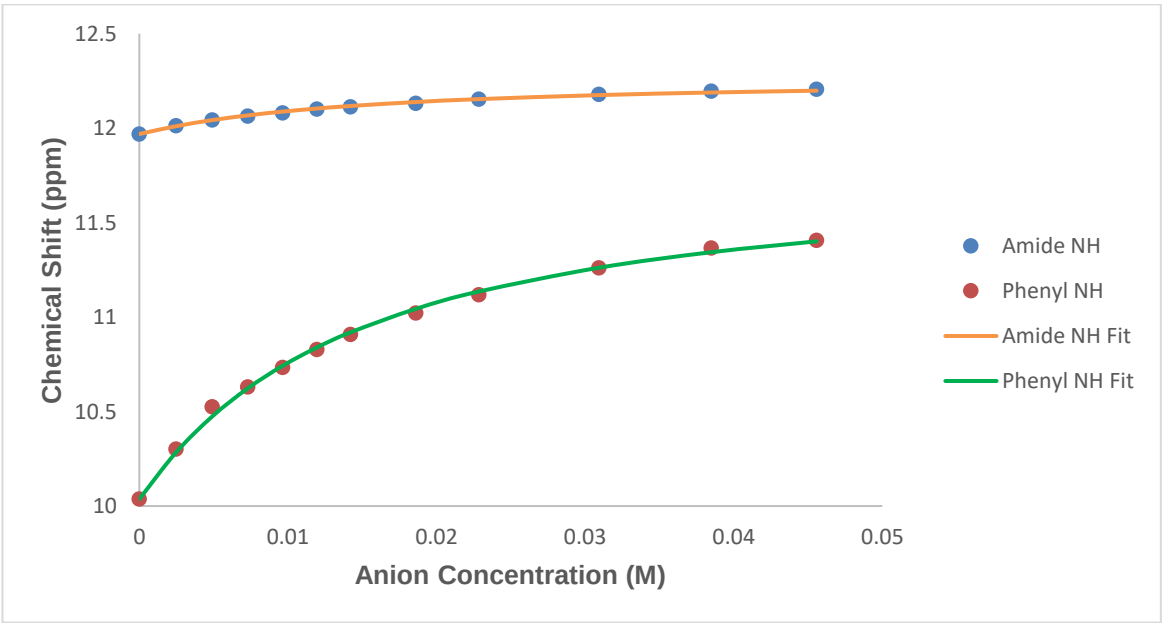

Figure C5. Fitted binding isotherm for the titration of **2.27** (2.5 X 10^{-6} M) in the presence of increasing concentrations of Cl^- in DMSO-*d*$_6$/0.5% H_2O). The data is fitted to a 1:1 binding model and shows the chemical shift of the NH signals throughout the titration.

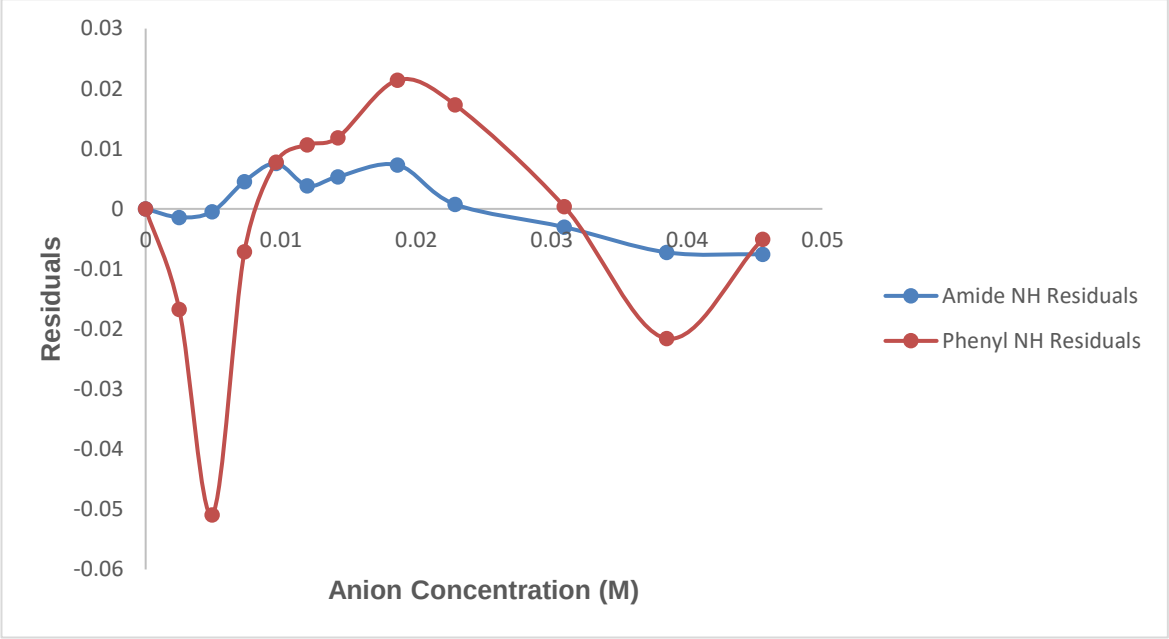

Figure C6 Residual plot of **2.27**

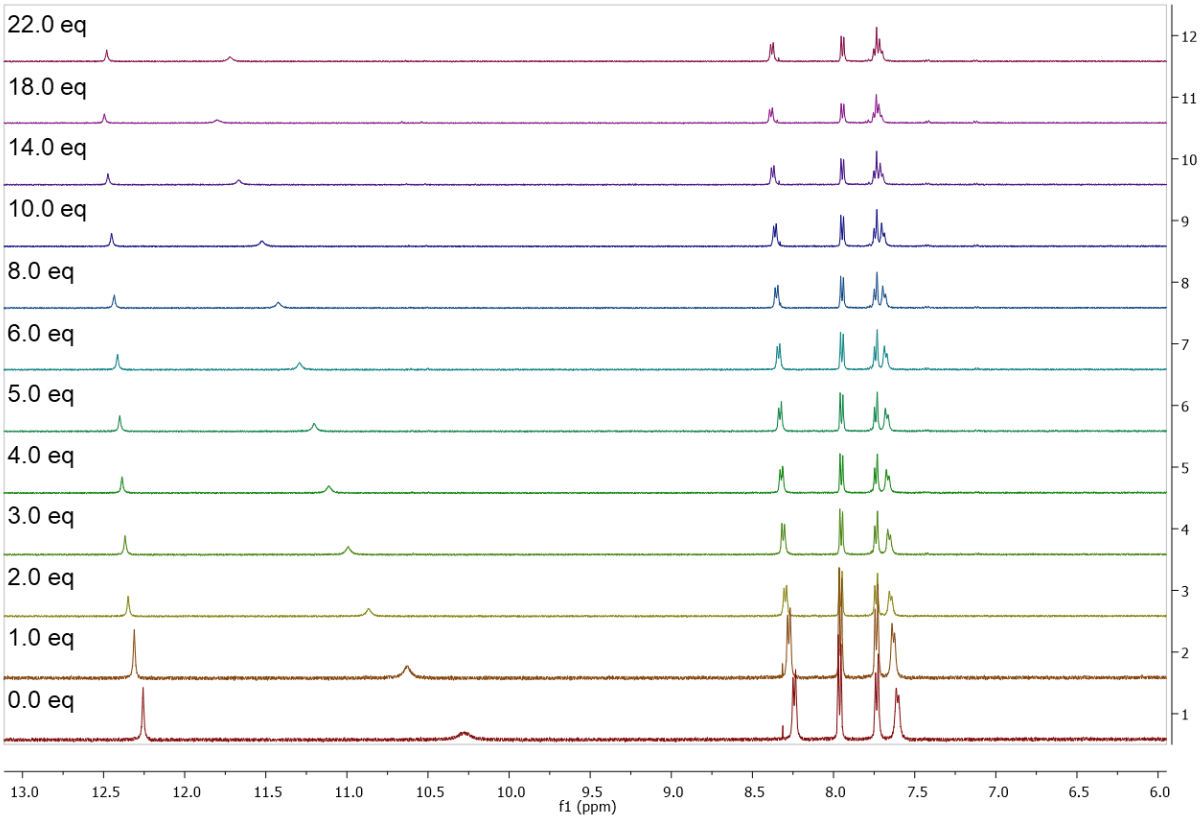

Figure C7. ^{1}H NMR stackplot, 6.0 ppm – 13.0 ppm, of receptor **2.28** with 0.0 – 22.0 equiv. TBACl in DMSO-d_6/0.5% H_2O.

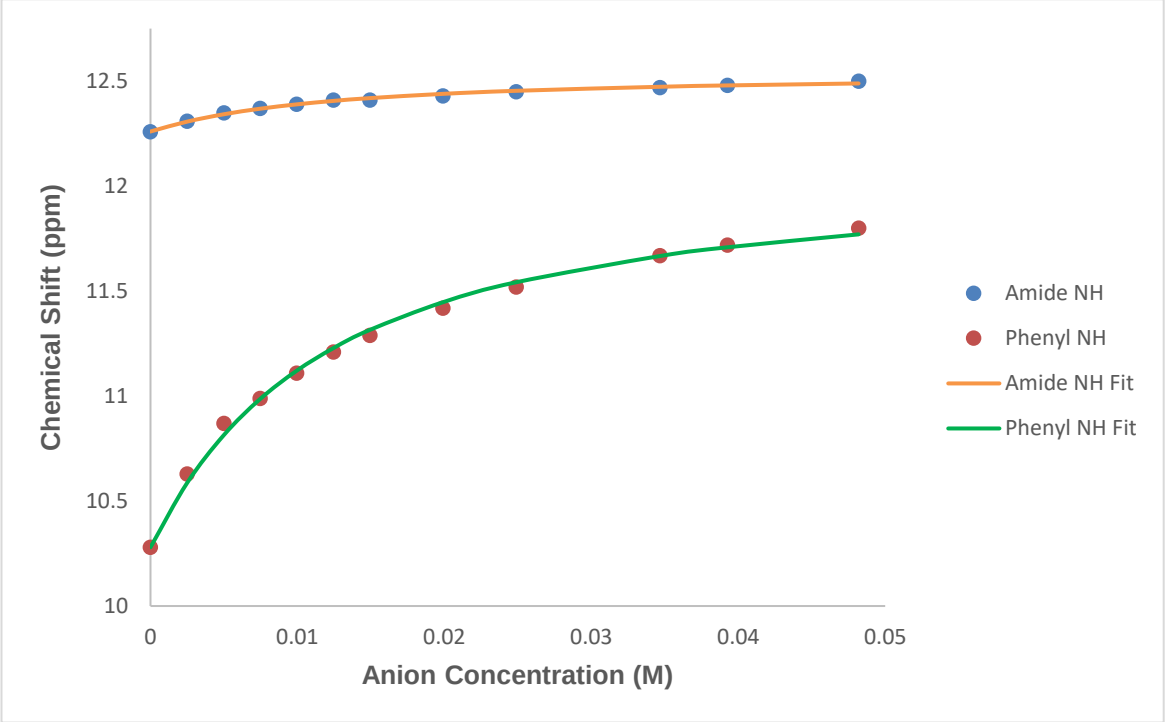

Figure C8. Fitted binding isotherm for the titration of **2.28** (2.5 X 10^{-6} M) in the presence of increasing concentrations of Cl^- in DMSO-d_6/0.5% H_2O). The data is fitted to a 1:1 binding model and shows the chemical shift of the NH signals throughout the titration.

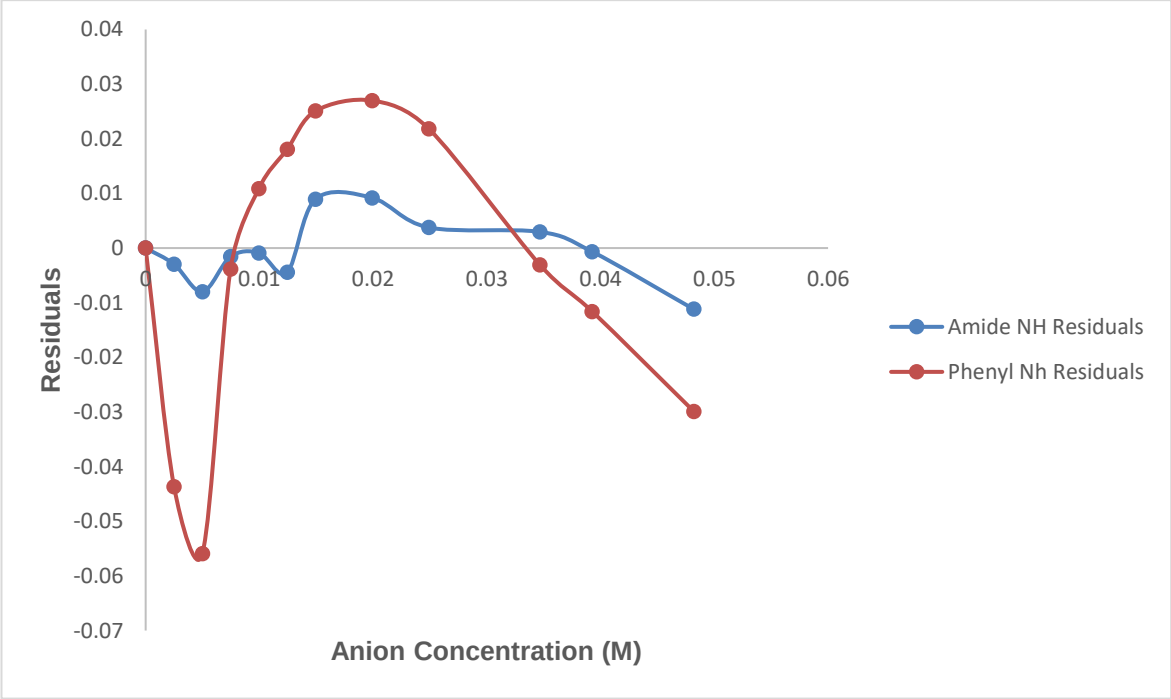

Figure C9. Residual plot of **2.28**

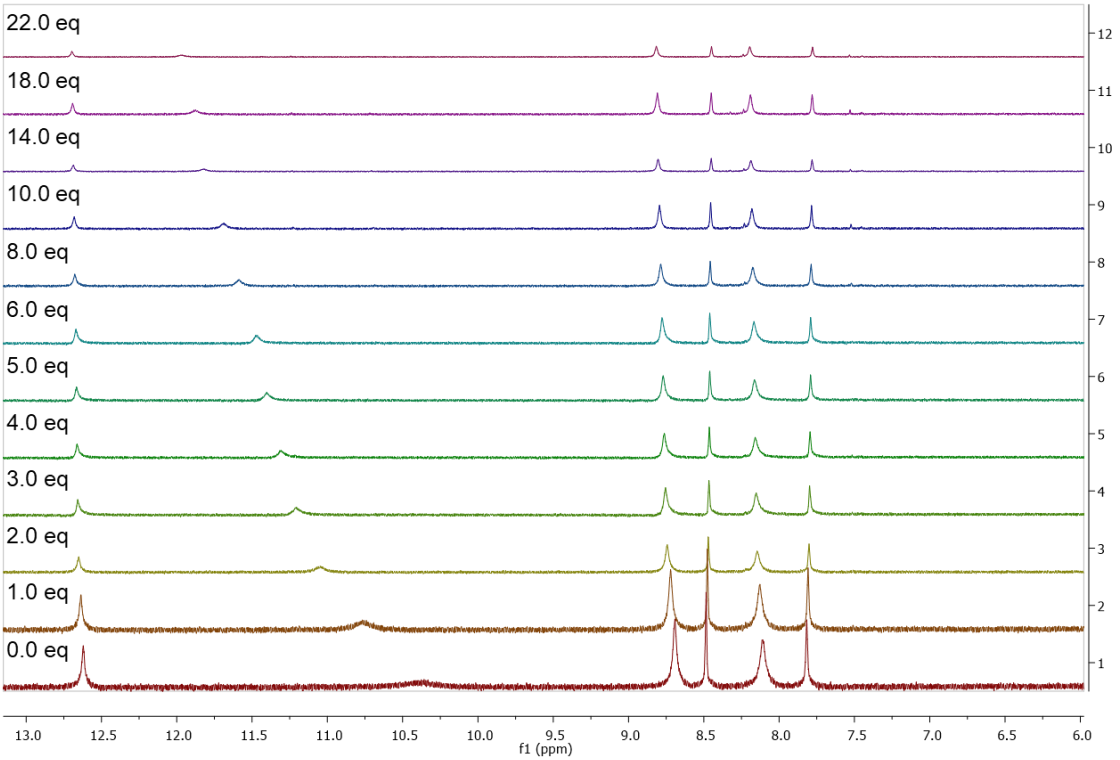

Figure C10. ^{1}H NMR stackplot, 6.0 ppm – 13.0 ppm, of receptor **2.29** with 0.0 – 22.0 equiv. TBACl in DMSO-d_6/0.5% H_2O.

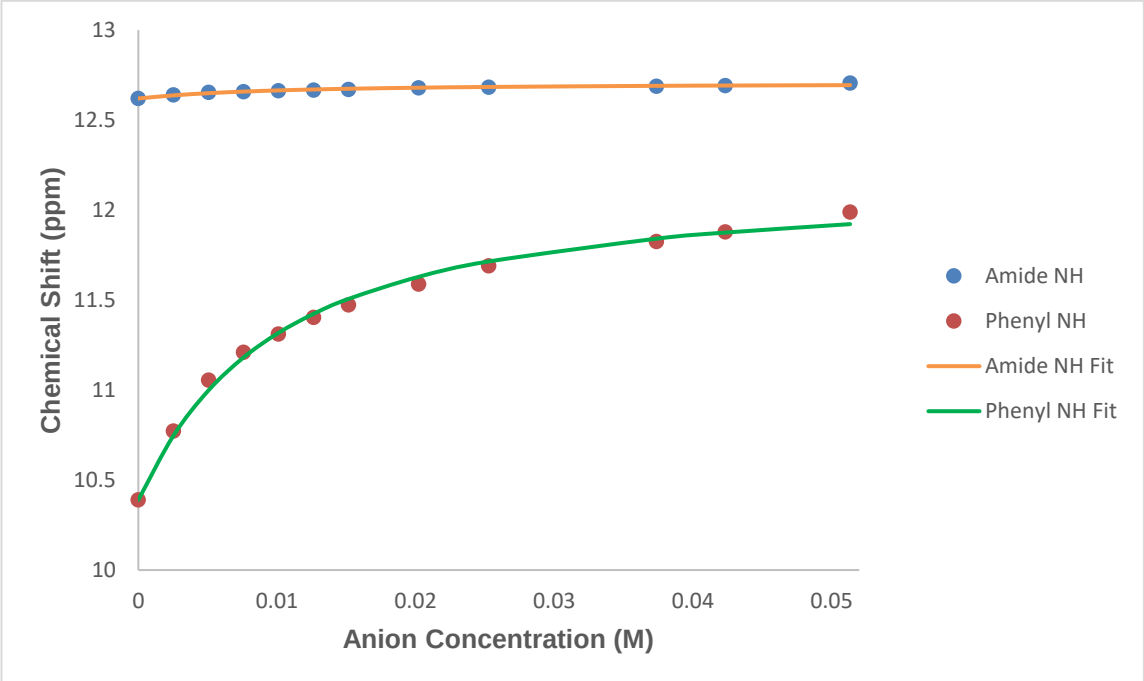

Figure C11. Fitted binding isotherm for the titration of **2.29** (2.5 X 10^{-6} M) in the presence of increasing concentrations of Cl^- in DMSO-d_6/0.5% H_2O). The data is fitted to a 1:1 binding model and shows the chemical shift of the NH signals throughout the titration.

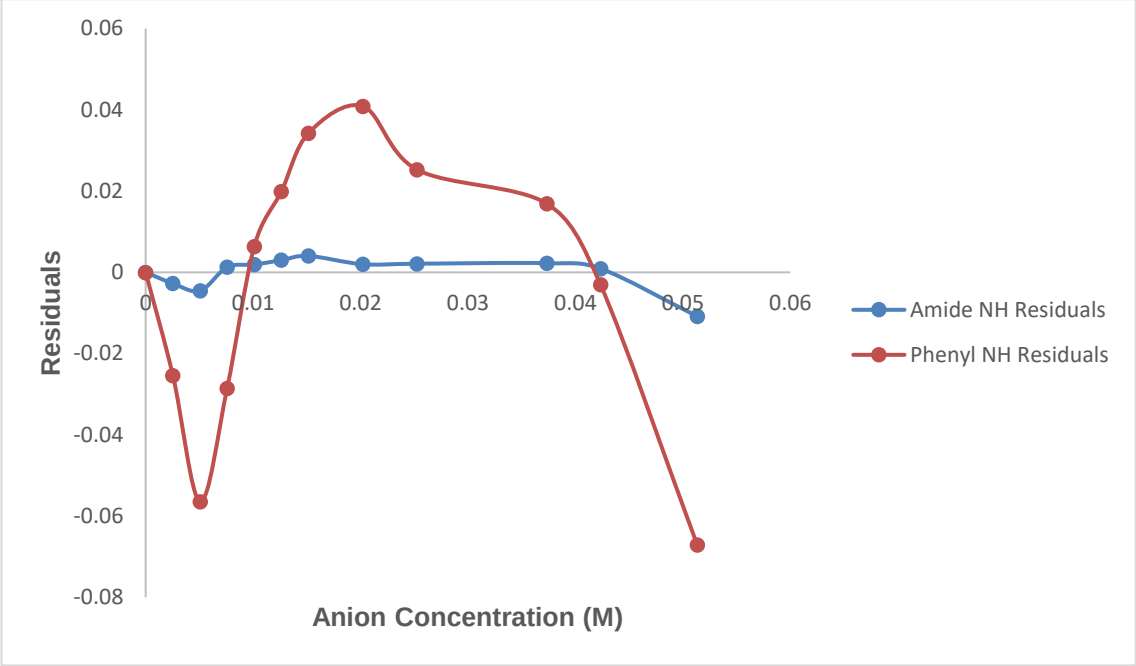

Figure C12. Residual plot of **2.29**

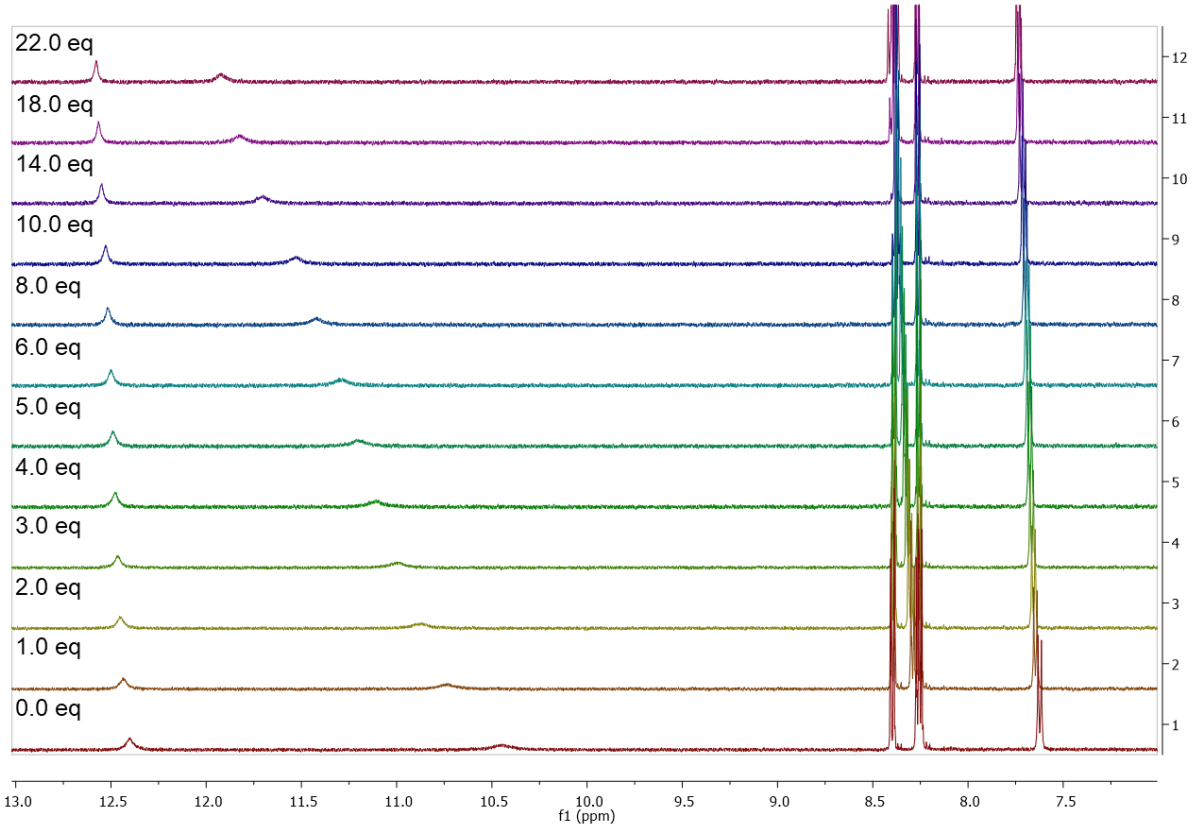

Figure C13. ^{1}H NMR stackplot, 6.0 ppm – 13.0 ppm, of receptor **2.30** with 0.0 – 22.0 equiv. TBACl in DMSO-d_6/0.5% H_2O.

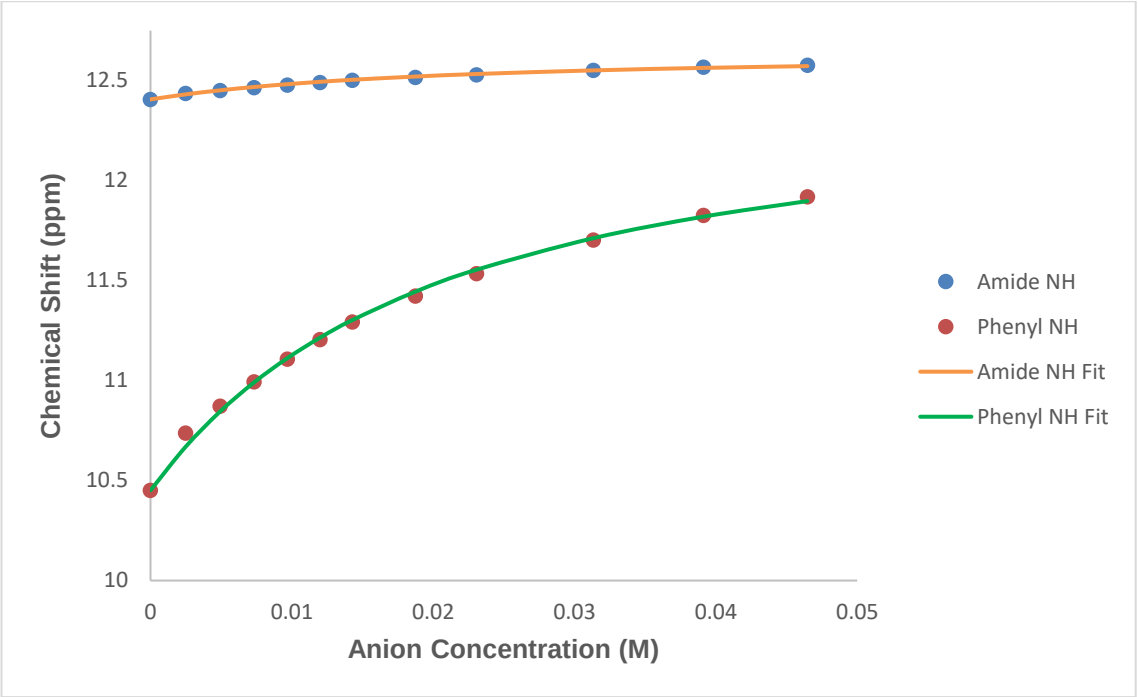

Figure C14. Fitted binding isotherm for the titration of **2.30** (2.5 X 10^{-6} M) in the presence of increasing concentrations of Cl^- in DMSO-d_6/0.5% H_2O). The data is fitted to a 1:1 binding model and shows the chemical shift of the NH signals throughout the titration.

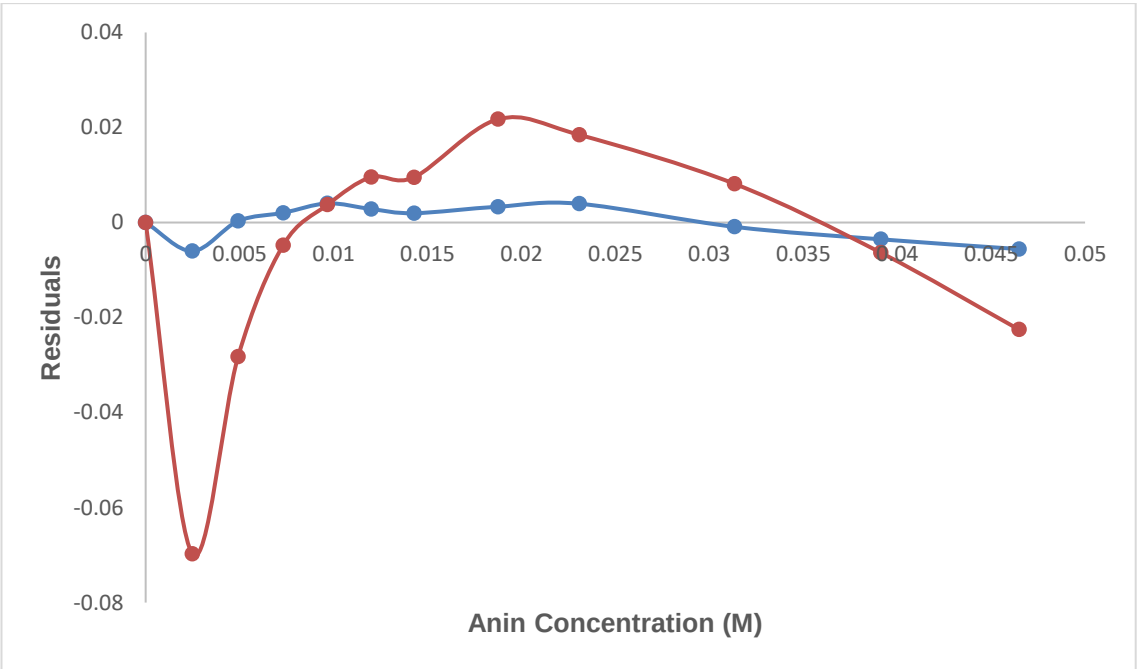

Figure C15. Residual plot of **2.30**

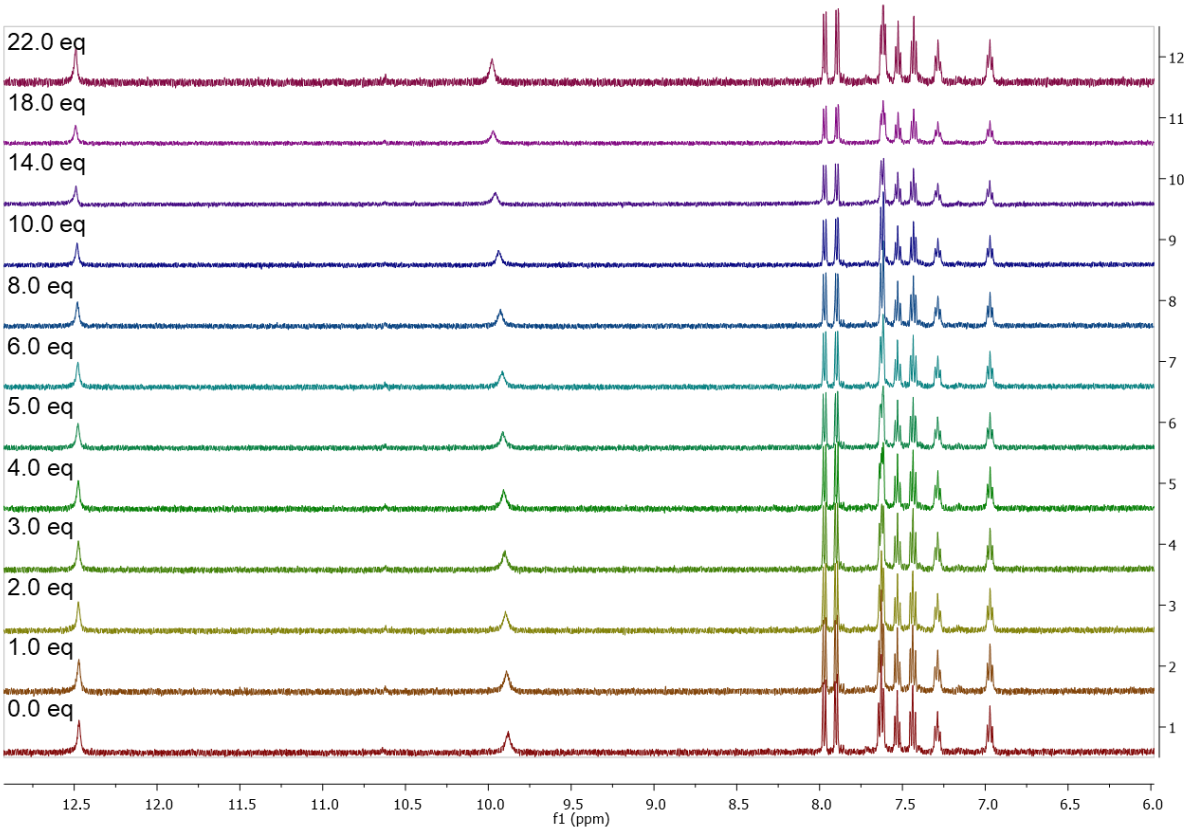

Figure C16. ^{1}H NMR stackplot, 6.0 ppm – 13.0 ppm, of receptor **2.31** with 0.0 – 22.0 equiv. TBACl in DMSO-d_6/0.5% H_2O.

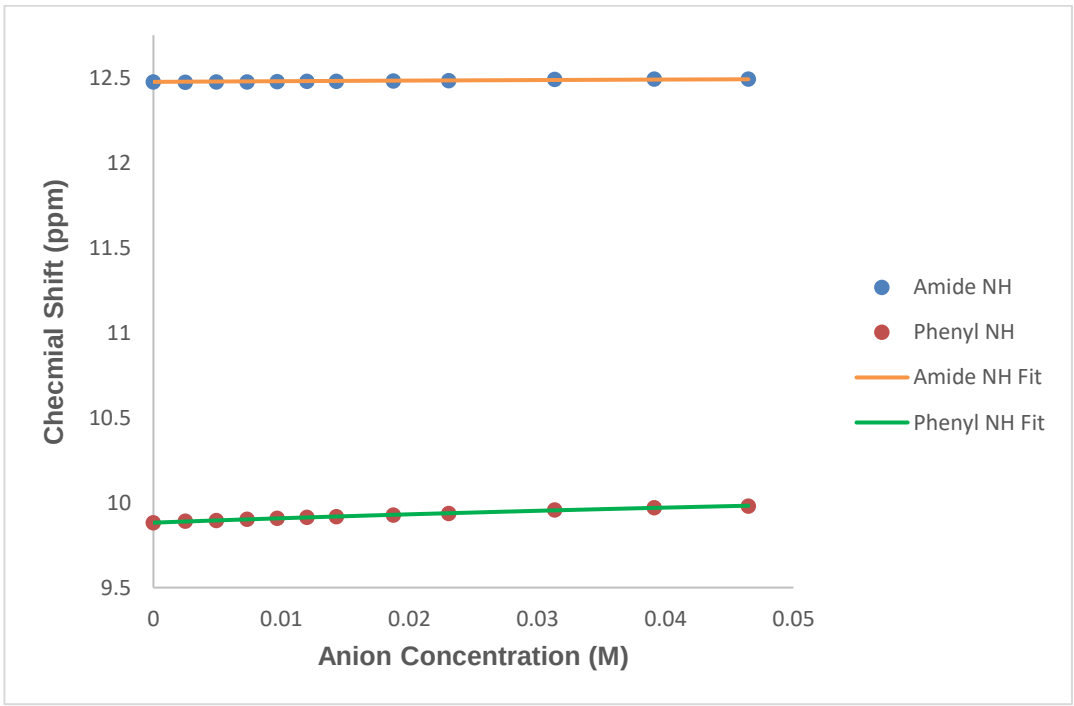

Figure C17. Fitted binding isotherm for the titration of **2.31** (2.5 X 10^{-6} M) in the presence of increasing concentrations of Cl^- in DMSO-d_6/0.5% H_2O). The data is fitted to a 1:1 binding model and shows the chemical shift of the NH signals throughout the titration.

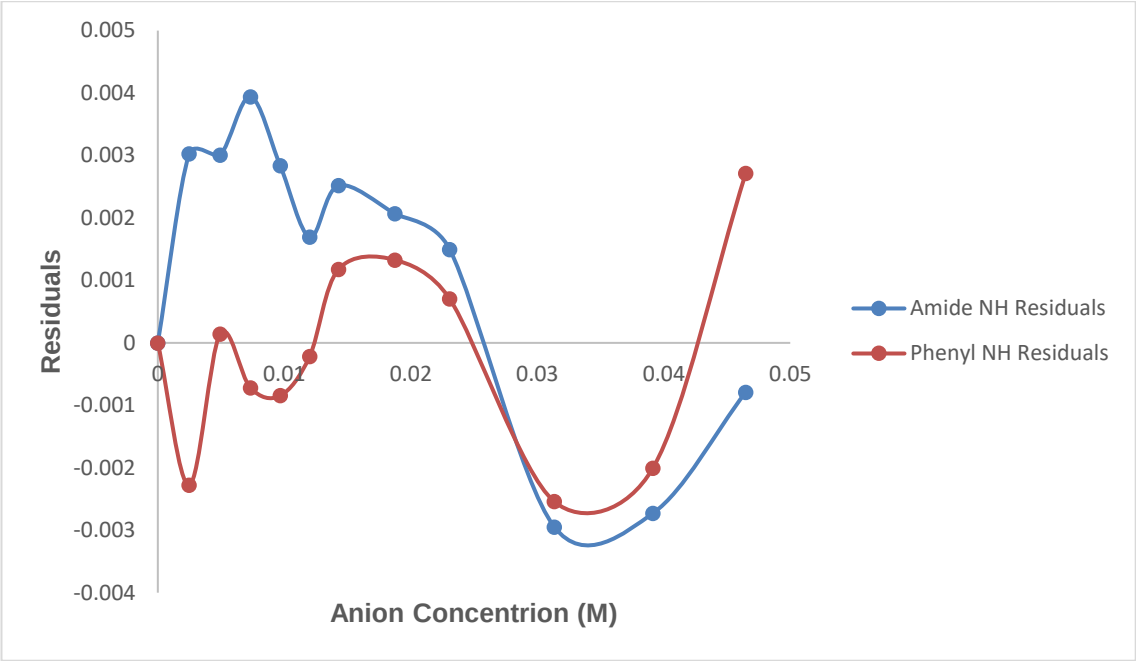

Figure C18. Residual plot of **2.31**

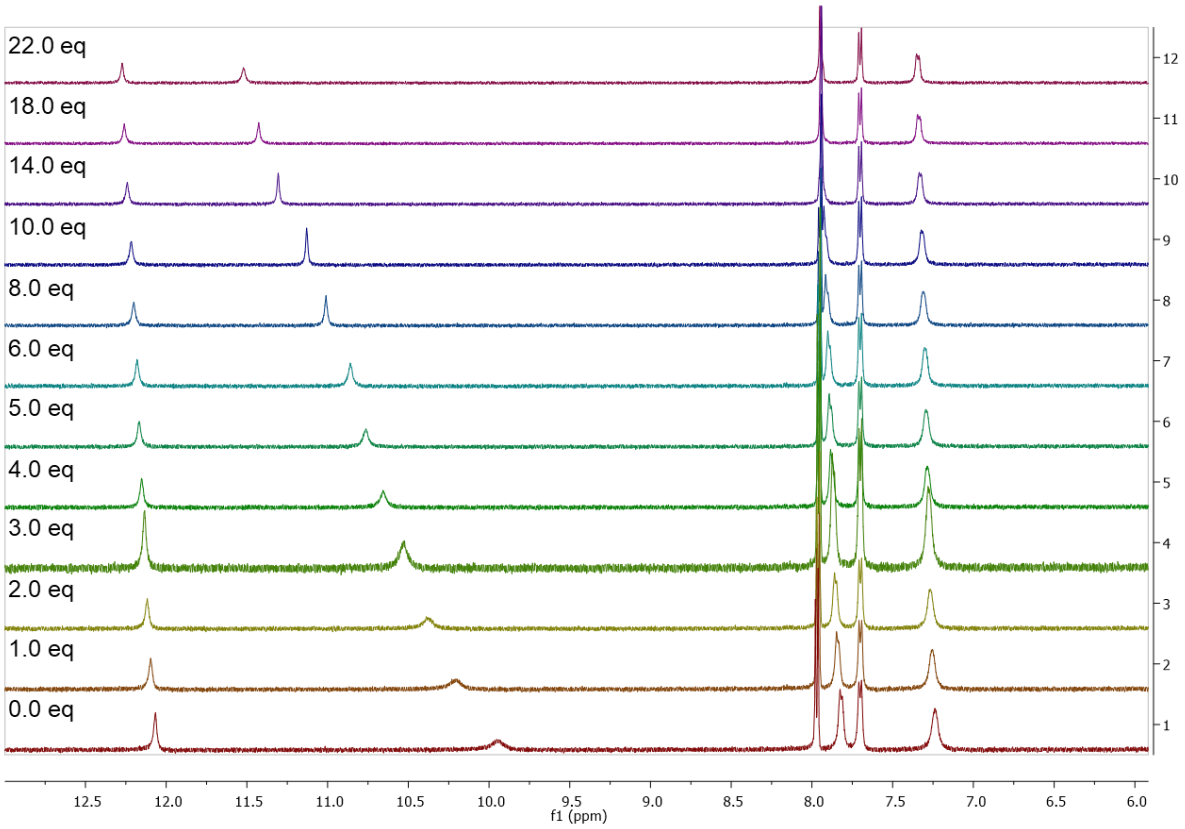

Figure C19. ^{1}H NMR stackplot, 6.0 ppm – 13.0 ppm, of receptor **2.32** with 0.0 – 22.0 equiv. TBACl in DMSO-d_6/0.5% H_2O.

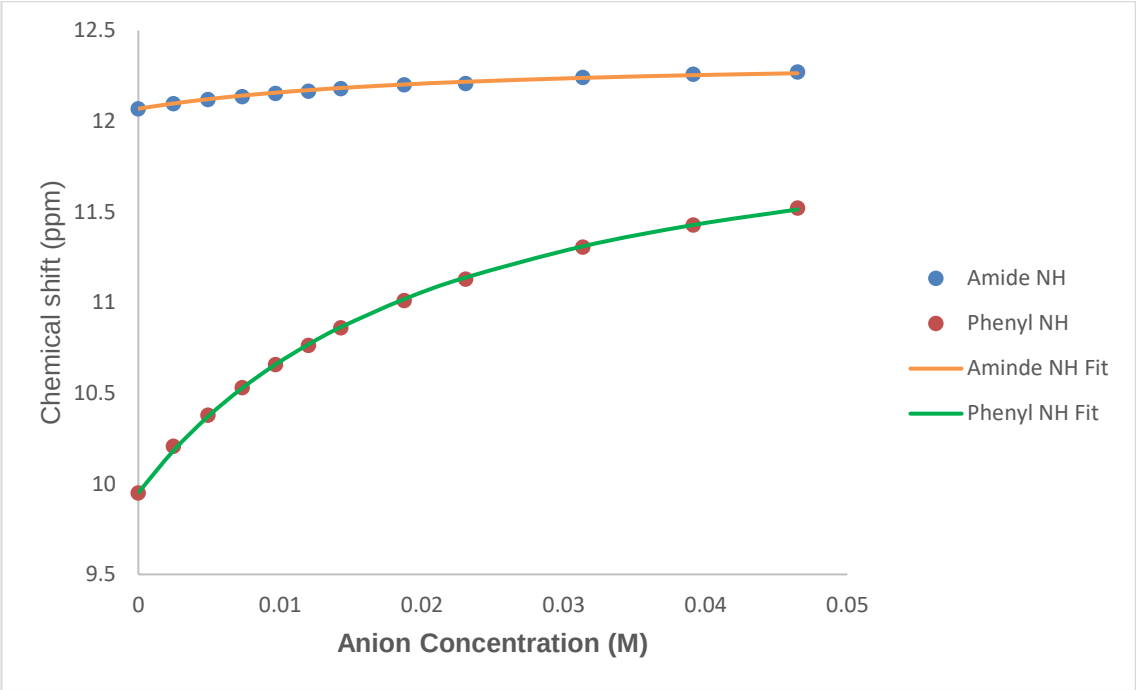

Figure C20. Fitted binding isotherm for the titration of **2.32** (2.5 X 10^{-6} M) in the presence of increasing concentrations of Cl^- in DMSO-d_6/0.5% H_2O). The data is fitted to a 1:1 binding model and shows the chemical shift of the NH signals throughout the titration.

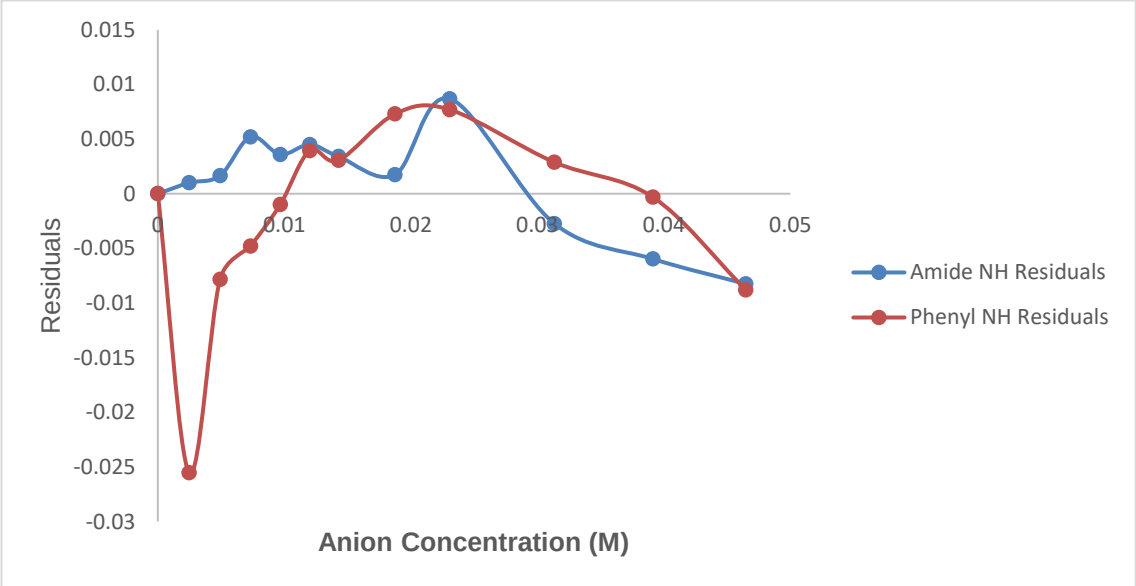

C21. Residual plot of **2.32**

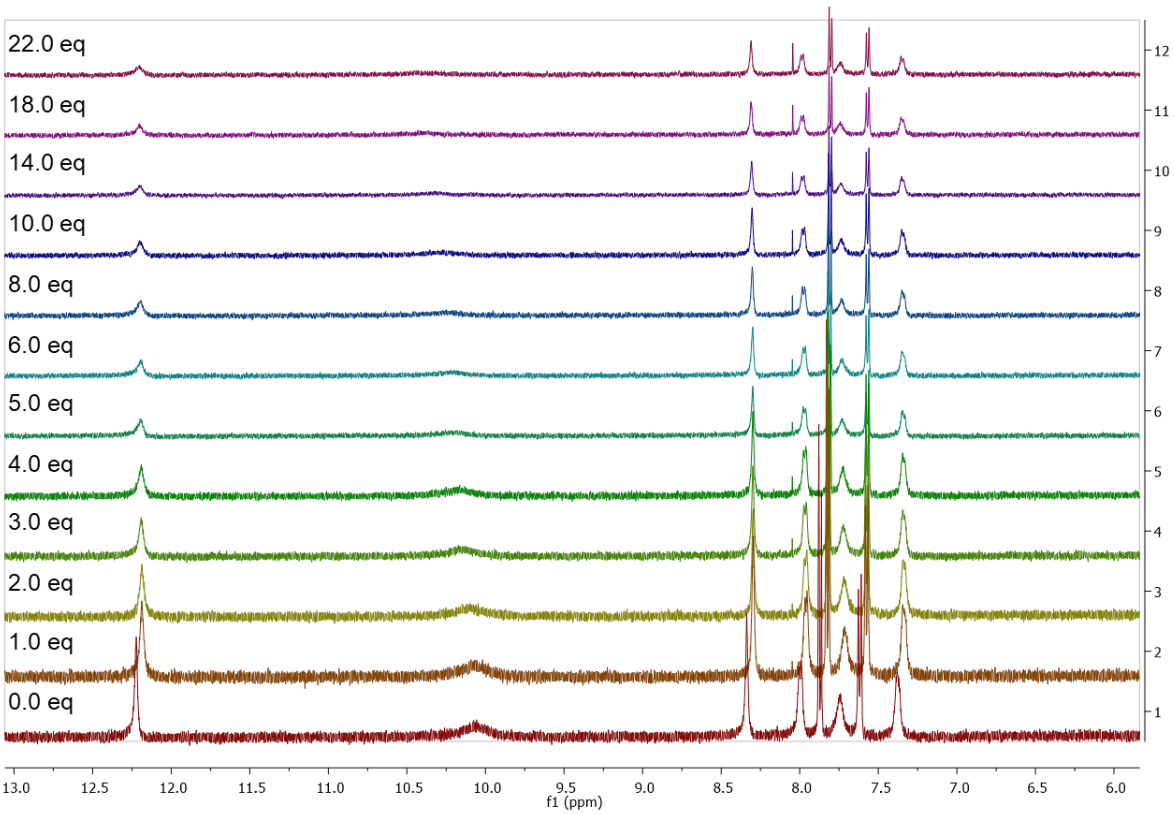

Figure C22. ^{1}H NMR stackplot, 6.0 ppm – 13.0 ppm, of receptor **2.33** with 0.0 – 22.0 equiv. TBACl in DMSO-d_6/0.5% H_2O.

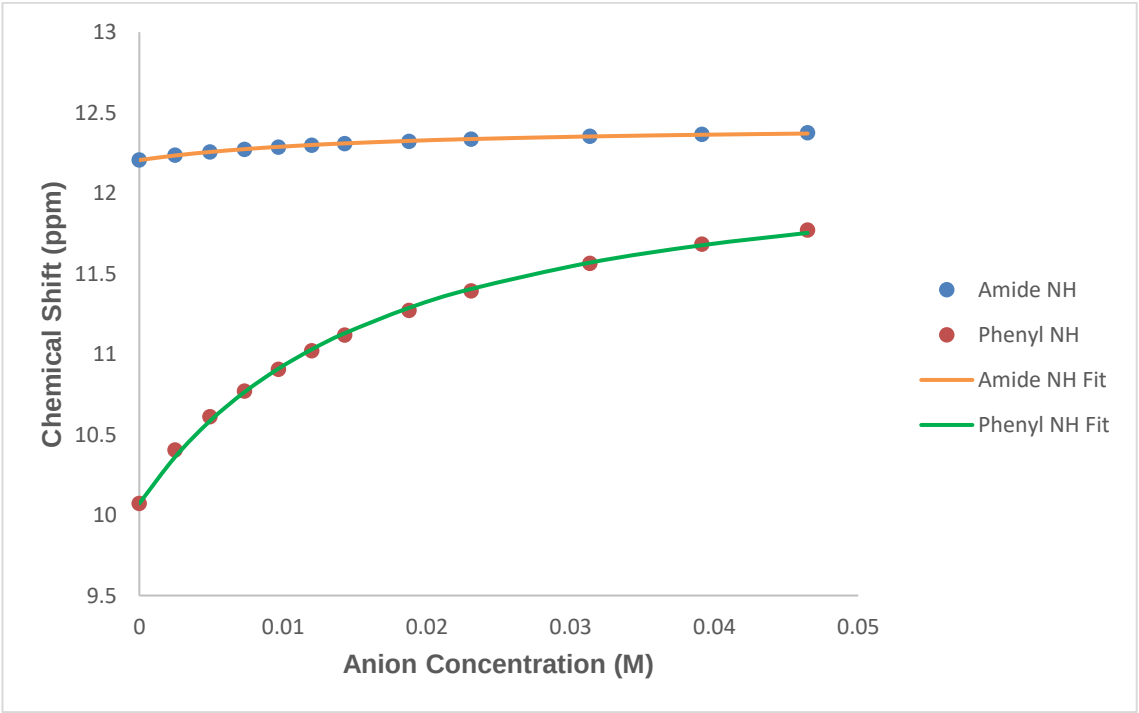

Figure C23. Fitted binding isotherm for the titration of **2.33** (2.5 X 10^{-6} M) in the presence of increasing concentrations of Cl^- in DMSO-d_6/0.5% H_2O). The data is fitted to a 1:1 binding model and shows the chemical shift of the NH signals throughout the titration.

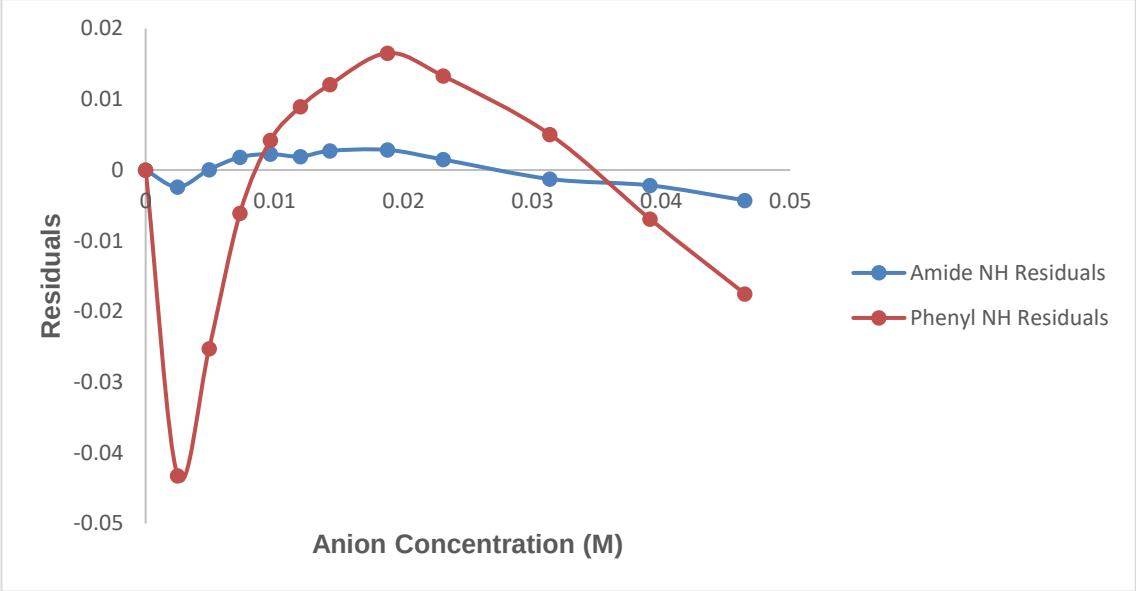

Figure C24. Residual plot of **2.33**

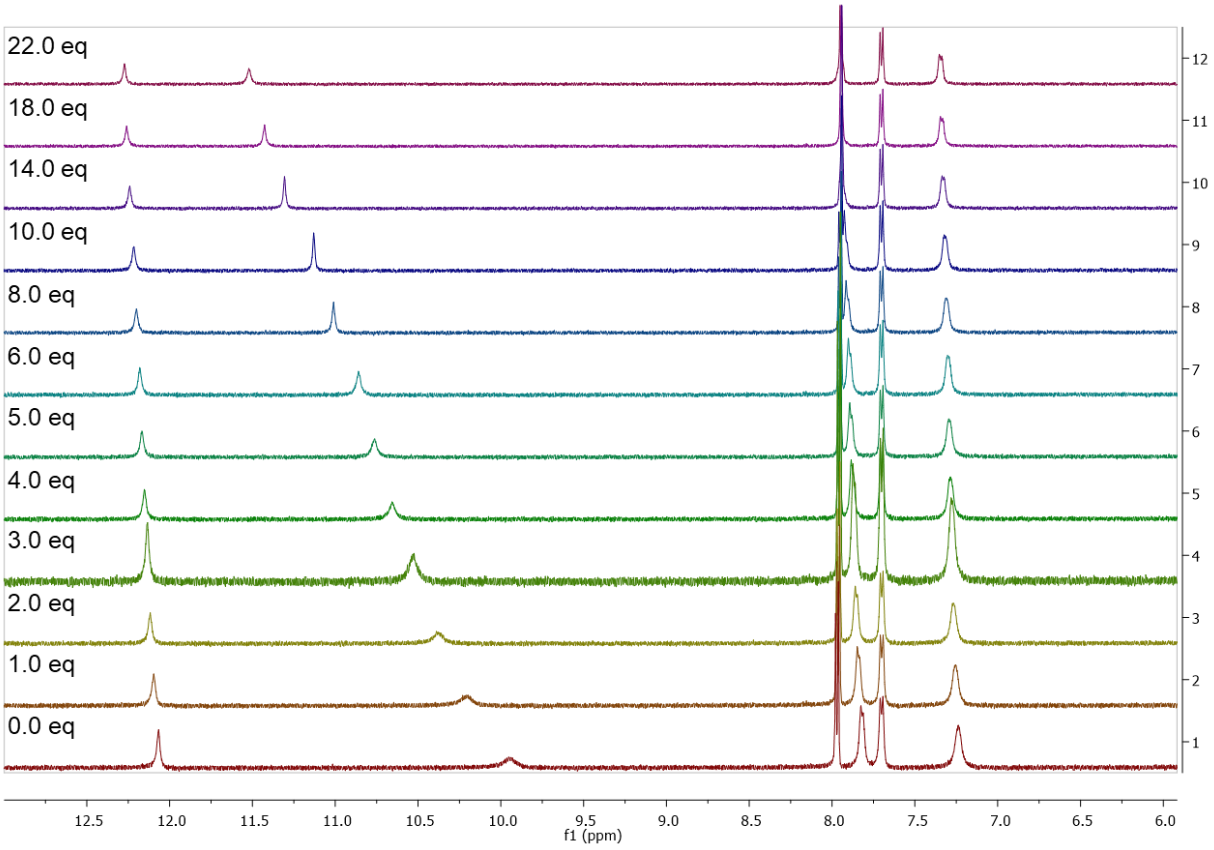

Figure C25. ^{1}H NMR stackplot, 6.0 ppm – 13.0 ppm, of receptor **2.34** with 0.0 – 22.0 equiv. TBACl in DMSO-d_6/0.5% H_2O.

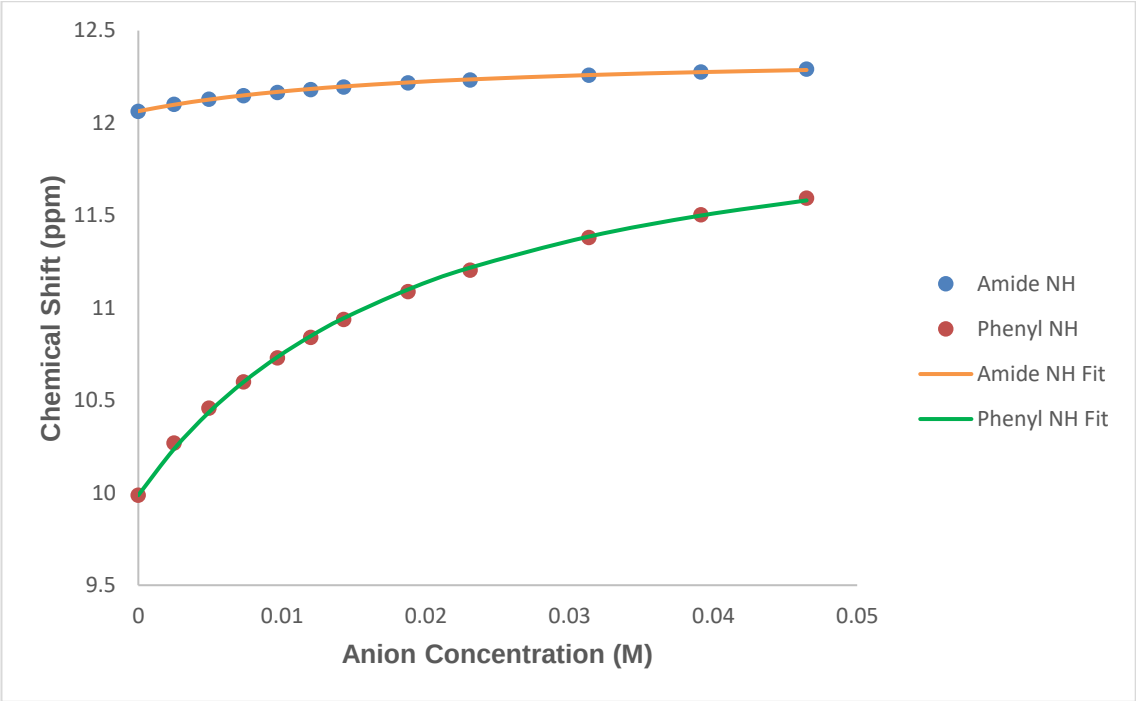

Figure C26. Fitted binding isotherm for the titration of **2.34** (2.5 X 10^{-6} M) in the presence of increasing concentrations of Cl^- in DMSO-d_6/0.5% H_2O). The data is fitted to a 1:1 binding model and shows the chemical shift of the NH signals throughout the titration.

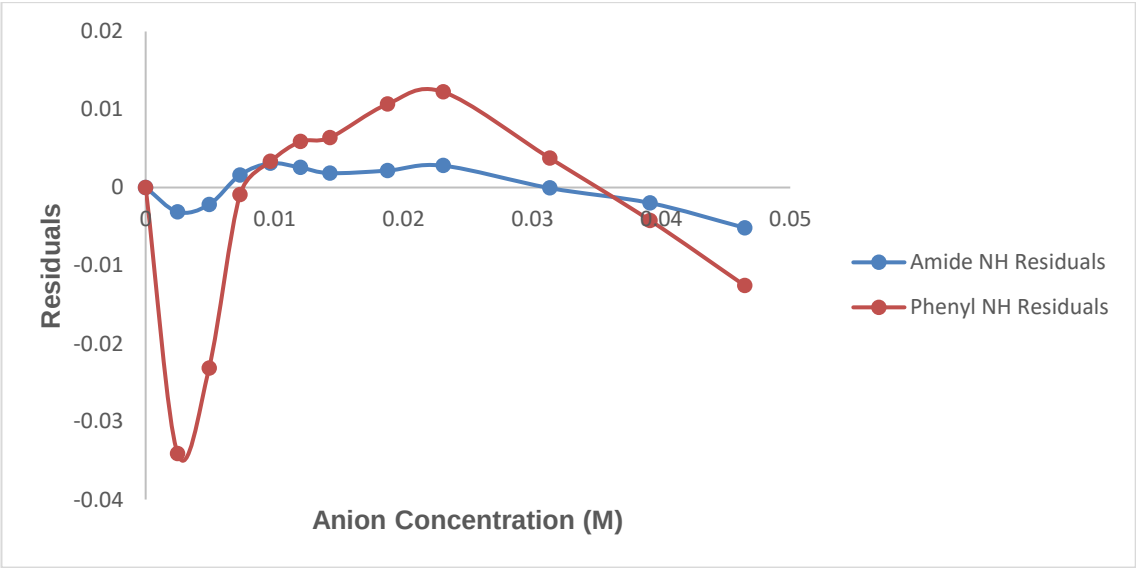

Figure C27. Residual plot of **2.34**

D. Chapter 3 Characterisation Data

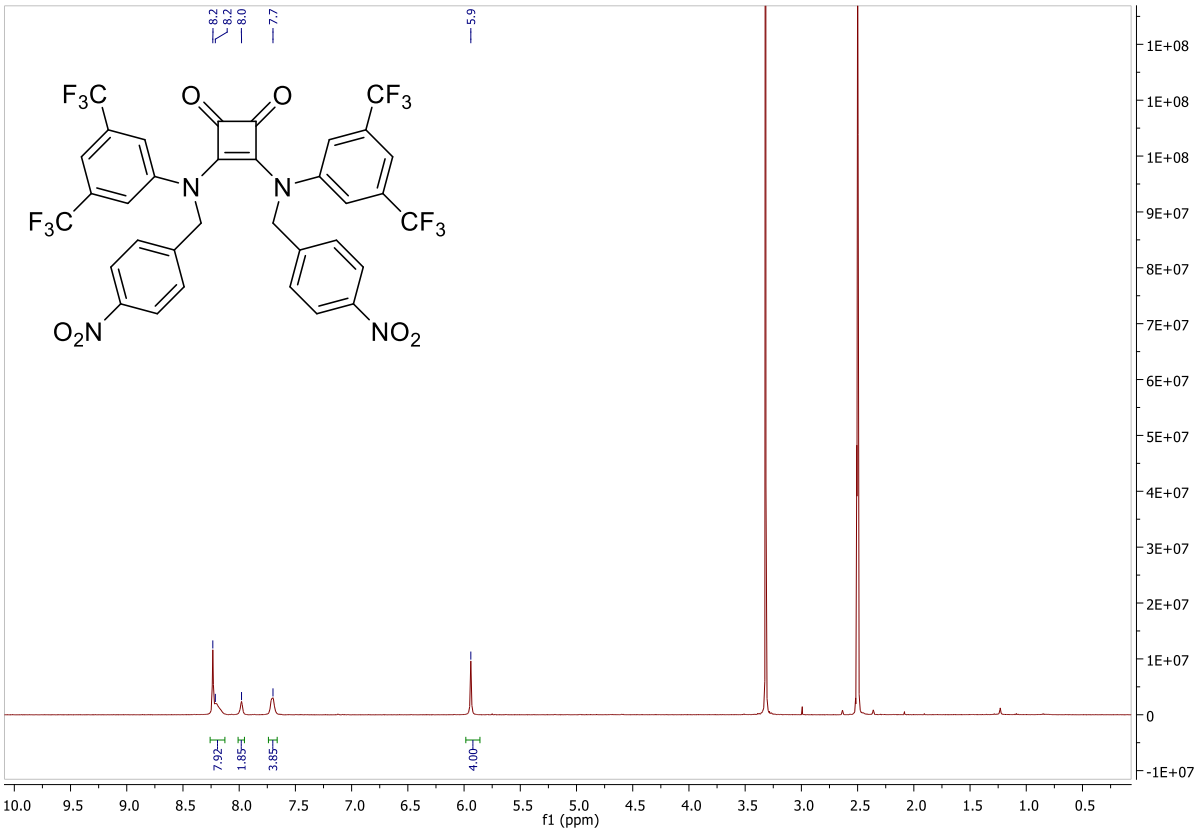

Figure D1. ^{1}H NMR (DMSO-d_6, 126 MHz) spectrum of **3.17**

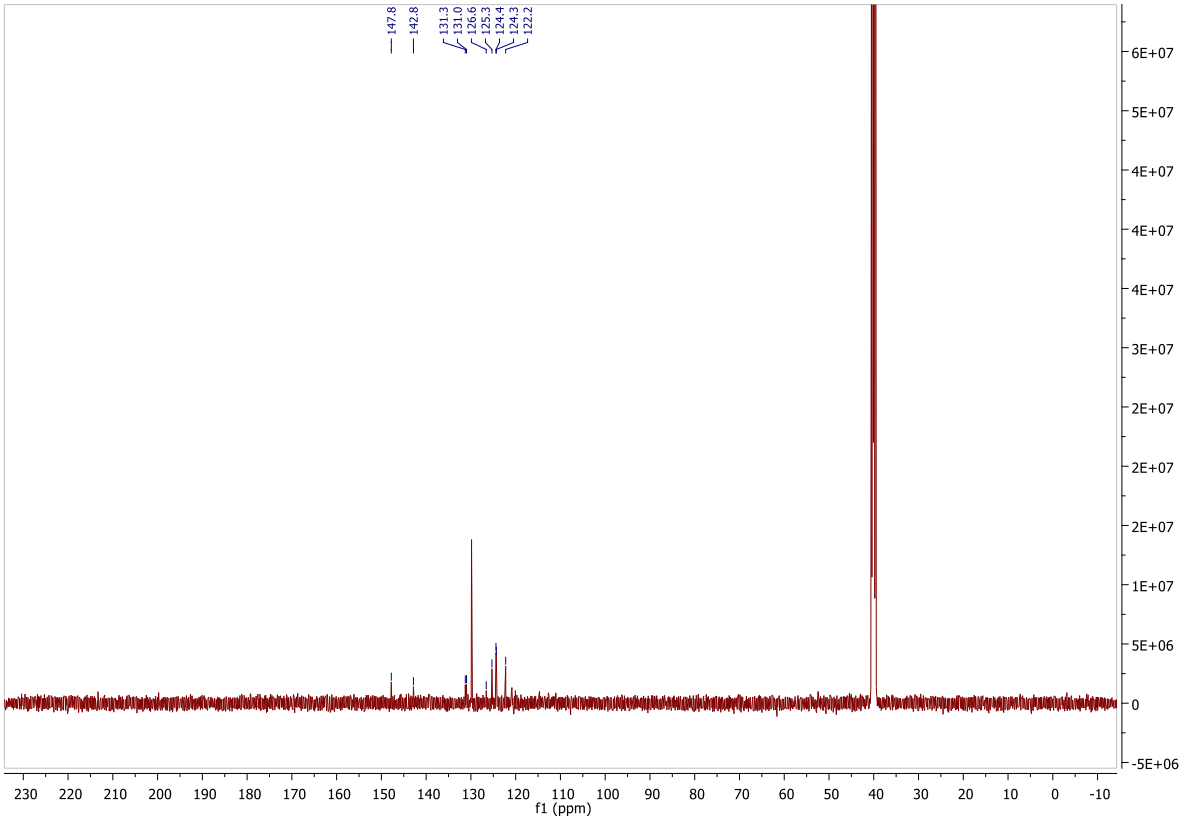

Figure D2. ^{13}C NMR (DMSO-d_6, 126 MHz) spectrum of **3.17**

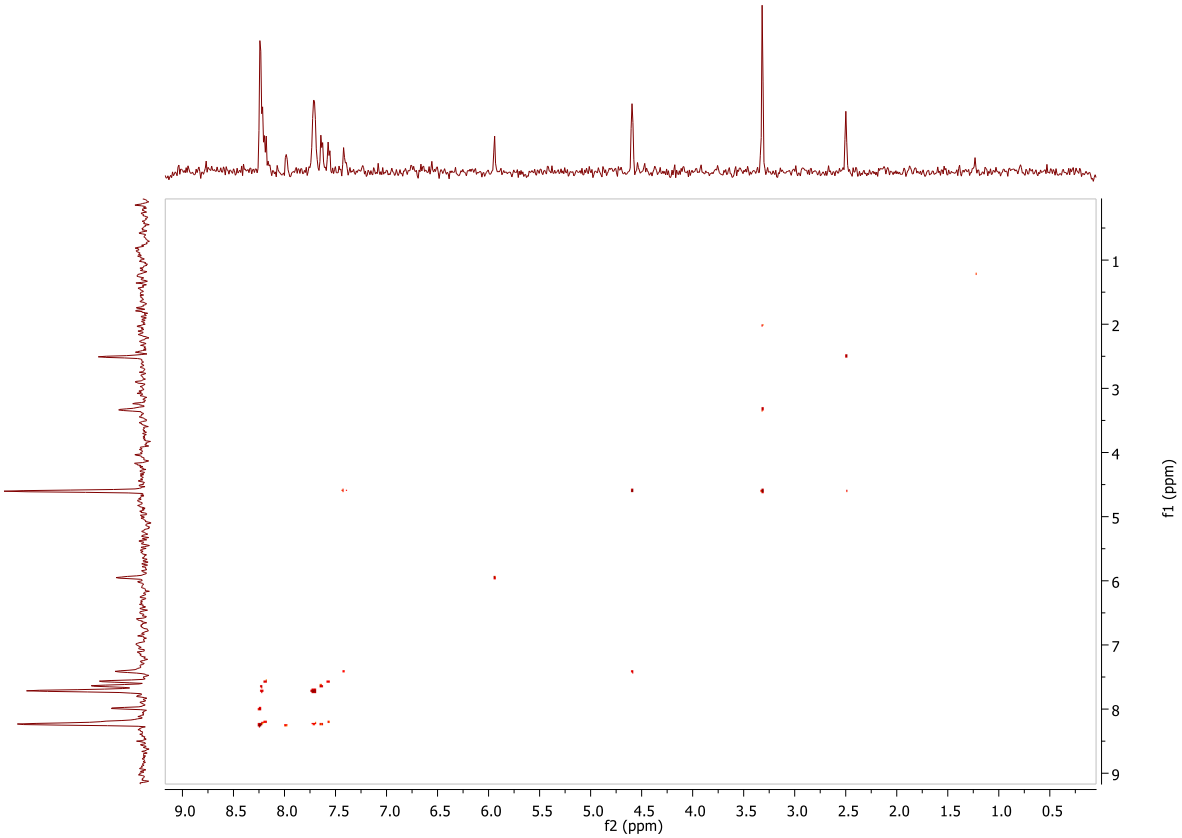

Figure D3. ^{1}H-^{1}H COSY spectrum of **3.17**

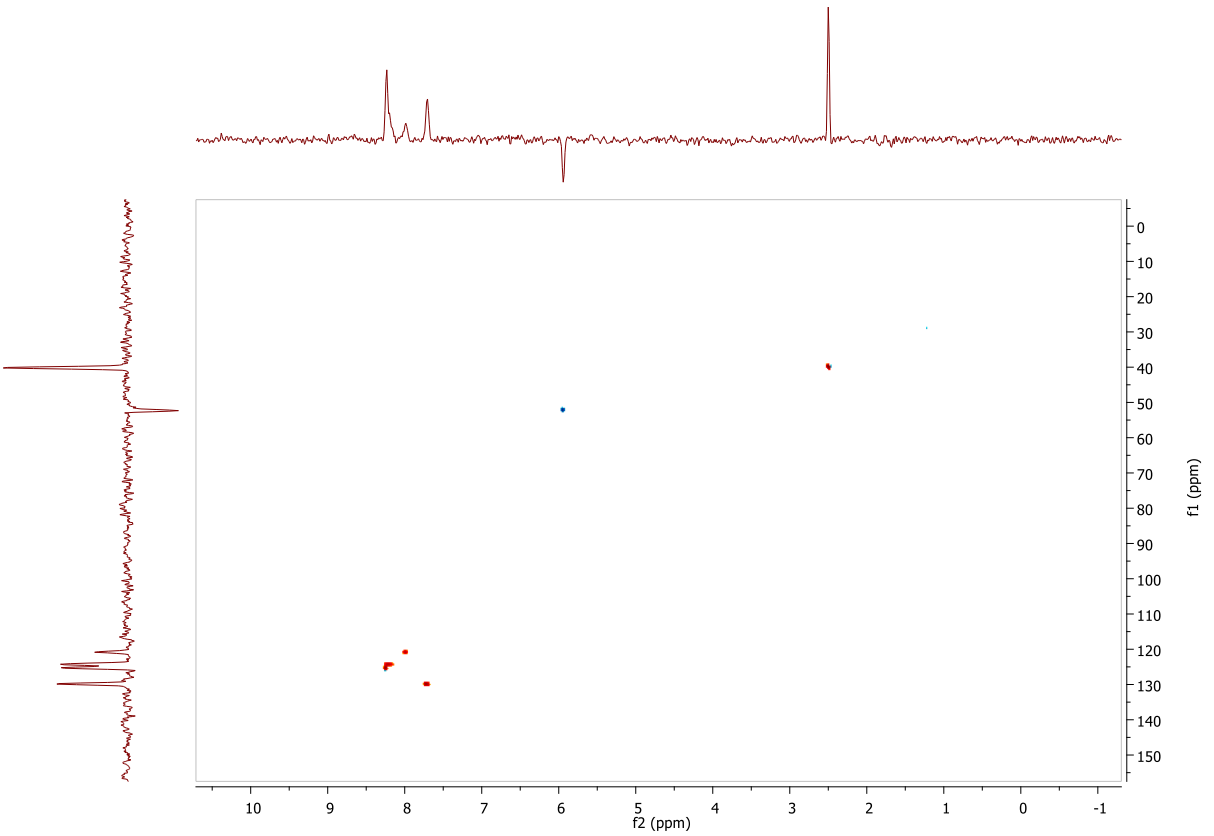

Figure D4. HSQC spectrum of **3.17**

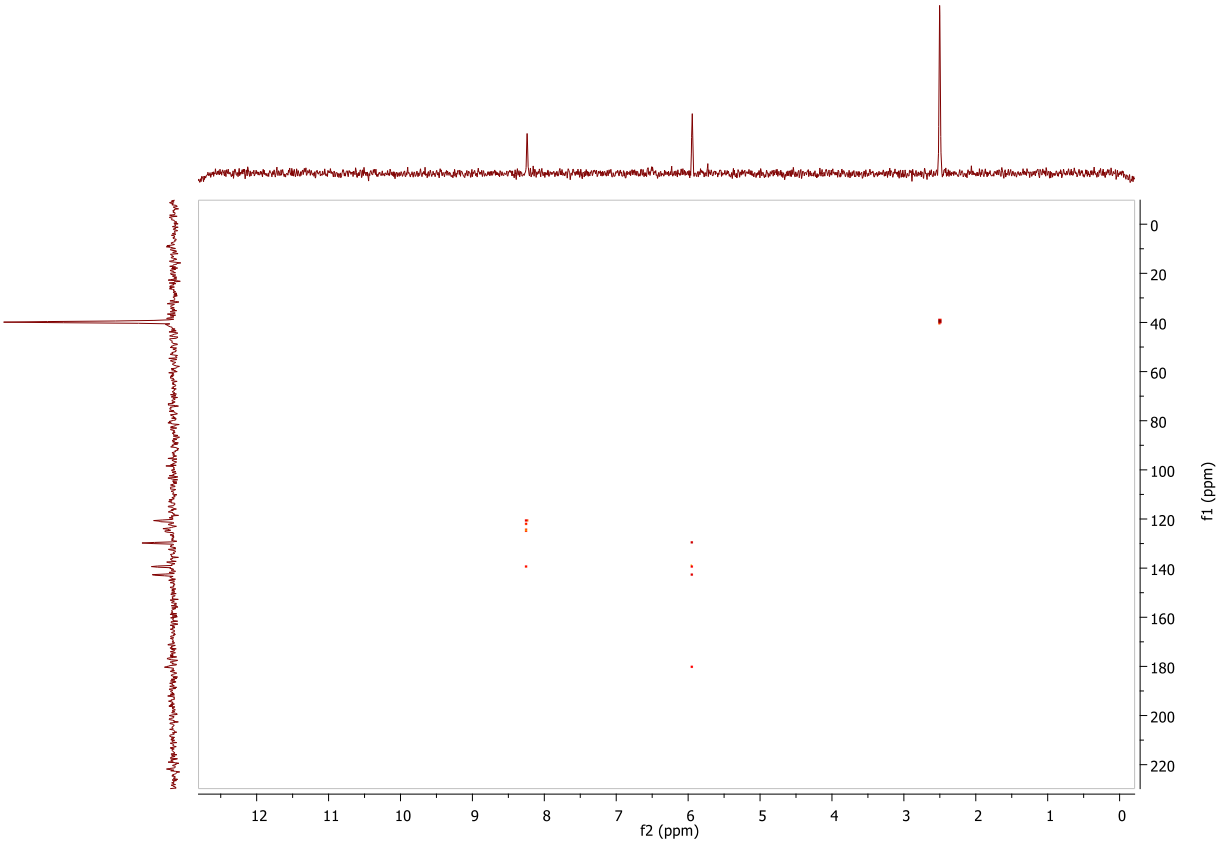

Figure D5. HMBC spectrum of **3.17**

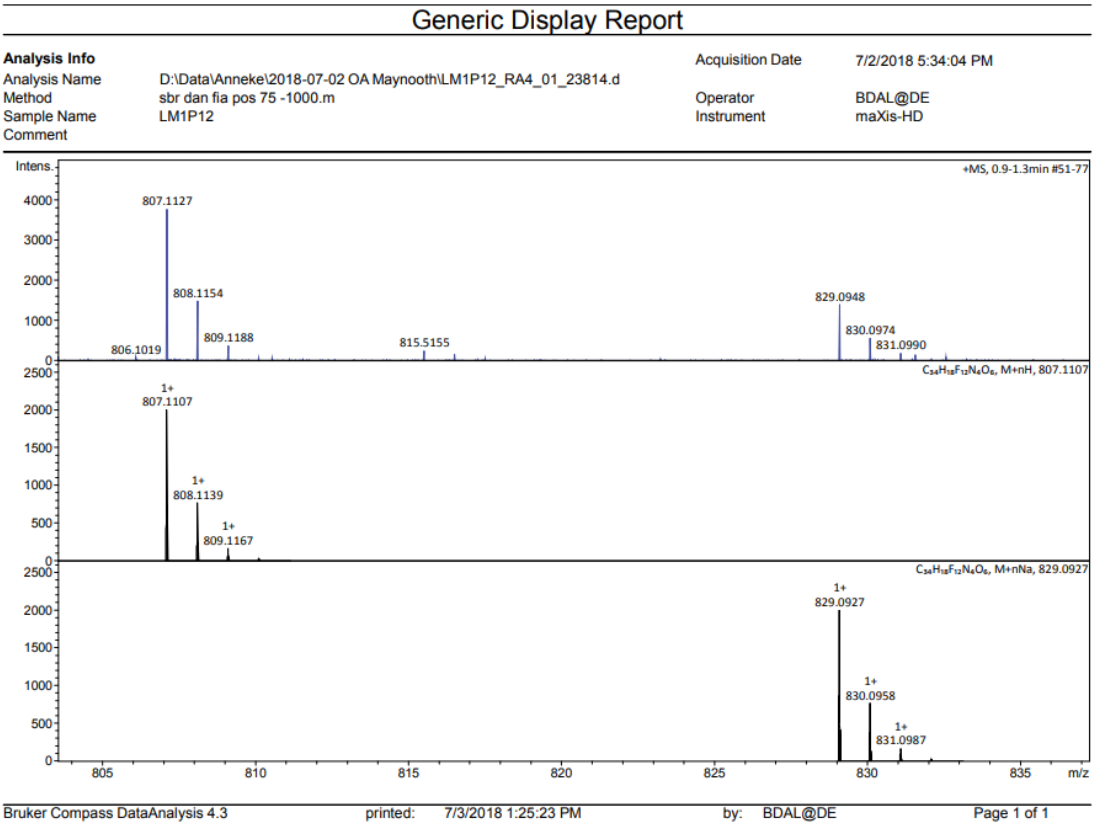

Figure D6. HRMS of **3.17**

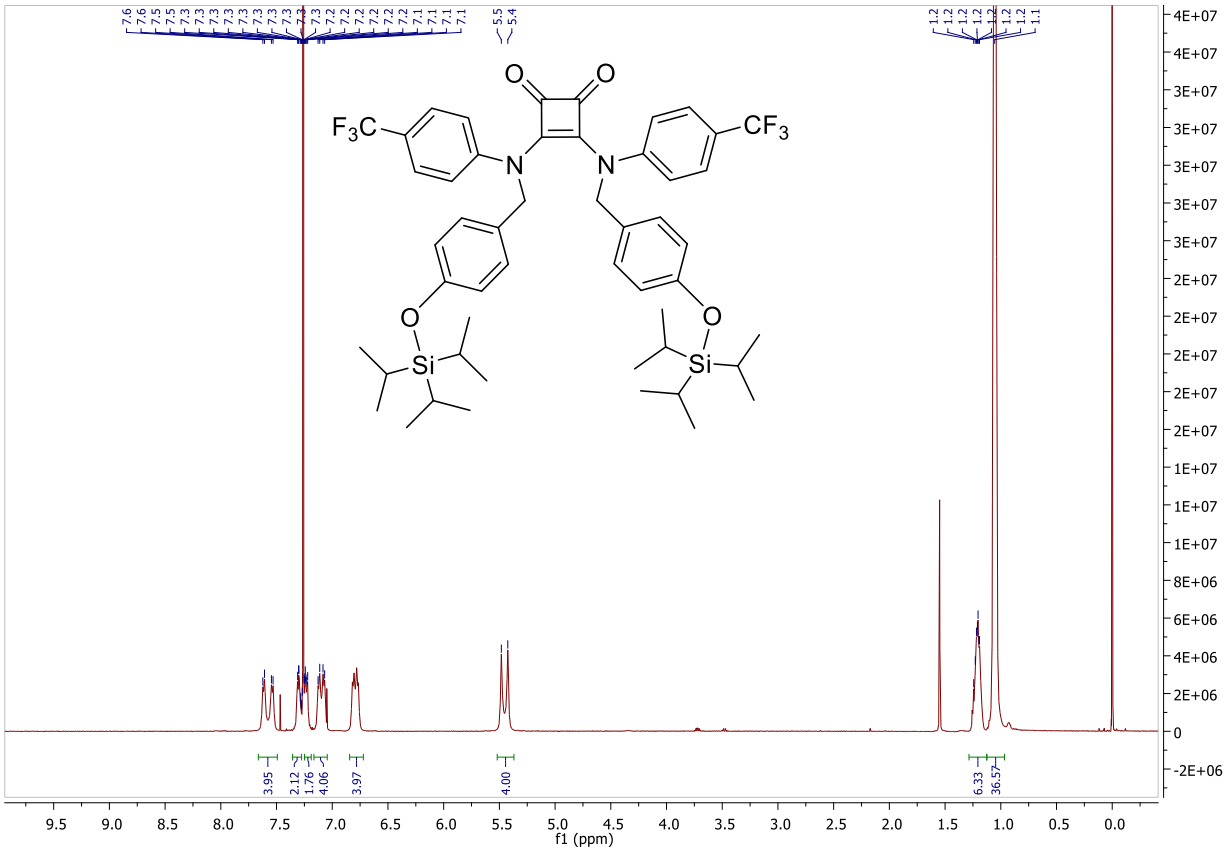

Figure D7. ^{1}H NMR ($CDCl_3$, 500 MHz) spectrum of **3.18**

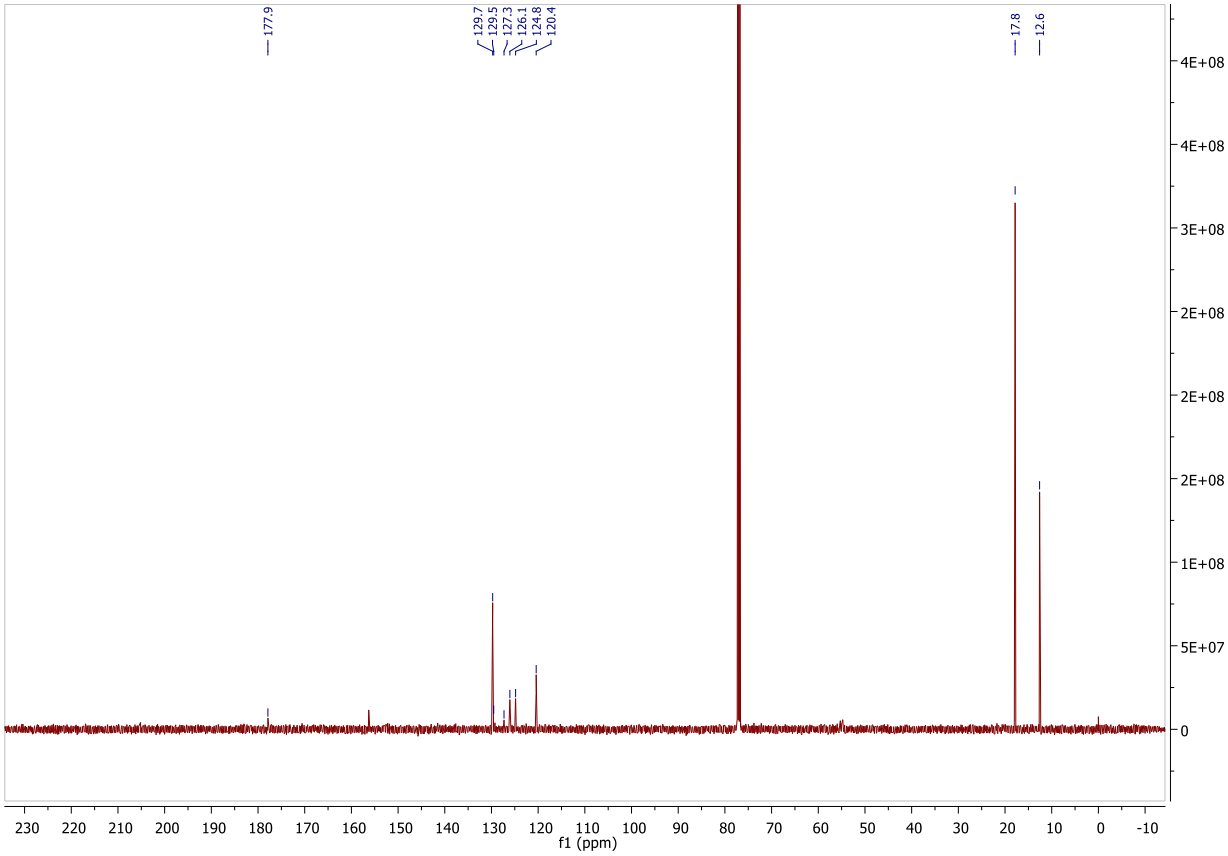

Figure D8. ^{13}C NMR ($CHCl_3$, 126 MHz) spectrum of **3.18**

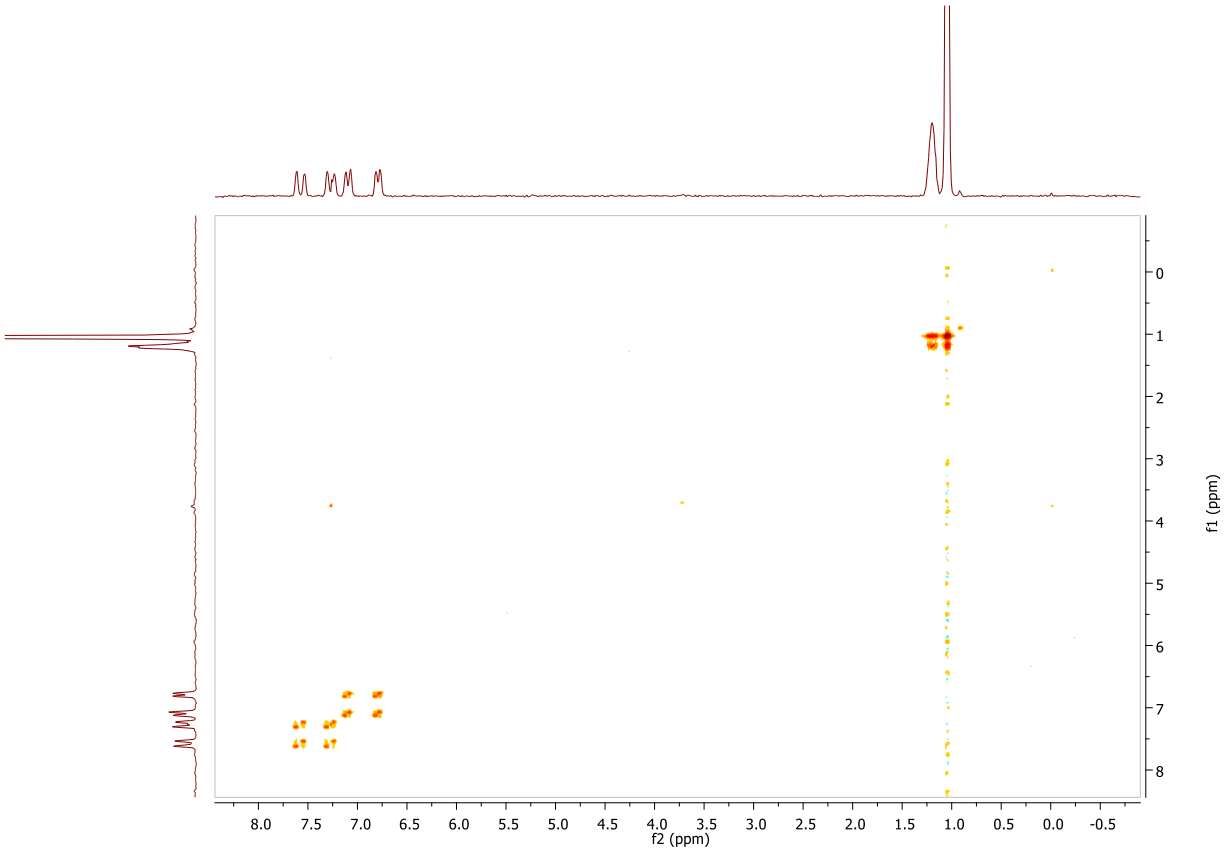

Figure D9. ^{1}H-^{1}H COSY spectrum of **3.18**

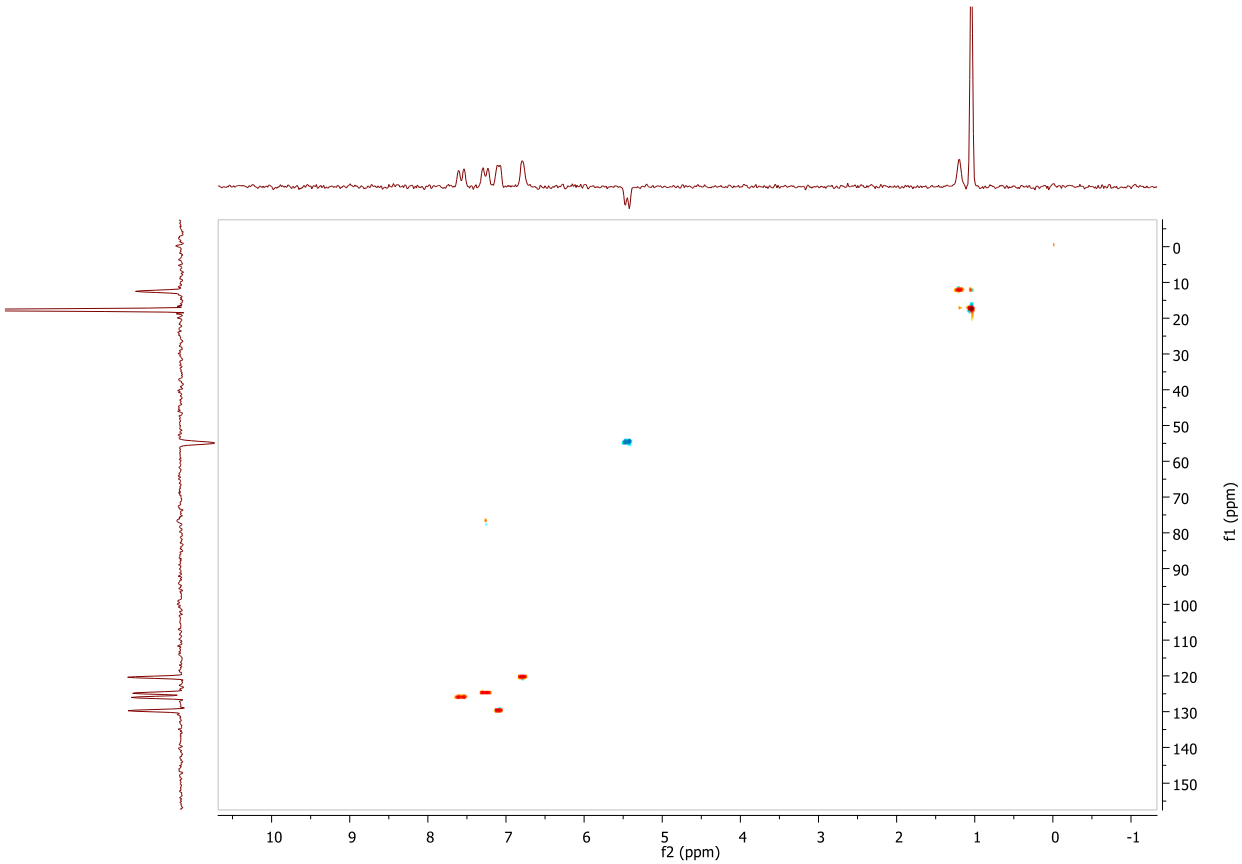

Figure D10. HSQC spectrum of **3.18**

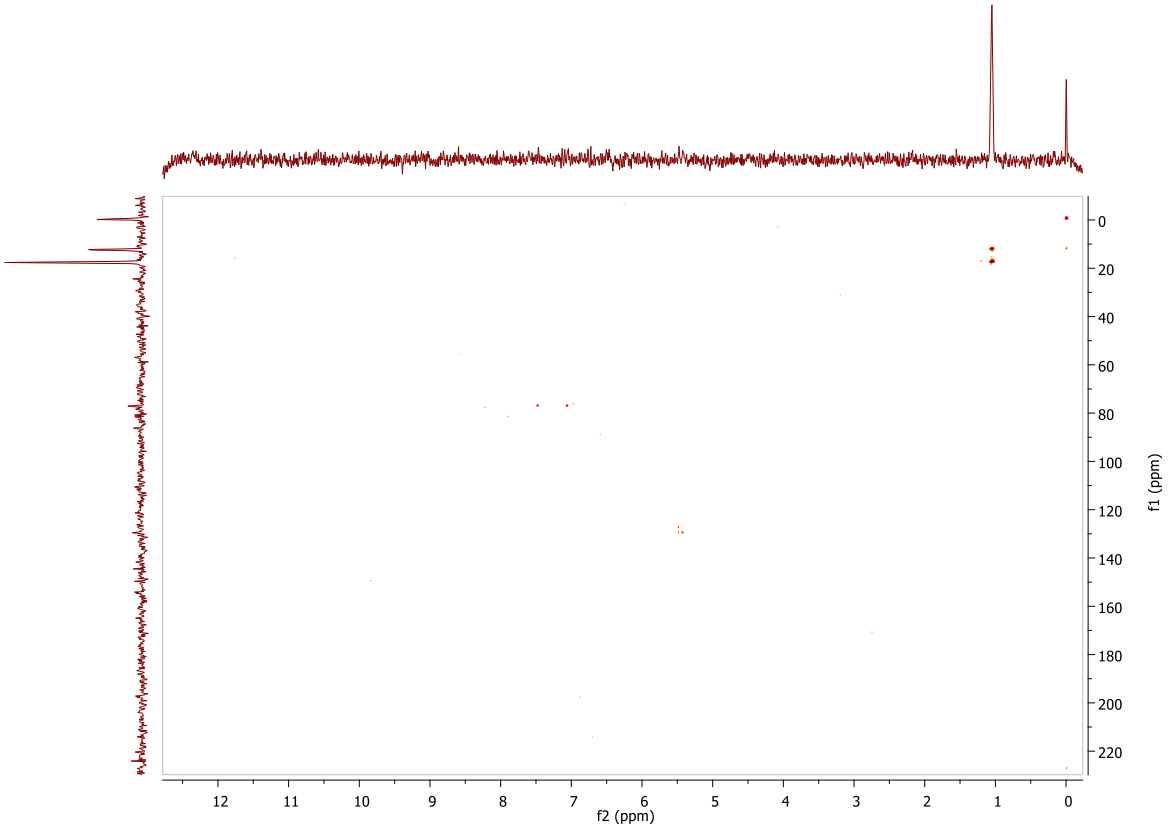

Figure D11. HMBC spectrum of **3.18**

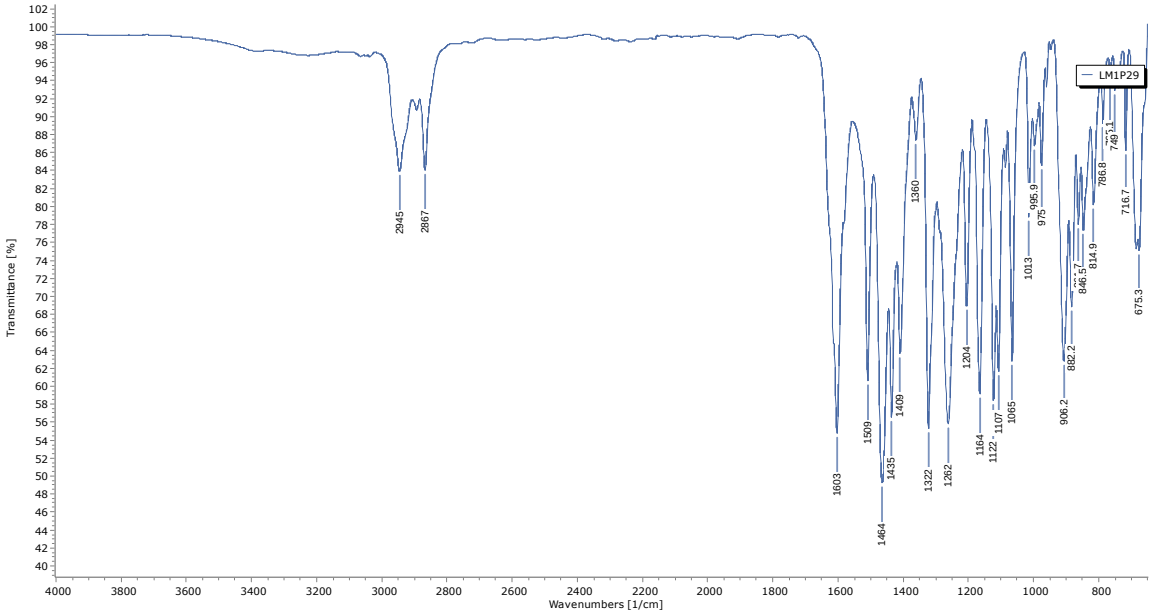

Figure D12. IR spectrum of **3.18**

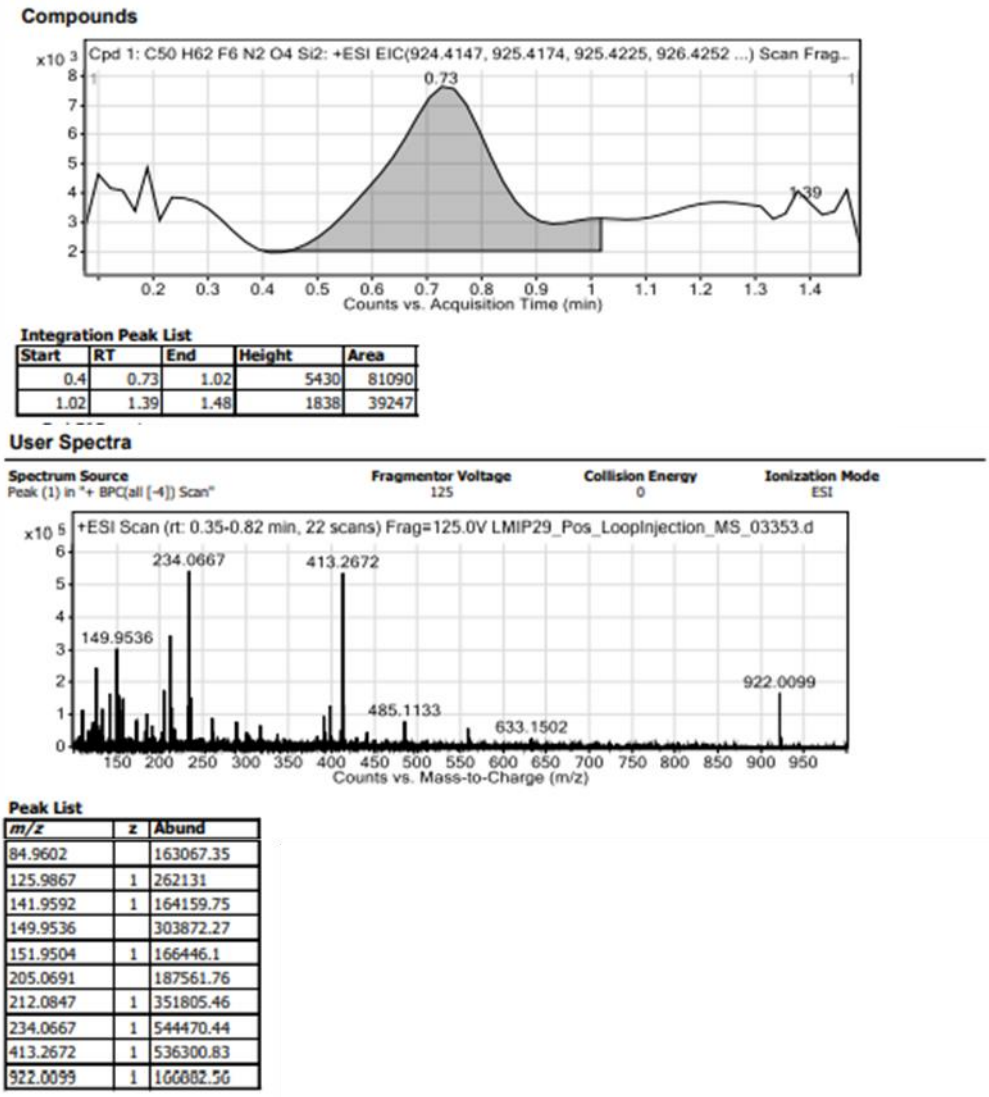

Figure D13. HRMS of **3.18**

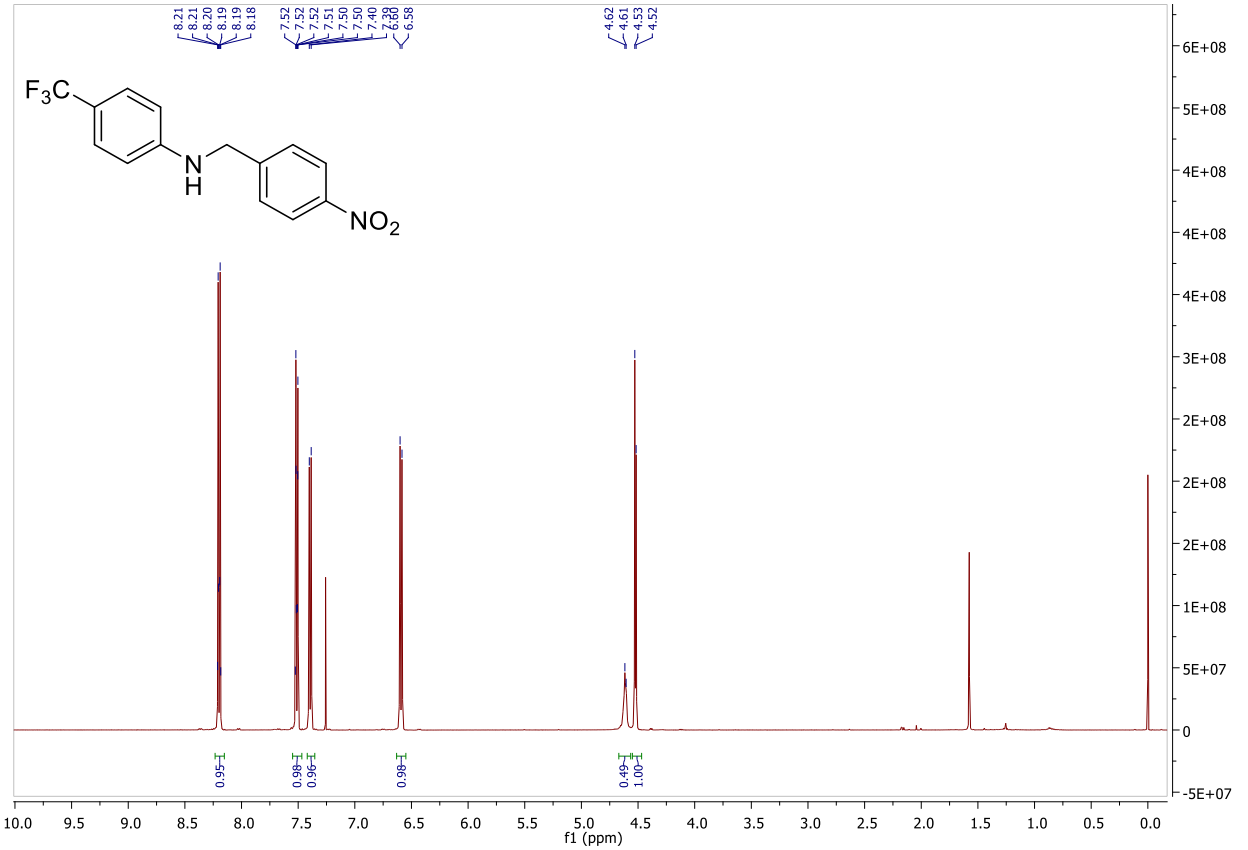

Figure D14. ^{1}H NMR (DMSO-d_6, 500 MHz) spectrum of **3.20**

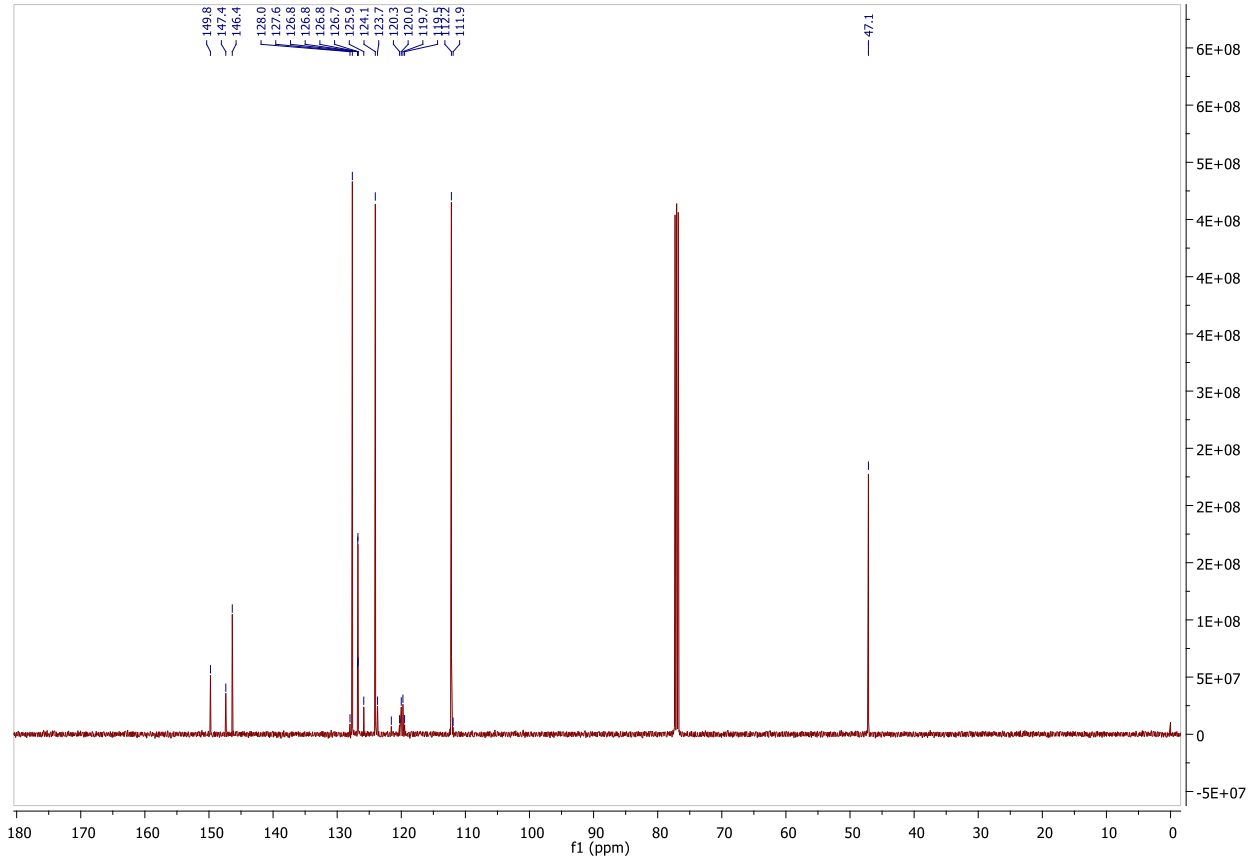

Figure D15. ^{13}C NMR (DMSO-d_6, 126 MHz) spectrum of **3.20**

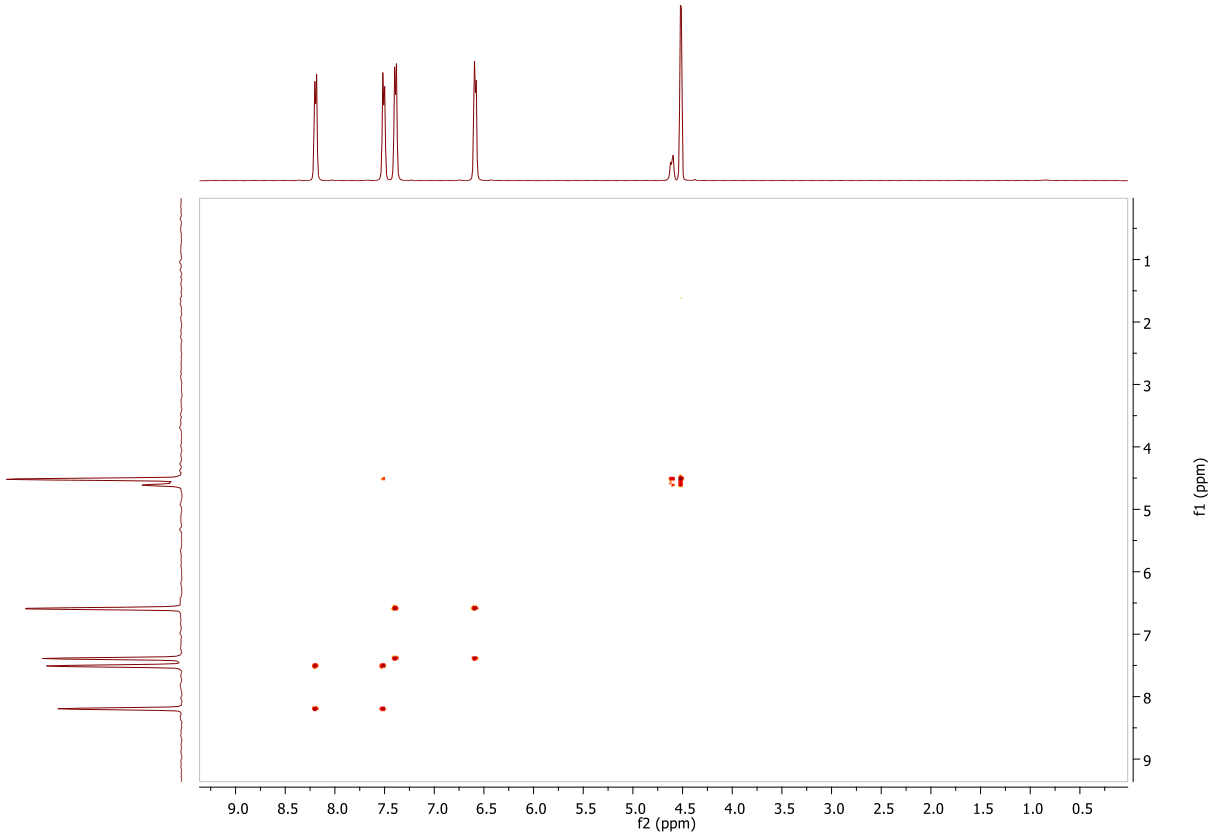

Figure D16. ^{1}H-^{1}H COSY spectrum of **3.20**

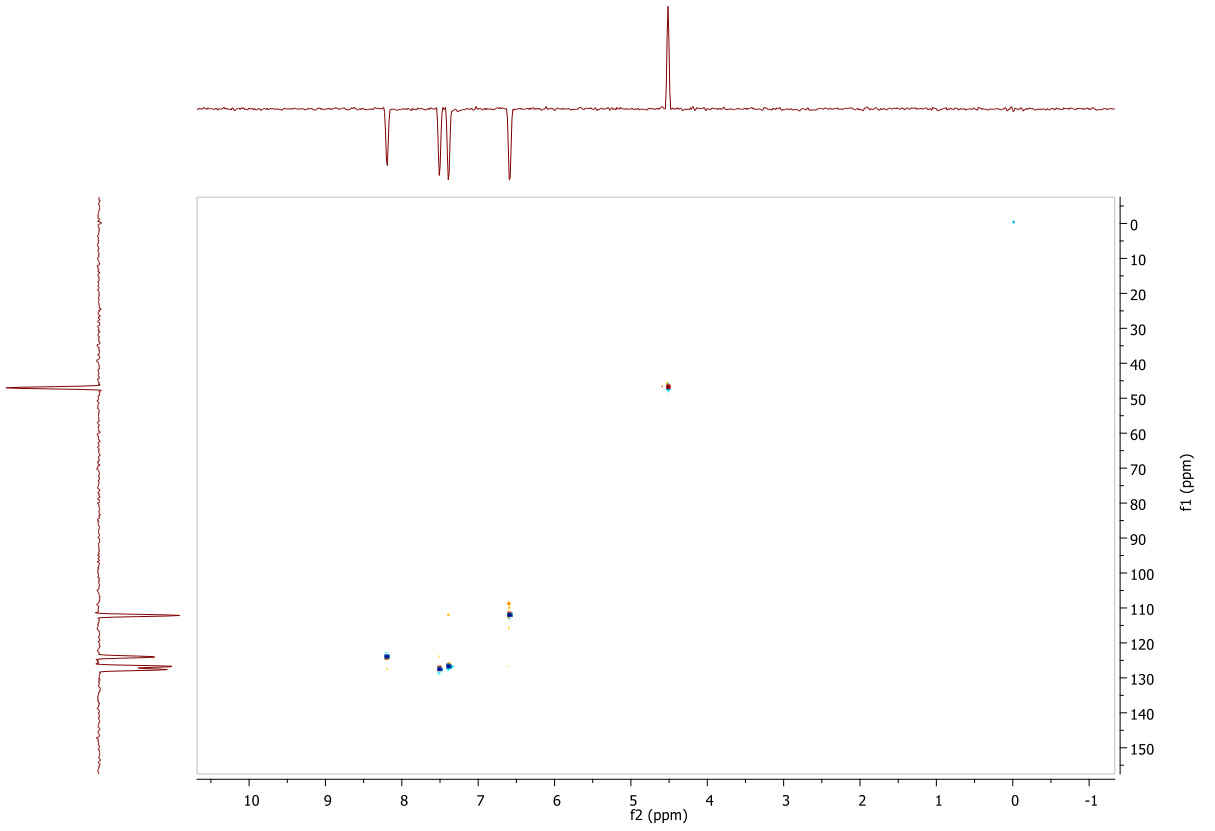

Figure D17. HSQC spectrum of **3.20**

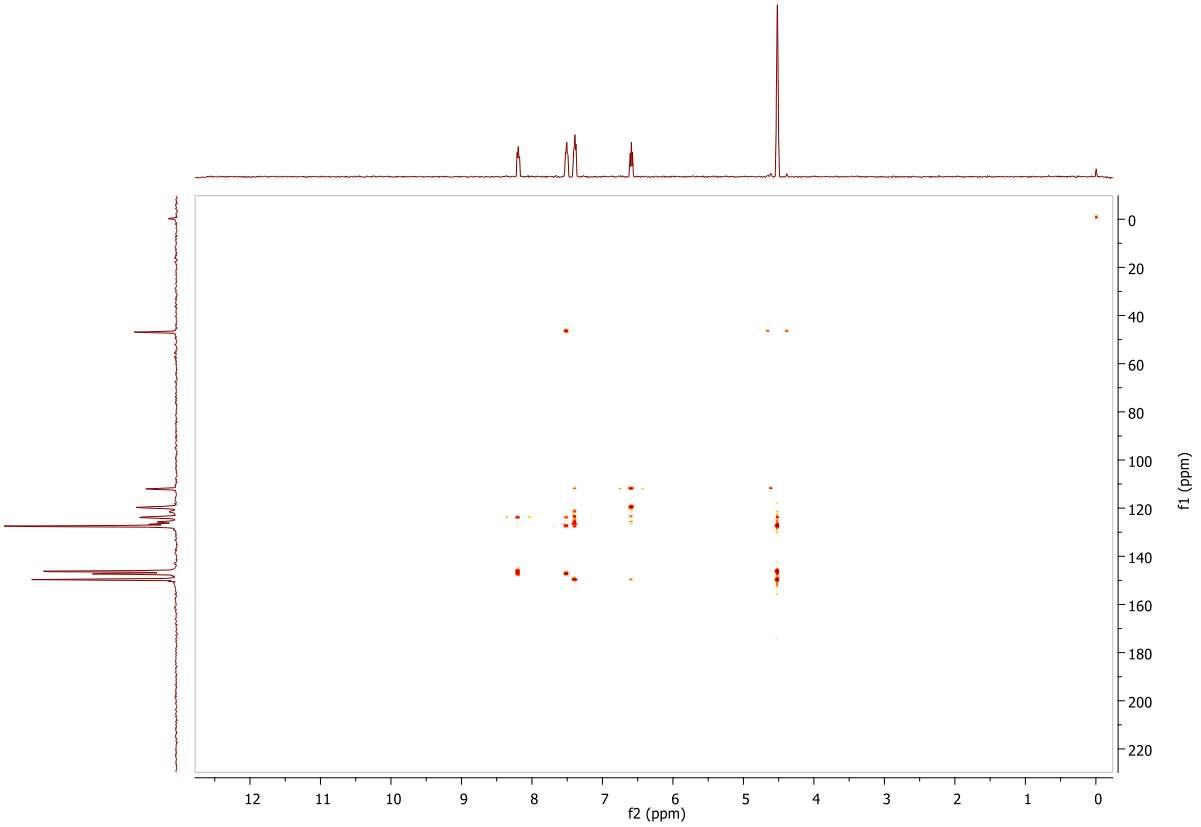

Figure D18. HMBC spectrum of **3.20**

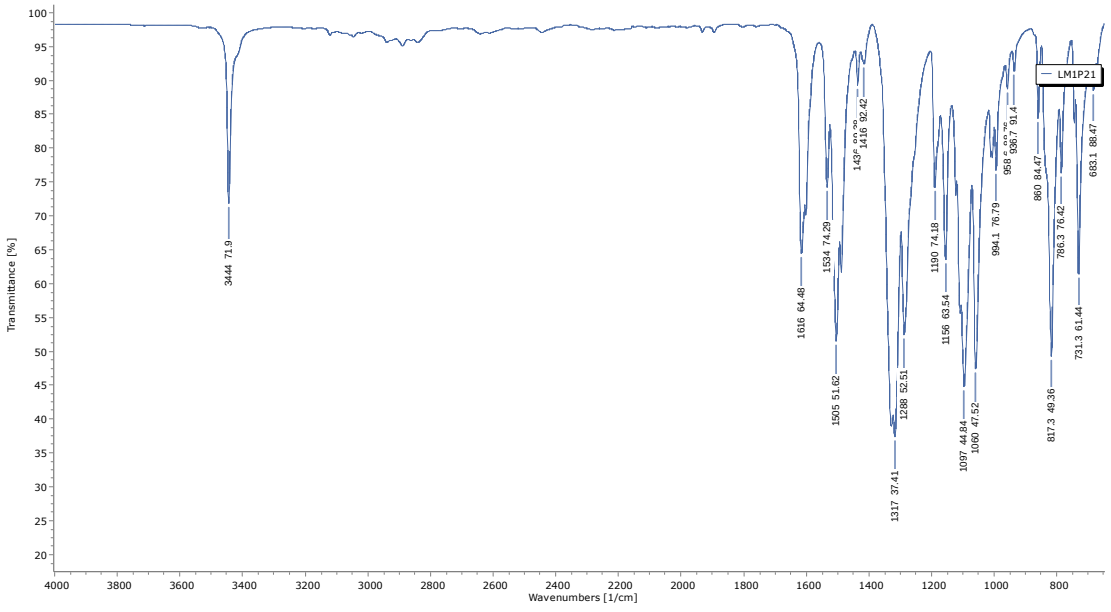

Figure D19. IR spectrum of **3.20**

+MS, 1.0-1.3min #(119-153), -Spectral Bkgrnd

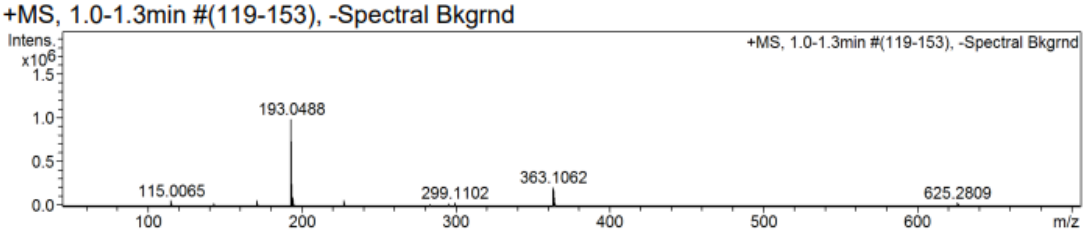

#	m/z	I	I %	Area	S/N
1	115.0065	55950	5.7	1041	3998.3
2	171.0653	60124	6.1	1824	1852.8
3	193.0488	987338	100.0	39236	18352.4
4	194.0501	91896	9.3	3202	1677.7
5	227.0885	61454	6.2	2490	1909.0
6	295.1497	32601	3.3	1674	1013.4
7	299.1102	35754	3.6	1787	1150.1
8	363.1062	212150	21.5	13058	4895.7
9	364.1089	34991	3.5	2097	795.5
10	625.2809	36818	3.7	3708	3178.1

Generate Molecular Formula Parameters

Charge	Tolerance	SearchRadius	H/C Ratio min.	H/C Ratio max.	Electron Conf.	Nitrogen Rule	sigma limit
positive	50 ppm	0.05 m/z	0	3	both	true	0.05

Expected Formula C8H10O4 **Adduct(s):** H, Na

#	meas. m/z	theo. m/z	Err[ppm]	Sigma	Formula
1	171.0653	171.0652	0.70	0.0134	C 8 H 11 O 4
1	193.0488	193.0471	8.80	0.0040	C 8 H 10 Na 1 O 4

Note: Sigma fits < 0.05 indicates high probability of correct MF.

Figure D20. HRMS of **3.20**

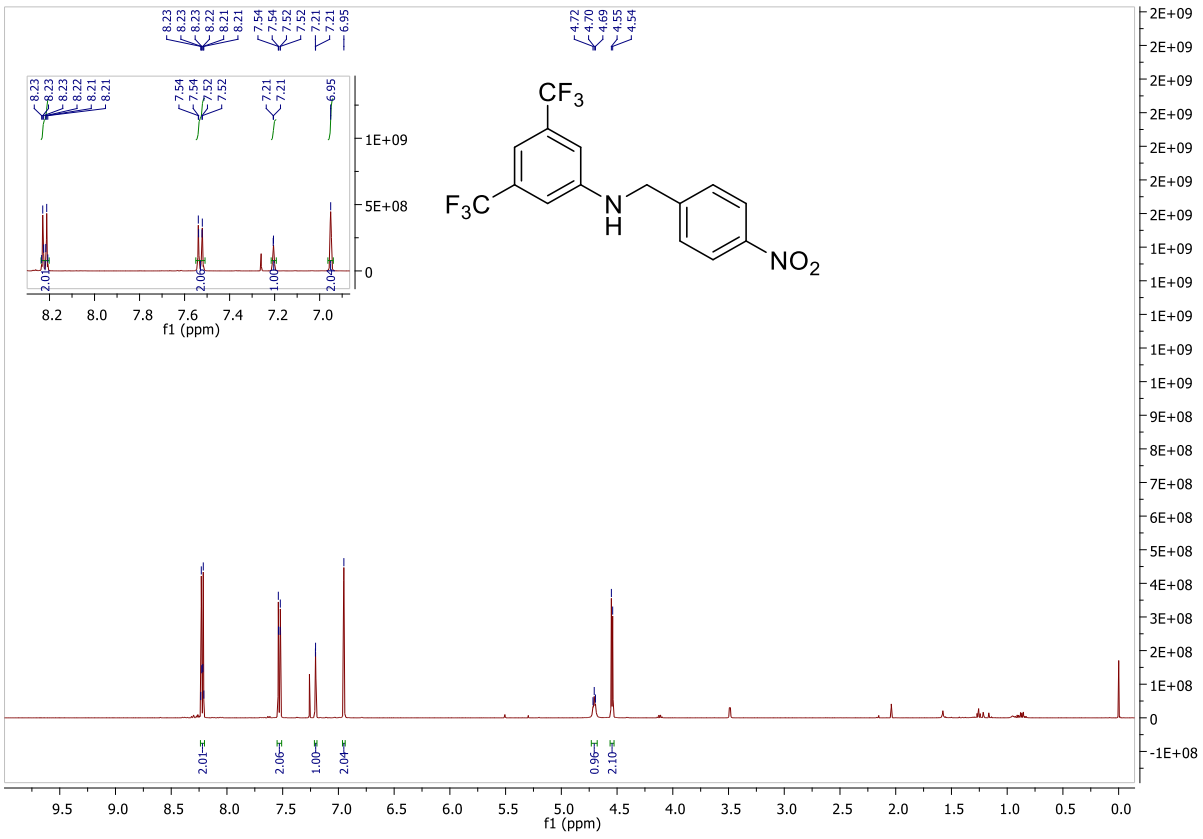

Figure D21. ^{1}H NMR (DMSO-d_6, 500 MHz) spectrum of **3.21**

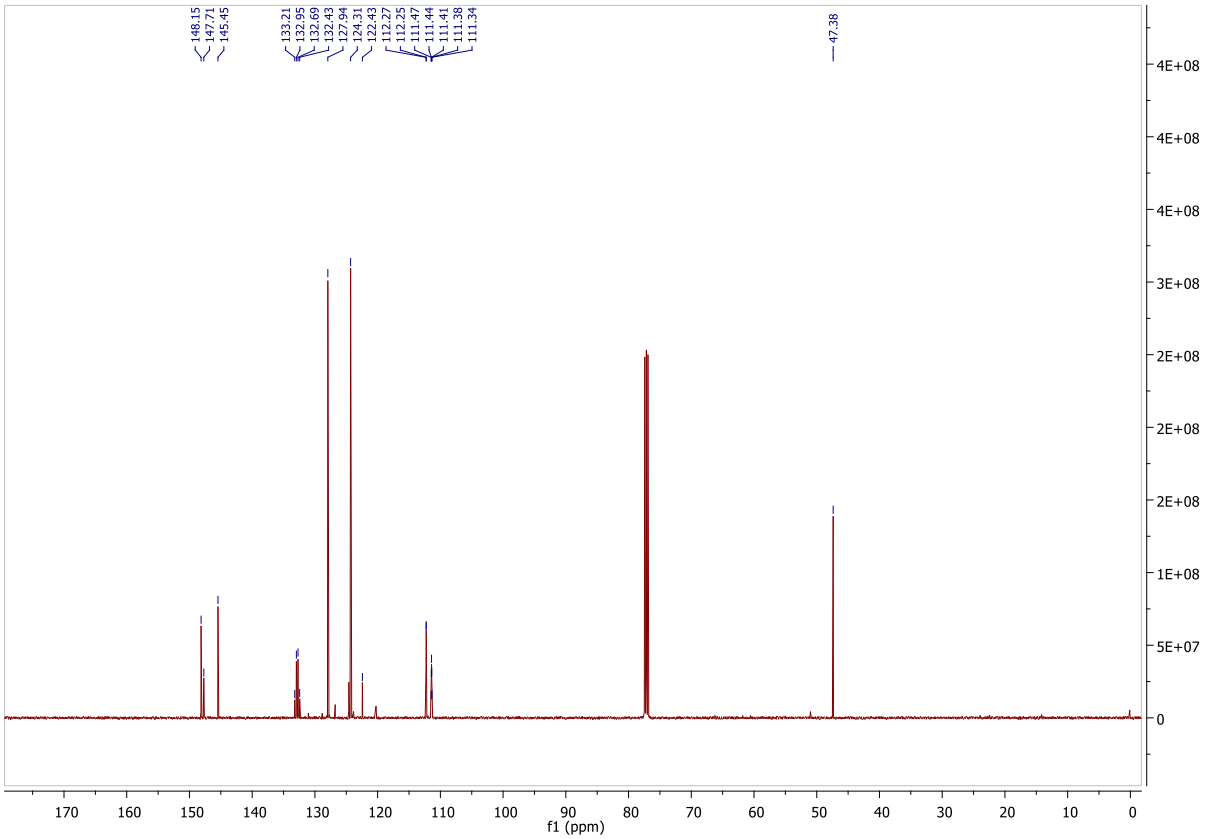

Figure D22. ^{13}C NMR (DMSO-d_6, 126 MHz) spectrum of **3.21**

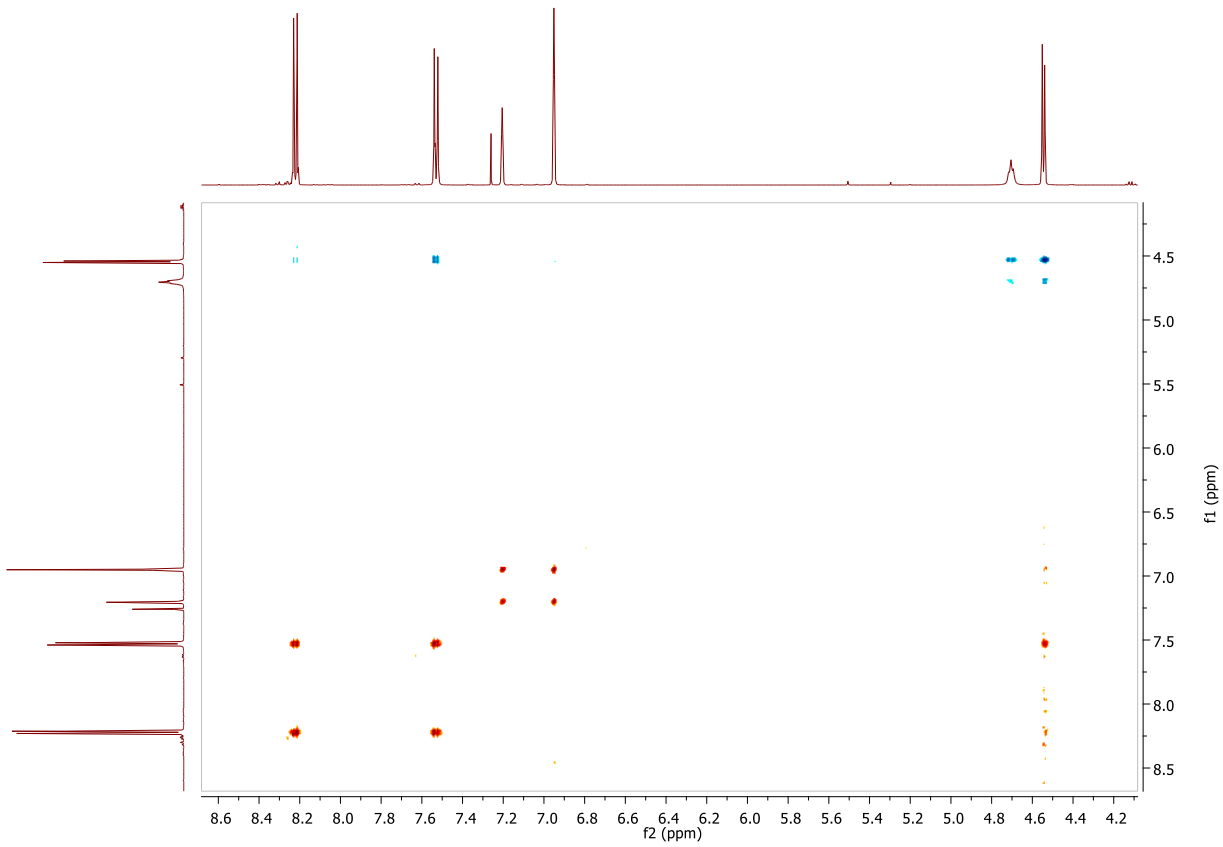

Figure D23. ^{1}H-^{1}H COSY spectrum of **3.21**

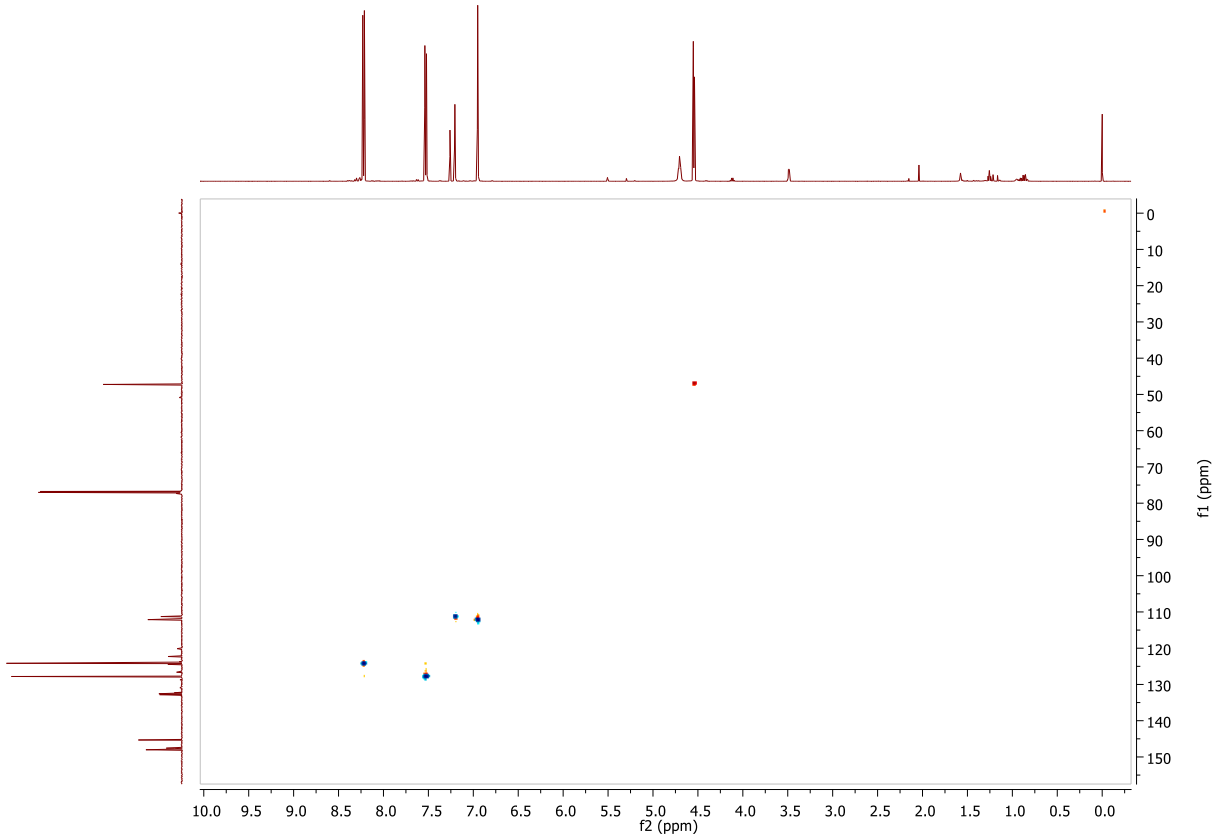

Figure D24. HSQC spectrum of **3.21**

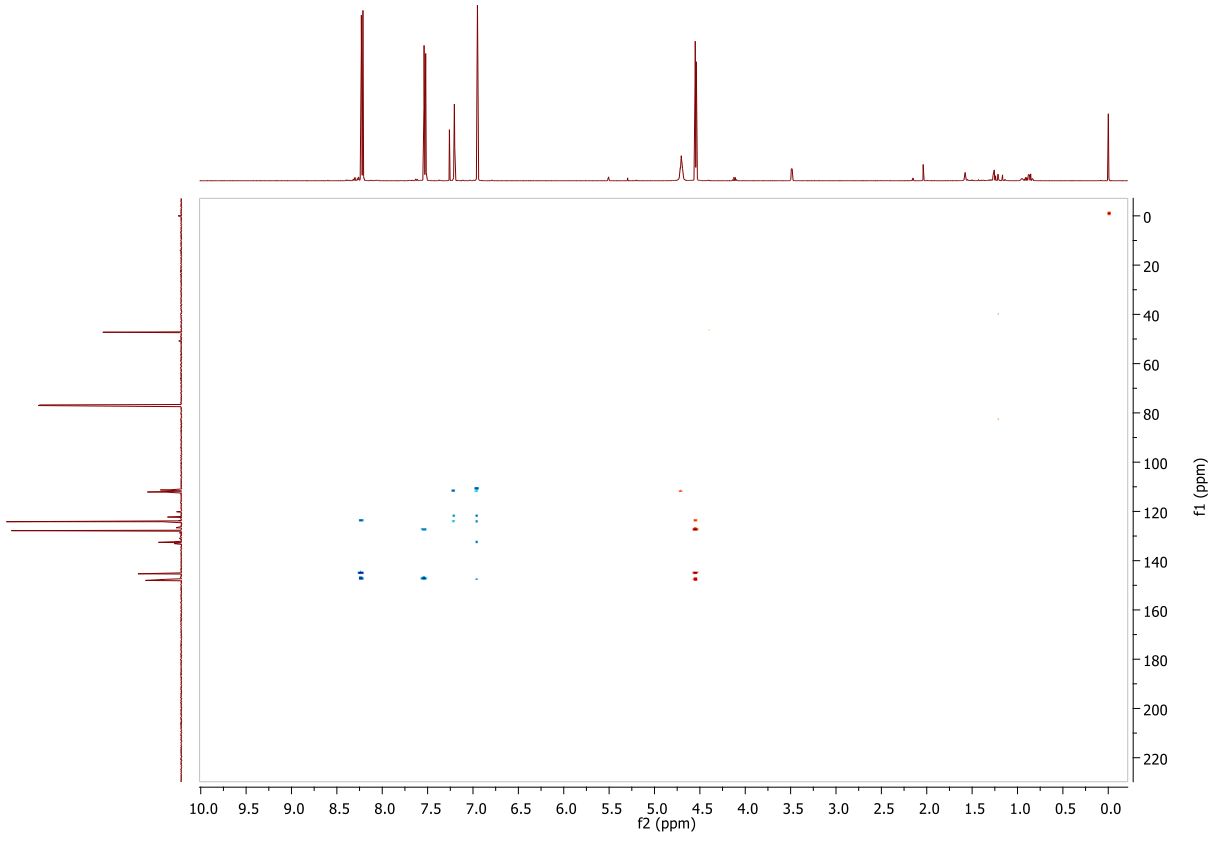

Figure D25. HMBC spectrum of **3.21**

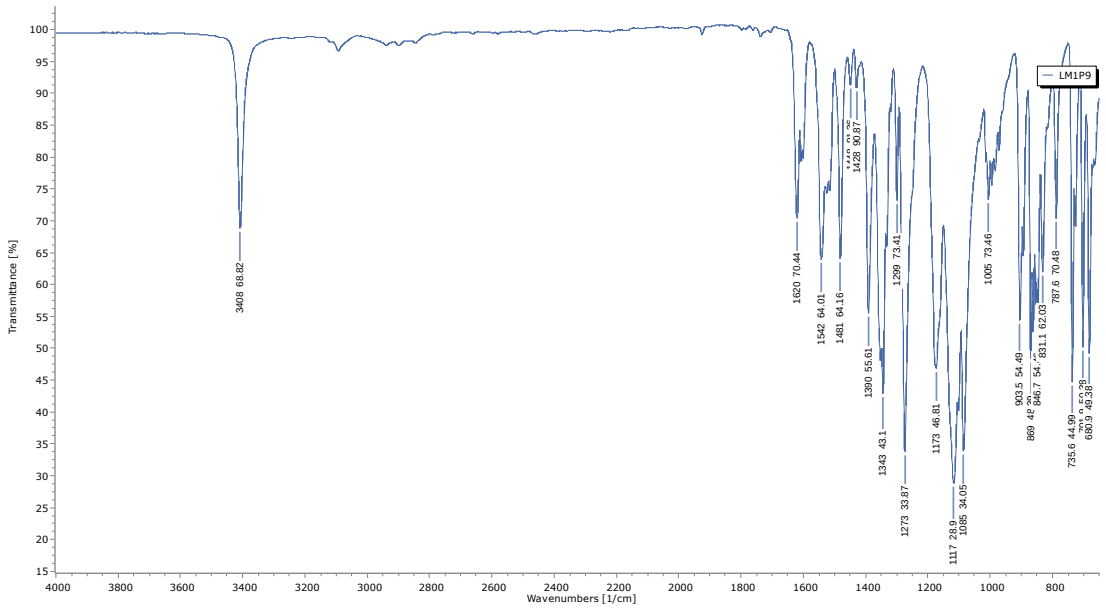

Figure D26. IR spectrum of **3.21**

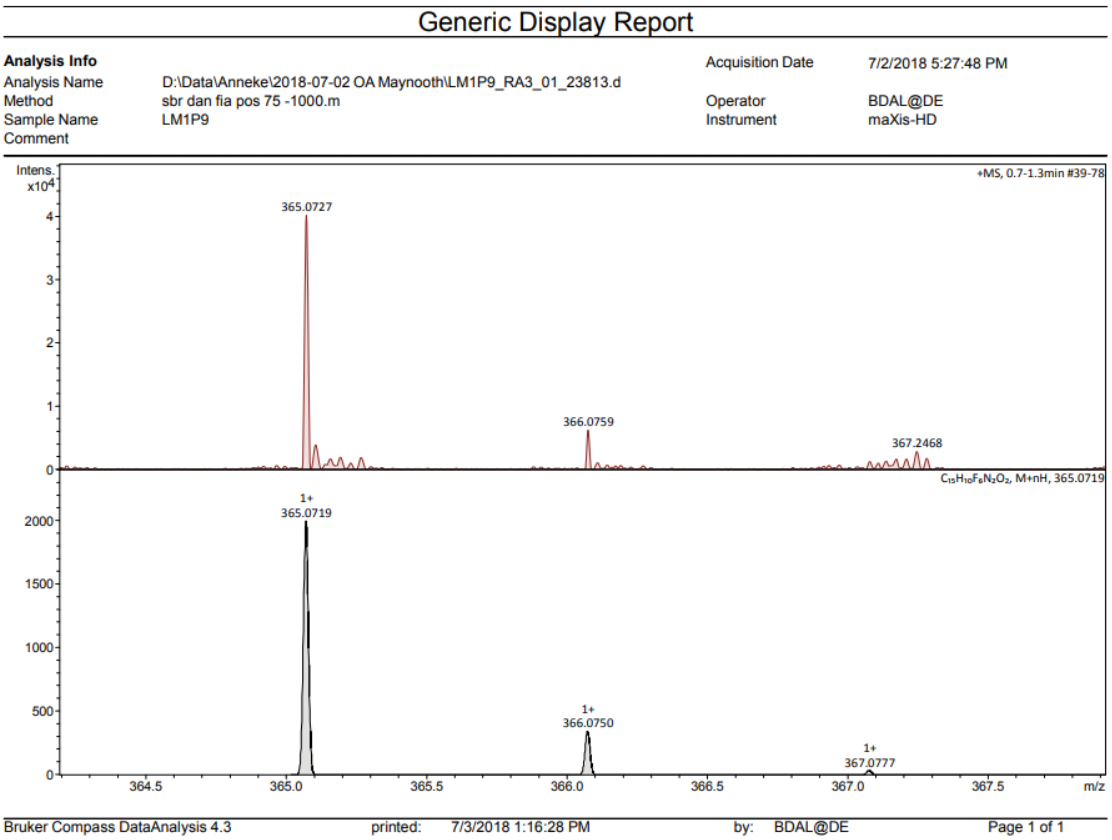

Figure D27. HRMS of **3.21**

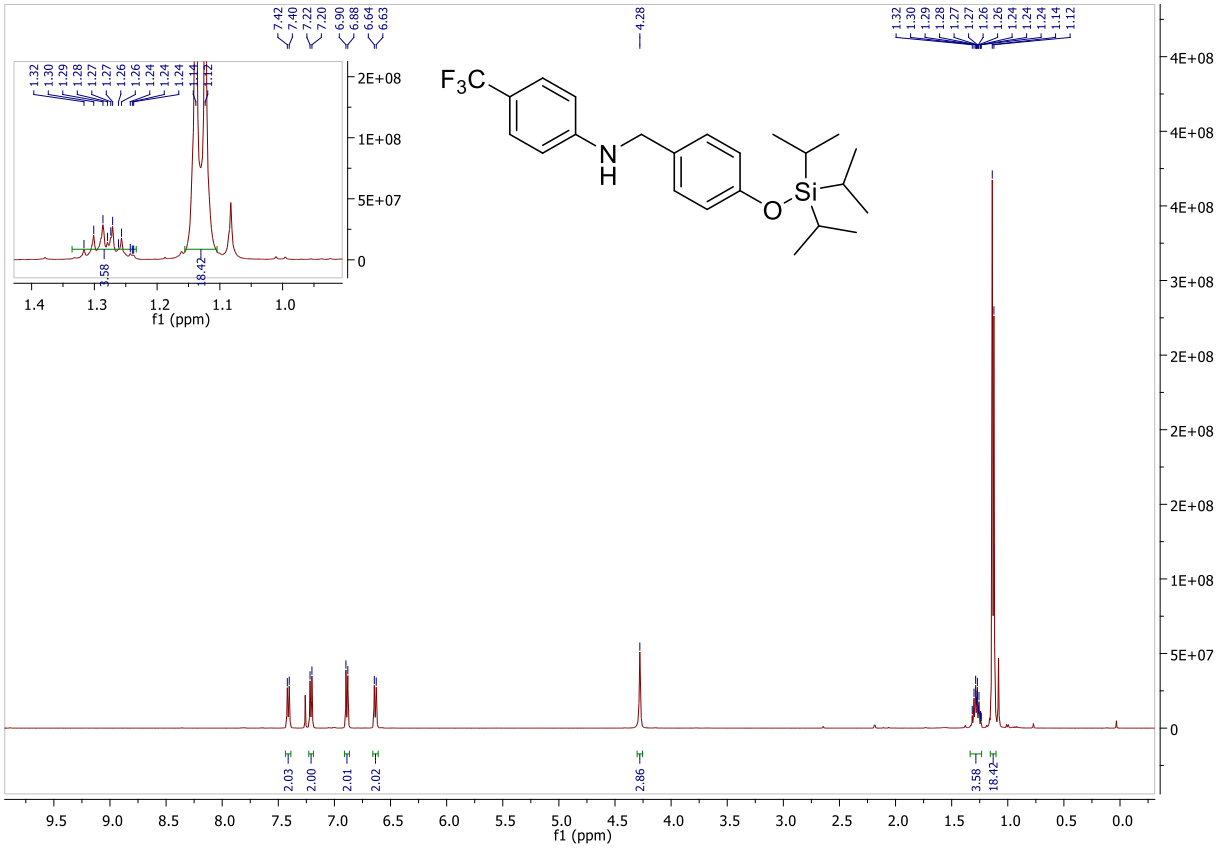

Figure D28. ^{1}H NMR (DMSO-d_6, 500 MHz) spectrum of **3.22**

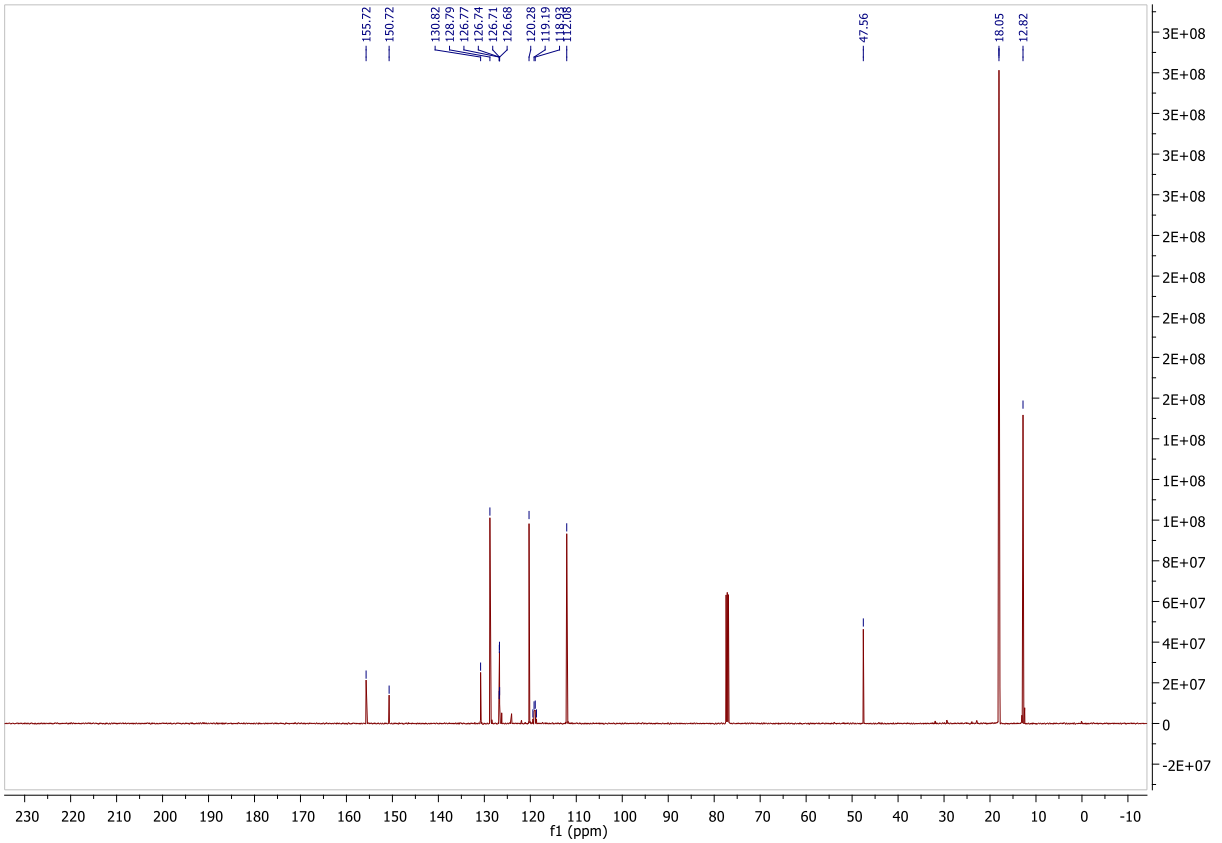

Figure D29. ^{13}C NMR (DMSO-d_6, 126 MHz) spectrum of **3.22**

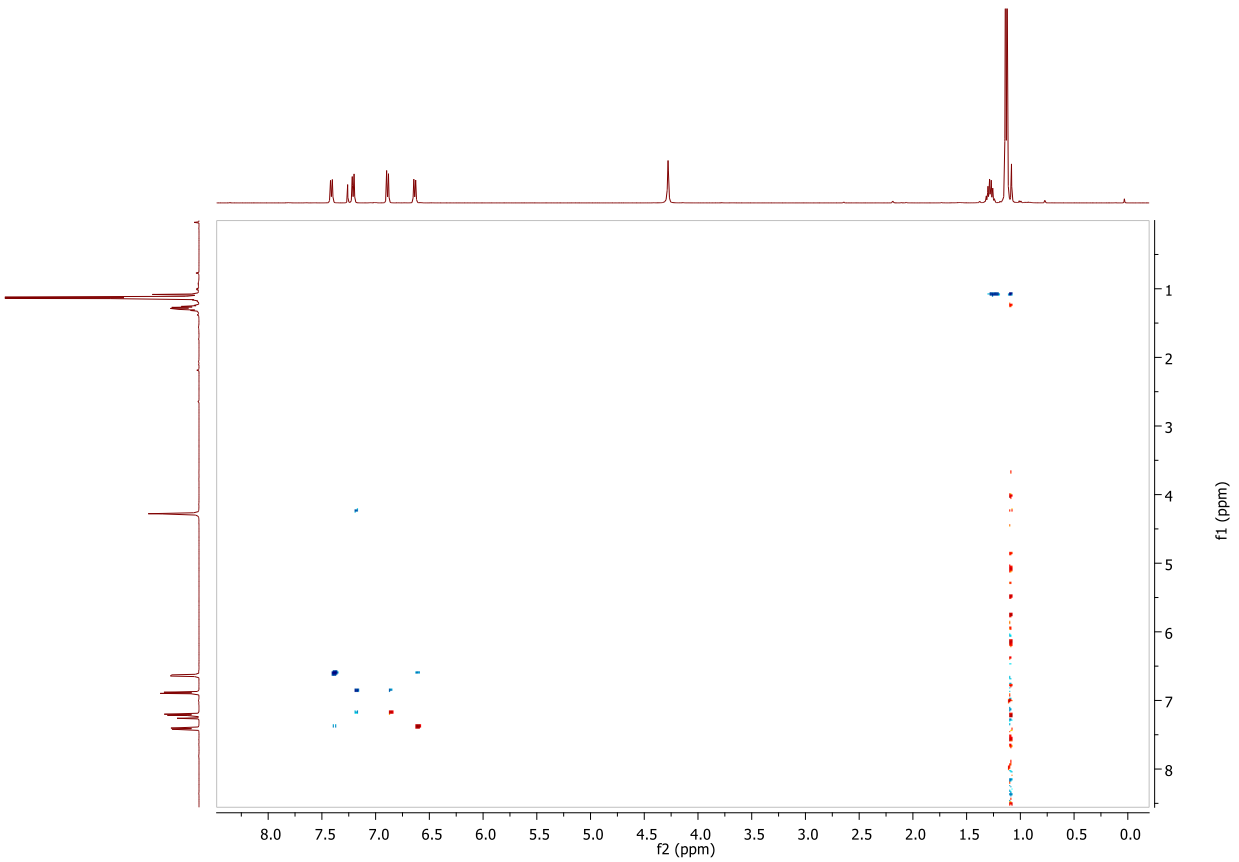

Figure D30. ^{1}H-^{1}H COSY spectrum of **3.22**

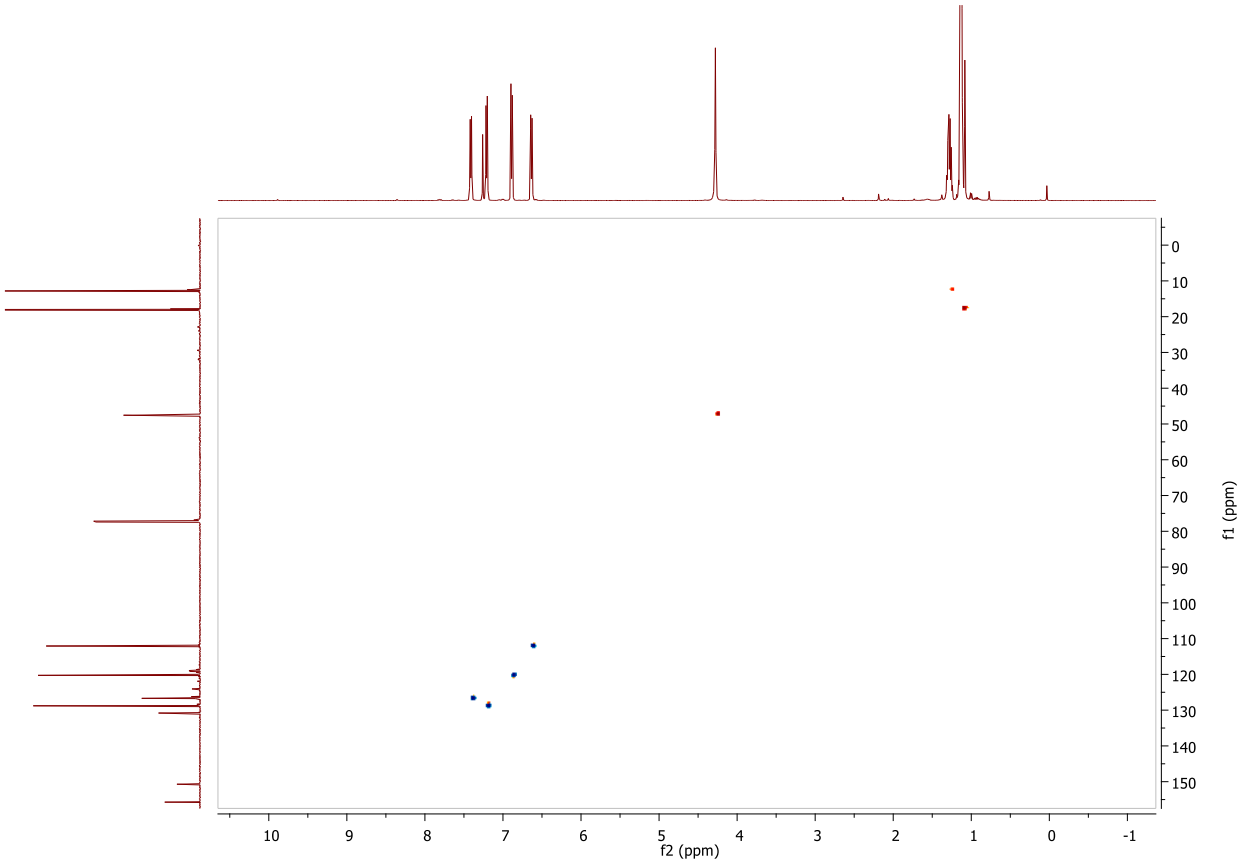

Figure D31. HSQC spectrum of **3.22**

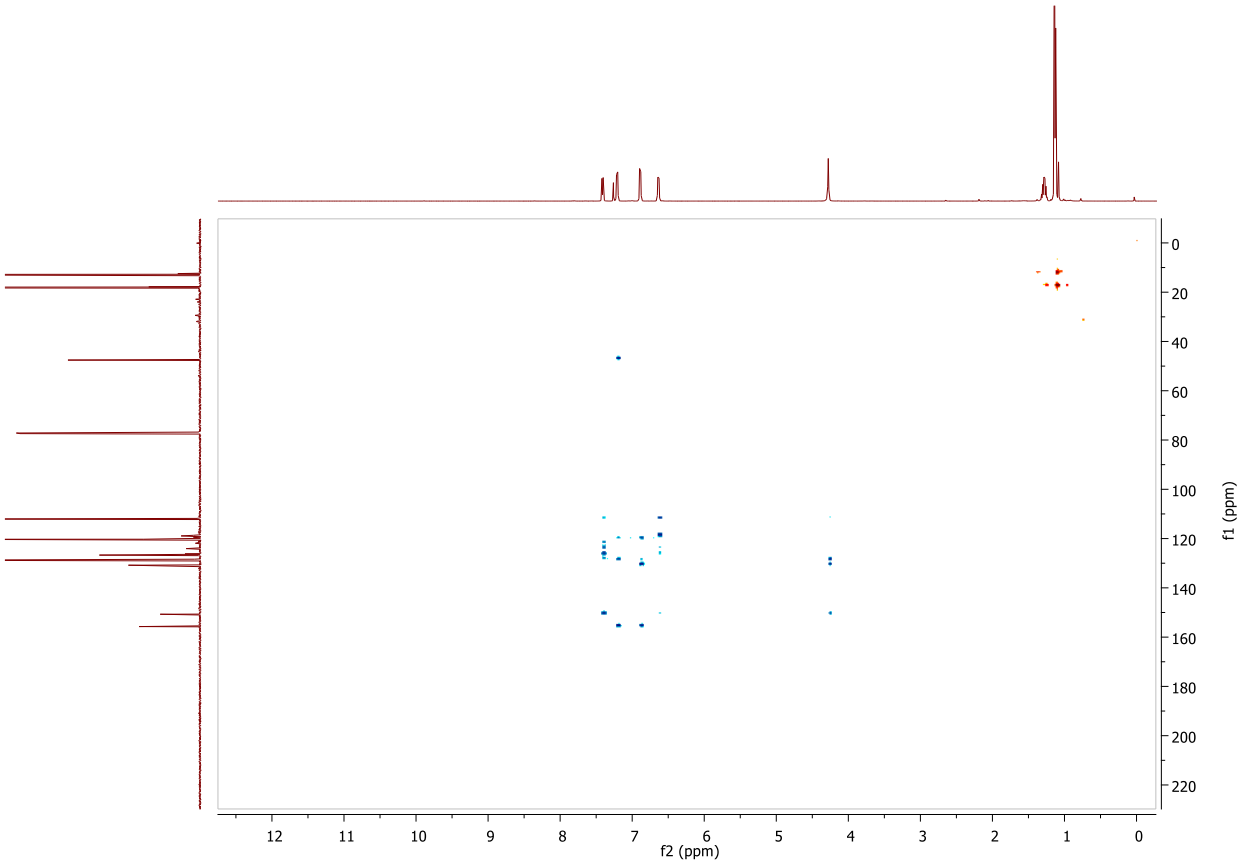

Figure D32. HMBC spectrum of **3.22**

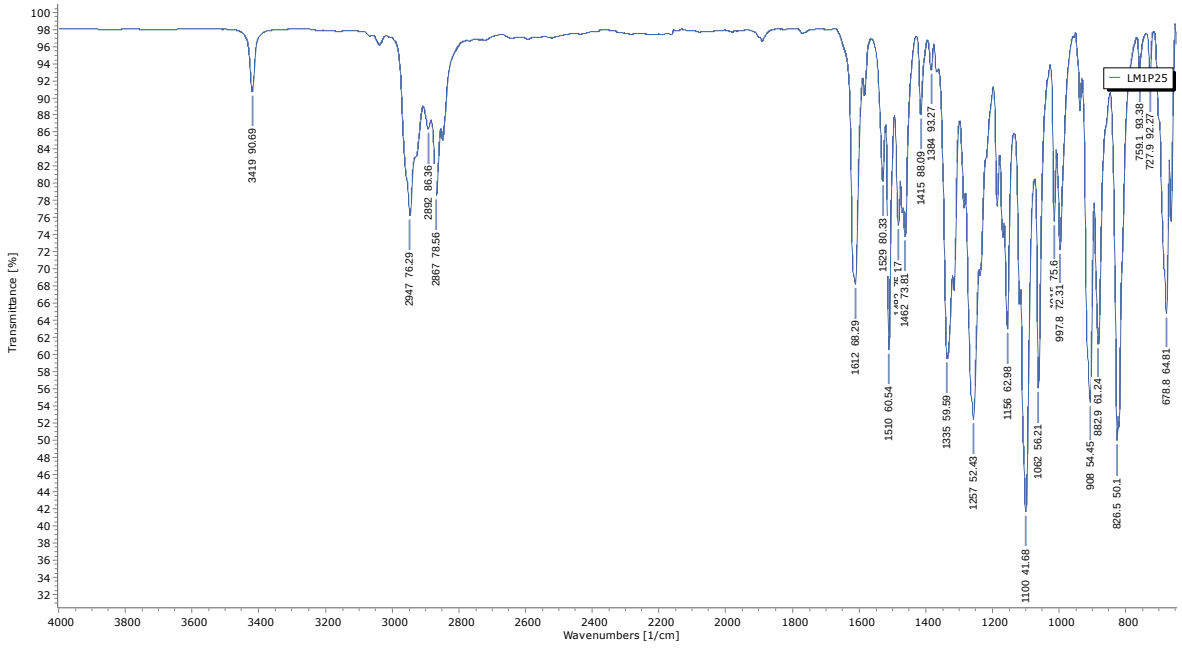

Figure D33. IR spectrum of **3.22**

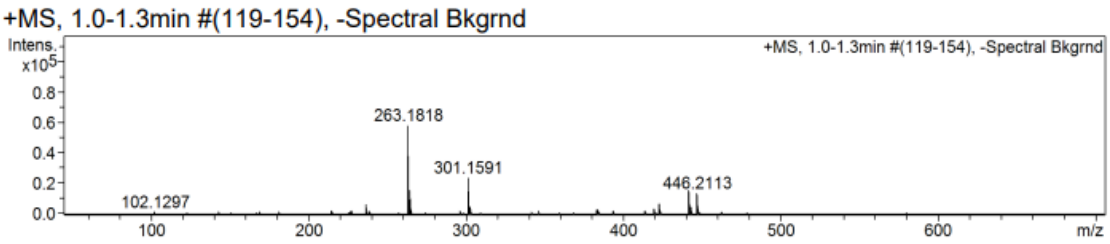

#	m/z	I	I %	Area	S/N
1	236.0929	6532	11.2	81	566.3
2	263.1818	58146	100.0	2856	4865.5
3	264.1876	15982	27.5	672	1342.8
4	301.1591	23725	40.8	1249	2616.6
5	302.1644	5065	8.7	223	566.2
6	422.2141	7199	12.4	502	742.3
7	441.3198	12010	20.7	550	810.8
8	442.3269	4941	8.5	128	327.6
9	446.2113	13684	23.5	1108	848.8
10	447.2117	4097	7.0	309	250.0

Generate Molecular Formula Parameters

Charge	Tolerance	SearchRadius	H/C Ratio min.	H/C Ratio max.	Electron Conf.	Nitrogen Rule	sigma limit
positive	25 ppm	0.05 m/z	0	3	both	true	0.05

Expected Formula C23H32F3NOSi **Adduct(s):** H, Na

#	meas. m/z	theo. m/z	Err[ppm]	Sigma	Formula
1	446.2113	446.2097	3.60	0.0069	C 23 H 32 F 3 N 1 Na 1 O 1 Si 1

Note: Sigma fits < 0.05 indicates high probability of correct MF.

Figure D34. HRMS of **3.22**

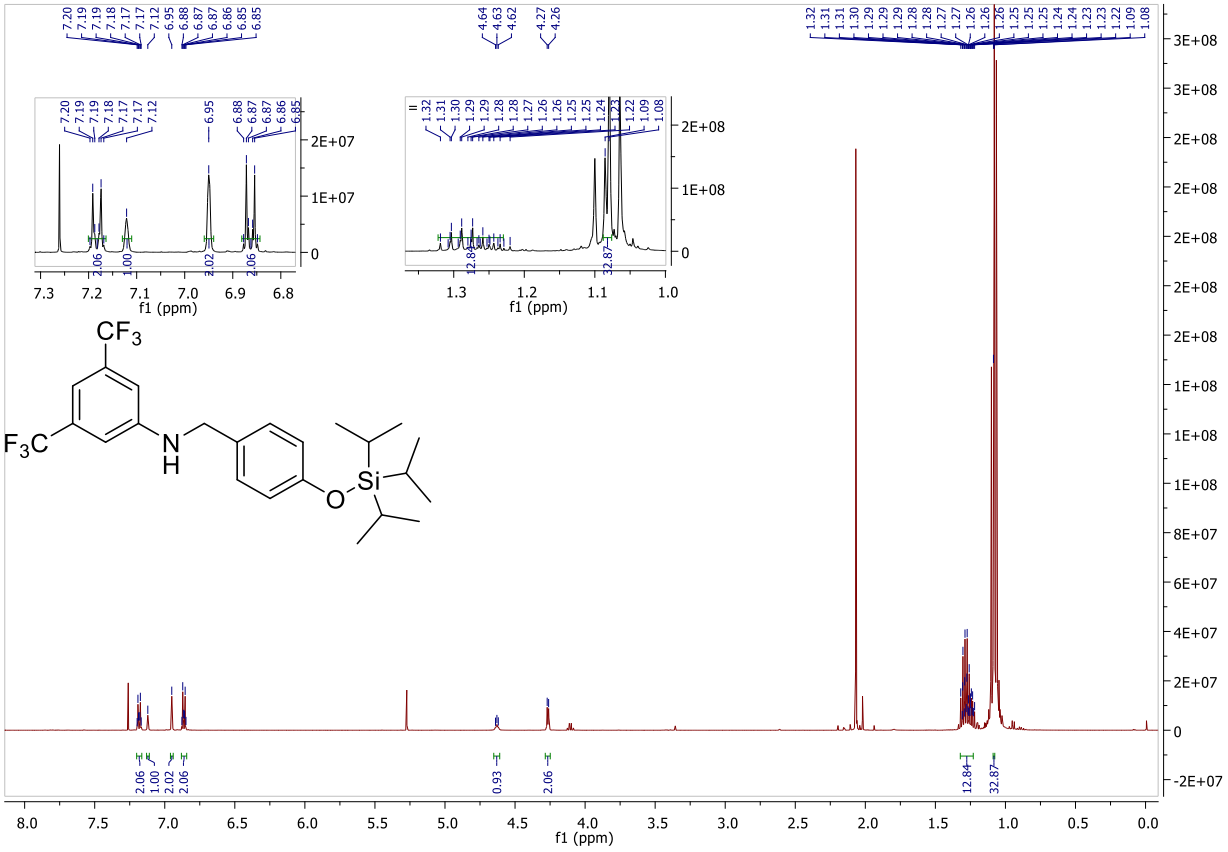

Figure D35. ^{1}H NMR (DMSO-d_6, 5 00 MHz) spectrum of **3.23**

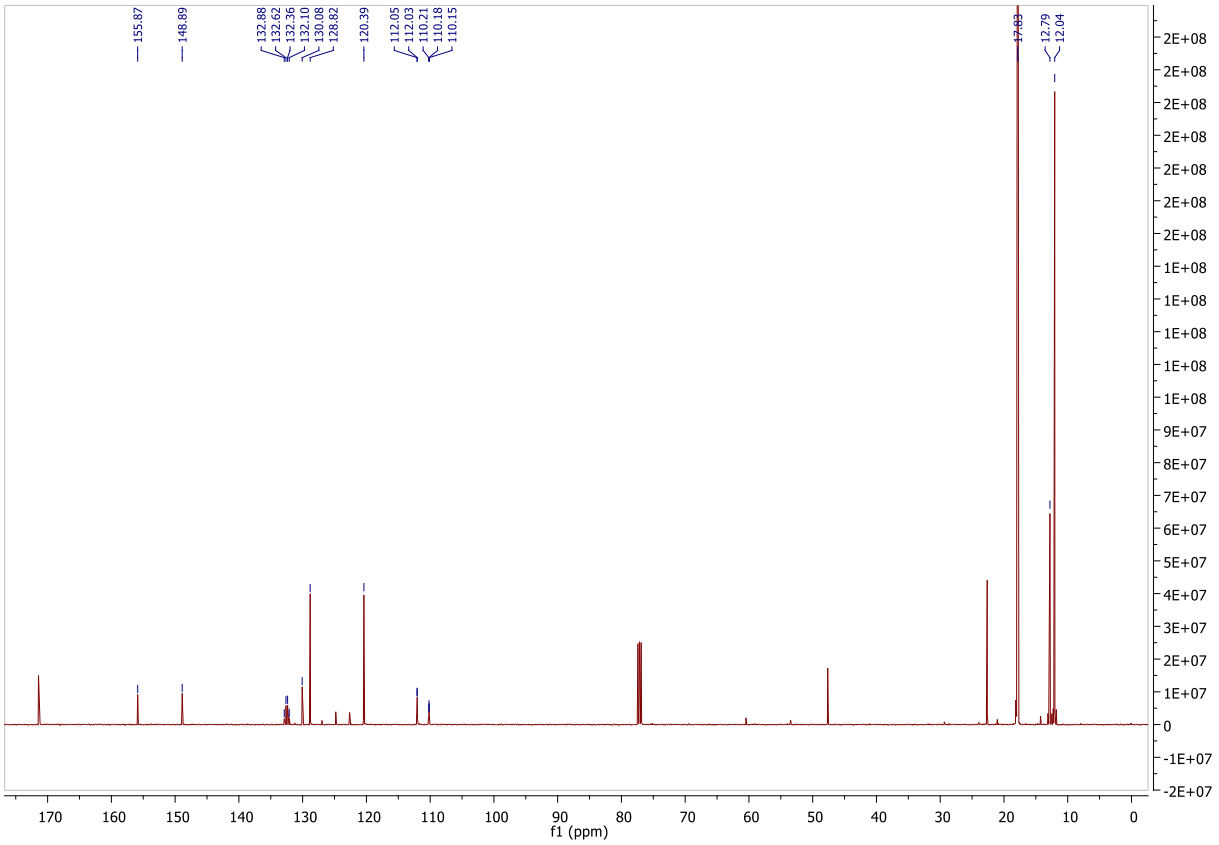

Figure D36. ^{13}C NMR (DMSO-d_6, 126 MHz) spectrum of **3.23**

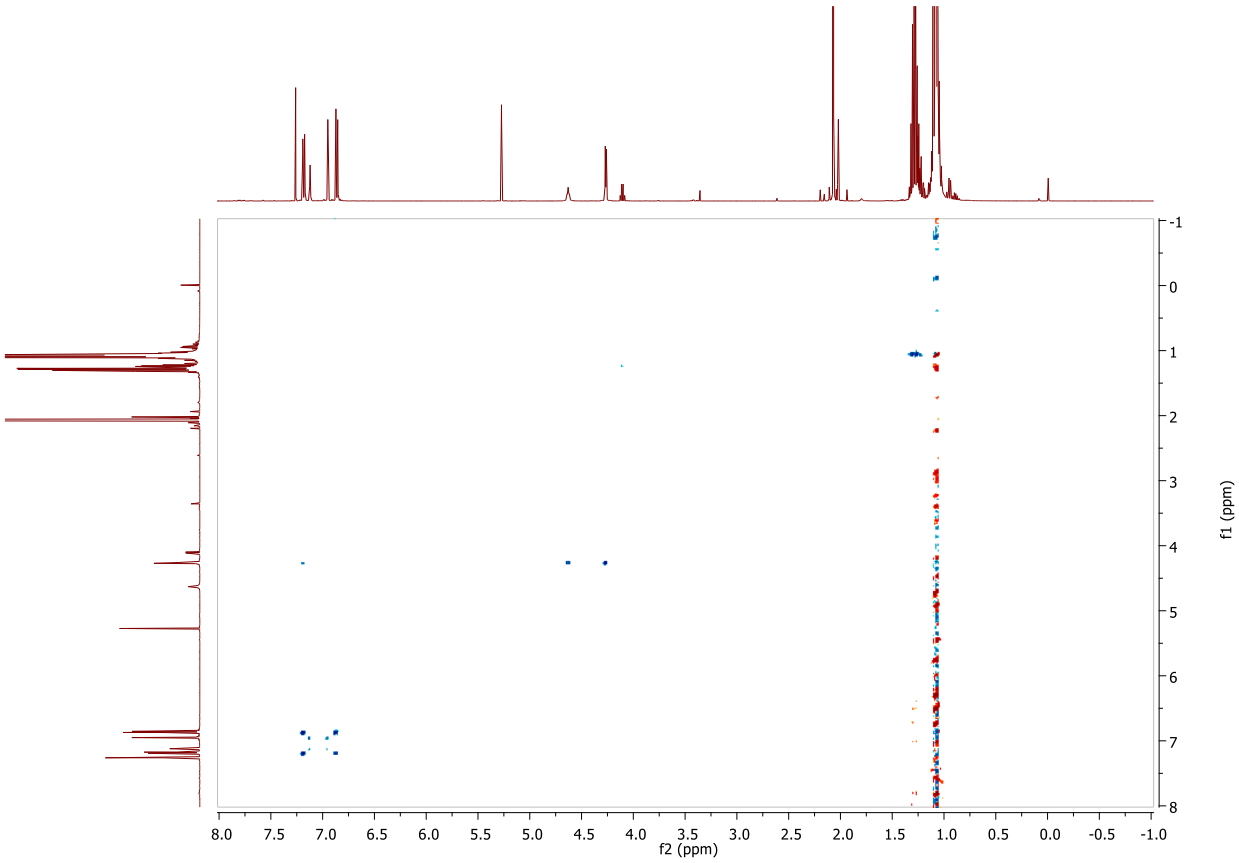

Figure D37. ^{1}H-^{1}H COSY spectrum of **3.23**

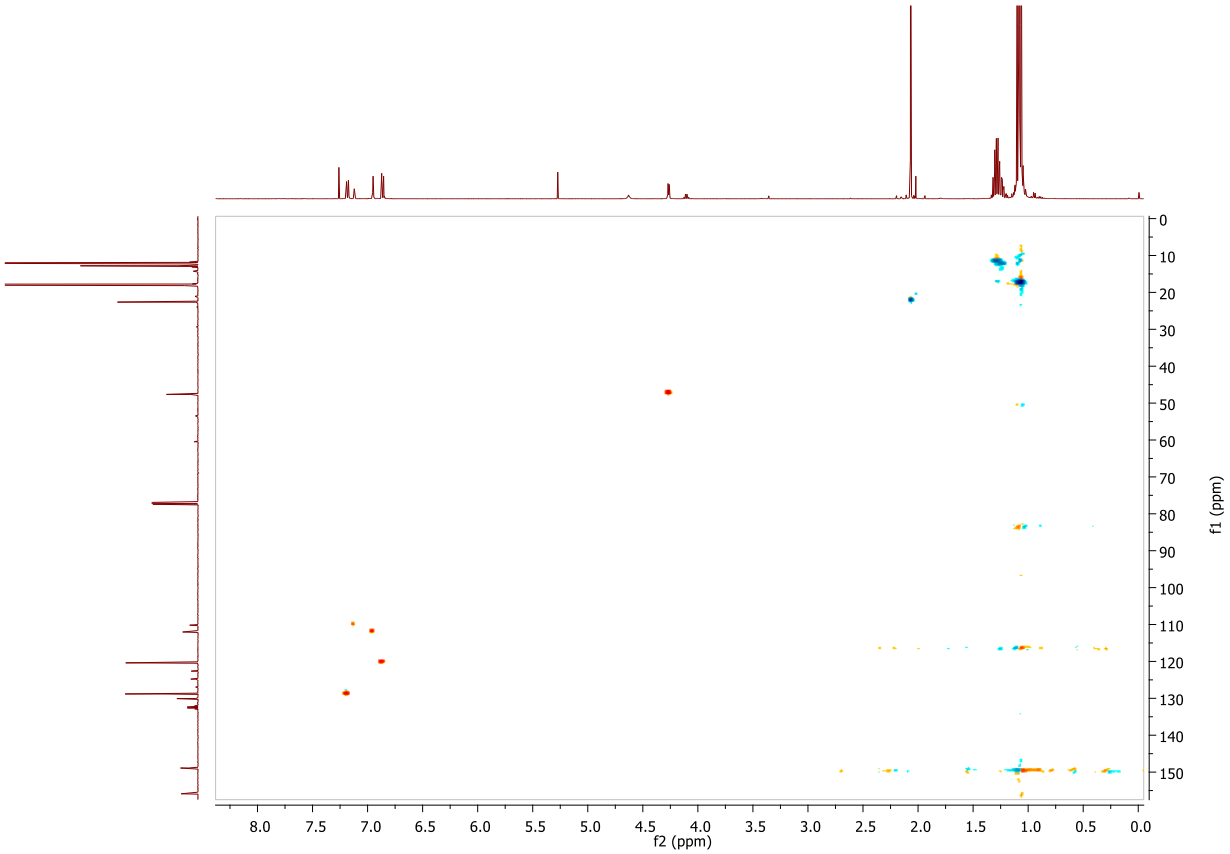

Figure D38. HSQC spectrum of **3.23**

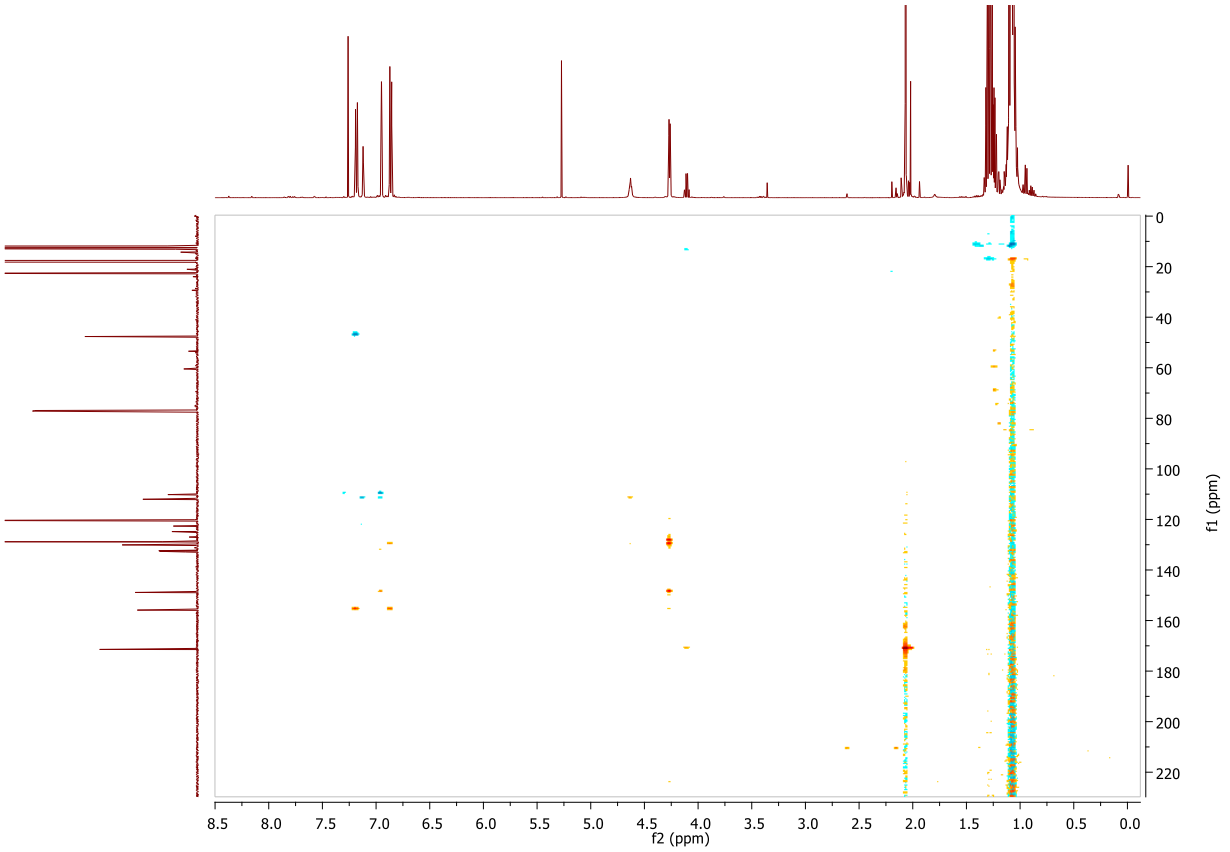

Figure D39. HMBC spectrum of **3.23**

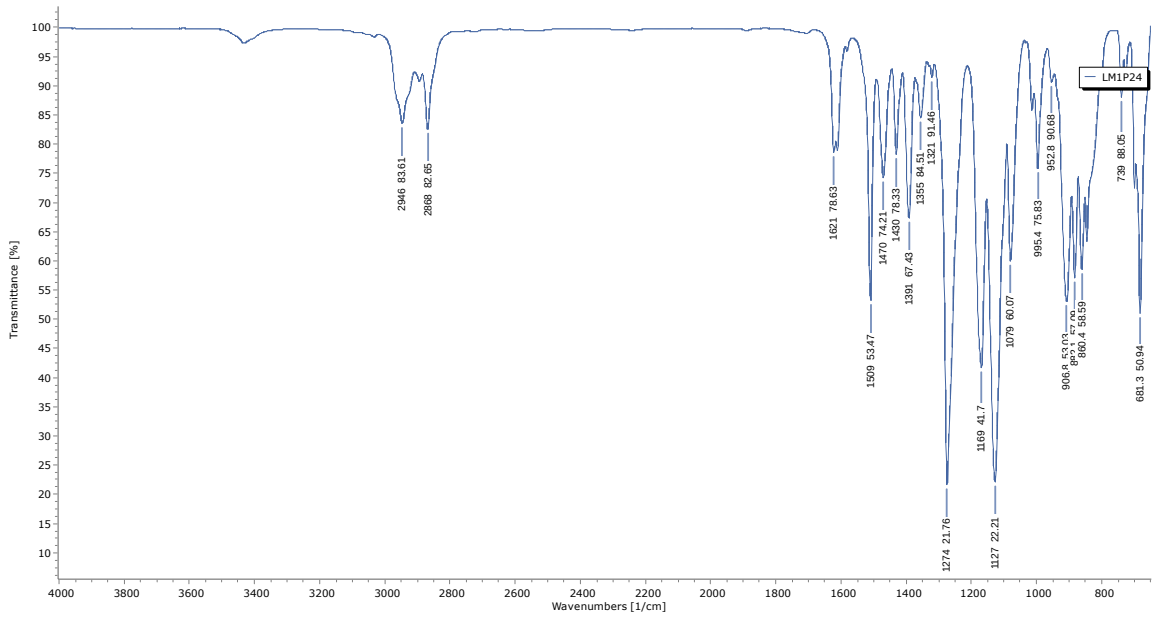

Figure D40. IR spectrum of **3.23**

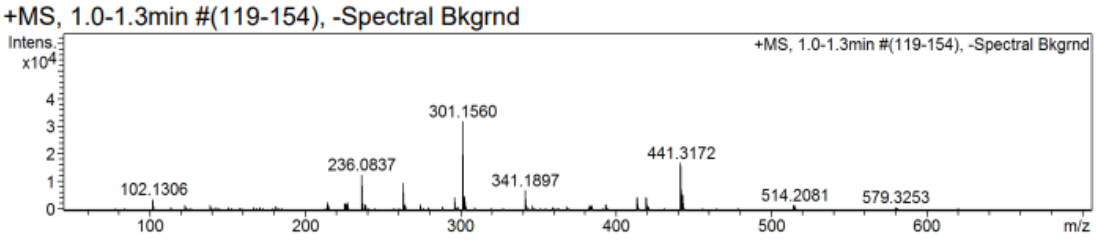

#	m/z	I	I %	Area	S/N
1	236.0837	12629	39.9	145	1147.8
2	263.1833	9734	30.7	426	753.8
3	296.1183	4391	13.9	73	355.6
4	301.1560	31675	100.0	1827	2713.6
5	302.1607	5173	16.3	262	448.3
6	341.1897	6904	21.8	397	902.5
7	413.2820	4648	14.7	174	680.2
8	419.3260	4561	14.4	238	675.0
9	441.3172	16764	52.9	553	2077.5
10	442.3293	5463	17.2	141	671.9

Generate Molecular Formula Parameters

Charge	Tolerance	SearchRadius	H/C Ratio min.	H/C Ratio max.	Electron Conf.	Nitrogen Rule	sigma limit
positive	25 ppm	0.05 m/z	0	3	both	true	0.05

Expected Formula C24H31F6NOSi **Adduct(s):** H, Na

#	meas. m/z	theo. m/z	Err[ppm]	Sigma	Formula
1	514.2081	514.1971	21.40	0.0074	C 24 H 31 F 6 N 1 Na 1 O 1 Si 1

Note: Sigma fits < 0.05 indicates high probability of correct MF.

Figure D41. HRMS of **3.23**

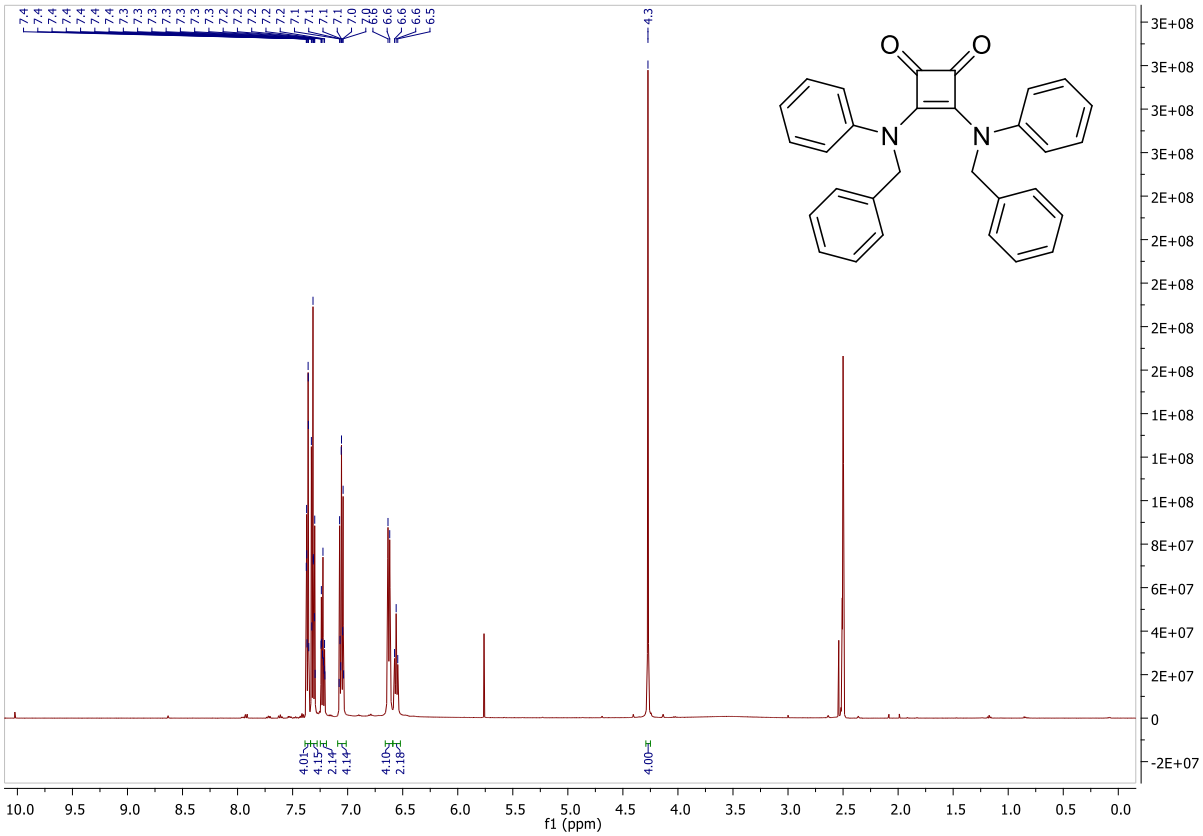

Figure D42. ^{1}H NMR (DMSO-d_6, 500 MHz) spectrum of **3.24**.

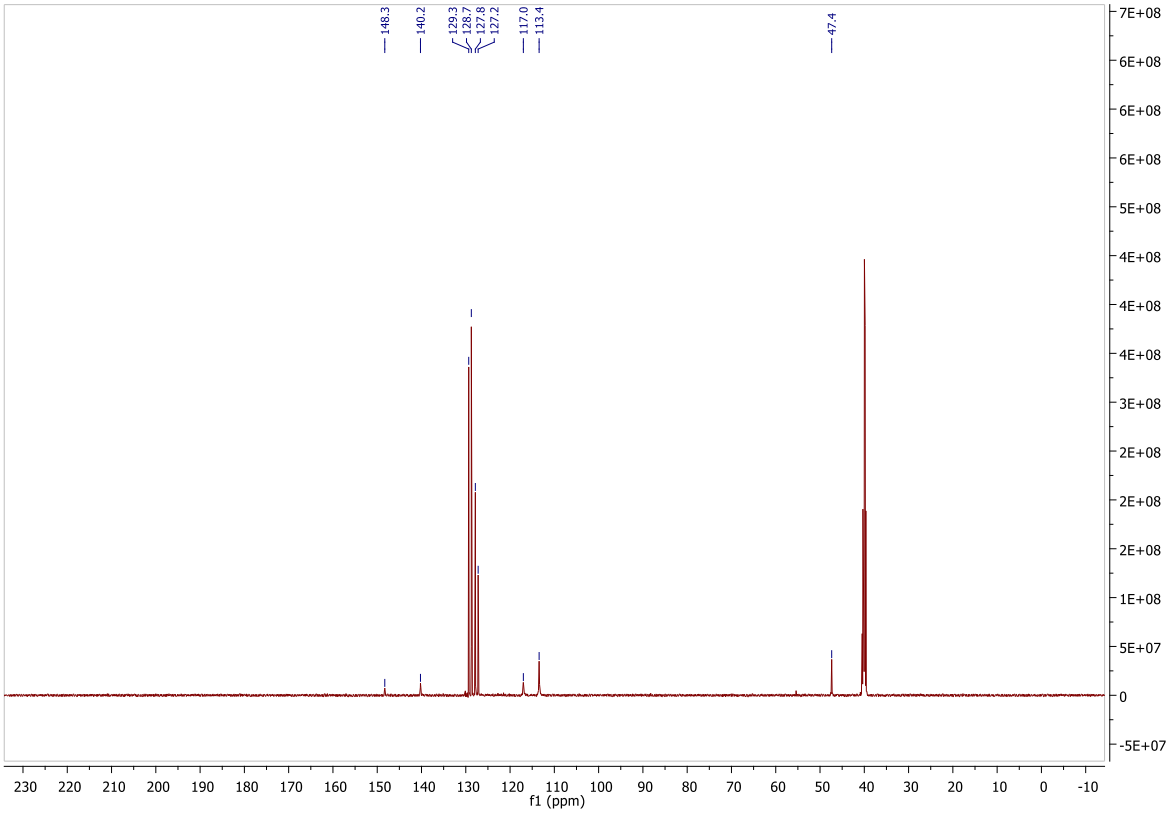

Figure D43. ^{13}C NMR (DMSO-d_6, 126 MHz) spectrum of **3.24**.

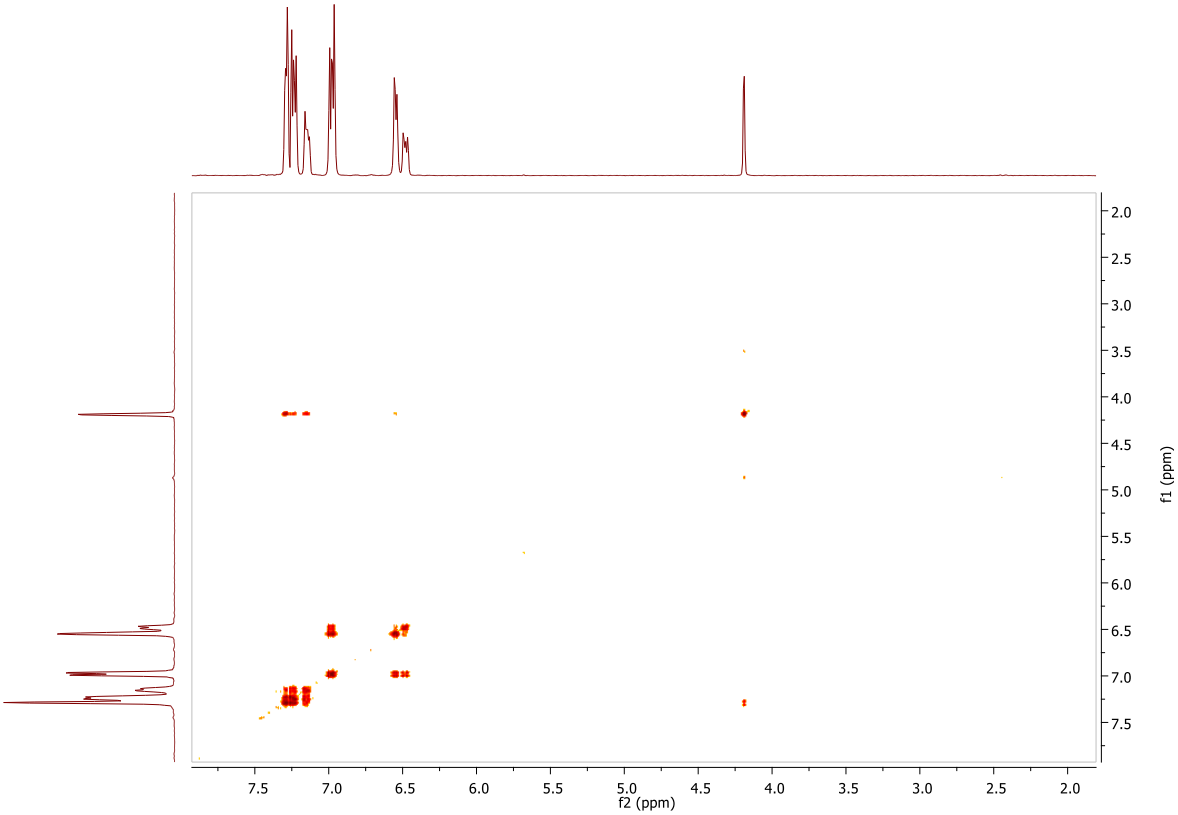

Figure D44. ^{1}H-^{1}H COSY NMR spectrum of **3.24**.

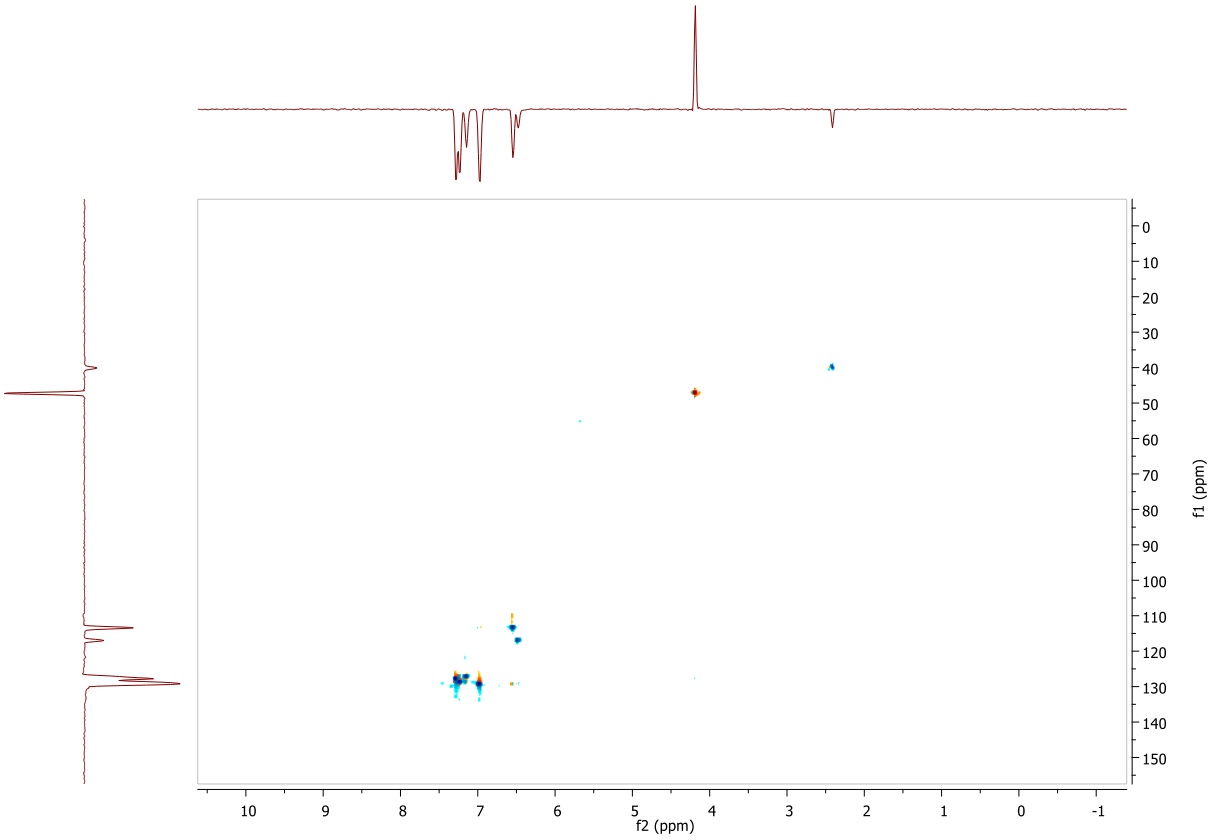

Figure D45. HSQC spectrum of **3.24**.

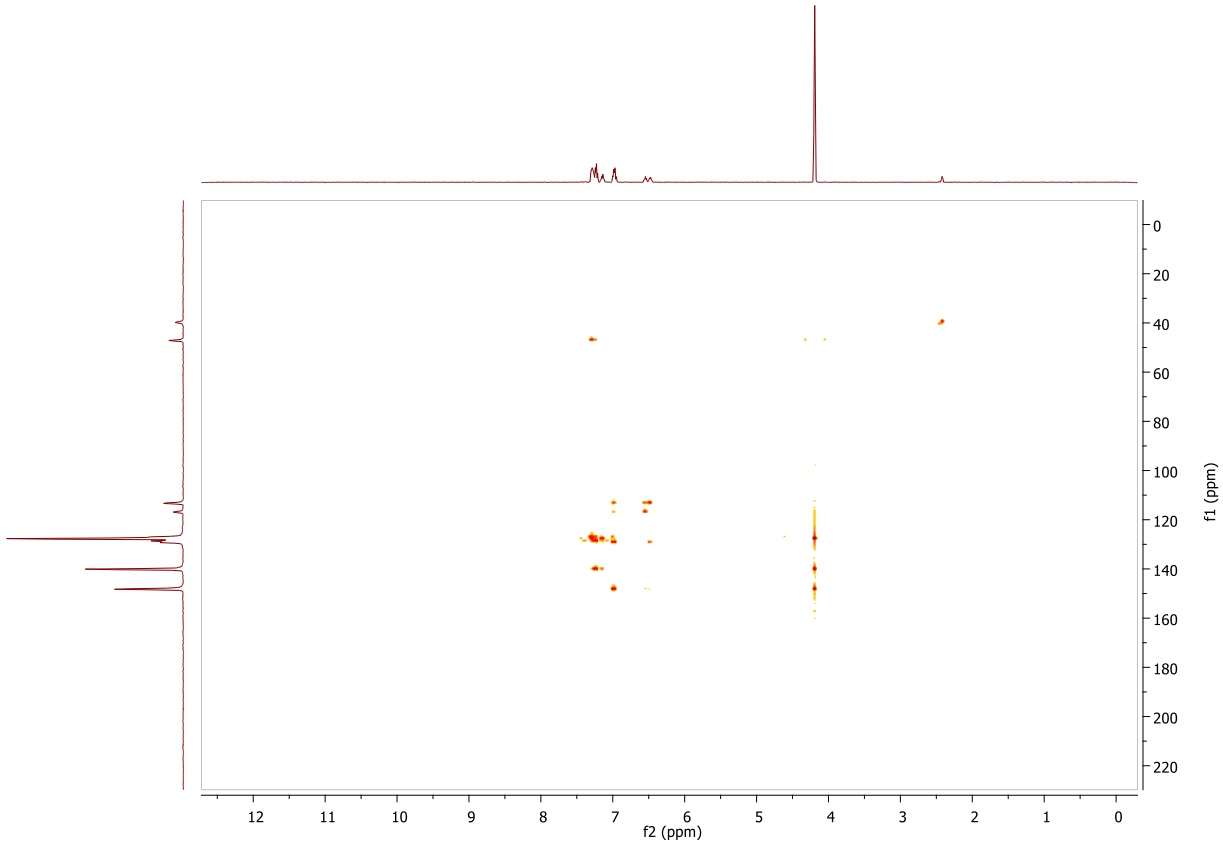

Figure D46. HMBC spectrum of **3.24**.

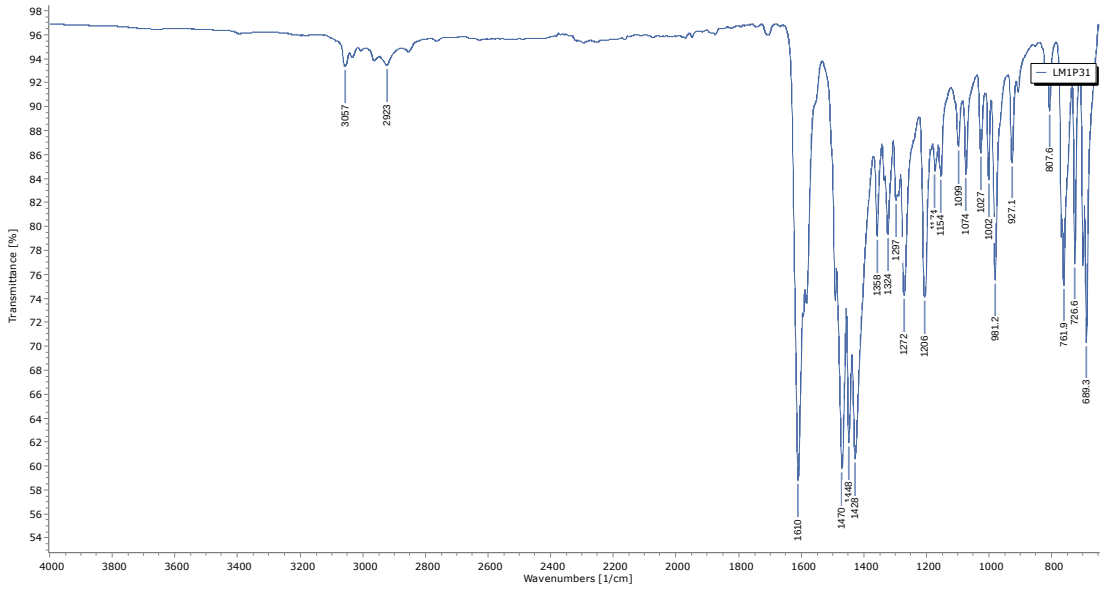

Figure D47. IR spectrum of **3.24**.

Compounds

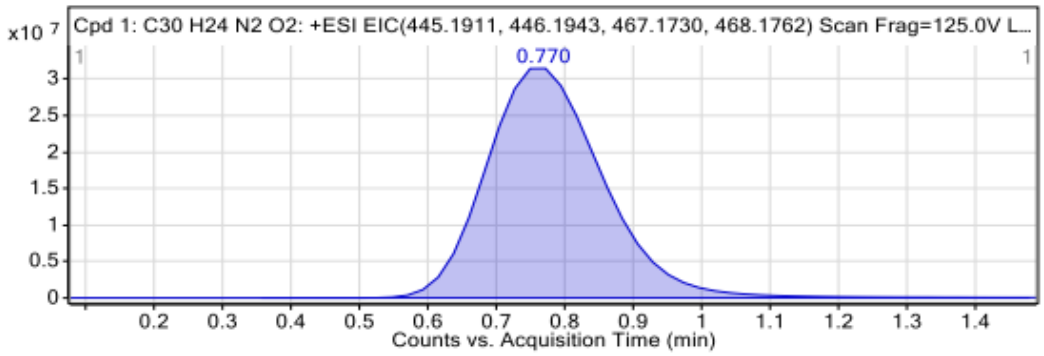

Integration Peak List

Start	RT	End	Height	Area
0.358	0.77	1.479	31469288	373389158

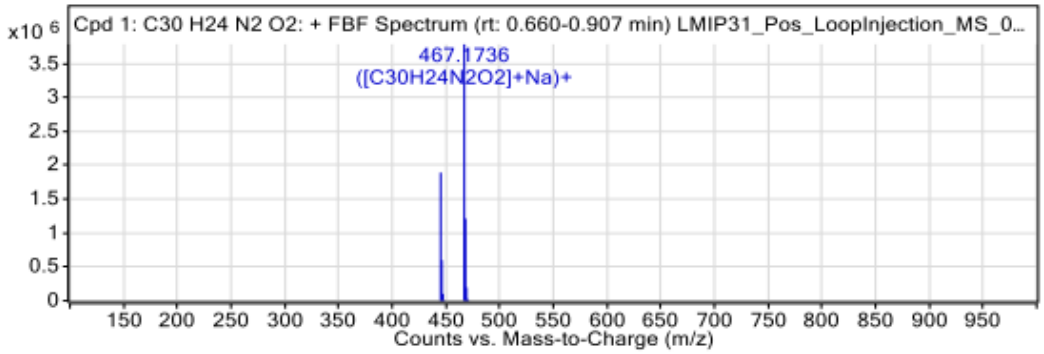

Peak List

m/z	z	Abund	Formula	Ion
445.1913	1	1890975.88	C30H24N2O2	(M+H)+
446.195	1	599152.81	C30H24N2O2	(M+H)+
447.1977	1	101484.63	C30H24N2O2	(M+H)+
448.2004	1	12395.29	C30H24N2O2	(M+H)+
467.1736	1	3783326.25	C30H24N2O2	(M+Na)+
468.1768	1	1211222.63	C30H24N2O2	(M+Na)+
469.1799	1	197024.08	C30H24N2O2	(M+Na)+
470.1826	1	23129	C30H24N2O2	(M+Na)+
471.1821	1	3207.05	C30H24N2O2	(M+Na)+

--- End Of Report ---

Figure D48. HRMS of **3.24**.

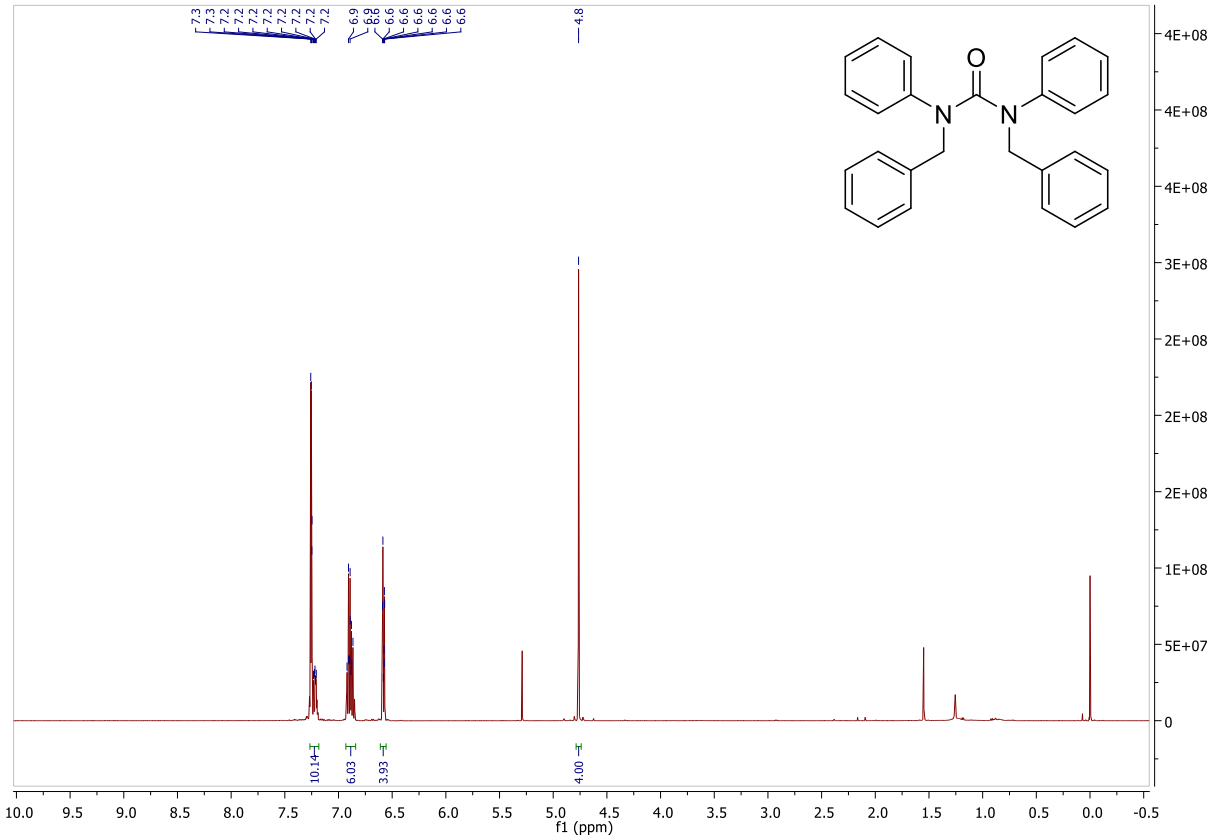

Figure D49. ^{1}H NMR (DMSO-d_6, 500 MHz) spectrum of **3.30**.

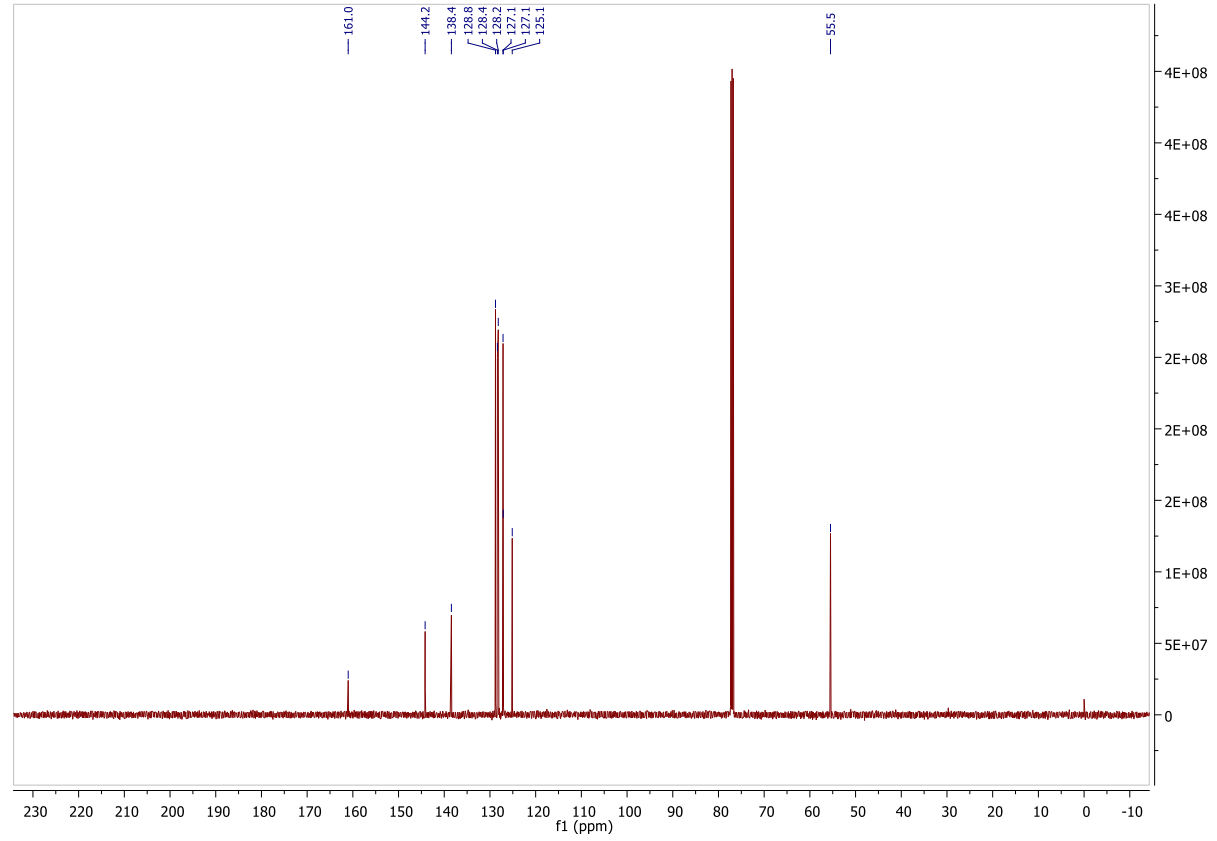

Figure D50. ^{13}C NMR (DMSO-d_6, 126 MHz) spectrum of **3.30**.

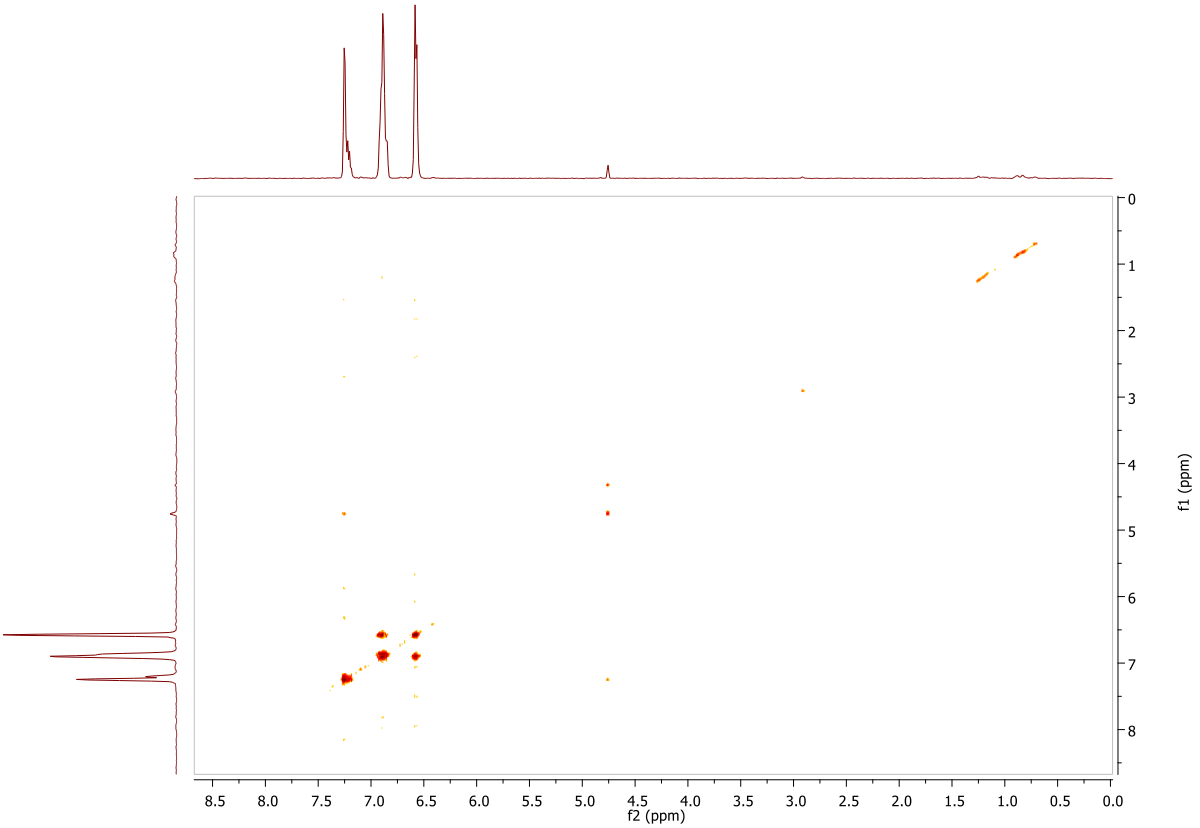

Figure D51. ^{1}H-^{1}H COSY NMR spectrum of **3.30**.

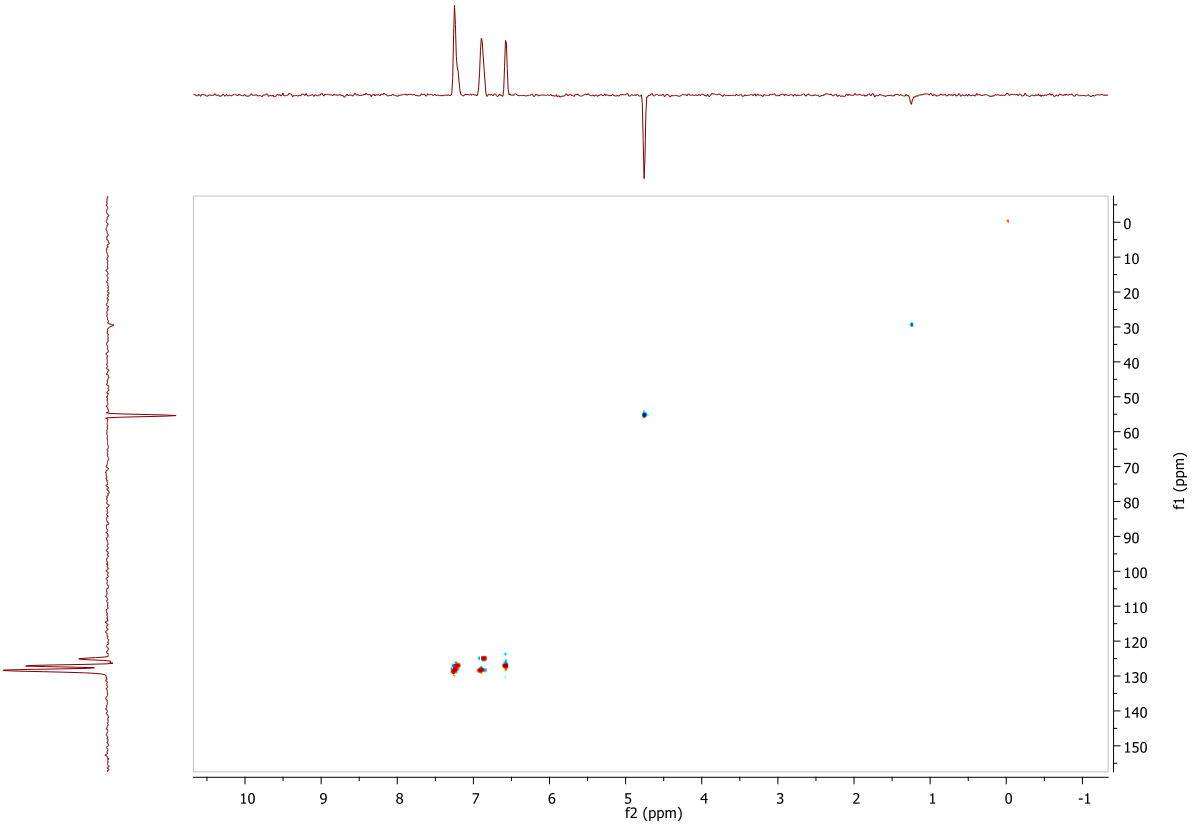

Figure D52. HSQC spectrum of **3.30**.

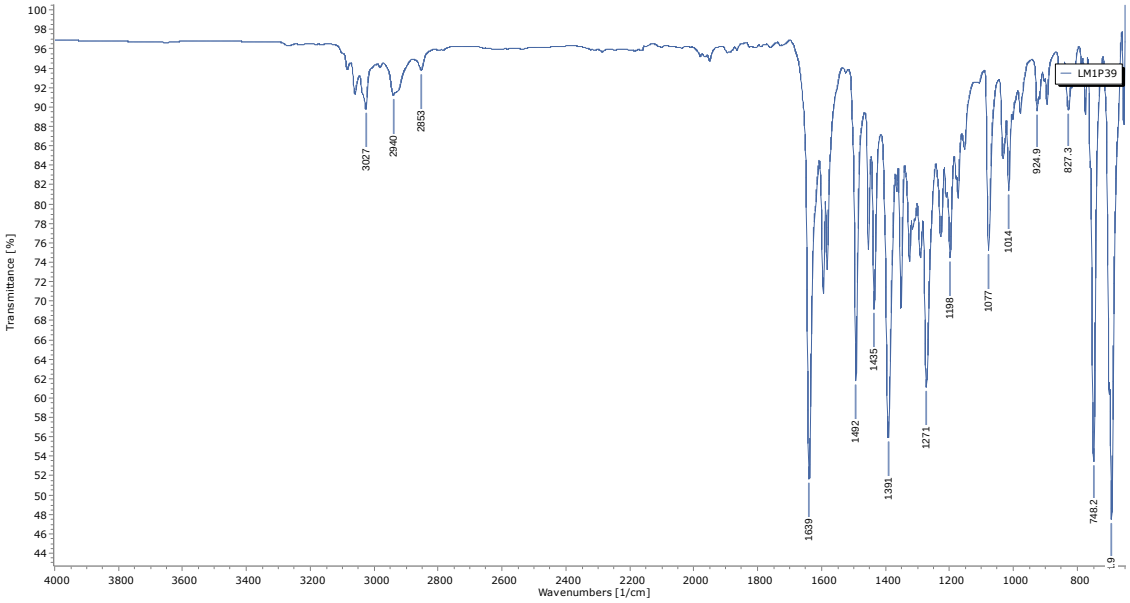

Figure D53. IR spectrum of **3.30**.

Compounds

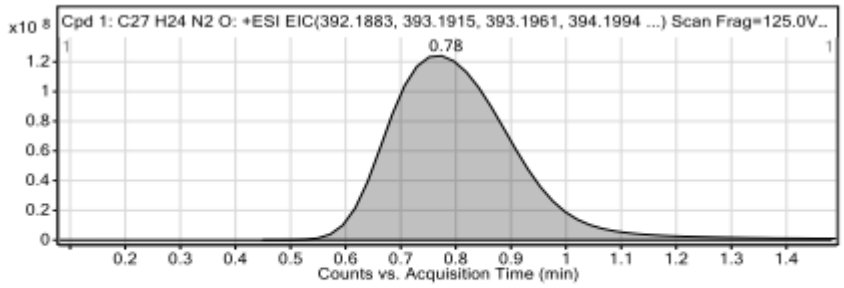

Integration Peak List

Start	RT	End	Height	Area
0.45	0.78	1.48	124534653	1950921431

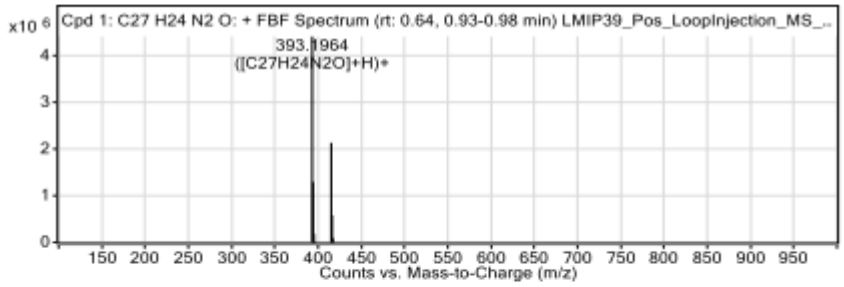

Peak List

m/z	z	Abund	Formula	Ion
393.1964	1	4412795	C27H24N2O	(M+H)+
394.1995	1	1293643.63	C27H24N2O	(M+H)+
395.2028	1	180398.58	C27H24N2O	(M+H)+
396.2062	1	20374.55	C27H24N2O	(M+H)+
415.178	1	2134517.5	C27H24N2O	(M+Na)+
416.1816	1	578408	C27H24N2O	(M+Na)+
417.1848	1	86390.72	C27H24N2O	(M+Na)+
418.1886	1	9745.88	C27H24N2O	(M+Na)+

--- End Of Report ---

Figure D54. HRMS of **3.30**.

E. Chapter 4 Characterisation Data

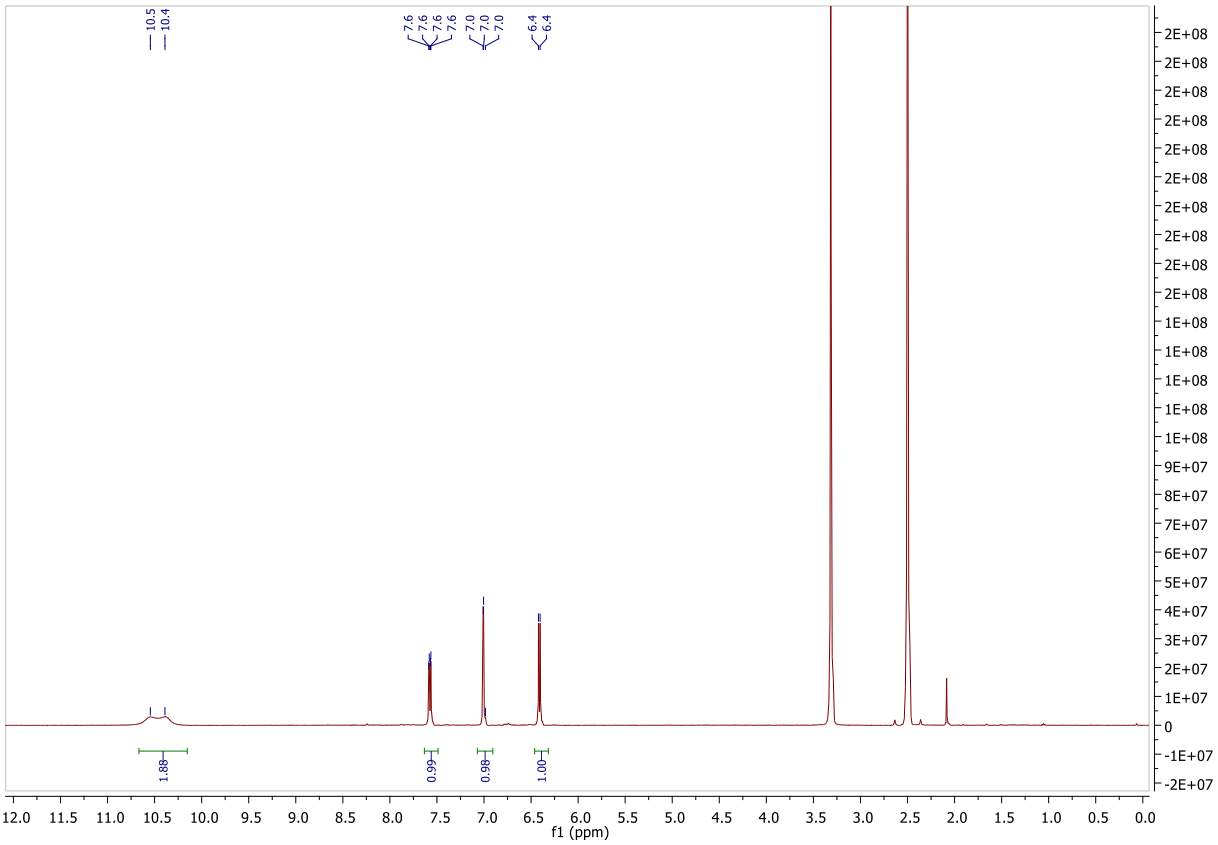

Figure E1. ^{1}H NMR (DMSO-d_6, 500 MHz) spectrum of **4.17**.

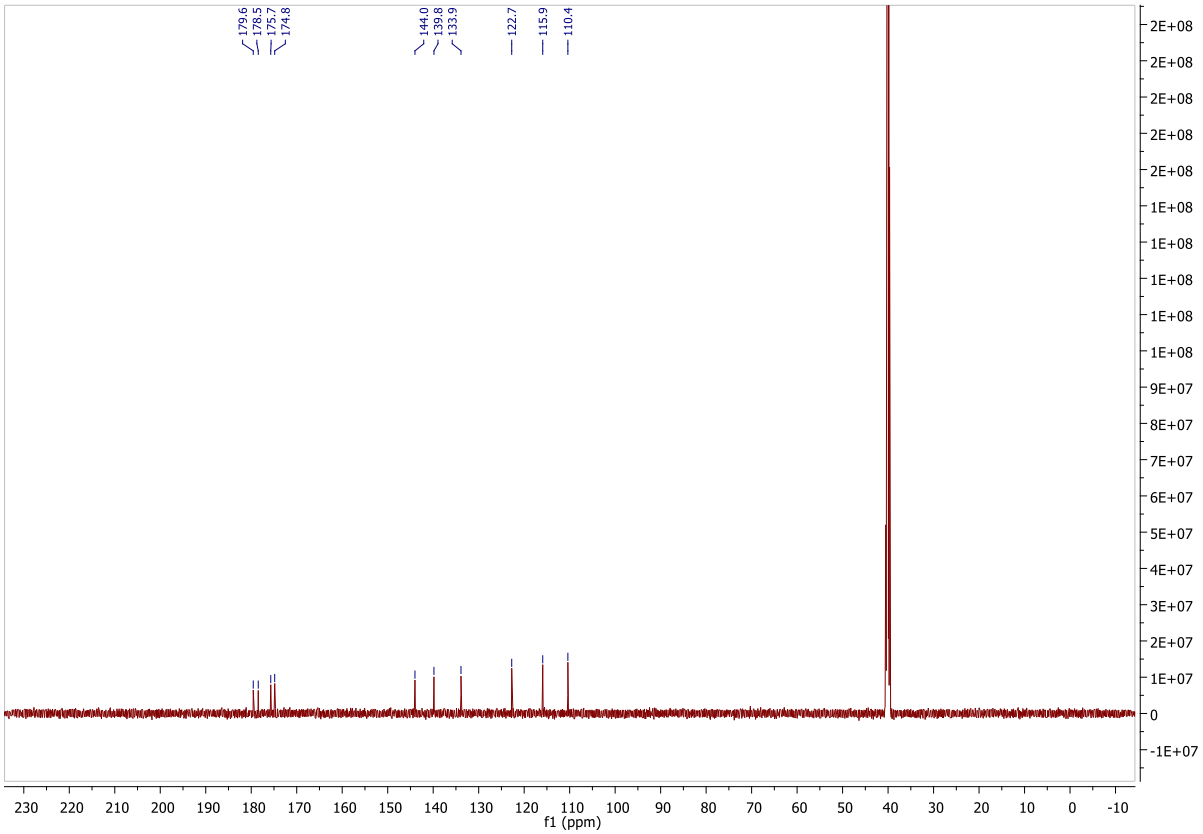

Figure E2. ^{13}C NMR (DMSO-d$_6$, 126 MHz) spectrum of **4.17**.

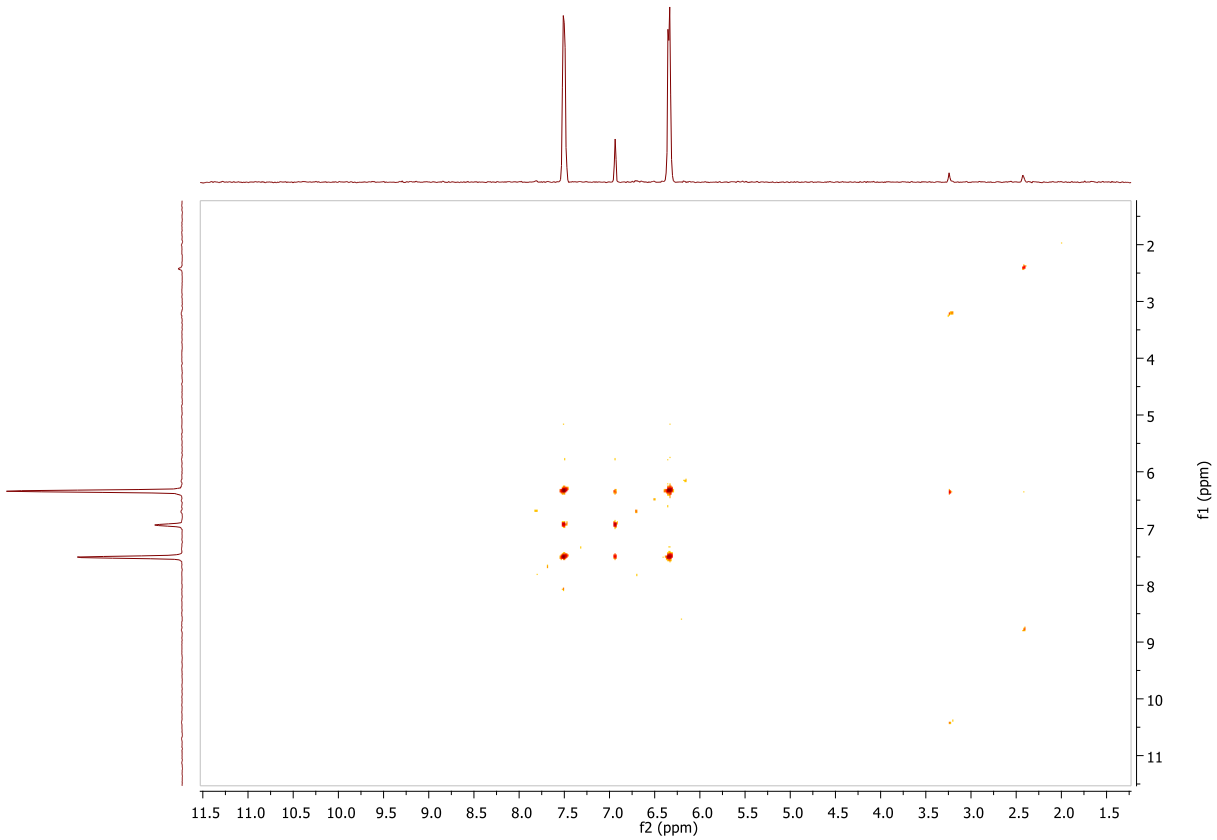

Figure E3. ^{1}H-^{1}H COSY spectrum of **4.17**.

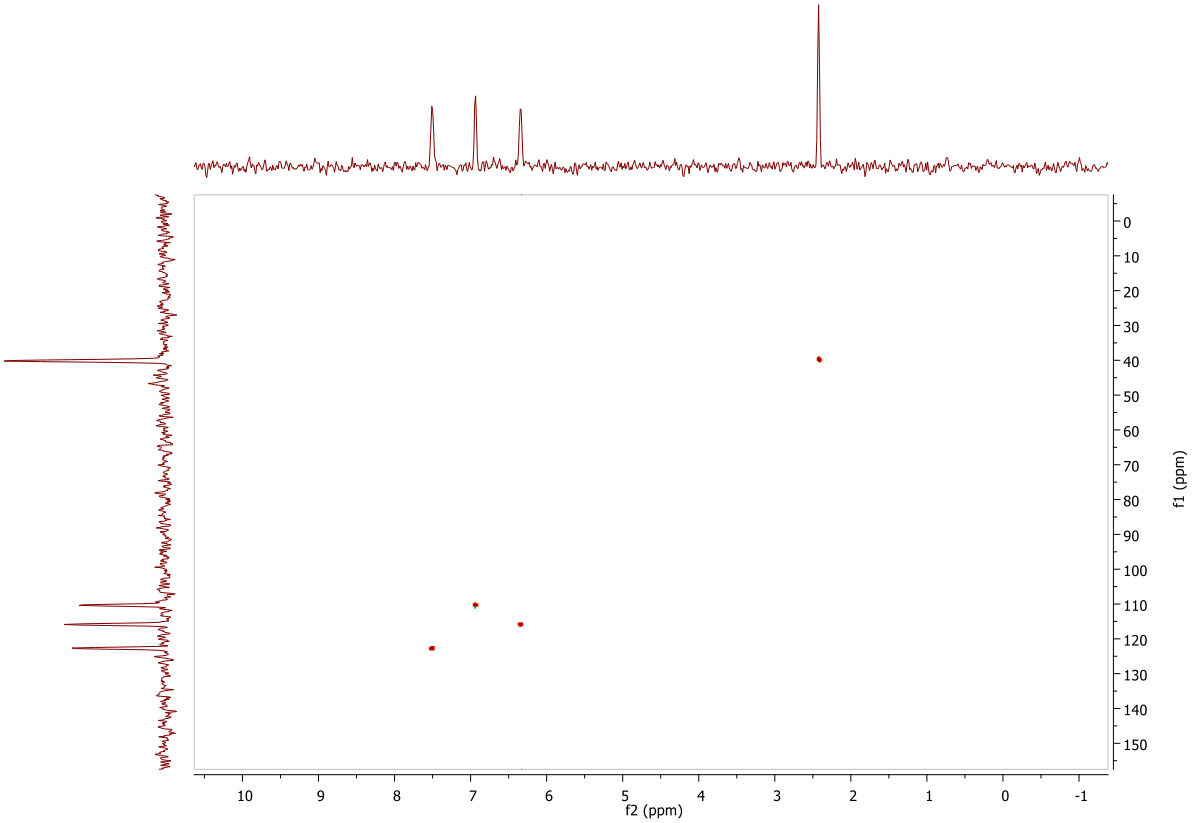

Figure E4. HSQC spectrum of **4.17**.

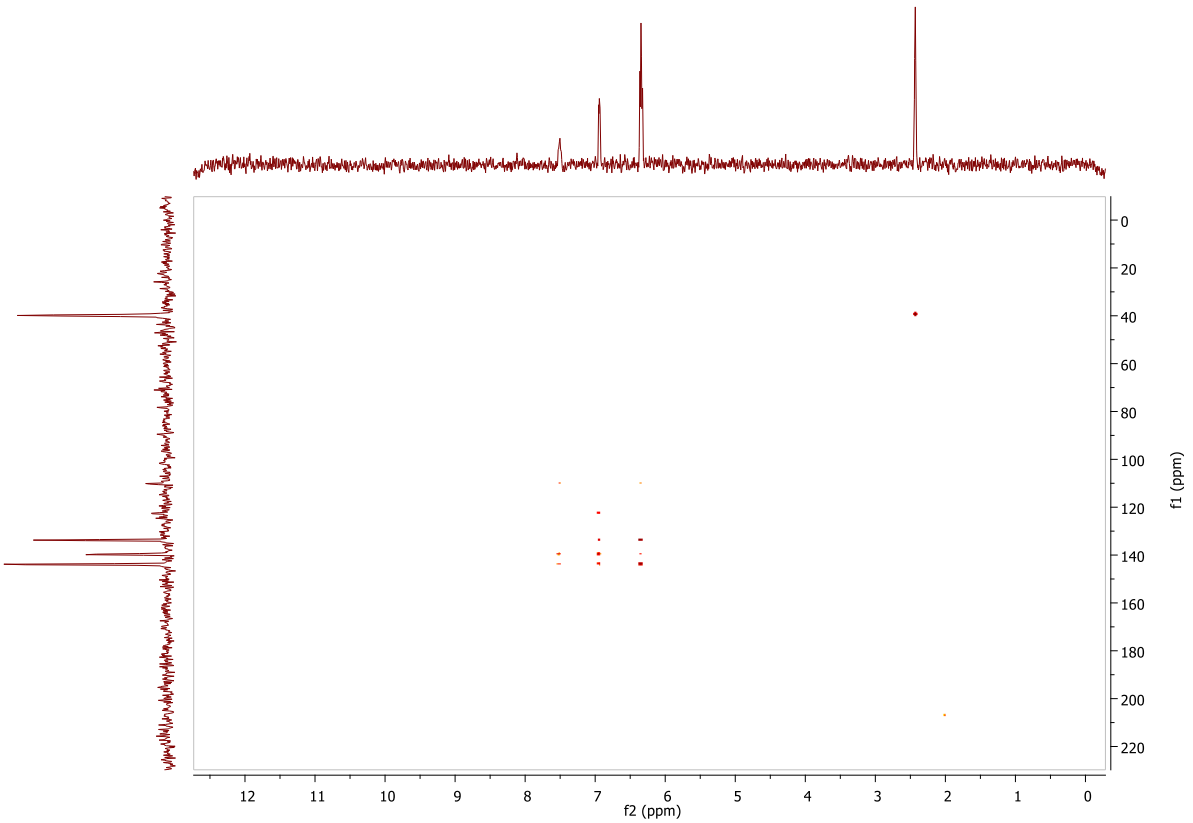

Figure E5. HMBC spectrum of **4.17**

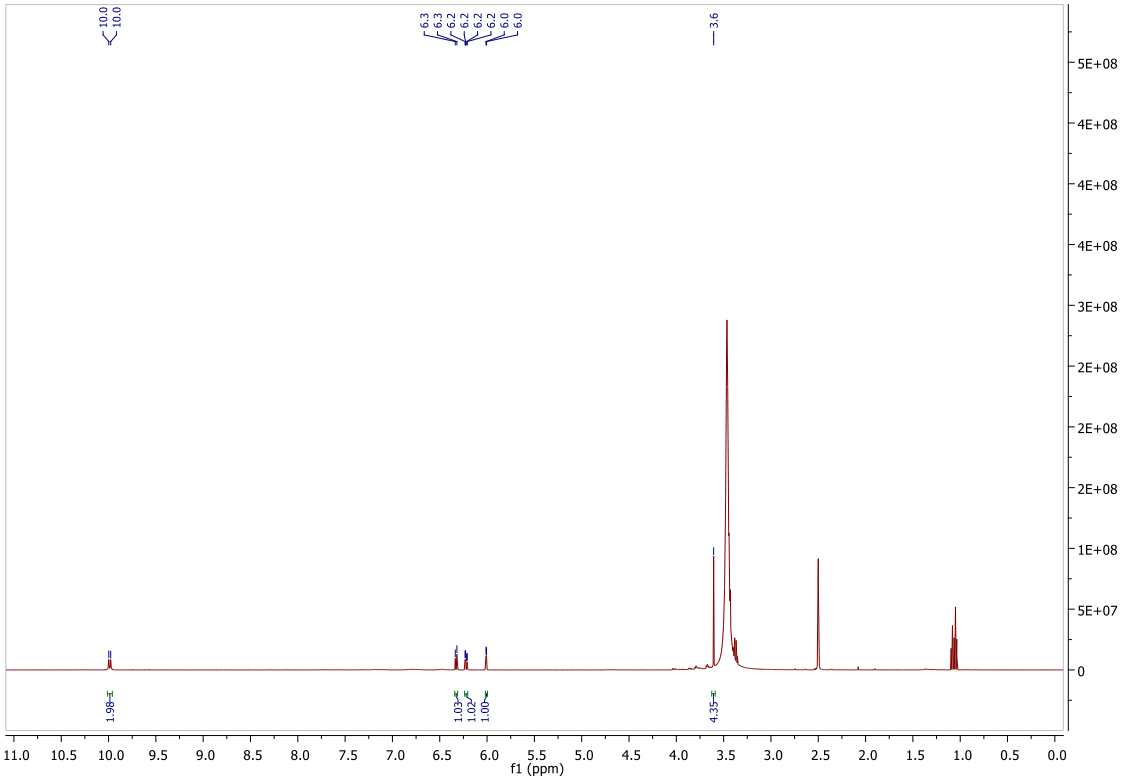

Figure E6. ^{1}H NMR (DMSO-d$_6$, 500 MHz) spectrum of **4.18**.

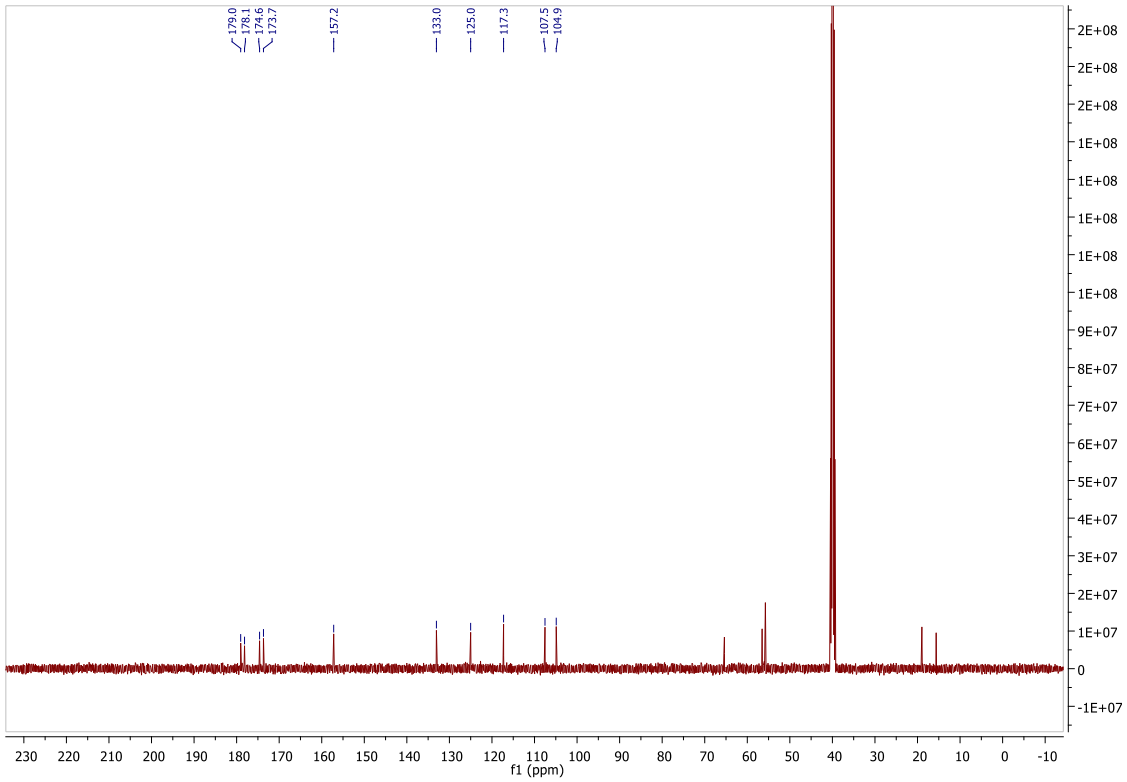

Figure E7. ^{13}C NMR (DMSO-d$_6$, 126 MHz) spectrum of **4.18**.

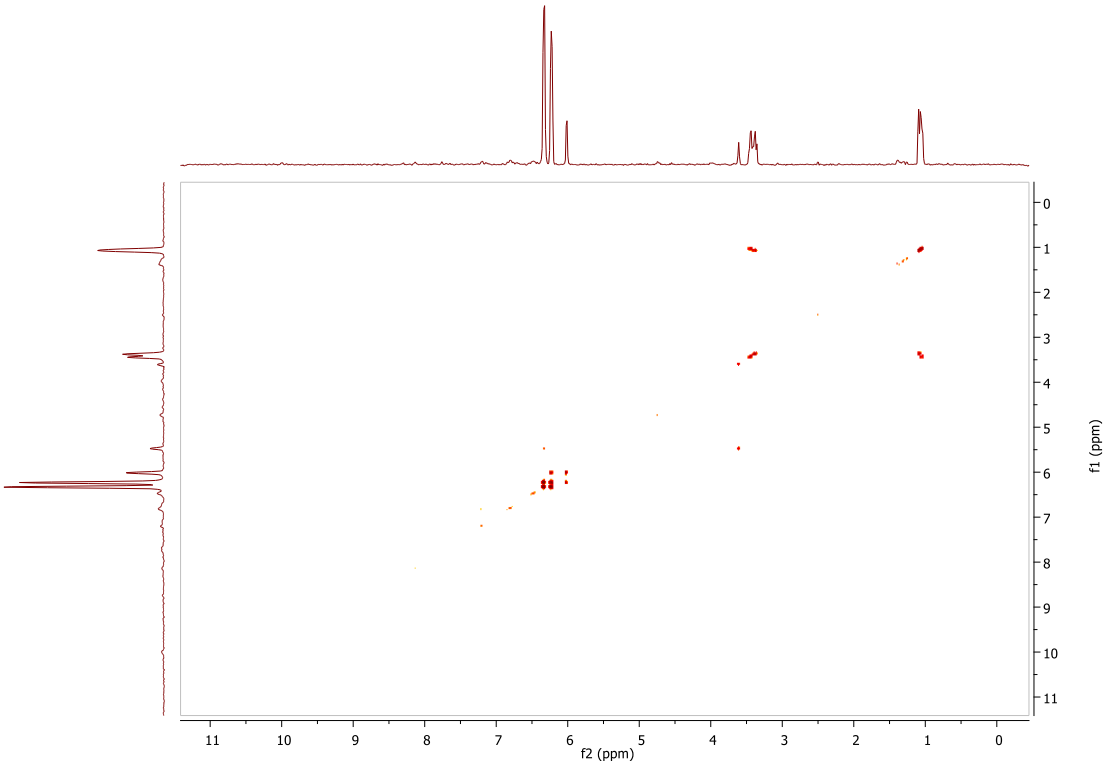

Figure E8. ^{1}H-^{1}H COSY spectrum of **4.18**.

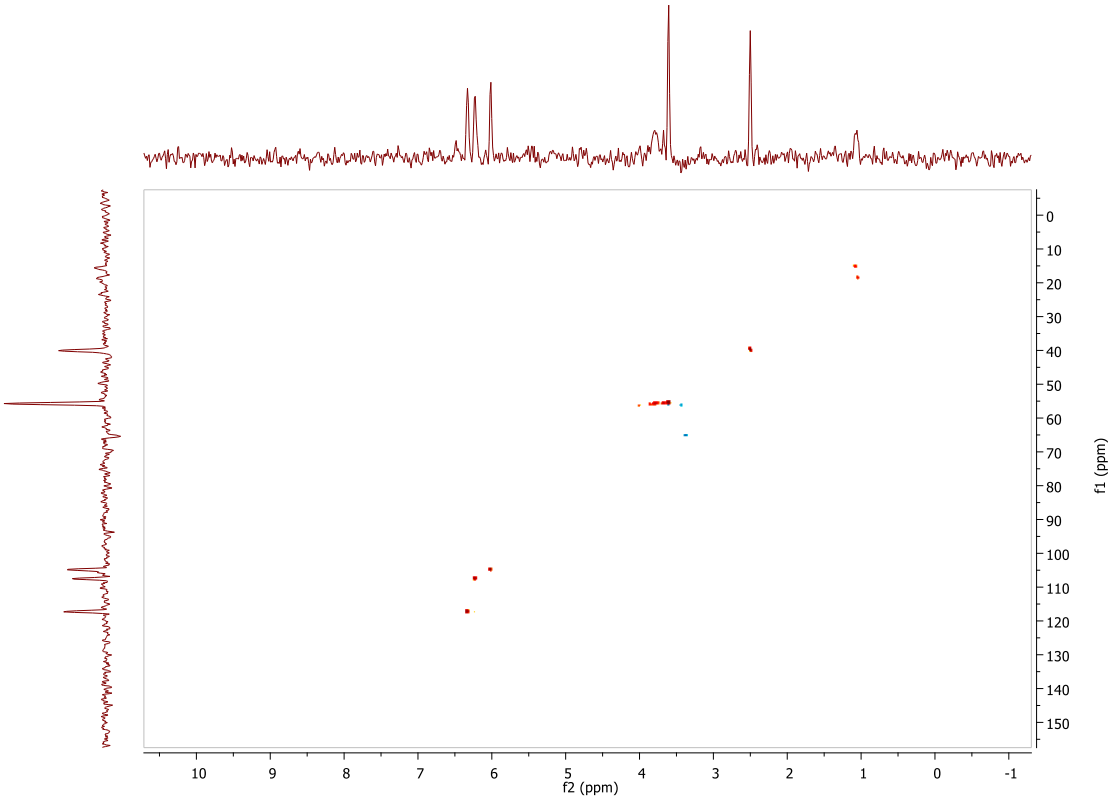

Figure E9. HSQC spectrum of **4.18**.

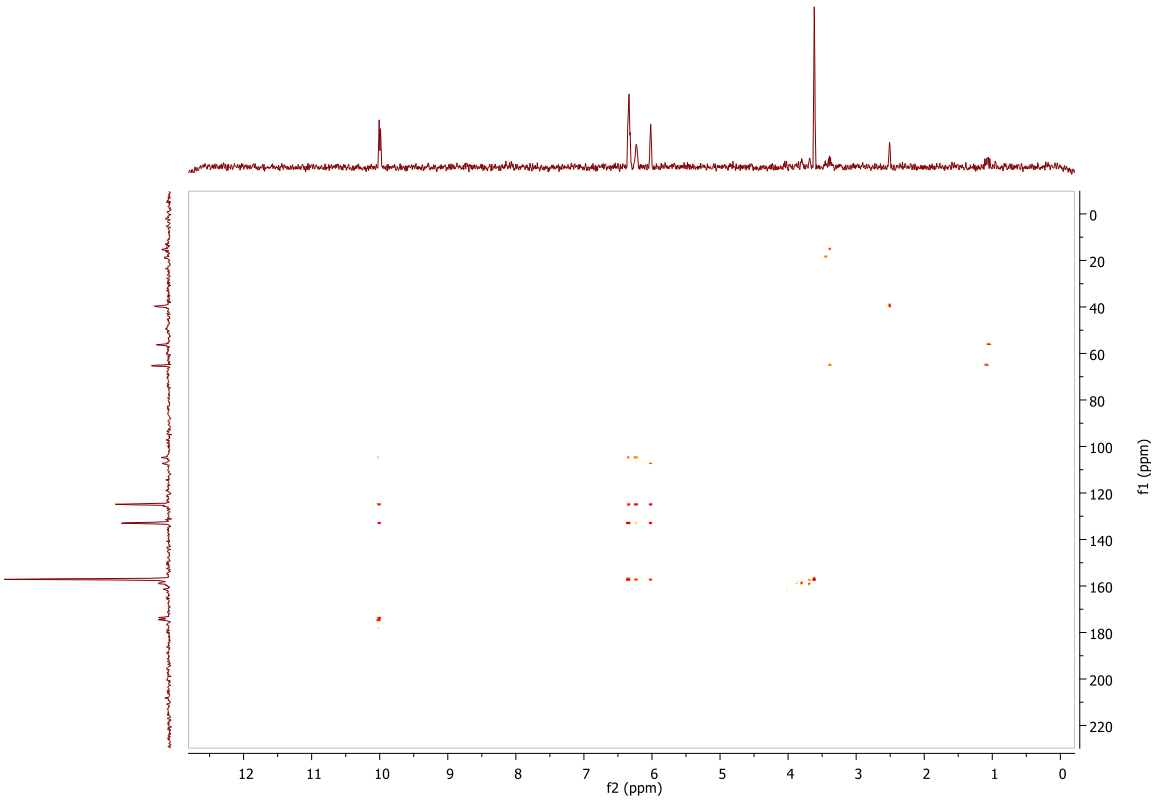

Figure E10. HMBC spectrum of **4.18**.

F. Chapter 4 UV-Vis Data

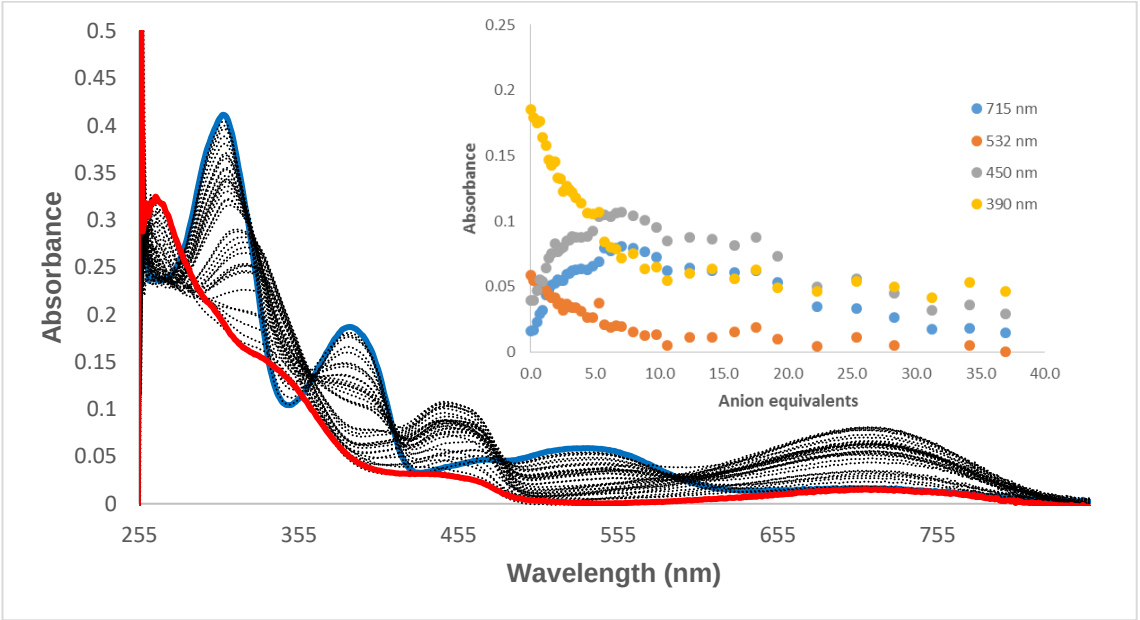

Figure F1. Changes observed in the absorption spectrum of **4.17** (1 x 10^{-5} M) upon addition of TBAF (0 – 0.37 mM) in 0.5% H_2O in DMSO solution. 0 mM in blue, 0.37 mM in red. *Inset:* Absorbance changes observed at 715 nm, 532 nm, 450 nm and 390 nm.

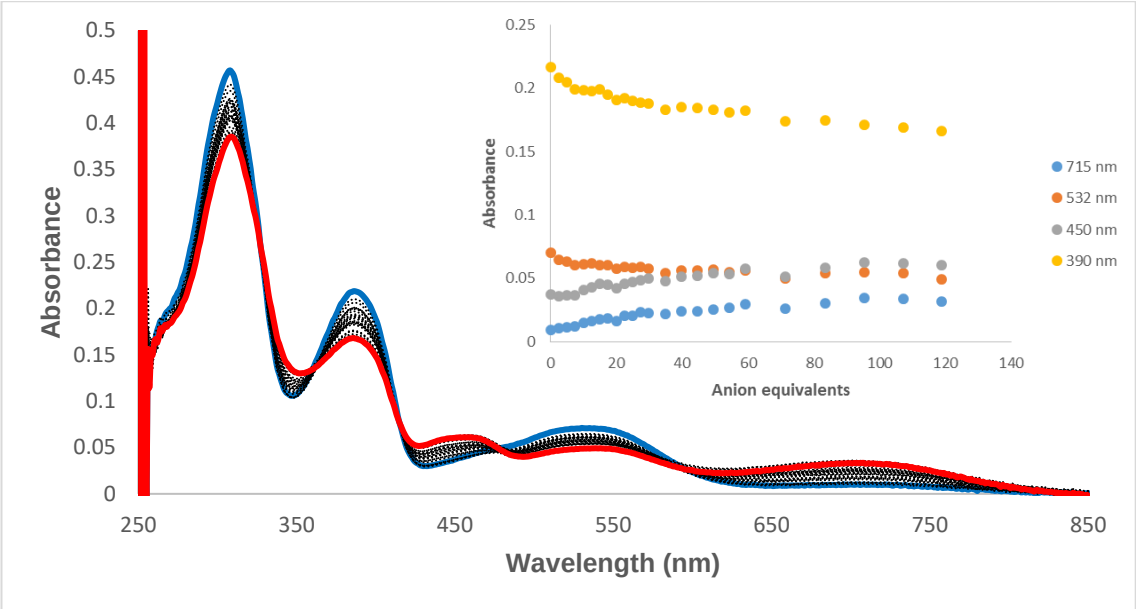

Figure F2. Changes observed in the absorption spectrum of **4.17** (1 x 10^{-5} M) upon addition of TBACl (0 – 0.37 mM) in 0.5% H_2O in DMSO solution. 0 mM in blue, 0.37 mM in red. *Inset:* Absorbance changes observed at 715 nm, 532 nm, 450 nm and 390 nm.

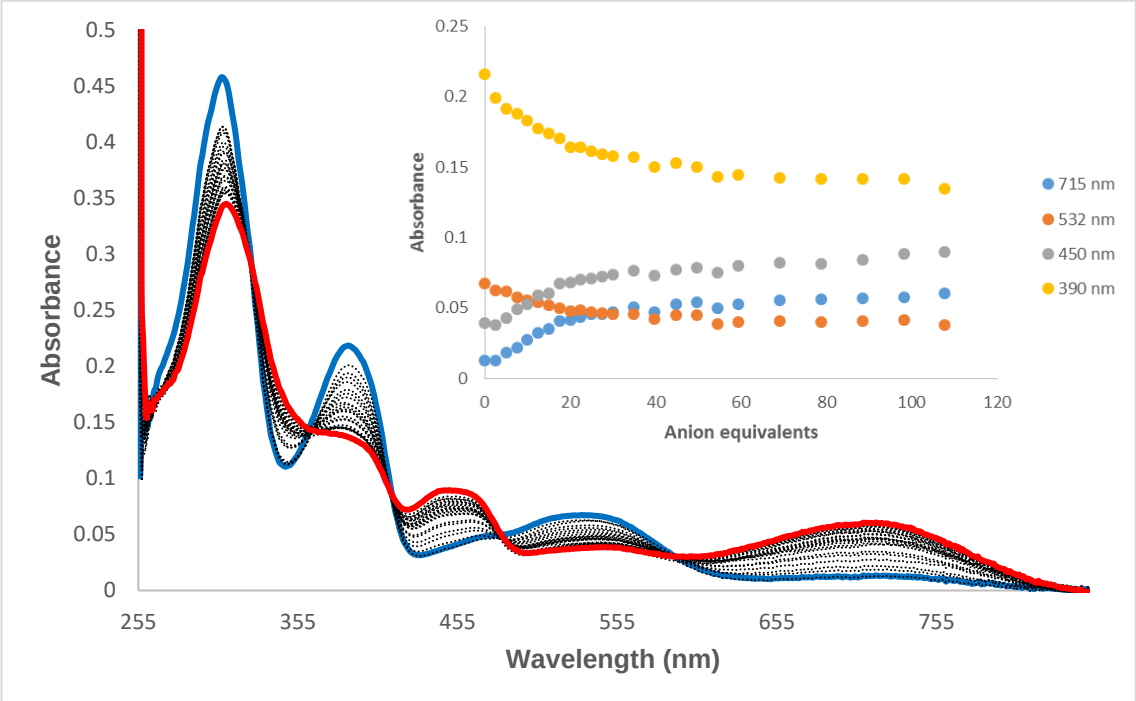

Figure F3. Changes observed in the absorption spectrum of **4.17** (1 x 10^{-5} M) upon addition of TBABr (0 – 0.37 mM) in 0.5% H_2O in DMSO solution. 0 mM in blue, 0.37 mM in red. *Inset:* Absorbance changes observed at 715 nm, 532 nm, 450 nm and 390 nm.

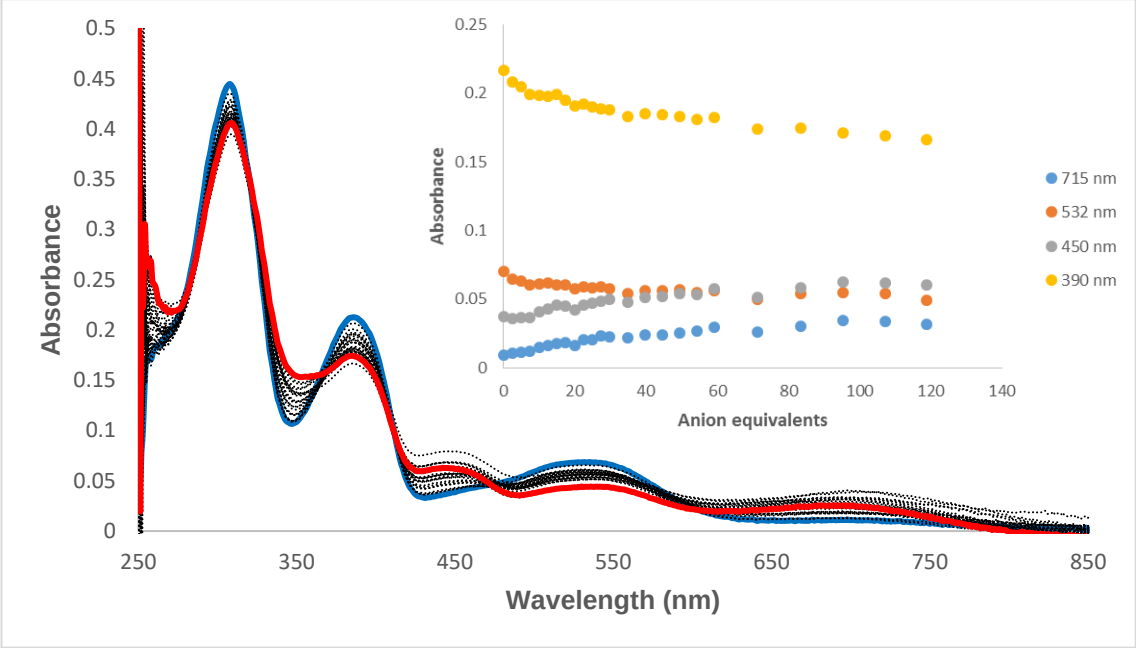

Figure F4. Changes observed in the absorption spectrum of **4.17** (1 x 10^{-5} M) upon addition of TBAI (0 – 0.37 mM) in 0.5% H_2O in DMSO solution. 0 mM in blue, 0.37 mM in red. *Inset:* Absorbance changes observed at 715 nm, 532 nm, 450 nm and 390 nm.

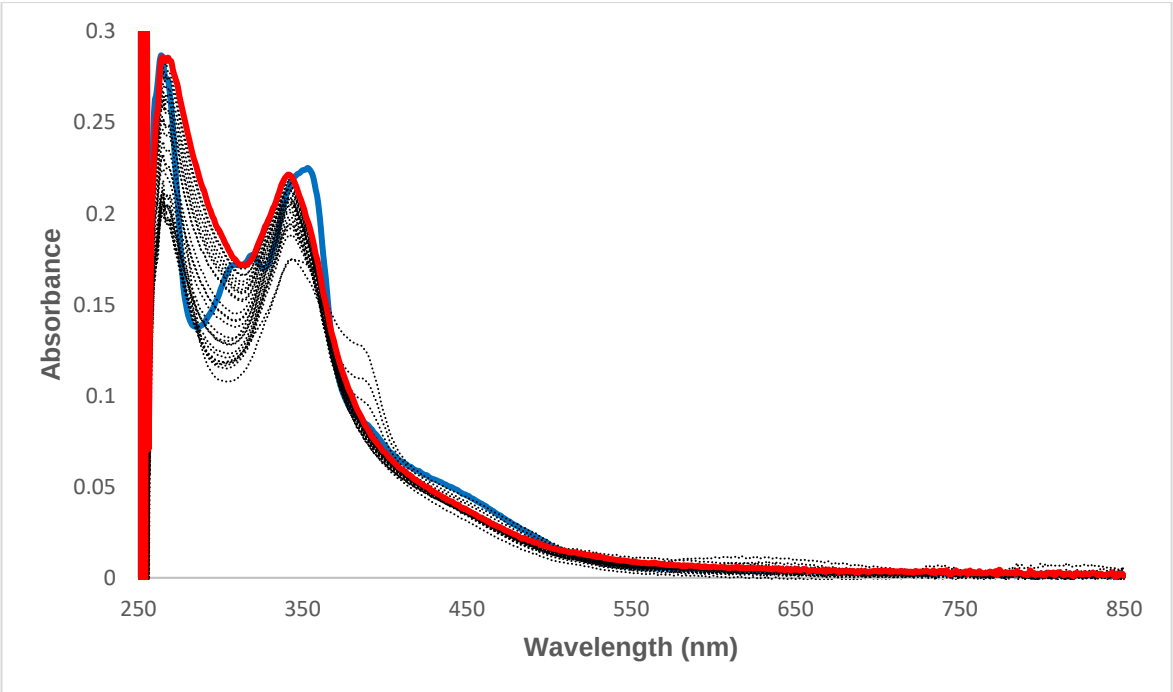

Figure F5. Changes observed in the absorption spectrum of **4.18** (1 x 10^{-5} M) upon addition of TBAF (0 – 1 mM) in 0.5% H_2O in DMSO solution. 0 mM in blue, 1 mM in red.

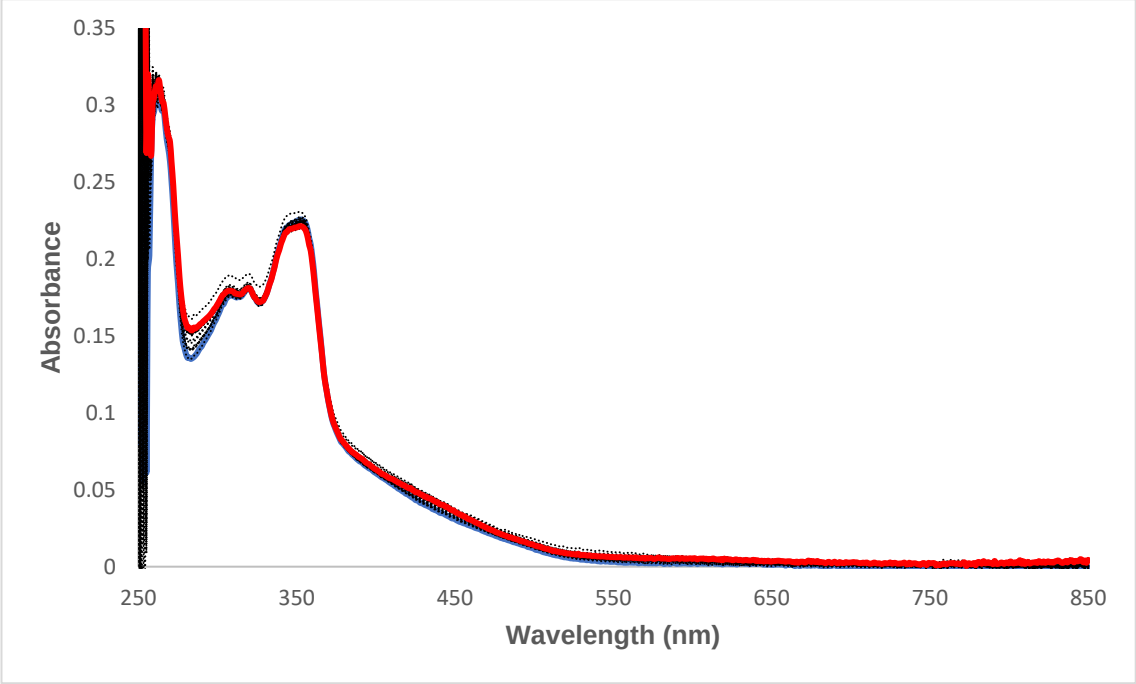

Figure F6. Changes observed in the absorption spectrum of **4.18** (1 x 10^{-5} M) upon addition of TBACl (0 – 1 mM) in 0.5% H_2O in DMSO solution. 0 mM in blue, 1 mM in red.

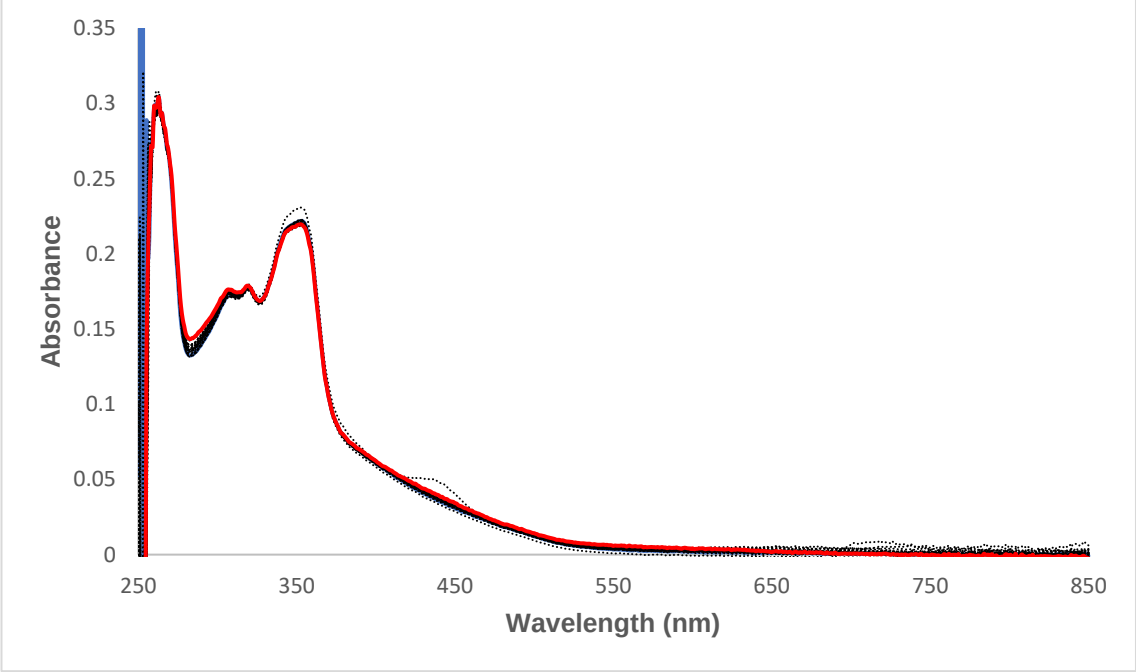

Figure F7. Changes observed in the absorption spectrum of **4.18** (1 x 10^{-5} M) upon addition of TBABr (0 – 1 mM) in 0.5% H_2O in DMSO solution. 0 mM in blue, 1 mM in red.

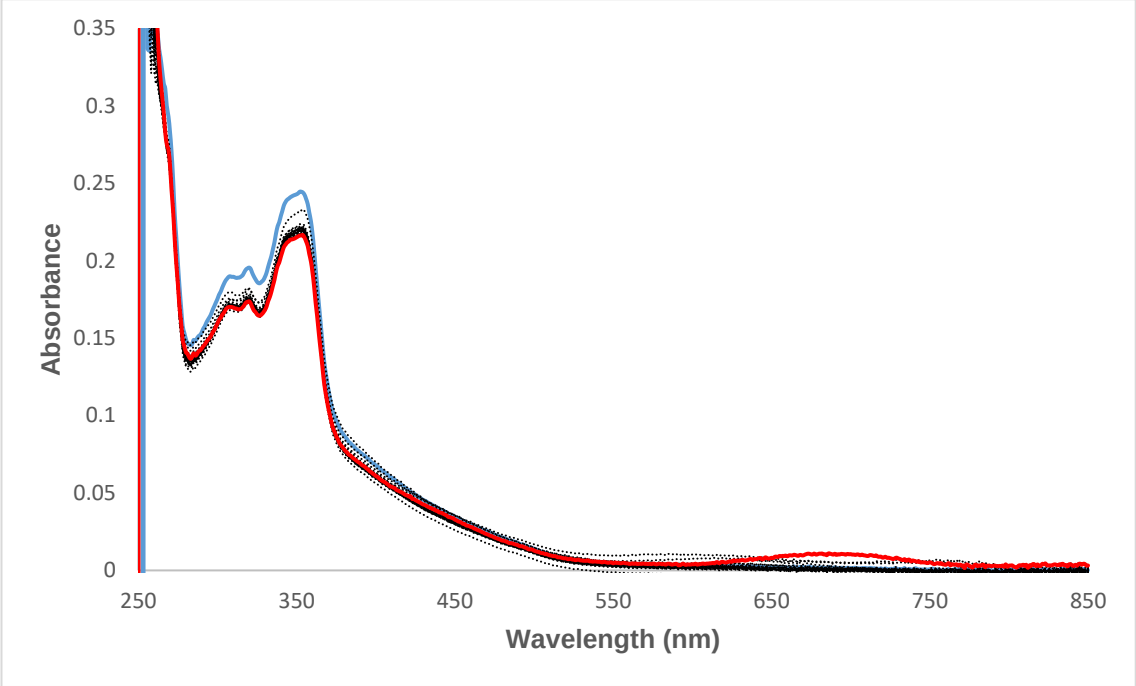

Figure F8. Changes observed in the absorption spectrum of **4.18** (1 x 10^{-5} M) upon addition of TBAI (0 – 1 mM) in 0.5% H_2O in DMSO solution. 0 mM in blue, 1 mM in red.

G. Chapter 4 ^{1}H NMR Titration Data

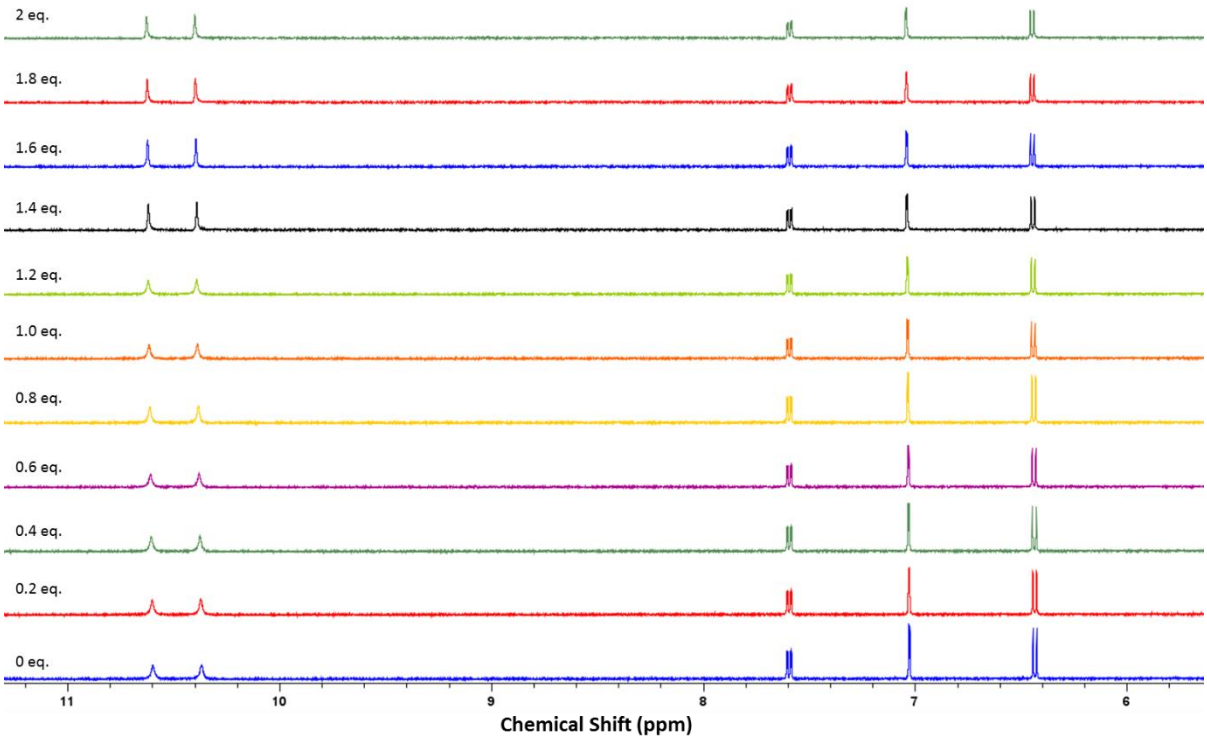

Figure G1 Stack plot of ^{1}H NMR spectra of **4.17** (2.5 x 10^{-3} M) upon addition of TBACl (0 - 2 equiv.) in DMSO-d_6 at 25 °C.

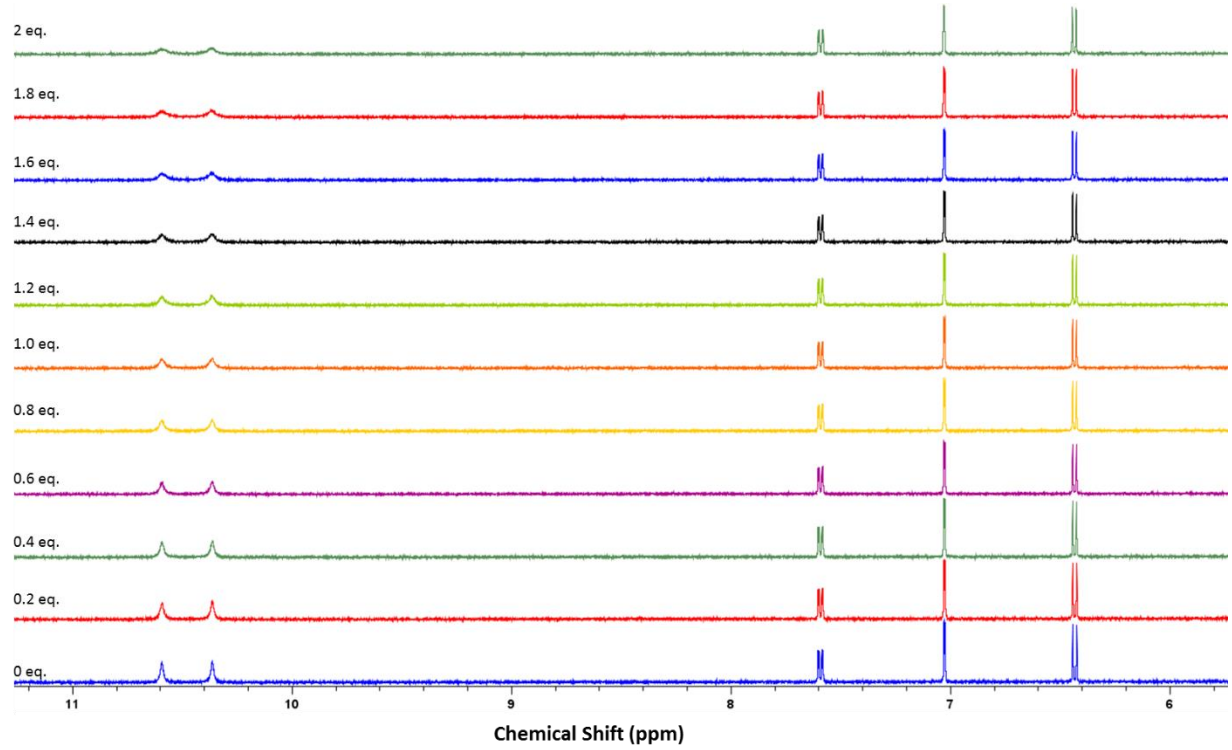

Figure G2 Stack plot of ^{1}H NMR spectra of **4.17** (2.5 x 10^{-3} M) upon addition of TBABr (0 - 2 equiv.) in DMSO-d_6 at 25 °C

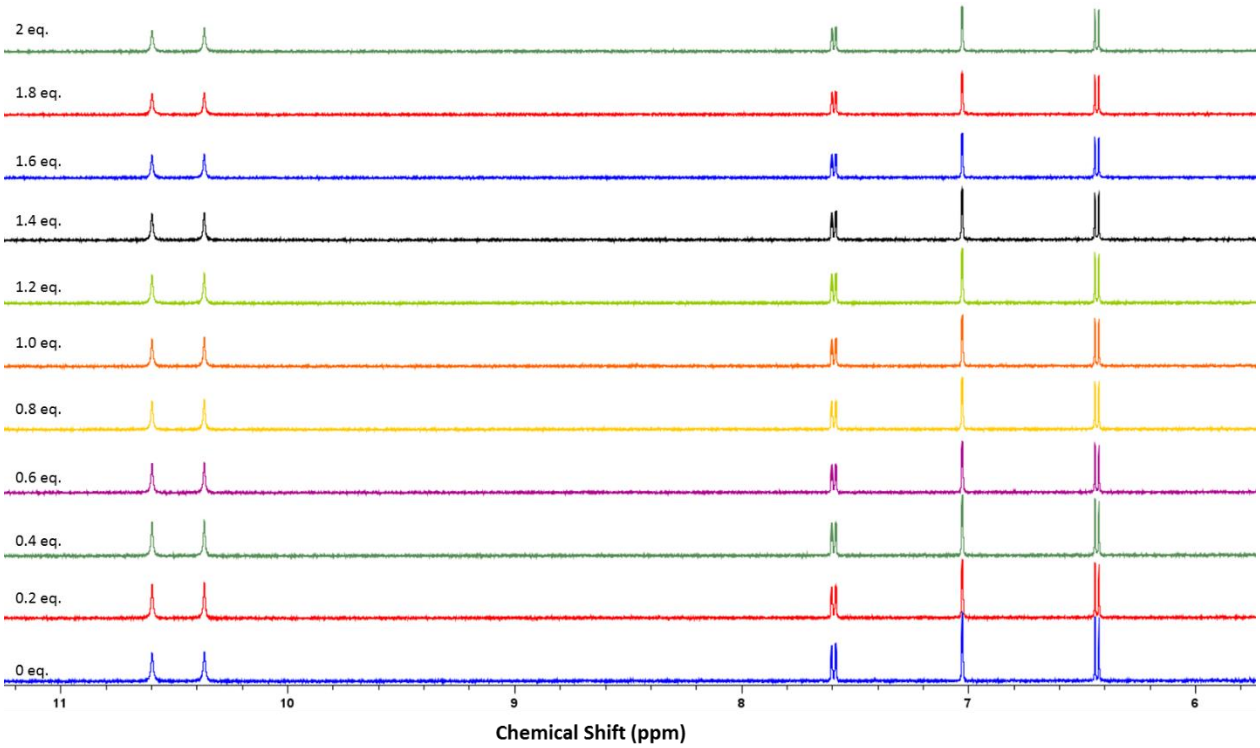

Figure G3 Stack plot of ^{1}H NMR spectra of **4.17** (2.5 x 10^{-3} M) upon addition of TBAI (0 - 2 equiv.) in DMSO-d_6 at 25 °C

H. Chapter 4 TD-DFT Data

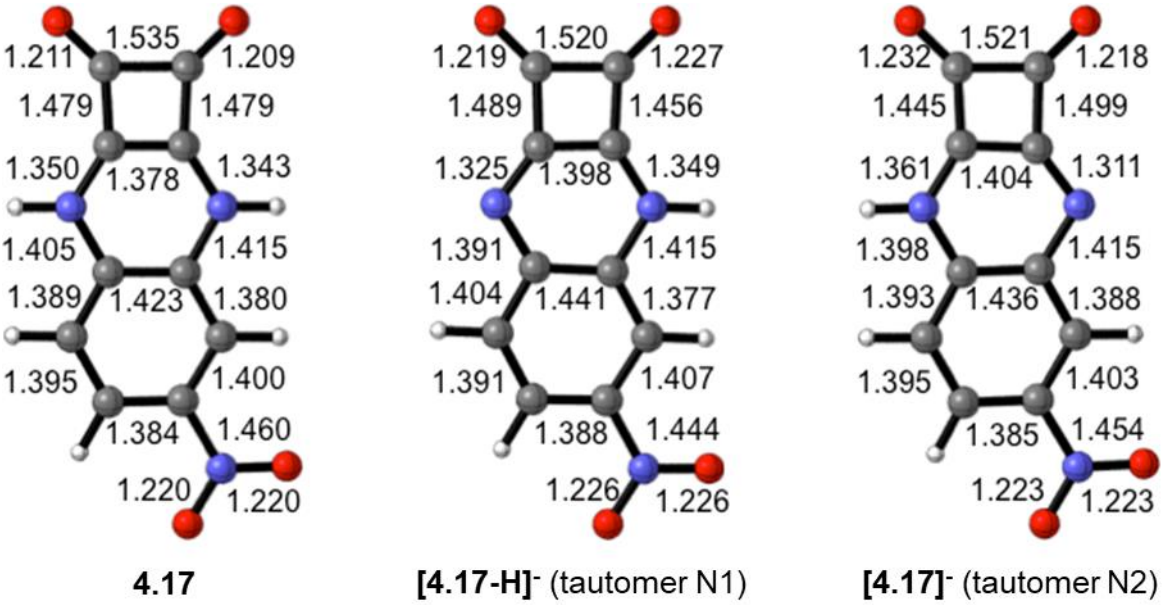

Figure G4 DFT-optimized geometries of compound **4.17**, and the tautomers of **[4.17-H]**$^{-}$. Bond distances are given in Å. [SMD-PCM(DMSO)/M06-2X/aug-cc-pVDZ].

	State	Excitation energy (λ_{max})	Oscillator strength	CI coefficient
4.17	S_0	549.34 nm	f = 0.1129	59 → 60 0.69394 59 → 61 0.12507
	S_1	382.17 nm	f = 0.1533	57 → 60 –0.11150 59 → 60 –0.11783 59 → 61 0.68207
	S_6	301.12 nm	f = 0.6980	57 → 60 –0.45023 59 → 62 –0.51865
[4.17–H]$^{-}$ (N1)	S_0	653.39 nm	f = 0.2166	59 → 60 0.69131 59 → 61 0.14918
	S_1	420.47 nm	f = 0.2059	57 → 60 –0.10056 59 → 60 –0.14309 59 → 61 0.67947

	S_3	337.87 nm	f = 0.0420	57 → 60 –0.20556 59 → 62 0.60175 59 → 63 0.27915
	S_6	319.12 nm	f = 0.4906	57 → 60 0.64438 59 → 62 0.24626
$[4.17–H]^-$ (N2)	S_0	730.03 nm	f = 0.0996	59 → 60 0.69670 59 → 61 –0.11807
	S_2	425.41 nm	f = 0.1488	57 → 60 0.10548 59 → 60 0.11092 59 → 61 0.68481
	S_7	319.15 nm	f = 0.5079	57 → 60 0.66816 59 → 62 0.16912
	S_8	301.14 nm	f = 0.2546	56 → 60 0.18108 59 → 62 –0.16284 59 → 63 0.64857

Table G1 Calculated excited state energies, oscillator strengths and largest coefficients of the CI expansion (MO contribution to particular state). [SMD-PCM(DMSO)/B3LYP/6-311G+(2d,p).

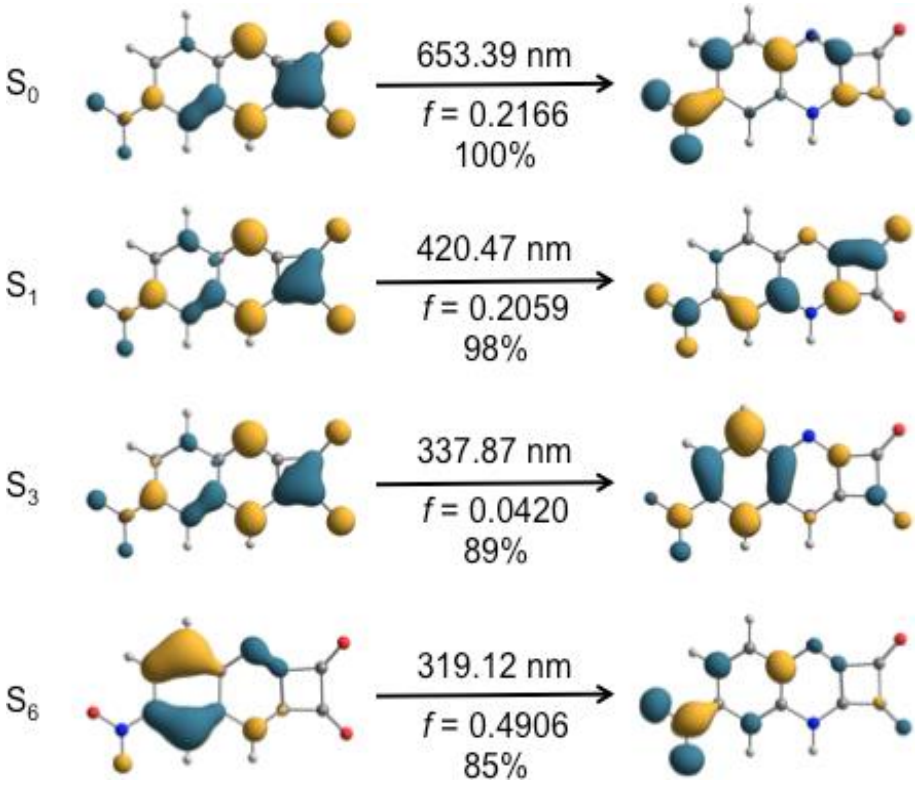

Figure G5 NTO plots (isovalue = 0.05) for key electronic transitions in tautomer N1 of **[4.17-H]⁻**. Excitation energies are given along with oscillator strengths and weight of contributing NTO pair to each transition. [PCM(DMSO)/B3LYP/6-311+G(2d,p)].

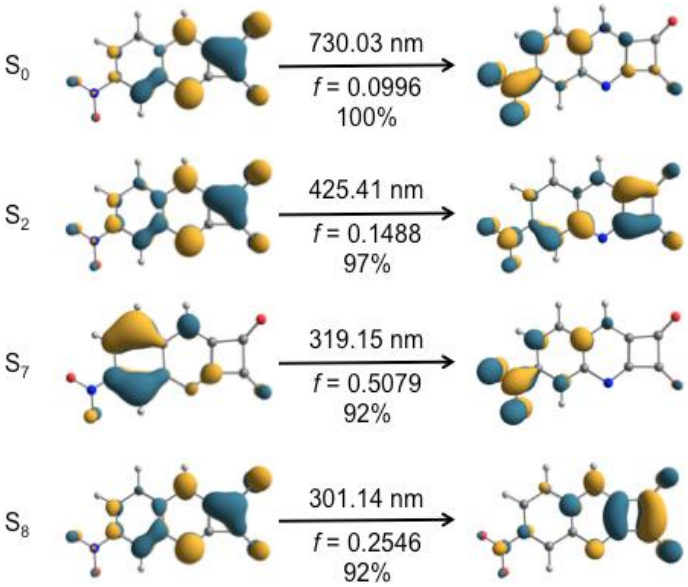

Figure G6 NTO plots (isovalue = 0.05) for key electronic transitions in tautomer N2 of **[4.17-H]⁻**. Excitation energies are given along with oscillator strengths and weight of contributing NTO pair to each transition. [SMD-PCM(DMSO)/B3LYP/6-311+G(2d,p)].

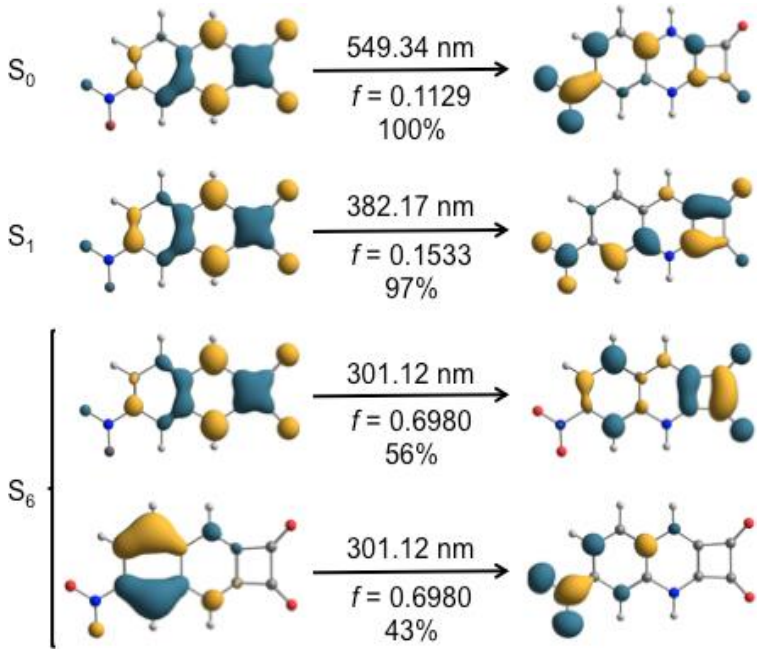

Figure G7 NTO plots (isovalue = 0.05) for key electronic transitions in **4.17**. Excitation energies are given along with oscillator strengths and weight of contributing NTO pair to each transition. [PCM(DMSO)/B3LYP/6-311+G(2d,p)].